

Lattice Boltzmann Methods for Partial Differential Equations

Zur Erlangung des akademischen Grades eines

DOKTORS DER NATURWISSENSCHAFTEN

von der KIT-Fakultät für Mathematik
des Karlsruher Instituts für Technologie (KIT)

genehmigte

DISSERTATION

von

Stephan Simonis

Tag der mündlichen Prüfung:

Hauptreferent:

Korreferenten:

28.06.2023

PD Dr. Mathias J. Krause

Prof. Dr. Siddhartha Mishra

Assoc. Prof. Dr. Timothy Reis

Abstract

Lattice Boltzmann methods provide a robust and highly scalable numerical technique in modern computational fluid dynamics. Besides the discretization procedure, the relaxation principles form the basis of any lattice Boltzmann scheme and render the method a bottom-up approach, which obstructs its development for approximating broad classes of partial differential equations. This work introduces a novel coherent mathematical path to jointly approach the topics of constructability, stability, and limit consistency for lattice Boltzmann methods. A new constructive ansatz for lattice Boltzmann equations is introduced, which highlights the concept of relaxation in a top-down procedure starting at the targeted partial differential equation. Modular convergence proofs are used at each step to identify the key ingredients of relaxation frequencies, equilibria, and moment bases in the ansatz, which determine linear and nonlinear stability as well as consistency orders of relaxation and space-time discretization. For the latter, conventional techniques are employed and extended to determine the impact of the kinetic limit at the very foundation of lattice Boltzmann methods. To computationally analyze nonlinear stability, extensive numerical tests are enabled by combining the intrinsic parallelizability of lattice Boltzmann methods with the platform-agnostic and scalable open-source framework OpenLB. Through upscaling the number and quality of computations, large variations in the parameter spaces of classical benchmark problems are considered for the exploratory indication of methodological insights. Finally, the introduced mathematical and computational techniques are applied for the proposal and analysis of new lattice Boltzmann methods. Based on stabilized relaxation, limit consistent discretizations, and consistent temporal filters, novel numerical schemes are developed for approximating initial value problems and initial boundary value problems as well as coupled systems thereof. In particular, lattice Boltzmann methods are proposed and analyzed for temporal large eddy simulation, for simulating homogenized nonstationary fluid flow through porous media, for binary fluid flow simulations with higher order free energy models, and for the combination with Monte Carlo sampling to approximate statistical solutions of the incompressible Euler equations in three dimensions.

Acknowledgement

The present work has been conducted at the Institute for Applied and Numerical Mathematics (IANM) at Karlsruhe Institute of Technology (KIT). I send my sincere gratitude to my supervisors at KIT, Mathias J. Krause, Martin Frank, Willy Dörfler and Gudrun Thäter, who provided the work facilities and generated the splendid academic surrounding. I would like to thank the external referees of my work, Siddhartha Mishra and Tim Reis for the careful review. Thank you all for opening your doors and the ones of others every time I knocked, whether in person or online, during the day or at night. Further, I would like to acknowledge all of my colleagues, coworkers, coauthors, and students for the countless hours of discussing and working together.

Parts of the computations in this work have been performed on supercomputers at the Steinbuch Centre for Computing (SCC) at KIT, namely on bwUniCluster, bwUniCluster 2.0, ForHLR I, ForHLR II and HoreKa funded by the Ministry of Science, Research and the Arts Baden-Württemberg and by the Federal Ministry of Education and Research. I am thankful to SCC for providing the compute resources to carry out the numerical experiments documented in this work. In addition, I would like to acknowledge the Karlsruhe House of Young Scientists (KHYS) at KIT for the support through a KHYS Networking Grant in 2022.

Besides, I thank my friends and family who accompanied me during the past years and helped me balancing my life outside of work. I send a special thank you to my parents for making all of this even possible in the first place.

At long last, I thank Luisa and Ludwig with all my heart for the love, the support and for being always there.

Contents

1	Introduction	1
1.1	Motivation and objectives	1
1.2	Contribution	2
1.3	Structure	3
2	Mathematical Notations, Methods and Models	5
2.1	Partial differential operators	5
2.2	Targeted partial differential equations	7
2.2.1	Advection–diffusion equation	7
2.2.2	Cahn–Hilliard equation	7
2.2.3	Navier–Stokes equations	8
2.2.4	Bhatnagar–Gross–Krook–Boltzmann equation	9
2.3	Diffusive limit	11
2.4	Temporal filtering	17
2.4.1	Time-filtered Navier–Stokes equations	17
2.4.2	Time-filtered Bhatnagar–Gross–Krook–Boltzmann equation	19
2.5	Homogenization	20
2.5.1	Geometric setup	21
2.5.2	Homogenized stationary Navier–Stokes equations	22
2.5.3	Homogenized nonstationary Navier–Stokes equations	24
2.5.4	Applicability of the homogenized model	26
2.6	Coupled systems	29
2.6.1	Free energy models	29
2.6.2	Higher order free energy models	33
2.6.3	Navier–Stokes–Cahn–Hilliard equations	35
2.7	Lyapunov functionals	35
3	Numerical Methodology	37
3.1	Constructive design principles	38
3.1.1	Constructing relaxation systems	38
3.1.2	Closed equations and relaxation functions	41
3.1.3	Transformed relaxation system	45
3.1.4	Stability and convergence	48
3.2	Space-time-velocity discretization	52
3.2.1	Discrete velocity models	52
3.2.2	Discrete velocity stability and convergence	55
3.2.3	Space-time Discretization	59
3.2.4	Limit consistency	68
3.2.5	Stability	69
3.2.6	Convergence	71
3.2.7	Limit control	71
3.3	Lattice Boltzmann methods	74
3.3.1	Lattice Boltzmann equations	75
3.3.2	Initial and boundary conditions	91

3.3.3	Postprocessing and other operations	93
3.3.4	Implementation	94
4	Numerical Experiments	99
4.1	Advection–Diffusion equation	99
4.1.1	Relaxation stability prediction	100
4.1.2	Experimental order of convergence	101
4.2	Cahn–Hilliard equation	106
4.2.1	Sharp interface limit consistency	107
4.3	Navier–Stokes equations	108
4.3.1	Taylor–Green vortex flow	110
4.3.2	Turbulence quantities	111
4.3.3	Linear and brute force stability	112
4.3.4	Spectral effects of controlled relaxation	124
4.3.5	Computation of statistical solutions	136
4.4	Time-filtered Navier–Stokes equations	141
4.4.1	Reference data	141
4.4.2	Model calibration	142
4.4.3	Comparison to the spectral element method	145
4.4.4	Numerical error quantification	149
4.4.5	Scaling, consistency and experimental order of convergence	152
4.5	Homogenized Navier–Stokes equations	154
4.5.1	Porous Poiseuille flow	155
4.5.2	Consistency of the pressure difference	155
4.6	Navier–Stokes–Cahn–Hilliard equations	158
4.6.1	Volume loss of small droplets	159
4.6.2	Binary shear flow	160
4.6.3	Binary extensional flow	163
5	Conclusions	165
5.1	Summary	165
5.2	Limitations and outlook	167
	Bibliography	171
	A Acronyms and Symbols	189
	B Publications	195
	List of Figures	197
	List of Tables	203

1 Introduction

The lattice Boltzmann method (LBM) is an established numerical technique [172] for the approximate solution of transport problems, especially in computational fluid dynamics (CFD). Due to the combination of discretization and relaxation limits, the LBM provides distinct advantages in terms of parallelizability [158, 164, 265]. Primarily for this reason, LBMs are well-suited for various applicative scenarios [59, 116, 162, 190, 229] in CFD where good scalability on high performance computing (HPC) machines is crucial. For example, the feasibility of transient computer simulations of turbulent fluid flow is drastically improved toward overnight runtime on an industrial scale [181] via combining the LBM with implicit numerical diffusion [232] or large eddy simulation (LES) in space [236] and in time [233]. On industry relevant scales, the pairing of LBMs with LES provides significant speedup over traditional methods such as finite volume methods (FVM) [19, 115, 144, 181]. Moreover, the intrinsically mesoscopic derivation of LBMs naturally allows for thermodynamically consistent and stable method extensions for approximating partial differential equations (PDEs) in general, and particularly well in coupled initial boundary value problems (IBVPs) for multiphysics applications. Highly efficient simulations of turbulent [115], reactive, particulate [249] and thermal fluid flow models [236], coupled radiative transport [93, 190] or melting and conjugate heat transfer [94], as well as compressible fluid flows with strong discontinuities [54, 68, 145, 260] and crack propagation in linear elastic solids [197] are realizable. In summary, even standard LBM formulations offer an easy to implement and mostly second order accurate, intrinsically matrix-free algorithm in space-time which is well-suited for approximating PDE problems and, if optimized properly, also capable of saturating [166, 167] modern-day HPC machinery.

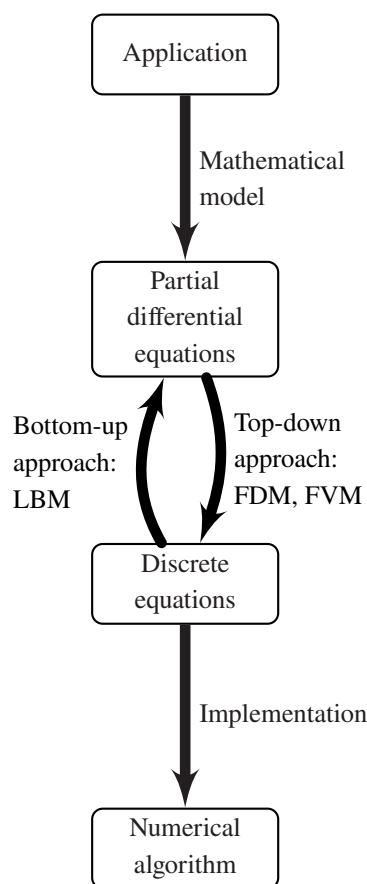


Figure 1.1: From application to numerical algorithm.

1.1 Motivation and objectives

Meanwhile, the perspectives on LBMs are shifting. Initially being exclusively well-suited for CFD, the LBM is further developed toward providing a standalone numerical method for approximating solutions to PDE systems in general. Nonetheless, the relaxation principle of the LBM does come at the price of inducing a bottom-up method, standing against conventional top-down discretizations applied for example, in finite difference methods (FDM) or FVM (see Figure 1.1). This essential feature complicates the rigorous numerical analysis of LBMs. On the one hand, approaches toward constructing LBMs exist (for example [50, 201–204, 270]), and several authors have contributed toward the aim of rigor (for example [16, 64, 69, 76, 117, 138, 142, 143, 171, 250] and recently [26, 28, 91, 92, 113, 185, 215, 262]). On the other hand, the limitations of analysis and scheme construction techniques for LBM formulations to approximate

specific PDEs persist. To the knowledge of the author, no coherent and constructive theory has been established, which suggests an LBM for approximating any given PDE, where only the PDE itself is known. To this end, we formulate the following objectives (OBJs):

(OBJ1) Top-down construction for LBMs from a targeted PDE,

(OBJ2) Convergence analysis of the combined limits in LBMs,

(OBJ3) Description of the kinetic information in LBMs,

(OBJ4) Establishment of novel LBMs for newly targeted PDEs.

The present work is thus motivated by the progress gained from trailblazing the combination of top-down construction as well as relaxation limit consistent and stable discretizations as a coherent methodology for transforming the LBM into a generically applicable solver for PDEs. To the knowledge of the author, (OBJ1–OBJ4) have not been addressed in this combination and explicitness before.

1.2 Contribution

The main contribution of the present work is the introduction of a novel coherent mathematical path to specify and approach the above-mentioned issues of constructability, and analysis of stability and limit consistency jointly for various LBMs. The particular contributions (CTNs) to achieve the Objectives (OBJ1–OBJ4) are summarized as follows:

(CTN1) Development of a constructive ansatz. A novel construction of LBMs is introduced, which highlights the mathematical concept of relaxation in a top-down procedure starting at the target equation (TEQ). Additionally, the notion of relaxation frequencies is extended toward relaxation functions, which are used to pass through stability domains under the premise of upholding the correct limit toward the TEQ.

(CTN2) Application of modular convergence proofs. At each step within the ansatz, a stability and consistency analysis is carried out to identify key ingredients within the constructive process that trigger certain numerical features. To this end, we employ and extend techniques to include the relaxation limit at the very foundation of the LBM.

(CTN3) Extensive numerical testing. The LBM itself is intrinsically parallel, which allows for a drastic upscaling of the number and quality of feasible computations. Based on this fact, we use large variations in the parameter spaces of classical benchmark problems for the exploratory indication of novel methodological insights.

(CTN4) Proposal and analysis of new models. We use the proposed methodology to obtain e.g. stabilized relaxation, limit consistent discretizations, and target conforming temporal filters for developing novel numerical schemes based on LBMs. The latter in turn are used for approximating initial value problems (IVPs) and IBVPs as well as coupled systems thereof.

Consequently, the novel coherent LBM framework (see Figure 1.2) contributes to the unfolding and analysis of the specific enforcing of numerical features, such as numerical dissipation, under the preservation of limit consistency already at the level of construction for a vast range of applications.

Parts of this work have been published by the author in advance. Contribution (CTN1) first appears in [231], where the constructive approach for obtaining an LBM limiting to a one-dimensional advection–diffusion equation is proposed. The d -dimensional extension thereof with multiple relaxation times is proposed in [234]. In both publications [231, 234], convergence proofs for the relaxation limit are carried out with respect to (CTN2), and stability notions for

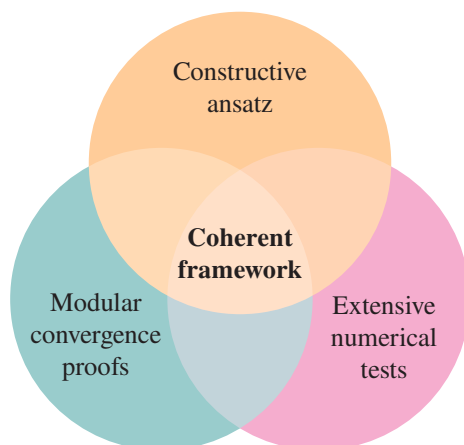


Figure 1.2: Present contributions toward a coherent mathematical framework for LBMs.

uniform relaxation are given. Considering (CTN3), based on numerical observations, the notion of brute force stability for LBM is proposed in [232], which is nonlinearity perceptive and includes discretization effects by construction. Published results of Contribution (CTN4) are the proposal of the first temporal large eddy simulation with LBM based on temporal direct deconvolution in [233] and a computational study including method extensions of free energy LBMs with high order functionals [235]. In addition, applications of LBMs for several types of PDEs are published in [59, 114, 116, 162, 190, 236]. A summary of the author’s publications, including preprints and open source software is provided in Appendix B.

1.3 Structure

The realization of the high-level Contributions (CTN1–CTN4) to achieve the Objectives (OBJ1–OBJ4) forms the content of this work. In Chapter 2, we introduce the mathematical models in the form of PDEs that are to be approximated with LBMs. The advection–diffusion equation is used as a paragon throughout this work to highlight the numerical analysis of the relaxation systems and the numerical schemes to be derived. Further, LBMs are applied to approximate incompressible, filtered and homogenized nonstationary Navier–Stokes equations as well as statistical solutions to incompressible Euler equations. Moreover, we approximate coupled Navier–Stokes–Cahn–Hilliard equations for simulating binary fluid flow of immiscible components. All targeted PDEs are summarized in Chapter 2, where possible extensions and novel interpretations thereof are discussed.

Based on the derived target PDEs, Chapter 3 establishes the numerical methodology of Contributions (CTN1–CTN4). A constructive ansatz is proposed to obtain LBMs for a given d -dimensional hyperbolic-parabolic PDE in advection–diffusion form. The procedure is divided into four steps: constructing a relaxation system, spectral decomposition toward a transformed relaxation system, parameter choices conforming to discrete velocity Boltzmann equations, and finally the relaxation limit consistent discretization that yields the lattice Boltzmann evolution equations on the space-time grid. On each level, we analyze the current result with respect to convergence or conformity to the previous step to unfold the mechanisms of the derivation. We modulate the relaxation frequencies to enforce numerical effects in the LBM along the coupled relaxation–discretization limit toward the TEQ. Several novel numerical schemes are proposed for the IBVPs to be approximated in the exploratory computations and numerical experiments presented in Chapter 4.

The numerical results in Chapter 4 contribute to (CTN3, CTN4) via the computation of advection–diffusion IVPs, benchmark Navier–Stokes problems as well as coupled Navier–Stokes–Cahn–Hilliard systems within the parallel C++

framework OpenLB¹ [162] executed on Top500 HPC machinery (e.g. HoreKa²). Specific results include the brute force computation of stability sets and Fourier transformed relaxation functions in deterministic and stochastic Taylor–Green vortex flows, the computational analysis of a novel temporal LES LBMs, the application of free energy LBMs to binary shear and extensional flows, as well as benchmark computations with the homogenized LBM for fluid flow through simplified porous media.

Appendix A lists the abbreviations and symbols used below. Since parts of this work are published in scientific journals and as preprints, or are included in open source code releases, frequent references are made throughout the text. A detailed overview is provided in Appendix B.

¹ <https://www.openlb.net>.

² <https://www.scc.kit.edu/dienste/horeka.php>.

2 Mathematical Notations, Methods and Models

The present chapter states modeling assumptions and introduces the PDEs that are to be approximated with LBMs. Besides the introduction, possible extensions and novel interpretations of the targeted PDEs in terms of mathematical modeling are presented, supporting Contribution (CTN4). As it turns out, the relaxation mechanism at the very foundation of any LBM demands the presence of transport terms in the targeted PDE. Thus, an initial modification of the PDE is to be carried out to create the structure of a typical material derivative (additive partial derivatives with first order in time and first order in space) on the left hand side. Here, we target only PDEs, which naturally show this form. In addition, we recall the Boltzmann equation with a simplified collision operator. From a thermodynamic perspective, the LBM can be derived via discretization on this mesoscopic level. In the present context, however, it is more convenient to try circumventing the knowledge of the scale-bridging limit within Hilbert's sixth problem for the most part. Although it is found possible to remove the thermodynamic information in simple examples, a discussion is hitherto inevitable and thus carried out as soon as the problem at hand becomes more complex. Finally, basic dynamical systems theory is used to recall the notion of nonlinear stability in terms of Lyapunov functionals.

2.1 Partial differential operators

Let $\Omega \subseteq \mathbb{R}^d$ be open and bounded, where $d \in \mathbb{N}$, and let $\Omega_T := \Omega \times I$ denote the space-time horizon, where $I = (0, T]$ and $T \in \mathbb{R}_{>0}$. Further, let

$$\rho : \overline{\Omega}_T \rightarrow \mathbb{R}, (\mathbf{x}, t) \mapsto \rho(\mathbf{x}, t) \quad (2.1)$$

be of class C^m with $m > 0$. A PDE of second order with the spatio-temporal unknown ρ is formed via (for the sake of simplicity) homogeneously equating a partial differential operator (PDO)

$$F_{\sharp}(\nabla_{\mathbf{x}}^2 \rho, \nabla_{\mathbf{x}} \rho, \partial_{tt} \rho, \partial_t \rho, \rho, \mathbf{x}, t) = 0 \quad \text{in } \Omega_T, \quad (2.2)$$

with supplementary boundary and initial conditions, where ∂_t denotes the partial derivative with respect to t . A collection of several PDEs (2.2) with several unknowns is called PDE system [78].

Definition 2.1.1. Let F_{\sharp}^{ϵ} component-wise denote a PDO such that

$$F_{\sharp}^{\epsilon}(\boldsymbol{\rho}^{\epsilon}) = \mathbf{0} \quad \text{in } \Omega_T \quad (2.3)$$

is the corresponding PDE system, which is dependent on a scaling parameter $\epsilon > 0$. If the limit conditions for the PDE system and its solutions, respectively

$$(i) \quad \lim_{\epsilon \searrow 0} F_{\sharp}^{\epsilon} = (F_{\sharp}, F_{\sharp}^{\text{ar}})^{\text{T}}, \quad (2.4)$$

$$(ii) \quad \lim_{\epsilon \searrow 0} \boldsymbol{\rho}^{\epsilon} = (\rho, \boldsymbol{\rho}^{\text{ar}})^{\text{T}}, \quad (2.5)$$

hold true, then F_{\sharp}^{ϵ} is called relaxation operator. In this case, (2.3) describes a relaxation system (RS).

Remark 2.1.1. The superscripts \cdot^ϵ denote artificially introduced ϵ -dependent instances of operators and variables, respectively. One aspect of the present work deals with the constructive definition of these quantities such that the obtained RS is in turn suitable to derive an LBM. The first aim is thus to design an RS via injecting the ϵ -dependence into a given PDO F_{\sharp}^ϵ through perturbative construction. In the following, the action of defining F_{\sharp}^ϵ via introducing artificial variables and perturbations to F_{\sharp} is occasionally called extension. The reverse action, passing to the limit $\epsilon \searrow 0$, is named contraction. Further, the superscript \cdot^{ar} denotes remainder terms of the extension in the smallness limit $\epsilon \searrow 0$.

We will frequently make use of the following special case.

Definition 2.1.2. Let

$$L(\rho) = - \sum_{i,j=1}^d a_{ij}(\mathbf{x}, t) \partial_{x_i x_j} \rho + \sum_{i=1}^d b_i(\mathbf{x}, t) \partial_{x_i} \rho + c(\mathbf{x}, t) \rho \quad (2.6)$$

define a linear second order spatial differential operator in transport form with diffusion. The coefficient functions \mathbf{a} , \mathbf{b} and c map componentwise $\bar{\Omega}_T \rightarrow \mathbb{R}$. The PDO

$$F_{\sharp}^\epsilon \in \{F_{\text{ell}} := L, F_{\text{par}} := \partial_t + L, F_{\text{hyp}} := \partial_{tt} + L\} \quad (2.7)$$

is possibly elliptic, parabolic or hyperbolic, respectively, and thus is occasionally called generic below.

Unless stated otherwise, we assume that $\Omega = \mathbb{R}^d$ and neglect the specific treatment of boundaries in this chapter. Hence, if Ω is stated as an interval, the solutions to the PDE at hand are assumed to be periodic. By construction, the PDE is similarly generic in terms of its generating PDO.

Example 2.1.1. With the previous definitions, the procedure we proposed in [231] leads from F_{par} to a relaxation operator

$$F_{\text{par}}^\epsilon(\rho^\epsilon) = \partial_t \rho^\epsilon + b_1^\epsilon \partial_x \rho^\epsilon + \mathbf{S}^\epsilon [\rho^\epsilon - \mathbf{g}^\epsilon(\rho^\epsilon)], \quad (2.8)$$

where $d = 1$ and two artificial variables are introduced such that $\rho^\epsilon = (\rho^\epsilon, \phi^\epsilon, \psi^\epsilon)^\top$ and (2.3) forms a 3×3 RS with a relaxation matrix \mathbf{S}^ϵ and a generalized Maxwellian \mathbf{g}^ϵ which are determined later. Moreover, a scalar, closed form expression of $F_{\text{par}, \rho^\epsilon}^\epsilon(\rho^\epsilon) = 0$ in terms of ρ^ϵ only is obtained via reverse insertion. The closed form allows the direct identification of added perturbation terms compared to $F_{\text{par}}(\rho)$. For $d > 1$, the corresponding derivation is condensed in [234] and extended in Chapter 3.

Remark 2.1.2. In case of $\sharp \in \{\text{ell}, \text{hyp}\}$, a preparative modification of the PDE in the sense of Definition 2.1.2 can be applied to bring it into parabolic form. For F_{hyp} , a substitution of the first order time derivative leads to a parabolic formulation. In turn, the final numerical scheme then requires an additional approximation of the preparatory substitution of $\partial_t \rho$ (see for example [109, 170] in the context of LBMs). For approximating F_{ell} with an LBM, either an artificial time derivative has to be suppressed with correction terms or a modification of the equilibrium function is required (see for example [49, 205]). We thus focus on PDEs in the form of F_{par} below.

Since the smallness parameters akin to ϵ are essential in the present context, we use the following notation for asymptotically bounding functions of ϵ .

Definition 2.1.3. Let $g(\epsilon)$ be a given real-valued function on an unbounded subset of $\mathbb{R}_{>0}$, which is asymptotically positive (i.e. $g(\epsilon) > 0$ for sufficiently large ϵ). Then, $\mathcal{O}(g(\epsilon))$ denotes the set of functions

$$\mathcal{O}(g(\epsilon)) = \{f(\epsilon) \mid \exists c_1, c_2, \epsilon_0 > 0: 0 \leq c_1 g(\epsilon) \leq f(\epsilon) \leq c_2 g(\epsilon) \forall \epsilon \geq \epsilon_0\}. \quad (2.9)$$

Remark 2.1.3. Despite $\mathcal{O}(g(\epsilon))$ being a set [57], below we occasionally align with common practice via writing for an exemplary real- or complex-valued function $f(\epsilon)$ that $f(\epsilon) = \mathcal{O}(g(\epsilon))$ instead of $f(\epsilon) \in \mathcal{O}(g(\epsilon))$. The equality sign is motivated by the observation that, if $f(\epsilon) = \mathcal{O}(g(\epsilon))$, then $f(\epsilon)$ is equal to $g(\epsilon)$ within a constant factor, such that $g(\epsilon)$ is an asymptotically tight bound for $f(\epsilon)$. In the case that we are dealing with tensors, the notation $\mathcal{O}(\cdot)$ is to be understood as for each element.

2.2 Targeted partial differential equations

This section provides a summary of the PDEs which are to be approximated with LBMs. As stated above, solely PDEs are targeted which have been transformed to, or naturally show the form of F_{par} . In addition, we presently focus on IVPs. Boundary conditions are discussed in Section 3.3 from an applicative point of view when setting up the complete numerical method. Unless stated otherwise, we assume that $\Omega = \mathbb{R}^d$ and neglect the specific treatment of boundaries in this chapter. Starting with the advection–diffusion equation as a paragon, the complexity is increased to Cahn–Hilliard equations and nonstationary Navier–Stokes equations. Moreover, we recall the Boltzmann equation with a simplified collision operator to analyze its diffusive macroscopic limit. The latter is carried out in Section 2.3. Further below, as a preparative part for Contribution (CTN4), we make use of homogenization (Section 2.5) and temporal filtering (Section 2.4) to derive modified versions of the Navier–Stokes equations which are to be approximated with LBMs. Also with respect to (CTN4), a coupled Navier–Stokes–Cahn–Hilliard model is configured, including existing free energy functionals with novel higher order terms (Section 2.6). Lastly in Section 2.7, Lyapunov functionals are briefly discussed for the purpose of nonlinear stabilization of the numerical method (see Section 3.2.7).

2.2.1 Advection–diffusion equation

Let $\rho : \Omega_T \rightarrow \mathcal{R} \subseteq \mathbb{R}$, $(\mathbf{x}, t) \mapsto \rho(\mathbf{x}, t)$ denote the conserved variable of an IVP based on a scalar linear d -dimensional advection–diffusion equation (ADE)

$$\begin{cases} \partial_t \rho(\mathbf{x}, t) + \nabla_{\mathbf{x}} \cdot \mathbf{F}(\rho(\mathbf{x}, t)) - \mu \Delta_{\mathbf{x}} \rho(\mathbf{x}, t) = 0 & \text{in } \Omega_T, \\ \rho|_{t=0} = \rho_0(\mathbf{x}) & \text{in } \Omega, \end{cases} \quad (2.10)$$

where $\mathbf{F} : \mathcal{R} \rightarrow \mathbb{R}^d$, $\rho \mapsto \mathbf{F}(\rho)$ is smooth, Lipschitz continuous and possibly nonlinear in ρ , the solution ρ is sought for to be periodic, and $\mu > 0$ specifies a given diffusivity. Below we assume the form $\mathbf{F}(\rho) = \mathbf{u}\rho$, where $\mathbf{u} \in \mathbb{R}^d$ denotes the convection speed. If not stated otherwise, let $d \in \{1, 2, 3\}$. We make the assumption that the initial value ρ_0 shares the periodicity of ρ , such that existence and uniqueness of bounded solutions to (2.10) are given by nondegeneracy and thus uniform parabolicity (see [37, 196]).

2.2.2 Cahn–Hilliard equation

The convective Cahn–Hilliard equation (CHE) reads

$$\begin{cases} \partial_t \phi(\mathbf{x}, t) + \nabla_{\mathbf{x}} \cdot (\phi(\mathbf{x}, t) \mathbf{u}(\mathbf{x}, t)) = \nabla_{\mathbf{x}} \cdot (M_{\phi} \nabla_{\mathbf{x}} \mu_{\phi}(\mathbf{x}, t)) & \text{in } \Omega_T, \\ \phi|_{t=0} = \phi_0(\mathbf{x}) & \text{in } \Omega, \end{cases} \quad (2.11)$$

where $\phi : \Omega_T \rightarrow \mathbb{R}$ denotes the order parameter, $M_{\phi} > 0$ is the diffusivity, μ_{ϕ} defines the chemical potential, $\mathbf{u} \in \mathbb{R}^3$ is a given velocity. The chemical potentials can be chosen according to different free energy models which are specified further below. Supplied with a specific chemical potential and periodic boundary conditions, global well-posedness and decay of solutions is proven in [278]. Further, when interpreted as a dynamical system the existence of a global

and exponential attractor is proven [71, 72]. In case of a vanishing advection term ($\mathbf{u} = \mathbf{0}$), all solutions converge to an equilibrium due to the fact that the CHE admits a Lyapunov functional (in terms of a free energy functional) [12, 101, 102]. Extensive reviews are provided by Miranville [191, 192].

2.2.3 Navier–Stokes equations

In the force-free, viscous case ($\nu > 0$), incompressible Newtonian fluid flows can be described by the incompressible Navier–Stokes equations (NSE)

$$\begin{cases} \operatorname{div}_{\mathbf{x}}(\mathbf{u}) = 0 & \text{in } \Omega_T, \\ \partial_t \mathbf{u} + \operatorname{div}_{\mathbf{x}}(\mathbf{u} \otimes \mathbf{u}) - \nu \Delta_{\mathbf{x}} \mathbf{u} + \nabla_{\mathbf{x}} p = \mathbf{F} & \text{in } \Omega_T, \\ \mathbf{u}|_{t=0} = \mathbf{u}_0 & \text{in } \Omega, \end{cases} \quad (2.12)$$

where $\operatorname{div}_{\mathbf{x}}(\mathbf{u}) = \nabla_{\mathbf{x}} \cdot \mathbf{u}$ refers to the divergence operator. Under an additional inviscid flow assumption ($1/Re \sim \nu \rightarrow 0$), (2.12) reduces to the incompressible Euler equations (EE), where $Re = u_c L_c / \nu$ is the Reynolds number defined by the characteristic flow velocity u_c and the characteristic domain length L_c . Below, we refer to (2.12) in both cases. Here, $\mathbf{u}: \Omega_T \rightarrow U := \mathbb{R}^d$, $(\mathbf{x}, t) \mapsto \mathbf{u}(\mathbf{x}, t)$ is the flow velocity as a function of space and time, where $d \in \{2, 3\}$, and $p: \Omega_T \rightarrow \mathbb{R}$, $(\mathbf{x}, t) \mapsto p(\mathbf{x}, t)$ denotes the pressure acting as a Lagrange multiplier. The density is assumed to be constant and \mathbf{F} and p are rescaled accordingly. The initial data is defined by $\mathbf{u}_0: \Omega \rightarrow \mathbb{R}^d$ which is assumed to be weakly divergence-free and in $L^2(\Omega; U)$, i.e.

$$\mathbf{u}_0 \in L^2_{\operatorname{div}}(\Omega; U) = \left\{ \mathbf{u} \in L^2(\Omega) \mid \operatorname{div}_{\mathbf{x}} \mathbf{u} = 0, \int_{\Omega} \mathbf{u} \, d\mathbf{x} < \infty \right\}. \quad (2.13)$$

The kinematic viscosity $\nu > 0$ and the external forces \mathbf{F} are given. In the case of $\Omega \subset \mathbb{R}^d$, system (2.12) is supplied with boundary conditions to form an IBVP. Even under the premise of spatial periodicity ($\Omega = \mathbb{R}^d$), global in time well-posedness of classical solutions to the 3D incompressible NSE has not been established yet.

The existence of weak solutions for $d \in \{2, 3\}$ has been pioneered by Leray [177] and Hopf [121]. Albeit the uniqueness has been proven for $d = 2$, the uniqueness of such solutions to the incompressible NSE for $d = 3$ is still an open problem [80]. Recent promising efforts have evolved around the concept of statistical solutions of incompressible NSE [86, 87] in the sense of Young measures [105] and the inviscid limit toward statistical solutions of the incompressible EE for $\nu \searrow 0$ in (2.12) [48, 85]. Further, the notion of exponential attractors is usable for the incompressible NSE [73–75]. Considering statistical solutions (defined as families of probability measures on the tensor products U^k for $k \in \mathbb{N}$), let $\mathbf{u}_0 \in L^2_{\operatorname{div}}(\Omega; U)$ and interpret (2.12) as a Liouville equation on a function space which defines the solution as a mapping of time $t \in I$ to a probability measure on $L^2_{\operatorname{div}}(\Omega; U)$ [86, 87].

Definition 2.2.1. A family of probability measures

$$\boldsymbol{\mu}^\nu = (\mu_t^\nu)_{0 \leq t \leq T}, \quad \text{on } L^2_{\operatorname{div}}(\Omega; U) \quad (2.14)$$

is a statistical solution of (2.12) with initial data μ_0^ν and fixed viscosity $\nu > 0$, if the function

$$t \mapsto \int_{L^2_{\operatorname{div}}(\Omega; U)} \boldsymbol{\zeta}(\mathbf{u}) \, d\mu_t^\nu(\mathbf{u}) \quad (2.15)$$

is measurable on $[0, T]$ for every $\varrho \in C_b(L^2_{\text{div}}(\Omega; U))$ (bounded continuous functions on $L^2_{\text{div}}(\Omega; U)$), and μ^ν satisfies the additional conditions listed in [85, Definition 3.6 (b–d)], namely, a weak functional formulation of (2.12) for cylindrical test functions, a strengthened mean energy inequality, and that the function

$$t \mapsto \int_{L^2_{\text{div}}(\Omega; U)} \varrho \left(\|\mathbf{u}\|_{L^2(\Omega)}^2 \right) d\mu_t^\nu(\mathbf{u}) \quad (2.16)$$

is continuous at $t = 0$ from the right for any $\varrho \in C^1(\mathbb{R}, \mathbb{R})$ nonnegative and nondecreasing with bounded derivative.

Remark 2.2.1. For the incompressible EE, a decay of the structure functions has been proved [173] to be implied by the decay of time-averaged energy spectrum functions. Further, if a scaling assumption on the structure functions is fulfilled, it has been proven that the statistical solutions of the incompressible NSE converge with $\nu \searrow 0$ to the statistical solutions of the EE [85, Theorem 4.8]. Based on that, in Chapter 4, the evaluation of energy spectra in the sense of Kolmogorov’s theory (K41) [155, 156] is used to at least indicate, whether a computed sample is an approximation of a weak solution to the incompressible NSE for $d = 3$. Moreover, if the sequence of expectations of the energy spectra of several samples show an asymptotic power law in the sense of K41 theory for $\nu \searrow 0$, we deduce that a statistical solution the incompressible EE is approximated [85]. Further details are given in Section 4.3.5.

2.2.4 Bhatnagar–Gross–Krook–Boltzmann equation

Let $\Omega \subseteq \mathbb{R}^d$ with $d = 3$ be a volume of rarefied gas which comprises many interacting particles. Via equalizing the mass $m \in \mathbb{R}_{>0}$, we interpret the particles as point masses. The state of a one-particle system is assumed to depend on position $\mathbf{x} \in \Omega$ and velocity $\mathbf{v} \in \Xi$ at time $t \in I = [t_0, t_1] \subseteq \mathbb{R}$ with $T \geq t_1 > t_0 > 0$, where $\Omega \subseteq \mathbb{R}^d$ denotes the positional space, $\Xi = \mathbb{R}^d$ is the velocity space, $\mathfrak{P} := \Omega \times \Xi$ is the phase space, and the crossing $\mathfrak{R} := \Omega \times \Xi \times I$ defines the phase-time tuple.

Definition 2.2.2. The probability density function

$$f: \mathfrak{R} \rightarrow \mathbb{R}_{>0}, (\mathbf{x}, \mathbf{v}, t) \mapsto f(\mathbf{x}, \mathbf{v}, t) \quad (2.17)$$

for the particles’ positions $\mathbf{x} \in \Omega$ and velocities $\mathbf{v} \in \Xi$ at time $t \in I$ defines the state of the dynamical system which is governed by the Boltzmann equation (BE)

$$\left(\partial_t + \mathbf{v} \cdot \nabla_{\mathbf{x}} + \frac{\mathbf{F}}{m} \cdot \nabla_{\mathbf{v}} \right) f = J(f, f) \quad \text{in } \mathfrak{R}, \quad (2.18)$$

where

$$f|_{t=0} = f_0 \quad \text{in } \mathfrak{P} \quad (2.19)$$

supplements a suitable initial condition. The operator

$$J(f, f) = \int_{\mathbb{R}^3} \int_{S^2} |\mathbf{v} - \mathbf{w}| [f(\mathbf{x}, \mathbf{v}', t) f(\mathbf{x}, \mathbf{w}', t) - f(\mathbf{x}, \mathbf{v}, t) f(\mathbf{x}, \mathbf{w}, t)] d\mathbf{N} d\mathbf{w} \quad (2.20)$$

models the collision, where $d\mathbf{N}$ is the normalized surface integral with the unit vector $\mathbf{N} \in S^2$ and $(\mathbf{v}', \mathbf{w}')^T = T_{\mathbf{N}}(\mathbf{v}, \mathbf{w})^T$ result from the transformation $T_{\mathbf{N}}$ that models hard sphere collision [14].

Definition 2.2.3. Let f be given in the sense of (2.17). Then, via prefactored integration over $\Xi = \mathbb{R}^d$, we define the moments

$$n_f: \begin{cases} \Omega \times I \rightarrow \mathbb{R}_{>0}, \\ (\mathbf{x}, t) \mapsto n_f(\mathbf{x}, t) := \int_{\mathbb{R}^d} f(\mathbf{x}, \mathbf{v}, t) \, d\mathbf{v}, \end{cases} \quad (2.21)$$

$$\rho_f: \begin{cases} \Omega \times I \rightarrow \mathbb{R}_{>0}, \\ (\mathbf{x}, t) \mapsto \rho_f(\mathbf{x}, t) := mn_f(\mathbf{x}, t), \end{cases} \quad (2.22)$$

$$\mathbf{u}_f: \begin{cases} \Omega \times I \rightarrow \mathbb{R}^d, \\ (\mathbf{x}, t) \mapsto \mathbf{u}_f(\mathbf{x}, t) := \frac{1}{n_f(\mathbf{x}, t)} \int_{\mathbb{R}^d} \mathbf{v} f(\mathbf{x}, \mathbf{v}, t) \, d\mathbf{v}, \end{cases} \quad (2.23)$$

$$\mathbf{P}_f: \begin{cases} \Omega \times I \rightarrow \mathbb{R}^{d \times d}, \\ (\mathbf{x}, t) \mapsto \mathbf{P}_f(\mathbf{x}, t) := m \int_{\mathbb{R}^d} [\mathbf{v} - \mathbf{u}_f(\mathbf{x}, t)] \otimes [\mathbf{v} - \mathbf{u}_f(\mathbf{x}, t)] f(\mathbf{x}, \mathbf{v}, t) \, d\mathbf{v}, \end{cases} \quad (2.24)$$

$$p_f: \begin{cases} \Omega \times I \rightarrow \mathbb{R}_{>0}, \\ (\mathbf{x}, t) \mapsto p_f(\mathbf{x}, t) := \frac{1}{d} \sum_{i=1}^d (\mathbf{P}_f)_{i,i}(\mathbf{x}, t), \end{cases} \quad (2.25)$$

respectively as particle density, mass density, velocity, stress tensor, and pressure. Here and below, the moments of f are indexed with \cdot_f .

Notably, the absolute temperature θ is determined implicitly by an ideal gas assumption

$$p_f = n_f R \theta, \quad (2.26)$$

where $R > 0$ is the universal gas constant. To a dedicated order of magnitude in characteristic scales, the above moments approximate the macroscopic quantities conserved by the incompressible NSE [107]. Equilibrium states f^{eq} , defined by

$$J(f^{\text{eq}}, f^{\text{eq}}) = 0 \quad \text{in } \mathfrak{R}, \quad (2.27)$$

exist [107]. Via the gas constant $R = k_{\text{B}}/m \in \mathbb{R}_{>0}$ (where $k_{\text{B}} \in \mathbb{R}_{>0}$ is the Boltzmann constant) and $\theta \in \mathbb{R}_{>0}$, n_f as well as \mathbf{u}_f , the equilibrium state is found to be of Maxwellian form

$$f^{\text{eq}}(\mathbf{x}, \mathbf{v}, t): \begin{cases} \mathfrak{R} \rightarrow \mathbb{R}, \\ (\mathbf{x}, \mathbf{v}, t) \mapsto \frac{n_f(\mathbf{x}, t)}{(2\pi R \theta)^{\frac{d}{2}}} \exp\left(-\frac{[\mathbf{v} - \mathbf{u}_f(\mathbf{x}, t)]^2}{2R\theta}\right). \end{cases} \quad (2.28)$$

Remark 2.2.2. We identify f^{eq}/n_f as d -dimensional normal distribution for $\mathbf{v} \in \mathbb{R}^d$ with expectation \mathbf{u}_f and covariance $R\theta \mathbf{I}_d$. In this regard, the arguments of f^{eq} regularly appear in terms of moments $f^{\text{eq}}(n_f, \mathbf{u}_f, \theta)$ (see for example [117, 143, 158, 171]).

Lemma 2.2.1. *The moments ρ_f , \mathbf{u}_f and p_f are conserved by collision.*

Proof. From f^{eq}/n_f being a density function, we find

$$\rho_{f^{\text{eq}}} \stackrel{(2.22)}{=} m \int_{\mathbb{R}^d} f^{\text{eq}}(\mathbf{x}, \mathbf{v}, t) \, d\mathbf{v} = mn_f = \rho_f, \quad (2.29)$$

$$\mathbf{u}_{f^{\text{eq}}} \stackrel{(2.23)}{=} \frac{1}{n_{f^{\text{eq}}}} \int_{\mathbb{R}^d} \mathbf{v} f^{\text{eq}}(\mathbf{x}, \mathbf{v}, t) \, d\mathbf{v} = \mathbf{u}_f. \quad (2.30)$$

The covariance matrix of f^{eq}/n_f for a perfect gas (2.26), verifies the conservation of pressure

$$p_{f^{\text{eq}}} \stackrel{(2.25)}{=} \frac{1}{d} m \int_{\mathbb{R}^d} (\mathbf{v} - \mathbf{u}_{f^{\text{eq}}})^2 f^{\text{eq}}(\mathbf{x}, \mathbf{v}, t) d\mathbf{v} = \frac{1}{d} m \int_{\mathbb{R}^d} (\mathbf{v} - \mathbf{u}_f)^2 f^{\text{eq}}(\mathbf{x}, \mathbf{v}, t) d\mathbf{v} = \frac{1}{d} m n_f \sum_{i=1}^d R\theta = p_f. \quad (2.31)$$

□

Definition 2.2.4. According to Bhatnagar, Gross and Krook (BGK) [31] we simplify the collision operator J in (2.18) to

$$Q(f) := -\frac{1}{\tau}(f - M_f^{\text{eq}}) \quad \text{in } \mathfrak{A}, \quad (2.32)$$

where $\tau > 0$ denotes the relaxation time between collisions, and $M_f^{\text{eq}} := f^{\text{eq}}(\mathbf{x}, \mathbf{v}, t)$ is a formal particular Maxwellian determined by n_f and \mathbf{u}_f .

Remark 2.2.3. The conservation of both, ρ_f and \mathbf{u}_f , respectively (2.29) and (2.30), is upheld, since $\ln(M_f^{\text{eq}})$ is a collision invariant of Q (cf. [158, Theorem 1.5]).

Definition 2.2.5. With Q from (2.32) implanted in (2.18), the BGK–Boltzmann equation (BGKBE) reads

$$\underbrace{\left(\partial_t + \mathbf{v} \cdot \nabla_{\mathbf{x}} + \frac{\mathbf{F}}{m} \cdot \nabla_{\mathbf{v}} \right)}_{= \frac{D}{Dt}} f = Q(f) \quad \text{in } \mathfrak{A}, \quad (2.33)$$

where $D/(Dt)$ is referred to as material derivative, and $f(\cdot, \cdot, 0) = f_0$ sets a suitable initial condition. Here and below, the variable f is renamed to obey (2.33) instead of (2.18).

Remark 2.2.4. The global existence of solutions to the BGKBE (2.33) has been rigorously proven in [207]. Weighted L^∞ bounds and uniqueness have later been established on bounded domains [208] and in \mathbb{R}^d [193].

2.3 Diffusive limit

We connect the BGKBE (2.33) to the NSE (2.12) via diffusive limiting. To this end, a formal verification of the continuum balance equations (2.12) for the moments ρ_f and \mathbf{u}_f in Definition 2.2.3 is conducted. It is to be noted that parts of the following derivation are taken from [158] and [230]. Where possible, we make links to other approaches which are based on similar ideas, irrespective of the order in time of publication. We also stress that neither the derivation, nor the references follow the aim of completeness, but rather are meant to illustrate the scale-bridging from the BGKBE toward the incompressible NSE only. The limiting is done in three steps [158, 230].

Step 1: Mass conservation and momentum balance. Let f^* be a solution to the BGKBE (2.33). Multiplying $m \times (2.33)$ and integrating over $\Xi = \mathbb{R}^d$ yields

$$\partial_t \rho_{f^*} + \nabla_{\mathbf{x}} \cdot (\rho_{f^*} \mathbf{u}_{f^*}) + \underbrace{\int_{\mathbb{R}^d} \mathbf{F} \cdot \nabla_{\mathbf{v}} f^* d\mathbf{v}}_{=0} = -\frac{1}{\tau} \underbrace{(\rho_{f^*} - \rho_{M_{f^*}^{\text{eq}}})}_{\stackrel{(2.29)}{=}0} \quad (2.34)$$

$$\iff \partial_t \rho_{f^*} + \nabla_{\mathbf{x}} \cdot (\rho_{f^*} \mathbf{u}_{f^*}) = 0 \quad \text{in } \Omega \times I, \quad (2.35)$$

where the force term nulls out (cf. [158, Corollary 5.2] with $g = 1$ and $a = F$ in the respective notation). Dividing by the formal constant ρ_{f^*} , the conservation of mass in the NSE is recovered. To balance momentum, we integrate $m\mathbf{v} \times (2.33)$ over $\Xi = \mathbb{R}^d$ and obtain that

$$\partial_t (\rho_{f^*} \mathbf{u}_{f^*}) + \nabla_{\mathbf{x}} \cdot \mathbf{P}_{f^*} + (\rho_{f^*} \mathbf{u}_{f^*} \cdot \nabla_{\mathbf{x}}) \mathbf{u}_{f^*} + \mathbf{F} = 0 \quad \text{in } \Omega \times I. \quad (2.36)$$

The derivation of (2.36) closely follows a standard procedure documented for example in [158, Subsection 1.3.1]. Finally, via (2.36)/ ρ_{f^*} a balance law of momentum in conservative form is recovered. Thus, when suitably determining \mathbf{P}_{f^*} according to the assumption of incompressible Newtonian flow, the incompressible NSE appears as the diffusive limit system.

Step 2: Incompressible limit. The incompressible limit regime of the BGKBE (2.33) is obtained via aligning parameters to the diffusion terms [158, 230]. Let l_f be the mean free path, \bar{c} the mean absolute thermal velocity, and $\nu > 0$ a kinematic viscosity. Assuming that a characteristic length L and a characteristic velocity U are given, we define the Knudsen number, the Mach number and the Reynolds number, respectively

$$Kn := \frac{l_f}{L}, \quad (2.37)$$

$$Ma := \frac{U}{\bar{c}_s}, \quad (2.38)$$

$$Re := \frac{UL}{\nu}. \quad (2.39)$$

These nondimensional numbers relate as

$$Re = \frac{l_f \bar{c}_s}{\nu} \frac{Ma}{Kn} = \sqrt{\frac{24}{\pi}} \frac{Ma}{Kn}, \quad (2.40)$$

via defining $\nu := \pi \bar{c} l_f / 8$ and the isothermal speed of sound $\bar{c}_s := \sqrt{3R\theta}$ (see also [223] and references therein).

Definition 2.3.1. To link the mesoscopic distributions with the macroscopic continuum we inversely substitute \bar{c}_s with an artificial parameter $\epsilon \in \mathbb{R}_{>0}$ through

$$\bar{c}_s \leftarrow \frac{1}{\epsilon}. \quad (2.41)$$

Here, and in the following the symbol \leftarrow denotes the assignment operator.

In the limit $\epsilon \searrow 0$, the incompressible continuum is reached, since Kn and Ma tend to zero while Re remains constant [223]. Based on that, we assign

$$\bar{c} = \sqrt{\frac{8k_B\theta}{m\pi}} \leftarrow \sqrt{\frac{8}{3\pi}} \frac{1}{\epsilon}, \quad (2.42)$$

$$l_f \leftarrow \sqrt{\frac{24}{\pi}} \nu \epsilon \quad (2.43)$$

and (2.42) unfold the relaxation time

$$\tau = \frac{l_f}{\bar{c}} \leftarrow 3\nu\epsilon^2. \quad (2.44)$$

Definition 2.3.2. Consequently, we define the ϵ -parametrized BGKBE (2.33) as

$$\frac{D}{Dt}f = -\frac{1}{3\nu\epsilon^2} \left(f - M_f^{\text{eq}} \right) \quad \text{in } \mathfrak{R}, \quad (2.45)$$

where the ϵ -parametrized Maxwellian distribution evaluated at (n_f, \mathbf{u}_f) is

$$M_f^{\text{eq}} = \frac{n_f \epsilon^d}{\left(\frac{2}{3}\pi\right)^{\frac{d}{2}}} \exp\left(-\frac{3}{2}(\mathbf{v}\epsilon - \mathbf{u}_f\epsilon)^2\right) \quad \text{in } \mathfrak{R}. \quad (2.46)$$

Lemma 2.3.1. *The population distribution function solving (2.45) can be formally expressed as a power series in ϵ around t , i.e.*

$$f = \sum_{i=0}^{\infty} \left(-3\nu\epsilon^2 \frac{D}{Dt} \right)^i M_f^{\text{eq}} \quad \text{in } \mathfrak{R}. \quad (2.47)$$

Proof. The BGKBE (2.45) transforms to

$$f = M_f^{\text{eq}} - 3\nu\epsilon^2 \frac{D}{Dt}f \quad \text{in } \mathfrak{R}. \quad (2.48)$$

Repeating $(D/Dt)(2.48)$ gives

$$\frac{D}{Dt}f = \frac{D}{Dt}M_f^{\text{eq}} - 3\nu\epsilon^2 \left(\frac{D}{Dt} \right)^2 f \quad \text{in } \mathfrak{R}. \quad (2.49)$$

The expression (2.49) substitutes $(D/Dt)f$ in (2.48). Thus

$$f = M_f^{\text{eq}} - 3\nu\epsilon^2 \frac{D}{Dt}M_f^{\text{eq}} + \left(3\nu\epsilon^2 \frac{D}{Dt} \right)^2 f \quad \text{in } \mathfrak{R}. \quad (2.50)$$

Subsequent repetition produces higher order terms and substitutions which proves the claim. \square

Remark 2.3.1. Up to lower order, equation (2.47) can also be obtained via Maxwell iteration [275] and references therein. The derivation in [275] is however based on an initial Taylor expansion of the material derivative, whereas the present formulation starts with repeated application of the material derivative. Further, similarities to classical Chapman–Enskog expansion (see e.g. [265] and references therein) are present. Comparisons of several expansion techniques for a discretized model BGKBE can be found for example in [45].

Step 3: Newton’s hypothesis. For a solution f^* of (2.33) the remaining stress tensor \mathbf{P}_{f^*} in (2.36) has to fulfill Newton’s hypothesis which is (in the present context) equivalent to

$$\mathbf{P}_{f^*} \stackrel{!}{=} -p_{f^*}\mathbf{I}_d + 2\nu\rho\mathbf{D}_{f^*} + \mathcal{O}(\epsilon^b) \quad \text{in } \Omega \times I \quad (2.51)$$

up to order $b > 0$, where the rate of strain is denoted by

$$\mathbf{D}_f = \frac{1}{2} \left[\nabla_{\mathbf{x}}\mathbf{u}_f + (\nabla_{\mathbf{x}}\mathbf{u}_f)^{\text{T}} \right]. \quad (2.52)$$

Due to the assumption that for $\epsilon \searrow 0$, higher order terms become sufficiently small, if the order b is large enough. This formally provides evidence for the recovery of the NSE in the diffusive limit. The following lemma illustrates the argument.

Lemma 2.3.2. *With a cutoff at order $b = 2$ we obtain*

$$\mathbf{P} = p\mathbf{I}_d - 2\nu\rho\mathbf{D}. \quad (2.53)$$

Proof. Equation (2.47) cut off at order $b = 2$, provides the ansatz

$$f^\star = M_{f^\star}^{\text{eq}} - 3\nu\epsilon^2 \frac{D}{Dt} M_{f^\star}^{\text{eq}} \quad \text{in } \mathfrak{R}. \quad (2.54)$$

Based on that, the stress tensor is computed by its definition (2.24). To keep the notation compact, f -indices at moments of f are omitted below. First, the material derivative and (2.34) is used to obtain

$$\begin{aligned} \frac{D}{Dt} M_f^{\text{eq}} &= \left(\frac{1}{\rho} \frac{D}{Dt} \rho + 3\epsilon^2 \mathbf{c} \cdot \frac{D}{Dt} \mathbf{u} - \frac{3\epsilon^2}{m} \mathbf{c} \cdot \mathbf{F} \right) M_f^{\text{eq}} \\ &= \left[\frac{1}{\rho} (\partial_t + \mathbf{v} \cdot \nabla_{\mathbf{x}}) \rho + 3\epsilon^2 \mathbf{c} \cdot (\partial_t + \mathbf{v} \cdot \nabla_{\mathbf{x}}) \mathbf{u} - \frac{3\epsilon^2}{m} \mathbf{c} \cdot \mathbf{F} \right] M_f^{\text{eq}} \\ &= \left[\frac{1}{\rho} (-\mathbf{u} \cdot \nabla_{\mathbf{x}} \rho - \rho \nabla_{\mathbf{x}} \cdot \mathbf{u} + \mathbf{v} \cdot \nabla_{\mathbf{x}} \rho) + 3\epsilon^2 \mathbf{c} \cdot (\partial_t + \mathbf{v} \cdot \nabla_{\mathbf{x}}) \mathbf{u} - \frac{3\epsilon^2}{m} \mathbf{c} \cdot \mathbf{F} \right] M_f^{\text{eq}} \\ &= \left[\underbrace{-\nabla_{\mathbf{x}} \cdot \mathbf{u}}_{=: a_f} + \underbrace{\frac{\mathbf{c}}{\rho} \cdot \nabla_{\mathbf{x}} \rho}_{=: b_f} + \underbrace{3\epsilon^2 \mathbf{c} \cdot \partial_t \mathbf{u}}_{=: c_f} + \underbrace{3\epsilon^2 \mathbf{c} \cdot (\mathbf{v} \cdot \nabla_{\mathbf{x}}) \mathbf{u}}_{=: d_f} - \underbrace{\frac{3\epsilon^2}{m} \mathbf{c} \cdot \mathbf{F}}_{=: e_f} \right] M_f^{\text{eq}} \end{aligned} \quad (2.55)$$

in \mathfrak{R} , where

$$\mathbf{c} := \mathbf{v} - \mathbf{u} \quad (2.56)$$

defines the relative velocity. Plugging the derivative (2.55) into (2.54) gives

$$f = M_f^{\text{eq}} [1 - 3\epsilon^2 \nu (-a_f + b_f + c_f + d_f + e_f)] \quad \text{in } \mathfrak{R}. \quad (2.57)$$

Second, the velocity integrals of terms a_f, b_f, \dots, e_f are individually evaluated. We use the symmetry of M_f^{eq} and that M_f^{eq}/n is a normal distribution with covariance $1/(3\epsilon^2)\mathbf{I}_d$. In $\Omega \times I$ and for any $i, j, k, l \in \{1, 2, \dots, d\}$ holds

$$m \int_{\mathbb{R}^d} c_i c_j M_f^{\text{eq}} d\mathbf{v} = \frac{\rho}{3\epsilon^2} \delta_{ij}, \quad (2.58)$$

$$m \int_{\mathbb{R}^d} c_i c_j c_k M_f^{\text{eq}} d\mathbf{v} = 0, \quad (2.59)$$

$$m \int_{\mathbb{R}^d} c_i c_j c_k v_l M_f^{\text{eq}} d\mathbf{v} = \frac{\rho}{9\epsilon^4} (\delta_{ij} \delta_{kl} + \delta_{ik} \delta_{jl} + \delta_{il} \delta_{jk}). \quad (2.60)$$

Hence, we obtain

$$m \int_{\mathbb{R}^d} c_i c_j a_f M_f^{\text{eq}} d\mathbf{v} = \left(m \int_{\mathbb{R}^d} c_i c_j M_f^{\text{eq}} d\mathbf{v} \right) \partial_{x_k} u_k \stackrel{(2.58)}{=} \frac{\rho}{3\epsilon^2} \partial_{x_k} u_k, \quad (2.61)$$

$$m \int_{\mathbb{R}^d} c_i c_j b_f M_f^{\text{eq}} d\mathbf{v} = \left(m \int_{\mathbb{R}^d} c_i c_j c_k M_f^{\text{eq}} d\mathbf{v} \right) \frac{1}{\rho} \partial_{x_k} \rho \stackrel{(2.59)}{=} 0, \quad (2.62)$$

$$m \int_{\mathbb{R}^d} c_i c_j c_f M_f^{\text{eq}} d\mathbf{v} = \left(m \int_{\mathbb{R}^d} c_i c_j c_k M_f^{\text{eq}} d\mathbf{v} \right) 3\epsilon^2 \partial_t u_k \stackrel{(2.59)}{=} 0, \quad (2.63)$$

$$m \int_{\mathbb{R}^d} c_i c_j d_f M_f^{\text{eq}} d\mathbf{v} = \left(m \int_{\mathbb{R}^d} c_i c_j c_k v_l M_f^{\text{eq}} d\mathbf{v} \right) 3\epsilon^2 \partial_{x_l} u_k \stackrel{(2.60)}{=} \frac{\rho}{3\epsilon^2} (\delta_{ij} \delta_{kl} + \delta_{ik} \delta_{jl} + \delta_{il} \delta_{jk}) \partial_{x_l} u_k, \quad (2.64)$$

$$m \int_{\mathbb{R}^d} c_i c_j e_f M_f^{\text{eq}} d\mathbf{v} = \left(m \int_{\mathbb{R}^d} c_i c_j c_k M_f^{\text{eq}} d\mathbf{v} \right) \frac{3\epsilon^2}{m} F_k \stackrel{(2.59)}{=} 0. \quad (2.65)$$

Third, for any $i, j \in \{1, 2, \dots, d\}$, the component $P_{ij} := (\mathbf{P})_{i,j}$ can be computed in \mathfrak{A} . Reordering its terms, we achieve

$$\begin{aligned}
P_{ij} &= m \int_{\mathbb{R}^d} c_i c_j [1 - 3\nu\epsilon^2 (-a_f + b_f + c_f + d_f + e_f)] M_f^{\text{eq}} d\mathbf{v} \\
&= p\delta_{ij} - 3\nu\epsilon^2 \left[-\frac{\rho}{3\epsilon^2} \partial_{x_k} u_k + \partial_{x_l} u_k \frac{\rho}{3\epsilon^2} (\delta_{ij}\delta_{kl} + \delta_{ik}\delta_{jl} + \delta_{il}\delta_{jk}) \right] \\
&= p\delta_{ij} + \nu\rho [\delta_{ij}\partial_{x_k} u_k - \partial_{x_l} u_k (\delta_{ij}\delta_{kl} + \delta_{ik}\delta_{jl} + \delta_{il}\delta_{jk})] \\
&= p\delta_{ij} - \nu\rho (\partial_{x_i} u_j + \partial_{x_j} u_i), \tag{2.66}
\end{aligned}$$

which proves the claim. \square

Remark 2.3.2. Extending the formal result, the vanishing of higher order terms in the diffusive limit $\epsilon \searrow 0$ is rigorously proven by Saint-Raymond [223] with notation ε instead of ϵ for the case $\Omega = \mathbb{R}^3$ and an initial condition

$$f_\epsilon(0, \mathbf{x}, \mathbf{v}) = M(1 + \epsilon g_\epsilon^0(\mathbf{x}, \mathbf{v})) \tag{2.67}$$

which is close to an absolute equilibrium

$$M(\mathbf{v}) = \frac{1}{(2\pi)^{d/2}} \exp\left(-\frac{|\mathbf{v}|^2}{2}\right), \tag{2.68}$$

with $\mathbf{u}_f = \mathbf{0}$, and $\rho_f = 1 = R\theta$ and initial fluctuations g_ϵ^0 . There, solutions f_ϵ to the ϵ -scaled BGKBE are passed to the limit, where the corresponding velocity moments \mathbf{u}_{f_ϵ} are consequently identified as limiting to Leray's weak solutions [177] of the incompressible NSE [223, Theorem 1.2]. It is to be noted that we adapted the initial wording "hydrodynamic limit" from [223] toward the more generic term "diffusive limit" to underline the presence of diffusion terms in the limiting equation. For the sake of clarity, we restate the main result of Saint-Raymond [223] in the present notation below.

It is to be stressed that we neglect the additional temperature equation appearing in the limit via imposing an ideal gas. Let the Hilbert space $L^2(\mathbb{R}^d, M d\mathbf{v})$ be defined by the scalar product

$$(f, g) \mapsto \int_{\mathbb{R}^d} f(\mathbf{v}) g(\mathbf{v}) M(\mathbf{v}) d\mathbf{v}, \tag{2.69}$$

where $M d\mathbf{v}$ is a positive unit measure on \mathbb{R}^d which allows the definition of an average

$$\langle \xi \rangle := \int_{\mathbb{R}^d} \xi(\mathbf{v}) M(\mathbf{v}) d\mathbf{v} \tag{2.70}$$

over $\Xi = \mathbb{R}$ for any integrable function ξ .

Definition 2.3.3. For any pair (f, g) of functions which are measurable and almost everywhere nonnegative on the phase space \mathfrak{B} , define the relative entropy

$$H(f | g) := \int_{\mathbb{R}^d} \int_{\mathbb{R}^d} \left(f \log\left(\frac{f}{g}\right) - f + g \right) d\mathbf{v} d\mathbf{x} \geq 0. \tag{2.71}$$

Based on that, we recall the following preparative result from [222]. Locally integrable functions on $X \subseteq \mathbb{R}^d$ and Sobolev spaces based on L^2 are denoted with

$$L_{\text{loc}}^1(X) = \left\{ f: X \rightarrow \mathbb{R} \mid \forall \mathbf{x} \in X \exists r > 0: B_r(\mathbf{x}) \subseteq X \wedge f|_{B_r(\mathbf{x})} \in L^1(B_r(\mathbf{x})) \right\}, \tag{2.72}$$

$$H^k(X) = W^{k,2}(X) = \left\{ f \in L^2(X) \mid \forall |\alpha| \leq k \exists \text{ weak derivative } \partial^\alpha f \in L^2(X) \right\}, \tag{2.73}$$

respectively. The latter are Hilbert spaces and the dual of $H^k(X)$ is denoted with $H^{-k}(X)$.

Theorem 2.3.1. *Let $\epsilon > 0$ and $0 \leq f_\epsilon^0 \in L^1_{\text{loc}}(\mathfrak{F})$ such that the entropy is bounded $H(f_\epsilon^0 | M) < \infty$. Then there exists a weak solution f_ϵ to (2.45) that is global and nonnegative, and fulfills*

$$f_\epsilon - M \in C(\mathbb{R}_{>0}, L^2(\mathfrak{F}) + L^1(\mathfrak{F})) \quad (2.74)$$

and for all $t > 0$:

$$H(f_\epsilon(t) | M) + \frac{1}{\epsilon^2 \nu} \int_0^t \int_{\mathbb{R}^d} \int_{\mathbb{R}^d} D(f_\epsilon)(s) \, d\mathbf{v} \, d\mathbf{x} \, ds \leq H(f_\epsilon^0 | M), \quad (2.75)$$

where the dissipation $D(f_\epsilon)$ is defined by

$$D(f_\epsilon) = (M_{f_\epsilon} - f_\epsilon) \log \left(\frac{M_{f_\epsilon}}{f_\epsilon} \right) \geq 0. \quad (2.76)$$

Additionally, the weak solution fulfills the moment integrated conservation laws (2.29), (2.30), and (2.31) at zeroth, first, and second order, respectively [222].

Via a boundedness assumption in $L^2(\mathfrak{F}, d\mathbf{x}M \, d\mathbf{v})$ of initial parametrized fluctuation data (g_ϵ^0) defined from

$$g_\epsilon^0 = \frac{1}{\epsilon} \left(\frac{f_\epsilon^0}{M} - 1 \right), \quad (2.77)$$

a constantly prefactored entropy bound $C_0 \epsilon^2$ is obtained and in turn weak compactness on (Mg_ϵ) holds in $L^1_{\text{loc}}(\mathbb{R}_{>0} \times \mathbb{R}^d, L^1(\mathbb{R}^d))$ [20, 223]. Within this setting, for $1 \leq p < \infty$ we define

$$w - L^p := \begin{cases} \text{weak topology } \sigma(L^p, L^{p'}) & \text{if } p < \infty, \\ \text{weak-}^* \text{ topology } \sigma(L^\infty, L^1) & \text{if } p = \infty, \end{cases} \quad (2.78)$$

to restate the following main result of [223].

Theorem 2.3.2. *Let (g_ϵ^0) be a family of measurable functions on \mathfrak{F} which satisfy almost everywhere*

$$1 + \epsilon g_\epsilon^0 \geq 0 \quad (2.79)$$

and

$$H(M(1 + \epsilon g_\epsilon^0) | M) \leq C_0 \epsilon^2, \quad (2.80)$$

and with $\nabla_{\mathbf{x}} \cdot \mathbf{u}_0 = 0$ additionally fulfill that

$$\langle g_\epsilon^0 \mathbf{v} \rangle \xrightarrow[w - L^2(\mathbb{R}^d)]{\epsilon \searrow 0} \mathbf{u}_0. \quad (2.81)$$

Further, let $f_\epsilon = M(1 + \epsilon g_\epsilon)$ be a solution of (2.45). Then

$$\exists \rho, \mathbf{u} \in L^\infty(\mathbb{R}_{>0}, L^2(\mathbb{R}^d)) \cap L^2(\mathbb{R}_{>0}, H^1(\mathbb{R}^d)) \quad (2.82)$$

and we have weak convergence such that, modulo a zero-limiting subsequence (ϵ_n) holds

$$\langle g_\epsilon \rangle \xrightarrow[w - L^1_{\text{loc}}(\mathbb{R}_{>0} \times \mathbb{R}^d)]{\epsilon \searrow 0} \rho, \quad (2.83)$$

$$\langle g_\epsilon \mathbf{v} \rangle \xrightarrow[\omega - L_{\text{loc}}^1(\mathbb{R}_{>0} \times \mathbb{R}^d)]{\epsilon \searrow 0} \mathbf{u}. \quad (2.84)$$

In addition, ρ and \mathbf{u} are weak solutions of the incompressible NSE (2.12), where the pressure is determined from the solenoidal condition [223].

2.4 Temporal filtering

In CFD, the filtering of the model equation provides an opportunity of generating significant simulation speedup in comparison to approximating the unfiltered PDE as is with scale-resolving grid resolutions. As a technique for approximating (2.12) in turbulent regimes (e.g. $Re \gg 1000$), the LBM has attracted increased attention due to efficient scalability on large HPC machines, especially in combination with LES [3]. Several studies (e.g. see [133] and references therein) have approved the applicability of LBMs to DNS and LES.

Based on space filtering and the standard Smagorinsky eddy viscosity, a first LES model for LBMs has been proposed by Hou *et al.* [129] and has been extended for example by Dong *et al.* [67]. Subsequently, via Hermite expansion, Malaspina and Sagaut [184] have proposed consistent subgrid closures for the space-filtered BGKBE.

Apart from these classical results from spatial filtering, Pruetz [211] has put forward several advantages of filtering the time domain instead. For the purpose of temporal large eddy simulation (TLES), a temporal variant of the approximate deconvolution model has been introduced. Moreover, due to the possibility of Eulerian time domain filtering of (2.12), a temporal direct deconvolution model (TDDM) has been proposed by Oberle *et al.* [200]. Our work [233] pioneers the usage of the TDDM in combination with LBMs and is part of Contribution (CTN4). Below, we recall the first TLES LBM derivation based on consistently time-filtering the BGKBE¹.

2.4.1 Time-filtered Navier–Stokes equations

The TDDM [200, 233] is based on an Eulerian time domain filtering

$$\bar{g}(\cdot, t; \Theta) = \int_{-\infty}^t G(t' - t; \Theta) g(\cdot, t') dt', \quad (2.85)$$

where $g: \cdot \times I_\infty \rightarrow \mathbb{R}$ is a time dependent function with other optional arguments and filtered version \bar{g} , G is the filter kernel, and the scalar $\Theta > 0$ specifies the filter width. Note that we have extended the positive time horizon I to allow values within the complete real line $I_\infty \subseteq \mathbb{R}$.

Proposition 2.4.1. *Let the filter kernel be exponential, i.e.*

$$G(t' - t; \Theta) = \frac{1}{\Theta} \exp\left(-\frac{t' - t}{\Theta}\right). \quad (2.86)$$

Then, for an unfiltered quantity Υ , the differential form of the filter operation can be written as

$$\partial_t \bar{\Upsilon} = \frac{\Upsilon - \bar{\Upsilon}}{\Theta}. \quad (2.87)$$

¹ Parts of this section are reproduced from [233], Copyright (2022), with permission from the authors and Elsevier Inc.

Proof. Let $\Upsilon(t)$ be a time-dependent function, where we suppressed other arguments in space for the sake of simplicity. We recall the computations given in [200]. Let $\hat{t} = t' - t$. Applying the time derivative to a time-filtered quantity $\bar{\Upsilon}(t; \Theta)$ yields

$$\begin{aligned}
 \partial_t \bar{\Upsilon}(t; \Theta) &\stackrel{(2.85)}{=} \partial_t \int_{-\infty}^0 G(\hat{t}; \Theta) \Upsilon(t + \hat{t}) \, d\hat{t} \\
 &= \int_{-\infty}^0 G(\hat{t}; \Theta) \partial_t \Upsilon(t + \hat{t}) \, d\hat{t} \\
 &= \int_{-\infty}^t G(t' - t; \Theta) \partial_{t'} \Upsilon(t') \, dt' \\
 &= G(t' - t; \Theta) \Upsilon(t') \Big|_{-\infty}^t - \int_{-\infty}^t \partial_{t'} G(t' - t; \Theta) \Upsilon(t') \, dt' \\
 &\stackrel{(2.86)}{=} G(t' - t; \Theta) \Upsilon(t') \Big|_{-\infty}^t - \frac{1}{\Theta} \int_{-\infty}^t G(t' - t; \Theta) \Upsilon(t') \, dt' \\
 &= G(0; \Theta) \Upsilon(t) - \left[\lim_{t' \rightarrow -\infty} G(t' - t; \Theta) \Upsilon(t') \right] - \frac{1}{\Theta} \bar{\Upsilon}(t, \Theta) \\
 &\stackrel{(2.86)}{=} \frac{1}{\Theta} \Upsilon(t) - \frac{1}{\Theta} \bar{\Upsilon}(t; \Theta). \tag{2.88}
 \end{aligned}$$

□

Definition 2.4.1. By simple rearrangement of (2.87) the filtering operation is reversed to

$$\Upsilon = \bar{\Upsilon} + \Theta \partial_t \bar{\Upsilon}. \tag{2.89}$$

As proposed in [200], we refer to this process as (temporal) direct deconvolution.

Let $\Upsilon \in \{\mathbf{u}, p\}$. Hence, temporally filtering (2.12) with $\mathbf{F} = 0$ results in [200]

$$\operatorname{div}_{\mathbf{x}}(\bar{\mathbf{u}}) = 0, \tag{2.90}$$

$$\partial_t \bar{\mathbf{u}} + \operatorname{div}_{\mathbf{x}}(\bar{\mathbf{u}} \otimes \bar{\mathbf{u}}) - \nu \Delta_{\mathbf{x}} \bar{\mathbf{u}} + \nabla_{\mathbf{x}} \bar{p} = -\operatorname{div}_{\mathbf{x}}(\mathbf{T}), \tag{2.91}$$

where $\bar{\mathbf{u}}$ and \bar{p} are the time-filtered velocity and pressure, respectively,

$$T_{\alpha\beta} = \overline{u_{\alpha} u_{\beta}} - \bar{u}_{\alpha} \bar{u}_{\beta} \tag{2.92}$$

is the temporal residual stress tensor and the tensor divergence of \mathbf{T} is defined as

$$\operatorname{div}_{\mathbf{x}}(\mathbf{T}) = \nabla_{\mathbf{x}} \cdot \mathbf{T} = (\partial_{x_{\beta}} T_{\alpha\beta}) \mathbf{e}_{\alpha} \tag{2.93}$$

with \mathbf{e}_{α} being the α th unit vector. Note that here and below, we neglect stating the explicit dependence on the filter width Θ of filtered quantities.

Proposition 2.4.2. *The time evolution of the temporal residual stress tensor \mathbf{T} is described by the ordinary differential equation*

$$\partial_t \mathbf{T} = -\frac{1}{\Theta} \mathbf{T} + \Theta (\partial_t \bar{\mathbf{u}}) \otimes (\partial_t \bar{\mathbf{u}}). \tag{2.94}$$

Proof. Via direct deconvolution we obtain the time derivative of \mathbf{T} as [200]

$$\begin{aligned}\partial_t T_{\alpha\beta} &= \partial_t \overline{u_\alpha u_\beta} - (\partial_t \overline{u_\alpha}) \overline{u_\beta} - \overline{u_\alpha} (\partial_t \overline{u_\beta}) \\ &\stackrel{(2.87)}{=} \frac{1}{\Theta} (u_\alpha u_\beta - \overline{u_\alpha u_\beta}) - (\partial_t \overline{u_\alpha}) \overline{u_\beta} - \overline{u_\alpha} (\partial_t \overline{u_\beta}) \\ &\stackrel{(2.89)}{=} \frac{1}{\Theta} [(\overline{u_\alpha} + \Theta \partial_t \overline{u_\alpha}) (\overline{u_\beta} + \Theta \partial_t \overline{u_\beta}) - \overline{u_\alpha u_\beta}] - (\partial_t \overline{u_\alpha}) \overline{u_\beta} - \overline{u_\alpha} (\partial_t \overline{u_\beta}).\end{aligned}\quad (2.95)$$

Rearranging terms proves the claim. \square

Remark 2.4.1. The equations (2.90), (2.91) and (2.94) form a closed system which compared to (2.12) features an analytically tunable filter in time manifested in the coupling term \mathbf{T} .

2.4.2 Time-filtered Bhatnagar–Gross–Krook–Boltzmann equation

In general, applying a filter operation to (2.45) with $\mathbf{F} = 0$ results in [184]

$$\frac{D}{Dt} \bar{f} = -\frac{1}{\tau} \left[\bar{f} - M_f^{\text{eq}}(\bar{f}) \right] + \frac{1}{\tau} \mathcal{R}, \quad (2.96)$$

where $\bar{f} : \mathfrak{X} \rightarrow \mathbb{R}$, $(\mathbf{x}, \boldsymbol{\xi}, t) \mapsto \bar{f}(\mathbf{x}, \boldsymbol{\xi}, t)$ is the filtered version of f , and

$$\mathcal{R} = \left[\overline{M_f^{\text{eq}}} - M_f^{\text{eq}}(\bar{f}) \right] \quad (2.97)$$

defines the residual.

Remark 2.4.2. Irrespective which function arguments are filtered, we can use (2.96) analogously for space and time domain filtering.

Via Hermite expanding M_f^{eq} to N th order, we obtain

$$\mathcal{R} = w(\boldsymbol{\xi}) \sum_{n=0}^N \mathbb{H}^{(n)}(\boldsymbol{\xi}) : \mathbb{R}^{(n)}, \quad (2.98)$$

where

$$\mathbb{H}^{(n)}(\boldsymbol{\xi}) = (-1)^n (2\pi)^{\frac{d}{2}} \exp\left(\frac{\boldsymbol{\xi}^2}{2}\right) \mathbb{D}^{(n)} \left[\frac{1}{(2\pi)^{\frac{d}{2}}} \exp\left(-\frac{\boldsymbol{\xi}^2}{2}\right) \right] \quad (2.99)$$

denotes the n th order multi-dimensional Hermite polynomial and $\mathbb{D}^{(n)}$ being a tensor of rank n with entries

$$D_{\alpha_1 \dots \alpha_n}^{(n)} = \partial_{\alpha_1} \dots \partial_{\alpha_n} \quad (2.100)$$

for multi-indices $\alpha_i = 1, \dots, d$ for all $i = 1, \dots, n$. Here and below, the symbol $:$ denotes full tensor contraction in terms of Hadamard multiplication (see Section 3.1.3) and subsequent summation of components. This yields an order by order expression with increasing tensorial rank [184]. Hence, up to second order ($N = 2$) we obtain

$$\mathbb{R}^{(0)} = 0, \quad (2.101)$$

$$\mathbb{R}^{(1)} = \mathbf{0}, \quad (2.102)$$

$$\mathbb{R}^{(2)} = \mathbf{T}^{\text{sg}} + \theta^{\text{sg}} \mathbf{I}_d, \quad (2.103)$$

where \mathbf{T}^{sg} and θ^{sg} are subgrid stress and subgrid temperature, respectively.

Remark 2.4.3. Due to an isothermal configuration, the second order truncation effectuates that $\theta^{\text{sg}} = 0$. Injecting the temporal residual stress as a subgrid stress $\mathbf{T}^{\text{sg}} \leftrightarrow \mathbf{T}$ and interpreting the filtering residual as a forcing term on the second moment, we obtain a diffusive limit toward the time-filtered NSE $\{(2.90), (2.91)\}$ up to leading order. Upon complete discretization, we obtain a lattice Boltzmann equation which is coupled to a discrete direct deconvolution rule as outlined in Section 3.3.1.5.

2.5 Homogenization

For the mathematical modeling of fluid flow through porous media, the incompressible NSE (2.12) can be modified to include the effects of the solid matrix on the fluid flow in the void. Various different mathematical models exist ([122, 198] and references therein). Here, we choose to recall the rigorous construction of porous media models formulated in Allaire’s seminal works [4–11]. Therein, the geometrical perception of porous media as equidistant perforations in flow domains is considered to construct model equations via homogenization. As a result, several homogenization limits are derived, where the homogenized equations depend on the geometric configuration. We distinguish between three classical cases of homogenization limits:

1. incompressible NSE,
2. Brinkman law (BL),
3. Darcy’s law (DL).

The respective limits in this categorization have been rigorously proved for the stationary [10] and nonstationary Stokes [9] regime as well as for the stationary NSE [8] as starting points. Although suggested by Allaire, to the knowledge of the author the validity of this distinction is not completely proven for the nonstationary NSE. Nevertheless, the works of Mikelić [188, 189] and Feireisl *et al.* [82] cover the homogenization limit toward the BL and the DL in the nonstationary case in a different framework. Other contributions also used this structural categorization [108, 154, 174]. Although these models are likely to be interconnected, rigorous proofs of the underlying relations are rare and limited to linear and stationary settings. Exemplarily, Allaire [5] proved the compliance of a formally derived DL and the DL derived via homogenization (low volume fraction limit). Further, Feppon [83] and Feppon *et al.* [84] proved high-order homogenization limits for the Stokes equations in a unified procedure. To the knowledge of the author, the latter is the first and only derivation covering all three classical cases together with the low volume fraction limit at once. It remains to be stressed, that such unified studies have not been conducted for homogenizing the nonstationary NSE. Below, we summarize proven results and formulate the corresponding hypotheses to complete the framework.

Besides the mathematically rigorous model derivation, application-based model construction has been found suitable for fluid flow in porous media [111, 199, 238]. Typically, empirical observations and matching terms are used to introduce model systems akin to Brinkman- [41], Forchheimer- [89], Darcy- [60], or mixed-type equations [198]. Depending on the characteristic scales of porosity in the application in question, the heuristically derived models can correctly recover the flow physics or severely disagree with experiments [198]. However, due to the large variation of involved spatial scales, the model equations often are numerically solved with highly parallelizable methods. For example, Spaid and Phelan [238] have proposed an LBM for approximating Stokes and Stokes–Brinkman equations as target models. The latter only apply to large obstacle sizes in the porous matrix and solely recover stationary flows. To the knowledge of the author, no LBM has yet been employed to approximate the nonstationary void flow through critically sized porous matrix structures. Additionally to the formal completion of a unified framework for several regimes, we evaluate its applicability and isolate a single target PDE which holds in the critical regime and is then to be approximated with LBMs. This process of model derivation and evaluation is part of Contribution (CTN4). Unless stated otherwise, C and C_n are constants, where $n \in \mathbb{N}_0$.

2.5.1 Geometric setup

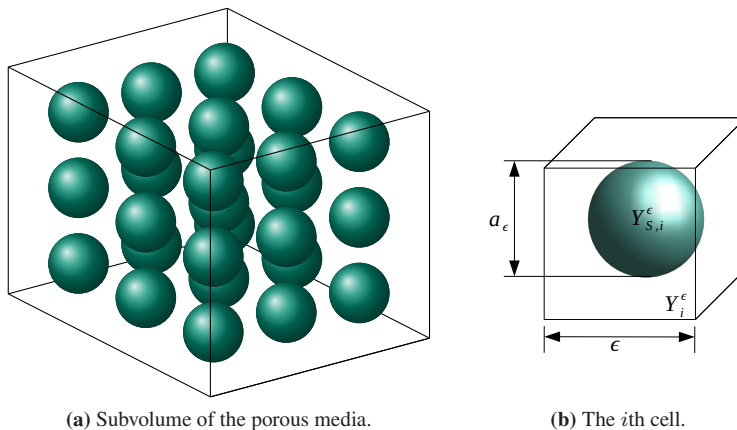


Figure 2.1: Illustrations of the geometric model of a porous structure in $d = 3$ dimensions. The i th void cell is denoted with Y_i^ϵ containing a spherical matrix obstacle $Y_{S,i}^\epsilon$ with radius a_ϵ . Each cell is cubic with side length ϵ .

We geometrically model the flow through porous media via perforating the fluid domain with regularly arranged obstacles (i.e. holes) of equal size [4, 6, 8, 11]. Let the domain $\Omega \subseteq \mathbb{R}^N$, $N \geq 2$ be redefined as an open, bounded, and connected set. The boundary $\partial\Omega$ is assumed to be smooth of class C^1 . The domain Ω is covered with a regular mesh of period $\epsilon > 0$ (see Figure 2.1a), prescribing the cells $Y_i^\epsilon = (0, \epsilon)^d$, for $1 \leq i \leq N(\epsilon)$ (see Figure 2.1b), where

$$N(\epsilon) = |\Omega| \epsilon^{-d} (1 + \mathcal{O}(1)) \quad (2.104)$$

counts their number. Each cubical cell contains a solid spherical obstacle $Y_{S,i}^\epsilon$ of size a_ϵ located in its center and a complementary part filled with fluid

$$Y_{F,i}^\epsilon = Y_i^\epsilon \setminus Y_{S,i}^\epsilon. \quad (2.105)$$

The overall fluid void is thus obtained via removal of the collective solid matrix, i.e.

$$\Omega_\epsilon = \Omega \setminus \bigcup_{i=1}^{N(\epsilon)} Y_{S,i}^\epsilon. \quad (2.106)$$

Further, we assume that all obstacles are similar to a model obstacle Y_S^m of size a_ϵ . Under the assumption that $a_\epsilon \ll \epsilon$, or equivalently

$$\lim_{\epsilon \searrow 0} \frac{a_\epsilon}{\epsilon} = 0, \quad (2.107)$$

we define the critical obstacle size

$$a_\epsilon^{\text{crit}} = \begin{cases} C_0 \epsilon^{\frac{d}{d-2}} & \text{for } d \geq 3, \\ e^{-\frac{C_0}{\epsilon^2}} & \text{for } d = 2, \end{cases} \quad (2.108)$$

with $0 < C_0 < \infty$ as well as the ratio

$$\sigma_\epsilon = \begin{cases} \left(\frac{\epsilon^d}{a_\epsilon^{d-2}} \right)^{\frac{1}{2}} & \text{for } d \geq 3, \\ \epsilon \left| \log \left(\frac{a_\epsilon}{\epsilon} \right) \right|^{\frac{1}{2}} & \text{for } d = 2. \end{cases} \quad (2.109)$$

Proposition 2.5.1. *For a critical size a_ϵ^{crit} , the ratio σ_ϵ reaches the nonnegative constant homogenization limit*

$$\lim_{\epsilon \searrow 0} \sigma_\epsilon = \begin{cases} (C_0)^{\frac{2-d}{2}} & \text{for } d \geq 3, \\ (C_0)^{\frac{1}{2}} & \text{for } d = 2. \end{cases} \quad (2.110)$$

Proof. Injecting (2.108) into (2.109) completes the proof. \square

2.5.2 Homogenized stationary Navier–Stokes equations

In the case of independence of time, the incompressible fluid flow in Ω_ϵ is modeled by the stationary nonlinear Navier–Stokes equations

$$\begin{cases} \mathbf{u}_\epsilon \cdot \nabla_{\mathbf{x}} \mathbf{u}_\epsilon - \nu \Delta_{\mathbf{x}} \mathbf{u}_\epsilon = \mathbf{F} - \nabla_{\mathbf{x}} p_\epsilon & \text{in } \Omega_\epsilon, \\ \operatorname{div}_{\mathbf{x}} \mathbf{u}_\epsilon = 0 & \text{in } \Omega_\epsilon, \\ \mathbf{u}_\epsilon = \mathbf{0} & \text{on } \partial\Omega_\epsilon, \end{cases} \quad (2.111)$$

where $\mathbf{u}_\epsilon: \Omega_\epsilon \rightarrow \mathbb{R}^d$ denotes the velocity field, $p_\epsilon: \Omega_\epsilon \rightarrow \mathbb{R}$ is the scalar-valued pressure, $\mathbf{F} \in L^2(\Omega)^d$ defines a given force, and $\nu > 0$ is a constant viscosity. Additionally, to comply with (2.106), we define the extension to Ω of a pair of solutions $(\mathbf{u}_\epsilon, p_\epsilon)$ of (2.111) as

$$(\tilde{\mathbf{u}}_\epsilon, \tilde{p}_\epsilon) = \begin{cases} (\mathbf{u}_\epsilon, p_\epsilon) & \text{in } \Omega_\epsilon, \\ \left(0, \frac{1}{|C_i^\epsilon|} \int_{C_i^\epsilon} p_\epsilon \, d\mathbf{x}\right) & \text{in each obstacle } Y_{S,i}^\epsilon, \end{cases} \quad (2.112)$$

where C_i^ϵ denotes a control volume containing $Y_{S,i}^\epsilon$ [8].

Based on the above definitions, Allaire [8, Corollary 1.4] proved homogenization limits for different obstacle sizes expressed in the ratio (2.109). The results of homogenizing (2.111) are summarized in the following statements which are recalled without proof. Let the index \cdot_0 of a function space denote the classical vanishing trace operator, e.g. for $X \subseteq \mathbb{R}^d$ let

$$H_0^1(X) = \{f \in H^1(X) \mid f|_{\partial X} = 0\}. \quad (2.113)$$

Theorem 2.5.1. *According to the scaling of the obstacle size, we distinguish between three homogenization limits [8].*

(i) *If the obstacles are too small, i.e. $\lim_{\epsilon \searrow 0} \sigma_\epsilon = +\infty$, then $(\tilde{\mathbf{u}}_\epsilon, \tilde{p}_\epsilon)$ converges strongly in $H_0^1(\Omega)^d \times L^2(\Omega)/\mathbb{R}$ to (\mathbf{u}, p) , a solution of the stationary nonlinear NSE*

$$\begin{cases} \mathbf{u} \cdot \nabla_{\mathbf{x}} \mathbf{u} - \nu \Delta_{\mathbf{x}} \mathbf{u} = \mathbf{F} - \nabla_{\mathbf{x}} p & \text{in } \Omega, \\ \operatorname{div}_{\mathbf{x}} \mathbf{u} = 0 & \text{in } \Omega, \\ \mathbf{u} = \mathbf{0} & \text{on } \partial\Omega. \end{cases} \quad (2.114)$$

(ii) *If the obstacles have a critical size, i.e. $\lim_{\epsilon \searrow 0} \sigma_\epsilon = \sigma > 0$, then $(\tilde{\mathbf{u}}_\epsilon, \tilde{p}_\epsilon)$ converges weakly in $H_0^1(\Omega)^d \times L^2(\Omega)/\mathbb{R}$ to (\mathbf{u}, p) , a solution of the stationary nonlinear BL*

$$\begin{cases} \mathbf{u} \cdot \nabla_{\mathbf{x}} \mathbf{u} - \nu \Delta_{\mathbf{x}} \mathbf{u} + \frac{\nu}{\sigma^2} \mathbf{M} \mathbf{u} = \mathbf{F} - \nabla_{\mathbf{x}} p & \text{in } \Omega, \\ \operatorname{div}_{\mathbf{x}} \mathbf{u} = 0 & \text{in } \Omega, \\ \mathbf{u} = \mathbf{0} & \text{on } \partial\Omega. \end{cases} \quad (2.115)$$

(iii) If the obstacles are too big, i.e. $\lim_{\epsilon \searrow 0} \sigma_\epsilon = 0$, then the rescaled solution $(\frac{\tilde{\mathbf{u}}_\epsilon}{\sigma_\epsilon}, \tilde{p}_\epsilon)$ converges strongly in $L^2(\Omega)^d \times L^2(\Omega)/\mathbb{R}$ to (\mathbf{u}, p) , the unique solution of the DL

$$\begin{cases} \mathbf{u} = \frac{1}{\nu} \mathbf{M}^{-1} (\mathbf{F} - \nabla_{\mathbf{x}} p) & \text{in } \Omega, \\ \operatorname{div}_{\mathbf{x}} \mathbf{u} = 0 & \text{in } \Omega, \\ \mathbf{u} = \mathbf{0} & \text{on } \partial\Omega. \end{cases} \quad (2.116)$$

In all three regimes (i–iii), \mathbf{M} is a $d \times d$ symmetric matrix, which depends only on the model obstacle Y_S^m .

The porosity matrix \mathbf{M} , which inversely represents a permeability tensor, is computable via a model problem defined locally around Y_S^m (see [8, Proposition 1.2] and [11, Proposition 1.3.2]). The following result, obtained from merging [8, Proposition 1.2] and [11, Proposition 1.3.2], unfolds the computation of \mathbf{M} .

Proposition 2.5.2. Let $\{e_k\}_{1 \leq k \leq d}$ denote the unit basis of \mathbb{R}^d . Hence, the local model problem is defined for each k as

$$\begin{cases} \nabla_{\mathbf{x}} q_k - \Delta_{\mathbf{x}} \mathbf{w}_k = \mathbf{0} & \text{in } \mathbb{R}^d \setminus Y_S^m, \\ \operatorname{div}_{\mathbf{x}} \mathbf{w}_k = \mathbf{0} & \text{in } \mathbb{R}^d \setminus Y_S^m, \\ \mathbf{w}_k = \mathbf{0} & \text{on } \partial Y_S^m, \\ \mathbf{w}_k \begin{cases} \rightarrow e_k & \text{for } d \geq 3 \\ \sim e_k \log(|\mathbf{x}|) & \text{for } d = 2 \end{cases} & \text{as } |\mathbf{x}| \rightarrow \infty. \end{cases} \quad (2.117)$$

The matrix \mathbf{M} is then assembled through

$$\mathbf{M} = \begin{cases} \left[\int_{\mathbb{R}^d \setminus Y_S} \nabla_{\mathbf{x}} \mathbf{w}_k \cdot \nabla_{\mathbf{x}} \mathbf{w}_j \, d\mathbf{x} \right]_{1 \leq j, k \leq d} & \text{for } d \geq 3, \\ 4\pi \mathbf{I}_d & \text{for } d = 2. \end{cases} \quad (2.118)$$

Remark 2.5.1. Note that the standard derivation of the DL uses the assumption that the obstacle size $a_\epsilon = \mathcal{O}(\epsilon)$. Presently, so far we have assumed a smaller obstacle size. Hence, the typical permeability tensor (often referred to as \mathbf{K}) is computed from a different model problem as the local model problem (2.117). Allaire [5] closely examines the relation of permeability and porosity tensors, and states the following result.

Let the obstacle size be redefined as $a_\epsilon := \delta_\epsilon = \mathcal{O}(\epsilon)$. Let ι_i^ϵ define a linear homeomorphism, mapping each cell to the unit cell $Y = (0, 1)^d$ and allocating solid and fluid parts therein, $Y_S = \iota_i^\epsilon(Y_{S,i}^\epsilon)$ and $Y_F = \iota_i^\epsilon(Y_{F,i}^\epsilon)$, respectively. Hence, the unit cell Y now is split into a fluid part $Y_F = Y \setminus Y_S$ and an obstacle Y_S which is of size $\delta > 0$ due to ι_i^ϵ resembling a rescaling with a homothety factor of ϵ^{-1} [189]. The following theorem from [11] states the outcome of the homogenization in this case.

Theorem 2.5.2. Let the case specific constant in [11, Theorem 1.2.5] be fixed at $\gamma = 4$ and $\beta > 1$ as given therein. Then an extension $(\tilde{\mathbf{u}}_\epsilon, \tilde{p}_\epsilon)$ of the solution $(\mathbf{u}_\epsilon, p_\epsilon)$ of (2.111) exists, such that $\tilde{\mathbf{u}}_\epsilon$ converges weakly in $L^2(\Omega)^d$ to \mathbf{u} , and \tilde{p}_ϵ converges strongly in $L^{q'}(\Omega)/\mathbb{R}$ to p , for any $1 < q' < \beta$, where (\mathbf{u}, p) is the unique solution of the DL

$$\begin{cases} \mathbf{u} = \frac{1}{\nu} \mathbf{A} (\mathbf{F} - \nabla_{\mathbf{x}} p) & \text{in } \Omega, \\ \operatorname{div}_{\mathbf{x}} \mathbf{u} = 0 & \text{in } \Omega, \\ \mathbf{u} = \mathbf{0} & \text{on } \partial\Omega. \end{cases} \quad (2.119)$$

In the DL (2.119), the porosity matrix \mathbf{A} is defined by

$$\mathbf{A} = \left[\int_{Y_F} \nabla_{\mathbf{x}} \mathbf{v}_k \cdot \nabla_{\mathbf{x}} \mathbf{v}_j \, d\mathbf{x} \right]_{1 \leq j, k \leq d}, \quad (2.120)$$

where for the canonical basis vector \mathbf{e}_k , $1 \leq k \leq d$, of \mathbb{R}^d , \mathbf{v}_k is the unique solution in $H_{\#}^1(Y_F)$ of the unit cell problem

$$\begin{cases} \nabla_{\mathbf{x}} p_k - \Delta_{\mathbf{x}} \mathbf{v}_k = \mathbf{e}_k & \text{in } Y_F, \\ \operatorname{div}_{\mathbf{x}} \mathbf{v}_k = 0 & \text{in } Y_F, \\ \mathbf{v}_k = \mathbf{0} & \text{on } \partial(Y_S). \end{cases} \quad (2.121)$$

Further, the continuity in the low volume fraction limit ($\delta \searrow 0$) is verified through the following theorem (Allaire [5, Theorem 3.1]), which links the permeability tensor \mathbf{A} (2.120) in the DL (2.119) to the porosity matrix \mathbf{M} (2.118) in the DL (2.116).

Theorem 2.5.3. *Let (p_k, \mathbf{v}_k) be the unique solution of the unit cell problem. Rescaling it, for $\mathbf{x} \in \delta^{-1}(Y \setminus Y_S)$, we can define*

$$\mathbf{v}_k^{\delta}(\mathbf{x}) = \delta^{d-2} \mathbf{v}_k(\delta \mathbf{x}), \quad (2.122)$$

$$p_k^{\delta}(\mathbf{x}) = \delta^{d-1} p_k(\delta \mathbf{x}). \quad (2.123)$$

Further, let (q_i, \mathbf{w}_i) be the unique solution of the local model problem. Then $(p_k^{\delta}, \mathbf{v}_k^{\delta})$ converges weakly to

$$\sum_{i=1}^d (\mathbf{e}_i^T \mathbf{M}^{-1} \mathbf{e}_k) (q_i, \mathbf{w}_i) \quad (2.124)$$

in $[L_{\text{loc}}^2(\mathbb{R}^d \setminus Y_S) / \mathbb{R}] \times [H_{\text{loc}}^1(\mathbb{R}^d \setminus Y_S)]^d$. Additionally, the low volume fraction limit for the permeability tensor is given as

$$\begin{cases} \lim_{\delta \searrow 0} \delta^{d-2} \mathbf{A}(\delta) = \mathbf{M}^{-1}, & \text{for } d \geq 3, \\ \lim_{\delta \searrow 0} \frac{1}{|\log \delta|} \mathbf{A}(\delta) = \mathbf{M}^{-1}, & \text{for } d = 2. \end{cases} \quad (2.125)$$

Remark 2.5.2. With the above limiting systems, homogenized stationary equations are given for the complete range of $a_{\epsilon} \leq \mathcal{O}(\epsilon)$, where the sharp inequality is covered in Theorem 2.5.1 via (i–iii) and the equality in Theorem 2.5.2 provides a complementary case (iv).

2.5.3 Homogenized nonstationary Navier–Stokes equations

Let $d \in \{2, 3\}$ and the model geometry be defined as above. The incompressible fluid flow, now being dependent on time $t \in I = (0, T)$, is governed by the nonstationary nonlinear NSE $_{\epsilon}$

$$\begin{cases} \partial_t \mathbf{u}_{\epsilon} + \epsilon^4 \mathbf{u}_{\epsilon} \cdot \nabla_{\mathbf{x}} \mathbf{u}_{\epsilon} - \epsilon^2 \nu \Delta_{\mathbf{x}} \mathbf{u}_{\epsilon} = \mathbf{F} - \nabla_{\mathbf{x}} p_{\epsilon} & \text{in } \Omega_{\epsilon} \times I, \\ \operatorname{div}_{\mathbf{x}} \mathbf{u}_{\epsilon} = 0 & \text{in } \Omega_{\epsilon} \times I, \\ \mathbf{u}_{\epsilon} = \mathbf{0} & \text{on } \partial \Omega_{\epsilon} \times I, \\ \mathbf{u}_{\epsilon}(\mathbf{x}, 0) = \mathbf{u}_{0, \epsilon} & \text{in } \Omega_{\epsilon}, \end{cases} \quad (2.126)$$

where $\mathbf{u}_{\epsilon}: \Omega_{\epsilon} \times I \rightarrow \mathbb{R}^d$ denotes the velocity field, $p_{\epsilon}: \Omega_{\epsilon} \times I \rightarrow \mathbb{R}$ is the scalar-valued pressure, $\mathbf{F} \in L^2(I; L^2(\Omega_{\epsilon})^d)$ defines a given force, $\nu > 0$ is a constant viscosity, and $\partial \Omega_{\epsilon}$ is supposed to be sufficiently regular.

Remark 2.5.3. Note that the individual terms of (2.126) are properly rescaled by prefactors of ϵ to ensure a non-vanishing limit velocity [11].

Further, following [82], let

$$\begin{cases} \mathbf{u}_{0,\epsilon} \in L^2(\Omega_\epsilon)^d, \\ \operatorname{div}_{\mathbf{x}} \mathbf{u}_{0,\epsilon} = 0 & \text{in } \Omega_\epsilon, \\ \mathbf{u}_{0,\epsilon} \cdot \mathbf{n} = 0 & \text{on } \partial\Omega_\epsilon, \end{cases} \quad (2.127)$$

where \mathbf{n} is the outward pointing normal vector. In this configuration, at least one weak solution to (2.126) exists [82], which is obtained in $\mathbf{u}_\epsilon \in L^2(I; H^1(\Omega_\epsilon)^d)$ and $p_\epsilon \in H^{-1}(I; L^2_0(\Omega_\epsilon))$, respectively [189]. To formulate the evolutionary version of Theorem 2.5.1, the works of Feireisl *et al.* [82], Allaire [9], and Mikelić [188] serve as a basis. Since only parts of the limit cases have been proven, we formulate the following conjecture.

Definition 2.5.1. Let

$$\begin{cases} \partial_t \mathbf{w}^j - \nu \Delta_{\mathbf{x}} \mathbf{w}^j + \nabla_{\mathbf{x}} \pi^j = \mathbf{0} & \text{in } Y_F \times I, \\ \operatorname{div}_{\mathbf{x}} \mathbf{w}^j = 0 & \text{in } Y_F \times (0, T), \\ \mathbf{w}^j(\mathbf{x}, 0) = \mathbf{e}^j & \text{in } Y_F, \\ \mathbf{w}^j = \mathbf{0} & \text{on } (\partial Y_S \setminus \partial Y) \times I \end{cases} \quad (2.128)$$

define a time-dependent unit cell problem [189], where \mathbf{w}^j is $H^1(Y)$ -periodic and π^j is $L^2(Y)$ -periodic. The matrix $\tilde{\mathbf{A}}(t)$ is then assembled through

$$\tilde{A}_{ij}(t) = \frac{1}{|Y|} \int_{Y_F} w_j^i(\mathbf{y}, t) \, d\mathbf{y}, \quad (2.129)$$

for $1 \leq i, j \leq d$.

Conjecture 2.5.1. Let $(\tilde{\mathbf{u}}_\epsilon, \tilde{p}_\epsilon)$ be a weak solution to (2.126). According to the scaling regimes of the obstacle size, we distinguish between the following homogenization limits.

(i) If the obstacles are too small, i.e. $\lim_{\epsilon \searrow 0} \sigma_\epsilon = +\infty$, then $(\tilde{\mathbf{u}}_\epsilon, \tilde{p}_\epsilon)$ converges to (\mathbf{u}, p) , a solution of the nonstationary nonlinear NSE

$$\begin{cases} \partial_t \mathbf{u} + \mathbf{u} \cdot \nabla_{\mathbf{x}} \mathbf{u} - \nu \Delta_{\mathbf{x}} \mathbf{u} = \mathbf{F} - \nabla_{\mathbf{x}} p & \text{in } \Omega, \\ \operatorname{div}_{\mathbf{x}} \mathbf{u} = 0 & \text{in } \Omega, \\ \mathbf{u} = \mathbf{0} & \text{on } \partial\Omega. \end{cases} \quad (2.130)$$

(ii) If the obstacles have a critical size, i.e. $\lim_{\epsilon \searrow 0} \sigma_\epsilon = \sigma > 0$, then $(\tilde{\mathbf{u}}_\epsilon, \tilde{p}_\epsilon)$ converges in $L^2(\Omega \times I)$ and weakly in $L^2(I; W_0^{1,2}(\Omega))$ to (\mathbf{u}, p) , respectively, a solution of the nonstationary nonlinear BL

$$\begin{cases} \partial_t \mathbf{u} + \mathbf{u} \cdot \nabla_{\mathbf{x}} \mathbf{u} - \nu \Delta_{\mathbf{x}} \mathbf{u} + \frac{\nu}{\sigma^2} \mathbf{M} \mathbf{u} = \mathbf{F} - \nabla_{\mathbf{x}} p & \text{in } \Omega, \\ \operatorname{div}_{\mathbf{x}} \mathbf{u} = 0 & \text{in } \Omega, \\ \mathbf{u} = \mathbf{0} & \text{on } \partial\Omega. \end{cases} \quad (2.131)$$

(iii) If the obstacles are smaller than $\mathcal{O}(\epsilon)$, but exceed the critical size, such that $\lim_{\epsilon \searrow 0} \sigma_\epsilon = 0$, then a suitably rescaled version of $(\tilde{\mathbf{u}}_\epsilon, \tilde{p}_\epsilon)$ converges to (\mathbf{u}, p) , the unique solution of the time-dependent DL

$$\begin{cases} \partial_t \mathbf{u} + \nu \mathbf{M} \mathbf{u} = \mathbf{F} - \nabla_{\mathbf{x}} p & \text{in } \Omega \times I, \\ \operatorname{div}_{\mathbf{x}} \mathbf{u} = 0 & \text{in } \Omega, \\ \mathbf{u} = \mathbf{0} & \text{on } \partial\Omega. \end{cases} \quad (2.132)$$

(iv) If the obstacles are of size $\mathcal{O}(\epsilon)$, then the rescaled solution $(\epsilon^2 \tilde{\mathbf{u}}_\epsilon, \partial_t \tilde{p}_\epsilon)$ converges in $L^2(I; \Omega)^d$ and weakly in $H^{-1}(I; L_0^2(\Omega))$, respectively to (\mathbf{u}, p) , the unique solution of the DL with memory

$$\begin{cases} \nu \mathbf{u} - \tilde{\mathbf{A}}(t) \mathbf{u}_0 = \int_0^t \tilde{\mathbf{A}}(t-s) [\mathbf{F}(s) - \nabla_{\mathbf{x}} p(s)] \, ds & \text{in } \Omega, \\ \operatorname{div}_{\mathbf{x}} \mathbf{u} = 0 & \text{in } \Omega, \\ \mathbf{u} = \mathbf{0} & \text{on } \partial\Omega. \end{cases} \quad (2.133)$$

Further, if the flow stabilizes after a finite period of time, the DL with memory (2.133) contracts for $t \rightarrow \infty$ to the classical DL (2.119) with

$$A_{ij} = \int_0^\infty \tilde{A}_{ij}(t) \, dt, \quad (2.134)$$

for $1 \leq i, j, \leq d$.

In the regimes (i-iii), \mathbf{M} is the same $d \times d$ symmetric matrix as in Proposition 2.5.2 and depends only on the model obstacle Y_S^m . In case of (iv), $\tilde{\mathbf{A}}(t)$ is constructed from Definition 2.5.1.

Proof of cases (ii) and (iv). In contrast to the stationary case, only some of the limiting proofs in Conjecture 2.5.1 and none of the interconnections of cases have been established yet. Hence we recall the available proofs only.

Case (ii). Feireisl *et al.* [82] consider obstacles of critical size smaller than $\mathcal{O}(\epsilon)$ and propose a differing methodology to the one used by Allaire to pass to the limit equations. Via the techniques used therein, the above assumptions on the shape and location of the obstacles can be loosened. The resulting homogenized equations however, are a BL which is similar to the one obtained in the framework introduced above. Thus, the limit in case (ii) is proven.

Case (iv). Mikelić [189, Theorem 1.2 (with $\beta = 4$)] completely covers the present setting for this size of obstacles which proves this case. \square

Remark 2.5.4. Cases (i) and (iii) are based on the conclusive evidence which has been stated for example in [6, 82] that this extension is possible in a similar manner. Starting from the homogenization limits of the nonstationary Stokes equations established in [9] could also be promising, since as stated in [6], the inclusion of a nonlinear advective term to the Stokes equations resembles a compact perturbation of the ϵ -dependent stationary nonlinear NSE (2.111). It is also notable that for case (iii), a proof for the homogenization of the evolutionary Stokes equations (without the nonlinear advective term) is given in [9]. Concerning the low volume fraction limit which connects cases (iv) to (iii), the memory effective terms of the DL with memory (2.133) might induce the time-dependency in the time-dependent DL (2.132). Hence, an import of stationary effects and an additional solving for time-dependent eigenvalue problems in respective cell spaces [5] might be insightful.

2.5.4 Applicability of the homogenized model

Assumption 2.5.1. To establish a connection to experimentally conforming model equations, we make the following assumptions:

1. According to [23, 189], the stabilization of the DL with memory (2.133) toward the classical DL (2.119) is understood to happen in a short period of time. Hence, we assume a stabilized flow in case of obstacle sizes which obey Conjecture 2.5.1 case (iv), i.e. the homogenization limit is constituted by an ordinary DL. Similarly, we assume stabilization for case (iii). Typically this involves adding Brinkman terms (diffusion) or other necessary features to the DL in case (iv). Though these artificial features are effective in the void and within the porous–void interface, they are contracted to zero within the porous media under the necessary local assumptions of highly viscous and stabilized (stationary) flow.
2. The porosity is determined to be constant in Ω_T .
3. The medium is isotropic, which results in regular symmetric, hence diagonal or diagonalizable matrices \mathbf{M} and \mathbf{A} . Further, we may thus reduce the matrix \mathbf{A} or \mathbf{M}^{-1} to its only eigenvalue, which yields a scalar multiplication. Below we assume this simplification and unless stated otherwise, denote the single eigenvalue of \mathbf{A} with A .

Remark 2.5.5. Assumption 2.5.1 explains the commonly formulated Brinkman equation [122, 198], which is constituted by a classical DL plus a diffusion term. Neglecting the time-dependency in the BL derived above as well as its inertial terms, results in a simplified equation which solely respects diffusion. To match the porous–void interface, Spaid and Phelan [238] used such a Brinkman equation as a stationary limit for their simulations. A note in [238] additionally states that far from the interface, and within the porous domain region, the governing equation reduces again, to the classical DL [238]. It is however notable that along the stationary limit, the nonstationary solution to the method in [238] is rather a BL as presently formulated, which was not further examined therein.

For $d = 3$ (see Figure 2.1b, σ_ϵ describes the square root of the ratio of the cell volume to the obstacle diameter

$$\sigma_\epsilon = \left(\frac{\epsilon^3}{a_\epsilon} \right)^{\frac{1}{2}}. \quad (2.135)$$

We use the classical notion of porosity [122] to assess the above framework in terms of applicability.

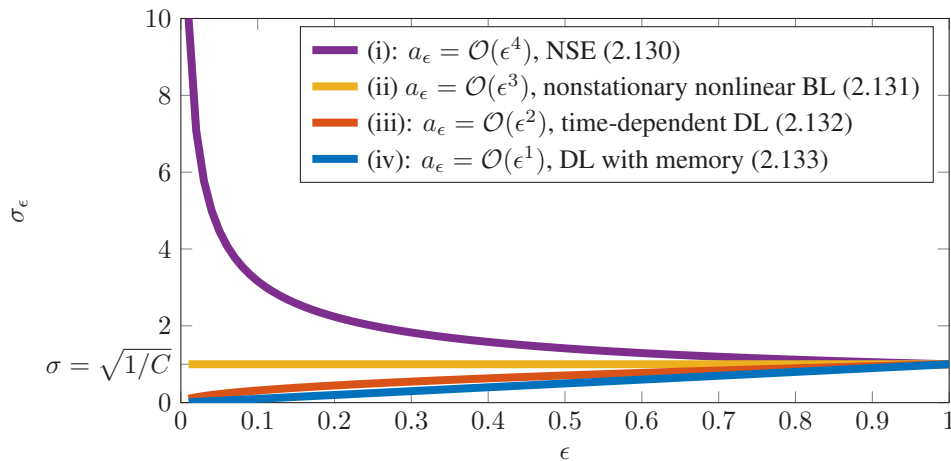


Figure 2.2: Graph of ratio $\sigma_\epsilon(\epsilon)$ (2.135) for $d = 3$ and $C = 1$.

Proposition 2.5.3. For Conjecture 2.5.1(iv) we obtain the minimal porosity of $\varphi \approx 0.4764$.

Proof. Recalling Conjecture 2.5.1, the size a_ϵ of the obstacles for $d = 3$ can be distinguished as follows. Let $C > 0$.

- (i) Let $a_\epsilon = C\epsilon^4 = \mathcal{O}(\epsilon^4)$. Then $\sigma_\epsilon = \left(\frac{1}{C\epsilon} \right)^{\frac{1}{2}} \Rightarrow \lim_{\epsilon \searrow 0} \sigma_\epsilon = +\infty$.

(ii) Let $a_\epsilon = C\epsilon^3 = \mathcal{O}(\epsilon^3)$. Then $\sigma_\epsilon = \left(\frac{1}{C}\right)^{\frac{1}{2}} \Rightarrow \lim_{\epsilon \searrow 0} \sigma_\epsilon = \sigma > 0$.

(iii) Let $a_\epsilon = C\epsilon^2 = \mathcal{O}(\epsilon^2)$. Then $\sigma_\epsilon = \left(\frac{\epsilon}{C}\right)^{\frac{1}{2}} \Rightarrow \lim_{\epsilon \searrow 0} \sigma_\epsilon = 0$.

(iv) Let $a_\epsilon = C\epsilon^1 = \mathcal{O}(\epsilon^1)$. Then $\sigma_\epsilon = \left(\frac{\epsilon^2}{C}\right)^{\frac{1}{2}} \Rightarrow \lim_{\epsilon \searrow 0} \sigma_\epsilon = 0$.

The limits of σ_ϵ for all cases are plotted in Figure 2.2 with a fixed constant $C = 1$. Subsequent to forming the porosity parameter φ as the ratio of void and full domain, the injection of the magnitude approximation implies physical reasoning for the specific homogenization limit equations. By definition, we obtain

$$\varphi = \frac{|\Omega_\epsilon|}{|\Omega|} = \frac{\left| \Omega - \bigcup_{i=1}^{N(\epsilon)} Y_{S,i}^\epsilon \right|}{|\Omega|} = 1 - \frac{\left| \bigcup_{i=1}^{N(\epsilon)} Y_{S,i}^\epsilon \right|}{|\Omega|} = 1 - \frac{\pi a_\epsilon^3}{6\epsilon^3} = \begin{cases} 1 - \frac{C\pi}{6}\epsilon^9 & \text{in case (i),} \\ 1 - \frac{C\pi}{6}\epsilon^6 & \text{in case (ii),} \\ 1 - \frac{C\pi}{6}\epsilon^3 & \text{in case (iii),} \\ 1 - \frac{C\pi}{6} & \text{in case (iv)} \end{cases} \quad (2.136)$$

$$\xrightarrow{\epsilon \searrow 0} \begin{cases} 1 & \text{in cases (i-iii),} \\ 1 - \frac{C\pi}{6} & \text{in case (iv),} \end{cases} \quad (2.137)$$

where $|\cdot|$ denotes the Lebesgue measure of the standard Euclidean space. \square

Remark 2.5.6. Proposition 2.5.3 frames the modeling possibilities of the presented approach, since the minimal attainable porosity is similar to a square sphere packing [100, 198].

Remark 2.5.7. A lower porosity could be obtained by considering three-dimensional flow through two-dimensional porous media, or by choosing three-dimensional obstacles in different arrangements [58, 198]. Whereas the former becomes reasonable when modeling for example fibers as obstacles with a circular cross-section [17] and repeating above calculations for $d = 2$, the latter renders rather complicated, due to the necessity of proving Conjecture 2.5.1 under loosened initial topological assumptions on the obstacles [82]. The question if all four cases would be retained under a differentiability-breaking change of shape or cell-crossing shifts in location, remains to be answered.

Remark 2.5.8. Under Assumption 2.5.1 we formulate a unified BL for case Conjecture 2.5.1(ii) below (Definition 2.5.2), which depends on σ and formally limits

- either to the nonstationary nonlinear NSE in case (i) for $\sigma \rightarrow \infty$
- or (via rescaling the solution to $\tilde{\mathbf{u}}/\sigma_\epsilon^2$) to the stabilized DL in case (iii) and (iv) for $\sigma \searrow 0$.

Further, since the continuity in the low volume fraction limit [5] implies that \mathbf{M}^{-1} is the limit of \mathbf{A} , we use \mathbf{A} in the modified BL and, due to Assumption 2.5.1(3.), reduce it to its single eigenvalue A . In summary, the resulting model equation is assumed to be valid for all herein considered porosities and permeabilities. We additionally motivate the procedure of emulating all four regimes by recent observations that turbulence prevails for porosity values approaching unity in aligned arrays of spheres [212].

Definition 2.5.2. Based on Conjecture 2.5.1, Assumption 2.5.1, Proposition 2.5.3 and Remark 2.5.8, we construct a unified nonstationary nonlinear BL

$$\begin{cases} \partial_t \mathbf{u} + \mathbf{u} \cdot \nabla_{\mathbf{x}} \mathbf{u} - \nu \Delta_{\mathbf{x}} \mathbf{u} + \frac{\nu}{\sigma^2} A^{-1} \mathbf{u} = \mathbf{F} - \nabla_{\mathbf{x}} p & \text{in } \Omega, \\ \operatorname{div}_{\mathbf{x}} \mathbf{u} = 0 & \text{in } \Omega, \\ \mathbf{u} = \mathbf{0} & \text{on } \partial\Omega, \end{cases} \quad (2.138)$$

which is used as a target PDE system for the LBM derivations and computer simulations further below in Chapters 3 and 4. Due to the unified perspective, the PDE system (2.138) is now referred to as homogenized NSE (HNSE).

2.6 Coupled systems

For the purpose of simulating fluid mixture flows [47] with diffuse-interface methods based on LBMs, we use coupled PDEs akin to the Navier–Stokes–Cahn–Hilliard equations (NSCHE) as target systems. Taylor [245] established experimental machinery to study the deformations of droplets induced by shear and extensional flow of binary fluids. Here, the latter refers to a fluid mixture consisting of two components. The deformation of the interface is dictated by the balance of surface tension and external forces. Once in favor of deformation, the droplet will break apart. The breakup process can be modified in terms of the resulting droplet size distribution. This is of primary interest for example in manufacturing processes, where the efficiency of creating emulsions is to be maximized [46, 257]. When simulating multicomponent or multiphase flows with LBMs, the diffuse interfacial zone brings forth additional physics. The added dynamics can be described by coupling the CHE to the NSE, where free energy models (FRMs) (e.g. [224, 242]) offer consistent thermodynamics to derive the chemical potential μ_ϕ . The dynamics of a binary fluid can be categorized among others into shear and extensional flows. A specific free energy LBM to approximate a coupled PDE model for a simple binary fluid (equal density and viscosity) is described and tested for such dynamic configurations further below (see Sections 3.3 and 4.6, respectively). Here, we derive the target PDE system. The ternary FRM by Semprebon *et al.* [224] is simplified to obtain the target PDEs for binary fluid flow. Subsequently, we indicate its asymptotic equivalence in the formal incompressible limit to the target equations of the FRM proposed by Kendon *et al.* [150]. In addition, both models are extended to higher order FRMs for sharpening the diffuse interface².

2.6.1 Free energy models

Definition 2.6.1. Let $\Omega \subseteq \mathbb{R}^d$. We define the free energy functional

$$\Psi(\phi(\mathbf{x})) = \int_{\Omega} (f_B + f_I)(\mathbf{x}, \phi(\mathbf{x}), \nabla_{\mathbf{x}}\phi(\mathbf{x}), \nabla_{\mathbf{x}}^2\phi(\mathbf{x}), \dots, \nabla_{\mathbf{x}}^K\phi(\mathbf{x})) \, d\mathbf{x}, \quad (2.139)$$

where $f_B: \Omega_T \rightarrow \mathbb{R}$ denotes the bulk free energy and $f_I: \Omega_T \rightarrow \mathbb{R}$ is the interfacial free energy. Here and below, we occasionally suppress other arguments of the order parameter such as time.

Definition 2.6.2. The chemical potential μ_ϕ required for the CHE (2.11) is then computed by the functional derivative $\delta_\cdot = \delta/(\delta\cdot)$ of Ψ with respect to the order parameter $\phi(\mathbf{x})$, thus

$$\mu_\phi = \delta_\phi \Psi(\phi) = \partial_\phi(f_B + f_I) + \sum_{k=1}^K (-1)^k \nabla_{\mathbf{x}}^k \cdot \partial_{\nabla_{\mathbf{x}}^k \phi} (f_B + f_I). \quad (2.140)$$

Definition 2.6.3. The thermodynamic pressure tensor $\mathbf{P}^{\text{th}}: \mathfrak{R} \rightarrow \mathbb{R}^{d \times d}$ is split into

$$\mathbf{P}^{\text{th}} = \mathbf{P}^{\text{ch}} + P\mathbf{I}_d, \quad (2.141)$$

where $P: \Omega_T \rightarrow \mathbb{R}$ is the unscaled isotropic pressure and $\mathbf{P}^{\text{ch}}: \Omega_T \rightarrow \mathbb{R}^{d \times d}$ is the partly anisotropic chemical pressure tensor [150, 242].

² Parts of this section are reproduced from [235], Copyright (2023), with permission from the authors and the American Institute of Mathematical Sciences.

Remark 2.6.1. The corresponding thermodynamics for multiphase and multicomponent flow can be modeled consistently through \mathbf{P}^{chem} . For single phase and single component flow, \mathbf{P}^{th} reduces to $P\mathbf{I}_d$.

The FRM structure typically used for simulating multicomponent fluid flow with LBMs is based on the isothermal, weakly compressible NSE coupled to the CHE for capturing the interface dynamics via \mathbf{P}^{th} and μ_ϕ , respectively as

$$\begin{cases} \partial_t \rho + \operatorname{div}_{\mathbf{x}}(\rho \mathbf{u}) = 0 & \text{in } \Omega_T, \\ \partial_t(\rho \mathbf{u}) + \operatorname{div}_{\mathbf{x}}(\rho \mathbf{u} \otimes \mathbf{u}) = \operatorname{div}_{\mathbf{x}}\{\eta[\nabla_{\mathbf{x}} \mathbf{u} + (\nabla_{\mathbf{x}} \mathbf{u})^T] + \tilde{\eta}(\operatorname{div}_{\mathbf{x}} \mathbf{u}) \mathbf{I}_d\} - \operatorname{div}_{\mathbf{x}} \mathbf{P}^{\text{th}} + \mathbf{F} & \text{in } \Omega_T, \\ \partial_t \phi + \operatorname{div}_{\mathbf{x}}(\phi \mathbf{u}) = M_\phi \Delta_{\mathbf{x}} \mu_\phi & \text{in } \Omega_T, \end{cases} \quad (2.142)$$

where $\rho: \Omega_T \rightarrow \mathbb{R}$ denotes the density, $\mathbf{u}: \Omega_T \rightarrow \mathbb{R}^d$ is the fluid velocity, $\eta > 0$ is a dynamic viscosity, and the factor $\tilde{\eta} = (\eta_B - 2\eta/3) \geq 0$ contains the bulk viscosity $\eta_B \geq 0$. Complemented with respective initial and boundary conditions, (2.142) forms a closed system. Additionally, to form the final FRM, definitions for \mathbf{P}^{th} , μ_ϕ and \mathbf{F} have to be supplied.

Remark 2.6.2. Alternatively to the pressure-based thermodynamic coupling via \mathbf{P}^{th} , for example to uphold the pressure structure in the weakly compressible NSE for computational purposes, the thermodynamics can be injected through the force field. Defining

$$\mathbf{F} \leftarrow \mathbf{F}^{\text{th}} = \mathbf{F} - \operatorname{div}_{\mathbf{x}} \mathbf{P}^{\text{ch}} \quad (2.143)$$

and reducing $\mathbf{P}^{\text{th}} = P\mathbf{I}_d$, will lead to a similar PDE system.

The FRM proposed by Kendon *et al.* [150] (KFRM) is based on the following definitions.

Definition 2.6.4. The KFRM defines the interfacial free energy between two continuous phases as

$$f_{\text{I}}^{\text{K}}(\phi) = \frac{\kappa}{2} |\nabla_{\mathbf{x}} \phi|^2, \quad (2.144)$$

where $\kappa > 0$ is a constant related to the mixture properties. The bulk free energy as

$$f_{\text{B}}^{\text{K}}(\phi) = -\frac{1}{2}A\phi^2 - \frac{1}{4}B\phi^4 + \frac{1}{3}\rho \ln(\rho), \quad (2.145)$$

where $A > 0$ is a model parameter.

Proposition 2.6.1. *The chemical potential of the KFRM is*

$$\mu_\phi^{\text{K}}(\phi) = -A\phi - B\phi^3 - \kappa \Delta_{\mathbf{x}} \phi. \quad (2.146)$$

Proof. We compute (2.140) from Definition 2.6.2 to obtain

$$\begin{aligned} \mu_\phi^{\text{K}} &= \partial_\phi (f_{\text{B}}^{\text{K}} + f_{\text{I}}^{\text{K}}) - \nabla_{\mathbf{x}} \cdot \partial_{\nabla_{\mathbf{x}} \phi} (f_{\text{B}}^{\text{K}} + f_{\text{I}}^{\text{K}}) \\ &= -A\phi - B\phi^3 - \nabla_{\mathbf{x}} \cdot \partial_{\nabla_{\mathbf{x}} \phi} \left(\frac{\kappa}{2} |\nabla_{\mathbf{x}} \phi|^2 \right). \end{aligned} \quad (2.147)$$

□

Definition 2.6.5. We define the divergence of the chemical pressure tensor for the KFRM as

$$\operatorname{div}_{\mathbf{x}} \mathbf{P}^{\text{th,K}} = \overbrace{\phi \nabla_{\mathbf{x}} \mu_\phi^{\text{K}}} = \operatorname{div}_{\mathbf{x}} \mathbf{P}^{\text{ch,K}} + \nabla_{\mathbf{x}} P$$

$$= -A\phi\nabla_{\mathbf{x}}\phi + B\phi\nabla_{\mathbf{x}}\phi^3 - \kappa\phi\nabla_{\mathbf{x}}^3\phi + \nabla_{\mathbf{x}}P. \quad (2.148)$$

For simplicity, we choose $B = -A$. Solving for $\mu_{\phi}^K = 0$ on a planar interface, we obtain the representative one-dimensional profile

$$\phi(x) = \phi^* \tanh\left(\frac{x}{\xi^K}\right), \quad (2.149)$$

with the equilibrium values $\phi^* = \pm\sqrt{A/(-B)} = \pm 1$ and the interface thickness

$$\xi^K = \sqrt{\frac{2\kappa}{A}}. \quad (2.150)$$

Remark 2.6.3. The bulk free energy f_B^K depends on the chosen model for the components or phases. The gradient of the order parameter $\phi \in [-1; 1]$ increases the total free energy across the interface. This results in an interface minimization in order to minimize the overall free energy.

Via the deriving the excess free energy [150] the surface tension reads

$$\sigma^K = \int_{-\phi^*}^{+\phi^*} \{2\kappa [f_B^K(\phi) - f_B^K(\phi^*)]\}^{\frac{1}{2}} d\phi \quad (2.151)$$

$$= \frac{4}{3}\kappa \frac{(\phi^*)^2}{\xi^K} \quad (2.152)$$

$$= \frac{4\kappa}{3\xi^K}. \quad (2.153)$$

The FRM proposed by Semprebon *et al.* [224] (SFRM) is based on the following definitions.

Definition 2.6.6. The SFRM defines the interfacial free energy between two continuous phases as

$$f_I^S(\phi) = \frac{\alpha^2\kappa_1}{8}(\nabla_{\mathbf{x}}\rho + \nabla_{\mathbf{x}}\phi)^2 + \frac{\alpha^2\kappa_2}{8}(\nabla_{\mathbf{x}}\rho - \nabla_{\mathbf{x}}\phi)^2, \quad (2.154)$$

where $\kappa_1, \kappa_2, \alpha > 0$ are constants related to the mixture properties. The bulk free energy as

$$f_B^S(\phi) = \frac{\kappa_1}{32}(\rho + \phi)^2(\rho + \phi - 2)^2 + \frac{\kappa_2}{32}(\rho - \phi)^2(\rho - \phi - 2)^2. \quad (2.155)$$

Proposition 2.6.2. *The chemical potentials of the SFRM are*

$$\begin{aligned} \mu_{\rho}^S &= \frac{\delta\Psi}{\delta\rho} = \frac{\kappa_1}{8}(\rho + \phi)(\rho + \phi - 2)(\rho + \phi - 1) + \frac{\kappa_2}{8}(\rho - \phi)(\rho - \phi - 2)(\rho - \phi - 1) \\ &\quad + \frac{\alpha^2}{4} [(\kappa_1 + \kappa_2)(-\nabla_{\mathbf{x}}^2\rho) + (\kappa_2 - \kappa_1)\nabla_{\mathbf{x}}^2\phi] \end{aligned} \quad (2.156)$$

and

$$\begin{aligned} \mu_{\phi}^S &= \frac{\delta\Psi}{\delta\phi} = \frac{\kappa_1}{8}(\rho + \phi)(\rho + \phi - 2)(\rho + \phi - 1) - \frac{\kappa_2}{8}(\rho - \phi)(\rho - \phi - 2)(\rho - \phi - 1) \\ &\quad + \frac{\alpha^2}{4} [(\kappa_1 + \kappa_2)(-\nabla_{\mathbf{x}}^2\phi) + (\kappa_2 - \kappa_1)\nabla_{\mathbf{x}}^2\rho]. \end{aligned} \quad (2.157)$$

Proof. We compute (2.140) from Definition 2.6.2 for both ρ and ϕ , respectively. The complete derivation is given in [224]. \square

Definition 2.6.7. We define the divergence of the chemical pressure tensor for the SFRM as

$$\operatorname{div}_{\mathbf{x}} \mathbf{P}^{\text{th},S} = \overbrace{\rho \nabla_{\mathbf{x}} \mu_{\rho}^S + \phi \nabla_{\mathbf{x}} \mu_{\phi}^S}^{= \operatorname{div}_{\mathbf{x}} \mathbf{P}^{\text{ch},S}} + \nabla_{\mathbf{x}} P. \quad (2.158)$$

An explicit definition of $\mathbf{P}^{\text{th},S}$ is given in [224]. For simplicity, we choose $\kappa_2 = \kappa_1$. In terms of the concentration fractions C_m of component $m = 1, 2$, where

$$\rho = C_1 + C_2, \quad (2.159)$$

$$\phi = C_1 - C_2, \quad (2.160)$$

a representative one-dimensional profile is obtained [224]

$$C_m(x) = \frac{1 + \tanh\left(\frac{x}{\xi^S}\right)}{2}, \quad (2.161)$$

with the equilibrium values $C_m^{\text{eq}} \in \{0, 1\}$ and the interface thickness

$$\xi^S = 2\alpha. \quad (2.162)$$

Via the deriving the excess free energy [224] the surface tension reads

$$\begin{aligned} \sigma^S &= \frac{\alpha}{6} (\kappa_1 + \kappa_2) \\ &= \frac{\alpha \kappa_1}{3}. \end{aligned} \quad (2.163)$$

Remark 2.6.4. A mixture flow with three or more components can be realized in a straightforward extension of the equation system (2.142) by adding a similarly coupled CHE (through pressure or force) for each additional order parameter [224].

Proposition 2.6.3. *In a formal incompressible limit, the KFRM is a special case of the SFRM.*

Proof. With $\kappa_2 = \kappa_1$, the chemical potentials simplify to

$$\mu_{\rho}^S = \frac{\kappa_1}{4} (\rho - 1) (\rho^2 - 2\rho + 3\phi^2) - \frac{\alpha^2 \kappa_1}{2} \Delta_{\mathbf{x}} \rho, \quad (2.164)$$

$$\mu_{\phi}^S = \frac{\kappa_1}{4} \phi [\phi^2 + (3\rho^2 - 6\rho + 2)] - \frac{\alpha^2 \kappa_1}{2} \Delta_{\mathbf{x}} \phi, \quad (2.165)$$

respectively. Thus, the incompressible limit yields

$$\lim_{\rho \rightarrow 1} \mu_{\rho}^S = 0, \quad (2.166)$$

$$\lim_{\rho \rightarrow 1} \mu_{\phi}^S = \frac{\kappa_1}{4} \phi (\phi^2 - 1) - \frac{\alpha^2 \kappa_1}{2} \Delta_{\mathbf{x}} \phi. \quad (2.167)$$

Identifying the parameters, we obtain

$$A = \frac{\kappa_1}{4}, \quad (2.168)$$

$$\kappa = \frac{\alpha^2 \kappa_1}{2}, \quad (2.169)$$

and thus $\xi^S = \xi^K$ and $\sigma^S = \sigma^K$. \square

Remark 2.6.5. In the case of $\kappa_2 \neq \kappa_1$, the incompressible limit yields the respective chemical potentials

$$\lim_{\rho \rightarrow 1} \mu_\rho^S = \frac{\kappa_1 - \kappa_2}{8} \phi (\phi^2 - 1) - \frac{\alpha^2 (\kappa_1 - \kappa_2)}{4} \Delta_{\mathbf{x}} \phi, \quad (2.170)$$

$$\lim_{\rho \rightarrow 1} \mu_\phi^S = \frac{\kappa_1 + \kappa_2}{8} \phi (\phi^2 - 1) - \frac{\alpha^2 (\kappa_1 + \kappa_2)}{4} \Delta_{\mathbf{x}} \phi, \quad (2.171)$$

which frames the difference between the SFRM and the KFRM in terms of the tunability parameters κ_1 and κ_2 preceding the added thermodynamical pressure derivatives via the additional chemical potential with respect to ρ .

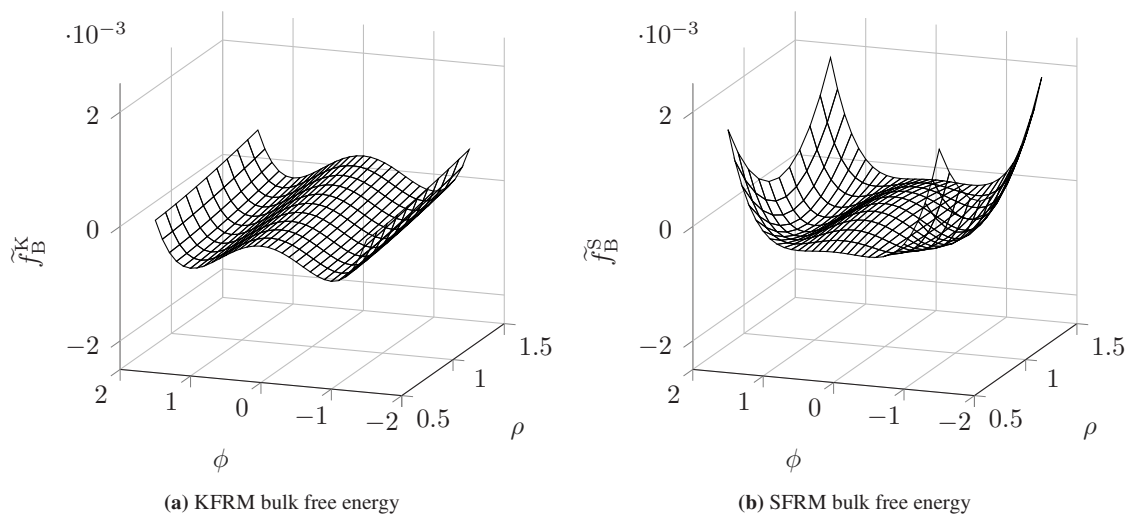


Figure 2.3: Double-well bulk free energy potentials of (a) the KFRM and (b) the SFRM. For the purpose of illustration, the values are scaled around null ($\tilde{f}_B^K = f_B^K - ((1 - 10^{-3})/3)\rho \ln(\rho)$ and $\tilde{f}_B^S = f_B^S - (\kappa_1 + \kappa_2)/32$) and cut off. The exemplary parameters $A = 0.002$, $B = -A$, $\kappa_1 = 0.008 = \kappa_2$ are chosen.

Remark 2.6.6. Proposition 2.6.3 and Remark 2.6.5 underline the differences of the models, which take effect mostly at density variations around unity. Whereas the bulk free energy potential of the SFRM is symmetric in the variations in ρ (double-well with minima at $\rho \in \{0, 2\}$), the KFRM has a with ρ increasing potential in the bulk free energy. Scaled versions of the double-well potentials of both models are visualized in Figure 2.3.

2.6.2 Higher order free energy models

Mass leakage, or more specifically volume loss of subcritical droplet sizes is known to be a fundamental mechanism in diffuse interface CHE models akin to FRMs. Particularly in the context of LBM simulations, Zheng *et al.* [279] proposed an estimate for the critical droplet radius such that any smaller droplet will vanish due to volume loss in a FRM LBM multiphase flow simulation. Previous results, relating the spontaneous drop shrinkage to the interface thickness, have been obtained for phase-field finite-element simulations by Yue *et al.* [271]. Shin *et al.* [227] have proposed a remedy for the volume loss via increasing the polynomial order of the bulk free energy in ϕ . As a consequence of the higher order leading terms in ϕ , the shape of the bulk free energy is steepened in the outer region near the minima and flattened in between. The positive effect of this polynomial reshaping (see Figure 2.4) is based on the following reasoning. The requirement $\phi = \pm 1$ in the bulk depends on the comparably negligible volume of the interface. Hence,

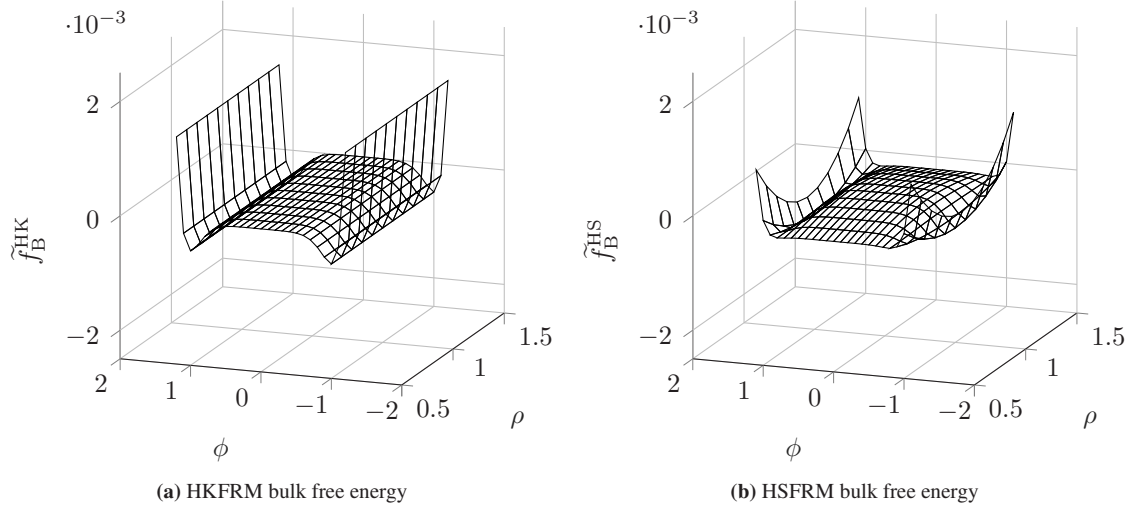


Figure 2.4: Double-well bulk free energy potentials of (a) the HKFRM and (b) the HSFRM, both for $m = 6$. For the purpose of illustration, the values are scaled around null ($\hat{f}_B^{\text{HK}} = f_B^{\text{HK}} - ((1 - 10^{-3})/3)\rho \ln(\rho)$ and $\hat{f}_B^{\text{HS}} = f_B^{\text{HS}} - (\kappa_1 + \kappa_2)/32$) and cut off. The exemplary parameters $A = 0.002$, $B = -A$, $\kappa_1 = 0.008 = \kappa_2$ are chosen.

only the bulk free energy should influence the energy minimization. Since this is not the case for nonplanar interfaces (e.g. droplets), the free energy is also concentrated on the interface. Based on the finiteness of the bulk volume, it is thus possible to reduce the total energy via shifting ϕ and shrinking the drop at the same time (cf. [271, Figure 1]). Henceforth, the energy exchange between bulk and interface moves its location causing a loss of volume when deforming an initially equilibrated drop by shear or extensional flow. Numerically, a careful parameter choice or adaptive discretization near the interface can ensure small ratios of interface width to drop radius a , i.e. small Cahn numbers, and thus reduces the volume loss [271]. From a modeling perspective, the shape of the free energy determines the strength of volume loss, which is minimized when using higher order polynomial bulk functionals. Thus, we extend the approach of Shin *et al.* [227] to steepen the KFRM and the SFRM with a flexible higher order leading term.

Definition 2.6.8. For $B = -A$, the bulk free energy of the higher order KFRM (HKFRM) reads

$$f_{B,m}^{\text{HK}}(\phi) = \frac{1}{4}A(\phi^m - 1)^2 - \frac{1}{4}A + \frac{1}{3}\rho \ln(\rho). \quad (2.172)$$

Remark 2.6.7. The KFRM is a special case of the HKFRM with $f_{B,2}^{\text{HK}} = f_B^{\text{K}}$.

Definition 2.6.9. The bulk free energy of the higher order SFRM (HSFRM) reads

$$f_{B,m}^{\text{HS}} = \frac{\kappa_1}{32}(\rho + \phi^{\frac{m}{2}})^2(\rho + \phi^{\frac{m}{2}} - 2)^2 + \frac{\kappa_2}{32}(\rho - \phi^{\frac{m}{2}})^2(\rho - \phi^{\frac{m}{2}} - 2)^2. \quad (2.173)$$

Remark 2.6.8. The SFRM is a special case of the HSFRM with $f_{B,2}^{\text{HS}} = f_B^{\text{S}}$.

Proposition 2.6.4. For $\kappa_1 = \kappa_2 = 4$, the HSFRM asymptotically leads to the bulk free energy model of Shin *et al.* [227] in the incompressible limit.

Proof. Let $\kappa_1 = \kappa_2$, which yields

$$\begin{aligned} \lim_{\rho \rightarrow 1} f_{B,m}^{\text{HS}} &= \lim_{\rho \rightarrow 1} \frac{\kappa_1}{16} \left\{ [\phi^m + (3\rho^2 - 6\rho + 2)]^2 - (3\rho^2 - 6\rho + 2)^2 + \rho^2(\rho - 2)^2 \right\} \\ &= \frac{\kappa_1}{16} [\phi^m - 1]^2. \end{aligned} \quad (2.174)$$

□

2.6.3 Navier–Stokes–Cahn–Hilliard equations

Taking into consideration the above, we construct the target equation which models incompressible binary fluid flow and is approximated by the (K/S/HK/HS)FRMLBM in the diffusive limit. The chemical potential is chosen according to Kendon *et al.* [150]

$$\mu_\phi = A(\phi - \phi^3) - \kappa \Delta_{\mathbf{x}} \mu_\phi. \quad (2.175)$$

Thus, for the incompressible NSE (2.12) we define a force term

$$\begin{aligned} \mathbf{F}^{\text{th}} &= \mathbf{F} - \phi \nabla_{\mathbf{x}} \mu_\phi \\ &= \mathbf{F} - \phi \nabla_{\mathbf{x}} [A(\phi - \phi^3) - \kappa \Delta_{\mathbf{x}} \phi] \\ &= \mathbf{F} - A\phi (\nabla_{\mathbf{x}} \phi - \nabla_{\mathbf{x}} \phi^3) + \kappa \phi \nabla_{\mathbf{x}}^3 \phi. \end{aligned} \quad (2.176)$$

The coupling term in the CHE (2.11) is then explicitly written as

$$M_\phi \Delta_{\mathbf{x}} \mu_\phi = AM_\phi (\Delta_{\mathbf{x}} \phi - \Delta_{\mathbf{x}} \phi^3) - \kappa M_\phi \Delta_{\mathbf{x}}^2 \phi. \quad (2.177)$$

Definition 2.6.10. The incompressible NSCHE for incompressible binary fluid flow reads

$$\begin{cases} \operatorname{div}_{\mathbf{x}}(\mathbf{u}) = 0 & \text{in } \Omega_T, \\ \partial_t \mathbf{u} + \operatorname{div}_{\mathbf{x}}(\mathbf{u} \otimes \mathbf{u}) - \nu \Delta_{\mathbf{x}} \mathbf{u} + \nabla_{\mathbf{x}} p + A\phi (\nabla_{\mathbf{x}} \phi - \nabla_{\mathbf{x}} \phi^3) - \kappa \phi \nabla_{\mathbf{x}}^3 \phi = \mathbf{F} & \text{in } \Omega_T, \\ \partial_t \phi + \mathbf{u} \cdot \nabla_{\mathbf{x}} \phi - AM_\phi (\Delta_{\mathbf{x}} \phi - \Delta_{\mathbf{x}} \phi^3) + \kappa M_\phi \Delta_{\mathbf{x}}^2 \phi = 0 & \text{in } \Omega_T, \\ \mathbf{u}|_{t=0} = \mathbf{u}_0 & \text{in } \Omega, \\ \phi|_{t=0} = \phi_0 & \text{in } \Omega, \end{cases} \quad (2.178)$$

together with appropriate boundary conditions.

2.7 Lyapunov functionals

For determining nonlinear stability of PDEs in terms of dynamical systems, Lyapunov functionals can be used. Let $I \subseteq \mathbb{R}_{\geq 0}$ denote the time horizon and

$$\frac{d}{dt} \mathbf{f}(t) = \mathbf{Q}(\mathbf{f}(t)) \quad (2.179)$$

denote a nonlinear autonomous system, where $\mathbf{f}: I \rightarrow \mathcal{F} \subseteq \mathbb{R}^q$ and $\mathbf{Q}: \mathcal{F} \rightarrow \mathbb{R}^q$ is locally Lipschitz (i.e. existence of constants such that the bounded distance of points in \mathcal{F} implies the distance of function evaluations at these points being bounded). Let $\mathbf{f}^* \in \mathcal{F}$ denote an equilibrium point such that $\mathbf{Q}(\mathbf{f}^*) = 0$. Without loss of generality, we translate the equilibrium point to the origin $\mathbf{f}^* = \mathbf{0}$. Considering the stability of (2.179) at \mathbf{f}^* we use the following definition from [151].

Definition 2.7.1. The equilibrium $\mathbf{f}^* = \mathbf{0}$ is

- stable, if for each $a > 0$, there is $b = b(a) > 0$ such that

$$\|\mathbf{f}(0)\| < b \Rightarrow \|\mathbf{f}(t)\| < a \quad \forall t \geq 0, \quad (2.180)$$

- unstable if it is not stable, and
- asymptotically stable if it is stable and b can be chosen such that

$$\|\mathbf{f}(0)\| < b \Rightarrow \lim_{t \rightarrow \infty} \mathbf{f}(t) = 0. \quad (2.181)$$

Definition 2.7.2. A function $V : \mathcal{F} \rightarrow \mathbb{R}$ of class C^∞ defined on a domain $\mathcal{F} \in \mathbb{R}^q$ that contains the origin is called a Lyapunov function, if

- $V(\mathbf{0}) = 0$,
- $V(\mathbf{f}) > 0$ if $\mathbf{f} \neq \mathbf{0}$,
- $\frac{d}{dt}V(\mathbf{f}) \leq 0$ in \mathcal{F} .

We restate Lyapunov's stability theorem (see [151] and references therein).

Theorem 2.7.1. Let $\mathbf{f}^* = \mathbf{0}$ be an equilibrium point of (2.179). If there exists a Lyapunov function V for \mathbf{f}^* , then the equilibrium point is stable. Further, if

$$\frac{d}{dt}V(\mathbf{f}^*) < 0 \quad \text{in } \mathcal{F} \setminus \mathbf{0}, \quad (2.182)$$

then \mathbf{f}^* is asymptotically stable.

Definition 2.7.3. A functional

$$H: f \mapsto H[f], \quad (2.183)$$

is called Lyapunov functional if $H[f]$ is a Lyapunov function.

Remark 2.7.1. The entropy defined in Boltzmann's H -theorem plays the role of a Lyapunov functional (see e.g. [34]). Moreover, the free energy functional used in the classical stationary CHE can be identified as a Lyapunov functional which leads to well-posedness [33, 71] and the separation of components for $t \rightarrow \infty$.

3 Numerical Methodology

Based on the target PDEs specified in Chapter 2, we now establish the methodology toward the Objectives (OBJ1–OBJ4) introduced in Chapter 1. Embedded in the Contributions (CTN1–CTN4) this chapter particularly comprises¹:

- A coherent framework for constructing LBM based on a given PDE,
- The numerical analysis of the scheme alongside its construction,
- The introduction of the notion of limit consistency,
- The proposal of LBM for PDE (systems) which in parts have not been approximated by it before,
- The definition of brute force stability.

The constructive ansatz for (CTN1) is proposed in Section 3.1 to obtain an LBM for a given d -dimensional parabolic PDE $F_{\text{par}} = 0$ in advection–diffusion form. As mentioned above (Remark 2.1.2), a preparative modification to bring a generic PDE in the sense of Definition 2.1.2 into parabolic form is realizable. The proposed ansatz is separated in four steps: constructing a relaxation system, spectral decomposition toward a transformed relaxation system, parameter choices conforming to discrete velocity Boltzmann equations and finally the relaxation limit consistent discretization which yields the lattice Boltzmann evolution equation on the space-time grid. The latter two form the content of Section 3.2. On each level, we analyze the current result with respect to convergence to the previous step to unfold the mechanisms of the derivation (CTN2). We modify the relaxation frequencies to enforce numerical stability of the LBM along the coupled relaxation and discretization limit toward the TEQ.

It has to be stressed that rigorous convergence of the numerical schemes at the center of LBMs to several PDEs has been previously proved in the literature. However, the focus and novelty of the present approach is modularity and generality in terms of interchanging parts of the LBM (relaxation, discretization, equilibria) without affecting usability of the approach for the evaluation of overall convergence up to leading order. The constraints which are necessary for doing so are derived below.

In Section 3.3, the approximation of the target PDEs with LBMs is completed via summarizing the main ingredients and adding initial, boundary and coupling methods to the bulk scheme. Concerning Contribution (CTN4), besides the assembly of existing methodology, several novel numerical schemes are proposed for the IBVPs to be approximated in the numerical experiments. Finally, preparing the latter, we sketch sample algorithms in terms of LBM collision kernels and stability estimates for complex problems to incorporate grid effects, relaxation mechanisms and nonlinear terms which leads to Contribution (CTN3). Parts of this chapter are already published by the author in [230–232, 234, 235].

¹ Parts of this chapter have been published in advance and are reproduced from several sources: [231], Copyright (2020), with permission from the authors and the Royal Society; [232], Copyright (2021), with permission from the authors and the Royal Society; [234], Copyright (2022), with permission from the authors and Elsevier Ltd; [233], Copyright (2022), with permission from the authors and Elsevier Inc; [235], Copyright (2023), with permission from the authors and the American Institute of Mathematical Sciences.

3.1 Constructive design principles

This section describes the top-down construction of relaxation operators in the form of relaxation systems (RSs) for the ADE (2.10) (see Figure 3.1). The procedure forms the main result of Contribution (CTN1). Whereas for the model IVP (2.10), a rigorously converging RS is obtained, the other targeted PDEs (Section 2.2) require switching to rather formal approaches in the case of nonlinear equilibria or nonuniform relaxation. In addition, as part of Contribution (CTN2), the resulting RS is analyzed with respect to its closed form expression in the conserved variables, the conditions and assumptions for its spectral transformation, rigorous convergence conditions involving the generic Maxwellian on its right hand side, and with respect to linear stability for non uniform relaxation. Subsequent to studying the relaxation limit, we derive lattice Boltzmann equations (LBEs) from RSs in Section 3.2. Thus, for a PDE in the form of (2.10), we establish a novel coherent methodology from recalling, combining and extending the previous results from Simonis *et al.* [230–232, 234]. Limits of the approach and future applications to more complex equation systems are discussed in Chapter 5.

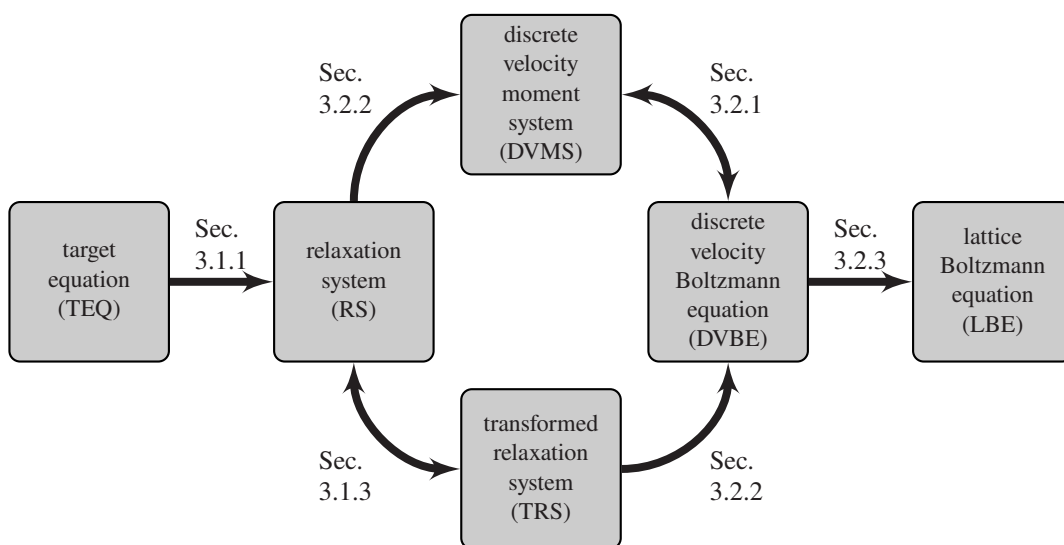


Figure 3.1: Schematic overview of the constructive approach (from left to right) proposed in [231]. Parts of this figure are reproduced from [231], Copyright (2020), with permission from the authors and the Royal Society.

3.1.1 Constructing relaxation systems

Definition 3.1.1. Conforming to Definition 2.1.1, we denote a perturbed quantity with \cdot^ϵ , i.e. a quantity which solves the relaxation induced perturbed version of the PDE solved by \cdot . A repeatedly exponentiation with ϵ corresponds to repeated perturbation with relaxation terms.

Remark 3.1.1. With respect to the previous sections, we can interpret the action constructing a relaxation operator $F_{\#}^\epsilon$ via perturbation as a reverse homogenization or inverse relaxation limit. It becomes clear that the notion of top-down construction in the present context needs to be envisioned in the metaphorical sense of constructing elements of equivalence classes of RSs. Hence, the parameters of the obtained RSs are not unique by construction. This viewpoint (in our version initially proposed in [231] and extended in [234]) that the relaxation mechanism adds another layer of information which is present in – though not uniquely recoverable from – the macroscopic equation, independently reappears in the literature on more or less discretized levels (e.g. see [28] and references therein).

The commutative construction of an RS (or relaxation operator) pertaining to the TEQ (2.10) is based on a hyperbolic conservation law

$$\partial_t \rho + \nabla_{\mathbf{x}} \cdot \mathbf{F}(\rho) = 0 \quad \text{in } \Omega_T, \quad (3.1)$$

where $\rho: \Omega_T \rightarrow \mathbb{R}$, $(\mathbf{x}, t) \mapsto \rho(\mathbf{x}, t)$, $\Omega_T = \Omega \times I \subseteq \mathbb{R}^d \times \mathbb{R}_{\geq 0}$, and $\mathbf{F}: \mathbb{R} \rightarrow \mathbb{R}^d$, $\rho \mapsto \mathbf{F}(\rho)$ is a component-wise Lipschitz continuous real-valued function. Initial and boundary conditions are discussed further below.

Remark 3.1.2. It is to be noted that also for other TEQs than (2.10), e.g. described by a PDO F_{\sharp} different from F_{par} , the starting point should be a PDE of similar form. The first step in the construction of an RS should thus be to bring the TEQ into an advection–diffusion (hyperbolic/parabolic) form and then to discard the diffusion terms which are to be regained asymptotically in the relaxation limit.

Let $\alpha \in \{1, \dots, d\}$. We denote with τ_b , $a_{\alpha}^{(1)}$, $a_{\alpha}^{(2)}$ variable stability parameters which are to be determined later, $\gamma > 0$ and $\delta = 2(\gamma - 1)$, where b is a tensor of flexible order. The latter are represented by the artificial variables introduced below and are later linked to physical moment tensors (cf. [66, 232]). For the sake of clarity, we neglect consistent notation of unambiguous arguments. To obtain a relaxation-based system of equations up to the first energy shell [148], two subsequent steps are performed. Each step consists of

- the introduction of artificial variables (AV) and
- the addition of perturbation terms (AP),

respectively [231, 234].

Step 1. Starting from (3.1) we define the first artificial variables

$$\underline{\text{AV}}: \quad \phi_{\alpha} = F_{\alpha}(\rho) \quad (3.2)$$

and obtain

$$\begin{cases} \partial_t \rho + \sum_{k=1}^d \partial_k \phi_k & = 0, \\ 0 & = F_{\alpha}(\rho) - \phi_{\alpha}, \end{cases} \quad (3.3)$$

which, by subsequent addition of perturbation terms to (3.2) for all α via

$$\underline{\text{AP}}: \quad \epsilon^{\gamma} \tau_{\phi} \left(\partial_t \phi_{\alpha}^{\epsilon} + \frac{a_{\alpha}^{(1)}}{\epsilon^{\delta}} \partial_{\alpha} \rho^{\epsilon} \right) = F_{\alpha}(\rho^{\epsilon}) - \phi_{\alpha}^{\epsilon}, \quad (3.4)$$

becomes a $(d+1) \times (d+1)$ RS

$$\begin{cases} \partial_t \rho^{\epsilon} + \sum_{k=1}^d \partial_k \phi_k^{\epsilon} & = 0, \\ \partial_t \phi_{\alpha}^{\epsilon} + \frac{a_{\alpha}^{(1)}}{\epsilon^{\delta}} \partial_{\alpha} \rho^{\epsilon} & = -\frac{1}{\epsilon^{\gamma} \tau_{\phi}} (\phi_{\alpha}^{\epsilon} - F_{\alpha}(\rho^{\epsilon})). \end{cases} \quad (3.5)$$

Step 2. We add a second set of artificial variables

$$\underline{\text{AV}}: \quad \psi_{\alpha}^{\epsilon} = \frac{a_{\alpha}^{(1)}}{\epsilon^{\delta}} \rho^{\epsilon} \quad (3.6)$$

for all α , which yields

$$\begin{cases} \partial_t \rho^\epsilon + \sum_{k=1}^d \partial_k \phi_k^\epsilon & = 0, \\ \partial_t \phi_\alpha^\epsilon + \partial_\alpha \psi_\alpha^\epsilon & = -\frac{1}{\epsilon^\gamma \tau_\phi} (\phi_\alpha^\epsilon - F_\alpha(\rho^\epsilon)), \\ 0 & = \frac{a_\alpha^{(1)}}{\epsilon^\delta} \rho^\epsilon - \psi_\alpha^\epsilon. \end{cases} \quad (3.7)$$

Adding a second set of perturbation terms to (3.6) for all α via

$$\underline{\mathbf{AP}}: \quad \epsilon^\gamma \tau_\psi \left(\partial_t \psi_\alpha^{\epsilon\epsilon} + \frac{a_\alpha^{(2)}}{\epsilon^\delta} \partial_\alpha \phi_\alpha^{\epsilon\epsilon} \right) = \frac{a_\alpha^{(1)}}{\epsilon^\delta} \rho^{\epsilon\epsilon} - \psi_\alpha^{\epsilon\epsilon} \quad (3.8)$$

transforms (3.7) into a $(2d+1) \times (2d+1)$ RS

$$\begin{cases} \partial_t \rho^{\epsilon\epsilon} + \sum_{k=1}^d \partial_k \phi_k^{\epsilon\epsilon} & = 0, \\ \partial_t \phi_k^{\epsilon\epsilon} + \partial_\alpha \psi_\alpha^{\epsilon\epsilon} & = -\frac{1}{\epsilon^\gamma \tau_\phi} (\phi_\alpha^{\epsilon\epsilon} - F_\alpha(\rho^{\epsilon\epsilon})), \\ \partial_t \psi_\alpha^{\epsilon\epsilon} + \frac{a_\alpha^{(2)}}{\epsilon^\delta} \partial_\alpha \phi_\alpha^{\epsilon\epsilon} & = -\frac{1}{\epsilon^\gamma \tau_\psi} \left(\psi_\alpha^{\epsilon\epsilon} - \frac{a_\alpha^{(1)}}{\epsilon^\delta} \rho^{\epsilon\epsilon} \right), \end{cases} \quad (3.9)$$

in Ω_T .

Definition 3.1.2. Compressing the above notation of (3.9), the RS reads

$$\partial_t \boldsymbol{\rho}^{\epsilon\epsilon} + \sum_{\alpha} \mathbf{A}_\alpha \partial_\alpha \boldsymbol{\rho}^{\epsilon\epsilon} = -\frac{1}{\epsilon^\gamma} \mathbf{S} [\boldsymbol{\rho}^{\epsilon\epsilon} - \hat{\boldsymbol{\rho}}^{\epsilon\epsilon}] \quad (3.10)$$

and governs the perturbed conservative variable

$$\boldsymbol{\rho}^{\epsilon\epsilon} = \begin{pmatrix} \rho^{\epsilon\epsilon} \\ \boldsymbol{\phi}^{\epsilon\epsilon} \\ \boldsymbol{\psi}^{\epsilon\epsilon} \end{pmatrix} \in \mathbb{R}^{2d+1}, \quad (3.11)$$

where

$$\mathbf{A}_\alpha = \begin{bmatrix} \mathbf{0}_{1 \times 1} & \mathbf{e}_\alpha^T & \mathbf{0}_{1 \times d} \\ \mathbf{0}_{d \times 1} & \mathbf{0}_{d \times d} & \text{diag}(\mathbf{e}_\alpha) \\ \mathbf{0}_{d \times 1} & \text{diag}\left(\frac{a_\alpha^{(2)}}{\epsilon^\delta} \mathbf{e}_\alpha\right) & \mathbf{0}_{d \times d} \end{bmatrix} \in \mathbb{R}^{(2d+1) \times (2d+1)} \quad (3.12)$$

is diagonalizable by construction,

$$\mathbf{S} = \text{diag}\left(\frac{1}{\tau_\rho} \mathbf{1}_{1 \times 1}, \frac{1}{\tau_\phi} \mathbf{1}_{d \times 1}, \frac{1}{\tau_\psi} \mathbf{1}_{d \times 1}\right) \in \mathbb{R}^{(2d+1) \times (2d+1)} \quad (3.13)$$

denotes the relaxation matrix with $\mathbf{r}_{a \times b} \in \mathbb{R}^{a \times b}$ being the all- r tensor of size $a \times b$ for $a, b \in \mathbb{N}$ and $r \in \mathbb{R}$, and $\mathbf{e}_\alpha \in \mathbb{R}^d$ is the α th unit vector. The function

$$\hat{\boldsymbol{\rho}}^{\epsilon\epsilon}: \mathbb{R} \rightarrow \mathbb{R}^{(2d+1) \times (2d+1)}, \rho^{\epsilon\epsilon} \mapsto \hat{\boldsymbol{\rho}}^{\epsilon\epsilon}(\rho^{\epsilon\epsilon}) = \begin{pmatrix} \rho^{\epsilon\epsilon} \\ \mathbf{F}(\rho^{\epsilon\epsilon}) \\ \frac{a_\alpha^{(1)}}{\epsilon^\delta} \rho^{\epsilon\epsilon} \end{pmatrix} \quad (3.14)$$

is named equilibrium.

Remark 3.1.3. Since the equilibrium is solely dependent on $\rho^{\epsilon\epsilon}$. A suitable choice for the initial condition complementing (3.10) is thus given by

$$\rho^{\epsilon\epsilon}(\mathbf{x}, 0) = \hat{\rho}^{\epsilon\epsilon}|_{\rho^{\epsilon\epsilon}(\mathbf{x}, 0) = \rho_0(\mathbf{x})}, \quad \text{in } \Omega. \quad (3.15)$$

According to [27], this choice is natural with respect to the later derived LBM interpreted as multi-step finite difference scheme.

Proposition 3.1.1. *Together with (3.10), (3.15) forms a well-posed IVP [37].*

Proof. A similar statement is proved in [37]. □

3.1.2 Closed equations and relaxation functions

Remark 3.1.4. The present ansatz enables both, constructing an RS and expressing the added relaxation terms as higher order derivatives, for any conservation law akin to (3.1) and thus any PDE which is transformable into a similar form. Further, via suitable rescaling, diffusion terms of the TEQ can be recovered.

We can *a priori* determine that the relaxation limit is governed by additional terms which null out when $\epsilon \searrow 0$ with specific prefactored orders. To do so, we formulate a closed equation in $\rho^{\epsilon\epsilon}$ for two distinct settings:

- (I) $d \in \mathbb{N}$, $\mathbf{F}(\rho)$ is linear, \mathbf{S} is independent on space and time,
- (II) $d = 1$, $\mathbf{F}(\rho)$ is nonlinear, \mathbf{S} is independent on space and time.

A third case is discussed in Remark 3.1.8 where $d = 1$, $\mathbf{F}(\rho)$ is nonlinear and \mathbf{S} is space-time dependent.

Theorem 3.1.1. *Let $\rho^{\epsilon\epsilon}$ be smooth in space and time, let \mathbf{F} be linear and let \mathbf{S} be independent of space and time. The RS (3.10) forms a closed equation for $\rho^{\epsilon\epsilon}$, namely*

$$\partial_t \rho^{\epsilon\epsilon} + \sum_{\alpha} F_{\alpha}(\partial_{\alpha} \rho^{\epsilon\epsilon}) - \epsilon^{2-\gamma} \tau_{\phi} \sum_{\alpha} a_{\alpha}^{(1)} \partial_{\alpha\alpha} \rho^{\epsilon\epsilon} = \mathcal{R}_{(I)}^{\epsilon\epsilon}, \quad (3.16)$$

where the relaxation remainder terms are

$$\mathcal{R}_{(I)}^{\epsilon\epsilon} = \epsilon^{\gamma} \tau_{\phi} \left[- \left(1 + \frac{\tau_{\psi}}{\tau_{\phi}} \right) \partial_{tt} \rho^{\epsilon\epsilon} - \frac{\tau_{\psi}}{\tau_{\phi}} \sum_{\alpha} F_{\alpha}(\partial_{\alpha t} \rho^{\epsilon\epsilon}) - \epsilon^{\gamma} \tau_{\psi} \partial_{ttt} \rho^{\epsilon\epsilon} + \epsilon^{2-\gamma} \tau_{\psi} \sum_{\alpha} a_{\alpha}^{(2)} \partial_{\alpha\alpha t} \rho^{\epsilon\epsilon} \right]. \quad (3.17)$$

Proof. The proof is sketched in [234], where we have additionally used that for all α

$$\begin{aligned} \partial_{\alpha t} F_{\alpha}(\rho^{\epsilon\epsilon}) &= \partial_t (F'_{\alpha}(\rho^{\epsilon\epsilon}) \partial_{\alpha} \rho^{\epsilon\epsilon}) \\ &= F''_{\alpha}(\rho^{\epsilon\epsilon}) \partial_t \rho^{\epsilon\epsilon} + F'_{\alpha}(\rho^{\epsilon\epsilon}) \partial_{\alpha t} \rho^{\epsilon\epsilon} \\ &= F_{\alpha}(\partial_{\alpha t} \rho^{\epsilon\epsilon}) \end{aligned} \quad (3.18)$$

for linear \mathbf{F} . □

Remark 3.1.5. The remainder terms (3.17) in Theorem 3.1.1 (3.16) indicate that the relaxation limit is of order $\mathcal{O}(\epsilon^{\gamma})$ with respect to the ADE (2.10). In the formal limit $\epsilon \rightarrow 0$, the perturbation terms on the right-hand side of (3.16)

vanish due to their prefactor ϵ^γ . Thus, the presence of the diffusion term in the limit equation depends on the scaling exponent γ . In the case of $\gamma = 2$, formally μ is recovered in the limit through τ multiplied with the directionally dependent factor $a_\alpha^{(\alpha)}$.

Theorem 3.1.2. *Let $\rho^{\epsilon\epsilon}$ be of class C^∞ in space and time, let \mathbf{F} be nonlinear and let \mathbf{S} be independent of space and time. For $d = 1$, the RS (3.10) forms a closed equation for $\rho^{\epsilon\epsilon}$, namely*

$$\partial_t \rho^{\epsilon\epsilon} + \partial_x F_x(\rho^{\epsilon\epsilon}) - \epsilon^{2-\gamma} \tau_\phi a_x^{(1)} \partial_{xx} \rho^{\epsilon\epsilon} = \mathcal{R}_{(\text{II})}^{\epsilon\epsilon}, \quad (3.19)$$

where the relaxation remainder terms are

$$\mathcal{R}_{(\text{II})}^{\epsilon\epsilon} = \epsilon^\gamma \tau_\phi \left[- \left(1 + \frac{\tau_\psi}{\tau_\phi} \right) \partial_{tt} \rho^{\epsilon\epsilon} - \frac{\tau_\psi}{\tau_\phi} \partial_{xt} F_x(\rho^{\epsilon\epsilon}) - \epsilon^\gamma \tau_\psi \partial_{ttt} \rho^{\epsilon\epsilon} + \epsilon^{2-\gamma} \tau_\psi a_x^{(2)} \partial_{xxt} \rho^{\epsilon\epsilon} \right]. \quad (3.20)$$

Proof. We begin with $d \in \mathbb{N}$ and fix the dimension to unity later in the proof where we give reasons for the necessity of doing so. To reduce the notation, we reorder the equation system (3.9) for any α into natural and artificial variables to

$$\partial_t \rho^{\epsilon\epsilon} = - \sum_{k=1}^d \partial_k \phi_k^{\epsilon\epsilon}, \quad (3.21)$$

$$F_\alpha(\rho^{\epsilon\epsilon}) = (1 + \epsilon^\gamma \tau_\phi \partial_t) \phi_\alpha^{\epsilon\epsilon} + (\epsilon^\gamma \tau_\phi \partial_\alpha) \psi_\alpha^{\epsilon\epsilon}, \quad (3.22)$$

$$(\epsilon^{-\delta} a_\alpha^{(1)}) \rho^{\epsilon\epsilon} = (\epsilon^{\gamma-\delta} \tau_\psi a_\alpha^{(2)} \partial_\alpha) \phi_\alpha^{\epsilon\epsilon} + (1 + \epsilon^\gamma \tau_\psi \partial_t) \psi_\alpha^{\epsilon\epsilon}. \quad (3.23)$$

We recall the generalization of Schwarz's theorem for symmetric partial derivatives of arbitrary order which allows us to equate permutations in the ordering partial derivatives with respect to space and time. In the spirit of [231, 234], we perform the inverse insertion from the last artificial variable to the initial conservation law for $d \in \mathbb{N}$. For illustration purposes, we display the following linear combination of (3.21)–(3.23) in tabular form (see Table 3.1). Conclusively, the final row R_1 in Table 3.1 reads

$$\begin{aligned} & \left(\partial_t - \epsilon^{\gamma-\delta} \tau_\phi \sum_{\alpha=1}^d a_\alpha^{(1)} \partial_{\alpha\alpha} - \epsilon^\gamma \tau_\phi \partial_{tt} - \epsilon^\gamma \tau_\psi \partial_{tt} - \epsilon^{2\gamma} \tau_\phi \tau_\psi \partial_{ttt} \right) \rho^{\epsilon\epsilon} \\ & + \left(\sum_{\alpha=1}^d \partial_\alpha + \epsilon^\gamma \tau_\psi \sum_{\alpha=1}^d \partial_{t\alpha} \right) F_\alpha(\rho^{\epsilon\epsilon}) = -\epsilon^{2\gamma-\delta} \tau_\phi \tau_\psi \sum_{\alpha=1}^d a_\alpha^{(2)} \partial_{\alpha\alpha\alpha} \phi_\alpha^{\epsilon\epsilon}. \end{aligned} \quad (3.24)$$

In the case of $\mathbf{F}(\rho^{\epsilon\epsilon})$ being linear, the assumption can be made that the graph of $\phi^{\epsilon\epsilon}$ approximates the hyperplane graph of the linear flux \mathbf{F} . Based on that, higher order cross derivatives in spatial dimensions can be neglected [234] for $d \in \mathbb{N}$. In the setting of the present proof, the nonlinearity of \mathbf{F} prevents this assumption for $d \neq 1$ due to

$$-\text{tr}(\nabla_{\mathbf{x}}(\nabla_{\mathbf{x}}(\partial_t \rho^{\epsilon\epsilon}))) = \text{tr}(\nabla_{\mathbf{x}}(\nabla_{\mathbf{x}}(\nabla_{\mathbf{x}} \cdot \phi_\alpha^{\epsilon\epsilon}))) \quad (3.25)$$

$$\Leftrightarrow \sum_{\alpha=1}^d \partial_{t\alpha\alpha} \rho^{\epsilon\epsilon} = \sum_{\beta=1}^d \sum_{\alpha=1}^d \partial_{\alpha\beta\beta} \phi_\alpha^{\epsilon\epsilon} \quad (3.26)$$

$$\begin{aligned} & = \sum_{\beta=1}^d \left(\sum_{\alpha=\beta}^d \partial_{\alpha\beta\beta} \phi_\alpha^{\epsilon\epsilon} + \sum_{\substack{\alpha=1 \\ \alpha \neq \beta}}^d \partial_{\alpha\beta\beta} \phi_\alpha^{\epsilon\epsilon} \right) \\ & = \sum_{\alpha=1}^d \partial_{\alpha\alpha\alpha} \phi_\alpha^{\epsilon\epsilon} + \sum_{\beta=1}^d \sum_{\substack{\alpha=1 \\ \alpha \neq \beta}}^d \partial_{\alpha\beta\beta} \phi_\alpha^{\epsilon\epsilon} \end{aligned}$$

Table 3.1: Computation of closed equation in $\rho^{\epsilon\epsilon}$ for Theorem 3.1.2. The n th row of (3.10) is denoted with R_n for $n \in \mathbb{N}$. Equations for $\phi^{\epsilon\epsilon}$ and $\psi^{\epsilon\epsilon}$ are not shown in the last two steps.

$[\cdot]\rho^{\epsilon\epsilon}$	$[\cdot]F_\alpha(\rho^{\epsilon\epsilon})$	$[\cdot]\phi_\alpha^{\epsilon\epsilon}$	$[\cdot]\psi_\alpha^{\epsilon\epsilon}$	linear combination
∂_t	0	$-\sum_{\alpha=1}^d \partial_\alpha$	0	
0	1	1 $+\epsilon^\gamma \tau_\phi \partial_t$	$\epsilon^\gamma \tau_\phi \partial_\alpha$	$-\epsilon^\gamma \tau_\phi \partial_\alpha (3.23)$
$\epsilon^{-\delta} a_\alpha^{(1)}$	0	$\epsilon^{\gamma-\delta} \tau_\psi a_\alpha^{(2)} \partial_\alpha$	1 $+\epsilon^\gamma \tau_\psi \partial_t$	
∂_t	0	$-\sum_{\alpha=1}^d \partial_\alpha$	0	
$-\epsilon^{\gamma-\delta} \tau_\phi a_\alpha^{(1)} \partial_\alpha$	1	1 $+\epsilon^\gamma \tau_\phi \partial_t$ $-\epsilon^{2\gamma-\delta} \tau_\phi \tau_\psi a_\alpha^{(2)} \partial_{\alpha\alpha}$	$-\epsilon^{2\gamma} \tau_\phi \tau_\psi \partial_{t\alpha}$	$+\epsilon^\gamma \tau_\psi \partial_t (3.22)$
$\epsilon^{-\delta} a_\alpha^{(1)}$	0	$\epsilon^{\gamma-\delta} \tau_\psi a_\alpha^{(2)} \partial_\alpha$	1 $+\epsilon^\gamma \tau_\psi \partial_t$	
∂_t	0	$-\sum_{\alpha=1}^d \partial_\alpha$	0	$+\epsilon^\gamma \tau_\psi \partial_t (3.22)$
$-\epsilon^{\gamma-\delta} \tau_\phi a_\alpha^{(1)} \partial_\alpha$	1 $+\epsilon^\gamma \tau_\psi \partial_t$	1 $+\epsilon^\gamma \tau_\phi \partial_t$ $+\epsilon^\gamma \tau_\psi \partial_t$ $-\epsilon^{2\gamma-\delta} \tau_\phi \tau_\psi a_\alpha^{(2)} \partial_{\alpha\alpha}$ $+\epsilon^{2\gamma} \tau_\phi \tau_\psi \partial_{tt}$	0	
$\epsilon^{-\delta} a_\alpha^{(1)}$	0	$\epsilon^{\gamma-\delta} \tau_\psi a_\alpha^{(2)} \partial_\alpha$	1 $+\epsilon^\gamma \tau_\psi \partial_t$	
∂_t	0	$-\sum_{\alpha=1}^d \partial_\alpha$	0	$+\sum_{\alpha=1}^d \partial_\alpha (R_2)$
$-\epsilon^{\gamma-\delta} \tau_\phi a_\alpha^{(1)} \partial_\alpha$	1 $+\epsilon^\gamma \tau_\psi \partial_t$	1 $+\epsilon^\gamma \tau_\phi \partial_t$ $+\epsilon^\gamma \tau_\psi \partial_t$ $-\epsilon^{2\gamma-\delta} \tau_\phi \tau_\psi a_\alpha^{(2)} \partial_{\alpha\alpha}$ $+\epsilon^{2\gamma} \tau_\phi \tau_\psi \partial_{tt}$	0	
$\epsilon^{-\delta} a_\alpha^{(1)}$	0	$\epsilon^{\gamma-\delta} \tau_\psi a_\alpha^{(2)} \partial_\alpha$	1 $+\epsilon^\gamma \tau_\psi \partial_t$	
∂_t	$\sum_{\alpha=1}^d \partial_\alpha$	$\epsilon^\gamma \tau_\phi \sum_{\alpha=1}^d \partial_{t\alpha}$	0	$+\epsilon^\gamma \tau_\phi \partial_t (3.21)$ $+\epsilon^\gamma \tau_\psi \partial_t (3.21)$ $+\epsilon^{2\gamma} \tau_\phi \tau_\psi \partial_{tt} (3.21)$
$-\epsilon^{\gamma-\delta} \tau_\phi \sum_{\alpha=1}^d a_\alpha^{(1)} \partial_{\alpha\alpha}$	$+\epsilon^\gamma \tau_\psi \sum_{\alpha=1}^d \partial_{t\alpha}$	$+\epsilon^\gamma \tau_\psi \sum_{\alpha=1}^d \partial_{t\alpha}$ $-\epsilon^{2\gamma-\delta} \tau_\phi \tau_\psi \sum_{\alpha=1}^d a_\alpha^{(2)} \partial_{\alpha\alpha\alpha}$ $+\epsilon^{2\gamma} \tau_\phi \tau_\psi \sum_{\alpha=1}^d \partial_{tt\alpha}$		
∂_t	$\sum_{\alpha=1}^d \partial_\alpha$	$-\epsilon^{2\gamma-\delta} \tau_\phi \tau_\psi \sum_{\alpha=1}^d a_\alpha^{(2)} \partial_{\alpha\alpha\alpha}$	0	final R_1
$-\epsilon^{\gamma-\delta} \tau_\phi \sum_{\alpha=1}^d a_\alpha^{(1)} \partial_{\alpha\alpha}$	$+\epsilon^\gamma \tau_\psi \sum_{\alpha=1}^d \partial_{t\alpha}$			
$-\epsilon^\gamma \tau_\phi \partial_{tt}$				
$-\epsilon^\gamma \tau_\psi \partial_{tt}$				
$-\epsilon^{2\gamma} \tau_\phi \tau_\psi \partial_{ttt}$				

$$\neq \sum_{\alpha=1}^d \partial_{\alpha\alpha\alpha} \phi_{\alpha}^{\epsilon\epsilon}. \quad (3.27)$$

We thus set $d = 1$, which yields

$$\sum_{\beta=1}^d \sum_{\substack{\alpha=1 \\ \alpha \neq \beta}}^d \partial_{\alpha\beta\beta} \phi_{\alpha} = 0, \quad (3.28)$$

and induces that from $R_1 + \epsilon^{2\gamma-\delta} \tau_{\phi} \tau_{\psi} \sum_{\alpha=1}^d a_{\alpha}^{(2)} \partial_{\alpha\alpha}$ (3.21) we indeed obtain zeros in the third and fourth row of Table (3.1) i.e. a closed equation in $\rho^{\epsilon\epsilon}$. Reordering the terms completes the proof. \square

Remark 3.1.6. We can extend the linear combination in Table (3.1) via repeated addition of

$$R_1 + (\epsilon^{2\gamma-\delta} \tau_{\phi} \tau_{\psi})^k \sum_{\alpha=1}^d \left(a_{\alpha}^{(2)} \right)^k \partial_{\alpha(\alpha\alpha)^k} (R_2) \quad (3.29)$$

for $k > 1$, where we have performed $k = 0$ already. Consequently, all even spatial derivatives $\partial_{(\alpha\alpha)^n} \phi_{\alpha}$ for $n \in \mathbb{N}$ vanish and we are left with odd order ones prefactored by $\epsilon^{k(2\gamma-\delta)} = \epsilon^{2k}$. The present derivation hence abstracts the observations made by Geier *et al.* [95, 96] from the recursive insertion of Taylor expanded collisions [120, 143] into the collision scheme of a cumulant LBM. The abstraction is in terms of using mathematical relaxation and the derivation of a closed form equation instead of kinetic arguments. On the present relaxation level (prior to discretization) the repeated addition in terms of linear combinations generates the powers in ϵ similar to typical asymptotic expansion terms.

Remark 3.1.7. Theorem 3.1.2 and its proof naturally suggest that in $d > 1$ the coupling of the RS (3.10) is strong in the sense that a closed form in $\rho^{\epsilon\epsilon}$ is not derivable by linear combination if \mathbf{F} is nonlinear. Instead, the closed form is solely asymptotically reachable with an infinite number of linear combinations through

$$\begin{aligned} R_1 + \sum_{k=1}^{\infty} (\epsilon^{2\gamma-\delta} \tau_{\phi} \tau_{\psi})^k \sum_{\alpha=1}^d \left(a_{\alpha}^{(2)} \right)^k \partial_{\alpha(\alpha\alpha)^k} (R_2) \\ + \sum_{k=1}^{\infty} (\epsilon^{\gamma} \tau_{\phi})^k \partial_{t(\alpha\alpha)^k} (3.21) \\ + \sum_{k=1}^{\infty} (\epsilon^{\gamma} \tau_{\psi})^k \partial_{t(\alpha\alpha)^k} (3.21) \\ + \sum_{k=1}^{\infty} (\epsilon^{2\gamma} \tau_{\phi} \tau_{\psi})^k \partial_{tt(\alpha\alpha)^k} (3.21), \end{aligned} \quad (3.30)$$

and only up to nonvanishing cross derivatives of $\phi^{\epsilon\epsilon}$ akin to (3.25).

Remark 3.1.8. The results of Theorem 3.1.1 and Theorem 3.1.2 are based on relaxation times τ_i and prefactors $a_{\alpha}^{(i)}$ which, although being linked to for example nondimensional numbers and grid sizes, are assumed to be independent of space and time for any α and $i = 1, 2$. Similarly, the (recursive) asymptotic expansion [95, 96] uses this assumption. To the knowledge of the author, a similar consistency analysis up to high orders with space-time dependent relaxation functions has not been established yet, is of paramount interest and is planned for future work. It is to be noted that, due to the appearance of cross-derivatives and combined terms, the amount of algebra to arrive at a formula which includes more than leading order is drastically increased already in the case of $d = 1$, $\mathbf{F}(\rho)$ being nonlinear and space-time dependent \mathbf{S} .

3.1.3 Transformed relaxation system

The following transformation of the RS is motivated by decoupling its left hand side. At first, Hadamard operations on and between tensors (see e.g. Reams [213]) and other notations are defined.

Definition 3.1.3. Let $\mathbf{A} = (A_i) \in \mathbb{R}^{\mathbf{n}}$ and $\mathbf{B} = (B_i) \in \mathbb{R}^{\mathbf{n}}$ be tensors of rank $N \in \mathbb{N}$, where $\mathbf{i} = (i_1, i_2, \dots, i_N) \in \mathbb{N}^N$ and $\mathbf{n} = (n, n, \dots, n) \in \mathbb{N}^N$ are multi-indices.

1. The Hadamard product is defined as

$$\mathbf{A} \diamond \mathbf{B} = (A_i B_i). \quad (3.31)$$

2. The Hadamard inverse is defined as

$$\mathbf{A}^{\diamond^{-1}} = (A_i^{-1}). \quad (3.32)$$

3. For $m \in \mathbb{R}_{\geq 0}$, the m th Hadamard power is defined as

$$\mathbf{A}^{\diamond m} = (A_i^m). \quad (3.33)$$

Further, any exponent of a tensor and any operation between tensors preceded with \diamond is to be performed entrywise.

Definition 3.1.4. The all- r tensor of size $a \times b$ for $a, b \in \mathbb{N}$ and $r \in \mathbb{R}$ is denoted with

$$\mathbf{r}_{a \times b} \in \mathbb{R}^{a \times b}. \quad (3.34)$$

Moreover, let $\mathbf{e}_\alpha \in \mathbb{R}^d$ be the α th unit vector in \mathbb{R}^d .

Definition 3.1.5. Let $\mathbf{A} = (A_{ij}) \in \mathbb{R}^{n \times n}$ and $\mathbf{a} = (a_i) \in \mathbb{R}^n$ for $n \in \mathbb{N}$. The diagonal operator

$$\text{diag}: \mathbb{R}^{n \times n} \rightarrow \mathbb{R}, \mathbf{A} \mapsto \text{diag}(\mathbf{A}) = \sum_{i=1}^n (\mathbf{e}_i^T \mathbf{A} \mathbf{e}_i) \mathbf{e}_i \quad (3.35)$$

extracts the diagonal elements of a matrix into a correspondingly sized vector. Denoted with the same symbol,

$$\text{diag}: \mathbb{R}^n \rightarrow \mathbb{R}^{n \times n}, \mathbf{a} \mapsto \text{diag}(\mathbf{a}) = \sum_{i=1}^n \mathbf{I}_n (\mathbf{e}_i^T \mathbf{a}) \mathbf{e}_i \quad (3.36)$$

forms a quadratic matrix from argument vector entries as diagonal elements only, where \mathbf{I}_n denotes the identity matrix in $\mathbb{R}^{n \times n}$.

We can describe the modal matrix of \mathbf{A}_α for all α as follows.

Definition 3.1.6. With $\chi_\alpha^{(i)} := a_\alpha^{(i)} / \epsilon^\delta$ for $i \in \{1, 2\}$ and any α , define

$$\mathbf{C}^{(i)} = \text{diag}(\boldsymbol{\chi}^{(i)}) \in \text{GL}_d(\mathbb{R}) \quad (3.37)$$

and the unified (i.e. the same for all α) diagonalizer

$$\mathbf{D} = \begin{bmatrix} \mathbf{1}_{1 \times d} & \mathbf{1}_{1 \times 1} & \mathbf{1}_{1 \times d} \\ -(\mathbf{C}^{(2)})^{\diamond \frac{1}{2}} & \mathbf{0}_{d \times 1} & (\mathbf{C}^{(2)})^{\diamond \frac{1}{2}} \\ \mathbf{C}^{(2)} & \mathbf{0}_{d \times 1} & \mathbf{C}^{(2)} \end{bmatrix} \in \text{GL}_{2d+1}(\mathbb{R}). \quad (3.38)$$

Proposition 3.1.2. *For any α , the matrix \mathbf{A}_α can be diagonalized to its spectral counterpart*

$$\begin{aligned} \mathbf{A}_\alpha^d &:= \mathbf{D}^{-1} \mathbf{A}_\alpha \mathbf{D} \\ &= \text{diag} \left((\mathbf{C}^{(2)})^{\diamond \frac{1}{2}} \mathbf{e}_\alpha, \mathbf{0}_{1 \times 1}, (\mathbf{C}^{(2)})^{\diamond \frac{1}{2}} \mathbf{e}_\alpha \right). \end{aligned} \quad (3.39)$$

Proof. Computing

$$\mathbf{D}^{-1} = \begin{bmatrix} \mathbf{0}_{d \times 1} & -\frac{1}{2} (\mathbf{C}^{(2)})^{\diamond -\frac{1}{2}} & \frac{1}{2} (\mathbf{C}^{(2)})^{\diamond -1} \\ \mathbf{1}_{1 \times 1} & \mathbf{0}_{1 \times d} & -(\boldsymbol{\chi}^{(2)})^{\diamond -1} \\ \mathbf{0}_{d \times 1} & \frac{1}{2} (\mathbf{C}^{(2)})^{\diamond -\frac{1}{2}} & \frac{1}{2} (\mathbf{C}^{(2)})^{\diamond -1} \end{bmatrix} \quad (3.40)$$

and multiplication with $\mathbf{D}^{-1} \mathbf{A}_\alpha$ for all α gives the result. \square

Remark 3.1.9. The unified diagonalization is unique only up to permutation of diagonal entries of \mathbf{A}_α^d and scalar multiples of the columns of \mathbf{D} . We can thus formulate diagonalizations for all α

$$\mathbf{A}_\alpha = \mathbf{D}_1 \mathbf{A}_\alpha^{d,1} \mathbf{D}_1^{-1} = \mathbf{D}_2 \mathbf{A}_\alpha^{d,2} \mathbf{D}_2^{-1}, \quad (3.41)$$

where $\mathbf{D}_1 \neq \mathbf{D}_2$ and $\mathbf{A}_\alpha^{d,1} \neq \mathbf{A}_\alpha^{d,2}$.

We transform the RS (3.10) via spectral decomposition. The vectors $\mathbf{g} := \mathbf{D}^{-1} \boldsymbol{\rho}^{\epsilon\epsilon} \in \mathbb{R}^{2d+1}$ and $\hat{\mathbf{g}} := \mathbf{D}^{-1} \hat{\boldsymbol{\rho}}^{\epsilon\epsilon} \in \mathbb{R}^{2d+1}$ expressed in $\boldsymbol{\rho}^{\epsilon\epsilon}$ and $\hat{\boldsymbol{\rho}}^{\epsilon\epsilon}$ are inserted in (3.10), such that

$$\partial_t \mathbf{D} \mathbf{g} + \sum_{\alpha} \mathbf{A}_\alpha \partial_\alpha \mathbf{D} \mathbf{g} = -\frac{1}{\epsilon^\gamma} \mathbf{S} \mathbf{D} (\mathbf{g} - \hat{\mathbf{g}}) \quad (3.42)$$

multiplied with \mathbf{D}^{-1} from the left yields the following.

Definition 3.1.7. The vector

$$\mathbf{g} = \mathbf{D}^{-1} \boldsymbol{\rho}^{\epsilon\epsilon} \quad (3.43)$$

obeys the transformed RS (TRS)

$$\partial_t \mathbf{g} + \sum_{\alpha} \mathbf{A}_\alpha^d \partial_\alpha \mathbf{g} = -\frac{1}{\epsilon^\gamma} \mathbf{D}^{-1} \mathbf{S} \mathbf{D} [\mathbf{g} - \mathbf{G}(\mathbf{g})]. \quad (3.44)$$

Here, the function $\mathbf{G} = \mathcal{G} \circ \iota \circ \mathcal{D}$ is composed such that $\mathbf{G}(\mathbf{g}) \stackrel{\dagger}{=} \mathbf{D}^{-1} \hat{\boldsymbol{\rho}}^{\epsilon\epsilon}$, where the map $\iota : \boldsymbol{\rho}^{\epsilon\epsilon} \mapsto \hat{\boldsymbol{\rho}}^{\epsilon\epsilon}$ extracts the nonartificial variables. Further, the linear map $\mathcal{D} : \mathbb{R}^{2d+1} \rightarrow \mathbb{R}^{2d+1}$ is directly induced by \mathbf{D} . Let

$$\mathbf{a} = \mathbf{a}^{(1)} \diamond (\mathbf{a}^{(2)})^{\diamond -1} \in \mathbb{R}^d. \quad (3.45)$$

Based on the above, the generalized Maxwellian is defined as

$$\mathcal{G} : [0, 1] \times \mathbb{R} \rightarrow \mathbb{R}^{2d+1}, (\epsilon, \vartheta) \mapsto \mathcal{G}(\epsilon, \vartheta) = (\mathcal{G}_1, \dots, \mathcal{G}_{2d+1})^T(\epsilon, \vartheta) = \begin{pmatrix} \frac{1}{2} \left[\mathbf{a}\vartheta - (\mathbf{C}^{(2)})^{\diamond-\frac{1}{2}} \mathbf{F}(\vartheta) \right] \\ (1 - \mathbf{1}_{d \times 1} \cdot \mathbf{a}) \vartheta \\ \frac{1}{2} \left[\mathbf{a}\vartheta + (\mathbf{C}^{(2)})^{\diamond-\frac{1}{2}} \mathbf{F}(\vartheta) \right] \end{pmatrix}. \quad (3.46)$$

Within the present framework, we can algebraically characterize the collision, the artificial variables, and the equilibrium formulation. These features determine the relaxation limit of the RS and thus the limit equation of the nonartificial (conserved) variables. Looking ahead, we anticipate to unfold also the inherited relaxation procedure for LBMs.

Remark 3.1.10 (Collision). The multi-relaxation-time (MRT) collision matrix reads

$$\begin{aligned} \mathbf{K} &= \mathbf{D}^{-1} \mathbf{S} \mathbf{D} \\ &= \begin{bmatrix} \frac{1}{2} \left(\frac{1}{\tau_\phi} + \frac{1}{\tau_\psi} \right) \mathbf{I}_d & \mathbf{0}_{d \times 1} & -\frac{1}{2} \left(\frac{1}{\tau_\phi} - \frac{1}{\tau_\psi} \right) \mathbf{I}_d \\ \left(\frac{1}{\tau_\rho} - \frac{1}{\tau_\psi} \right) \mathbf{1}_{1 \times d} & \frac{1}{\tau_\rho} \mathbf{1}_{1 \times 1} & \left(\frac{1}{\tau_\rho} - \frac{1}{\tau_\psi} \right) \mathbf{1}_{1 \times d} \\ -\frac{1}{2} \left(\frac{1}{\tau_\phi} - \frac{1}{\tau_\psi} \right) \mathbf{I}_d & \mathbf{0}_{d \times 1} & \frac{1}{2} \left(\frac{1}{\tau_\phi} + \frac{1}{\tau_\psi} \right) \mathbf{I}_d \end{bmatrix}. \end{aligned} \quad (3.47)$$

It is notable that, compared to a single-relaxation-time (SRT) collision defined as

$$\begin{aligned} \check{\mathbf{K}} &= \mathbf{D}^{-1} \check{\mathbf{S}} \mathbf{D} \\ &= \tau_\rho^{-1} \mathbf{I}_{2d+1}, \end{aligned} \quad (3.48)$$

where $\check{\mathbf{S}} := \tau_\rho^{-1} \mathbf{I}_{2d+1}$, the MRT collision matrix shows nonzero off-diagonal blocks. The latter correlate nonequilibrium contributions

$$\mathbf{g}^{\text{neq}} = \mathbf{g} - \mathbf{G}(\mathbf{g}) \quad (3.49)$$

via prefactors from relaxation frequency sums. As a classic LBM staple, these relaxation effects are often tediously derived from a BGKBE in moment form [55].

Remark 3.1.11 (AV space). The previously made choice of defining the AV ($\phi^{\epsilon\epsilon}$ and $\psi^{\epsilon\epsilon}$) and adding the perturbation terms in the constructive ansatz narrows the possibilities of defining the unified diagonalizer \mathbf{D} . The latter in turn fixes the appearance of the TRS in terms of \mathbf{A}_α^d and \mathbf{G} . In particular, we have that

$$\text{colsp}(\mathbf{D}) = \text{span} \left(\bigcap_{\alpha} E(\mathbf{A}_\alpha) \right) \quad (3.50)$$

frames the choices for \mathbf{D} , where $E(\mathbf{A}_\alpha)$ is the eigenbasis of right eigenvectors of \mathbf{A}_α .

Remark 3.1.12. Here, we limit our discussion to raw and orthogonal moment bases only, since the TRS is obtained through eigendecomposition. In this setting, \mathbf{D} can be chosen to have orthogonal rows in the case that \mathbf{A}_α admits orthogonal eigenvectors for example if \mathbf{A}_α is normal for all α . The introduced methodology [234] differs from other approaches such as moment-matching or Gauss–Hermite quadrature (see for example [185] and references therein). The latter are based on thermodynamic concepts for example the recovery of Maxwellian equilibria to leading order. In contrast to that, the present framework is mathematically generic. This allows for example the derivation of closed equations (3.16) in special cases without expansions akin to Chapman–Enskog.

3.1.4 Stability and convergence

Without loss of generality, the flux is normalized by $\mathbf{F}(0) = \mathbf{0}_{d \times 1}$ so that

$$\mathcal{G}(\epsilon, 0) = \mathbf{0}_{(2d+1) \times 1} \quad \forall \epsilon \in (0, 1] \quad (3.51)$$

follows from (3.46). Additionally, we assume that $\mathcal{G}_i(\epsilon, \cdot)$ is monotone, i.e. nondecreasing in $\mathcal{N} = \{\vartheta \in \mathbb{R} : |\vartheta| \leq \|\rho_0\|_\infty\}$ for all $i \in \{1, 2, \dots, 2d+1\}$, which is called quasimonotonicity of \mathcal{G} [37]. Based on the rigorous derivations for classes of diffusive relaxation systems by Bouchut *et al.* [37], we can form the following convergence result depending on the generalized Maxwellian and a sub-characteristic condition. Let $q = 2d + 1$.

Lemma 3.1.1. *The generalized Maxwellian \mathcal{G} is a local Maxwellian function for equation (2.10) according to [37].*

Proof. The conditions (M_1-M_4) given in [37] are verified. In particular, after some algebra we have that

$$(M_1) \quad \sum_{i=1}^{2d+1} \mathcal{G}_i(\epsilon, \vartheta) = \vartheta \quad \forall \epsilon \in (0, 1] \quad \forall \vartheta \in \mathcal{N}, \quad (3.52)$$

$$(M_2) \quad \sum_{i=1}^{2d+1} (\mathbf{A}_\alpha^d)_{i,i} \mathcal{G}_i(\epsilon, \vartheta) = F_\alpha(\vartheta) \quad \forall \alpha \in \{1, 2, \dots, d\} \quad \forall \epsilon \in (0, 1] \quad \forall \vartheta \in \mathcal{N}, \quad (3.53)$$

$$(M_3) \quad \sum_{i=1}^{2d+1} \left[\sqrt{\epsilon^\delta} (\mathbf{A}_\alpha^d)_{i,i} \right] \left[\sqrt{\epsilon^\delta} (\mathbf{A}_\beta^d)_{i,i} \right] \mathcal{G}_i(0, \vartheta) = \mu \vartheta \delta_{\alpha,\beta} \quad \forall \alpha, \beta \in \{1, 2, \dots, d\} \quad \forall \vartheta \in \mathcal{N}, \quad (3.54)$$

$$(M_4) \quad \lim_{\epsilon \searrow 0} \mathcal{G}_i(\epsilon, \vartheta) = \mathcal{G}_i(0, \vartheta) \quad \text{uniformly for } \vartheta \in \mathcal{N}, \text{ for } i = 1, 2, \dots, 2d+1, \quad (3.55)$$

where (M_3) requires that $\sum_\alpha a_\alpha^{(1)} = \mu$ holds. \square

Definition 3.1.8. The TRS (3.44) is called relaxation stable if the stability parameters are chosen such that for all α holds

$$\sum_\alpha a_\alpha^{(1)} = \mu, \quad (3.56)$$

$$1 \geq \sum_\alpha a_\alpha, \quad (3.57)$$

$$\sum_\alpha a_\alpha \geq \left| \sum_\alpha \sqrt{\frac{\epsilon^\delta}{a_\alpha^{(2)}}} \partial \rho(F_\alpha(\rho)) \right|. \quad (3.58)$$

Remark 3.1.13. The relaxation stability conditions all emerge from properties on \mathcal{G} . Where (3.56) is necessary to uphold the Maxwellian locality in (M_1-M_4) , (3.57) and (3.58) ensure quasimonotonicity of \mathcal{G} (see [37, Proposition 2.2]).

Proposition 3.1.3. *Let $\tau_b = 1$ for all $b \in \{\rho, \phi, \psi\}$, $\rho_0 \in L^\infty(\Omega) \cap L^1(\Omega)$ and choose relaxation stable variables $\mathbf{a}^{(1)}, \mathbf{a}^{(2)}$. Initialize the TRS (3.44) with $\mathbf{g}(\cdot, 0) = \mathcal{G}(\epsilon, \rho_0)$, and let $\mathbf{g} \in C(I; L^1_{\text{loc}}(\Omega))^q \cap L^\infty(\Omega \times I)^q$ denote its solution. Then a bounded function \mathbf{g}^* exists, such that (along a subsequence)*

$$\lim_{\epsilon \searrow 0} \mathbf{g} = \mathbf{g}^* \quad \text{in } C(I; L^1_{\text{loc}}(\Omega)). \quad (3.59)$$

Further, $\rho_* = \iota(\mathbf{D}\mathbf{g}^*)$ is the unique entropy solution to the TEQ (2.10).

Proof. We identify the structure of the derived TRS (3.44) as a finite dimension diffusive BGK approximation of the TEQ (2.10) such that with relaxation stability and \mathcal{G} admitting the conditions (M_1-M_4) , the solution \mathbf{g} exists [37, Theorem 2.1]. Then, the claim follows from [37, Theorem 3.1 and Theorem 4.1]. \square

Remark 3.1.14. Albeit this result is rigorous, it does not treat the case that $\tau_b \neq 1$ for some b which is rather common in practice. Hence, we slightly drift away from rigor and study the formal consistency as well as linear stability of the relaxation limit.

Remark 3.1.15. Let $d = 1$. Based on the closed equation (3.19) we infer the following:

- The diffusion coefficient in the relaxation limit of the RS (3.10) can be altered via modifying τ_ϕ .
- Formally, the RS (3.10) is consistent of order $\mathcal{O}(\epsilon^\gamma)$ to the TEQ (2.10).
- The diffusivity in the limit is not affected when τ_ψ is modified within a certain bound. We can thus alter τ_ψ to modify the path we take toward the TEQ along $\epsilon \searrow 0$ in terms of consistency and stability.

To study the controlling mechanism of a relaxation time modification with respect to the limit $\epsilon \searrow 0$, we evaluate the linear stability of the TRS (3.44) with nonuniform τ_b .

Remark 3.1.16. At some point in the derivation, the dimension is fixed to $d = 1$ which is necessary to enable an analytic derivation of the spectral radius of the amplification matrix derived below (see Corollary 3.1.2).

To obtain a relaxation time dependent linear stability notion in the sense of von Neumann (VN), we split

$$\mathbf{g} = \bar{\mathbf{g}} + \tilde{\mathbf{g}} \quad (3.60)$$

into a global equilibrium $\bar{\mathbf{g}}$ (constant in space-time) plus its fluctuations $\tilde{\mathbf{g}}$, respectively. The equilibrium is Taylor expanded at the global state

$$\begin{aligned} \mathbf{G}(\mathbf{g}) &= \sum_{n=0}^{\infty} \frac{1}{n!} [(\partial_{\mathbf{g}})^n \mathbf{G}(\bar{\mathbf{g}})] \tilde{\mathbf{g}}^n \\ &= \mathbf{G}(\bar{\mathbf{g}}) + \mathbf{J}_{\mathbf{G}}(\bar{\mathbf{g}}) \tilde{\mathbf{g}} + \mathcal{O}(\tilde{\mathbf{g}}^2), \end{aligned} \quad (3.61)$$

where $\mathbf{J}_{\mathbf{G}}(\bar{\mathbf{g}})$ is the equilibrium Jacobian evaluated at the global equilibrium. We insert (3.60) and (3.61) in (3.44), assume that $\mathbf{G}(\bar{\mathbf{g}}) = \bar{\mathbf{g}}$ and neglect powers in fluctuations higher than two to obtain

$$\begin{aligned} \partial_t \tilde{\mathbf{g}} + \sum_{\alpha} \mathbf{A}_{\alpha}^d \partial_{\alpha} \tilde{\mathbf{g}} &= -\frac{1}{\epsilon^\gamma} \mathbf{K} (\bar{\mathbf{g}} + \tilde{\mathbf{g}} - \mathbf{G}(\mathbf{g})) \\ &= -\frac{1}{\epsilon^\gamma} \mathbf{K} [\bar{\mathbf{g}} - \mathbf{G}(\bar{\mathbf{g}}) + \tilde{\mathbf{g}} - \mathbf{J}_{\mathbf{G}}(\bar{\mathbf{g}}) \tilde{\mathbf{g}} - \mathcal{O}(\tilde{\mathbf{g}}^2)] \\ &= -\frac{1}{\epsilon^\gamma} \mathbf{K} [\mathbf{I}_q - \mathbf{J}_{\mathbf{G}}(\bar{\mathbf{g}})] \tilde{\mathbf{g}}. \end{aligned} \quad (3.62)$$

Fourier transforming the fluctuations gives

$$\tilde{\mathbf{g}} = \hat{\mathbf{g}} \exp(i(2\pi \mathbf{k} \cdot \mathbf{x} - \omega t)), \quad (3.63)$$

where $\hat{\mathbf{g}} \in \mathbb{C}^q$ denotes the Fourier transform of $\tilde{\mathbf{g}}$ and is a vector of amplitudes for monochromatic waves [264], $\mathbf{k} \in \mathcal{K} \subseteq \mathbb{R}^d$ denotes the wavevector and $\omega \in \mathbb{C}$. Insertion of $\hat{\mathbf{g}}$ into (3.62) yields an eigenvalue problem

$$\mathbf{V} \hat{\mathbf{g}} = \omega \hat{\mathbf{g}}, \quad (3.64)$$

where the amplification matrix $\mathbf{V} \in \mathbb{C}^{q \times q}$ reads

$$\mathbf{V}(\mathbf{k}, \mathbf{F}, \mathbf{S}) := \text{diag} \left(2\pi (\mathbf{k} \cdot \mathbf{A}_i^d)_{1 \leq i \leq q} \right) - \frac{i}{\epsilon^\gamma} \mathbf{K} (\mathbf{I}_q - \mathbf{J}_G(\bar{\mathbf{g}})), \quad (3.65)$$

with

$$\mathbf{A}_i^d = ((A_\alpha^d)_{i,i})_{1 \leq \alpha \leq d} \in \mathbb{R}^d. \quad (3.66)$$

Definition 3.1.9. The TRS (3.44) is termed von Neumann stable if the unit ball encloses the spectrum of \mathbf{V} , i.e.

$$\text{spec}(\mathbf{V}) \subseteq B_1(0). \quad (3.67)$$

Further, for given \mathbf{F} we define the von Neumann stability set

$$\mathcal{S}_F^{\text{lin}} = \{\mathbf{S} \mid \text{spec}(\mathbf{V}) \subseteq B_1(0) \forall \mathbf{k} \in \mathcal{K}\}. \quad (3.68)$$

We can further specify the amplification matrix by calculating the Jacobian $\mathbf{J}_G(\mathbf{g})$.

Corollary 3.1.1. Let G be defined by (3.46). Then $\mathbf{J}_G(\mathbf{g})$ is a projector (i.e. $(\mathbf{J}_G)^2(\mathbf{g}) = \mathbf{J}_G(\mathbf{g})$).

Proof. The columns of

$$\mathbf{J}_G(\mathbf{g}) = \begin{bmatrix} \frac{1}{2} \left[\mathbf{a} - (\mathbf{C}^{(2)})^{\diamond-\frac{1}{2}} \partial g_1 \mathbf{F}(\mathbf{g}) \right] & \frac{1}{2} \left[\mathbf{a} + (\mathbf{C}^{(2)})^{\diamond-\frac{1}{2}} \partial g_{2d+1} \mathbf{F}(\mathbf{g}) \right] \\ (1 - \mathbf{1}_{1 \times q} \cdot \mathbf{a}) & \dots & (1 - \mathbf{1}_{1 \times q} \cdot \mathbf{a}) \\ \frac{1}{2} \left[\mathbf{a} + (\mathbf{C}^{(2)})^{\diamond-\frac{1}{2}} \partial g_1 \mathbf{F}(\mathbf{g}) \right] & \frac{1}{2} \left[\mathbf{a} + (\mathbf{C}^{(2)})^{\diamond-\frac{1}{2}} \partial g_{2d+1} \mathbf{F}(\mathbf{g}) \right] \end{bmatrix} \in \mathbb{R}^{(2d+1) \times (2d+1)} \quad (3.69)$$

sum up to 1, which completes the proof. \square

Corollary 3.1.2. Let $d = 1$. The TRS (3.44) admits the von Neumann stability set

$$\mathcal{S}_F^{\text{lin}} = \left\{ \mathbf{S} = \text{diag}(1, \tau_\phi^{-1}, \tau_\psi^{-1}) \mid \tau_\phi^{-1} = \frac{\epsilon^{2-\gamma} a_1^{(1)}}{\mu}, \tau_\psi^{-1} \leq \frac{\epsilon^\gamma - 2\pi\epsilon\sqrt{a_1^{(2)}} - \frac{\epsilon^{2-\gamma} a_1^{(1)}}{\mu} \left(\sum_{j=1}^3 \left| \frac{\epsilon^{\gamma-1}}{2\sqrt{a_1^{(2)}}} \frac{\partial F_1}{\partial g_j} \right| + 1 \right)}{\frac{3}{2} \left| \frac{a_1^{(1)}}{a_1^{(2)}} \right| + 1} \right\}. \quad (3.70)$$

Proof. Let $\mathbf{k} \in \mathcal{K}$. We express some of the matrices appearing in (3.65) in block form such that

$$\mathbf{K} = \begin{bmatrix} \mathbf{K}_{11} & \mathbf{K}_{12} & \mathbf{K}_{13} \\ \mathbf{K}_{21}^T & \mathbf{K}_{22} & \mathbf{K}_{23}^T \\ \mathbf{K}_{31} & \mathbf{K}_{32} & \mathbf{K}_{33} \end{bmatrix}, \quad \mathbf{J}_G(\bar{\mathbf{g}}) = \begin{bmatrix} \mathbf{J}_{11} & \mathbf{J}_{12} & \mathbf{J}_{13} \\ \mathbf{J}_{21}^T & \mathbf{J}_{22} & \mathbf{J}_{23}^T \\ \mathbf{J}_{31} & \mathbf{J}_{32} & \mathbf{J}_{33} \end{bmatrix}, \quad \mathbf{\Pi} = \text{diag} \left(2\pi (\mathbf{k} \cdot \mathbf{A}_i^d)_{1 \leq i \leq d} \right) \quad (3.71)$$

gives (with slight evasion of tensor order highlighting) that

$$\mathbf{V} = \begin{bmatrix} \Pi_{11} - \frac{i}{\epsilon^\gamma} \left[\mathbf{K}_{11} - \sum_{\alpha} \mathbf{K}_{1\alpha} \mathbf{J}_{\alpha 1} \right] & \Pi_{12} - \frac{i}{\epsilon^\gamma} \left[\mathbf{K}_{12} - \sum_{\alpha} \mathbf{K}_{1\alpha} \mathbf{J}_{\alpha 2} \right] & \Pi_{13} - \frac{i}{\epsilon^\gamma} \left[\mathbf{K}_{13} - \sum_{\alpha} \mathbf{K}_{1\alpha} \mathbf{J}_{\alpha 3} \right] \\ \Pi_{21} - \frac{i}{\epsilon^\gamma} \left[\mathbf{K}_{21} - \sum_{\alpha} \mathbf{K}_{2\alpha} \mathbf{J}_{\alpha 1} \right] & \Pi_{22} - \frac{i}{\epsilon^\gamma} \left[\mathbf{K}_{22} - \sum_{\alpha} \mathbf{K}_{2\alpha} \mathbf{J}_{\alpha 2} \right] & \Pi_{23} - \frac{i}{\epsilon^\gamma} \left[\mathbf{K}_{23} - \sum_{\alpha} \mathbf{K}_{2\alpha} \mathbf{J}_{\alpha 3} \right] \\ \Pi_{31} - \frac{i}{\epsilon^\gamma} \left[\mathbf{K}_{31} - \sum_{\alpha} \mathbf{K}_{3\alpha} \mathbf{J}_{\alpha 1} \right] & \Pi_{32} - \frac{i}{\epsilon^\gamma} \left[\mathbf{K}_{32} - \sum_{\alpha} \mathbf{K}_{3\alpha} \mathbf{J}_{\alpha 2} \right] & \Pi_{33} - \frac{i}{\epsilon^\gamma} \left[\mathbf{K}_{33} - \sum_{\alpha} \mathbf{K}_{3\alpha} \mathbf{J}_{\alpha 3} \right] \end{bmatrix} \quad (3.72)$$

$$= \begin{bmatrix} \Pi_{1 \leq i \leq d} - \frac{i}{\epsilon^\gamma} \mathbf{K}_{11} - \mathbf{W}^+ & -\Lambda_{d+1}^+ & -\frac{i}{\epsilon^\gamma} \mathbf{K}_{13} - \mathbf{U}^+ \\ -\Gamma \mathbf{1}_{1 \times d} & \Pi_{d+1} - \frac{i}{\epsilon^\gamma} \frac{1}{\tau_\psi} - \Gamma & -\Gamma \mathbf{1}_{1 \times d} \\ -\frac{i}{\epsilon^\gamma} \mathbf{K}_{31} - \mathbf{W}^- & -\Lambda_{d+1}^- & \Pi_{d+2 \leq i \leq 2d+1} - \frac{i}{\epsilon^\gamma} \mathbf{K}_{33} - \mathbf{U}^- \end{bmatrix}, \quad (3.73)$$

where

$$\Gamma = \frac{i}{\epsilon^\gamma} \frac{1}{\tau_\psi} \left(-1 + \sum_{\alpha} \frac{a_{\alpha}^{(1)}}{a_{\alpha}^{(2)}} \right) \in \mathbb{C}, \quad (3.74)$$

$$\Lambda_i^{\pm} = \frac{i}{\epsilon^\gamma} \left(\pm \frac{1}{\tau_\phi} \frac{1}{2\sqrt{\chi_\alpha^{(2)}}} \frac{\partial F_\alpha}{\partial g_i} - \frac{1}{\tau_\psi} \frac{a_{\alpha}^{(1)}}{2a_{\alpha}^{(2)}} \right)_{1 \leq \alpha \leq d} \in \mathbb{C}^d, \quad \text{for } 1 \leq i \leq 2d+1, \quad (3.75)$$

$$\Pi_{m \leq i \leq n} = \text{diag} \left((2\pi \mathbf{k} \cdot \mathbf{A}_i^d)_{m \leq i \leq n} \right) \in \mathbb{R}^{m-n+1}, \quad \text{for } 1 \leq m \leq n \leq 2d+1, \quad (3.76)$$

$$\mathbf{U}^{\pm} = \frac{i}{\epsilon^\gamma} \left(\pm \frac{1}{\tau_\phi} \frac{1}{2\sqrt{\chi_\alpha^{(2)}}} \frac{\partial F_\alpha}{\partial g_i} - \frac{1}{\tau_\psi} \frac{a_{\alpha}^{(1)}}{2a_{\alpha}^{(2)}} \right)_{\substack{1 \leq \alpha \leq 3 \\ d+2 \leq i \leq 2d+1}} \in \mathbb{C}^{d \times d}, \quad (3.77)$$

$$\mathbf{W}^{\pm} = \frac{i}{\epsilon^\gamma} \left(\pm \frac{1}{\tau_\phi} \frac{1}{2\sqrt{\chi_\alpha^{(2)}}} \frac{\partial F_\alpha}{\partial g_i} - \frac{1}{\tau_\psi} \frac{a_{\alpha}^{(1)}}{2a_{\alpha}^{(2)}} \right)_{\substack{1 \leq \alpha \leq 3 \\ 1 \leq i \leq d}} \in \mathbb{C}^{d \times d}. \quad (3.78)$$

Now fix $d = 1$. Thus $\mathbf{U}^{\pm} = \Lambda_3^{\pm}$ and $\mathbf{W}^{\pm} = \Lambda_1^{\pm}$, such that

$$\mathbf{V}(k, F, \mathbf{S}) = \begin{bmatrix} \Pi_1 - \frac{i}{\epsilon^\gamma} K_{11} - \Lambda_1^+ & -\Lambda_2^+ & -\frac{i}{\epsilon^\gamma} K_{13} - \Lambda_3^+ \\ -\Gamma & \Pi_2 - \frac{i}{\epsilon^\gamma} \frac{1}{\tau_\psi} - \Gamma & -\Gamma \\ -\frac{i}{\epsilon^\gamma} K_{31} - \Lambda_1^- & -\Lambda_2^- & \Pi_3 - \frac{i}{\epsilon^\gamma} K_{33} - \Lambda_3^- \end{bmatrix}. \quad (3.79)$$

In analogy to Corollary 3.1.1, we bound the sum of the absolute valued components in the i th row of \mathbf{V} in (3.79) to

$$\sum_{j=1}^3 |V_{ij}| \leq \begin{cases} |\Pi_i| + \sum_{j=1}^3 |-\Lambda_j^{\pm}| \sum_{j \in \{1,3\}} \left| -\frac{i}{\epsilon^\gamma} K_{ij} \right|, & \text{if } i = 1, 3, \\ |\Pi_i| + \sum_{j=1}^3 |-\Gamma| + \left| -\frac{i}{\epsilon^\gamma \tau_\psi} \right|, & \text{if } i = 2 \end{cases} \quad (3.80)$$

$$\leq \max_{i \in \{1,2,3\}} |\Pi_i| + \sum_{j=1}^3 \frac{1}{\epsilon^\gamma \tau_\phi} \left| \frac{1}{2\sqrt{\chi_1^{(2)}}} \frac{\partial F_1}{\partial g_j} \right| + \frac{3}{2} \frac{1}{\epsilon^\gamma \tau_\psi} \left| \frac{a_1^{(1)}}{a_1^{(2)}} \right| + \frac{1}{\epsilon^\gamma} \left(\frac{1}{\tau_\phi} + \frac{1}{\tau_\psi} \right) \quad (3.81)$$

$$\leq 2\pi \sqrt{\frac{a_1^{(2)}}{\epsilon^{2(\gamma-1)}}} + \sum_{j=1}^3 \frac{1}{\epsilon^\gamma \tau_\phi} \left| \frac{1}{2\sqrt{\chi_1^{(2)}}} \frac{\partial F_1}{\partial g_j} \right| + \frac{3}{2} \frac{1}{\epsilon^\gamma \tau_\psi} \left| \frac{a_1^{(1)}}{a_1^{(2)}} \right| + \frac{1}{\epsilon^\gamma} \left(\frac{1}{\tau_\phi} + \frac{1}{\tau_\psi} \right) =: b \quad (3.82)$$

for all i . We can infer from the Gerschgorin circle theorem that

$$r_{\text{spec}}(\mathbf{V}) = \max_{\lambda \in \text{spec}(\mathbf{V})} |\lambda| \leq \|\mathbf{V}\|_{\infty} \leq b. \quad (3.83)$$

Finally, from $b \leq 1$ in Definition 3.1.9 we obtain an upper bound for the artificial relaxation frequency $s_{\psi} = 1/\tau_{\psi}$ reading

$$s_{\psi} \leq \frac{\epsilon^{\gamma} - 2\pi\epsilon\sqrt{a_1^{(2)}} - \frac{1}{\tau_{\phi}} \left(\sum_{j=1}^3 \left| \frac{\epsilon^{\gamma-1}}{2\sqrt{a_1^{(2)}}} \frac{\partial F_1}{\partial g_j} \right| + 1 \right)}{\frac{3}{2} \left| \frac{a_1^{(1)}}{a_1^{(2)}} \right| + 1}. \quad (3.84)$$

The claim follows from Theorem 3.1.2. □

Remark 3.1.17. Albeit, the validity of the derived von Neumann stability set (3.70) holds only in the sense of a nonsharp bound, we have still proven that the stability of the relaxation limit can be consistently regulated via modulating τ_{ψ} within a certain regime.

3.2 Space-time-velocity discretization

The final step in the constructive ansatz (see Figure 3.1) is to discretize the TRS (3.44) in a consistent way in space and time such that the relaxation limit is upheld. *A priori* identifying the parameters of the TRS (3.44) with typical ones obtained from discrete velocity Boltzmann models yields an LBE on the space-time grid.

Based on the discretization, a second limit is introduced, which is analyzed with respect to both, consistency to the relaxation limit running already in the background and to the targeted PDE. To the knowledge of the author, the former notion (limit consistency) was initially motivated by Krause [158] and has been explicitly proposed for the first time in [230]. The latter work of the present author is part of Contribution (CTN2). The second notion of consistency (LBE to TEQ) is classical, and found to be implied if limit consistency is proved.

In addition to the consistency, stability is analyzed linearly in terms of von Neumann and the use of Lyapunov functionals for nonlinear target PDEs is discussed. A third, new notion of nonlinear stability (brute force stability [232]) is proposed, which includes grid effects by construction. Since the relaxation frequencies prefactor the relaxation terms in the closed form of the RS (see Section 3.1), the influence on the convergence in the coupled limit is crucial. This observation is outsourced in the proposal of a novel collision scheme which is based on flexible relaxation times dependent on nondimensional numbers present in the targeted PDE. Additionally, the key ingredient (entropy controlled relaxation) for nonlinear stability is isolated from the entropic MRT collision proposed by Karlin, Bösch and Chikatamarla (KBC) [148] and paired with a computationally efficient discrete velocity set and equilibrium.

3.2.1 Discrete velocity models

In the following, a $DdQq$ discrete velocity BGK–Boltzmann equation (DVBE) is derived classically from the BGKBE (2.33) and its equivalence to the generic TRS (3.44) with specific parameter choices is shown. This equivalence then implies rigorous relaxation convergence of the DVBE to the TEQ by construction.

The top-down ansatz proposed in Section 3.1 is currently applied, proved for convergence, and further analyzed for the case of the ADE (2.10) only. With increased complexity of the PDE to be approximated, thermodynamic information based on the (diffusive) limit of the BGKBE (see Section 2.3) is necessary. Nevertheless, the other parts of the coherent

framework (CTN2) are applicable, e.g. assessing linear stability for nonuniform relaxation based on understanding the DVBE as an RS, irrespective of its derivation being top-down or bottom-up.

Classically, the DVBE is a result of reducing the velocity space Ξ of the BGKBE (2.33) to a countable finite set $\mathcal{Q} := \{\mathbf{c}_i\}_{i=1,2,\dots,q} \subset \Xi = \mathbb{R}^d$ with $\#\mathcal{Q} = q$, which is abbreviated with $DdQq$. Examples of velocity sets are sketched in Figure 3.2. Note that since our definition of the velocity set is only unique up to ordering of its elements, we handle the numbering carelessly below. Let

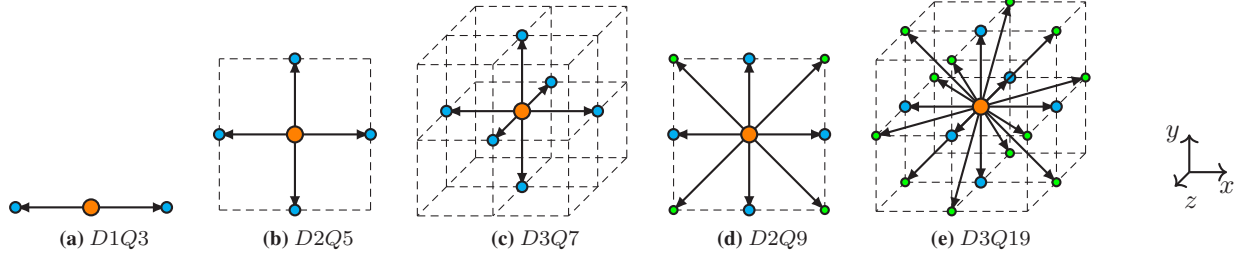


Figure 3.2: Discrete velocity sets $DdQ(2d+1)$ for $d = 1, 2, 3$, respectively (a–c), $D2Q9$ (d) and $D3Q19$ (e). Coloring refers to the corresponding energy shell, where orange, cyan and green denote zeroth, first and second order nodes, respectively.

$$w(\tilde{\mathbf{c}}_i) := \left(\frac{2}{3}\pi\right)^{\frac{d}{2}} \epsilon^{-d\delta} \exp\left(\frac{3}{2}\tilde{\mathbf{c}}_i^2\right) \in \mathcal{O}(\epsilon^{-d}) \quad (3.85)$$

define a weight function for $\tilde{\mathbf{c}}_i = \epsilon^{\delta/2}\mathbf{c}_i$. Unless stated otherwise, we assume unity particle mass $m = 1$ below.

Definition 3.2.1. For $d \in \mathbb{N}$, the $DdQ(2d+1)$ velocity set is defined through its elements

$$\mathbf{c}_i = \epsilon^{-\frac{\delta}{2}} \begin{cases} \mathbf{0}_{d \times 1} & \text{if } i = 1, \\ \pm \mathbf{e}_\alpha \forall \alpha & \text{if } i = 2, 3, \dots, 2d+1, \end{cases} \quad (3.86)$$

distributed on two energy shells. To each element, we attach a weight

$$w_i = w \begin{cases} \frac{\theta-d}{\theta} & \text{if } i = 1, \\ \frac{1}{2\theta} & \text{if } i \neq 1. \end{cases} \quad (3.87)$$

Unless stated otherwise, we use $\theta = 3$ if $d = 1, 2$ and $\theta = 4$ in case of $d = 3$.

Definition 3.2.2. The $D2Q9$ velocity set is defined through its elements

$$\mathbf{c}_i = \epsilon^{-\frac{\delta}{2}} \begin{cases} \mathbf{0}_{d \times 1} & \text{if } i = 1, \\ \pm \mathbf{e}_\alpha \forall \alpha & \text{if } i = 2, 3, \dots, 5, \\ (\pm 1, \pm 1)^T, & \text{if } i = 6, 7, \dots, 9 \end{cases} \quad (3.88)$$

distributed on three energy shells. To each element, we attach a weight

$$w_i = w \begin{cases} \frac{4}{9} & \text{if } i = 1, \\ \frac{1}{9} & \text{if } i = 2, 3, \dots, 5, \\ \frac{1}{36} & \text{if } i = 6, 7, \dots, 9. \end{cases} \quad (3.89)$$

Definition 3.2.3. The $D3Q19$ velocity set is defined through its elements

$$\mathbf{c}_i = \epsilon^{-\frac{\delta}{2}} \begin{cases} (0, 0, 0)^T & \text{if } i = 1, \\ (\pm 1, 0, 0)^T, (0, \pm 1, 0)^T, (0, 0, \pm 1)^T & \text{if } i = 2, 3, \dots, 7, \\ (0, \pm 1, \pm 1)^T, (\pm 1, \pm 1, 0)^T, (\pm 1, 0, \pm 1)^T & \text{if } i = 8, 9, \dots, 19, \end{cases} \quad (3.90)$$

distributed on three energy shells. To each element, we attach a weight

$$w_i = w \begin{cases} \frac{1}{3} & \text{if } i = 1, \\ \frac{1}{18} & \text{if } i = 2, 3, \dots, 7, \\ \frac{1}{36} & \text{if } i = 8, 9, \dots, 19. \end{cases} \quad (3.91)$$

Definition 3.2.4. Based on $DdQq$, the ϵ -parametrized DVBE derived from (2.45) with BGK collision, generalized scaling and multiple relaxation times reads

$$\partial_t \mathbf{f} + \sum_{\alpha=1}^d \mathbf{V}_\alpha \partial_\alpha \mathbf{f} = -\frac{1}{\epsilon^\gamma} \mathbf{M}^{-1} \mathbf{S} \mathbf{M} (\mathbf{f} - \mathbf{f}^{\text{eq}}(\mathbf{f})) \quad \text{in } \Omega_T, \quad (3.92)$$

where $\mathbf{f}: \Omega_T \rightarrow \mathbb{R}^q$ denote discrete velocity distribution functions, $\mathbf{S} = \text{diag}(\mathbf{s})$ is the relaxation matrix with $\mathbf{s} = (1/\tau_i)_{1 \leq i \leq q}$ and $\mathbf{V}_\alpha = \text{diag}((c_i)_\alpha)_{1 \leq i \leq q}$. The moment matrix \mathbf{M} and the truncated Maxwellian equilibria \mathbf{f}^{eq} are dependent on the TEQ and specified below. If $\tau_i = \tau$ for all i , the matrix $\mathbf{M}^{-1} \mathbf{S} \mathbf{M}$ reduces to the SRT BGK collision.

Remark 3.2.1. Notably the equilibrium formulation (2.46) used in the BGKBE is suitably expandable to yield a first order truncated model which is similar to (3.92) (see for example [184]). For the case of $D3Q19$ a derivation of a DVBE via velocity discretization of the ϵ -parametrized BGKBE and its consistency order in terms of ϵ is provided in [158, 230]. The velocity discrete equation thus still limits toward the NSE for $\epsilon \searrow 0$ and $\gamma = 2$, respecting the convergence result in Theorem 2.3.2. Hence, similarly to the TRS, the DVBE can be seen as a perturbed system providing the background limit which has to be taken account for in the discretization of space and time.

Definition 3.2.5. For the $DdQ(2d+1)$ let

$$\mathbf{M} = \begin{bmatrix} \mathbf{1}_{1 \times 1} & \mathbf{1}_{1 \times d} & \mathbf{1}_{1 \times d} \\ \mathbf{0}_{d \times 1} & -\epsilon^{-\frac{\delta}{2}} \mathbf{I}_d & \epsilon^{-\frac{\delta}{2}} \mathbf{I}_d \\ \mathbf{0}_{d \times 1} & \epsilon^{-\delta} \mathbf{I}_d & \epsilon^{-\delta} \mathbf{I}_d \end{bmatrix} \quad (3.93)$$

define a raw moment basis $\mathbf{m} = \mathbf{M} \mathbf{f}$ and set the relaxation times $\tau_1 = 0$, $\tau_{\alpha+1} = \tau$ and $\tau_{\alpha+(d+1)} = \tau_k$. The conserved moment is defined as

$$\rho_{\mathbf{f}} = \sum_{i=1}^q f_i. \quad (3.94)$$

Further, a first order truncation of the Taylor expanded Maxwellian equilibrium yields

$$f_i^{\text{eq}}(\mathbf{x}, t) := \left[\frac{w_i}{w} \rho_{f_i} (1 + 3\epsilon^\delta \mathbf{c}_i \cdot \mathbf{u}_{f_i}) \right] (\mathbf{x}, t). \quad (3.95)$$

Definition 3.2.6. For the $D3Q19$ DVBE approximating the incompressible NSE (2.12), the conserved moments and the equilibrium read

$$\rho_{f_i}(\mathbf{x}, t) := \sum_{i=1}^q f_i(\mathbf{x}, t), \quad (3.96)$$

$$\mathbf{u}_{f_i}(\mathbf{x}, t) := \frac{1}{\rho_{f_i}(\mathbf{x}, t)} \sum_{i=1}^q \mathbf{c}_i f_i(\mathbf{x}, t), \quad (3.97)$$

$$f_i^{\text{eq}}(\mathbf{x}, t) := \left\{ \frac{w_i}{w} \rho_{f_i} \left[1 + 3\epsilon^\delta \mathbf{c}_i \cdot \mathbf{u}_{f_i} - \frac{3}{2} \epsilon^\delta \mathbf{u}_{f_i}^2 + \frac{9}{2} \epsilon^{2\delta} (\mathbf{c}_i \cdot \mathbf{u}_{f_i})^2 \right] \right\}(\mathbf{x}, t), \quad (3.98)$$

respectively.

Below, the parameter combination $c_s := 1/\sqrt{3\epsilon^\delta}$ is called lattice speed of sound. In the present work, we consider two different moment bases for the $D3Q19$ velocity set. In both cases, the moment matrix $\mathbf{M} \in \text{GL}_q(\mathbb{R})$ is constructed with the mapping

$$m_i = \langle \phi^i, \mathbf{f} \rangle \quad (3.99)$$

based on the standard inner product $\langle \cdot, \cdot \rangle$ on \mathbb{R}^q , where $\phi^i = (\phi_j^i)_j \in \mathbb{R}^q$ are q vectorial representations of q linearly independent polynomials in discrete velocity vector entries. The polynomials P_{p_1, p_2, \dots, p_d} are constructed via generic moments

$$\rho_{p_1, p_2, \dots, p_d}^\Gamma = \left\langle \underbrace{((c_i)_1^{p_1} (c_i)_2^{p_2} \cdots (c_i)_d^{p_d})}_{{=P_{p_1, p_2, \dots, p_d}(c_i)}}, \mathbf{f} \right\rangle. \quad (3.100)$$

The compression of ϕ^i as rows of a matrix defines

$$\mathbf{M} = (M_{i,j})_{i,j} = (\phi_j^i)_{i,j} \in \mathbb{R}^{q \times q}, \quad (3.101)$$

inducing an isomorphic map $\mathbf{m} = \mathbf{M}\mathbf{f}$ from population to moment space. Further, let $\mathbf{W}^j = (W_i^j)_i \in \mathbb{R}^q$ denote the columns of \mathbf{M}^{-1} which are linearly independent by construction. Table 3.2 summarizes the natural moments constructed for $D3Q19$. Table 3.3 groups the moments into kinematic, shear, and kinetic types and assigns relaxation frequencies to the each group. The former two are regarded as hydrodynamic moments. Table 3.4 summarizes the orthogonal moments constructed for $D3Q19$ in a Gram–Schmidt process [66] and the corresponding relaxation frequencies. Additionally, the relaxation frequency configurations proposed in [66] and [52] are given.

Remark 3.2.2. The natural moment basis (Table 3.2) comprises nonorthogonalized linearly independent monomials (thus raw moments) except for N_{xz} , N_{yz} , and T . The additive redefinition of these moments is necessary to decouple shear and bulk viscosity [55, Equation (40)]. The orthogonal moment basis initially proposed in [66] has to be reduced to obtain the one in [52] (see for example [55]).

3.2.2 Discrete velocity stability and convergence

We prove linear stability for the $DdQ(2d+1)$ DVBE. Since space and time are still continuous, the present stability is solely with respect to the relaxation limit toward the TEQ. The first derivation is based on realizing that the $DdQ(2d+1)$ model is a special parameter configuration of the $(2d+1) \times (2d+1)$ TRS admitting a rigorous result from Bouchut *et al.* [37]. The second derivation evaluates the stability structures [219] for the $DdQ(2d+1)$ DVBE.

Table 3.2: Summary of natural moments and physical tensor notation used in the $D3Q19$ MRT collision.

physical tensor	moment
1	$\Gamma_{0,0,0}$
u_x, u_y, u_z	$\Gamma_{1,0,0}, \Gamma_{0,1,0}, \Gamma_{0,0,1}$
N_{xz}, N_{yz}	$\Gamma_{2,0,0} - \Gamma_{0,2,0}, \Gamma_{0,2,0} - \Gamma_{0,0,2}$
$\Pi_{xy}, \Pi_{yz}, \Pi_{xz}$	$\Gamma_{1,1,0}, \Gamma_{0,1,1}, \Gamma_{1,0,1}$
T	$\Gamma_{2,0,0} + \Gamma_{0,2,0} + \Gamma_{0,0,2}$
$Q_{xxz}, Q_{yzz}, Q_{xxz}, Q_{yyz}, Q_{xxy}, Q_{xyy}$	$\Gamma_{1,0,2}, \Gamma_{0,1,2}, \Gamma_{2,0,1}, \Gamma_{0,2,1}, \Gamma_{2,1,0}, \Gamma_{1,2,0}$
A_{xy}, A_{xz}, A_{yz}	$\Gamma_{2,2,0}, \Gamma_{2,0,2}, \Gamma_{0,2,2}$

Table 3.3: Summary of relaxation frequencies and orders of physical tensors resembling natural moments in the $D3Q19$ MRT collision. Note that moments of kinematic and shear type are considered to be hydrodynamic.

type	tensor	order	relaxation frequency s
kinematic	1	0	$s_k = 0$
	\mathbf{u}	1	
shear	N	2	$s_\nu = 2\beta = \frac{2c_s^2}{2\nu + c_s^2}$
	Π	2	
kinetic	T	2	$s := \beta\gamma^*$
	Q	3	
	A	4	

entropy controlled

Table 3.4: Summary of moments and corresponding relaxation frequencies used in $D3Q19$ MRT formulations in [66], [52], and the present work, respectively. The frequencies are in discrete form, where the lattice sound speed is denoted by c_s and physical interpretations for the tensors $\rho, \rho\mathbf{u}, e, P, \mathbf{q}, \boldsymbol{\mu}, \varepsilon,$ and Π are given in [66]. This table is reproduced from [232]. Copyright (2021), with permission from the authors and the Royal Society.

moment type	physical tensor	moment order	\tilde{s} [66]	\hat{s} [52]	s (present)
hydro-dynamic	ρ	0	0	0	0
	$\rho u_x, \rho u_y, \rho u_z$	1	0	0	0
	e	2	1.19	1.19 or $\frac{2c_s^2}{2\nu + c_s^2}$	s_e
	$3P_{xx}, P_{yy} - P_{zz}, P_{xy}, P_{yz}, P_{xz}$	2	$\frac{2c_s^2}{2\nu + c_s^2}$	$\frac{2c_s^2}{2\nu + c_s^2}$	s_P
kinetic	q_x, q_y, q_z	3	1.2	\hat{s}_q	s_q
	μ_x, μ_y, μ_z	3	1.98	\hat{s}_μ	s_μ
	ε	4	1.4	1.4	s_ε
	$3\Pi_{xx}, \Pi_{yy} - \Pi_{zz}$	4	1.4	1.4	s_Π

Let $q = 2d + 1$ (see Figure 3.2) and $\alpha = 1, 2, \dots, d$. Based on (3.91) we define a weight vector $\mathbf{w} = (w_i)_i$. Further, let $\mathbf{v}_\alpha = ((c_i)_\alpha)_i \in \mathbb{R}^q$ denote the vectors comprising the α th components of $\mathbf{c}_i \in \mathcal{Q}$ which are linearly independent

by construction and equal to $\Gamma_{e_\alpha^T}$. The rows of \mathbf{M} (3.93) are thus generated by $\Gamma_{\mathbf{0}_{1 \times d}}$, \mathbf{v}_α^T and $\Gamma_{2e_\alpha^T}$. Let the velocity model set be generalized by a variable speed $\lambda > 0$ such that $\mathcal{Q} \leftarrow \lambda \mathcal{Q}$. By construction, we have that

$$\mathbf{v}_\alpha^{\circ n} = \begin{cases} \mathbf{1}_{q \times 1}, & \text{if } n = 0, \\ \lambda^{n-1} \mathbf{v}_\alpha, & \text{if } n \text{ odd}, \\ \lambda^{n-2} \mathbf{v}_\alpha^{\circ 2}, & \text{if } n \text{ even}. \end{cases} \quad (3.102)$$

The structure relations for $DdQ(2d+1)$ are given by

$$\langle \mathbf{v}_\alpha^{\circ 0}, \mathbf{w} \rangle = 1, \quad \langle \mathbf{v}_\alpha^{\circ 1}, \mathbf{w} \rangle = 0, \quad \langle \mathbf{v}_\alpha^{\circ 2}, \mathbf{w} \rangle = \frac{\lambda^2}{\epsilon^\delta \theta}, \quad \langle \mathbf{v}_\alpha^{\circ 3}, \mathbf{w} \rangle = 0. \quad (3.103)$$

Remark 3.2.3. From identification of ρ_f with the conservative variable in (2.10), the relations (3.103) can be used to construct \mathbf{f}^{eq} based on the injection of the latter directly into the TEQ and removal of terms dependent on ϵ . Solving the resulting linear system then leads to (3.95).

Proposition 3.2.1. *The $DdQ(2d+1)$ DVBE (3.92) is a special case of the $(2d+1) \times (2d+1)$ RS (3.10).*

Proof. Comparing (3.92) to (3.44), equivalence of the $DdQ(2d+1)$ DVBE and the $(2d+1) \times (2d+1)$ TRS is obtained via fixing the parameters

$$\mathbf{A}_\alpha = \mathbf{V}_\alpha, \quad \mathbf{D} = \mathbf{M}, \quad \mathcal{G} = \mathbf{f}^{\text{eq}}, \quad \mathbf{a}^{(1)} := \frac{\lambda^2}{\theta} \mathbf{1}_{d \times 1}, \quad \mathbf{a}^{(2)} := \lambda^2 \mathbf{1}_{d \times 1}, \quad \mathbf{F}(\rho) = \mathbf{u}\rho. \quad (3.104)$$

□

Proposition 3.2.2. *The $DdQ(2d+q)$ DVBE (3.92) is formally consistent of order $\mathcal{O}(\epsilon^\gamma)$ to the ADE (2.10).*

Proof. The closed form (3.16) in Theorem 3.1.1 proves the claim. As discussed above (see Remark 3.1.6), an asymptotic expansion or a truncation error analysis could have been applied to obtain the same result. □

Theorem 3.2.1. *Let $\tau_i = 1$ for all i and $\rho_0 \in L^\infty(\Omega) \cap L^1(\Omega)$. Let $\mathbf{F}(\rho) = \mathbf{u}\rho$ be linear. If*

$$\frac{d\lambda^2}{\theta} = \mu, \quad (3.105)$$

$$\theta \geq d, \quad (3.106)$$

$$\frac{d\lambda}{\theta\sqrt{\epsilon^\delta}} \geq \sum_\alpha |u_\alpha|, \quad (3.107)$$

then the solution $\mathbf{f} \in C(I; L^1_{\text{loc}}(\Omega))^q \cap L^\infty(\Omega \times I)^q$ of the $DdQ(2d+1)$ DVBE (3.92) with initial data $\mathbf{f}(\mathbf{x}, 0) = \mathbf{f}^{\text{eq}}(\rho_0)$ converges (along a subsequence) to a bounded function

$$\lim_{\epsilon \searrow 0} \mathbf{f} = \mathbf{f}^* \quad \text{in } C(I; L^1_{\text{loc}}(\Omega)). \quad (3.108)$$

Further, $\rho_ = \iota(\mathbf{M}\mathbf{f}^*)$ is the unique solution to the TEQ (2.10) with periodic boundary conditions.*

Proof. Proposition 3.2.1 directly implies that \mathbf{f}^{eq} is a generalized Maxwellian in the sense of (M_1-M_4) . Additionally, the DVBE is relaxation stable based on the given conditions (3.105), (3.106), (3.107), such that convergence to (2.10) follows from Proposition 3.1.3 and [37]. □

Remark 3.2.4. The parameter setting (3.104) additionally generates equivalence of the initially constructed RS (3.10) to the moment system obtained from

$$\langle \mathbf{v}_\alpha^{\diamond 0}, (3.92) \rangle, \quad (3.109)$$

$$\langle \mathbf{v}_\alpha^{\diamond 1}, (3.92) \rangle, \quad (3.110)$$

$$\langle \mathbf{v}_\alpha^{\diamond 2}, (3.92) \rangle, \quad (3.111)$$

for all α . Hence, this moment summation reflects the reverse action of the spectral decomposition in Proposition 3.1.2.

Remark 3.2.5. With Proposition 3.1.3, we have verified rigorous structural stability of the TRS for uniform relaxation $\tau_b = 1$. Likewise, for the DVBE, (3.106) and (3.107) constitute rigorous stability conditions under the premise of uniform relaxation. Similar conditions for linear stability in combination with positivity constraints on \mathbf{f} have been found sufficient for stability of LBMs by Hosseini *et al.* [124].

We make a cross-comparison to the stability structures proposed by Banda *et al.* [15] for the DVBE and extended by Rheinländer [219] to a self-contained *a priori* stability notion for LBM. The pre-stability in [219] is used to obtain structural stability for the $DdQ(2d+1)$ DVBE. The following derivations are simplified by the assumed linearity of \mathbf{F} , which transforms the collision to a linear map induced by its Jacobian. In the case that \mathbf{F} is nonlinear and thus is \mathbf{Q} , the conceptual procedure [15] linearizes the collision around an equilibrium state to allow for stability structure conditions. We recall the following definition from [219].

Definition 3.2.7. The collision operator

$$\mathbf{Q}(\mathbf{f}) = -\frac{1}{\epsilon^\gamma} \mathbf{M}^{-1} \mathbf{S} \mathbf{M}(\mathbf{f} - \mathbf{f}^{\text{eq}}(\mathbf{f})) \quad \text{in } \Omega_T \quad (3.112)$$

in (3.92) admits a pre-stability structure, if there exists $\mathbf{H} \in \text{GL}_q(\mathbb{R})$ and $\mathbf{p} = (p_1, \dots, p_q)^\top, \mathbf{r} = (r_1, \dots, r_q)^\top \in \mathbb{R}^q$ such that

$$\begin{cases} \mathbf{H} \mathbf{J}_Q = -\text{diag}(\mathbf{p}) \mathbf{H}, \\ \mathbf{H}^\top \mathbf{H} = \text{diag}(\mathbf{r}), \end{cases} \quad (3.113)$$

where \mathbf{J}_Q denotes the Jacobian matrix of $\mathbf{Q}(\mathbf{f})$.

Corollary 3.2.1. The $DdQ(2d+1)$ collision operator (Definition 3.2.5), admits a pre-stability structure, if

$$\theta > d \quad \text{and} \quad \frac{d\lambda}{\theta \epsilon^{\frac{\delta}{2}}} > \sum_{\alpha} |\partial_{\rho} F_{\alpha}|. \quad (3.114)$$

Proof. The Jacobian matrix of the collision reads

$$\mathbf{J}_Q(\mathbf{f}) = -\frac{1}{\epsilon^\gamma} \mathbf{K}(\mathbf{I}_q - \mathbf{J}_{\mathbf{f}^{\text{eq}}}(\mathbf{f})), \quad (3.115)$$

where with (3.46) holds that

$$\mathbf{J}_G(\mathbf{g}) = \begin{bmatrix} \frac{1}{2} [\mathbf{a} - (\mathbf{C}^{(2)})^{\diamond -\frac{1}{2}} \partial_{\rho} \mathbf{F}] & \cdots & \frac{1}{2} [\mathbf{a} - (\mathbf{C}^{(2)})^{\diamond -\frac{1}{2}} \partial_{\rho} \mathbf{F}] \\ (1 - \mathbf{1}_{d \times 1} \cdot \mathbf{a}) & \cdots & (1 - \mathbf{1}_{d \times 1} \cdot \mathbf{a}) \\ \frac{1}{2} [\mathbf{a} + (\mathbf{C}^{(2)})^{\diamond -\frac{1}{2}} \partial_{\rho} \mathbf{F}] & \cdots & \frac{1}{2} [\mathbf{a} + (\mathbf{C}^{(2)})^{\diamond -\frac{1}{2}} \partial_{\rho} \mathbf{F}] \end{bmatrix}$$

$$\begin{aligned}
& \stackrel{\text{Prop. 3.2.1}}{=} \begin{bmatrix} \left[\frac{1}{2\theta} \mathbf{1}_{d \times 1} - \frac{\epsilon^{\frac{\delta}{2}}}{2\lambda} \partial_{\rho} \mathbf{F} \right] & \cdots & \left[\frac{1}{2\theta} \mathbf{1}_{d \times 1} - \frac{\epsilon^{\frac{\delta}{2}}}{2\lambda} \partial_{\rho} \mathbf{F} \right] \\ & \frac{\theta-d}{\theta} & \cdots & \frac{\theta-d}{\theta} \\ \left[\frac{1}{2\theta} \mathbf{1}_{d \times 1} + \frac{\epsilon^{\frac{\delta}{2}}}{2\lambda} \partial_{\rho} \mathbf{F} \right] & \cdots & \left[\frac{1}{2\theta} \mathbf{1}_{d \times 1} + \frac{\epsilon^{\frac{\delta}{2}}}{2\lambda} \partial_{\rho} \mathbf{F} \right] \end{bmatrix} \\
& = \mathbf{J}_{f^{\text{eq}}}(\mathbf{f}).
\end{aligned} \tag{3.116}$$

Each column of $\mathbf{J}_{f^{\text{eq}}}$ sums up to 1. Hence, the Jacobian matrix is a projector (cf. Corollary 3.1.1)

$$\mathbf{J}_{f^{\text{eq}}} \mathbf{J}_{f^{\text{eq}}} = \mathbf{J}_{f^{\text{eq}}}. \tag{3.117}$$

Henceforth,

$$\mathbf{Y} = \text{diag} \left(\left[\frac{1}{2\theta} \mathbf{1}_{d \times 1} - \frac{\epsilon^{\frac{\delta}{2}}}{2\lambda} \partial_{\rho} \mathbf{F} \right]^{\text{T}}, \frac{\theta-d}{\theta}, \left[\frac{1}{2\theta} \mathbf{1}_{d \times 1} + \frac{\epsilon^{\frac{\delta}{2}}}{2\lambda} \partial_{\rho} \mathbf{F} \right]^{\text{T}} \right) \tag{3.118}$$

is a unique symmetrizer for $\mathbf{J}_{f^{\text{eq}}}$. Condition (3.114) implies that \mathbf{Y} is positive definite. Via [219, Theorem 6, Proposition 13] the definitions of \mathbf{H} , \mathbf{p} and \mathbf{r} provide their respective existence which proves the claim. \square

Remark 3.2.6. Notably, the pre-stability structure conditions (3.114) differ from the relaxation stability conditions (3.57) and (3.58) solely in the additional equality case. Thus, in case of uniform relaxation, the existence of a pre-stability structure is a sufficient condition [219] for linear stability.

Remark 3.2.7. Below, we unfold the typical discretization of the LBM as a chaining of finite differences and Taylor's theorem. The thus induced shift in the relaxation matrix leads to a stability structure under an additional condition on the final relaxation frequencies. Stability bounds for space-time discrete evolution rules are specified below. Comparisons between the linear equilibrium (3.95) and the second order truncated one (3.98) used for relaxation toward the ADE (2.10) in the context of LBMs are provided for example in [53]. It is to be noted that the inclusion of equilibria akin to (3.98) into the current framework would require using extended perturbation terms for in the constructive ansatz. Such terms would in turn add more options for modulating the relaxation limit based on the right-hand side of the closed form (3.16).

3.2.3 Space-time Discretization

To obtain the final numerical scheme, we apply a limit consistent discretization through chaining Taylor expansions and finite difference operators². The following derivation is part of Contributions (CTN1) and (CTN2), completing the top-down construction in the former and upholding the overall convergence studied in the latter. The modular character of the following discretization procedure has to be stressed. Any given TRS or DVBE with a previously imposed scaling can be discretized in the following way to obtain an intrinsically parallel discrete evolution equation which forms the centerpiece of the LBM and limits toward the TEQ. The two subsequent sections provide an order analysis of the consistency as well as stability estimates for the here derived discretization.

Remark 3.2.8. For now, the limit consistency is with respect to the relaxation limit $\epsilon \searrow 0$ passing the TRS (3.44) to the targeted ADE (2.10). Compared to [230], we circumvent the path from DVBE to the BGKBE by directly connecting the DVBE to its macroscopic TEQ. The former pathway considering thermodynamic background information is treated further below for the HNSE (2.138) as a target. Compared to previous approaches which regard the space-time and velocity discretizations by separate methods, the distinct feature of the present methodology is thus manifested in its

² Parts of this section are reproduced from [230], Copyright (2022), with permission from the authors.

generic modularity. Hence, we postulate and enable to use thermodynamic information only if necessary to approximate the model PDE.

Remark 3.2.9. We motivate the following Definition 3.2.10 by comparison to existing approaches with the help of Figure 3.3. The illustration is based on a given relaxation (or kinetic) limit $\mathcal{A}^\epsilon \rightarrow \mathcal{C}$ for $\epsilon \searrow 0$ from a relaxation scheme

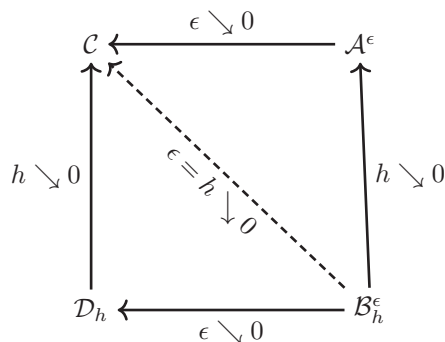


Figure 3.3: Schematic concept of kinetic and relaxation limits. The limit PDE of the relaxation operator is denoted with \mathcal{C} , the kinetic equation or RS is denoted with \mathcal{A}^ϵ , the kinetic scheme or relaxation scheme is denoted with \mathcal{B}_h^ϵ and the corresponding macroscopic scheme or relaxed scheme is \mathcal{D}_h . Here, h defines a space-time discretization. The diagonal limit $\mathcal{B}_h^\epsilon \rightarrow \mathcal{C}$ for $\epsilon = h \searrow 0$ is the present focus.

\mathcal{A}^ϵ induced by a relaxation operator (Definition 2.1.1) to its limit PDE \mathcal{C} which is the TEQ completed with artificial equations \mathbf{F}^{ar} . Considering the space-time discretization of the relaxation scheme \mathcal{B}_h^ϵ , the property of asymptotic preserving defines whether a stable and consistent space-time discretization \mathcal{D}_h exists in the macroscopic limit $\epsilon \searrow 0$ [113, 134, 137] (cf. Figure 3.3). If this is the case, the formal limit equality of equations

$$\lim_{h \searrow 0} \underbrace{\left(\lim_{\epsilon \searrow 0} \mathcal{B}_h^\epsilon \right)}_{=\mathcal{D}_h} \stackrel{!}{=} \lim_{\epsilon \searrow 0} \underbrace{\left(\lim_{h \searrow 0} \mathcal{B}_h^\epsilon \right)}_{=\mathcal{A}^\epsilon} = \mathcal{C} \quad (3.119)$$

should hold. In contrast to that, here the parameter ϵ is glued to the grid, i.e. $\epsilon \leftrightarrow h$, such that, in the context of LBMs we work with the formal limit equality

$$\lim_{\substack{\epsilon=h \\ h \searrow 0}} \mathcal{B}_h^\epsilon \stackrel{!}{=} \lim_{\epsilon \searrow 0} \underbrace{\left(\lim_{h \searrow 0} \mathcal{B}_h^\epsilon \right)}_{=\mathcal{A}^\epsilon} = \mathcal{C}, \quad (3.120)$$

rather than with (3.119). Drawing the analogy to limits and continuity of multivariate functions [88] (via $\mathcal{B}_h^\epsilon = \mathcal{B}(\epsilon, h)$), we expect that other shapes of paths than $\epsilon = h$ can be used. In fact, the mapping function $h \leftrightarrow \mathcal{O}(\epsilon^{\alpha_0})$ is analyzed in [113]. The overall order α_0 is the minimum of exponents from space Δx and time Δt discretization in the order of ϵ , respectively, and leads to distinct features of the scheme \mathcal{B}_h^ϵ . Presently, we focus on the order at which the limit point is approximated by the diagonal path ($\epsilon = h$). For the sake of completeness, we recall the abstract definition of limit consistency below which is firstly introduced by the author in [230] and has been motivated by Krause [158]. Notably, hybrid schemes have been derived e.g. by Klar [152], which are based on a DVBE but completed with an asymptotic preserving discretization to achieve uniform functionality for all ranges in ϵ .

Definition 3.2.8. Let $d \in \mathbb{N}$ and $X \subseteq \mathbb{R}^d$ with a discretization $X_h \subseteq X$ for any $h \in \mathbb{R}_{>0}$. Let $U(X)$ and $W_h(X_h)$ denote Hilbert spaces on X and X_h , respectively, where W_h contains the grid functions of $\{v_h: X_h \rightarrow \mathbb{R}\}$. Via

$$\mathcal{A}^\epsilon = (A^\epsilon(\cdot) = 0 \quad \text{in } U)_{\epsilon > 0}, \quad (3.121)$$

$$\mathcal{B}_h^\epsilon = (B_h^\epsilon(\cdot) = 0 \quad \text{in } W_h)_{\epsilon > 0, h > 0}, \quad (3.122)$$

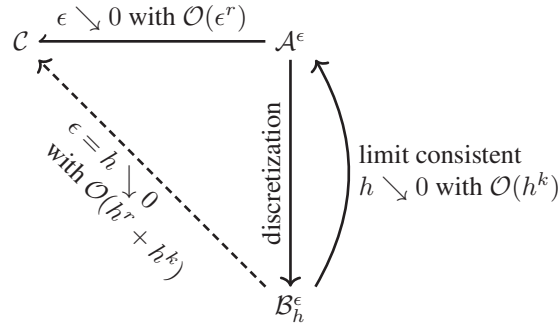


Figure 3.4: Schematic concept of limit consistency. Notation is similar to Figure 3.3. This figure is reproduced from [230].

families of PDEs are defined by continuous and discrete relaxation operators A^ϵ and B_h^ϵ , respectively. Solutions to instances of (3.121) and (3.122) are denoted with $a^\epsilon \in U$ for all $\epsilon > 0$ and $b_h^\epsilon \in W_h$ for all $\epsilon, h > 0$, respectively.

Conforming to Definition 3.2.8, we occasionally adopt the notation

$$\mathcal{C} = \left(C(\cdot) = 0 \quad \text{in } \tilde{U} \right) \quad (3.123)$$

for a single PDE with a solution c in the Hilbert space $\tilde{U}(X)$.

Definition 3.2.9. Let A^ϵ and \mathcal{C} be given as in (3.121) and (3.123), respectively. The abstracted solution limit of a solution a^ϵ to A^ϵ toward a solution c to \mathcal{C} for $\epsilon \searrow 0$ is denoted with

$$a^\epsilon \rightharpoonup c \quad (3.124)$$

and defines convergence in the broadest sense (e.g. formal, weak or strong). The formal order $r \geq 0$ of this convergence is $A^\epsilon(c) \in \mathcal{O}(\epsilon^r)$. The information of both, the formal PDE convergence and the solution convergence is compressed in the notation

$$A^\epsilon \xrightarrow[\mathcal{O}(\epsilon^r)]{\epsilon \searrow 0} \mathcal{C}. \quad (3.125)$$

Remark 3.2.10. Let A^ϵ be an RS induced by the relaxation operator F_{\sharp}^ϵ . Then \mathcal{C} is the contraction limit $(F_{\sharp}, F_{\sharp}^{\text{ar}})^{\text{T}}$, (2.4) in Definition 3.2.9. Similarly, the solution limit $a \rightharpoonup c$ is the relaxation limit of ρ^ϵ to $(\rho, \rho^{\text{ar}})^{\text{T}}$, (2.5) in Definition 3.2.9.

Based on the abstracted but formally determined background limit in Definition 3.2.9, we propose the following specialized notion of consistency.

Definition 3.2.10. Let A^ϵ admit an abstracted solution limit of order $\mathcal{O}(\epsilon^r)$ in $\epsilon \searrow 0$ to a solution c of a PDE system \mathcal{C} as in Definition 3.2.9. Then, B_h^ϵ is called limit consistent of order $k > 0$ to A^ϵ in $W_h(X_h)$, if for any fixed $\epsilon > 0$ holds that

- (i) $B_h^\epsilon(a^\epsilon|_{X_h}) \in \mathcal{O}(h^k)$ in W_h , and
- (ii) $k \geq r$.

The residual expression $B_h^\epsilon(a^\epsilon|_{X_h})$ is called truncation error.

Lemma 3.2.1. *Let \mathcal{B}_h^ϵ be limit consistent of order k to \mathcal{A}^ϵ in $W_h(X_h)$. Then for any fixed $\epsilon > 0$ we have*

$$[B_h^\epsilon(a^\epsilon|_{X_h}) \in \mathcal{O}(h^k) \quad \text{in } W_h] \iff \lim_{h \searrow 0} \sup_{x \in X_h} \left| \frac{B_h^\epsilon(a^\epsilon|_{X_h})(x)}{h^k} \right| < \infty. \quad (3.126)$$

Proof. We interpret the operation

$$\cdot|_{X_h} : U \rightarrow W_h, f \mapsto f|_{X_h} \quad (3.127)$$

as an interpolation which is exact at the grid nodes of X_h . Let $\epsilon > 0$ be fixed. Forming the local truncation error of B_h^ϵ with respect to A^ϵ , via insertion of the exact solution a^ϵ evaluated at the grid nodes [178], gives

$$B_h^\epsilon(a^\epsilon|_{X_h}) = Kh^k + \mathcal{O}(h^{k+1}), \quad (3.128)$$

with a constant $K < \infty$. Due to consistency, i.e. the local truncation nulling out for $h \searrow 0$, we can limit

$$\lim_{h \searrow 0} \|B_h^\epsilon(a^\epsilon|_{X_h})\| = 0, \quad (3.129)$$

where $\|\cdot\| := \sup_{x \in X_h} |\cdot|$ defines a supremum norm on W_h . Similarly, we have that

$$\lim_{h \searrow 0} \left\| \frac{B_h^\epsilon(a^\epsilon|_{X_h})}{h^k} \right\| = \lim_{h \searrow 0} \left\| \frac{Kh^k + \mathcal{O}(h^{k+1})}{h^k} \right\| = K + \mathcal{O}(1) < \infty. \quad (3.130)$$

□

Remark 3.2.11. It is to be stressed, that the difference to classical consistency is with respect to the exact solution a^ϵ being already parametrized in ϵ . Via the assignment of the artificial parameter $\epsilon \leftarrow h$ and the interpolation $a^{\epsilon \leftarrow h}|_{X_h}$ onto the grid nodes, the relaxation process is irreversibly coupled to the discretization. The process of discretization has thus to be consistent to the relaxation to at least uphold its limit. If this is the case, the limit consistency implies classical consistency with concatenated orders as described further below.

Remark 3.2.12. In Definition 3.2.10, we have purposely not specified the limit $\mathcal{A}^\epsilon \xrightarrow{\epsilon \searrow 0} \mathcal{C}$ further. Dependent on the situation at hand, this limit can be e.g. weak or strong. For example, the former is the case when approximating weak solutions of the incompressible NSE (2.12) with the BGKBE (2.33) [223] in diffusive scaling. The latter is given when using an RS (3.10) (or the corresponding BGK model, see Proposition 3.2.1), for the approximation of scalar, linear, d -dimensional ADE (2.10). The limit can also be in terms of unique entropy solutions, if \mathbf{F} is nonlinear [37].

Remark 3.2.13. Note that by Lemma 3.2.1, we have identified $B_h^\epsilon(a^\epsilon|_{X_h})$ as the abstracted local truncation error

$$-T_h^\epsilon := \underbrace{B_h^\epsilon(b_h^\epsilon)}_{=0} - B_h^\epsilon(a^\epsilon|_{X_h}) \quad (3.131)$$

(e.g. see [21, 178]) with an additional relaxation limit running in the background. As a consequence, demanding stability seems natural to complete the convergence result.

Let the global error be defined by

$$E_h^\epsilon = b_h^\epsilon - a^\epsilon|_{X_h}. \quad (3.132)$$

We cut off the Taylor expansion of $B_h^\epsilon(b_h^\epsilon)$ at $a^\epsilon|_{X_h}$ given by

$$B_h^\epsilon(b_h^\epsilon) = \sum_{n=0}^{\infty} \frac{1}{n!} (\partial_{b_h^\epsilon})^n B_h^\epsilon(a^\epsilon|_{X_h}) (E_h^\epsilon)^n \quad (3.133)$$

to obtain a linearized expression

$$J_{B_h^\epsilon}(a^\epsilon|_{X_h}) E_h^\epsilon = -T_h^\epsilon + \mathcal{O}(\|E_h^\epsilon\|^2), \quad (3.134)$$

where $J_{B_h^\epsilon}(a^\epsilon|_{X_h})$ denotes the Jacobian of the discrete relaxation PDO B_h^ϵ at exact solutions a^ϵ of A^ϵ evaluated on the grid. The nonlinear terms are gathered in $\mathcal{O}(\|E_h^\epsilon\|^2)$. Following [178] we can define the following notion of stability with respect to the linearized discretization.

Definition 3.2.11. For fixed ϵ , the linearized discrete relaxation PDO B_h^ϵ is stable in some norm $\|\cdot\|_{W_h}$ on W_h if its inverse Jacobian at the exact solution evaluated at X_h is uniformly bounded for $h \searrow 0$ in the sense that there exist constants $K > 0$ and h_0 such that

$$\left\| (J_{B_h^\epsilon}(a^\epsilon|_{X_h}))^{-1} \right\| \leq K \quad \text{for all } h < h_0. \quad (3.135)$$

Remark 3.2.14. In the context of the LBM, where B_h^ϵ is the lattice Boltzmann equation (LBE) for $\epsilon \leftrightarrow h$, several previous works derived bounds for linearized amplification matrices in the sense of von Neumann (e.g. [231]) and proved weighted L^2 -stability [142] for linearized collisions which admit a stability structure. As a matter of fact, nonlinear stability estimates for LBMs naturally involve the notion of entropy in a mathematical (relaxation) [43] or thermodynamical [34] sense. To the knowledge of the author, coherent methodologies for evaluating the nonlinear stability of LBMs for realistic IBVPs involving $d \geq 2$ have not been established so far.

Remark 3.2.15. Upon condition that the lattice Boltzmann discretizations are stable in some norm, limit consistency can be used to infer classical consistency and hence convergence [178, 243] toward the target PDE. Below, the overall notion of convergence is to be understood in terms of the kind of relaxation or kinetic background limit $\mathcal{A}^\epsilon \xrightarrow{\epsilon \searrow 0} \mathcal{C}$ only (e.g. formal, weak or strong).

Lemma 3.2.2. Let \mathcal{A}_h^ϵ and \mathcal{B}_h^ϵ be given as in Definition 3.2.10 and let

- (i) \mathcal{B}_h^ϵ be limit consistent of order k to \mathcal{A}^ϵ ,
- (ii) its underlying PDO B_h^ϵ be stable and linear in the sense of Definition 3.2.11.

Then we obtain an overall convergence result of solutions in the sense of

$$\mathcal{B}_h^\epsilon \xrightarrow[\mathcal{O}(\epsilon^r)|_{X_h} + \mathcal{O}(\epsilon^k)]{(\epsilon, h) \searrow (0,0)} \mathcal{C} \equiv \left(\mathcal{A}^\epsilon \xrightarrow[\mathcal{O}(\epsilon^r)]{\epsilon \searrow 0} \mathcal{C} \right) \circ \left(\mathcal{B}_h^\epsilon \xrightarrow[\mathcal{O}(h^k)]{h \searrow 0} \mathcal{A}^\epsilon \right), \quad (3.136)$$

where the symbol \equiv denotes arrow equality irrespective of the nature of the mappings. Further, if $\epsilon = \iota(h)$ via $\iota = \text{id}$, b_h^ϵ converges at order r to c .

Proof. For fixed $\epsilon > 0$, limit consistency of \mathcal{B}_h^ϵ and the stability of B_h^ϵ imply classically [175] that

$$\begin{aligned} \|E_h^\epsilon\| &= \left\| - (J_{B_h^\epsilon}(a^\epsilon|_{X_h}))^{-1} T_h^\epsilon + \mathcal{O}(\|E_h^\epsilon\|^2) \right\| \\ &\leq \left\| (J_{B_h^\epsilon}(a^\epsilon|_{X_h}))^{-1} \right\| \|T_h^\epsilon\| \\ &\leq K \mathcal{O}(h^k) \end{aligned} \quad (3.137)$$

and hence

$$b_h^\epsilon = a^\epsilon|_{X_h} + \mathcal{O}(h^k). \quad (3.138)$$

Similarly, from the background relaxation limit, we have that

$$a^\epsilon = c + \mathcal{O}(\epsilon^r). \quad (3.139)$$

Combining (3.138) and (3.139) we obtain

$$b_h^\epsilon = c|_{X_h} + \mathcal{O}(\epsilon^r)|_{X_h} + \mathcal{O}(h^k). \quad (3.140)$$

Now let $\epsilon \leftarrow \iota(h)$. Thus, since $\mathcal{O}(\epsilon^r)|_{X_h}$ are higher order terms interpolated on the grid nodes, we see that their leading order in h is r . Conclusively, (3.140) becomes

$$\begin{aligned} b_h^\epsilon &= c|_{X_h} + \mathcal{O}(\iota(h)^r + h^k) \\ &= c|_{X_h} + \mathcal{O}(h^{\min\{r,k\}}) \\ &= c|_{X_h} + \mathcal{O}(h^r), \end{aligned} \quad (3.141)$$

due to the limit consistent discretization. \square

Remark 3.2.16. Rheinländer [218, Corollary 3.4.] has rigorously proved second order convergence of zeroth moments of a $D1Q3$ DVBE to the solution of a reaction–diffusion equation akin to (2.10) with equal scaling, zero flux ($\mathbf{F} = \mathbf{0}$) and an additional linear reaction term. Further, first and second order moments are proven to converge toward first and second order spatial derivatives of the conserved variable. The convergence rates of the rescaled moments are also two, provided the prefactor is ϵ^{-o} , where o is the respective moment order. As already indicated in the closed form (3.24), the convergence is of order $\mathcal{O}(\epsilon^2)$ for $\gamma = 2$ for $\rho^{\epsilon\epsilon}$. We thus anticipate the overall convergence of the below derived LBE to be of second order in the grid parameters.

In regard to Definition 3.2.10 and above derived consequences, we provide limit consistent discretizations of the ϵ -parametrized DVBE. In particular, we use finite differences and Taylor series to obtain a space-time discrete evolution equation which defines the numerical scheme for periodic solutions. To implement the result of Lemma 3.2.2, we further generalize the relaxation scaling when mapping the discretization of space and time to ϵ .

Let $\mathbf{K}_i \in \mathbb{R}^q$ denote the i th row of \mathbf{K} and \hat{c}_j be the dimensionless integer discrete velocities. The i th component of equation (3.92) reads

$$\partial_t f_i + \frac{1}{\hat{\sigma}(\epsilon)} \hat{c}_i \cdot \nabla_{\mathbf{x}} f_i = -\frac{1}{\sigma(\epsilon)} \mathbf{K}_i (\mathbf{f} - \mathbf{f}^{\text{eq}}(\mathbf{f})) \quad (3.142)$$

and defines the scaled component-wise material derivative

$$\frac{D}{Dt} := \partial_t + \frac{1}{\hat{\sigma}(\epsilon)} \hat{c}_i \cdot \nabla_{\mathbf{x}}, \quad (3.143)$$

where $\sigma(\epsilon), \hat{\sigma}(\epsilon) \in \mathcal{P}(\epsilon)$ are scaling monomials defined by

$$\hat{\sigma}: (0, 1) \rightarrow \mathbb{R}, (\epsilon) \mapsto \epsilon^{\hat{s}}, \quad (3.144)$$

$$\sigma: (0, 1) \rightarrow \mathbb{R}, (\epsilon) \mapsto \epsilon^s, \quad (3.145)$$

where $s, \hat{s} \in \mathbb{N}_0$. Note that we have suppressed the i -dependence of D/Dt for the sake of simplicity. The imposed scaling of the RS (3.10) can be recovered via $\hat{s} = \delta/2$ and $s = \gamma$.

Definition 3.2.12. Using the notation from Definition 3.2.8, let the ϵ -parametrized DVBE (3.142) define the family

$$\mathcal{A}^\epsilon := \left(\frac{D}{Dt} f_i^\epsilon + \frac{1}{\sigma(\epsilon)} \mathbf{K}_i(\mathbf{f}^\epsilon - \mathbf{f}^{\text{eq},\epsilon}(\mathbf{f}^\epsilon)) = 0 \quad \text{in } \Omega \times I \times Q \right)_{\epsilon > 0}, \quad (3.146)$$

where Q denotes the velocity space $DdQq$ with $q = 2d + 1$ and $i = 1, 2, \dots, q$. Note that the conserved variables in (3.146) now display an upper index ϵ to highlight the dependence on relaxation parameters.

Remark 3.2.17. Compared to our previous work [230], (3.146) is a generalized version of the classical discrete velocity BGKBE with first order equilibrium in both, the scaling as well as the moment-wise relaxation, albeit for $DdQ(2d+1)$.

We synchronize the relaxation with the discretization limit with the help of the scaling function σ . A Cartesian grid $\Omega_{\Delta x} \subseteq \Omega$ with $N + 1$ nodes x per dimension is embedded. The largest cubic subdomain $\tilde{\Omega}_{\Delta x} \subseteq \Omega_{\Delta x}$ dictates the discretization intervals in space $\Delta x = |\tilde{\Omega}_{\Delta x}|^{1/d}/N$. To obtain an evolution rule on the space-time cylinder Ω_T , the discrete time interval is defined regularly as

$$I_{\Delta t} := \{t = t_0 + k\Delta t \mid t_0 \in I, k \in \mathbb{N}\} \subseteq I. \quad (3.147)$$

Here and below, the parametrization obeys

$$\Delta x \sim \hat{\sigma}(\epsilon), \quad (3.148)$$

$$\Delta t \sim \sigma(\epsilon). \quad (3.149)$$

The positioning in the discrete velocity is set through

$$c_{i\alpha} = \frac{\hat{\sigma}(\epsilon)}{\sigma(\epsilon)} c_{i\alpha} \quad \text{for all } \alpha, \quad (3.150)$$

where $c_{i\alpha} \in \{0, \pm 1\}$, and provides an evolution rule through the discrete space-time cylinder connecting the corresponding neighbors via $\hat{c}_i = (c_{i\alpha})_{1 \leq \alpha \leq d}$ on up to two energy shells ($|\hat{c}_i| \leq 1$ for all i). We can thus reduce the arguments of f^ϵ to time only as follows.

Definition 3.2.13. Let f_i^h denote a solution to the parametrized DVBE (3.146). For $i = 1, 2, \dots, q$ and $\zeta \in \mathbb{R}$, we define the i th population

$$f_i^\epsilon(t + \zeta\sigma(h)) = f_i^\epsilon(\cdot, t + \zeta\sigma(h)) := f_i^\epsilon\left(\mathbf{x} + \zeta \frac{\sigma(h)}{\hat{\sigma}(h)} \hat{c}_i, t + \zeta\sigma(h)\right) \quad (3.151)$$

for (\mathbf{x}, t) in the discrete space-time cylinder $Z_h := \Omega_{\Delta x} \times I_{\Delta t} \subseteq \Omega \times I$.

Based on the definition of space-time coupled population arguments (3.151), the grid conforming space-time coupling (3.149), and the scaled material derivative (3.143), we project space onto time and consider Taylor expansions in the temporal argument only. Let f^ϵ be at least of class C^3 with respect to D/Dt . Unless stated otherwise, $\mathcal{O}(h^0 + \epsilon^0) = \mathcal{O}(1)$.

To derive the LBE, we approximate the DVBE (3.146) using three discrete points in time $(t, t + \sigma(h)/2, t + \sigma(h))$ (see Figure 3.5), where the midpoint $t + \sigma(h)/2$ is a ghost node for the derivation and cancels in the final evolution equation of the scheme. Since the width of the stencil is linked to the relaxation scaling, limit consistency is implicitly ensured.

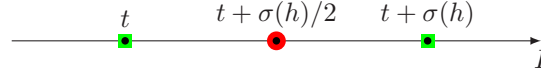


Figure 3.5: Time steps used for the discretization. The final LBE operates on the green squares only. Red points are canceled in the derivation.

Definition 3.2.14. Let $r: \mathbb{R} \rightarrow \mathbb{R}, y \mapsto r(y)$ denote a C^∞ -function and $a \in \mathbb{R}_{\geq 0}$ be a point on the nonnegative real line. We define the following finite difference operations:

1. central difference

$$r'(y) = \frac{1}{a} \left(r\left(y + \frac{a}{2}\right) - r\left(y - \frac{a}{2}\right) \right) + \mathcal{O}(a^2), \quad (3.152)$$

2. forward difference

$$r'(y) = \frac{1}{a} (r(y+a) - r(y)) + \mathcal{O}(a), \quad (3.153)$$

3. Taylor's theorem

$$r(y) = r(a) + r'(a)(y-a) + \mathcal{O}(|y-a|^2). \quad (3.154)$$

Definition 3.2.15. Let $q = 2d + 1$. To prevent trivial solutions let

$$\left(\frac{D}{Dt} \right)^j f_i^\epsilon \in \mathcal{O}(1) \quad (3.155)$$

for all $1 \geq i \geq q$ and for $j = 0, 1, \dots, \hat{\alpha}$. Let $\hat{\alpha} = 3$. For a given population \mathbf{f}^ϵ , we denote its moments with an explicit selfsame index

$$\rho_{\mathbf{f}^\epsilon} = \mathbf{M} \mathbf{f}^\epsilon. \quad (3.156)$$

and realize with (3.38) that

$$\rho_{\mathbf{f}^\epsilon} = \mathbf{M}_1 \cdot \mathbf{f}^\epsilon \in \mathcal{O}(1), \quad (3.157)$$

$$\phi_{\mathbf{f}^\epsilon, \alpha} = \mathbf{M}_{\alpha+1} \cdot \mathbf{f}^\epsilon \in \mathcal{O}(\hat{\sigma}^{-1}(\epsilon)), \quad (3.158)$$

$$\psi_{\mathbf{f}^\epsilon, \alpha} = \mathbf{M}_{\alpha+(d+1)} \cdot \mathbf{f}^\epsilon \in \mathcal{O}(\hat{\sigma}^{-2}(\epsilon)), \quad (3.159)$$

where M_j denotes the j th row of the unified diagonalizer \mathbf{M} of \mathbf{V}_α .

Remark 3.2.18. Here, conservation of moments can thus be understood in terms of limiting values for $\epsilon \searrow 0$ being nonzero which implies the order of magnitude $\mathcal{O}(1)$. The value of $\hat{\alpha}$ will be unfolded further below (see Proposition 3.2.4). Moreover, since (3.156) is a result of our constructive ansatz and thus doubly perturbed with ϵ , we immediately observe the connection to Remark 3.2.16. Hence, the introduction of artificial variables implies the necessity of rescaling the nonconserved moments to equalize the convergence order of (3.157), (3.158), and (3.159).

Proposition 3.2.3. *The h -parametrized LBE*

$$\mathcal{B}_h^{\epsilon \leftarrow h} = (f_i^h(t + \sigma(h)) - f_i^h(t) + \mathbf{K}_i^s(\mathbf{f}^h(t) - \mathbf{f}^{\text{eq},h}(t))) = 0 \quad \text{in } Z_h \times Q)_{h>0} \quad (3.160)$$

can be derived as explicit evolution rule from the DVBE (3.146) using three points in time $(t, t + \sigma(h)/2, t + \sigma(h))$ only. Here, \mathbf{K}_i^s denotes the i th row of the shifted collision matrix

$$\mathbf{K}^s = \mathbf{M}^{-1} \mathbf{S}^s \mathbf{M}, \quad (3.161)$$

with the shifted relaxation matrix

$$\mathbf{S}^s = \text{diag} \left(\frac{1}{\frac{1}{S_{ii}} + \frac{1}{2}} \right)_{1 \leq i \leq q}. \quad (3.162)$$

Proof. We evaluate $\sigma(\epsilon) \times (3.146)|_{(\mathbf{x}+(1/2)(\sigma(h)/\hat{\sigma}(h))\hat{\mathbf{c}}_i, t+(1/2)\sigma(h))}$ and proceed on the time domain only due to (3.151). To remove the function evaluations on the ghost node $t + \sigma(h)$ (cf. Figure 3.5), the finite difference operations (3.152), (3.153) and (3.154) are linked up as follows. Let $R_t^{(n)}$ denote the n th remainder term for $n \in \mathbb{N}$ with respect to the space-time discretization adhered according to the scaling functions $\hat{\sigma}$ and σ . A central difference of $(D/Dt)f_i^\epsilon$ at the node $t + \sigma(h)/2$ yields

$$\sigma(h) \frac{D}{Dt} f_i^\epsilon \left(t + \frac{1}{2} \sigma(h) \right) = f_i^\epsilon(t + \sigma(h)) - f_i^\epsilon(t) + R_t^{(1)} \quad \text{in } \Omega_T, \quad (3.163)$$

where

$$R_t^{(1)} \in \mathcal{O}(\sigma(h)^3), \quad (3.164)$$

provided that $(D/Dt)^3 f_i^\epsilon \in \mathcal{O}(1)$. Taylor's theorem applied to f_i^ϵ at $t + \sigma(h)/2$ with the expansion point t , and a forward difference of $(D/Dt)f_i^\epsilon$ at t gives

$$\begin{aligned} f_i^\epsilon \left(t + \frac{1}{2} \sigma(h) \right) &= f_i^\epsilon(t) + \frac{1}{2} \sigma(h) \frac{D}{Dt} f_i^\epsilon(t) + R_t^{(2)} \\ &= f_i^\epsilon(t) + \frac{1}{2} [f_i^\epsilon(t + \sigma(h)) - f_i^\epsilon(t)] + R_t^{(3)} \end{aligned} \quad (3.165)$$

in Ω_T , where

$$R_t^{(2)} \in \mathcal{O}(\sigma(h)^2), \quad (3.166)$$

$$R_t^{(3)} \in \mathcal{O}(\sigma(h)^2), \quad (3.167)$$

provided that $(D/Dt)^2 f_i^\epsilon \in \mathcal{O}(1)$. At last, we apply Taylor's theorem to the equilibrium to obtain

$$f_i^{\text{eq}, \epsilon} \left(t + \frac{1}{2} \sigma(h) \right) = f_i^{\text{eq}, \epsilon}(t) + \frac{1}{2} \sigma(h) \frac{D}{Dt} f_i^{\text{eq}, \epsilon}(t) + R_t^{(4)} \quad (3.168)$$

$$= f_i^{\text{eq}, \epsilon}(t) + R_t^{(5)}, \quad (3.169)$$

in Ω_T . By construction $f_i^\epsilon, (D/Dt)f_i^\epsilon \in \mathcal{O}(1)$ (cf. Definition 3.2.15), thus

$$R_t^{(4)} \in \mathcal{O}(\sigma(h)). \quad (3.170)$$

We use (3.46) and (3.157) to see that $(D/Dt)f^{\text{eq}, \epsilon} \in \mathcal{O}(1)$. Hence, from the latter being prefactored by $\sigma(h)$ in (3.168), we have

$$R_t^{(5)} \in \mathcal{O}(\sigma(h)). \quad (3.171)$$

As planned, we insert (3.151), (3.163), (3.165), and (3.168), in $\sigma(\epsilon) \times (3.146)|_{(\mathbf{x}+(1/2)(\sigma(h)/\hat{\sigma}(h))\hat{\mathbf{e}}_i, t+(1/2)\sigma(h))}$ to obtain in matrix form

$$\begin{aligned} 0 &= \sigma(\epsilon) \frac{\mathfrak{D}}{\mathfrak{D}t} \diamond \mathbf{f}^\epsilon \left(t + \frac{1}{2}\sigma(h) \right) + \mathbf{K} \left(\mathbf{f}^\epsilon \left(t + \frac{1}{2}\sigma(h) \right) - \mathbf{f}^{\text{eq},\epsilon} \left(t + \frac{1}{2}\sigma(h) \right) \right) \\ &= \underbrace{\frac{\sigma(\epsilon)}{\sigma(h)}}_{\sigma^s} \left[\mathbf{f}^\epsilon(t + \sigma(h)) - \mathbf{f}^\epsilon(t) + \mathbf{R}_t^{(1)} \right] + \mathbf{K} \left\{ \mathbf{f}^\epsilon(t) + \frac{1}{2} [\mathbf{f}(t + \sigma(h)) - \mathbf{f}(t)] + \mathbf{R}_t^{(3)} - \mathbf{f}^{\text{eq},\epsilon}(t) - \mathbf{R}_t^{(5)} \right\} \\ &= \left(\sigma^s \mathbf{I}_q + \frac{1}{2} \mathbf{K} \right) [\mathbf{f}^\epsilon(t + \sigma(h)) - \mathbf{f}^\epsilon(t)] + \underbrace{\mathbf{K} [\mathbf{f}^\epsilon(t) - \mathbf{f}^{\text{eq},\epsilon}(t)] + \mathbf{K} (\mathbf{R}_t^{(3)} - \mathbf{R}_t^{(5)}) + \sigma^s \mathbf{R}_t^{(1)}}_{=:\tilde{\mathbf{R}}_t}, \end{aligned} \quad (3.172)$$

where

$$\frac{\mathfrak{D}}{\mathfrak{D}t} := \partial_t \mathbf{1}_{q \times 1} + \sum_{k=\alpha}^d \mathbf{V}_\alpha (\partial_\alpha \mathbf{1}_{q \times 1}) \in \mathbb{R}^q \quad (3.173)$$

denotes the vector material derivative with $\mathbf{V}_\alpha = \mathbf{A}_\alpha^d \in \mathcal{O}(\hat{\sigma}^{-1}(\epsilon))$ from (3.39) and $\mathbf{R}_t^{(n)} = R_t^{(n)} \mathbf{1}_{q \times 1}$. The multiplication $(\sigma^s \mathbf{I}_q + (1/2)\mathbf{K})^{-1} \times (3.172)$ yields

$$\mathbf{f}^\epsilon(t + \sigma(h)) - \mathbf{f}^\epsilon(t) + \underbrace{\left(\sigma^s \mathbf{I}_q + \frac{1}{2} \mathbf{K} \right)^{-1} \mathbf{K} [\mathbf{f}^\epsilon(t) - \mathbf{f}^{\text{eq},\epsilon}(t)]}_{=:\mathbf{K}^s} = -\tilde{\mathbf{R}}_t. \quad (3.174)$$

Using the Woodbury matrix identity [266] we have that

$$\begin{aligned} \mathbf{K}^s &= \left[(\sigma^s \mathbf{I}_q) + \mathbf{M}^{-1} \left(\frac{1}{2} \mathbf{S} \right) \mathbf{M} \right]^{-1} \mathbf{K} \\ &= \left\{ \mathbf{M}^{-1} (\sigma^s \mathbf{I}_q)^{-1} \mathbf{M} - (\sigma^s \mathbf{I}_q)^{-2} \mathbf{M}^{-1} \left[2\mathbf{S}^{-1} + (\sigma^s \mathbf{I}_q)^{-1} \right]^{-1} \mathbf{M} \right\} \mathbf{M}^{-1} \mathbf{S} \mathbf{M} \\ &= \mathbf{M}^{-1} \underbrace{\left[(\sigma^s \mathbf{I}_q)^{-1} - (\sigma^s \mathbf{I}_q)^{-2} \left(2\mathbf{S}^{-1} + (\sigma^s \mathbf{I}_q)^{-1} \right)^{-1} \right]}_{=:\mathbf{S}^s} \mathbf{S} \mathbf{M}. \end{aligned} \quad (3.175)$$

The precise order of magnitude of $-\tilde{\mathbf{R}}_t$ in (3.174) is determined further below. From the present derivation, it is obviously at least of order $\sigma(h)$ which permits us to use (3.174) as an approximation of 0 for $h \searrow 0$. In case of $\mathbf{S} = \text{diag}(S_{ii})_{1 \leq i \leq q}$ all operations in the shifted relaxation matrix \mathbf{S}^s are Hadamard which yields

$$\mathbf{S}^s = \text{diag} \left(\frac{1}{\sigma^s (S_{ii}^{-1} + \frac{1}{2\sigma^s})} \right) \in \mathcal{O} \left(\frac{\sigma(h)}{\sigma(\epsilon)} \right). \quad (3.176)$$

Finally, the assignment $\epsilon \leftarrow h$ proves the claim. \square

3.2.4 Limit consistency

Proposition 3.2.4. *For given $h, \mu > 0$, let \mathbf{f}^ϵ denote a weak solution of the ϵ -parametrized DVBE (3.146) with the conserved moment $\rho_{\mathbf{f}^\epsilon}$. Further, let*

$$\rho_{\mathbf{f}^\epsilon} \in \mathcal{O}(1) \quad \text{in } Z_h, \quad (3.177)$$

$$\left(\frac{D}{Dt}\right)^j f_i^\epsilon \in \mathcal{O}(1) \quad \text{in } Z_h, \quad \text{for } j = 0, 1, 2, 3, \quad (3.178)$$

for $i = 1, 2, \dots, q$ understood as functions of h . Then, the family $\mathcal{B}_h^{\epsilon \leftarrow h}$ of LBEs (3.160) is limit consistent of order $\sigma(h)$ to the ϵ -parametrized DVBE \mathcal{A}^ϵ (3.146) in $Z_h \times Q$.

Proof. With (3.164), (3.166), (3.167), (3.170), (3.171), and (3.176), we asymptotically estimate (3.174)

$$\mathbf{f}^\epsilon(t + \sigma(h)) - \mathbf{f}^\epsilon(t) = -\mathbf{K}^s [\mathbf{f}^\epsilon(t) - \mathbf{f}^{\text{eq}, \epsilon}(t)] - \tilde{\mathbf{R}}_t \in \mathcal{O}\left(\frac{\sigma(h)}{\sigma(\epsilon)} + \sigma(h) + \sigma(\epsilon)\sigma(h)^2\right), \quad (3.179)$$

which is consistent to \mathcal{A}^ϵ with order $\mathcal{O}(\sigma(h))$ for fixed $\epsilon > 0$. The relaxation consistency of $\mathcal{O}(\sigma(\epsilon))$ approves Definition 3.2.10 and thus proves the claim. \square

Remark 3.2.19. At this point, we see that the notion of limit consistency is stronger than consistency in the classical sense, due to the additional requirement on the order of the limiting process. Each limit (relaxation and discretization) contributes individual stability and consistency estimates of which both have been proven for the relaxation process. Consistency and limit consistency are proved for the discretization so far. Hence, the stability of the discretization limit is analyzed below in order to prove the overall convergence.

3.2.5 Stability

To account for nonuniform and nonconstant relaxation frequencies, we use a linear von Neumann estimate on the fully discrete scheme. As proposed by the author in [232], based on the notion of stability, we define stability sets for the relaxation times which is part of (CTN2). The stability sets underline that the relaxation is and has to be flexible to uphold both, stability via counteracting coarse resolutions and limit consistency through vanishing for high resolutions. Further below, Lyapunov functionals are used to indicate nonlinear stability with respect to an approximate equilibrium. Moreover, based on empirical observations for fine discretizations of parameter spaces in numerical experiments (CTN3), a third notion of stability is proposed by the author in [232] (see Definition 3.3.8 and Section 4.3.3).

Upon full discretization in space and time, the structure of the collision operator is upheld such that we can transfer the notion of linear stability in the sense of von Neumann used for the TRS (see Section 3.1.4) onto the LBE (3.160). The von Neumann analysis for LBEs has been pioneered by [240, 267]. Along the process from the TEQ toward the final LBE, we have merged all limits according to $\epsilon \leftarrow h = \Delta x$ and $(\Delta x / \Delta t) \sim (\hat{\sigma} / \sigma)$ and thus drop any corresponding indices below such that any appearing \mathbf{f} is understood as conserved quantity of the LBE (3.160). Recall that both, the relaxation matrix \mathbf{S}^s and thus \mathbf{K}^s are now shifted as a result of the limit consistent discretization.

As before, a Taylor–Maclaurin expanded evolution equation is obtained via splitting the populations into global mean and fluctuation

$$\mathbf{f}_i(\mathbf{x}, t) = \bar{\mathbf{f}} + \tilde{\mathbf{f}}(\mathbf{x}, t) \quad (3.180)$$

into a global equilibrium $\bar{\mathbf{f}}$ (constant in space-time) plus its fluctuations $\tilde{\mathbf{f}}$, respectively. The space-time discrete equilibrium is Taylor expanded at the global state

$$\begin{aligned} \mathbf{f}^{\text{eq}}(\mathbf{f}) &= \sum_{n=0}^{\infty} \frac{1}{n!} [(\partial_{\mathbf{f}})^n \mathbf{f}^{\text{eq}}(\bar{\mathbf{f}})] \tilde{\mathbf{f}}^n \\ &= \mathbf{f}^{\text{eq}}(\bar{\mathbf{f}}) + \mathbf{J}_{\mathbf{f}^{\text{eq}}}(\bar{\mathbf{f}}) \tilde{\mathbf{f}} + \mathcal{O}(\tilde{\mathbf{f}}^2), \end{aligned} \quad (3.181)$$

where $\mathbf{J}_{f^{\text{eq}}}(\bar{\mathbf{f}})$ is the equilibrium Jacobian evaluated at the global equilibrium state. We insert (3.180) and (3.181) in (3.160), assume that $f^{\text{eq}}(\mathbf{f}) = \bar{\mathbf{f}}$ and neglect powers in fluctuations higher than two to obtain

$$\begin{aligned}\tilde{\mathbf{f}}(t + \Delta t) - \tilde{\mathbf{f}}(t) &= \mathbf{f}(t + \Delta t) - \mathbf{f}(t) \\ &= -\mathbf{K}^s \left(\bar{\mathbf{f}} + \tilde{\mathbf{f}}(t) - f^{\text{eq}}(\mathbf{f})(t) \right) \\ &= -\mathbf{K}^s \left[\bar{\mathbf{f}} - f^{\text{eq}}(\bar{\mathbf{f}}) + \tilde{\mathbf{f}}(t) - \mathbf{J}_{f^{\text{eq}}}(\bar{\mathbf{f}}) \tilde{\mathbf{f}}(t) - \mathcal{O}(\tilde{\mathbf{f}}^2(t)) \right] \\ &= -\mathbf{K}^s \left[\mathbf{I}_q - \mathbf{J}_{f^{\text{eq}}}(\bar{\mathbf{f}}) \right] \tilde{\mathbf{f}}(t).\end{aligned}\quad (3.182)$$

We unfold the space-time scaling to Fourier transform the fluctuations

$$\tilde{\mathbf{f}}(\mathbf{x}, t) = \hat{\mathbf{f}} \exp(i(2\pi \mathbf{k} \cdot \mathbf{x} - \omega t)), \quad (3.183)$$

where the amplitudes $\hat{\mathbf{f}} \in \mathbb{C}^q$ denote the discrete Fourier transform of $\tilde{\mathbf{f}}$ and $\mathbf{k} \in \mathcal{K} \subseteq \mathbb{R}^d$ is the wavevector and $\omega \in \mathbb{C}$. Insertion of $\hat{\mathbf{f}}$ into (3.182) and reordering terms yields an eigenvalue problem

$$\mathbf{H} \hat{\mathbf{f}} = \exp(-i\omega \Delta t) \hat{\mathbf{f}}, \quad (3.184)$$

where the discrete amplification matrix appears as

$$\mathbf{H}(\mathbf{k}, \bar{\mathbf{f}}, \mathbf{s}) = \text{diag}((\exp(-2\pi i \Delta t \mathbf{k} \cdot \mathbf{c}_i))_i) \left[\mathbf{I}_q + \mathbf{K}^s(\mathbf{s}) (\mathbf{J}_{f^{\text{eq}}}(\bar{\mathbf{f}}) - \mathbf{I}_q) \right]. \quad (3.185)$$

Remark 3.2.20. The linearized equilibrium Jacobian $\mathbf{J}_{f^{\text{eq}}}(\bar{\mathbf{f}})$ is directly obtained for linear equilibria and can be extended to nonlinear ones. For example for *D3Q19*, we obtain

$$(\mathbf{J}_{f^{\text{eq}}}(\bar{\mathbf{f}}))_{i,j} = \frac{w_i}{w} \left\{ 1 + \frac{1}{c_s^2} \mathbf{c}_i \cdot \mathbf{c}_j + \frac{1}{2c_s^4} \left[2(\mathbf{c}_i \cdot \mathbf{c}_j)(\mathbf{c}_i \cdot \bar{\mathbf{u}}) - (\mathbf{c}_i \cdot \bar{\mathbf{u}})^2 \right] - \frac{1}{2c_s^2} [2\mathbf{c}_j \cdot \bar{\mathbf{u}} - \bar{\mathbf{u}} \cdot \bar{\mathbf{u}}] \right\}, \quad (3.186)$$

where $\mathbf{k} \in \mathcal{K}$ and $c_s = 1/\sqrt{3\delta(\epsilon)}$ and the $\bar{\mathbf{f}}$ -dependency of $\mathbf{J}_{f^{\text{eq}}}$ reduces to the background (mean) flow $\bar{\mathbf{u}}$.

Having fixed \mathbf{M} due to the moment basis, \mathbf{H} in (3.185) is to be determined by the wavevector $\mathbf{k} \in \mathcal{K}$, the mean flow $\bar{\mathbf{u}}$ and the relaxation frequency vector \mathbf{s} . We define the following notion for von Neumann stability of the fully discrete scheme [232].

Definition 3.2.16. Let the LBE (3.160) be determined by a moment basis \mathbf{M} on *DdQq*. Further, let $\mathcal{K} \subseteq \mathbb{R}^d$ and $\bar{\mathbf{u}}$ be given in advance. The scheme is termed von Neumann stable for \mathbf{s} if the spectrum of \mathbf{H} is enclosed in the unit ball, i.e.

$$\text{spec}(\mathbf{H}) \subseteq B_1(0). \quad (3.187)$$

The set \mathcal{S} containing relaxation frequency vectors which render the scheme von Neumann stable is called von Neumann stability set.

Remark 3.2.21. With the linearized Jacobian (3.186) at hand, we might specify the stability set analytically such that for all $\mathbf{s} \in \mathcal{S}$ holds

$$r_{\text{spec}}(\mathbf{H}(\mathbf{k}, \bar{\mathbf{u}}, \mathbf{s})) = \max_{\lambda \in \text{spec}(\mathbf{H})} |\lambda| \leq 1 \quad \forall \mathbf{k} \in \mathcal{K}. \quad (3.188)$$

However, when the spectral radius r_{spec} has to be calculated for a $q \times q$ matrix with $q \geq 5$ we consider numerical approximations of r_{spec} based on the QR algorithm instead (see Section 3.3.3).

3.2.6 Convergence

Theorem 3.2.2. *In case of diffusive scaling $\sigma(h) = h^2$ and linear flux \mathbf{F} , solutions to the family of LBEs $\mathcal{B}_h^{\epsilon \leftarrow h}$ (3.160) converge to a solution of the ADE \mathcal{C} (2.10) with second order consistency and a truncation error $\mathcal{O}(\Delta x^2) = \mathcal{O}(\Delta t)$ under the premise of von Neumann stability.*

Proof. Lemma 3.2.2 gives strong convergence in the sense of

$$\mathcal{B}_h^{\epsilon \leftarrow h} \xrightarrow[\mathcal{O}(\epsilon^r)|_{x_h} + \mathcal{O}(\epsilon^k)]{(\epsilon, h) \searrow (0,0)} \mathcal{C} \equiv \mathcal{B}_h^h \xrightarrow[\mathcal{O}(h^2)]{(h, h) \searrow (0,0)} \mathcal{C} \quad (3.189)$$

with $\epsilon^2 \leftarrow h^2 \sim \Delta t \sim \Delta x^2$. □

Remark 3.2.22. Since the above derivation is modular, we can swap the background limit with any other relaxation approximation which is stable and consistent of order $\mathcal{O}(\epsilon^2)$ or less. In [230], we have used the methodology to obtain limit consistency and thus convergence of the classical $D3Q19$ DVBE with a second order truncated equilibrium. Below we provide consistent discretizations toward other TEQs in the form of homogenized NSE, CHEs and filtered NSE. It is to be stressed that other approaches are available and rigorous convergence to ADEs, and NSE has been proven in the literature. The present benefit is modularity and generality which allow to interchange parts of the LBM (relaxation, discretization, equilibria) without affecting the validity of the framework to evaluate overall convergence up to leading order.

3.2.7 Limit control

As elaborated in the previous sections, based on existing and present results, we have observed the freedom to modify or even control the relaxation limit via scaling and relaxation frequencies. To be precise, we have explicated that, whereas the consistency of the conservation relaxation dictates the overall limiting, the artificial relaxation provides numerical correction terms provided that the order of discretization is large enough. Below, two options to control the artificial relaxation frequencies contained in \mathbf{S}^s are discussed. The first one (relaxation functions) is an extension of previous results and developed by the author. The novel collision scheme is part of the Contributions (CTN3) and (CTN4). The second modification is an established technique based on entropy control, which is however motivated by thermodynamics and has thus received marginal attention in terms of numerical analysis so far. Both methods are here used on a $D3Q19$ velocity set with a second order equilibrium limiting toward the incompressible NSE (2.12).

3.2.7.1 Relaxation functions for orthogonal moment collision

In [232] we provide numerical evidence that it is beneficial for classical MRT collision [66] (i.e. collision in a moment space spanned by unweighted product orthogonal moments, see Table 3.4) to generalize the kinetic relaxation time scaling to predefined self-tuning functions for automatically triggering certain numerical features.

This measure of defining the freely tunable kinetic relaxation times as relaxation functions, for example enables the hybridization of MRT and SRT BGK collision along the incompressibility limit under diffusive scaling. In the spirit of ghost Reynolds numbers proposed by Dellar [63], the fully discretized evolution rule should stream to a SRT BGK collision scheme up to machine precision at some point in the limit $h \searrow 0$. Dependent on the choice of the relaxation functions, the specific interval within which a certain coincidence to the SRT BGK is reached should be flexible along the limit. The thus obtained multi-relaxation-function (MRF) collision hence represents the activity of moving from a fixed MRT setting toward the SRT BGK collision (see Figure 3.6). This specific feature is realized via contracting the kinetic relaxation times toward the hydrodynamic one for $Ma \rightarrow 0$.

Further, as indicated in [233], we interpret the use of MRFs as implicit turbulence modeling via the definition of hyperviscosities which are respectively connected to the kinetic moments. Hence, the sooner the additional higher order moment viscosities vanish via contraction of the kinetic relaxation times to τ , the sooner the MRFs merge with the SRT BGK collision scheme (see Figure 3.6). Up to that point in the limit, MRFs resemble variable MRTs and offer the possibility to implicitly tune the properties of the LBM for the following specific reasons. Firstly, in terms of purely numerical intentions, the stability region of the SRT BGK scheme can be exceeded without breaking the thermodynamic limit consistency. Secondly, with regards to controlling the flow physics, specific features such as turbulent flow quantities can be amplified or reduced.

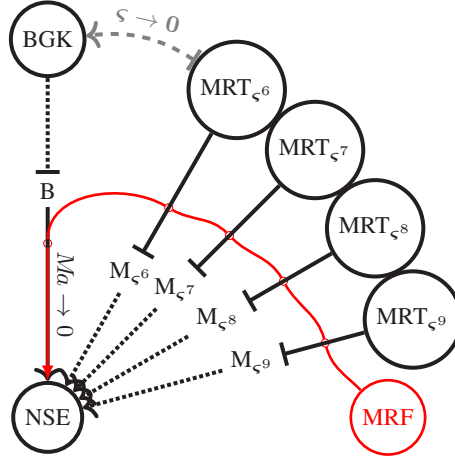


Figure 3.6: Schematic view of diffusive scaling limits ($Ma \sim h \searrow 0$) of LBM schemes (SRT BGK LBE and exemplary instances of $n \in \mathbb{N}$ parametrized MRT_{ζ^n} LBE) toward the NSE, respectively. Dashed lines denote instability regions along the limit. The points B and M_{ζ^n} mark the (coarse resolution dependent [114, 267]) instability onset of the SRT BGK scheme and the (Mach induced [62, 114]) instability onsets of fixed MRT_{ζ^n} schemes, respectively. Solid lines specify stable configurations.

To uphold the SRT BGK collision limit toward the incompressible NSE, the hydrodynamic relaxation frequencies are coupled to the bulk viscosity via

$$s_e = \frac{2}{2\nu + c_s^2}, \quad (3.190)$$

$$s_P = \frac{2}{2\nu + c_s^2}, \quad (3.191)$$

where for the $D3Q19$ velocity set, the lattice speed of sound is $c_s = 1/\sqrt{3}$. Note that the appearance of s_e and s_P with an additional sum is a result from the space-time discretization discussed in Section 3.2.3. The remaining relaxation frequencies (which are also written in fully discrete form) are parametrized by a variable ς_b , which is injected in

$$\left(\frac{1}{s_b} - \frac{1}{2}\right) = \underbrace{2^{\varsigma_b}}_{=: \hat{\varsigma}_b} \left(\frac{1}{s_P} - \frac{1}{2}\right), \quad (3.192)$$

and tracks the deviation of s_b from the viscosity connected relaxation frequency s_P , where $b \in \{e, q, \mu, \varepsilon, \Pi\}$. Further, the kinetic relaxation times are grouped by the order of their moments. In summary, the relaxation frequencies $s_e, s_{q,\mu}$, and $s_{\varepsilon,\Pi}$ vary with $\varsigma = (\varsigma_{q,\mu}, \varsigma_e, \varsigma_{\varepsilon,\Pi})^T \in \{n \in \mathbb{N}_0 \mid 0 \leq n \leq 10\}^3$, where $\varsigma \rightarrow \mathbf{0}$ limits to the SRT BGK collision. The present relaxation functions used for the MRF collision are thus

$$s_b = \begin{cases} \frac{1}{\hat{\varsigma}_b \left(\frac{1}{s_P} - \frac{1}{2}\right) + \frac{1}{2}} & \text{if } \varsigma_b > 0 \text{ (MRF mode),} \\ s_P & \text{otherwise (SRT BGK mode),} \end{cases} \quad (3.193)$$

such that in both modes the background limit toward the incompressible NSE is upheld via reduction to the SRT BGK scheme based on suitable MRFs. The definition of the reduction point however is subject to current investigation and so far is determined empirically from brute force stability results (see Section 4.3).

Remark 3.2.23. The above proposed relaxation functions introduce ghost Reynolds numbers [63] for each moment order larger than one. These in turn act as controllable hyperviscosity prefactors [185, 264]. The scaling with respect to the viscosity relaxation frequency s_P is similar to the magic parameter used in the two-relaxation-time collision scheme (see for example [103, 104]).

3.2.7.2 Entropic stabilizer for natural moment collision

The choice of the equilibrium population \mathbf{f}^{eq} can increase linear stability (see [123] and references therein). In addition, a thermodynamically consistent equilibrium obtained from minimizing an H -function can be used to guarantee isotropy in compressible, trans- and supersonic flows. Since the isotropy of the equilibrium is up to the order of the discretization [36], the second order truncated equilibrium is suitable for incompressible flows. Albeit this equilibrium does not obey a classical global H -theorem [255], we can still use the local H -value as a basis of approximation. To improve the relaxation stability in nonlinear regimes, we can modify the relaxation frequencies in \mathbf{S}^s to be space-time dependent functions. The grouping of relaxation frequencies given in Table 3.3 is similar to the KBC-N1 scheme proposed in [36] albeit for being defined on $D3Q19$ which is computationally less demanding. For the sake of clarity, we recall the classical derivation of KBC collision for entropic MRT LBMs on natural moments, i.e. all moments except the ones which are responsible for shear and bulk viscosity decoupling are raw and thus based on monomials. Let $\mathcal{M} = \{\nu, T, Q, A\}$. We split the population in additive modes separated in moment space [148, 149, 256]

$$\mathbf{f}^{\text{eq}} + \mathbf{f}^{\text{neq}} = \mathbf{f} = \sum_{b \in \mathcal{M}} \mathbf{f}_b = \sum_{b \in \mathcal{M}} \mathbf{f}_b^{\text{eq}} + \sum_{b \in \mathcal{M}} \mathbf{f}_b^{\text{neq}}. \quad (3.194)$$

Via \mathbf{M}^{-1} , we have the inversion

$$\mathbf{f}_b^{\text{neq}} = \sum_{l \in L_b} \langle \phi^l, \mathbf{f}^{\text{neq}} \rangle \mathbf{W}^l, \quad (3.195)$$

where $L_b \subseteq \{1, 2, \dots, q\}$ denotes the corresponding velocity indices of the vectorial entries of $b \in \mathcal{M}$. Conforming to [36, 148], we gather the post-collision nonequilibrium contribution of higher order moments

$$\mathbf{f}_{\text{hom}}^{\text{neq}} := \sum_{b \in \{T, Q, A\}} \mathbf{f}_b^{\text{neq}}, \quad (3.196)$$

such that, due to the diagonality of \mathbf{S}^s , the LBE (3.160) becomes

$$\begin{aligned} \mathbf{f}^{\text{poc}}(\mathbf{x}, t) &= \mathbf{f}(\mathbf{x}, t) - \mathbf{M}^{-1} \mathbf{S}^s \mathbf{M} \mathbf{f}^{\text{neq}}(\mathbf{x}, t) \\ &= \mathbf{f}(\mathbf{x}, t) - \sum_{b \in \mathcal{M}} s_b \mathbf{f}_b^{\text{neq}}(\mathbf{x}, t) \\ &= \mathbf{f}(\mathbf{x}, t) - s_\nu \mathbf{f}_\nu^{\text{neq}}(\mathbf{x}, t) - s \mathbf{f}_{\text{hom}}^{\text{neq}}(\mathbf{x}, t), \end{aligned} \quad (3.197)$$

where $\mathbf{f}^{\text{poc}}(\mathbf{x}, t)$ denotes the post-collision state.

Definition 3.2.17. The higher order relaxation frequency $s = \beta \gamma^*$ is entropy controlled in the sense that the controller γ^* is computed to maximize the discrete entropy of the post-collision state.

Recall that $\mathbf{f}_b^{\text{neq}} = \mathbf{f}_b - \mathbf{f}_b^{\text{neq}}$, hence [148] the critical point which minimizes the Lyapunov functional (understood as an H -function [146, 147])

$$H(\mathbf{f}^{\text{poc}}) = \sum_{i=1}^q f_i^{\text{poc}} \ln \left(\frac{f_i^{\text{poc}}}{w_i} \right), \quad (3.198)$$

is reached under the condition of

$$\sum_{i=1}^q f_{\text{hom},i}^{\text{neq}} \ln \left(1 + \frac{(1-s)f_{\text{hom},i}^{\text{neq}} + (1-s_\nu)f_{\nu,i}^{\text{neq}}}{f_i^{\text{eq}}} \right) \stackrel{!}{=} 0. \quad (3.199)$$

Definition 3.2.18. The entropic scalar product for $\mathbf{X}, \mathbf{Y} \in \mathbb{R}^q$ with respect to $\mathbf{f}^{\text{eq}} \in \mathbb{R}^q$ is defined as

$$\langle \mathbf{X} | \mathbf{Y} \rangle = \sum_{i=1}^q \frac{X_i Y_i}{f_i^{\text{eq}}}. \quad (3.200)$$

A truncation to first order in both terms of the enumerator of (3.199), results in an expression for the entropy controller [36]

$$\gamma^* = \frac{1}{\beta} - \left(2 - \frac{1}{\beta} \right) \frac{\langle \mathbf{f}_\nu^{\text{neq}} | \mathbf{f}_{\text{hom}}^{\text{neq}} \rangle}{\langle \mathbf{f}_{\text{hom}}^{\text{neq}} | \mathbf{f}_{\text{hom}}^{\text{neq}} \rangle}, \quad (3.201)$$

such that (3.199) is approximately fulfilled, in turn approximately minimizing the Lyapunov functional of the discrete dynamical system defined by (3.160). Notably, a search for different Lyapunov functionals which ensure nonlinear stability might lead to novel entropic stabilizer approximations (see [34, 128] and references therein).

3.3 Lattice Boltzmann methods

This section renders the LBM as a complete approximation technique to a given IBVP comprised by PDEs with supplementary initial and boundary conditions. Based on the above analyzed LBEs for the bulk flow approximating standard forms of the ADE, the NSE and the CHE, the scheme is complemented with modified equilibria for additional terms, initial and boundary methods as well as coupling conditions between the equations.

Remark 3.3.1. At some points in the description of the numerical scheme it is essential to separate the evolution rule (3.160) into two steps:

- Collision:

$$\mathbf{f}^{\text{poc}}(\mathbf{x}, t) = \mathbf{f}^{\text{prc}}(\mathbf{x}, t) - \mathbf{K}^{\text{S}} [\mathbf{f}^{\text{prc}}(\mathbf{x}, t) - \mathbf{f}^{\text{eq,prc}}(\mathbf{x}, t)], \quad (3.202)$$

- Streaming:

$$\mathbf{f}^{\text{pos}} \left(\mathbf{x} + \frac{\sigma(h)}{\hat{\sigma}(h)} \hat{\mathbf{c}}_i, t + \sigma(h) \right) = \mathbf{f}^{\text{prc}}(\mathbf{x}, t). \quad (3.203)$$

As it turns out, the possibility of doing so is the most prolific feature of the LBM in terms of parallelizability which allows to carry out all possibly nonlinear operations (collisions) locally at each node and all other nonlocal ones simply as mere pointer shifts between the node storage (see for example [166, 194]). The population states in between these

two steps are frequently called pre-/post-collision (prc/poc) and pre-/post-streaming (prs/pos) below. Obviously, if no other computations are performed in between, $f^{\text{poc}} = f^{\text{prs}}$ and $f^{\text{pos}} = f^{\text{prc}}$.

3.3.1 Lattice Boltzmann equations

For each TEQ addressed in this work we summarize the final composition of the LBM (velocity set, moments and equilibria) in the fully discrete form. Additionally, the shifted diffusion coefficient equation is provided. Unless stated otherwise, τ denotes the relaxation time associated with the diffusion terms in the TEQ and all equations can be approximated in any of the moment bases. In case no moment space is explicitly given, SRT BGK collision is applied and also referred to as SRT. Missing thermodynamic information is derived or recalled where necessary. All of the configurations below use the same evolution equation (3.160) except for additional forces and couplings, which are introduced where required. We make no claim to exhaustiveness since, as stated in Section 3.1, an RS of a given TEQ resembles a nonunique approximation. Occasionally, other options for LBM ingredients are given and referenced.

3.3.1.1 Lattice Boltzmann equation for advection–diffusion equations

From the constructive derivation above we have obtained a convergent scheme based on the $DdQ(2d+1)$ stencil with MRT collision and first order truncated equilibrium. Note that other velocity stencils and equilibria can be used to limit toward the ADE as a TEQ [53]. In summary, here the ADE (2.10) is approximated by an LBM consisting of

- velocity stencil: $DdQ(2d+1)$ (Figure 3.2);
- equilibrium: (3.95);
- moment space: raw moments (3.93) zeroth order conservation;
- diffusion coefficient:

$$\mu = c_s^2 \left(\tau - \frac{1}{2} \right). \quad (3.204)$$

Remark 3.3.2. When keeping the conservation order of the moments fixed and increasing the velocity stencil together with the equilibrium truncation results in the same TEQ. The limit of this increase in velocity space approximation order should lead to a continuous BGKBE which is exactly the thermodynamic information we successfully suppressed in the derivation of the LBM for the ADE.

3.3.1.2 Lattice Boltzmann equation for Cahn–Hilliard equations

Let \mathbf{u} be a given flow velocity. Based on substitution of the diffusive terms in the ADE, a relaxation approximation of the CHE can be derived. It is possible (but not necessary [273]) to use a second order equilibrium. Since Swift *et al.* [242] used a Taylor expanded LBE to match the terms in the CHE and the ternary model [224] is based on a similar equilibrium structure, we adopt the second order truncation here. Further, also the KFRM can be approximated with this structure, irrespective of the definition of the chemical potential μ_ϕ . Here, the CHE (2.11) is approximated by an LBM consisting of

- velocity stencil: $D2Q9, D3Q19$ (Figure 3.2);

- equilibrium:

$$f_i^{\text{eq}}(\mathbf{x}, t) = \left\{ \frac{w_i}{w} \left[\frac{1}{c_s^2} \Gamma_\phi \mu_\phi + \frac{1}{c_s^2} \phi_f \mathbf{c}_i \cdot \mathbf{u} - \frac{1}{2c_s^2} \phi_f \mathbf{u}_f^2 + \frac{1}{2c_s^4} \phi_f (\mathbf{c}_i \cdot \mathbf{u}_f)^2 \right] \right\} (\mathbf{x}, t) \quad (3.205)$$

if $i \neq 1$, and otherwise

$$f_1^{\text{eq}}(\mathbf{x}, t) = \phi_f(\mathbf{x}, t) - \sum_{i \neq 1} f_i^{\text{eq}}(\mathbf{x}, t); \quad (3.206)$$

- moment space: zeroth order conservation

$$\phi_f = \sum_{i=1}^q f_i = \sum_{i=1}^q f_i^{\text{eq}}; \quad (3.207)$$

- diffusion coefficient:

$$M_\phi = \Gamma_\phi \left(\tau - \frac{1}{2} \right). \quad (3.208)$$

3.3.1.3 Lattice Boltzmann equation for Navier–Stokes equations

In Section 3.2, we have constructed the LBE (3.160) from the ADE (2.10) and recalled possible equilibrium formulations and stencils, also leading to the NSE (2.12). Concerning the latter, we provide a similarly constructive derivation of both, the velocity and the space-time discretizations in [230] based on a procedure by Krause [158]. Whereas construction and convergence of LBMs for incompressible NSE has been carried out priorly for example by Junk *et al.* [136, 140, 141] an explicit link to RSs and artificial compressibility has been made recently by Ruhi *et al.* [221]. Here, upon limit consistent discretization, the NSE (2.12) is approximated by an LBM consisting of

- velocity stencil: $D2Q9$, $D3Q19$ (Figure 3.2);
- equilibrium: (2.46);
- moment space: orthogonal moments (Table 3.4), natural moments (Table 3.2), zeroth and first order conservation;
- diffusion coefficient:

$$\nu = c_s^2 \left(\tau - \frac{1}{2} \right). \quad (3.209)$$

3.3.1.4 Lattice Boltzmann equation for homogenized Navier–Stokes equations

For reasons of clarity, the novel scheme used for approximating the homogenized NSE (2.138) is derived after the summary of its main LBM building blocks. The LBM to obtain (2.138) in the relaxation and discretization limit is termed homogenized LBM (HLBM) and was initially proposed by Krause *et al.* [159] and revisited by Trunk *et al.* [249] to efficiently simulate large numbers of arbitrarily shaped particles submersed in a viscous fluid. Removing the particles inner (solid) and outer (fluid) region from the model, results in one coherent porous interface across the domain of interest. It is to be stressed that, in the low Reynolds number regime, the HLBM applied to porous media flows aligns with the model of Spaid *et al.* [238]. For other regimes however the HLBM approximates a different TEQ in the present setting which is to be seen as a progressive advantage of the here proposed framework of analyzing LBM.

Details are clarified in the derivation below. Upon limit consistent discretization, the homogenized NSE (2.138) is approximated by the HLBM consisting of

- velocity stencil: $D3Q19$ (Figure 3.2);
- equilibrium:

$$f_i^{\text{eq}}(\mathbf{x}, t) := \left\{ \frac{w_i}{w} \rho_f \left[1 + \frac{1}{c_s^2} d_h \mathbf{c}_i \cdot \mathbf{u}_f - \frac{1}{2c_s^2} d_h^2 \mathbf{u}_f^2 + \frac{1}{2c_s^4} d_h^2 (\mathbf{c}_i \cdot \mathbf{u}_f)^2 \right] \right\}(\mathbf{x}, t), \quad (3.210)$$

where

$$d_h = (1 - \tau \nu \Delta t K^{-1}) \quad (3.211)$$

is the lattice porosity;

- moment space: zeroth and first order conservation

$$\rho_f(\mathbf{x}, t) = \sum_{i=1}^q f_i(\mathbf{x}, t) = \sum_{i=1}^q f_i^{\text{eq}}(\mathbf{x}, t), \quad (3.212)$$

$$d_h \mathbf{u}_f(\mathbf{x}, t) = \frac{d_h}{\rho_f(\mathbf{x}, t)} \sum_{i=1}^q \mathbf{c}_i f_i(\mathbf{x}, t) = \frac{1}{\rho_f(\mathbf{x}, t)} \sum_{i=1}^q \mathbf{c}_i f_i^{\text{eq}}(\mathbf{x}, t); \quad (3.213)$$

- diffusion coefficient:

$$\nu = c_s^2 \left(\tau - \frac{1}{2} \right). \quad (3.214)$$

Below we make use of a formal thermodynamic background limit which is then successively discretized to obtain the evolution rule which forms the basis of the HLBM for fluid flow through porous media.

Homogenized BGK–Boltzmann collision As common to classical derivations in LBMs, we start with the mesoscopic viewpoint to formally assess the continuum limit toward the macroscopic TEQ. Apart from the procedure itself being classical, to the knowledge of the author the results below are novel. Let K denote the single eigenvalue of the permeability tensor \mathbf{A} according to the Definition 2.5.2. All other definitions are similar as in Section 2.2.4, Section 2.3 and Section 2.5, or follow the notation in [230].

Definition 3.3.1. Based on (2.28), the homogenized Maxwellian for the BGK collision (2.32) is defined as

$$M_f^{\text{eq}} = f^{\text{eq}}(n_f, \varpi \mathbf{u}_f, T) \quad (3.215)$$

with an additional prefactor called porosity control

$$\varpi = 1 - \nu \tau K^{-1} \quad (3.216)$$

in the velocity argument. For $\varpi = 1$, the collision reduces to the classical BGK operator (2.32).

For any ρ_f , \mathbf{u}_f , T and ϖ we obtain the zeroth, first and second order balance laws

$$\rho_{M_f^{\text{eq}}} = m \int_{\mathbb{R}^d} M_f^{\text{eq}} d\mathbf{v} = m \int_{\mathbb{R}^d} f^{\text{eq}}(n_f, \varpi \mathbf{u}_f, T) d\mathbf{v} = \rho_f, \quad (3.217)$$

$$\mathbf{u}_{M_f^{\text{eq}}} = \frac{1}{n_{M_f^{\text{eq}}}} \int_{\mathbb{R}^d} \mathbf{v} M_f^{\text{eq}} d\mathbf{v} = \frac{1}{n_f} \int_{\mathbb{R}^d} \mathbf{v} f^{\text{eq}}(n_f, \varpi \mathbf{u}_f, T) d\mathbf{v} = \varpi \mathbf{u}_f, \quad (3.218)$$

$$p_{M_f^{\text{eq}}} = \frac{m}{d} \int_{\mathbb{R}^d} (\mathbf{v} - \mathbf{u}_{M_f^{\text{eq}}})^2 M_f^{\text{eq}} d\mathbf{v} = \frac{m}{d} \int_{\mathbb{R}^d} (\mathbf{v} - \varpi \mathbf{u}_f)^2 f^{\text{eq}}(n_f, \varpi \mathbf{u}_f, T) d\mathbf{v} = p_f, \quad (3.219)$$

respectively. Notably, the hydrodynamic first order moment of M_f^{eq} in (3.218) differs from the one of f^{eq} due to the prefactored porosity control ϖ .

Definition 3.3.2. With the homogenized M_f^{eq} from (3.215) implanted in (2.32), the homogenized BGKBE (HBGKBE) reads

$$\frac{D}{Dt} f = Q(f) \quad \text{in } \mathfrak{R}. \quad (3.220)$$

Remark 3.3.3. In the present mesoscopic framework, the term homogenized refers to generalizing the BGKBE as a special case for $\varpi = 1$ (via $K \rightarrow \infty$) to a broader validity where $\varpi \neq 1$. Below, we formally indicate that for $\varpi < 1$ the homogenized Maxwellian (3.215) leads to imposing a nonstandard hydrodynamic similarity of the HBGKBE to the HNSE in the broadest sense of Hilbert's sixth problem. The artificial case of $\varpi > 1$ is neglected hereafter.

Homogenized diffusive limit Analogously to Section 2.3, we relate the HBGKBE (3.220) to the HNSE (2.138) in the sense of diffusive limiting. To this end, we formally verify that the assumed to be well-defined moments in Definition 2.2.3 obey the balance equations of the HNSE. To verify Step 1 (Mass conservation and momentum balance), let f^* be a solution to the HBGKBE (3.220). Multiplying (3.220) by m and integrating over the velocity space $\Xi = \mathbb{R}^d$ yields the solenoidal constraint in (2.138) after division by the constant ρ_{f^*} , where the force term vanishes when applying [158, Corollary 5.2] with $g = 1$ and $\mathbf{a} = \mathbf{F}$ in the respective notation. To balance momentum, we integrate $m\mathbf{v} \times (3.220)$ over the $\Xi = \mathbb{R}^d$ and obtain in Ω_T that

$$\begin{aligned} \partial_t (\rho_{f^*} \mathbf{u}_{f^*}) + \nabla_{\mathbf{x}} \cdot \mathbf{P}_{f^*} + (\rho_{f^*} \mathbf{u}_{f^*} \cdot \nabla_{\mathbf{x}}) \mathbf{u}_{f^*} + \mathbf{F} &= -\frac{1}{\tau} (\rho_{f^*} \mathbf{u}_{f^*} - \varpi \rho_{f^*} \mathbf{u}_{f^*}) \\ &= -\nu K^{-1} \rho_{f^*} \mathbf{u}_{f^*}. \end{aligned} \quad (3.221)$$

Besides the homogenization term on the right hand side, the derivation of (3.221) closely follows the procedure recalled in Section 2.3. In the end, via (3.221)/ ρ_{f^*} we recover a balance law of momentum in conservative form where the additional term $-\nu K^{-1} \mathbf{u}_{f^*}$ is induced by the homogenization controlled equilibrium and corresponds to $-(\nu/(\sigma^2)) \mathbf{A}^{-1} \mathbf{u}$ under the above assumptions on the porous structure made in Section 2.5 and specifically in Section 2.5.4. Hence, with a suitably defined \mathbf{P}_{f^*} conforming to the assumptions of incompressible Newtonian flow, the HNSE (2.138) is reached in the diffusive limit. This incompressible limit regime of the HBGKBE (3.220) arises from parameter alignment to diffusion terms. We thus extend the derivation given in [158, 230] for the classical BGKBE to the HBGKBE.

Definition 3.3.3. As a consequence of the assignments made in Section 2.3, we reassign the porosity controller

$$\varpi \leftarrow 1 - 3\nu^2 \epsilon^2 K^{-1} =: \varpi_{\epsilon}, \quad (3.222)$$

and define the ϵ -parametrized HBGKBE similarly to (2.45) as

$$\frac{D}{Dt} f = -\frac{1}{3\nu\epsilon^2} (f - M_f^{\text{eq}}) \quad \text{in } \mathfrak{R}, \quad (3.223)$$

where the homogenized Maxwellian distribution evaluated at $(n_f, \varpi_\epsilon \mathbf{u}_f)$ now reads

$$M_f^{\text{eq}} = \frac{n_f \epsilon^d}{\left(\frac{2}{3}\pi\right)^{\frac{d}{2}}} \exp\left(-\frac{3}{2}(\mathbf{v}\epsilon - \varpi_\epsilon \mathbf{u}_f \epsilon)^2\right) \quad \text{in } \mathfrak{R}. \quad (3.224)$$

The HBGKBE (3.223) is accordingly transformed to

$$f = M_f^{\text{eq}} - 3\nu\epsilon^2 \frac{D}{Dt} f \quad \text{in } \mathfrak{R}. \quad (3.225)$$

Repeating the material derivative through (D/Dt) (3.225) yields

$$\frac{D}{Dt} f = \frac{D}{Dt} M_f^{\text{eq}} - 3\nu\epsilon^2 \left(\frac{D}{Dt}\right)^2 f \quad \text{in } \mathfrak{R}. \quad (3.226)$$

The expression (3.226) serves to substitute $(D/Dt)f$ in (3.225) which gives

$$f = M_f^{\text{eq}} - 3\nu\epsilon^2 \frac{D}{Dt} M_f^{\text{eq}} + \left(3\nu\epsilon^2 \frac{D}{Dt}\right)^2 f \quad \text{in } \mathfrak{R}. \quad (3.227)$$

Repeating the above subsequently produces higher order terms and substitutions. The evolving sequence unfolds the power series

$$f = \sum_{i=0}^{\infty} \left(-3\nu\epsilon^2 \frac{D}{Dt}\right)^i M_f^{\text{eq}} \quad \text{in } \mathfrak{R}. \quad (3.228)$$

To complete the macroscopic limit the stress tensor \mathbf{P}_{f^*} in (3.221) has to be matched to (2.138) (Step 3: Newton's hypothesis), which for a solution f^* to the HBGKBE (3.220) yields

$$\mathbf{P}_{f^*} = -p_{f^*} \mathbf{I} + 2\nu\rho \mathbf{D}_{f^*} + \mathcal{O}(\epsilon^b) \quad \text{in } \Omega_T \quad (3.229)$$

up to an order $b > 0$. Using (3.228), an approximation ansatz of the form

$$f^* = M_{f^*}^{\text{eq}} - 3\nu\epsilon^2 \frac{D}{Dt} M_{f^*}^{\text{eq}} \quad \text{in } \mathfrak{R} \quad (3.230)$$

is chosen. As before, this choice is based upon the assumption that higher order terms are sufficiently small for $\epsilon \rightarrow 0$ such that the order b in turn is large enough. To verify (3.229), we compute the stress tensor according to its definition (2.24). In the following, f -indices at physical moment expressions are omitted for the sake of simplicity. At first, we inject the material derivative and use the mass conservation to obtain

$$\begin{aligned} \frac{D}{Dt} M_f^{\text{eq}} &= \left(\frac{1}{\rho} \frac{D}{Dt} \rho + 3\epsilon^2 \varpi_\epsilon \mathbf{c}_\varpi \cdot \frac{D}{Dt} \mathbf{u} - \frac{3\epsilon^2 \mathbf{c}_\varpi \cdot \mathbf{F}}{m} \right) M_f^{\text{eq}} \\ &= \left[\frac{1}{\rho} (\partial_t + \mathbf{v} \cdot \nabla_{\mathbf{x}}) \rho + 3\epsilon^2 \varpi_\epsilon \mathbf{c}_\varpi \cdot (\partial_t + \mathbf{v} \cdot \nabla_{\mathbf{x}}) \mathbf{u} - \frac{3\epsilon^2 \mathbf{c}_\varpi \cdot \mathbf{F}}{m} \right] M_f^{\text{eq}} \\ &= \left[\frac{1}{\rho} (-\mathbf{u} \cdot \nabla_{\mathbf{x}} \rho - \rho \nabla_{\mathbf{x}} \cdot \mathbf{u} + \mathbf{v} \cdot \nabla_{\mathbf{x}} \rho) + 3\epsilon^2 \varpi_\epsilon \mathbf{c}_\varpi \cdot (\partial_t + \mathbf{v} \cdot \nabla_{\mathbf{x}}) \mathbf{u} - \frac{3\epsilon^2 \mathbf{c}_\varpi \cdot \mathbf{F}}{m} \right] M_f^{\text{eq}} \\ &= \left[\underbrace{-\nabla_{\mathbf{x}} \cdot \mathbf{u}}_{=: a_f} + \underbrace{\frac{\mathbf{c}}{\rho} \cdot \nabla_{\mathbf{x}} \rho}_{=: b_f} + \underbrace{3\epsilon^2 \varpi_\epsilon \mathbf{c}_\varpi \cdot \partial_t \mathbf{u}}_{=: c_f} + \underbrace{3\epsilon^2 \varpi_\epsilon \mathbf{c}_\varpi \cdot (\mathbf{v} \cdot \nabla_{\mathbf{x}}) \mathbf{u}}_{=: d_f} - \underbrace{\frac{3\epsilon^2 \mathbf{c}_\varpi \cdot \mathbf{F}}{m}}_{=: e_f} \right] M_f^{\text{eq}} \end{aligned} \quad (3.231)$$

in \mathfrak{R} , where

$$\mathbf{c} := \mathbf{v} - \mathbf{u}, \quad (3.232)$$

$$\mathbf{c}_{\varpi} := \mathbf{v} - \varpi_{\epsilon} \mathbf{u}, \quad (3.233)$$

are relative velocities. Inserting the derivative (3.231) in (3.230) yields

$$f = M_f^{\text{eq}} [1 - 3\epsilon^2 \nu (-a_f + b_f + c_f + d_f + e_f)] \quad \text{in } \mathfrak{R}. \quad (3.234)$$

Secondly, we evaluate the velocity space integrals of the individual terms a_f, b_f, \dots, e_f . To this end, we use the symmetric properties of M_f^{eq} and the fact that M_f^{eq}/n is a normal distribution with covariance matrix $1/(3\epsilon^2)\mathbf{I}_d$. In Ω_T and for any $i, j, k, l \in \{1, 2, \dots, d\}$ we verify that

$$\begin{aligned} m \int_{\mathbb{R}^d} c_i c_j M_f^{\text{eq}} \, d\mathbf{v} &= m \int_{\mathbb{R}^d} c_{\varpi, i} c_{\varpi, j} M_f^{\text{eq}} \, d\mathbf{v} - m \int_{\mathbb{R}^d} (1 - \varpi_{\epsilon}) u_i [2v_j - (1 + \varpi_{\epsilon}) u_j] M_f^{\text{eq}} \, d\mathbf{v} \\ &= \frac{\rho}{3\epsilon^2} \delta_{ij} - \rho (1 - \varpi_{\epsilon})^2 u_i u_j \\ &= \rho \delta_{ij} + \mathcal{O}(\epsilon^4), \end{aligned} \quad (3.235)$$

$$\begin{aligned} m \int_{\mathbb{R}^d} c_i c_j c_k M_f^{\text{eq}} \, d\mathbf{v} &= m \underbrace{\int_{\mathbb{R}^d} c_{\varpi, i} c_{\varpi, j} c_{\varpi, k} M_f^{\text{eq}} \, d\mathbf{v}}_{=0} \\ &\quad + (\varpi_{\epsilon} - 1) \rho u_i \left[\frac{1}{3\epsilon^2} \delta_{jk} - (1 - \varpi_{\epsilon})^2 u_j u_k \right] \\ &\quad + (\varpi_{\epsilon} - 1) \rho u_j \left[\frac{1}{3\epsilon^2} \delta_{ik} - (1 - \varpi_{\epsilon})^2 u_i u_k \right] \\ &\quad + (\varpi_{\epsilon} - 1) \rho u_k \left[\frac{1}{3\epsilon^2} \delta_{ij} - (1 - \varpi_{\epsilon})^2 u_i u_j \right] \\ &= \sum_{\substack{\alpha\beta\gamma \in \\ \{ijk, jik, kij\}}} \left\{ (\varpi_{\epsilon} - 1) \rho u_{\alpha} \left[\frac{1}{3\epsilon^2} \delta_{\beta\gamma} - (1 - \varpi_{\epsilon})^2 u_{\beta} u_{\gamma} \right] \right\} \\ &= \mathcal{O}(1), \end{aligned} \quad (3.236)$$

$$\begin{aligned} m \int_{\mathbb{R}^d} c_i c_j c_{\varpi, k} v_l M_f^{\text{eq}} \, d\mathbf{v} &= \rho \left\{ \frac{1}{9\epsilon^4} (\delta_{ij} \delta_{kl} + \delta_{ik} \delta_{jl} + \delta_{il} \delta_{jk}) \right. \\ &\quad + (\varpi_{\epsilon} - 1)^2 u_i u_j \left[\frac{1}{3\epsilon^2} \delta_{kl} - (1 - \varpi_{\epsilon})^2 u_k u_l \right] \\ &\quad + (\varpi_{\epsilon} - 1) \varpi_{\epsilon} u_i u_l \left[\frac{1}{3\epsilon^2} \delta_{jk} - (1 - \varpi_{\epsilon})^2 u_j u_k \right] \\ &\quad \left. + (\varpi_{\epsilon} - 1) \varpi_{\epsilon} u_j u_l \left[\frac{1}{3\epsilon^2} \delta_{ik} - (1 - \varpi_{\epsilon})^2 u_i u_k \right] \right\}, \\ &= \frac{\rho}{9\epsilon^4} (\delta_{ij} \delta_{kl} + \delta_{ik} \delta_{jl} + \delta_{il} \delta_{jk}) + \mathcal{O}(1). \end{aligned} \quad (3.237)$$

The order estimates hold since, by construction $\varpi_{\epsilon} - 1 \in \mathcal{O}(\epsilon^2)$. Hence, we obtain

$$\begin{aligned} m \int_{\mathbb{R}^d} c_i c_j a_f M_f^{\text{eq}} \, d\mathbf{v} &= \left(m \int_{\mathbb{R}^d} c_i c_j M_f^{\text{eq}} \, d\mathbf{v} \right) \partial_{x_k} u_k \\ &\stackrel{(3.235)}{=} \left(\frac{\rho}{3\epsilon^2} + \mathcal{O}(\epsilon^4) \right) \partial_{x_k} u_k \\ &= \frac{\rho}{3\epsilon^2} \partial_{x_k} u_k + \mathcal{O}(\epsilon^4), \end{aligned} \quad (3.238)$$

$$m \int_{\mathbb{R}^d} c_i c_j b_f M_f^{\text{eq}} d\mathbf{v} = \left(m \int_{\mathbb{R}^d} c_i c_j c_k M_f^{\text{eq}} d\mathbf{v} \right) \frac{1}{\rho} \partial_{x_k} \rho \stackrel{(3.236)}{=} \mathcal{O}(1), \quad (3.239)$$

$$m \int_{\mathbb{R}^d} c_i c_j c_f M_f^{\text{eq}} d\mathbf{v} = \left(m \int_{\mathbb{R}^d} c_i c_j c_k M_f^{\text{eq}} d\mathbf{v} \right) 3\epsilon^2 \varpi_\epsilon \partial_t u_k \stackrel{(3.236)}{=} \mathcal{O}(\epsilon^2), \quad (3.240)$$

$$m \int_{\mathbb{R}^d} c_i c_j d_f M_f^{\text{eq}} d\mathbf{v} = \left(m \int_{\mathbb{R}^d} c_i c_j c_{\varpi, k} v_l M_f^{\text{eq}} d\mathbf{v} \right) 3\epsilon^2 \varpi_\epsilon \partial_{x_l} u_k \stackrel{(3.237)}{=} 3\epsilon^2 \varpi_\epsilon \partial_{x_l} u_k \left[\frac{\rho}{9\epsilon^4} (\delta_{ij} \delta_{kl} + \delta_{ik} \delta_{jl} + \delta_{il} \delta_{jk}) + \mathcal{O}(1) \right] \stackrel{(3.222)}{=} \partial_{x_l} u_k \frac{\rho}{3\epsilon^2} (\delta_{ij} \delta_{kl} + \delta_{ik} \delta_{jl} + \delta_{il} \delta_{jk}) + \mathcal{O}(1), \quad (3.241)$$

$$m \int_{\mathbb{R}^d} c_i c_j e_f M_f^{\text{eq}} d\mathbf{v} = \rho (\varpi_\epsilon - 1) F_k u_j \delta_{ik} = \mathcal{O}(\epsilon^2). \quad (3.242)$$

Third and finally, each \mathbf{P} -component P_{ij} for $i, j \in \{1, 2, \dots, d\}$ is computable in \mathfrak{R} . Via reordering terms, we obtain

$$\begin{aligned} P_{ij} &= m \int_{\mathbb{R}^d} c_i c_j [1 - 3\nu\epsilon^2 (-a_f + b_f + c_f + d_f + e_f)] M_f^{\text{eq}} d\mathbf{v} \\ &= p\delta_{ij} - 3\nu\epsilon^2 \left[-\frac{\rho}{3\epsilon^2} \partial_{x_k} u_k + \partial_{x_l} u_k \frac{\rho}{3\epsilon^2} (\delta_{ij} \delta_{kl} + \delta_{ik} \delta_{jl} + \delta_{il} \delta_{jk}) + \mathcal{O}(1) \right] \\ &= p\delta_{ij} + \nu\rho [\delta_{ij} \partial_{x_k} u_k - \partial_{x_l} u_k (\delta_{ij} \delta_{kl} + \delta_{ik} \delta_{jl} + \delta_{il} \delta_{jk})] + \mathcal{O}(\epsilon^2) \\ &= p\delta_{ij} - \nu\rho (\partial_{x_i} u_j + \partial_{x_j} u_i) + \mathcal{O}(\epsilon^2) \end{aligned} \quad (3.243)$$

and thus equivalently

$$\mathbf{P} = p\mathbf{I}_d - 2\nu\rho\mathbf{D} + \mathcal{O}(\epsilon^2). \quad (3.244)$$

which formally proves the approximate recovery of the HNSE (2.138) in the hydrodynamic limit.

Discrete velocity homogenized BGK–Boltzmann equation Based on the above derived formal limit, the subsequent discretization in the velocity space yields, in the thermodynamic sense a moment approximation of the HBGKBE and, in the present context, a relaxation approximation of the HNSE. We estimate the order of the discrete velocity approximation in ϵ as follows.

Definition 3.3.4. From $\epsilon^2 \times (3.223)$, we construct the family of HBGKBEs

$$\mathcal{F} := \left(\epsilon^2 \frac{D}{Dt} f^\epsilon + \frac{1}{3\nu} (f^\epsilon - M_{f^\epsilon}^{\text{eq}}) = 0 \quad \text{in } \mathfrak{R} \right)_{\epsilon > 0}. \quad (3.245)$$

Since, in the present setting we instead aim at proving conformity of sequences of equations in the sense of limit alignment under discretization the consistency in ϵ with respect to the TEQ can be interpreted as limit consistency also in the velocity discretization [230]. To discretize the velocity space, let $\epsilon \in \mathbb{R}_{>0}$, K and ν be fixed, and define the discrete velocity set $\mathcal{Q} = \{c_i \mid i = 1, 2, \dots, q\} \subseteq \Xi = \mathbb{R}^d$. Unless stated otherwise, we use $D3Q19$ as given in Definition 3.2.3. We assume that a solution f^ϵ to (3.223) exists and creates well-defined moments n_{f^ϵ} and \mathbf{u}_{f^ϵ} . As in the previous sections, the dependence of f^ϵ on ϵ , carries over to n_{f^ϵ} and \mathbf{u}_{f^ϵ} which are related to the macroscopic targeted HNSE (2.138). Therefore, $n_{f^\epsilon}, \mathbf{u}_{f^\epsilon} \in \mathcal{O}(1)$ is assumed to hold by construction. Further, $\varpi_\epsilon \in \mathcal{O}(1)$ and

$\varpi_\epsilon - 1 \in \mathcal{O}(\epsilon^2)$ via (3.222). Under the above conditions, we expand $M_{f^\epsilon}^{\text{eq}}(\mathbf{x}, t, \mathbf{c}_i)$ in (3.224) as Taylor series in ϵ such that in \mathfrak{X} a second order partition yields

$$\begin{aligned} M_{f^\epsilon}^{\text{eq}}(\mathbf{x}, t, \mathbf{c}_i) &= \frac{n_{f^\epsilon}(\mathbf{x}, t)\epsilon^d}{\left(\frac{2}{3}\pi\right)^{\frac{d}{2}}} \exp\left(-\frac{3}{2}\tilde{\mathbf{c}}_i^2\right) \exp\left(3\epsilon\varpi_\epsilon\tilde{\mathbf{c}}_i \cdot \mathbf{u}_{f^\epsilon}(\mathbf{x}, t) - \frac{3}{2}\epsilon^2\varpi_\epsilon^2\mathbf{u}_{f^\epsilon}^2(\mathbf{x}, t)\right) \\ &= \frac{n_{f^\epsilon}(\mathbf{x}, t)\epsilon^d}{\left(\frac{2}{3}\pi\right)^{\frac{d}{2}}} \exp\left(-\frac{3}{2}\tilde{\mathbf{c}}_i^2\right) \underbrace{\left[1 + 3\epsilon\varpi_\epsilon\tilde{\mathbf{c}}_i \cdot \mathbf{u}_{f^\epsilon}(\mathbf{x}, t) - \frac{3}{2}\epsilon^2\varpi_\epsilon^2\mathbf{u}_{f^\epsilon}^2(\mathbf{x}, t) + \frac{9}{2}\epsilon^2\varpi_\epsilon^2(\tilde{\mathbf{c}}_i \cdot \mathbf{u}_{f^\epsilon}(\mathbf{x}, t))^2\right]}_{=: \widetilde{M}_{f^\epsilon}^{\text{eq}}} \\ &\quad + R_{\mathbf{x}, t, \mathbf{c}_i}^{(0)}, \end{aligned} \quad (3.246)$$

where $R_{\mathbf{x}, t, \mathbf{c}_i}^{(0)} \in \mathcal{O}(\epsilon^{d+3})$ is the remainder term for each $(\mathbf{x}, t, \mathbf{c}_i) \in \Omega_T \times Q$. Where unambiguous, we drop the corresponding indexes below. The prefactored discrete velocities $\tilde{\mathbf{c}}_i := \mathbf{c}_i\epsilon$ do not depend on ϵ . With the weights $w_i \in \mathbb{R}_{>0}$ for $i = 1, 2, \dots, q$ we have that in Ω_T

$$n_{f^\epsilon} = \sum_{i=1}^q w_i \widetilde{M}_{f^\epsilon}^{\text{eq}}, \quad (3.247)$$

$$n_{f^\epsilon}\varpi_\epsilon\mathbf{u}_{f^\epsilon} = \sum_{i=1}^q w_i\mathbf{c}_i\widetilde{M}_{f^\epsilon}^{\text{eq}}. \quad (3.248)$$

This is a particular approximation in form of

$$\begin{aligned} \int_{\mathbb{R}^d} f^\epsilon \, d\mathbf{v} &= n_{f^\epsilon} = \sum_{i=1}^q w_i \widetilde{M}_{f^\epsilon}^{\text{eq}} = \sum_{i=1}^q w_i M_{f^\epsilon}^{\text{eq}} + R_{\mathbf{x}, t}^{(1)} \\ &= \sum_{i=1}^q w_i \left(f^\epsilon + 3\nu\epsilon^2 \frac{D}{Dt} f^\epsilon \right) + R_{\mathbf{x}, t}^{(1)} \\ &= \sum_{i=1}^q w_i f^\epsilon + R_{\mathbf{x}, t}^{(2)} \end{aligned} \quad (3.249)$$

and

$$\begin{aligned} \int_{\mathbb{R}^d} \mathbf{v} f^\epsilon \, d\mathbf{v} &= n_{f^\epsilon}\mathbf{u}_{f^\epsilon} = n_{f^\epsilon} [\varpi_\epsilon\mathbf{u}_{f^\epsilon} - (\varpi_\epsilon - 1)\mathbf{u}_{f^\epsilon}] \\ &= n_{f^\epsilon}\varpi_\epsilon\mathbf{u}_{f^\epsilon} + R_{\mathbf{x}, t}^{(3)} \\ &= \sum_{i=1}^q w_i\mathbf{c}_i\widetilde{M}_{f^\epsilon}^{\text{eq}} + R_{\mathbf{x}, t}^{(3)} \\ &= \sum_{i=1}^q w_i\mathbf{c}_i M_{f^\epsilon}^{\text{eq}} + R_{\mathbf{x}, t}^{(4)} \\ &= \sum_{i=1}^q w_i\mathbf{c}_i \left(f^\epsilon + 3\nu\epsilon^2 \frac{D}{Dt} f^\epsilon \right) + R_{\mathbf{x}, t}^{(4)} \\ &= \sum_{i=1}^q (w_i\mathbf{c}_i f^\epsilon) + R_{\mathbf{x}, t}^{(5)} \mathbf{1}_{d \times 1}, \end{aligned} \quad (3.250)$$

respectively. Based on $w_i \in \mathcal{O}(\epsilon^{-d})$ the product $w_i(D/Dt)f^\epsilon(\mathbf{x}, t, \mathbf{c}_i) \in \mathcal{O}(1)$ for all $(\mathbf{x}, t, \mathbf{c}_i) \in \Omega_T \times Q$. Further, recall from (3.246) that $M_{f^\epsilon}^{\text{eq}}$ is approximated by $\widetilde{M}_{f^\epsilon}^{\text{eq}}$ with an error in $\mathcal{O}(\epsilon^{3+d})$ for all $(\mathbf{x}, t, \mathbf{c}_i) \in \Omega_T \times Q$. Henceforth, with $\varpi_\epsilon - 1 \in \mathcal{O}(\epsilon^2)$ and $\mathbf{c}_i \in \mathcal{O}(\epsilon^{-1})$ by construction, we obtain for all $(\mathbf{x}, t) \in \Omega_T$ that

- $R_{\mathbf{x},t}^{(1)} \in \mathcal{O}(\epsilon^3)$,
- $R_{\mathbf{x},t}^{(2)}, R_{\mathbf{x},t}^{(3)}, R_{\mathbf{x},t}^{(4)} \in \mathcal{O}(\epsilon^2)$, and
- $R_{\mathbf{x},t}^{(5)} \in \mathcal{O}(\epsilon)$.

Finally, in Ω_T we can classify

$$n_{f^\epsilon} - \sum_{i=1}^q w_i f^\epsilon \in \mathcal{O}(\epsilon^2), \quad (3.251)$$

$$\mathbf{u}_{f^\epsilon} - \frac{\sum_{i=1}^q w_i \mathbf{c}_i f^\epsilon}{\sum_{i=1}^q w_i f^\epsilon} \in \mathcal{O}(\epsilon). \quad (3.252)$$

Shortening the notation, we define for $i = 1, 2, \dots, q$ and in Ω_T that

$$f_i^\epsilon(\mathbf{x}, t) = w_i f^\epsilon(\mathbf{x}, t, \mathbf{c}_i), \quad (3.253)$$

$$\rho_{f^\epsilon}(\mathbf{x}, t) = \sum_{i=1}^q f_i^\epsilon(\mathbf{x}, t), \quad (3.254)$$

$$\mathbf{u}_{f^\epsilon}(\mathbf{x}, t) = \frac{1}{\rho_{f^\epsilon}(\mathbf{x}, t)} \sum_{i=1}^q \mathbf{c}_i f_i^\epsilon(\mathbf{x}, t), \quad (3.255)$$

$$\overline{M}_{f^\epsilon, i}^{\text{eq}}(\mathbf{x}, t) = \frac{w_i}{w} \rho_{f^\epsilon}(\mathbf{x}, t) \left[1 + 3\epsilon^2 \varpi_\epsilon \mathbf{c}_i \cdot \mathbf{u}_{f^\epsilon}(\mathbf{x}, t) - \frac{3}{2} \epsilon^2 \varpi_\epsilon^2 \mathbf{u}_{f^\epsilon}^2(\mathbf{x}, t) + \frac{9}{2} \epsilon^4 \varpi_\epsilon^2 (\mathbf{c}_i \cdot \mathbf{u}_{f^\epsilon}(\mathbf{x}, t))^2 \right]. \quad (3.256)$$

Definition 3.3.5. Multiplying the HBGKBE (3.223) with all weights w_i and injecting the above definitions, we obtain the discrete velocity HBGKBE as a system of q equations

$$\frac{D}{Dt} f_i^\epsilon = -\frac{1}{3\nu\epsilon^2} \left(f_i^\epsilon - \overline{M}_{f^\epsilon, i}^{\text{eq}} \right) \quad \text{in } \Omega_T, \quad (3.257)$$

for $i = 1, 2, \dots, q$. The upheld parametrization with ϵ now generates the sequence of discrete velocity HBGKBEs

$$\mathcal{FG} := \left(\frac{D}{Dt} f_i^\epsilon + \frac{1}{3\nu\epsilon^2} \left(f_i^\epsilon - \overline{M}_{f^\epsilon, i}^{\text{eq}} \right) = 0 \quad \text{in } \Omega_T \times Q \right)_{\epsilon > 0}. \quad (3.258)$$

Theorem 3.3.1. Suppose that for given $\epsilon, \nu, K \in \mathbb{R}_{>0}$, f^ϵ is a solution of the HBGKBE (3.245) with moments n_{f^ϵ} and \mathbf{u}_{f^ϵ} and that for $n_{f^\epsilon}, \mathbf{u}_{f^\epsilon}, w_i \frac{D}{Dt} f^\epsilon$ understood as functions of ϵ holds

$$n_{f^\epsilon} \in \mathcal{O}(1) \quad \text{in } \Omega_T, \quad (3.259)$$

$$\mathbf{u}_{f^\epsilon} \in \mathcal{O}(1) \quad \text{in } \Omega_T, \quad (3.260)$$

$$w_i \frac{D}{Dt} f^\epsilon \in \mathcal{O}(1) \quad \text{in } \Omega_T \times Q. \quad (3.261)$$

Then, the sequence \mathcal{FG} of discrete velocity HBGKBE (3.258) is limit consistent of order two to the sequence \mathcal{F} of HBGKBE (3.245) in $\Omega_T \times Q$, and for $i = 1, 2, \dots, q$ the truncation error is

$$\epsilon^2 \frac{D}{Dt} f_i^\epsilon + \frac{1}{3\nu} \left(f_i^\epsilon - \overline{M}_{f^\epsilon, i}^{\text{eq}} \right) \in \mathcal{O}(\epsilon^2) \quad \text{in } \Omega_T \times Q. \quad (3.262)$$

Proof. As a direct consequence of measuring the remainder terms which gives (3.251) and (3.252), the conditions in Definition 3.2.10 are verified and complete the proof. \square

Remark 3.3.4. Note that we can use the result of Theorem 3.3.1 to unfold the convergence of \mathcal{FG} to the HNSE (2.138). In particular, via \mathcal{FG} being limit consistent to \mathcal{F} and the latter in turn converges toward the macroscopic target, we obtain similar convergence information of the former. In the present case, the resulting convergence is formal, since the background limit is formal only.

Homogenized lattice Boltzmann equation As a last step within the derivation of HLBM, we completely discretize the parametrized equations and verify that the limit consistency is preserved. By doing so, the parameter ϵ is glued to the space-time grid resembled by h as described in Section 3.2. We aim for diffusive scaling only which is why $\sigma(\epsilon) = \epsilon^2 = \hat{\sigma}^2(\epsilon)$ holds for $\gamma = 2$. Let Ω be discretized by a regular (uniform Cartesian) grid Ω_h with $N + 1$ nodes per dimension, such that for the largest cubic subdomain $\tilde{\Omega}_h \subseteq \Omega_h \subseteq \Omega$ we define $\Delta x = |\tilde{\Omega}_h|^{1/d}/N$. Via imposing the space-time coupling $\Delta t \sim \Delta x^2$, we uphold a positioning constraint $v_{i\alpha} = \iota \Delta x / \Delta t$ for $\iota \in \{0, \pm 1\}$ (up to three shells) and define the discrete time interval $I_{\Delta t} := \{t = t_0 + k\Delta t \mid t_0 \in I, k \in \mathbb{N}\} \subseteq I$. Here and below we use the parametrization $\epsilon \leftrightarrow h \sim \Delta x \sim \sqrt{\Delta t}$. In contrast to Section 3.2, we glue the limit parameters first and then discretize the equation, since we already fixed the scaling. This agrees also to the merged functioning of the limits (cf. Figure 3.4).

Definition 3.3.6. Let $\Omega_h \times I_h \times Q$ be constructed as above, and f^h denote a solution to the HBGKBE (3.223). Continuing from (3.253), for $i = 1, 2, \dots, q$ we define the i -th population

$$f_i^h(t + \chi h) = f_i^h(\cdot, t + \chi h) = f_i^h(\mathbf{x} + \mathbf{c}_i \chi h, t + \chi h) \quad (3.263)$$

on the space-time cylinder $Z_h = \Omega_h \times I_h$.

Let f^h at least of class C^3 with respect to D/Dt be a solution to the HBGKBE (3.223). We apply Proposition 3.2.3 under the assumption that $(D/Dt)^3 f_i^h \in \mathcal{O}(1)$ for $i = 1, 2, \dots, q$ in terms of functions of h . We use the central difference approximation

$$h^2 \frac{D}{Dt} f_i^h \left(t + \frac{1}{2} h^2 \right) = f_i^h(t + h^2) - f_i^h(t) + R_t^{(6)} \quad \text{in } Z_h. \quad (3.264)$$

Taylor expanding f_i^h and forward differencing $(D/Dt)f_i^h$ yields

$$\begin{aligned} f_i^h \left(t + \frac{1}{2} h^2 \right) &= f_i^h(t) + \frac{1}{2} h^2 \frac{D}{Dt} f_i^h(t) + R_{\mathbf{x},t}^{(7)} \\ &= f_i^h(t) + \frac{1}{2} [f_i^h(t + h^2) - f_i^h(t)] + R_{\mathbf{x},t}^{(8)} \end{aligned} \quad (3.265)$$

in Z_h . Under the assumption that $(D/Dt)^2 f_i^h \in \mathcal{O}(1)$, we deduce

- $R_{\mathbf{x},t}^{(6)} \in \mathcal{O}(h^6)$,
- $R_{\mathbf{x},t}^{(7)} \in \mathcal{O}(h^4)$, and
- $R_{\mathbf{x},t}^{(8)} \in \mathcal{O}(h^4)$ for $(\mathbf{x}, t) \in Z_h$.

To interpret the discrete moments as functions of h , we shift ρ_{f^h} and \mathbf{u}_{f^h} by $h^2/2$, respectively in space-time. Recalling the macroscopic diffusive limit (cf. (2.34) and (3.221)), $(D/Dt)\rho_{f^h} = 0$ and $(D/Dt)\mathbf{u}_{f^h} = -\nu K^{-1}\mathbf{u}_{f^h}$ directly follows for $\epsilon \leftrightarrow h$. Via $(D/Dt)(3.251)$ and $(D/Dt)(3.252)$, we have for $(\mathbf{x}, t) \in Z_h$ that

$$\frac{D}{Dt} \rho_{f^h} = \mathcal{O}(h^2), \quad (3.266)$$

$$\frac{D}{Dt} \mathbf{u}_{f^h} + \nu K^{-1} \mathbf{u}_{f^h} = \mathcal{O}(h), \quad (3.267)$$

respectively. Taylor expanding both moments for $(\mathbf{x}, t) \in Z_h$ leads to the respective approximations

$$\begin{aligned} \rho_{f^h} \left(t + \frac{1}{2} h^2 \right) &= \rho_{f^h}(t) + \frac{1}{2} h^2 \frac{D}{Dt} \rho_{f^h}(t) + R_{\mathbf{x},t}^{(9)} \\ &= \rho_{f^h}(t) + R_{\mathbf{x},t}^{(10)}, \end{aligned} \quad (3.268)$$

$$\begin{aligned} \mathbf{u}_{f^h} \left(t + \frac{1}{2} h^2 \right) &= \mathbf{u}_{f^h}(t) + \frac{1}{2} h^2 \frac{D}{Dt} \mathbf{u}_{f^h}(t) + R_{\mathbf{x},t}^{(11)} \mathbf{1}_{d \times 1} \\ &= \mathbf{u}_{f^h}(t) + \frac{1}{2} \nu h^2 K^{-1} \mathbf{u}_{f^h}(t) + R_{\mathbf{x},t}^{(12)} \mathbf{1}_{d \times 1}, \end{aligned} \quad (3.269)$$

with remainder terms $R_{\mathbf{x},t}^{(9)}, R_{\mathbf{x},t}^{(10)}, R_{\mathbf{x},t}^{(11)} \in \mathcal{O}(h^4)$ and $R_{\mathbf{x},t}^{(12)} \in \mathcal{O}(h^3)$. Multiplying $\varpi_h \times (3.269)$ in Z_h gives

$$\begin{aligned} \varpi_h \mathbf{u}_{f^h} \left(t + \frac{1}{2} h^2 \right) &= (1 - 3\nu^2 h^2 K^{-1}) \mathbf{u}_{f^h}(t) + \frac{1}{2} \nu h^2 K^{-1} \mathbf{u}_{f^h}(t) + R_{\mathbf{x},t}^{(12)} \mathbf{1}_{d \times 1} \\ &= \underbrace{\left[1 - \left(3\nu + \frac{1}{2} \right) \nu h^2 K^{-1} \right]}_{=: d_h} \mathbf{u}_{f^h}(t) + R_{\mathbf{x},t}^{(12)} \mathbf{1}_{d \times 1}, \end{aligned} \quad (3.270)$$

where d_h is referred to as lattice porosity [153]. We inject the latter into (3.256) and define

$$\overline{\overline{M}}_{f^h,i}^{\text{eq}}(\mathbf{x}, t) := \left\{ \frac{w_i}{w} \rho_{f^h} \left[1 + 3h^2 d_h \mathbf{c}_i \cdot \mathbf{u}_{f^h} - \frac{3}{2} h^2 d_h^2 \mathbf{u}_{f^h}^2 + \frac{9}{2} h^4 d_h^2 (\mathbf{c}_i \cdot \mathbf{u}_{f^h})^2 \right] \right\}(\mathbf{x}, t), \quad (3.271)$$

With the help of (3.268), (3.269), (3.270), and (3.271), we construct the homogenized lattice Maxwellian for $(\mathbf{x}, t) \in Z_h$ from discretization and shift as

$$\widehat{M}_{f^h,i}^{\text{eq}} \left(\mathbf{x} + \mathbf{c}_i \frac{1}{2} h^2, t + \frac{1}{2} h^2 \right) = \overline{\overline{M}}_{f^h,i}^{\text{eq}}(\mathbf{x}, t) + R_{\mathbf{x},t}^{(13)}. \quad (3.272)$$

By construction, $R_{\mathbf{x},t}^{(13)} \in \mathcal{O}(h^4)$ for all $(\mathbf{x}, t) \in Z_h$.

Definition 3.3.7. We use Proposition 3.2.3 and the above derivations (3.263), (3.264), (3.265), (3.272), to construct the homogenized lattice Boltzmann equation (HLBE) from three points in time for a space-time grid Z_h and $i = 1, 2, \dots, q$ via reordering (3.257) $_{|(\mathbf{x} + \mathbf{c}_i(1/2)h^2, t + (1/2)h^2)}$ to

$$f_i^h(t + h^2) - f_i^h(t) = -\frac{1}{3\nu + \frac{1}{2}} \left[f_i^h(t) - \overline{\overline{M}}_{f^h,i}^{\text{eq}}(t) \right]. \quad (3.273)$$

Consequently, the sequence of HLBEs reads

$$\mathcal{G} := \left(f_i^h(t + h^2) - f_i^h(t) + \frac{1}{3\nu + \frac{1}{2}} \left[f_i^h(t) - \overline{\overline{M}}_{f^h,i}^{\text{eq}}(t) \right] = 0 \quad \text{in } Z_h \times Q \right)_{h>0}. \quad (3.274)$$

Theorem 3.3.2. Suppose that for given $h, \nu, K \in \mathbb{R}_{>0}$, f^h is a solution of the discrete velocity HBGKBE (3.258) with moments ρ_{f^h} and \mathbf{u}_{f^h} and that for $\rho_{f^h}, \mathbf{u}_{f^h}, f_i^h, (D/Dt)f_i^h, (D/Dt)^2 f_i^h, (D/Dt)^3 f_i^h$ understood as functions of h holds that

$$\rho_{f^h} \in \mathcal{O}(1) \quad \text{in } Z_h, \quad (3.275)$$

$$\mathbf{u}_{f^h} \in \mathcal{O}(1) \quad \text{in } Z_h, \quad (3.276)$$

$$f_i^h, \frac{D}{Dt} f_i^h, \left(\frac{D}{Dt}\right)^2 f_i^h, \left(\frac{D}{Dt}\right)^3 f_i^h \in \mathcal{O}(1) \quad \text{in } Z_h, \quad (3.277)$$

for $i = 1, 2, \dots, q$, respectively. Then, the sequence \mathcal{G} of HLBE (3.3.2) is limit consistent of order two to the sequence \mathcal{FG} of discrete velocity HBKBE (3.258) in $Z_h \times Q$.

Proof. Recall that we have already mapped $\epsilon \leftrightarrow h$. Let f^h be a solution of the HBKBE (3.223) with well-defined moments as specified above. Then, Theorem 3.3.1 dictates the truncation error with respect to velocity discretization

$$\mathcal{E}(h) = \frac{6\nu}{6\nu + 1} \left[h^2 \frac{D}{Dt} f_i^h + \frac{1}{3\nu} \left(f_i^h - \overline{M}_{f^h,i}^{\text{eq}} \right) \right] \in \mathcal{O}(h^2) \quad \text{in } \Omega_T \times Q. \quad (3.278)$$

Considering $\mathcal{E}(h)|_{(x+c_i(1/2)h^2, t+(1/2)h^2)}$ and substituting (3.264), (3.265), and (3.272), unfolds

$$\begin{aligned} & \frac{6\nu}{6\nu + 1} \left\{ h^2 \frac{D}{Dt} f_i^h \left(t + \frac{1}{2}h^2 \right) + \frac{1}{3\nu} \left[f_i^h \left(t + \frac{1}{2}h^2 \right) - \widehat{M}_{f^h,i}^{\text{eq}} \left(t + \frac{1}{2}h^2 \right) \right] \right\} \\ & \approx \frac{6\nu}{6\nu + 1} \left(f_i^h(t+h^2) - f_i^h(t) \right) \end{aligned} \quad (3.279)$$

$$\begin{aligned} & + \frac{1}{3\nu} \left\{ f_i^h(t) + \frac{1}{2} [f_i^h(t+h^2) - f_i^h(t)] - \overline{M}_{f^h,i}^{\text{eq}}(t) \right\} \\ & = f_i^h(t+h^2) - f_i^h(t) + \frac{1}{3\nu + \frac{1}{2}} [f_i^h(t) - \overline{M}_{f^h,i}^{\text{eq}}(t)] \in \mathcal{O}(h^2) \end{aligned} \quad (3.280)$$

for $i = 1, 2, \dots, q$ and for all $(x, t) \in Z_h$. □

Remark 3.3.5. Based on an application-oriented rationale for simulating porous media flow with a mathematical model (2.138), we have constructed a limit consistent discretization leading to an HLBE (3.273) to approximate the latter. The truncation errors of the governing parametrized equations are thus determined up to leading orders at each level of discretization yielding limit consistency and thus (if the discretization is stable) convergence of order two and one of the HLBE with respect to the pressure and velocity, respectively, of the HNSE 2.138. The validity of this limit is based on formal arguments which are however well motivated. Interestingly, the convergence order for the pressure is approved in numerical tests in Section 4.5.

3.3.1.5 Lattice Boltzmann equation for time-filtered Navier–Stokes equations

In [233] we propose for the first time a combination of the TDDM (2.89) developed in [200] and LBMs. The latter are based on MRT collision with relaxation functions for orthogonal moments (see Table 3.4) to achieve the sought for stabilization at coarse resolutions. The TDDM itself is paired with the LBM via consistently discretizing the consistently filtered BGKBE (3.286) and coupling it through the subgrid stress at moment order two to the ordinary differential equation for the temporal residual which is derived in Section 2.4.2. For the sake of completeness, we recall our derivation proposed in [233] after summarizing the main ingredients of the LBM for the bulk flow³. Upon limit consistent discretization, the temporally filtered NSE (2.90), (2.91) is approximated by the LBE (with an additional residual term see (3.288)) consisting of

- velocity stencil: $D3Q19$ (Figure 3.2);

³ Parts of this section are reproduced from [233], Copyright (2022), with permission from the authors and Elsevier Inc.

- equilibrium:

$$f_i^{\text{eq}}(\mathbf{x}, t) := \left\{ \frac{w_i}{w} \bar{\rho}_{\bar{\mathbf{f}}} \left[1 + \frac{1}{c_s^2} \mathbf{c}_i \cdot \bar{\mathbf{u}}_{\bar{\mathbf{f}}} - \frac{1}{2c_s^2} \bar{\mathbf{u}}_{\bar{\mathbf{f}}}^2 + \frac{1}{2c_s^4} \left(\mathbf{c}_i \cdot \bar{\mathbf{u}}_{\bar{\mathbf{f}}} \right)^2 \right] \right\}(\mathbf{x}, t); \quad (3.281)$$

- moment space: zeroth and first order conservation

$$\bar{\rho}_{\bar{\mathbf{f}}}(\mathbf{x}, t) := \sum_{i=1}^q \bar{f}_i(\mathbf{x}, t) = \sum_{i=1}^q f_i^{\text{eq}}(\mathbf{x}, t), \quad (3.282)$$

$$\bar{\mathbf{u}}_{\bar{\mathbf{f}}}(\mathbf{x}, t) := \frac{1}{\bar{\rho}_{\bar{\mathbf{f}}}(\mathbf{x}, t)} \sum_{i=1}^q \mathbf{c}_i \bar{f}_i(\mathbf{x}, t) = \frac{1}{\bar{\rho}_{\bar{\mathbf{f}}}(\mathbf{x}, t)} \sum_{i=1}^q \mathbf{c}_i f_i^{\text{eq}}(\mathbf{x}, t); \quad (3.283)$$

- diffusion coefficient (in the filtered TEQ):

$$\nu = c_s^2 \left(\tau - \frac{1}{2} \right). \quad (3.284)$$

Time-filtered discrete velocity BGK–Boltzmann equation Up to order two, the Hermite expansion of $M_f^{\text{eq}} = f^{\text{eq}}(\mathbf{x}, \mathbf{v}, t)$ (2.28) is given by

$$f_i^{\text{eq}}(\bar{\mathbf{f}}) = \frac{w_i}{w} \bar{\rho}_{\bar{\mathbf{f}}} \left[1 + \frac{1}{c_s^2} \mathbf{c}_i \cdot \bar{\mathbf{u}}_{\bar{\mathbf{f}}} + \frac{1}{2c_s^4} \mathbb{H}_i^{(2)} : \left(\bar{\mathbf{u}}_{\bar{\mathbf{f}}} \otimes \bar{\mathbf{u}}_{\bar{\mathbf{f}}} \right) \right], \quad (3.285)$$

and aligns with the Taylor expansion leading to (3.98) or (3.246) such that (3.285) is equivalent to (3.281). Here, w_i specify the classical weights for $D3Q19$, c_s denotes the corresponding lattice speed of sound and $\mathbb{H}_i^{(2)}$ is the second order multi-dimensional Hermite polynomial evaluated at \mathbf{c}_i for $i = 1, 2, \dots, q$. Note that the dependence of f_i^{eq} on $\bar{\mathbf{f}}$ via the zeroth and first order moment summation for recovering the hydrodynamic conservative variables is now with respect to the filtered conserved quantities $\bar{\rho}$ and $\bar{\mathbf{u}}$ [184] (we neglect the moment index notation $\cdot_{\bar{\mathbf{f}}}$). Thus, the discrete velocity approximation of (2.96) is analogously to (3.92) for the unfiltered NSE (2.12). With (2.103), the truncation of the series expansion at order two, and the use of a $D3Q19$ velocity stencil, the time-filtered BGKBE (2.96) is transformed to the scaled, filtered discrete velocity BGKBE (FDVBE)

$$\partial_t \bar{\mathbf{f}} + \sum_{\alpha=1}^d \mathbf{V}_\alpha \partial_\alpha \bar{\mathbf{f}} = -\frac{1}{\epsilon^\gamma} \left\{ \mathbf{K} [\bar{\mathbf{f}} - f^{\text{eq}}(\bar{\mathbf{f}})] - \mathbf{K} \left(\frac{1}{2c_s^4} w_i \mathbb{H}_i^{(2)} : \mathbf{T} \right)_{1 \leq i \leq q} \right\} \quad (3.286)$$

with $\gamma = 2$ and MRT collision. We define the discrete velocity subgrid remainder term $\mathbf{R} = R_{1 \leq i \leq q}$ with

$$R_i(\mathbf{x}, t) = \frac{1}{2c_s^4} w_i \mathbb{H}_i^{(2)} : \mathbf{T}(\mathbf{x}, t). \quad (3.287)$$

Hence, we can form a closed system of equations, consisting of (2.94), (3.286), and (3.285).

Time-filtered lattice Boltzmann equation Finally, by limit consistent discretization of (3.286) as before on a Cartesian grid with discrete time horizon $(\mathbf{x}, t) \in Z_h = \Omega_{\Delta x} \times I_{\Delta t}$ we obtain the (in time) filtered LBE (FLBE)

$$\bar{\mathbf{f}}(\mathbf{x} + \Delta t \mathbf{c}_i, t + \Delta t) = \bar{\mathbf{f}}(\mathbf{x}, t) - \mathbf{K}^s \left\{ [\bar{\mathbf{f}}(\mathbf{x}, t) - f^{\text{eq}}(\mathbf{x}, t)] + \mathbf{R}(\mathbf{x}, t) \right\}. \quad (3.288)$$

With the zeroth and first order moment summations leading to $\bar{\rho}$ and $\bar{\mathbf{u}}$, respectively, second order convergence in space and first order in time under diffusive scaling is expected [172, 184] toward (2.90) and (2.91). In case of reduction to

the SRT with $\mathbf{K}^s = 1/(\tau + 1/2)\mathbf{I}_q$ along the discretization and relaxation limit, the viscosity in the temporally filtered TEQ is recovered by

$$\nu = c_s^2 \left(\tau - \frac{1}{2} \right). \quad (3.289)$$

The MRT collision matrix \mathbf{K}^s (orthogonal moments, see Table 3.4) is introduced to stabilize the method for coarse grid resolutions. Notably, the orthogonal moment basis \mathbf{M} is defined as in [66]. However, we make the following modifications according to the results obtained so far. To ensure limit consistency to the TEQ, the equilibrium moments are consistent to SRT formulations (i.e. in terms of the notation of [66]: $w_\epsilon = 3$, $w_{\epsilon_j} = 17/2$, $w_{xx} = 2$). Additionally, it has to be stressed that the present definition of \mathbf{R} is unrelaxed in contrast to [184]. The relaxation matrix \mathbf{S} comprises both, the hydrodynamic relaxation rates as proposed in [66] and the optimized kinetic relaxation frequencies proposed in [52]. The essential difference in our work [233], is motivated by linear and brute force analysis [232] which yields dynamic relaxation functions with respect to the lattice Mach number Ma . The necessity of this modification is based on the following reasoning. The orthogonal MRT LBM [66] exhibits lattice Mach number instabilities found by Dellar [63] and numerically studied for example in our work [114]. The instabilities can however be removed when the kinetic relaxation parameters are defined as functions with a proper scaling. In [232], we found that also the optimized third order relaxation frequencies proposed in [52] are Ma -dependent. Thus, a polynomial fit can be used to respect this dependency [233]. As this procedure is dependent on the application and the discretization parameters used, we provide the actual relaxation functions further below (see Section 4.4).

Discrete direct deconvolution with finite differences Conforming to the limit consistent discretization based on Definition 3.2.14, we use finite difference approximations in time to compute the remainder term \mathbf{R} (3.287). We have proposed two versions in [233]. For a first order approximation of (2.94), the forward Euler method with forward differenced time derivatives of $\bar{\mathbf{u}}$ is used, which results in

$$\mathbf{T}(\mathbf{x}, t) = \left(1 - \frac{\Delta t}{\Theta} \right) \mathbf{T}(\mathbf{x}, t - \Delta t) + \frac{\Theta}{\Delta t} \{ [\bar{\mathbf{u}}(\mathbf{x}, t) - \bar{\mathbf{u}}(\mathbf{x}, t - \Delta t)] \otimes [\bar{\mathbf{u}}(\mathbf{x}, t) - \bar{\mathbf{u}}(\mathbf{x}, t - \Delta t)] \}. \quad (3.290)$$

Any unfiltered discrete variable Υ , for example solutions approximating the TEQ (2.12), can thus be easily recovered via backward differencing the deconvolution rule (2.89) through

$$\Upsilon(\mathbf{x}, t) = \bar{\Upsilon}(\mathbf{x}, t) + \frac{\Theta}{\Delta t} [\bar{\Upsilon}(\mathbf{x}, t) - \bar{\Upsilon}(\mathbf{x}, t - \Delta t)]. \quad (3.291)$$

Remark 3.3.6. As initially motivated in Section 2.4, it is remarkable that both (3.290) and (3.291) are local in space by construction which theoretically reduces the computational overhead of the turbulence model to a minimum. The price to pay however is the additional memory storage in the implementation when increasing the discretization order and requiring data from the previous timesteps. The memory consumption is hence directly correlated to the order of the model discretization, such that an accuracy trade-off might be reasonable in actual applications. To match the second order in time when not using diffusive scaling for the LBM, the residual stress formulation of the TDDM as well as the deconvolution rule should be approximated with second order.

A second order consistent discretization of (2.94) can be obtained with the two-step Adams–Bashforth method (see for example [178] and references therein). The derivatives of $\bar{\mathbf{u}}$ at $t - 2\Delta t$ and $t - \Delta t$ are approximated with second order forward and central differences, respectively. We thus transform (2.94) into

$$\begin{aligned} \mathbf{T}(\mathbf{x}, t) = & \left(1 - \frac{3\Delta t}{2\Theta} \right) \mathbf{T}(\mathbf{x}, t - \Delta t) + \frac{\Delta t}{2\Theta} \mathbf{T}(\mathbf{x}, t - 2\Delta t) \\ & - \frac{\Theta}{2\Delta t} \left[\frac{1}{2} \bar{\mathbf{u}}(\mathbf{x}, t) - 2\bar{\mathbf{u}}(\mathbf{x}, t - \Delta t) + \frac{3}{2} \bar{\mathbf{u}}(\mathbf{x}, t - 2\Delta t) \right] \end{aligned}$$

$$\begin{aligned} & \otimes \left[\frac{1}{2} \bar{\mathbf{u}}(\mathbf{x}, t) - 2\bar{\mathbf{u}}(\mathbf{x}, t - \Delta t) + \frac{3}{2} \bar{\mathbf{u}}(\mathbf{x}, t - 2\Delta t) \right] \\ & + \frac{3\Theta}{8\Delta t} \left[\bar{\mathbf{u}}(\mathbf{x}, t) - \bar{\mathbf{u}}(\mathbf{x}, t - 2\Delta t) \right] \otimes \left[\bar{\mathbf{u}}(\mathbf{x}, t) - \bar{\mathbf{u}}(\mathbf{x}, t - 2\Delta t) \right]. \end{aligned} \quad (3.292)$$

Using backward differences of second order for the deconvolution rule (2.89) gives

$$\Upsilon(\mathbf{x}, t) = \bar{\Upsilon}(\mathbf{x}, t) + \frac{\Theta}{\Delta t} \left[\frac{3}{2} \bar{\Upsilon}(\mathbf{x}, t) - 2\bar{\Upsilon}(\mathbf{x}, t - \Delta t) + \frac{1}{2} \bar{\Upsilon}(\mathbf{x}, t - 2\Delta t) \right] \quad (3.293)$$

for obtaining any unfiltered quantity Υ .

Remark 3.3.7. At the temporal boundary $t = 0$, the following procedure is used [233]. The equations (3.292) and (3.293) are for $t \geq 2\Delta t$ only. Initially, for $t = 0$ the residual stress is null by construction. This is due to the fact that filtered and unfiltered fields coincide [200] at $t = 0$. At the next timestep $t = \Delta t$, we use the first order approximations (3.290) and (3.291) instead of (3.292) and (3.293), respectively. Still, locality in space is preserved.

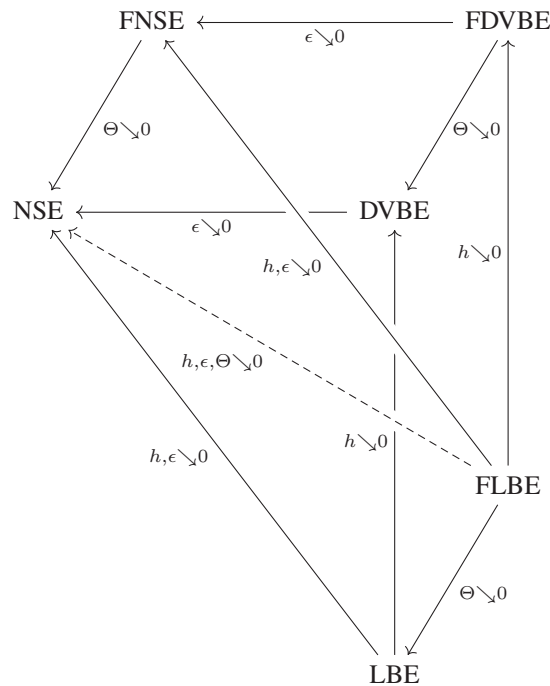


Figure 3.7: Schematic concept for merging relaxation, discretization and filtering of PDE. The abbreviations denote: filtered NSE (FNSE) {(2.90), (2.91), (2.94)}; filtered DVBE (FDVBE) {(3.286), (2.94)}; filtered LBE (FLBE) {(3.288), (3.293)}; NSE (2.12); DVBE (3.92); LBE (3.160). The parameters are defined as ϵ for the relaxation scaling, h for the space-time discretization and Θ for the filter width. The nature of arrows is hidden for the purpose of representation. The overall limit of the FLBE to the NSE is denoted as dashed line.

Remark 3.3.8. As a matter of fact, we have now added a third layer of limits to the already merged discretization and relaxation (see Figure 3.7). The filtering of the TLES (in terms of the filter width) is now running on top of the RS (in form of discrete velocities) and the LBE (in terms of discretization). To weakly converge in terms of equations and solutions from the FLBE (2.96) to the incompressible NSE (2.12) we have to connect three single limit arrows now and ensure that the overall order of consistency is still two in space. For spatial LES with direct NSE solvers, the matter of error estimation has been quantitatively analyzed by Geurts *et al.* [98, 99] and convergence toward weak solutions in the sense of Leray–Hopf has been rigorously proved by Berselli *et al.* [30]. For the present TLES nothing similar has

been done yet to the knowledge of the author. We provide first experimental error estimates in [233], which indicate the expected convergence when merging all limits accordingly, and summarize the results in Section 4.4.

3.3.1.6 Lattice Boltzmann equation for Navier–Stokes–Cahn–Hilliard equations

In [235] we use the SFRM [224] (see Section 2.6, Definition 2.6.6) and the novel HSFRM (see Section 2.6, Definition 2.6.9) to simulate shear and extensional flows of a binary fluid mixture with LBMs in two and three dimensions. To that end, two populations are used, one for approximating the CHE which governs the order parameter and another one for approximating the incompressible NSE with a forcing term which couples the PDEs (see below). The derivation of the two LBEs for approximating to TEQs can be done separately involving a generic force term or jointly by considering thermodynamics. In general, similarly to the single CHE, it is useful to use a second order equilibrium [242] which matches the discretization terms of the Taylor expanded LBE with the TEQ. Upon limit consistent discretization of the DVBE for each population, the LBM approximating (2.178) in the incompressible limit consists of

- velocity stencil: $D2Q9$, $D3Q19$ for both f_i and g_i (see Figure 3.2);
- equilibria:

$$f_i^{\text{eq}}(\mathbf{x}, t) = \left\{ \frac{w_i}{w} \rho_f \left[1 + \frac{1}{c_s^2} \mathbf{c}_i \cdot \mathbf{u}_f - \frac{1}{2c_s^2} \mathbf{u}_f^2 + \frac{1}{2c_s^4} (\mathbf{c}_i \cdot \mathbf{u}_f)^2 \right] \right\}(\mathbf{x}, t), \quad (3.294)$$

$$g_i^{\text{eq}}(\mathbf{x}, t) = \begin{cases} \left\{ \frac{w_i}{w} \left[\frac{1}{c_s^2} \Gamma_\phi \mu_\phi + \frac{1}{c_s^2} \phi_g \mathbf{c}_i \cdot \mathbf{u}_f - \frac{1}{2c_s^2} \phi_g \mathbf{u}_f^2 + \frac{1}{2c_s^4} \phi_g (\mathbf{c}_i \cdot \mathbf{u}_f)^2 \right] \right\}(\mathbf{x}, t), & \text{if } i \neq 1, \\ \phi_g(\mathbf{x}, t) - \sum_{i \neq 1} g_i^{\text{eq}}(\mathbf{x}, t), & \text{if } i = 1; \end{cases} \quad (3.295)$$

- moment space: zeroth and first order (for f_i) and zeroth (for g_i) conservation, respectively

$$\rho_f(\mathbf{x}, t) = \sum_{i=1}^q f_i(\mathbf{x}, t) = \sum_{i=1}^q f_i^{\text{eq}}(\mathbf{x}, t), \quad (3.296)$$

$$\rho_f(\mathbf{x}, t) \mathbf{u}_f(\mathbf{x}, t) = \sum_{i=1}^q \mathbf{c}_i f_i(\mathbf{x}, t) + \frac{1}{2} \mathbf{F}(\mathbf{x}, t) = \sum_{i=1}^q \mathbf{c}_i f_i^{\text{eq}}(\mathbf{x}, t) + \frac{1}{2} \mathbf{F}(\mathbf{x}, t), \quad (3.297)$$

$$\phi_g(\mathbf{x}, t) = \sum_{i=1}^q g_i(\mathbf{x}, t) = \sum_{i=1}^q g_i^{\text{eq}}(\mathbf{x}, t); \quad (3.298)$$

- diffusion coefficients:

$$\nu = c_s^2 \left(\tau_\nu - \frac{1}{2} \right), \quad (3.299)$$

$$M_\phi = \Gamma_\phi \left(\tau_{M_\phi} - \frac{1}{2} \right). \quad (3.300)$$

Forcing scheme The LBE with a general force term S reads

$$f_i(\mathbf{x} + \mathbf{c}_i, t + 1) = f_i(\mathbf{x}, t) + J_i(\mathbf{x}, t) + S_i(\mathbf{x}, t), \quad \text{for } i = 1, 2, \dots, q. \quad (3.301)$$

Since the forcing term \mathbf{F}^{th} (2.143) based on the thermodynamic pressure tensor (2.141) is included into the LBE, a second order consistent forcing scheme is required to uphold limit consistency. For example the classical forcing method by Guo *et al.* [112] defines

$$S_i(\mathbf{x}, t) = \left(1 - \frac{1}{2\tau_\nu}\right) w_i \left[\frac{\mathbf{c}_i - \mathbf{u}_f(\mathbf{x}, t)}{c_s^2} + \frac{(\mathbf{c}_i \cdot \mathbf{u}_f(\mathbf{x}, t)) \mathbf{c}_i}{c_s^4} \right] \cdot \mathbf{F}(\mathbf{x}, t), \quad \text{for } i = 1, 2, \dots, q. \quad (3.302)$$

Via this structure, the parts to be interchanged for using a different FRM would be the force term including the chemical potentials and the second lattice. Further, ternary mixtures or flows with more components can be modeled by coupling more CHEs to the NSE. The approximation with LBMs is thus realized via coupling one additional LBE per additional component with the respective order parameter as zeroth moment.

3.3.2 Initial and boundary conditions

3.3.2.1 Initialization

As observed by several authors [27, 44, 186, 252, 254] in an ongoing scientific discourse, it is essential to supply the LBE with initial conditions consistent to the target problem at hand. As proven above (see Proposition 3.1.3, Theorem 3.2.1), the equilibrium initialization with the given target initial conditions leads to convergence of the relaxation limit which agrees to the results in the literature. Due to the relaxation character of the LBM, the conserved quantities of the TEQ at $t = 0$ are the only known initial data in general. Several techniques exist to align the *a priori* unknown initial data of the constructed artificial variables (moments) with the conserved quantities. In the present work, if not stated otherwise, we initialize the populations with

$$\mathbf{f}(\mathbf{x}, 0) = \mathbf{f}^{\text{eq}}(\mathbf{x}, 0) \quad \text{in } \Omega. \quad (3.303)$$

Since we consider solely nonstationary PDEs, at several occasions in numerical experiments we align the nonequilibrium part of the kinetic moments (and thus the nonequilibrium populations) through repeated collisions to the initial conserved state preceding the actual simulation time horizon. The length of the process is bound by a variable percentage of the final simulation time interval which yields a sufficiently diminished oscillation up to a feasible tolerance in practice. Additionally, in the case of approximating fluid flow where an initial pressure function is given, we use the same procedure to obtain a more accurate zeroth order moment density profile at the initial time. On top of that, we use the method proposed by Mei *et al.* [186] and pressure correct the velocity in case of a solenoidal target.

3.3.2.2 Methods for imposing boundary conditions

Compared to the initialization methods, the treatment of boundaries in LBMs might be regarded as a self-standing research field. Since this is not the focus of the present work, we provide only the necessary details on the implementation of boundary conditions for the PDEs to be approximated. Krüger *et al.* [164] provide a comprehensive overview of boundary methods and schemes in LBMs which serves as a main reference for the summary below. We separate the methods in terms of their result in the relaxation limit, i.e. the macroscopic target condition on the respective moment order. For the purpose of illustration, let the space-time cylinder Ω_T be discretized with $(\Delta x, \Delta t)$ for $(\mathbf{x}, t) \in Z_h \subseteq \Omega_T$. All boundaries of the continuum are to be thought of as link-wise, i.e. the discretization is such that the continuum boundary lies in between two grid nodes.

Periodic boundary condition Let $\Omega \subseteq \mathbb{R}^d$ define a cube of size L^3 , which, when periodically repeated, covers the whole space. In case of the assumption that the specific solution ρ sought for in the target problem shares the same periodicity, we have that

$$\rho(\mathbf{x}, t) = \rho(\mathbf{x} + L\mathbf{p}, t) \quad \text{in } \Omega_T, \quad (3.304)$$

where $\mathbf{p} \in \mathbb{R}^d$ describes the periodicity directions of Ω . The same rule is imposed onto the populations governed by the corresponding LBE, such that the re-entry in the opposing domain side is given by

$$\mathbf{f}(\mathbf{x}, t) = \mathbf{f}(\mathbf{x} + L\mathbf{p}, t) \quad \text{in } \Omega_T, \quad (3.305)$$

which transfers to all moments $\mathbf{M}\mathbf{f}$.

Dirichlet condition for first order moments Let $\Omega \subset \mathbb{R}^d$ with boundary $\partial\Omega$ and let $\mathbf{x}_b \in \partial\Omega$ denote the boundary nodes in the discretization of $\bar{\Omega} = \Omega \cup \partial\Omega$. For example in the case of a no-slip wall boundary for a fluid continuum, a homogeneous Dirichlet condition

$$\mathbf{u} = \mathbf{0} \quad \text{on } \partial\Omega \times I \quad (3.306)$$

is successfully recovered by imposing a bounce-back rule (see [164] and references therein).

$$f_{\bar{i}}^{\text{POS}}(\mathbf{x}_b, t + \Delta t) = f_{\bar{i}}^{\text{PRS}}(\mathbf{x}_b, t), \quad (3.307)$$

where $f_{\bar{i}}$ denote the populations corresponding to $\mathbf{c}_{\bar{i}} = \mathbf{c}_i$. Similarly, a nonhomogeneous Dirichlet boundary condition

$$\mathbf{u} = \mathbf{u}_w \quad \text{on } \partial\Omega \times I \quad (3.308)$$

is obtained via

$$f_{\bar{i}}^{\text{POS}}(\mathbf{x}_b, t + \Delta t) = f_{\bar{i}}^{\text{PRS}}(\mathbf{x}_b, t) - 2 \frac{w_i}{w c_s^4} \rho_{\mathbf{f}}(\mathbf{x}_w, t) \mathbf{c}_i \cdot \mathbf{u}_{\mathbf{f}}(\mathbf{x}_w, t), \quad (3.309)$$

where $\mathbf{x}_w = \mathbf{x}_b + 0.5\mathbf{c}_i\Delta t$ is the wall location and $\mathbf{u}_{\mathbf{f}}(\mathbf{x}_w, \cdot) = \mathbf{u}_w(\cdot)$. The method can be applied for slip wall boundaries, inflows and outflows, or moving walls without mass flux. It is to be noted that in general, the standard bounce-back boundary methods are second order accurate in space only in special scenarios, for example for straight walls. Further details and method extensions are given for example in [164] and references therein.

Dirichlet condition for zeroth order moments A Dirichlet condition in the TEQ, e.g.

$$\rho = 0 \quad \text{on } \partial\Omega \times I, \quad (3.310)$$

can be imposed for the LBE via the anti-bounce-back rule

$$f_{\bar{i}}^{\text{POS}}(\mathbf{x}_b, t + \Delta t) = -f_{\bar{i}}^{\text{PRS}}(\mathbf{x}_b, t) + 2 \frac{w_i}{w} \rho_{\mathbf{f}}(\mathbf{x}_w, t) \left[1 + \frac{1}{2c_s^4} (\mathbf{c}_i \cdot \mathbf{u}_{\mathbf{f}}(\mathbf{x}_w, t))^2 - \frac{1}{2c_s^2} u_{\mathbf{f}}^2(\mathbf{x}_w, t) \right], \quad (3.311)$$

which is useful for example to realize pressure inflows or outflows, to set order parameters at domain boundaries or predefine the temperature in thermal flows (see [164, 236] and references therein).

Bouzidi's method for curved boundaries For approximating curved walls with second order accuracy (for an exemplary application see [116]), the method by Bouzidi *et al.* [38] can be used. The method extends the half-way

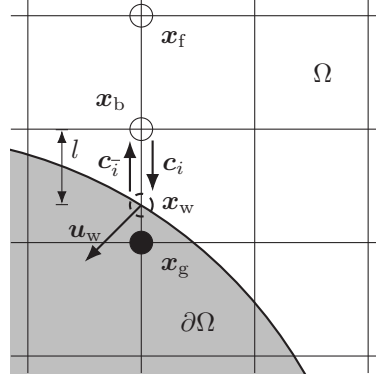


Figure 3.8: Illustration of a curved boundary layout [116].

implementation of the bounce-back boundary scheme. A linear interpolation recovers the approximate distance l to the boundary in the i th direction. Effectively taking into account the shape of the object or wall, hence increases the accuracy and theoretically retains second order for the boundary scheme also in this case. The post-streaming populations are computed via

$$f_i^{\text{pos}}(\mathbf{x}_b, t + \Delta t) = \begin{cases} 2lf_i^{\text{prS}}(\mathbf{x}_b, t) + (1 - 2l)f_i^{\text{prS}}(\mathbf{x}_f, t) - 2\frac{w_i}{wc_s^2}\mathbf{c}_i \cdot \mathbf{u}_f(\mathbf{x}_w, t) & \text{for } l < \frac{1}{2}, \\ \frac{1}{2l}f_i^{\text{prS}}(\mathbf{x}_b, t) + (1 - \frac{1}{2l})f_i^{\text{prS}}(\mathbf{x}_f, t) - \frac{1}{l}\frac{w_i}{wc_s^2}\mathbf{c}_i \cdot \mathbf{u}_f(\mathbf{x}_w, t) & \text{for } l \geq \frac{1}{2}. \end{cases} \quad (3.312)$$

A layout of grid nodes is sketched in Figure 3.8, where the indexed \mathbf{x}_g denotes the ghost node outside of the domain $\bar{\Omega}$ in i th direction. Note that the half-way bounce-back rule (3.308) is recovered for $l = 1/2$. An estimation of consistency and a detailed discussion is given in [164] and references therein.

3.3.3 Postprocessing and other operations

Besides the LBE kernel with initialization and boundary schemes, the numerical experiments below require several additional approximation methods. Among others, we need to approximate gradients, Fourier transforms and eigenvalues to dense matrices of intermediate size $\mathcal{O}(q)$.

Gradients At several occasions within the approximation of the solution to the TEQ, gradients are to be approximated. Conforming to the discretizations used so far, we use finite differences of order two and higher. Exemplarily, for postprocessing the computed velocity field in a turbulent flow simulation, central difference stencils of order eight have been found suitable (by us [114, 232, 233] and others [97]). Hence, given an approximate solution \mathbf{u} on Z_h to (2.12), we approximate its gradient with

$$\begin{aligned} \partial_\beta u_\alpha(\mathbf{x}) = \frac{1}{\Delta x} \left\{ \frac{4}{5} [u_\alpha(\mathbf{x} + \Delta x \mathbf{e}_\beta) - u_\alpha(\mathbf{x} - \Delta x \mathbf{e}_\beta)] \right. \\ + \frac{1}{5} [u_\alpha(\mathbf{x} - 2\Delta x \mathbf{e}_\beta) - u_\alpha(\mathbf{x} + 2\Delta x \mathbf{e}_\beta)] \\ + \frac{4}{105} [u_\alpha(\mathbf{x} + 3\Delta x \mathbf{e}_\beta) - u_\alpha(\mathbf{x} - 3\Delta x \mathbf{e}_\beta)] \\ \left. + \frac{1}{280} [u_\alpha(\mathbf{x} - 4\Delta x \mathbf{e}_\beta) - u_\alpha(\mathbf{x} + 4\Delta x \mathbf{e}_\beta)] \right\} + \mathcal{O}(\Delta x^8), \end{aligned} \quad (3.313)$$

where the temporal argument is neglected for the purpose of illustration. As another example for a derivative of order two, we compute the Laplacian finite difference operator of an order parameter ϕ in Z_h as approximate solution to the CHE (2.11) with a stable and isotropic d^3 -point stencil [210] of second order, e.g. on the $D2Q9$ lattice we use

$$\begin{aligned} \Delta_{\mathbf{x}}\phi(\mathbf{x}) = \frac{1}{\Delta x^2} \left\{ \frac{1}{2} [\phi(\mathbf{x} + \Delta x \mathbf{e}_1) + \phi(\mathbf{x} - \Delta x \mathbf{e}_1) + \phi(\mathbf{x} + \Delta x \mathbf{e}_2) + \phi(\mathbf{x} - \Delta x \mathbf{e}_2)] \right. \\ \left. + \frac{1}{4} [\phi(\mathbf{x} + \Delta x(\mathbf{e}_1 + \mathbf{e}_2)) + \phi(\mathbf{x} - \Delta x(-\mathbf{e}_1 + \mathbf{e}_2)) \right. \\ \left. + \phi(\mathbf{x} + \Delta x(\mathbf{e}_1 - \mathbf{e}_2)) + \phi(\mathbf{x} - \Delta x(-\mathbf{e}_1 - \mathbf{e}_2))] \right. \\ \left. - 3\phi(\mathbf{x}) \right\} + \mathcal{O}(\Delta x^2). \end{aligned} \quad (3.314)$$

Finally, also in the time domain, we use backward difference formulas at least of order two to obtain approximations of $\partial_t \cdot$ for postprocessing turbulence quantities of interest (further descriptions are given in our work [233]).

Fourier transforms To approximate the energy, dissipation, and relaxation spectra in the turbulent flow simulations in Chapter 4, we use component-wise discrete Fourier transforms. For example, given a computed vectorial quantity $\Upsilon: \Omega_{\Delta x} \times I_{\Delta t} \rightarrow \mathbb{R}^d$ on the grid nodes $\mathbf{x} = (n_1, n_2, \dots, n_d)$ and $n_i = 0, 1, \dots, N$ for all i , we compute the spatial discrete Fourier transform according to

$$\tilde{\Upsilon}_{\alpha}(\mathbf{k}, t) = \sum_{\mathbf{x}=\mathbf{0}_{1 \times d}}^{(N-1)\mathbf{1}_{1 \times d}} \Upsilon_{\alpha}(\mathbf{x}, t) \exp\left(-\frac{2\pi i}{N} \mathbf{k} \cdot \mathbf{x}\right) \quad (3.315)$$

for all $\alpha = 1, 2, \dots, d$, defined on the wave nodes $\mathbf{k} = (k_1, k_2, \dots, k_d)$ with $k_i = 0, 1, \dots, N$ for all i . Due to the real input symmetry, we mostly postprocess $k_i = 0, 1, \dots, \lfloor N/2 \rfloor$ below.

Eigenvalue problems In Section 3.2.5, the von Neumann stability of the collision operator defined by its linearized amplification matrix \mathbf{H} (see Definition 3.2.16) is determined through its spectrum. Since, $\mathbf{H} \in \mathbb{C}^{q \times q}$ and $3 \leq q \leq 19$ in the present work, the eigenvalues have to be approximated. Moreover, the arguments of \mathbf{H} are provided in the form of discrete parameter spaces (presently of the size $\mathcal{O}(10^2)$ up to $\mathcal{O}(10^7)$ each) and thus scale up quickly. As the matrices are independent of each other for each parameter tuple, parallelizability is perfect when approximating the eigenvalues separately. The present work employs a classical QR algorithm to compute the Schur decomposition of the matrix

$$\mathbf{H} = \mathbf{Q}\mathbf{U}\mathbf{Q}^{-1}, \quad (3.316)$$

where $\mathbf{Q} \in \mathbb{C}^{q \times q}$ is unitary and $\mathbf{U} \in \mathbb{C}^{q \times q}$ is upper triangular. Hence, with a costs of $\mathcal{O}(q^3)$ we obtain

$$\text{spec}(\mathbf{H}) = \text{spec}(\mathbf{U}) = \text{diag}(\mathbf{U}) \quad (3.317)$$

up to machine precision.

3.3.4 Implementation

Implementational details for the algorithms employed in the present work can be found in our publications [42, 59, 114, 116, 162, 190, 229–236] and code releases [160, 161, 165, 168]. Here, only a selection of methods is presented which depart from the common LBM bulk kernel structure (stream and collide) due to additional features or coupling. We thus document an advanced collision kernel, a coupled collision scheme, a single level Monte Carlo (SLMC) method wrapper which treats the LBM as a black box, and two possibilities to obtain stability maps for three-dimensional

artificial turbulence simulations. For the purpose of illustration, the notation in this section occasionally differs from the above made definitions. Unless stated otherwise, all numerical methods are implemented in, or added as external libraries to the open source C++ library OpenLB (releases 1.3, 1.4, 1.5, 1.6, or ongoing).

Entropy controlled kinetic moment relaxation The present work uses a KBC-N1 collision scheme [36], which has to the knowledge of the author not been extensively used before on a reduced $D3Q19$ lattice with natural moments combined with a second order truncated equilibrium. The here used kernel implementation is summarized in Algorithm 1. A preliminary study is provided in [163]. The implementation of entropy control approximations is ongoing research and other works treat this topic in more details. For example Wang [256] restated (3.201) in terms of a least squares problem for entropy-controlling individual moment collisions and suggested a solution via matrix decomposition. Moreover, various computational details of the entropic SRT and MRT collision models are discussed in [135] and [244]. It is observable that, the implementation of the additional entropic scalar product in the collision kernel does not add much load to the method and thus is expected to have a negligible impact on the overall scalability of the LBM on several hundreds of graphical processing units (GPUs) [168].

Algorithm 1 Realization of entropic MRT collision (KBC-N1 [35]) in OpenLB [168]

```

procedure collideKBC-N1( $\mathbf{f}$ ) ▷ Input: pre-collision  $\mathbf{f}$  at local node  $(\mathbf{x}, t)$ 
  compute hydrodynamic moments:  $(\rho, \mathbf{u}) \leftarrow (\sum_{i=1}^q f_i, \sum_{i=1}^q \mathbf{c}_i f_i / \rho)$ 
  compute equilibrium  $\mathbf{f}^{\text{eq}} \leftarrow \mathbf{f}^{\text{eq}}(\rho, \mathbf{u})$  ▷ (3.98)
  compute nonequilibrium  $\mathbf{f}^{\text{neq}} \leftarrow \mathbf{f} - \mathbf{f}^{\text{eq}}$ 
  compute all moments  $\mathbf{m} \leftarrow \mathbf{m}(\mathbf{f})$  ▷ (3.99)
  compute shear nonequilibrium populations  $\mathbf{f}_\nu^{\text{neq}} \leftarrow \mathbf{f}_\nu^{\text{neq}}(N, \Pi)$  ▷ (3.195)
  compute higher order nonequilibrium populations  $\mathbf{f}_{\text{hom}}^{\text{neq}} = \mathbf{f}^{\text{neq}} - \mathbf{f}_\nu^{\text{neq}}$  ▷ (3.196)
  assign viscosity relaxation frequency  $\beta \leftarrow \omega/2$  ▷  $\omega = 1/\tau$ 
  compute entropy controller  $\gamma^* \leftarrow \gamma^*(\beta, \mathbf{f}^{\text{eq}}, \mathbf{f}_\nu^{\text{neq}}, \mathbf{f}_{\text{hom}}^{\text{neq}})$  ▷ (3.201)
  local collision of  $\mathbf{f}^{\text{poc}} \leftarrow \mathbf{f}^{\text{poc}}(\beta, \gamma^*, \mathbf{f}, \mathbf{f}_\nu^{\text{neq}}, \mathbf{f}_{\text{hom}}^{\text{neq}})$  ▷ Collide populations via (3.197)
  return  $\mathbf{f}^{\text{poc}}$  ▷ Output: post-collision  $\mathbf{f}^{\text{poc}}$  at local node  $(\mathbf{x}, t)$ 
end procedure

```

Free energy coupling The approximation for the NSE with a thermodynamic pressure tensor (2.142) together with one coupled CHE (2.11) requires two LBEs for \mathbf{f} and \mathbf{g} , respectively. The computational steps implemented in one collision (jointly on both lattices) are summarized in Algorithm 2. The present work illustrates the bulk solver only and the initial and the boundary methods summarized in Section 3.3.2 are applied to impose boundary conditions for the binary fluid mixture.

Von Neumann stability analysis To compute the Schur decomposition (3.316) and thus approximate the eigenvalues of \mathbf{H} via (3.317), the linear algebra package Eigen [110] is linked with OpenLB [165]. An exemplary computation of linear stability maps for a given periodic PDE problem with a background flow of $\bar{\mathbf{u}} \in \mathbb{R}^d$ approximated with an MRT LBM is pseudocoded in Algorithm 3. The algorithm describes the computation of von Neumann stability sets spanned by kinetic relaxation times for approximating the incompressible NSE (2.12). Discrete parameter spaces are given as input. The relaxation frequencies $\mathbf{S}^s \in \mathfrak{S}$ are to be scanned for all background flow directions \mathcal{B} of interest and for all flow configurations (N, Ma, Re) gathered in the space $\mathfrak{N} \times \mathfrak{M} \times \mathfrak{R}$ with given initial data \mathbf{u}_0 . Note that in case of spatially inhomogeneous initial data, the mean flow is computed using the average $\text{ave}(\mathbf{u}_0)$ which depends on the actual problem configuration (see Chapter 4).

Algorithm 2 FRM LBM bulk collision kernel (SFRM [224]) in OpenLB [168] (reproduced from [235])

```

procedure collideSFRM( $f, g$ )                                ▷ Input: pre-collision  $f$  and  $g$  at local node  $(x, t)$ 
  compute zeroth moments:
    mixture density  $\rho \leftarrow \sum_i f_i$                                 ▷ (3.296)
    order parameter  $\phi \leftarrow \sum_i g_i$                                 ▷ (3.298)
  compute potentials:  $\mu_\rho \leftarrow \mu_\rho(\rho, \phi)$  and  $\mu_\phi \leftarrow \mu_\phi(\rho, \phi)$   ▷ (2.156), (2.157)
  Guo forcing, via:
    force  $F \leftarrow F(\rho, \mu_\rho, \phi, \mu_\phi)$                                 ▷ (2.143), (2.158)
    velocity  $u \leftarrow u(f, \rho, F)$                                 ▷ (3.297)
    force term  $S \leftarrow S(u, F)$                                 ▷ (3.302)
  compute equilibria:  $f^{\text{eq}} \leftarrow f^{\text{eq}}(\rho, u)$  and  $g^{\text{eq}} \leftarrow g^{\text{eq}}(\phi, \mu_\phi, u)$   ▷ (2.28), (3.205)
  local collision:  $f^{\text{poc}} \leftarrow f^{\text{poc}}(f, f^{\text{eq}}, S)$  and  $g^{\text{poc}} \leftarrow g^{\text{poc}}(g, g^{\text{eq}})$   ▷ (3.301), (3.160)
  return  $f^{\text{poc}}, g^{\text{poc}}$ 
end procedure                                            ▷ Output: post-collision  $f^{\text{poc}}$  and  $g^{\text{poc}}$  at local node  $(x, t)$ 

```

Algorithm 3 Von Neumann stability estimation in OpenLB [168] as used in [232] for approximating (2.12)

```

procedure computeLinearStabilitySets( $\mathcal{B}, \mathcal{S}, u_0, \mathfrak{N}, \mathfrak{M}, \mathfrak{R}$ )  ▷ Input: scan parameters, flow configurations
  load LBM structure from OpenLB: read in  $DdQq, M, f^{\text{eq}}$   ▷ e.g. Definition 3.2.3, Table 3.4, (3.98)
  for  $Re \in \mathfrak{R}$  do
     $\nu = 1/Re$                                 ▷ normalized characteristic scales
    for  $Ma \in \mathfrak{M}$  do
       $U_c = Mac_s$                                 ▷ characteristic lattice velocity
      for  $N \in \mathfrak{N}$  do
         $\Delta\kappa = 2\pi/(N-1)$                                 ▷ wave space discretization length
        for  $u_{\text{dir}} \in \mathcal{B}$  do
          compute Jacobian  $J_{f^{\text{eq}}}(U_c \text{ave}(u_0)u_{\text{dir}})$                                 ▷ (3.186)
          for  $S^s \in \mathcal{S}$  do
            compute  $K^s = M^{-1}SM$                                 ▷ (3.161)
            for  $k \in \mathcal{K}_{\Delta\kappa}$  do
              compute prefactor diagonal  $A = \text{diag}((\exp(-2\pi\Delta tk \cdot c_i))_i)$                                 ▷ (3.185)
              compute  $H = A[I_q + K^s(J_{f^{\text{eq}}} - I_q)]$                                 ▷ (3.185)
              compute Schur decomposition  $H = QUQ^{-1}$                                 ▷ (3.316)
              store  $\text{spec}(H) = \text{diag}(U)$                                 ▷ (3.317)
              compute and store spectral radius  $r_{\text{spec}}(H) = \max(\text{spec}(H))$                                 ▷ (3.188)
              compute  $\omega = \text{iln}(\text{spec}(H))/\Delta t$                                 ▷ (3.184)
              compute and store dispersion  $\text{Re}(\omega)$  and dissipation  $\text{Im}(\omega)$ 
            end for
            compute maximum  $r_{\text{spec}}^*(H) = \max_k(r_{\text{spec}}(H))$                                 ▷ (3.188)
          end for
          store spectral radius tensor  $\mathbb{r}_{\text{spec}}^*(H) \in \mathbb{R}^{\dim(\mathcal{S})}$ 
        end for
        compute component-wise maximum  $\mathbb{r}_{\text{spec}}^{**}(H) = \max_{u_{\text{dir}}}(r_{\text{spec}}^*(H))$ 
        store stability set  $\mathcal{S} = \{S^s \in \mathcal{S} \mid (\mathbb{r}_{\text{spec}}^{**}(H))_i \leq 1\}$                                 ▷ Definition 3.2.16
      end for
    end for
  end for
  return stability sets  $\mathcal{S}$  for each configuration  $(Re, Ma, N) \in \mathfrak{R} \times \mathfrak{M} \times \mathfrak{N}$ 
end procedure                                            ▷ Output: von Neumann stability sets

```

Brute force stability The notion of linear stability is commonly used for analyzing the robustness of LBMs in incompressible and compressible fluid flow configurations (see for example [54, 56, 124, 127, 264] and references therein). For large Reynolds numbers however, nonlinear terms gain more influence on the stability, such that spectral sampling [56] perturbs the result, even for discrete Fourier transformed data (3.315) resulting from nonlinear mean flow information which is automatically scaled by cutoff [232]. Moreover, nonlinear terms of order two and higher have been neglected from the Taylor expanded equilibrium in the first place such that \mathbf{H} describes amplification from linearized collision only. We thus introduce a purely numerical notion of stability in [232]. The procedure is based on computing through numerical and physical parameter spaces of a chosen benchmark test with a highly parallel software library. The obtained information is final in the sense that the scheme is completely discrete and implemented, yielding *a posteriori* stability including all possible numerical and modeling nonlinearities.

Definition 3.3.8. Let the LBE (3.160) be determined by an orthogonal moment MRT LBM on $DdQq$. Let \mathfrak{S} be a given scan parameter space for \mathbf{S} and $\mathfrak{N} \times \mathfrak{R}_1 \times \mathfrak{R}_2 \times \dots \times \mathfrak{R}_D$ be a given flow configuration, where \mathfrak{N} contains the resolutions N and $(\mathfrak{R}_i)_{1 \leq i \leq D}$ denotes a space tuple containing π -groups $(R_i)_{1 \leq i \leq D}$ for a periodic benchmark setting governed by the TEQ with a given initial condition (e.g. \mathbf{u}_0). Let φ denote a target length scale to be resolved in the simulation. Unless a simulated characteristic quantity $j = j(\varphi)$ exceeds an upper tolerance

$$j(\varphi) > \text{tol}, \quad (3.318)$$

the simulation is called nondivergent. The scheme is called brute force stable for \mathbf{S} and a given flow configuration, if the LBM computation initialized with $\mathbf{f}^{\text{eq}}(\mathbf{u}_0)$ is nondivergent until a given physical time step $t = t_{\text{end}}$. The set \mathcal{S} containing relaxation frequency vectors which render the scheme brute force stable is called brute force stability set.

An exemplary computation of brute force stability maps for a given periodic PDE problem with a background flow of $\bar{\mathbf{u}} \in \mathbb{R}^d$ approximated with an MRT LBM is pseudocoded in Algorithm 4. The algorithm describes the computation of brute force stability sets spanned by kinetic relaxation times for approximating the incompressible NSE (2.12). Discrete parameter spaces are given as input.

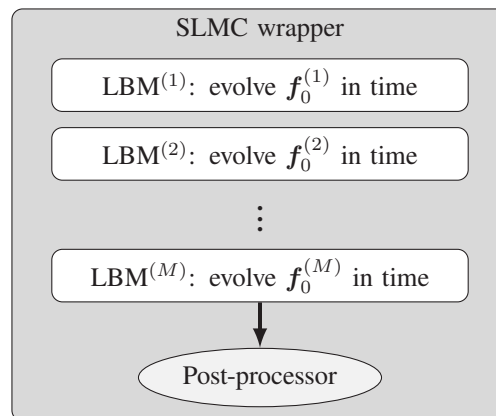


Figure 3.9: Schematic overview of SLMC LBM. The m th initial data sample is denoted with $\mathbf{f}_0^{(m)}$.

Algorithm 4 Brute force stability estimation in OpenLB [168] as used in [232] for approximating (2.12)

```

procedure computeBruteForceStabilitySets( $\mathfrak{S}, \mathbf{u}_0, \mathfrak{N}, \mathfrak{M}, \mathfrak{R}$ )  $\triangleright$  Input: scan parameters, flow configurations
  initialize LBM computation in OpenLB with  $\mathbf{u}_0, DdQq, \mathbf{M}, \mathbf{f}^{\text{eq}}$   $\triangleright$  e.g. Definition 3.2.3, Table 3.4, (3.98)
  pass flow configuration as variable arguments
  for  $Re \in \mathfrak{R}$  do
     $\nu = 1/Re$   $\triangleright$  normalized characteristic scales
    for  $Ma \in \mathfrak{M}$  do
       $U_c = Mac_s$   $\triangleright$  characteristic lattice velocity
      for  $N \in \mathfrak{N}$  do
        for  $\mathbf{S}^s \in \mathfrak{S}$  do
          for  $t \in [0, t_{\text{end}}]$  do
            for  $\mathbf{x} \in \Omega_{\Delta x}$  do
              collide MRT at node  $\mathbf{x}$   $\triangleright$  (3.160), (3.202)
            end for
            evolve LBE in time (streaming)  $\triangleright$  (3.160), (3.203)
            compute  $j(\varphi)$ 
            if  $j(\varphi) > \text{tol}$  then  $\triangleright$  (3.318)
              store divergence point in time  $t_{\text{div},1} = t$  in array  $\mathbf{t}_{\text{div},1} \in \mathbb{R}^{\dim(\mathfrak{S})}$ 
              store error  $t_{\text{div},2} = \text{NaN}$  in array  $\mathbf{t}_{\text{div},2} \in \mathbb{R}^{\dim(\mathfrak{S})}$ 
            end if
            if  $(t = t_{\text{end}}) \wedge (j(\varphi) \leq \text{tol})$  then
              store stability point  $t_{\text{div},1} = t_{\text{end}}$ 
              compute error  $\text{err}_{L^p}(j(\varphi))$  with respect to reference solution
              store error  $t_{\text{div},2} = \text{err}_{L^p}(j(\varphi))$ 
            end if
          end for
        end for
      end for
      store stability set  $\mathcal{S} = \{\mathbf{S}^s \in \mathfrak{S} \mid t_{\text{div},1} \geq t_{\text{end}}\}$  with error data  $\mathbf{t}_{\text{div},2}$   $\triangleright$  Definition 3.3.8
    end for
  end for
  end for
  return stability sets  $\mathcal{S}$  and error data for each configuration  $(Re, Ma, N) \in \mathfrak{R} \times \mathfrak{M} \times \mathfrak{N}$ 
end procedure  $\triangleright$  Output: brute force stability sets

```

Stochastic method wrapper To compute approximated statistical solution candidates to the incompressible NSE (2.12), a novel SLMC LBM is devised using a KBC-N1 kernel (see Algorithm 1) implemented in OpenLB as a black box. The SLMC wrapper is built on scripting multiple executables with random input data to evolve highly parallelized LBM instances (LBM^(m)) in Figure 3.9) on multiple central processing units (CPUs) and/or GPUs parallel in time. This layout is necessary to meet the sample size of $M = N$ also for high resolutions. The post-processor then uses the output stack of the samples to compute statistical quantities from hydrodynamic moments. In Chapter 4 proof-of-concept computations are given for the Taylor–Green vortex benchmark. Based on previous observations (e.g. [115]), the acceleration of time-to-solution gained from using LBMs implemented in OpenLB over traditional methods (e.g. FVM), both on GPUs, is estimated to a factor of $\mathcal{O}(10)$ for this purpose.

4 Numerical Experiments

This chapter documents results of the Contributions (CTN3) and (CTN4) summarized in Chapter 1. Parts of this chapter have been already published by the author in [59, 114, 162, 231–235]. Along the computation of test cases with gradually increasing complexity, we make reference to the theoretical predictions of stability and consistency derived in Chapter 3 as well as to the model extensions in Chapter 2. We first consider the stability of LBMs for the approximation of PDEs with linear flux (2.10) in Section 4.1 and then move on in Section 4.2 toward consistency studies for CHEs (2.11) which show higher complexity in the diffusion terms. Section 4.3 evaluates the methodology proposed in Chapter 3 for linear and nonlinear stability when approximating the incompressible NSE with SRT, MRT, MRF and KBC collision. The intrinsic parallelizability of LBMs allows for a drastic upscaling of the number and quality of feasible computations. We outsource this feature via using HPC machines to brute force through parameter spaces with the help of Algorithm 4. Exploratory indications of methodological insights are made for nonlinear stability and confronted to the theoretical predictions of von Neumann stability. In addition, the KBC-N1 scheme is extensively analyzed via the Fourier transformed entropy controller for the first time and then utilized as a sampling machine for a proof of concept of the novel SLMC LBM. In Section 4.4, the numerical investigation of our recently proposed TLES LBM [233] is presented with a focus on the experimental order of convergence (EOC) for the concatenated limits of relaxation, discretization and time filtering in Section 3.3.1.5. Additionally, the HNSE (2.138) is approximated with the above derived HLBM for fluid flow through porous media in Section 4.5. Finally we couple the LBM for the NSE to the approximation of the CHE in the simulation of binary fluid flows in Section 4.6 which contains investigations of the volume loss of small droplets with respect to grid resolutions and modeling assumptions. All results are produced with the open source softwares OpenLB [162], Eigen [110] and ParaView [2]. Occasionally, MATLAB [132] is used for data processing. The computations have been performed on several HPC machines at the Steinbuch Centre for Computing (SCC) [239] at KIT, namely on bwUniCluster, bwUniCluster 2.0, ForHLR I, ForHLR II and HoreKa funded by the Ministry of Science, Research and the Arts Baden-Württemberg and by the Federal Ministry of Education and Research.

4.1 Advection–Diffusion equation

Let $\mathbf{F}(\rho) = \mathbf{u}\rho$ be linear and $\Omega \subseteq \mathbb{R}^d$. For periodic boundary conditions on $\partial\Omega$ covering \mathbb{R}^d , analytical solutions to (2.10) are known (see for example [195]) and thus used below for the computation of the EOC of the numerical schemes derived above. Let $\mathbf{x} = (x_\alpha)_\alpha \in \Omega_{\Delta x} \subseteq \Omega = (-1, 1)^d$ and $t \in I_{\Delta t} = (t_0, t_M) \subseteq \mathbb{R}_{>0}$. Unless stated otherwise, we use SI units with the characteristic scales $l_c = 2[\text{m}]$ and $u_c = 2.5[\text{m/s}]$ and neglect further notation. We study two examples¹, where the first one obeys the assumptions made in the convergence Theorem 3.2.1 on the initial data and the second one breaks it gradually with increasing the governing nondimensional Péclet number

$$Pe = \frac{l_c u_c}{\mu}. \quad (4.1)$$

¹ Parts of this section have been published in advance and are reproduced from several sources: [231], Copyright (2020), with permission from the authors and the Royal Society; [59], Copyright (2021), with permission from the authors and Elsevier Ltd; [234], Copyright (2022), with permission from the authors and Elsevier Ltd.

Example 4.1.1 (Smooth initial data). Together with the initial condition

$$\rho_0^{(\text{sm})}(\mathbf{x}) = \prod_{\alpha=1}^d \sin(\pi x_\alpha) + 1, \quad (4.2)$$

the ADE (2.10) forms an IVP which admits the smooth analytical solution

$$\rho_\star^{(\text{sm})}(\mathbf{x}, t) = \left[\prod_{\alpha=1}^d \sin(\pi [x_\alpha - u_\alpha t]) \right] \exp(-d\mu\pi^2 t) + 1. \quad (4.3)$$

Example 4.1.2 (Nonsmooth initial data). Let $d = 3$. We form another IVP with the solution

$$\rho_\star^{(\text{ns})}(\mathbf{x}, t) = \frac{1}{\sqrt{4\pi\mu t}} \sum_{k \in \mathbb{Z}} \exp\left(-\frac{[x - (x_0 + u_x t) + 2k]^2}{4\mu t}\right) + 1, \quad (4.4)$$

where x_0 denotes the x -location of the peak at $t = 0$, which is the analytical solution to the ADE (2.10) with the initial condition

$$\lim_{t \searrow 0} \rho_\star^{(\text{ns})}(\mathbf{x}, t) = \text{III}_2(x - x_0) + 1, \quad (4.5)$$

where

$$\text{III}_\beta(x) = \sum_{i=-\infty}^{\infty} \delta(x - i\beta) \quad (4.6)$$

denotes the Dirac comb for the period $\beta > 0$. A proof of the limit is given in our publication [59]. To realize this numerically, we initialize the LBE with a superposition of discretized Gaussian hills along the x -axis. As such, the nondifferentiability is instantly smoothed out unless $Pe_g \nearrow \infty$ where it persists. The numerical initialization is done with $\mathbf{f}(\mathbf{x}, 0) = \mathbf{f}^{\text{eq}}(\rho_0^{(\text{ns})}(\mathbf{x}))$, where

$$\rho_0^{(\text{ns})}(\mathbf{x}) = \begin{cases} \frac{1}{\sqrt{4\pi\mu\Delta t}} + 1, & \text{if } x \in \left(-\frac{\Delta x}{2}, \frac{\Delta x}{2}\right), \\ 1, & \text{otherwise.} \end{cases} \quad (4.7)$$

4.1.1 Relaxation stability prediction

In Section 3.2.2 we have derived relaxation stability bounds (3.107) for the DVBE which are sufficient for convergence in Theorem 3.2.1. For a linear target PDE, the discretization respects these bounds. Inserting the parameters of the present test case, we predict that

$$\Delta x^{\gamma-1} \leq \frac{d}{\theta \sum_{\alpha=1}^d |u_\alpha|} \quad (4.8)$$

is a relaxation stable discretization for uniform continuous relaxation frequencies. The continuous uniformity relates to the discretized (shifted) relaxation by $1 = \tau_{\text{cont}} \leftrightarrow \tau_{\text{disc}} + 1/2$ such that the predicted relaxation bound is exact for $\tau_{\text{disc}} = 0.5$. The latter finding was experimentally observed with the help of stability structures by Rheinländer [219]. Figure 4.1 visualizes the relaxation stability bounds for the first three spatial dimensions in case of $\tau_{\text{disc}} = 0.5$ and diffusive scaling $\gamma = 2$. For $\gamma = 1$, relaxation stability is determined by the weights of the stencil only which also is in agreement to the literature [219].

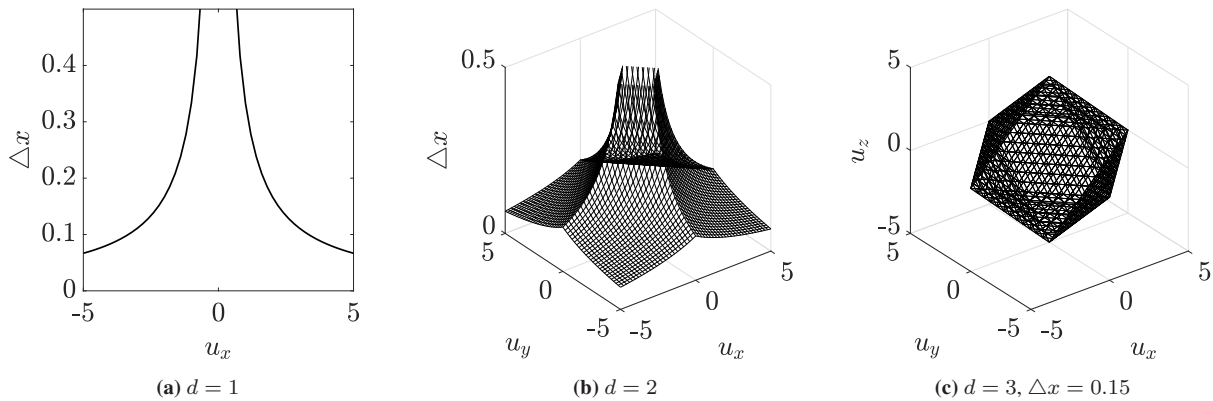


Figure 4.1: Relaxation stability maps for LBM (see Theorem 3.2.1) approximating the d -dimensional ADE (2.10). The volume of the stability octahedron (c) in u -coordinates grows inversely proportional to Δx . Plot (a) is redrawn from [231], Copyright (2020), with permission from the authors and the Royal Society.

4.1.2 Experimental order of convergence

We investigate the EOC of the $DdQ(2d+1)$ SRT LBM when approximating the ADE (2.10) for different parameter settings. The parameter dependence of the recovery of different features in the TEQ in Example 4.1.1 is investigated. The results are confronted to the predicted consistency and stability in Section 3.2. Further the effects of nonsmooth initial data on the consistency for increasing Péclet numbers are isolated in Example 4.1.2.

4.1.2.1 Parameter dependence

In [231] we study several cases of TEQs which can be obtained from (3.160). Via setting the parameters accordingly, we obtain either a diffusion equation ($\mathbf{F} = \mathbf{0}$, $\tau > 0.5$, $\gamma = 2$), a hyperbolic balance law ($\mathbf{F} \neq \mathbf{0}$, $\tau = 0.5$, $\gamma = 1$) or the full ADE (2.10) ($\mathbf{F} \neq \mathbf{0}$, $\tau > 0.5$, $\gamma = 2$) in the discretization and relaxation limit. Exemplary solutions for each target PDE are visualized in Figure 4.2. Both, the local error

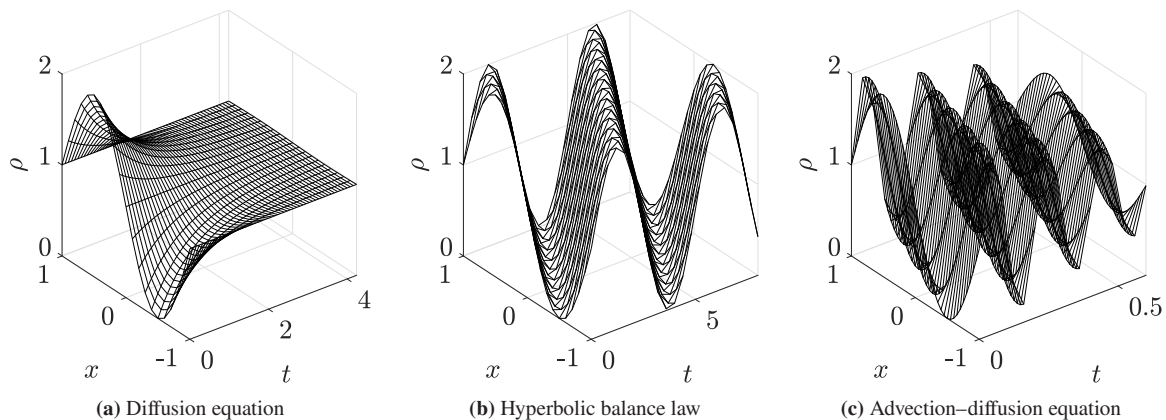


Figure 4.2: Exemplary computations with SRT BGK collision (images are downsampled for visualization) approximating (a) a diffusion equation ($\mathbf{F} = \mathbf{0}$, $\tau > 0.5$, $\gamma = 2$), (b) a hyperbolic balance law ($\mathbf{F} \neq \mathbf{0}$, $\tau = 0.5$, $\gamma = 1$) or (c) the full ADE (2.10) ($\mathbf{F} \neq \mathbf{0}$, $\tau > 0.5$, $\gamma = 2$). This figure is redrawn from [231], Copyright (2020), with permission from the authors and the Royal Society.

$$\text{err}_{L^p}(t_i) = \left(\frac{\sum_{\mathbf{x} \in \Omega_{\Delta x}} [\rho(\mathbf{x}, t_i) - \rho_\star(\mathbf{x}, t_i)]^p}{\sum_{\mathbf{x} \in \Omega_{\Delta x}} [\rho_\star(\mathbf{x}, t_i)]^p} \right)^{1/p} \quad (4.9)$$

at time $t_i \in I_{\Delta t}$ and the global error

$$\overline{\text{err}} = \frac{1}{M} \sum_{i=1}^M \text{err}_{L^p}(t_i) \quad (4.10)$$

are given for $p = 2$ in Table 4.3, Table 4.4, and Table 4.5, where a dash denotes divergence due to instability. Error plots of the local error at $\hat{t} = 0.3$ are provided in Figure 4.3.

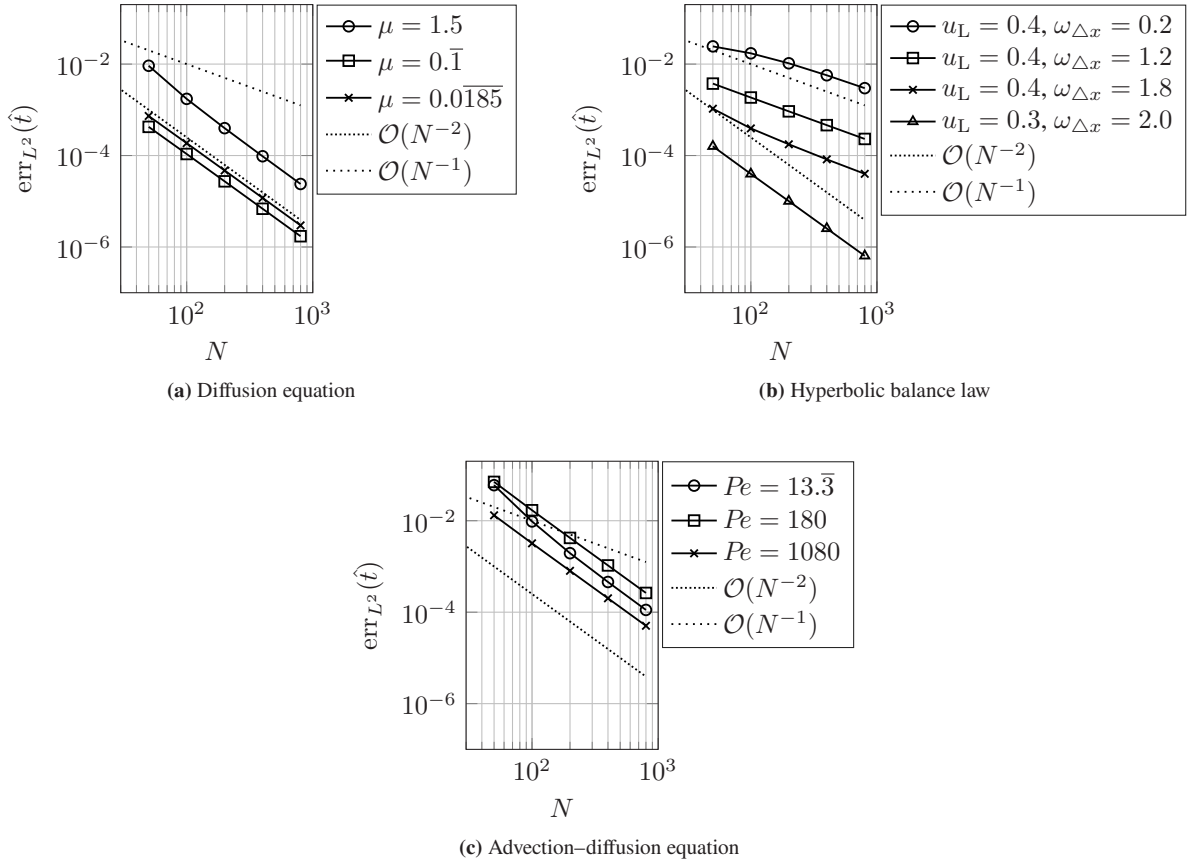


Figure 4.3: Local in time error $\text{err}_{L^2}(\hat{t})$ plots at $\hat{t} = 0.3$ for several Péclet numbers or corresponding characteristic scales (u_L denotes nondimensional lattice units). Computations with SRT BGK collision approximating (a) a diffusion equation ($\mathbf{F} = \mathbf{0}$, $\tau > 0.5$, $\gamma = 2$), (b) a hyperbolic balance law ($\mathbf{F} \neq \mathbf{0}$, $\tau \searrow 0.5$, $\gamma = 1$) or (c) the full ADE (2.10) ($\mathbf{F} \neq \mathbf{0}$, $\tau > 0.5$, $\gamma = 2$). This figure is reproduced from [231], Copyright (2020), with permission from the authors and the Royal Society.

Exemplary discretization parameters are given in Table 4.1 for diffusive scaling and in Table 4.2 for acoustic scaling. All other parameters used in the results are given in our publication [231]. The terminal time t_M for $\overline{\text{err}}$ in (4.10) is set (as in [231]) such that for each Pe in Table 4.1, the initial data ρ_0 is diffused to an amplitude of

$$\max_{\mathbf{x}_n \in \Omega_{\Delta x}} |\rho(x_n, t_M)| \leq 0.01. \quad (4.11)$$

Moreover, the respective EOC is denoted with \overline{EOC} and is calculated from the arithmetic mean of the convergence speeds

$$EOC_{N_i, N_j} = \frac{\ln\left(\frac{\text{err}^{(N_i)}}{\text{err}^{(N_j)}}\right)}{\ln\left(\frac{N_j}{N_i}\right)} \quad (4.12)$$

which are respectively obtained for two subsequent resolutions $N_i < N_j$ with any error notion $\text{err}^{(\cdot)}$ at a resolution N (see our publication [114]).

Table 4.1: Summary of LBM discretization parameters for diffusive scaling (\cdot_L denotes lattice units). Note that $\mu = \mu_L$ and $\omega_{\Delta x} = 1/\tau_{\Delta x}$. This table is reproduced from [231], Copyright (2020), with permission from the authors and the Royal Society.

N	diffusive scaling $\gamma = 2$			$\omega_{\Delta x}$		
	u_L	Δx	Δt	$Pe = 13.\bar{3}$ $\mu = 1.5$	$Pe = 180$ $\mu = 0.\bar{1}$	$Pe = 1080$ $\mu = 0.0\bar{185}$
50	4.00×10^{-1}	4.00×10^{-2}	1.60×10^{-3}	0.2	1.2	1.8
100	2.00×10^{-1}	2.00×10^{-2}	4.00×10^{-4}	0.2	1.2	1.8
200	1.00×10^{-1}	1.00×10^{-2}	1.00×10^{-4}	0.2	1.2	1.8
400	5.00×10^{-2}	5.00×10^{-3}	2.50×10^{-5}	0.2	1.2	1.8
800	2.50×10^{-2}	2.50×10^{-3}	6.25×10^{-6}	0.2	1.2	1.8

Table 4.2: Summary of LBM discretization parameters in acoustic scaling (\cdot_L denotes lattice units). Note that $u = u_L$. This table is reproduced from [231], Copyright (2020), with permission from the authors and the Royal Society.

N	acoustic scaling $\gamma = 1$		$\omega_{\Delta x}$			
	Δx	Δt	$u_L = 0.4$		$u_L = 0.3$	
50	4.0×10^{-2}	4.0×10^{-2}	0.2	1.2	1.8	2.0
100	2.0×10^{-2}	2.0×10^{-2}	0.2	1.2	1.8	2.0
200	1.0×10^{-2}	1.0×10^{-2}	0.2	1.2	1.8	2.0
400	5.0×10^{-3}	5.0×10^{-3}	0.2	1.2	1.8	2.0
800	2.5×10^{-3}	2.5×10^{-3}	0.2	1.2	1.8	2.0

In general, the EOC results approve our predictions for the consistency of order two in space toward the diffusion terms appearing in (2.10). Concerning the derived relaxation stability bound (4.8) (see Figure 4.1), we observe that the instability onset prediction becomes sharper for $\tau_{\Delta x} \searrow 0.5$ in Table 4.3 and Table 4.5. For example in Table 4.3, the instabilities appear after $t > 0.3$ for a parameter combination of $\omega_{\Delta x} = 1.8$ and $\Delta x = 0.04 > 0.0\bar{3}$. These observations match the results in [219, 241].

In case that the flux is nulled, the consistency to the diffusion equation of order two is upheld, which is in agreement with Weiss [258] who analyzed the Goldstein–Taylor model (formally equivalent to $\theta = 0$, hence a $D1Q2$ DVBE). It is to be noted that all conducted computations with zero flux and nonzero diffusion are stable which was expected from the theoretical predictions, since (4.8) becomes $\Delta x < \infty$. The latter yields unconditional relaxation stability for $\omega_{\Delta x} \in (0, 2)$.

For approximating a hyperbolic conservation law ($\mathbf{F} \neq \mathbf{0}$, $\mu = 0$, $\gamma = 1$), the corresponding simulation parameters (see Table 4.2 and Simonis *et al.* [231]) yield first order convergence to the TEQ for $0 < \omega_{\Delta x} < 2$ (see Table 4.5 and Figure 4.3b). Similar observations are documented for the $D1Q2$ LBE by Junk *et al.* [139]. The present results suggest that, though the overall $\overline{EOC} < 1.0$ in Table 4.5 for $\omega_{\Delta x} = 0.2$, the convergence speeds for two subsequent resolutions approach a value of 1.0 with increasing N . Plotted results in [231] approve the asymptotic alignment of the error curve for $\omega_{\Delta x} = 0.2$ with a first order reference line. In the case of zero diffusivity and $\gamma = 1$, the relaxation parameter has to be used as a prefactor nulling out the respective terms of $\mathcal{O}(\Delta x)$ in the closed form equation (3.16). The fully discrete version of the closed form yields a prefactor $\tau_{\Delta} - 0.5$ in terms the shifted relaxation time $\tau_{\Delta x}$ [139], which grows inversely linear for $\omega_{\Delta x} \searrow 0$ and thus for small but nonzero $\omega_{\Delta x}$ counteracts the first order along the discretization limit $\Delta x \searrow 0$. This modified factor is precisely nulled out for $\omega_{\Delta x} = 2$ which is responsible for the

sudden jump to second order convergence (from left to right in Table 4.5 and for $\omega_{\Delta x} \nearrow 2$ in Figure 4.3b). As a result of the combined relaxation and discretization, dependent on the PDE to target and the size of the velocity stencil used for its approximation with MRT LBMs, other relaxation times can also be used to cancel approximation terms. Several lines of research consider this topic in the literature see for example [103], or [95, 96] and references therein.

Table 4.3: Numerical errors of LBM computations in diffusive scaling to approximate the advection–diffusion equation (2.10) ($\mathbf{F} \neq \mathbf{0}$ linear, $\tau > 0.5$) measured in terms of global error $\overline{\text{err}}$ until terminal time t_M , local error $\text{err}_{L_2}(\hat{t})$ at $\hat{t} = 0.3$, and experimental order of convergence \overline{EOC} . This table is reproduced from [231], Copyright (2020), with permission from the authors and the Royal Society.

N	$Pe = 13.\bar{3}$		$Pe = 180$		$Pe = 1080$	
	$\text{err}_{L_2}(\hat{t})$	$\overline{\text{err}}$	$\text{err}_{L_2}(\hat{t})$	$\overline{\text{err}}$	$\text{err}_{L_2}(\hat{t})$	$\overline{\text{err}}$
50	5.98×10^{-2}	9.94×10^{-2}	7.07×10^{-2}	1.13×10^{-1}	1.31×10^{-2}	—
100	9.64×10^{-3}	2.48×10^{-2}	1.69×10^{-2}	1.88×10^{-2}	3.20×10^{-3}	1.88×10^{-2}
200	1.95×10^{-3}	5.83×10^{-3}	4.21×10^{-3}	4.31×10^{-3}	8.02×10^{-4}	4.32×10^{-3}
400	4.57×10^{-4}	1.42×10^{-3}	1.05×10^{-3}	1.05×10^{-3}	2.01×10^{-4}	1.05×10^{-3}
800	1.12×10^{-4}	3.55×10^{-4}	2.63×10^{-4}	2.63×10^{-4}	5.04×10^{-5}	2.63×10^{-4}
\overline{EOC}	2.26	2.03	2.01	2.18	2.00	2.05

Table 4.4: Numerical errors of LBM computations in diffusive scaling to approximate the diffusion equation (2.10) ($\mathbf{F} = \mathbf{0}$, $\tau > 0.5$, $\gamma = 2$), measured in terms of global error $\overline{\text{err}}$ until terminal time t_M , local error $\text{err}_{L_2}(\hat{t})$ at $\hat{t} = 0.3$, and experimental order of convergence \overline{EOC} . This table is reproduced from [231], Copyright (2020), with permission from the authors and the Royal Society.

N	$\mu = 1.5$		$\mu = 0.\bar{1}$		$\mu = 0.0\bar{1}8\bar{5}$	
	$\text{err}_{L_2}(\hat{t})$	$\overline{\text{err}}$	$\text{err}_{L_2}(\hat{t})$	$\overline{\text{err}}$	$\text{err}_{L_2}(\hat{t})$	$\overline{\text{err}}$
50	9.18×10^{-3}	2.41×10^{-2}	4.23×10^{-4}	1.95×10^{-4}	7.32×10^{-4}	3.52×10^{-4}
100	1.73×10^{-3}	6.47×10^{-3}	1.08×10^{-4}	4.98×10^{-5}	1.86×10^{-4}	8.98×10^{-5}
200	3.96×10^{-4}	1.59×10^{-3}	2.72×10^{-5}	1.25×10^{-5}	4.71×10^{-5}	2.26×10^{-5}
400	9.64×10^{-5}	3.96×10^{-4}	6.86×10^{-6}	3.17×10^{-6}	1.18×10^{-5}	5.69×10^{-6}
800	2.38×10^{-5}	9.89×10^{-5}	1.72×10^{-6}	7.95×10^{-7}	2.97×10^{-6}	1.43×10^{-6}
\overline{EOC}	2.14	1.98	1.98	1.98	1.98	1.98

Table 4.5: Numerical errors of LBM computations in acoustic scaling to approximate the hyperbolic conservation law (2.10) ($\mathbf{F} \neq \mathbf{0}$, $\mu = 0$, $\gamma = 1$) or the full ADE (2.10) ($\mathbf{F} \neq \mathbf{0}$, $\mu > 0$, $\gamma = 1$), measured in terms of global error $\overline{\text{err}}$ until terminal time $t_M = 8.12$, local error $\text{err}_{L_2}(\hat{t})$ at $\hat{t} = 0.3$, and experimental order of convergence \overline{EOC} . This table is reproduced from [231], Copyright (2020), with permission from the authors and the Royal Society.

N	$u_L = 0.4$				$u_L = 0.3$			
	$\omega_{\Delta x} = 0.2$		$\omega_{\Delta x} = 1.2$		$\omega_{\Delta x} = 1.8$		$\omega_{\Delta x} = 2.0$	
	$\text{err}_{L_2}(\hat{t})$	$\overline{\text{err}}$	$\text{err}_{L_2}(\hat{t})$	$\overline{\text{err}}$	$\text{err}_{L_2}(\hat{t})$	$\overline{\text{err}}$	$\text{err}_{L_2}(\hat{t})$	$\overline{\text{err}}$
50	2.43×10^{-2}	3.84×10^{-1}	3.74×10^{-3}	4.88×10^{-2}	1.05×10^{-3}	1.05×10^{-2}	1.59×10^{-4}	7.66×10^{-4}
100	1.72×10^{-2}	2.52×10^{-1}	1.85×10^{-3}	2.56×10^{-2}	3.92×10^{-4}	—	3.96×10^{-5}	2.27×10^{-4}
200	1.04×10^{-2}	1.48×10^{-1}	9.25×10^{-4}	1.31×10^{-2}	1.76×10^{-4}	—	1.00×10^{-5}	5.75×10^{-5}
400	5.69×10^{-3}	8.14×10^{-2}	4.61×10^{-4}	6.63×10^{-3}	8.25×10^{-5}	—	2.54×10^{-6}	1.44×10^{-5}
800	2.97×10^{-3}	4.28×10^{-2}	2.30×10^{-4}	3.33×10^{-3}	3.98×10^{-5}	—	6.40×10^{-7}	3.63×10^{-6}
\overline{EOC}	0.75	0.79	1.00	0.96	1.18	—	2.02	1.93

4.1.2.2 Dependence on initial data

In another batch of numerical tests, we approximate solutions to Example 4.1.1 and Example 4.1.2, both for $d = 3$. For the purpose of illustration, the solutions are visualized for exemplary configurations in Figure 4.4 and Figure 4.5, respectively.

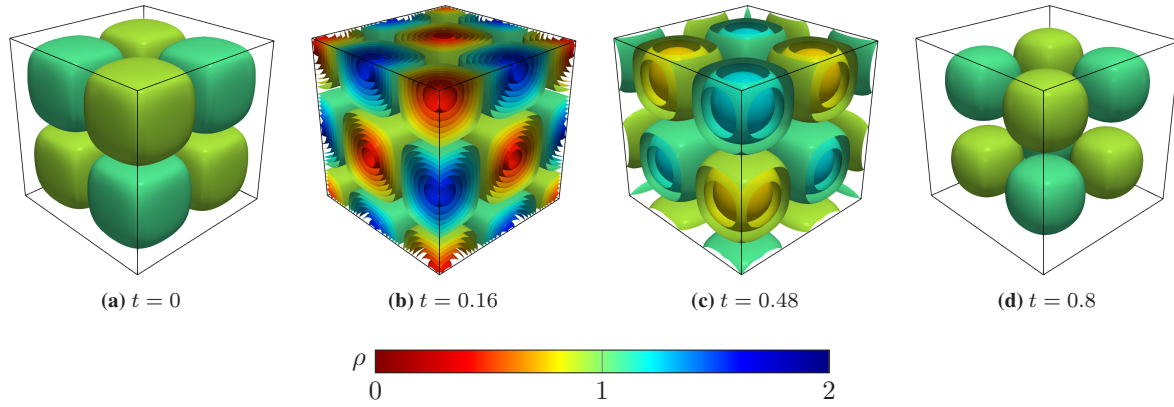


Figure 4.4: Approximated solution to Example 4.1.1 with resolution $N = 200$ for $Pe = 100$. Parts of this figure are reproduced from [59], Copyright (2021), with permission from the authors and Elsevier Ltd.

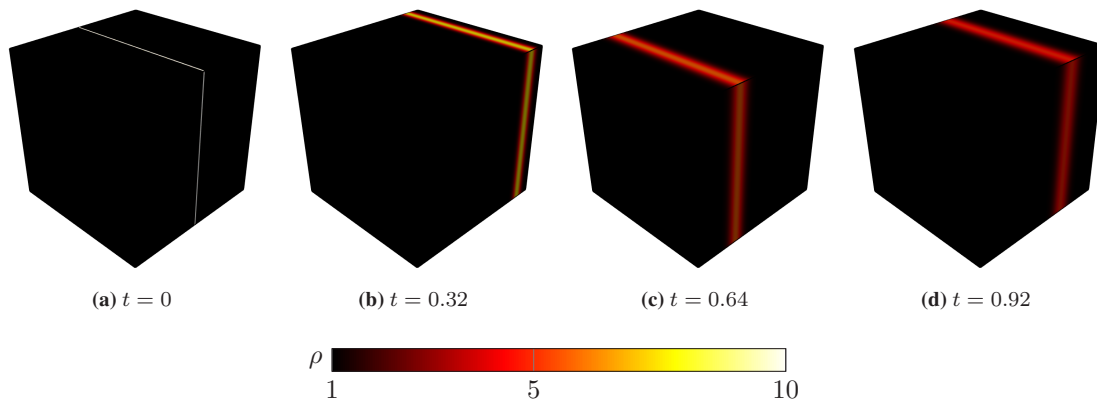


Figure 4.5: Approximated solution to Example 4.1.2 with resolution $N = 200$ for $Pe = 1000$.

The following computations were executed on at most four nodes comprising two Intel Xeon Platinum 8368 CPUs and four NVIDIA A100-40 GPUs each. The EOC is evaluated with specific choices of Ω_T , \mathbf{u} , μ , and ρ_0 for the ADE (2.10) with linear flux. The results are published for the $D3Q19$ velocity stencil in [59] and the $D3Q7$ velocity stencil in [234]. We average the relative L^2 -error with respect to the analytical solution ρ_* in the interval $(t_0, t_M) = (0, 1.52) \subseteq I$ to compute the global error $\overline{\text{err}}$. Several parameter configurations $(N, Pe) \in \mathfrak{N} \times \mathfrak{P}$ are computed, where $\mathfrak{N} = \{2^n \times 25 : n \in \{0, 1, \dots, 5\}\}$ and $\mathfrak{P} = \{10^n : n \in \{2, 3, 4, 5\}\}$. Hence, a series of grid Péclet numbers

$$Pe_g = \frac{Pe}{N} \quad (4.13)$$

and Courant numbers

$$Co = (u_c \Delta t) / \Delta x \quad (4.14)$$

is tested. Figure 4.6 shows the results in the parameter spaces $\mathfrak{N} \times \mathfrak{P}$ under diffusive scaling. By construction, the

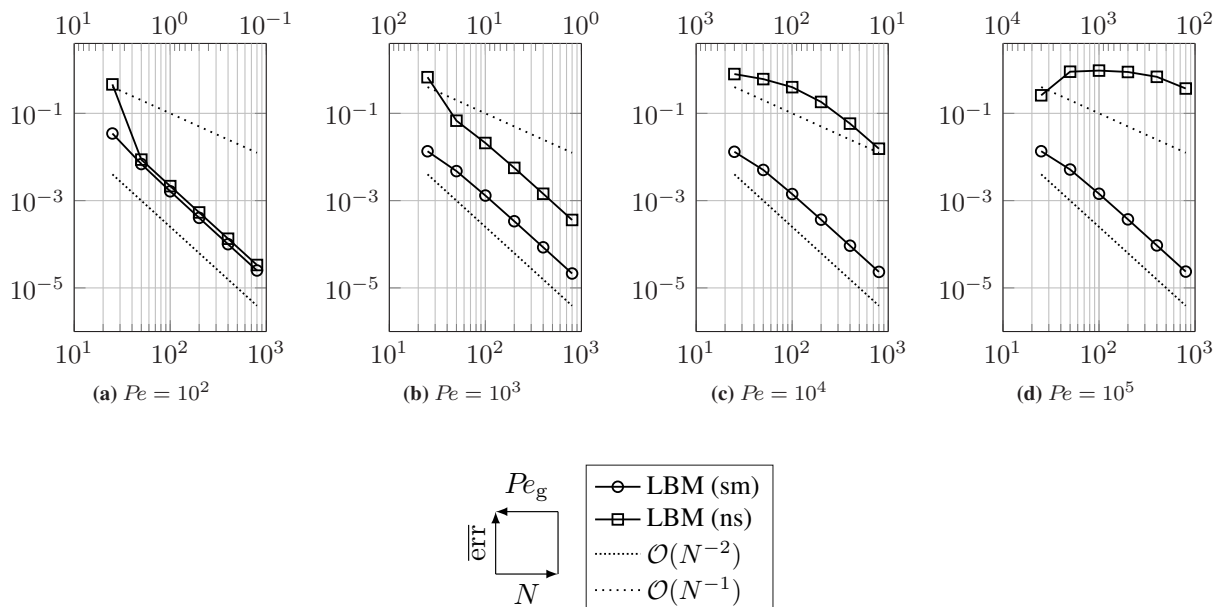


Figure 4.6: Errors of $D3Q7$ SRT LBM approximating (2.10) with smooth (sm) and nonsmooth (ns) initial data. This figure is reproduced from [234], Copyright (2022), with permission from the authors and Elsevier Ltd.

spatio-temporal grid size is $\Delta t = \Delta x^2 = (l_c/N)^2$. We use convection speeds of $\mathbf{u}^{(\text{sm})} = u_c \mathbf{1}_{d \times 1}$ and $\mathbf{u}^{(\text{ns})} = u_c e_x$ and a single relaxation time τ conforming to the Péclet number in the TEQ. In the chosen parameter spaces, the Courant number sequences over $Co = 0.5^n \times 0.2$ with $n \in \{0, 1, \dots, 4\}$ and the grid Péclet number passes several orders of magnitudes $Pe_g \in [\mathcal{O}(10^{-1}), \mathcal{O}(10^3)]$. For the smooth IVP, Figure 4.6 approves the EOC of two, as predicted in Section 3. The nonsmooth initialization however yields a reduction to first order accuracy at $Pe_g \gtrsim 10^2$. A further increase $Pe_g \nearrow 10^4$ in the nonsmooth case, yields a larger error contribution which eventually also breaks the EOC of one. For a further increase of Pe_g , the nonsmooth initial data exits the function space in Lemma 3.1.3. Thus we expect a blowup due to delayed smoothing. Our results with $D3Q19$ in [59] approve this observation. Therein, we suggest remedies to obtain stable solutions via using a combination of upwind and central finite differences of second order with an artificial diffusivity correction.

4.2 Cahn–Hilliard equation

In the present work, we interpret the CHE (2.11) as a diffuse interface model for the approximation of moving contact lines [272] between several fluid components. The approximation of the sharp interface is generally assumed to be of order $\mathcal{O}(Ch)$, where

$$Ch = \frac{\xi}{l_c} \quad (4.15)$$

denotes the Cahn number, ξ is the interface thickness and l_c is the characteristic length. Unless stated otherwise, we assume $l_c = a$, where a is the radius of a bubble or droplet of one fluid component submersed in the surrounding fluid component. For the purpose of clarity, we use lattice units, where time, space and the remaining quantities in the π -groups are nondimensionalized such that the grid spacing is one in every dimension. The term normalized corresponds to a physical analogue which is fixed irrespective of refinement in grid spacing. To numerically test the convergence toward a sharp interface of the SFRM LBM used in the coupled simulations further below, we compute

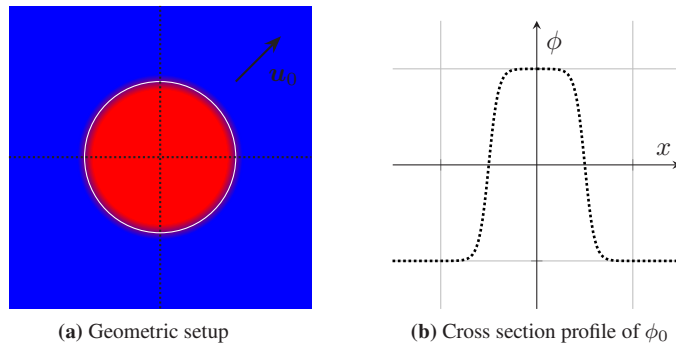


Figure 4.7: (a): Static ($\mathbf{u} = \mathbf{0}$) and moving interface ($\mathbf{u} = \mathbf{u}_0$) simulation setup, where the white circle denotes $\phi = 0$. The velocity \mathbf{u}_0 is constant and boundaries are periodic. (b): Cross section of the interface at $y = 0$ with profile of initial order parameter $\phi = \phi_0$ (dashed line). Scales differ for the purpose of representation.

a series of tests for static and moving circular interfaces in two dimensions forming a solution to (2.11). Here, the velocity \mathbf{u} is fixed and the Laplacian in the chemical potential is approximated with the stencil in (3.314). The circular interface in the benchmark test is initialized with a tanh-profile

$$\phi_0(\mathbf{x}) = \tanh\left(\frac{1}{\xi}\left[\sqrt{(x_1 - c_1)^2 + (x_2 - c_2)^2} - a\right]\right), \quad (4.16)$$

where $\mathbf{x} = (x_1, x_2)^T \in \Omega$, and $\mathbf{c} = (c_1, c_2)^T \in \Omega$ and $r \in \mathbb{R}$ are the center and the radius of the circular interface, respectively, as illustrated in Figure 4.7. The computational domain is set to $\Omega_{\Delta x} = [-0.5, 0.5]^d$, where $d = 2$, the radius of the interface is set to 0.25 and the $D2Q9$ velocity stencil is used. The interface width is dependent on the discretization via $\xi = 2\Delta x$, such that $Ch \searrow 0$ if $\Delta x \searrow 0$. To recover the diffusion terms in the CHE (2.11), we use diffusive scaling $\Delta t \sim \Delta x^2$. The relaxation frequencies are set to unity as is commonly done in the literature (see [164] and references therein).

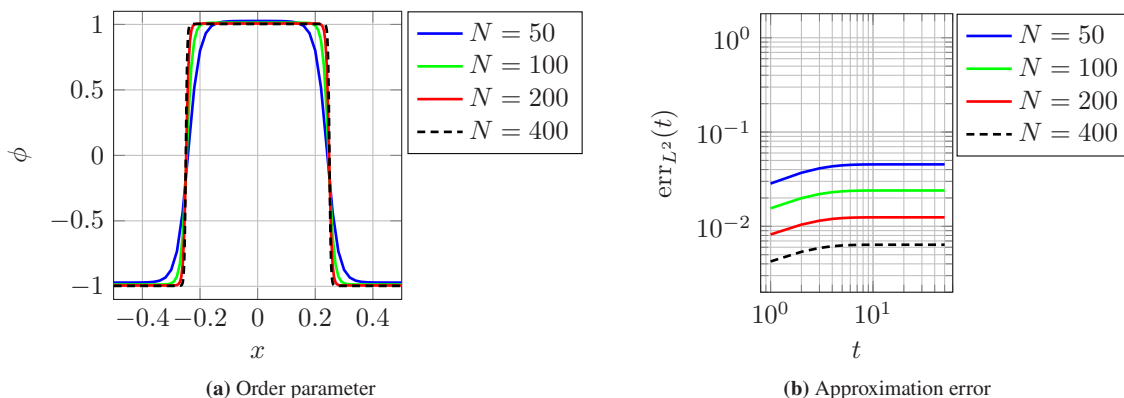


Figure 4.8: (a): Order parameter approximated with the SFRM LBM after 40 normalized timesteps for subsequent resolutions N . (b): Relative approximation error err_{L^2} with respect to tanh-profile within normalized time interval $t \in [1, 50]$.

4.2.1 Sharp interface limit consistency

Similarly to previous observations we have made thus far in this work, the sharp interface limit can be regarded as a third limit on top of the relaxation and the discretization. Since the lowest order is provided by the interface sharpening, we analyze the results in terms of consistency toward this limit. The procedure of approximating the sharp interface in the limit instead of a diffuse one, aligns with the conclusions in terms of physical validity of numerical results in [157, 272]. For techniques to even enforce a sharpening of the interface within the numerical algorithm the reader is

referred to [214, 216, 217]. Here, we compute the advection of a circular profile in two dimensions with the SFRM (see Definition 2.6.6) based on a $D2Q9$ LBE. To assess the difference of the numerical order parameter with respect to the analytical tanh-profile ϕ_0 for a static interface ($\mathbf{u} = 0$), we compute the time-dependent errors err_{L^p} for $p = 2$ at normalized time $t = 40$ for several resolutions and visualize it together with the ϕ -profile in Figure 4.8. The interface sharpening is clearly visible. The order of approximation in N toward the sharp interface (which results from the tanh-profile sharpening with $Ch \searrow 0$) is plotted in Figure 4.9a and asymptotically limits to one. We additionally observe that the error toward the analytical tanh-profile increases at first and then stagnates, which agrees with common knowledge in the literature that the interface develops after an initial period of time.

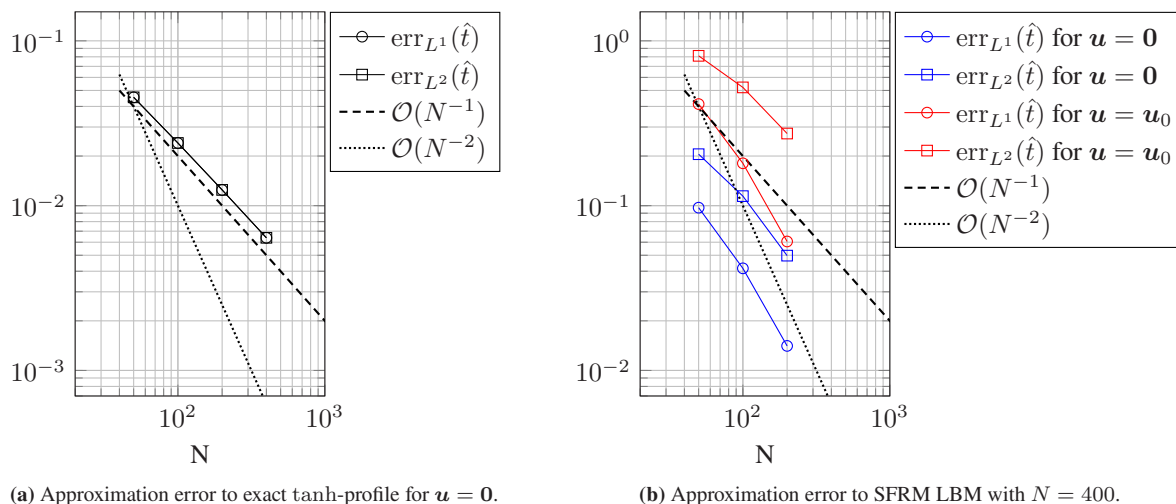


Figure 4.9: Normalized time of error measurements is $\hat{t} = 40$. (a): Time local error $\text{err}_L^p(\hat{t})$ of ϕ with respect to the initial analytical tanh-profile for circular interface for accuracy prediction toward sharp interface. (b): Time local error $\text{err}_L^p(\hat{t})$ of ϕ with respect to highest tested resolution $N = 400$ for consistency prediction of discretization.

To assess the portion of limit consistent error terms added by the discretization and relaxation, we compute an additional time-dependent err_{L^2} with respect to the highest tested resolution $N = 400$ and plot it in Figure 4.9b. The error is half an order shifted in magnitude but seems to bend toward $\mathcal{O}(N^{-2})$. We can explain this observation with the fact that our discretization is of order two limit consistent to the interface sharpening $Ch \searrow 0$. Further, moving the interface diagonally across the domain with $\mathbf{u} = \mathbf{u}_0$ results in another error contribution from the approximation of the flux, which shows however the same trend in bending toward the order of discretization. Figure 4.10 shows sample profiles warped by ϕ -values for $\mathbf{u} = \mathbf{u}_0$. The typical set in period of the interface thickness in approximations of the CHE is observable and should be evaluated as a positive effect in our case. Although initialized with a two-lattice-spacing interfacial width, the profile becomes sharper with time until a smaller interface thickness is reached asymptotically which produces the error increase in Figure 4.8 for the static case. Additionally, we observe that the location of the interface reaches an asymptotic limit for a certain amount of cycles passing through the domain with increasing N . Furthermore, the interface is tilted less toward the movement direction with increased N , which is also a commonly observed artifact for refining coarse grids. Overall, the qualitative features shown in Figure 4.10 underline the data gathered in the EOC plots above and numerically approve the limit consistency of relaxation, discretization and interface sharpening.

4.3 Navier–Stokes equations

In this section we evaluate the methodology introduced in Chapter 3 for approximating the incompressible NSE (2.12) with LBMs using SRT, MRT, MRF and KBC collision (e.g. Algorithm 1). Specifically, we compute EOC results as

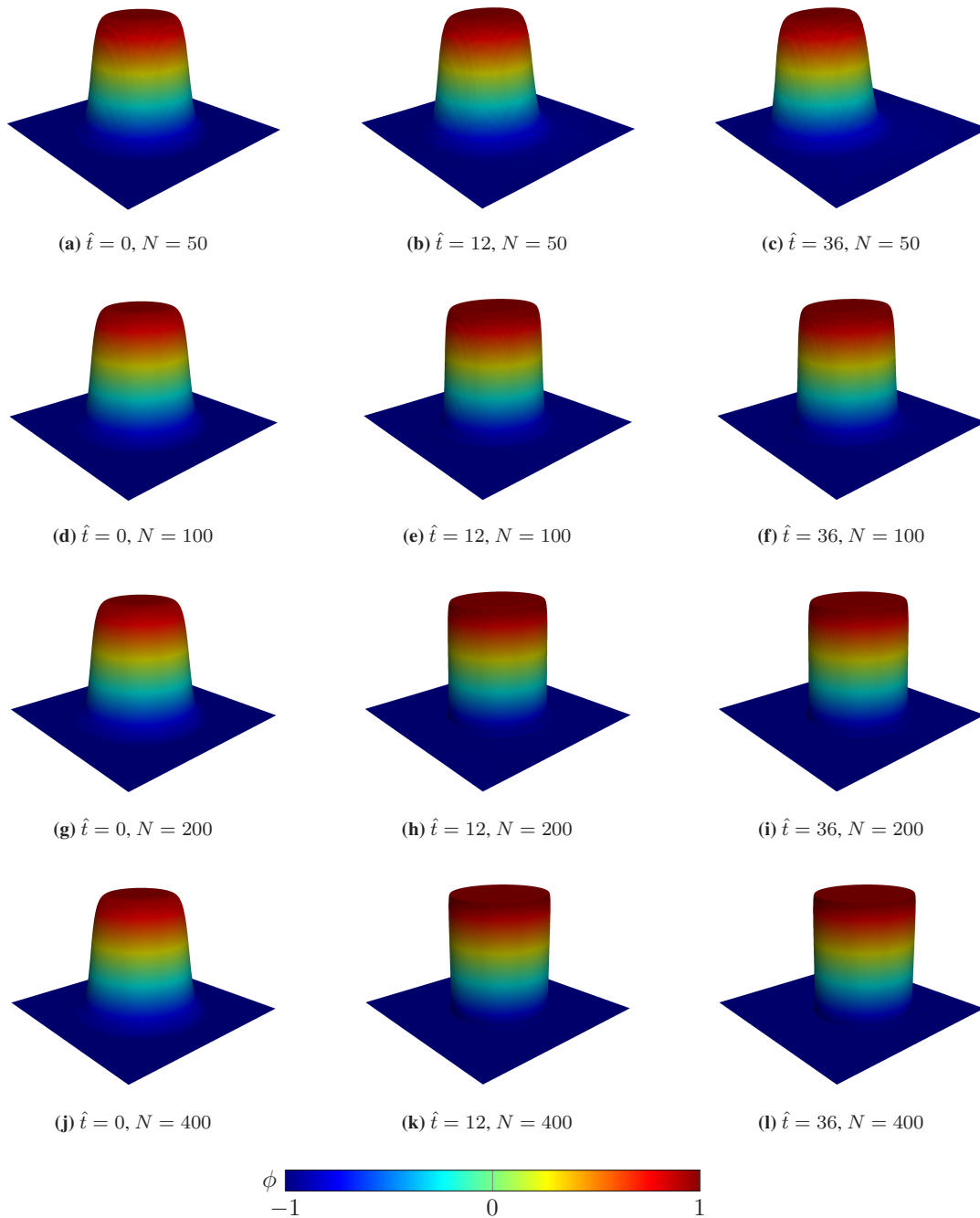


Figure 4.10: Warped order parameter ϕ from SFRM LBM simulations of moving circular interfaces ($\mathbf{u} = \mathbf{u}_0$) at fixed normalized timesteps $\hat{t} = 0, 12, 36$ (column-wise) which comprise several cycles of reaching the initial interface location for several resolutions $N = 50, 100, 200, 400$ (row-wise). The colorbar is cut off for the purpose of representation.

well as linear and nonlinear stability sets for the latter schemes. To obtain nonlinear stability information including the grid effects, we outsource the intrinsic parallelizability of LBMs via using HPC machines to brute force through parameter spaces with the help of Algorithm 4. The exploratory results are contrasted with the theoretical predictions of von Neumann stability (Algorithm 3). Further, the KBC-N1 scheme is analyzed via Fourier transforming the kinetic relaxation parameter. We finally use the scheme on a computationally feasible configuration to sample statistical solutions to the incompressible NSE (2.12) along the inviscid limit towards the EE with a novel SLMC LBM.

4.3.1 Taylor–Green vortex flow

Let $d = 3$. Due to the partly universal character of turbulent scales, an investigation of decaying homogeneous turbulence (DHIT) in simplified geometries serves as a natural testbed for numerical schemes. In a typical scenario, a periodic initial velocity field solution to (2.12) on a cubic flow domain is evolved in time based on the numerical method at hand. Besides the testing of the method, insights to the complexity of turbulent flows in a cleaned setting can be obtained when using a sufficiently accurate, robust and reliable scheme in a highly resolved configuration. Since pseudo-spectral (ps) direct numerical simulation (DNS) methods have been used for this very purpose and are the most reliable tool for computing DHIT, we use reference computations from the literature produced with akin methodology to evaluate the accuracy of the presented LBM derivatives. As an initial solution to the incompressible NSE (2.12), the Taylor–Green vortex (TGV) flow has been extensively studied in the past for a multitude of purposes by various authors (for example [39, 40, 52, 61, 79, 81, 97, 144, 206, 246, 247]) including the present one [114, 162, 232, 233]. Besides the incompressible regime, TGV simulations serve as benchmark cases in stratified flows [261], in coupled magnetohydrodynamic systems [106] or in turbulent reacting flows [1]. After a laminar large-scale vortex initialization, the convective terms in the NSE produce successively smaller structures [40, 79] which induces vortex-stretching and an eventual energy cascade as proposed by Kolmogorov [155, 156]. It has been observed that already at a Reynolds number of $Re \geq 1000$, the turbulent flow becomes nearly isotropic with a deletion of initial memory [79], and a power law asymptotic appears in the energy spectrum. Although we occasionally refer to this observation below as artificial turbulence, since it differs from a more realistic spectral initialization via randomized modes, we will abstain from a consistent classification throughout the text. Further, instead of spectral random initial conditions, a randomized version of the TGV initialization is proposed below. This random artificial turbulence eludes any realistic interpretation but instead serves as a purely mathematical example for a statistical solution of the incompressible NSE [105].

For the present purpose, we define the TGV flow on a domain $\Omega = [0, 2\pi l_c]^3$ with computationally periodic boundaries. Together with the assumption of uniform characteristic length $l_c = 1\text{m}$ and characteristic velocity $U_c = 1\text{m/s}$, we reduce

$$Re = \frac{1}{\nu} \quad (4.17)$$

for simplicity and neglect further notation of units from now on. The deterministic initial TGV velocity field reads [39, 114]

$$\mathbf{u}(\mathbf{x}, 0) = \begin{pmatrix} U_c \sin\left(\frac{x}{l_c}\right) \cos\left(\frac{y}{l_c}\right) \cos\left(\frac{z}{l_c}\right) \\ -U_c \cos\left(\frac{x}{l_c}\right) \sin\left(\frac{y}{l_c}\right) \cos\left(\frac{z}{l_c}\right) \\ 0 \end{pmatrix}. \quad (4.18)$$

Further, let ρ_c denote the characteristic density. Conforming to the solenoidal condition in (2.12), the initial pressure

$$p(\mathbf{x}, 0) = p_\infty + \frac{\rho_c U_c^2}{16} \left[\cos\left(\frac{2x}{l_c}\right) + \cos\left(\frac{2y}{l_c}\right) \right] \left[\cos\left(\frac{2z}{l_c}\right) + 2 \right], \quad (4.19)$$

where p_∞ labels a reference pressure, can be used in the LBM initialization routine due to the weak compressibility appearing as error terms in the LBM along the diffusive limit. To visualize the energy cascade already apparent at low Reynolds numbers, the energy and dissipation spectra (defined further below) are computed with the spectral element method (SEM) code Nek5000² for $Re = 800$ and plotted in Figure 4.11.

² Nek5000, 2019, Argonne National Laboratory, Illinois. Available: <https://nek5000.mcs.anl.gov>.

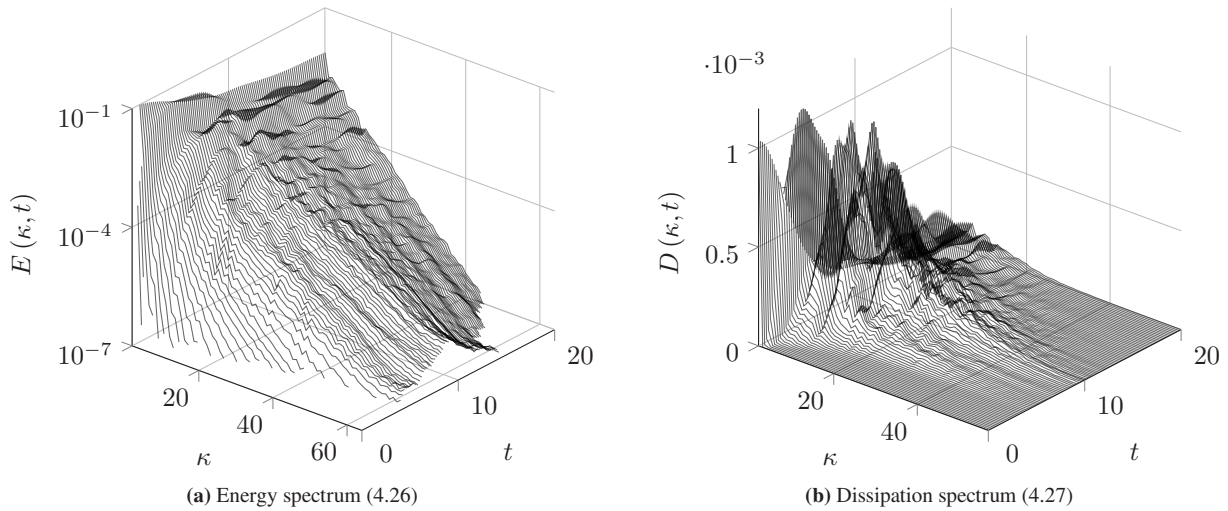


Figure 4.11: DNS results of the TGV flow computed with SEM ($N = 127$, $Re = 800$). Energy spectrum $E(\kappa, t)$ and dissipation spectrum $D(\kappa, t)$ plotted over time t and wavenumber κ . This figure is reproduced from [233], Copyright (2022), with permission from the authors and Elsevier Inc.

4.3.2 Turbulence quantities

We compute an approximate weak solution field \mathbf{u} to (2.12) via evolving the LBM in space-time initialized with (4.18) (and optionally (4.19)). The quality of approximation in terms of accuracy toward pseudo-spectral reference results or in terms of consistency to a high resolution LBM simulation is judged below with respect to several turbulence quantities computed from \mathbf{u} . These quantities of interest are continuously defined by the kinetic energy

$$k(t) = \frac{1}{|\Omega|} \int_{\Omega} \frac{1}{2} \mathbf{u}(\mathbf{x}, t) \cdot \mathbf{u}(\mathbf{x}, t) \, d\mathbf{x} \quad (4.20)$$

and the enstrophy

$$\zeta(t) = \frac{1}{|\Omega|} \int_{\Omega} \mathbf{r}(\mathbf{x}, t) \cdot \mathbf{r}(\mathbf{x}, t) \, d\mathbf{x}, \quad (4.21)$$

where the vorticity field $\mathbf{r} = \nabla_{\mathbf{x}} \times \mathbf{u}$ denotes the curl of the velocity, the total dissipation rate

$$\epsilon_{\text{tot}}(t) = -\frac{dk(t)}{dt} \quad (4.22)$$

and the resolved dissipation rate

$$\epsilon_{\text{res}}(t) = 2\pi\nu\zeta(t). \quad (4.23)$$

The difference of the latter two yields the model dissipation rate

$$\epsilon_{\text{mod}} = \epsilon_{\text{tot}} - \epsilon_{\text{res}}, \quad (4.24)$$

which isolates the artificial dissipation injected by the method in an underresolved setting [79]. If no abbreviation is used in the index, $\epsilon = \epsilon_{\text{tot}}$. The maximum vorticity magnitude

$$\omega(t) = \max_{\mathbf{x} \in \Omega} \|\mathbf{r}(\mathbf{x}, t)\|_2 \quad (4.25)$$

is used to measure the recovery of initial peak regions (IPR) [247]. Further, we compute the instantaneous nondirectional energy spectrum

$$E(\kappa, t) = \iint_{S(\kappa)} \frac{1}{2} \Phi(\mathbf{k}, t) \, dS(\kappa) \approx \sum_{\substack{\mathbf{k} \in \mathbb{N}^d \\ \kappa-1 < |\mathbf{k}| \leq \kappa}} \frac{1}{2} \Phi(\mathbf{k}, t) \quad (4.26)$$

and with it, the dissipation spectrum

$$D(\kappa, t) = 2\nu\kappa E(\kappa, t) \quad (4.27)$$

on spherical wave shells $S(\kappa) = \{\mathbf{k} \in \mathcal{K} : |\mathbf{k}| = \kappa\}$, where κ is the scalar wavenumber and

$$\Phi(\mathbf{k}, t) = \|\tilde{\mathbf{u}}(\mathbf{k}, t)\|_2^2 \quad (4.28)$$

squares the spatially Fourier-transformed velocity

$$\tilde{\mathbf{u}}(\mathbf{k}, t) = \frac{1}{\sqrt{2\pi}^d} \int_{\mathbb{R}^d} \mathbf{u}(\mathbf{x}, t) \exp(-i\mathbf{k} \cdot \mathbf{x}) \, d\mathbf{x}. \quad (4.29)$$

The latter is approximated by (3.315) as discussed in Section 3.3.3 and spatial gradients are finite differenced with eighth order (see (3.313)) unless stated otherwise. The above quantities are classical and have been studied extensively in the literature. In addition, motivated by [163], we propose the following novel quantity to specifically measure the relaxation in wave-time and with it, the entropic stabilization.

Definition 4.3.1. The instantaneous discrete control spectrum is defined as

$$C(\kappa, t) = \sum_{\substack{\mathbf{k} \in \mathbb{N}^d \\ \kappa-1 < |\mathbf{k}| \leq \kappa}} \frac{1}{2} \Psi(\mathbf{k}, t), \quad (4.30)$$

where

$$\Psi(\mathbf{k}, t) = |\hat{\gamma}^*(\mathbf{k}, t)| \quad (4.31)$$

denotes the absolute value of the discrete Fourier transformed wave-time dependent entropy control

$$\hat{\gamma}^*(\mathbf{k}, t) = \sum_{\mathbf{x}=\mathbf{0}_{1 \times d}}^{(N-1)\mathbf{1}_{1 \times d}} \gamma^*(\mathbf{x}, t) \exp\left(-\frac{2\pi i}{N} \mathbf{k} \cdot \mathbf{x}\right). \quad (4.32)$$

As γ^* defines a relaxation function of the grid nodes \mathbf{x} and the time steps t , the control spectrum (4.30) is occasionally called relaxation spectrum below.

4.3.3 Linear and brute force stability

The contribution of the present section to (CTN3) is a pilot study of brute-forcing methodological insights on HPC machines and contrasting the results to classical predictions. The contribution to (CTN4) is that, based on these exploratory insights, method development is accelerated. Specifically, we compute stability sets for orthogonal moment MRT LBMs in [232]. On the one hand, the results are used to investigate the capabilities of classical von Neumann techniques for the stability analysis of MRT LBMs applied to artificial homogeneous isotropic turbulence (HIT). On the other hand, the results indicate possible relaxation functions for the novel MRF scheme (see Section 3.2.7.1) which for example provides a background stabilization for advanced turbulence models since numerical dissipation is minimized.

On a third hand, the latter underpins the natural availability of *a posteriori* error measurements as a distinct advantage of computing through a grid of parameters with the actual method itself rather than a linearized version.

In the following³, stability sets are computed for an orthogonal moment MRT LBM (see Table 3.4) on $D3Q19$ when approximating the NSE (2.12). The choice of the kinetic relaxation times for MRT LBMs is frequently researched from several perspectives such that the present investigation only covers a small part of topics which open up in this context. The here used MRT model is known to diverge for constant relaxation times in diffusive scaling [63] which makes an investigation thereof interesting from the present perspective. In addition to the von Neumann stability (Algorithm 3), brute force stability (Algorithm 4) is used to scan large parameter spaces for the tunable relaxation frequencies. The motivation for using and comparing both notions is as follows.

The convergence criteria for the continuous RS (3.10) (see Proposition 3.1.3) and thus for the DVBE (3.92) are based on uniform relaxation (see Section 3.1.4 and Section 3.2.2, respectively). The stability structures in turn only take the consistency condition $\mathbf{s} = (1/\tau)\mathbf{1}_{q \times 1} \in (0, 2)^q$ for the hydrodynamic relaxation frequencies into account (see Definition 3.2.7 and Corollary 3.2.1), also for MRT collision operators [219]. Hence, using linearized von Neumann stability (Definition 3.2.16) is a natural choice to determine if the global error is bounded for nonuniform relaxation. Approving this observation, von Neumann stability has been used extensively in the recent years [125, 126, 185, 263, 264] to extract characteristic features of the numerical method for specific ranges of nondimensional numbers.

There are two main points of concern which generate demand for analyzing the discrepancies between linear stability predictions and overall brute force stability data from simulations. Firstly, the targeted PDE (2.12) is nonlinear such that the linearized amplification matrix (3.185) might be a very rough approximation to the actual propagation of initial data through the scheme. In particular for large Re , the nonlinear terms become disruptive for stability, which is unseen by the linearized notion. Second, the mapping from the spatial grid to wave space acts as a normalization, which obstructs the investigation of mesh dependent instabilities with von Neumann stability [56, 240, 267].

In [232] we detect grid-dependent instabilities for relaxation time tuning along diffusive scaling of orthogonal moment MRT LBMs. A comparison of von Neumann stability and the results obtained with brute force computations highlights the deficiencies of the former in the present setting. With the help of the latter applied to parametrized relaxation frequency tuning, the effect of the grid resolution on the overall stability is empirically documented. In summary, a sequence of more than 2.2×10^4 numerical experiments is conducted to further unfold LBM theory via outsourcing its parallelizability with the help of highly scalable implementations.

As a measure of accuracy, the temporal L^2 -error norm

$$\text{err}_{L^2}(\epsilon) = \sqrt{\frac{\sum_{n=0}^m |\epsilon^*(t_n) - \epsilon(t_n)|^2}{\sum_{n=0}^m |\epsilon^*(t_n)|^2}} \quad (4.33)$$

of the total dissipation rate $\epsilon(t)$ is used. Here, the reference solution $\epsilon^*(t)$ in (4.33) is taken from the pseudo-spectral results of Brachet *et al.* [40]. Let the LBE (3.160) be determined by an orthogonal moment basis on $D3Q19$ (see Table 3.4) and a second order truncated equilibrium (3.98).

Brute force stability The parameter spaces and the divergence criterion in Definition 3.3.8 are set as follows (see [232, Algorithm 3.1]). The parameter space configuration is $\mathbf{s} \in \mathfrak{S}$, $Re \in \mathfrak{R}$, $Ma \in \mathfrak{M}$ and $N \in \mathfrak{N}$. Let \wp denote the

³ Parts of this section have been published in advance and are reproduced from [232], Copyright (2021), with permission from the authors and the Royal Society.

Kolmogorov length scale [155, 156, 209]. Then the brute force stability results are based on computing the TGV flow initialized with (\mathbf{u}_0, p_0) until $t = 20\text{s}$. Unless the simulated dissipation rate (4.22) exceeds the upper bound

$$\epsilon_{\max} > \text{tol} = 2 \frac{\nu^3}{\varrho^4}, \quad (4.34)$$

indicating divergence, the MRT LBM is termed brute force (BF) stable for the parameter configuration if the final time step is reached.

Von Neumann stability The parameter spaces and other quantities in Definition 3.2.16 are set as follows. The mean flow $\bar{\mathbf{u}}$ is specified below and $\mathbf{k} \in \mathcal{K} = [-\pi, \pi]^3$ denotes the wavevector. Further, let $\mathbf{s} \in \mathfrak{S}$, $Re \in \mathfrak{R}$ and $Ma \in \mathfrak{M}$ be a given configuration. According to Definition 3.2.16, the VN stability results are based on computing the spectral radius $r_{\text{spec}}(\mathbf{H})$ via approximating the eigenvalues of (3.65) (see Algorithm 3). The MRT LBM is termed von Neumann stable for \mathbf{s} , if $r_{\text{spec}}(\mathbf{H}) \leq 1$.

As before, we use physical SI units without further notation. In the case that the explicit specification of lattice units is necessary, we continue with the notation \cdot^L . Since several spaces have to be discretized, the term resolution exclusively refers to the number of grid points N per dimension in the discrete physical space $\Omega_{\Delta x}$. The (lattice) Mach number is defined as $Ma = u^L/c_s$, where u^L is the dimensionless characteristic lattice velocity.

4.3.3.1 Third order moment relaxation and comparison of stability notions

In the following numerical experiments, the third order relaxation frequencies s_q and s_μ are varied in $[0, 2]$ with a precision of 0.05. All other components of \mathbf{S} are set according to $\mathbf{s} = \tilde{\mathbf{s}}$ (see Table 3.4). The simulations for BF stability are carried out with $N = 64$, where N is the spatial resolution per dimension and with a Reynolds number $Re = 1600$. Since we expect divergence of the scheme related to the Mach number [63], the sequence $Ma \in \mathfrak{M} = \{0.3, 0.2, 0.1, 0.05\}$ is computed. The BF results from Algorithm 4 are then cross-compared with the VN stability estimation gained from approximating $r_{\text{spec}} = \mathbf{H}$ with the corresponding parameter choices in \mathbf{H} (3.185). The LBM simulations in this section are carried out with OpenLB [161, 162] on a maximum of 75 nodes with two deca-core Intel Xeon E5-2660 v3 each.

In Figure 4.12 the data obtained from the BF computations is assembled to stability maps for each $Ma \in \mathfrak{M}$, which show the following characteristic features:

1. A shift and a contraction of the BF stability area dependent on the decreasing lattice Mach number (see Figures 4.12a, 4.12b, 4.12c, 4.12d) are visible. Two different instability regions are formed. Whereas one region of divergence is vanishing toward $(s_q, s_\mu) \rightarrow \mathbf{0}$ with decreasing Ma , the other is growing from $(s_q, s_\mu) = (2, 2)$ toward the center of the relaxation frequency domain.
2. The bottom row in Figure 4.12 indicates that the accuracy within the BF stable region also renders a transformation with decreasing Ma (see Figures 4.12e, 4.12h, 4.12g, 4.12h). The minima of the error measurement are located along a line at $s_q \approx 0.5$ for $Ma = 0.3$ in Figure 4.12e. Whereas this minimal error strip is shifted to the left and thinned out for smaller lattice Mach numbers, a second minimal region appears around $(s_q, s_\mu) \approx (2, 0.5)$ at $Ma = 0.05$ in Figure 4.12h.

Since the computations are underresolved, the dissipation rate is overall reduced compared to the DNS reference (see also [114] for several collision schemes). This implies that a small dissipation rate error for fixed $\mathbf{s} \in \mathfrak{S}$ indicates a small amount of numerical dissipation being added by the scheme.

The VN stability sets are evaluated with respect to the capability of reproducing the above observations made from Figure 4.12. The eigenvalues of \mathbf{H} for Algorithm 3 are computed and approximated with the C++ template library

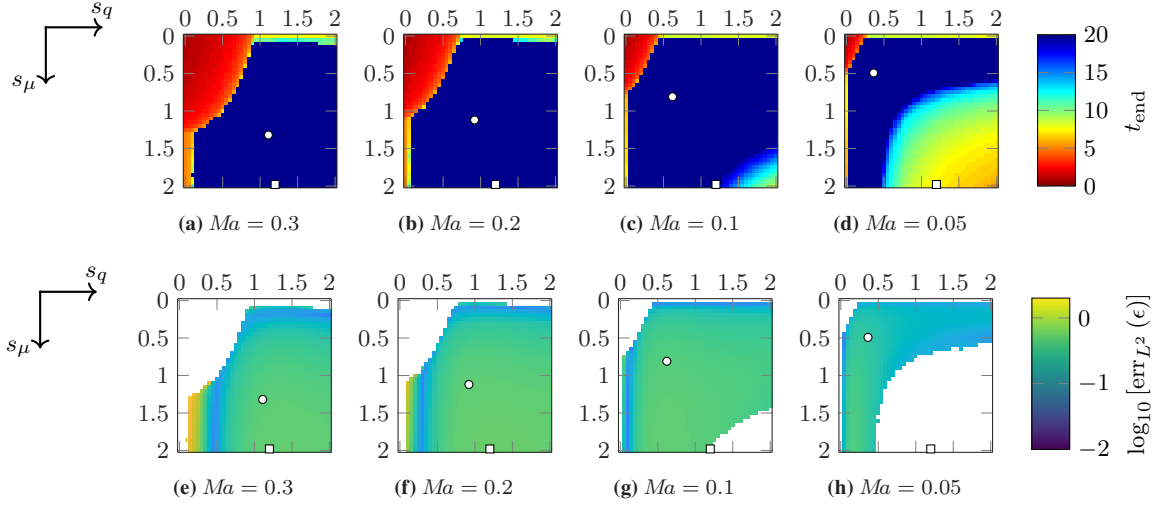


Figure 4.12: Top row (a–d): BF stability maps (Algorithm 4) for $Re = 1600$ and $N = 64$, where the pixel resolution of each map is 41×41 , one pixel equals one TGV computation with the MRT LBM (Table 3.4), and coloring refers to maximal stable computation time t_{end} . Bottom row (e–h): Corresponding BF error maps, with the same map resolution as above (only BF stable configurations shown). Coloring refers to the logarithm of $\text{err}_{L^2}(\epsilon)$ over the interval $t \in [0, 10]$. For all subfigures $Ma = 0.3, 0.2, 0.1, 0.05$, respectively, from left to right. White squares denote \hat{s} used in the classical MRT formulation [66]. The optimized MRT LBM [52] comprising \hat{s} is plotted as white circles. The optimized value for $Ma = 0.05$ is obtained by a polynomial fit through \hat{s}_q and \hat{s}_μ for larger Ma , respectively. This figure is reproduced from [232], Copyright (2021), with permission from the authors and the Royal Society.

Table 4.6: List of specifiers for scan regions of the VN stability maps plotted in Figure 4.14. Note that $\mathbf{b} \in \mathcal{B}$ denotes the mean flow variation in the first octant (4.35) and $\text{ave}(\mathbf{u}_0)$ accounts for scaling via the averaged TGV initial flow field magnitude (4.36). This table is reproduced from [232], Copyright (2021), with permission from the authors and the Royal Society.

specifier	background flow $\bar{\mathbf{u}}$	tested wavevectors \mathcal{K}'
<i>x-directional</i>	$\bar{\mathbf{u}} = (u^L, 0, 0)^T$	$\mathbf{k} \parallel \bar{\mathbf{u}}$
<i>orthogonal</i>	$\bar{\mathbf{u}} = (u^L, u^L, u^L)^T / \sqrt{3}$	$\mathbf{k} \perp \bar{\mathbf{u}}$
<i>parallel</i>	$\bar{\mathbf{u}} = (u^L, u^L, u^L)^T / \sqrt{3}$	$\mathbf{k} \parallel \bar{\mathbf{u}}$
<i>κ-partial</i>	$\bar{\mathbf{u}} = (u^L, u^L, u^L)^T / \sqrt{3}$	$\mathbf{k} \in \kappa\mathcal{K} = [-\kappa\pi, \kappa\pi]^3$
<i>full</i>	$\bar{\mathbf{u}} = (u^L, u^L, u^L)^T / \sqrt{3}$	$\mathbf{k} \in \mathcal{K}$
<i>octant</i>	$\bar{\mathbf{u}} \in \{u^L \mathbf{b} \mid \mathbf{b} \in \mathcal{B}\}$	$\mathbf{k} \in \mathcal{K}$
<i>scaled octant</i>	$\bar{\mathbf{u}} \in \{\text{ave}(\mathbf{u}_0) u^L \mathbf{b} \mid \mathbf{b} \in \mathcal{B}\}$	$\mathbf{k} \in \mathcal{K}$

Eigen [110]. Based on that, Algorithm 3 is then embedded in OpenLB. The configuration parameter spaces as well as the space \mathfrak{S} spanned by the discretized relaxation frequency intervals to be tested, are load balanced with existing routines in OpenLB.

As a first step, predefined regions of \mathcal{K} , are scanned for a fixed background flow with respect to Ma . The wave space resolution is set to $N_{\mathcal{K}} = 257$ grid points per dimension. Notably, a further increase in the number of discretization points did not lead to visible changes in the results. Several pairings of background flows and wavevectors are summarized in Table 4.6. The Nyquist–Shannon sampling theorem [225] allows to reduce the computational effort of the *full* wave space scans (see Table 4.6) via cutting the necessary wavevector values by half along $k_z = 0$.

The specifier *octant* refers to a scan over the full wave space with an additional variation of the background flow direction. The latter is realized as follows. Let $\mathcal{B}_{\Delta\chi, \Delta\theta}$ denote the first octant of the unit sphere [13, 22]

$$\mathcal{B} = \left\{ \left(\sqrt{1 - \chi^2} \cos(\theta), \sqrt{1 - \chi^2} \sin(\theta), \chi \right)^T \in \mathbb{R}^3 \mid \chi \in [0, 1], \theta \in \left[0, \frac{\pi}{2}\right] \right\}, \quad (4.35)$$

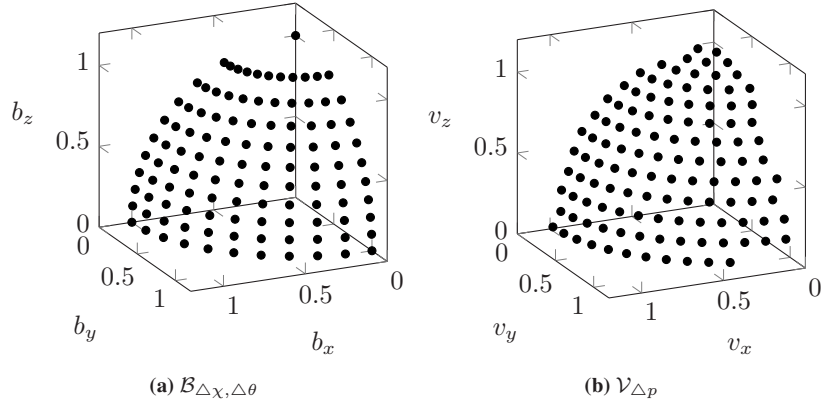


Figure 4.13: (a) Schematic visualization of $\mathcal{B}_{\Delta\chi, \Delta\theta}$ (elements are denoted with black dots). The discretization steps are $\Delta\chi = 0.1$ and $\Delta\theta = \pi/20$. The set comprises normalized vectors $\mathbf{b} = (b_x, b_y, b_z)^\top$ for the mean flow variation used in the (*scaled*) *octant* specifier according to Table 4.6. (b) Schematic visualization of $\mathcal{V}_{\Delta p}$ (elements are denoted with black dots). The number of points on the whole sphere is $p = 8.88 \times 10^2$. The set comprises normalized vectors $\mathbf{v} = (v_x, v_y, v_z)^\top$. Figure (a) is reproduced from [232], Copyright (2021), with permission from the authors and the Royal Society.

discretized with $\Delta\chi$ and $\Delta\theta$. The presently used discretization is given in Figure 4.13a and equidistantly parts the intervals for χ and θ . A second option of discretizing the unit sphere with is visualized in Figure 4.13b, where the whole sphere is first spiraled with a chosen discretization [22, Algorithm 4] and then chunked. The tests of both options favor the first one (Figure 4.13a) due to the regular inclusion of discretization points on the boundary. Nonetheless, the spiral method creates a better distribution of points over the surface and hence should be used when the initial mean flow is more randomly directed.

Finally, the specifier *scaled octant* denotes an additionally scaled mean flow on top of the configuration *octant*. The scaling is based on the ratio

$$\text{ave}(\mathbf{u}_0) = \frac{\int_{\Omega} \|\mathbf{u}_0\|_2 \, d\mathbf{x}}{|\Omega| \max_{\mathbf{x} \in \Omega} \|\mathbf{u}_0\|_2}. \quad (4.36)$$

For the specifiers *octant* and *scaled octant*, the maximum spectral radius

$$r_{\text{spec}}^{**}(\mathbf{H}) = \max_{\mathbf{b} \in \mathcal{B}} \underbrace{\max_{\mathbf{k} \in \mathcal{K}'} r_{\text{spec}}(\mathbf{H})}_{= r_{\text{spec}}^*(\mathbf{H})}, \quad (4.37)$$

is extracted. Here, $\mathcal{K}' \subseteq \mathcal{K}$ denotes the respective scan region (see Table 4.6).

The maps produced with Algorithm 3 for the specifiers in Table 4.6 are plotted in Figure 4.14 and 4.15. For the purpose of representation, the coloring refers to an individually normalized spectral radius

$$\tilde{r}_{\text{spec}}(\mathbf{H}) = \frac{r_{\text{spec}}(\mathbf{H}) - 1}{\max_{s_q, s_\mu} r_{\text{spec}}(\mathbf{H}) - 1}, \quad (4.38)$$

where the normalization is done per Ma and specifier.

The observations we made in [232] are summarized as follows. The stability regions obtained with the *x-directional* scan (Figures 4.14a, 4.14b, 4.14c, 4.14d) significantly differ from the remaining ones in Figure 4.14 which are based on a three-dimensional mean flow (see Table 4.6). In particular, when Ma is small enough in the *x-directional* scan, the optimized MRT LBM relaxation frequencies [52] (white circles) and the classical ones [66] (white squares) are VN stable. Further, the optimization of \hat{s} for variable Ma tracks a specific range of $\tilde{r}_{\text{spec}}^*(\mathbf{H})$ (see *x-dir.* row from left to right in Figure 4.14). In contrast to that, both $(\tilde{s}$ and $\hat{s})$ lie in a VN unstable domain when considering the

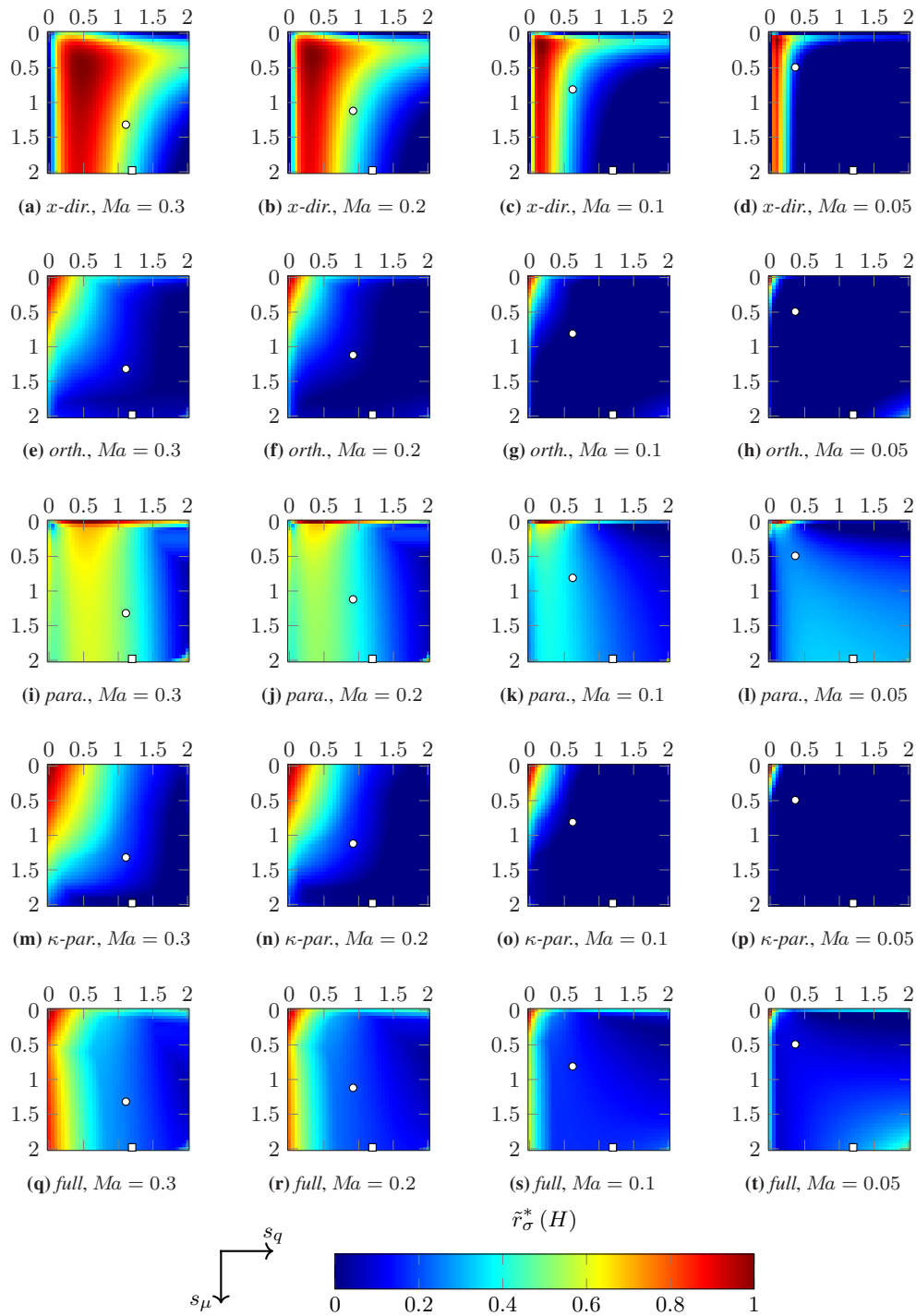


Figure 4.14: From top to bottom, row-wise: VN stability maps (Algorithm 3) for $Re = 1600$ and $N_{\mathcal{C}} = 257$ with scan regions according to Table 4.6: *x-directional* (a–d), *orthogonal* (e–h), *parallel* (i–l), *κ -partial* (m–p), *full* (q–t). From left to right, column-wise: $Ma = 0.3, 0.2, 0.1, 0.05$, respectively. Coloring refers to respectively normalized spectral radius approximation $\tilde{r}_{\text{spec}}^*(\mathbf{H})$ (4.38). White squares denote \tilde{s} used in the classical MRT formulation [66]. The optimized MRT LBM [52] comprising \hat{s} is plotted as white circles. Note that the optimized value for $Ma = 0.05$ is obtained by a polynomial fit through \hat{s}_q and \hat{s}_μ for larger Ma , respectively. This figure is reproduced from [232], Copyright (2021), with permission from the authors and the Royal Society.

full scan (Figures 4.14q, 4.14r, 4.14s, 4.14t). Hence, the *x-directional* scan used for example in [51, 52] to optimize MRT LBM versions for the TGV flow, is less reliable for being a valid indicator of VN stability in a three-dimensional setting. Nevertheless, the VN stability region for a *full* scan as well as the BF stability region in Figure 4.12 indicate

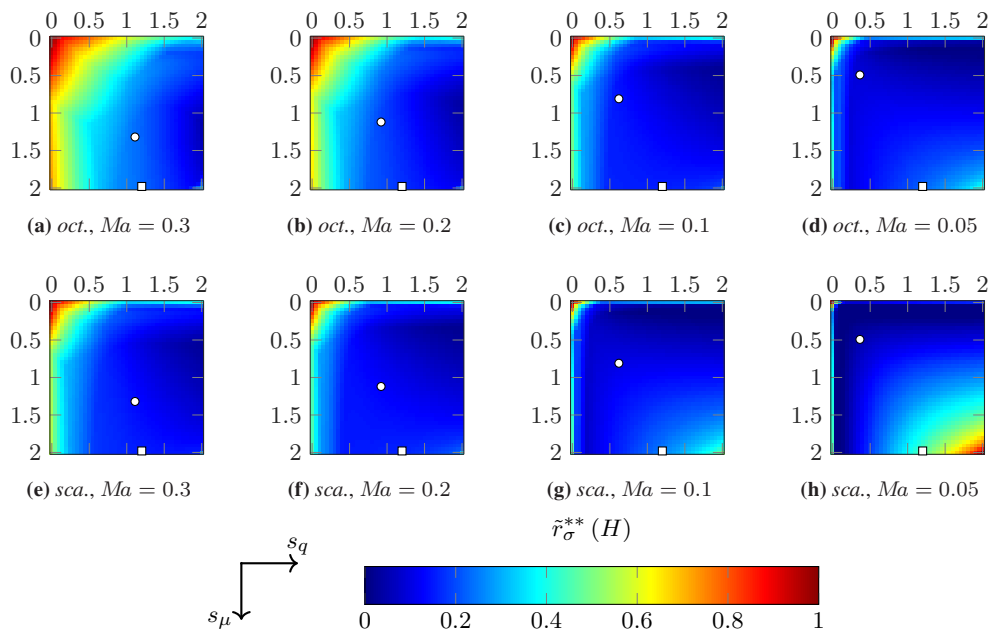


Figure 4.15: From top to bottom, row-wise: VN stability maps (Algorithm 3) for $Re = 1600$ and $N_{\mathcal{K}} = 257$ with scan region *octant* (a–d) and *scaled octant* (e–h) according to Table 4.6. From left to right, column-wise: $Ma = 0.3, 0.2, 0.1, 0.05$, respectively. Coloring refers to respectively normalized spectral radius approximation $\tilde{r}_{\text{spec}}^{**}(\mathbf{H})$. White squares denote \tilde{s} used in the classical MRT formulation [66]. The optimized MRT LBM [52] comprising \hat{s} is plotted as white circles. Note that the optimized value for $Ma = 0.05$ is obtained by a polynomial fit through \hat{s}_q and \hat{s}_μ for larger Ma , respectively. This figure is reproduced from [232], Copyright (2021), with permission from the authors and the Royal Society.

that the polynomially fitted relaxation pair (\hat{s}_q, \hat{s}_μ) upholds a certain distance to the increasing instability region when decreasing Ma .

Several options of reducing the number of necessary eigenvalue computations within \mathcal{K} for a three-dimensional mean flow were suggested in the literature [228, 268, 269], for example via computing solely *parallel* or *orthogonal* wave paths. The corresponding VN stability maps are shown in Figures 4.14i, 4.14j, 4.14k, 4.14l and Figures 4.14e, 4.14f, 4.14g, 4.14h, respectively.

Whereas the *orthogonal* scan highly overestimates the stability compared to the BF results, the *parallel* configuration isolates the accuracy line that was detected by BF (cf. bottom row in Figure 4.12, especially 4.12e). More precisely, the increased normalized spectral radius (e.g. $\tilde{r}_{\text{spec}}^*(\mathbf{H}) \approx 0.6$ at $s_q \approx 0.5$ in Figure 4.14i) approves the above stated conjecture that predicts decreased numerical dissipation within this region (cf. Figure 4.12e). Additionally, the *parallel* scan reproduces a second region which exhibits increased VN instability, but is larger and differing in shape from the BF instability. It is further notable, that for $Ma = 0.05$ (Figure 4.14l), the VN stability set (i.e. where strictly $r_{\text{spec}}(\mathbf{H}) \leq 1$ holds) detected by the *parallel* scan is located within the interval $(s_q, s_\mu) \in (0.5, 2) \times (0, 0.25)$ and is much smaller than the BF stable region (cf. Figure 4.12d).

Testing a third reduction of the wave space, the κ -*partial* scan for $\kappa = 0.5$ (see Figures 4.14m, 4.14n, 4.14o, 4.14p) indicates that a major portion of the VN instability located within the lower right region of the map is added in the remaining wave space section $\mathcal{K} \setminus \kappa\mathcal{K}$. The added portions particularly include the error minimal line as well as the (with Mach decrease) growing instability region. From this, we may imply the following.

First, the suggestion in [52] for transferring the cutoff wavenumber within the TGV flow directly onto the value of $\pi/2$ seems to be not applicable. Instead, the cutoff wavenumber for a given resolution is mapped to π . This is reasonable in regard to the projection from physical $\mathbf{k}/\Delta x \in (1/\Delta x)\mathcal{K} = [-N/2, N/2]^3$ to grid-normalized (i.e. nondimensionalized) $\mathbf{k} \in \mathcal{K} = [-\pi, \pi]^3$, initially described in [267]. As stated therein, this relation between resolution dependent and continuous wave space prevents the use of the linear VN analysis for investigating mesh dependent

instabilities in numerical simulations. The present observations conform to the *spectral sampling* mentioned in [56]. Second, the VN stability map provides theoretical evidence that the instability of the classical MRT scheme [66] roots in the increased spectral radius of its linearized version, which exclusively becomes effective in high wavenumbers and further, can be prevented by tuning certain relaxation times along with $Ma \rightarrow 0$ (see e.g. [63]).

Considering the *full* scan (Figures 4.14q, 4.14r, 4.14s, 4.14t) and the additional *octant* variation of the mean flow (Figures 4.15a, 4.15b, 4.15c, 4.15d), the latter reproduces a fair amount of the BF instability vanishing toward $(s_q, s_\mu) = (0, 0)$ with $Ma \rightarrow 0$ in terms of shape, if $\tilde{r}^{**}(\mathbf{H}) \approx 0.5$ is interpreted as stability bound. In contrast to that, the appearing BF instability (cf. Figures 4.12a, 4.12b, 4.12c, 4.12d) is recovered marginally by both scans across the complete wave space.

Figures 4.15e, 4.15f, 4.15g, 4.15h visualize the change of the VN stability maps with the *scaled octant* specifier for decreasing Ma . Compared to any of the preceding scan regions, this most adapted configuration, which scans all possible variations with an additionally fitted mean flow magnitude, recovers the highest amount of features with respect to BF stability (Figure 4.12). In particular, for $Ma = 0.05$ the instability region appearing in the BF stability map (Figure 4.12d) is fairly reproduced in shape.

Finally, it can be stated that reduced scans are suitable to detect specific spectral features of the numerical method. However, for reproducing the structure of the BF stability in a fully three-dimensional flow problem, solely the computation through the complete wave space together with a directionally varying background flow of conforming magnitude reaches at most acceptable quality.

4.3.3.2 Brute force stability of second, third and fourth order relaxation

The above comparison provides evidence, that the VN stability maps are less reliable than the BF results in the present test case. Particularly due to the observation that the VN stability maps solely include wave space normalized grid dependence, we conduct further BF computations to examine the relaxation frequency influence on the stability.

The BF computations (Algorithm 4) below are parametrized by a variable ς_b , which is injected in (3.192) and measuring the deviation of s_b from s_P , where $b \in \{e, q, \mu, \varepsilon, \Pi\}$. Thus, with the following TGV simulations, we compute through possible MRF ranges and determine if the current set of relaxation frequencies contained in \mathbf{S} is overall stable. Additionally, the error according to (4.33) is computed.

Table 4.7: Exemplary relaxation parameters calculated with (3.192) for $Re = 1600$, $Ma = 0.05$, $N = 128$, where $s_P = 1/\tau_P$ with $\tau_P = 0.50109$ according to Table 4.8. This table is reproduced from [232], Copyright (2021), with permission from the authors and the Royal Society.

ς_b	τ_b	s_b
0	0.50109	1.99563
1	0.50218	1.99128
2	0.50437	1.98264
3	0.50875	1.96559
4	0.51750	1.93234
5	0.53500	1.86912
6	0.57001	1.75432
7	0.64003	1.56240
8	0.78007	1.28192
9	1.06015	0.94326
10	1.62030	0.61716

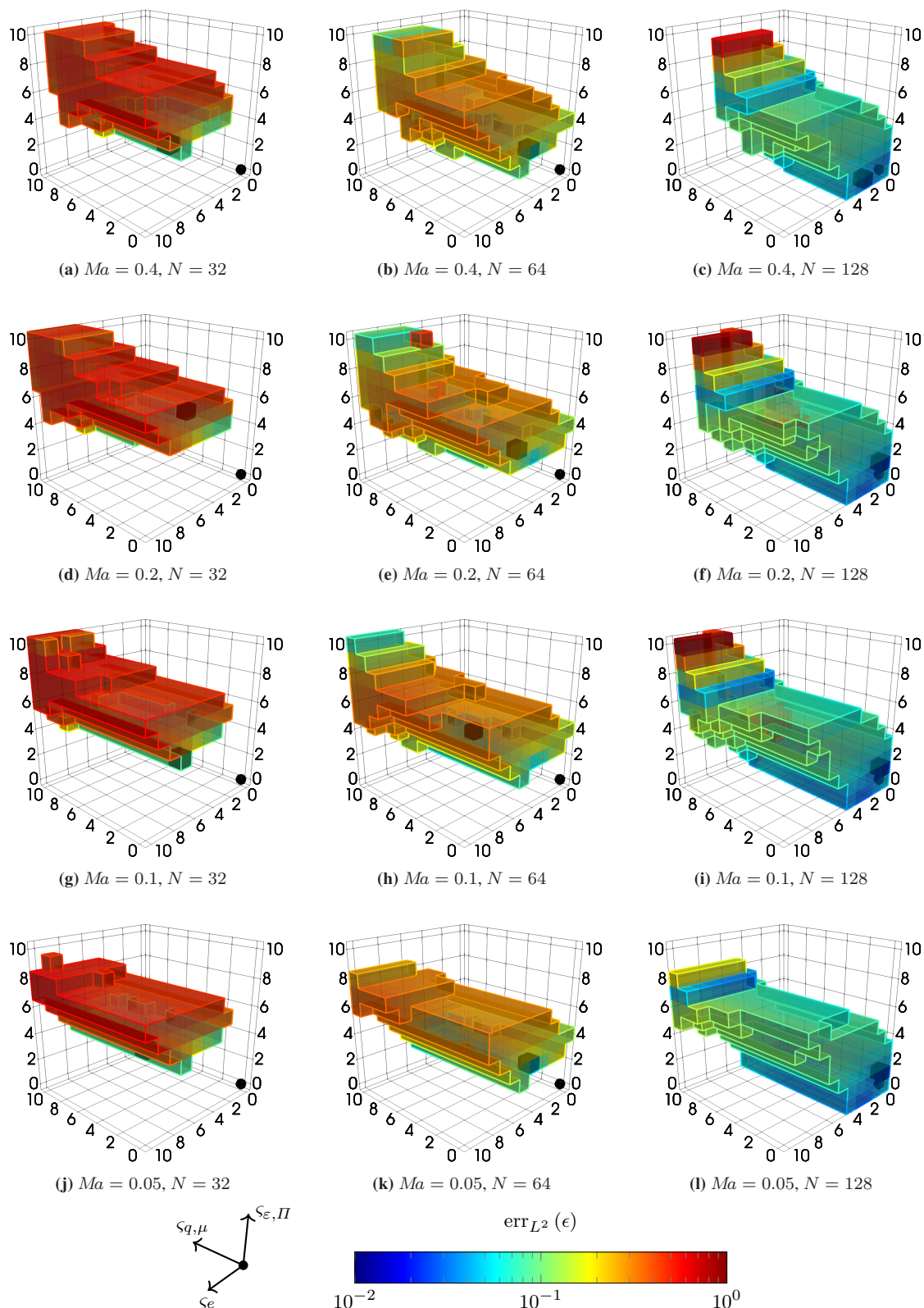


Figure 4.16: BF stability maps (Algorithm 4), only stable configurations shown) of ς -parametrized MRT LBM computations for TGV flow simulations with $Re = 1600$, $Ma = 0.4, 0.2, 0.1, 0.05$ (from top to bottom), and $N = 32, 64, 128$ (from left to right). The Cartesian x -, y -, and z -coordinate axes correspond to $\varsigma_{q,\mu}$, ς_e , and $\varsigma_{\Pi,e}$, respectively, and are shown for the interval $[0, 10]^3$. One map contains 11^3 TGV computations visualized as voxels. Coloring refers to $err_{L^2}(\epsilon)$ over the interval $t \in [0, 10]$. Black cubes denote stable ς configurations such that $err_{L^2}(\epsilon)$ is minimal. Black spheres indicate the corresponding origins $\varsigma = \mathbf{0}$, i.e. SRT BGK configurations. This figure is reproduced from [232], Copyright (2021), with permission from the authors and the Royal Society.

Table 4.8: LBM discretization parameters for TGV flow simulations at $Re = 1600$, where $\tau_P = 1/s_P$. This table is reproduced from [232], Copyright (2021), with permission from the authors and the Royal Society.

$Ma \backslash N$	32			64			128		
	τ_P	Δx	Δt	τ_P	Δx	Δt	τ_P	Δx	Δt
0.4	0.50213	0.20268	0.04680	0.50434	0.09973	0.02303	0.50875	0.04947	0.01142
0.2	0.50106	0.20268	0.02340	0.50217	0.09973	0.01151	0.50437	0.04947	0.00571
0.1	0.50053	0.20268	0.01170	0.50108	0.09973	0.00575	0.50218	0.04947	0.00285
0.05	0.50026	0.20268	0.00585	0.50054	0.09973	0.00287	0.50109	0.04947	0.00142

An example calculation of the thus tested relaxation frequencies for a specific combination of Re , Ma , and N is summarized in Table 4.7. To reduce the computational costs of a full variation of the five tunable relaxation frequencies (four kinetic ones plus one hydrodynamic), we group them by the order of their moments. In summary, the relaxation frequencies s_e , $s_{q,\mu}$, and $s_{\varepsilon,\Pi}$ vary with $\zeta = (\zeta_{q,\mu}, \zeta_e, \zeta_{\varepsilon,\Pi})^T \in \{n \in \mathbb{N}_0 \mid 0 \leq n \leq 10\}^3$, where $\zeta = \mathbf{0}$ corresponds to SRT BGK collision. With this procedure we introduce ghost Reynolds numbers [63] for each moment order larger than one. Hence with the scan over the parameter space induced by ζ , we test values of possible ghost Reynolds numbers, which in terms of (3.192) appear as controllable bulk viscosities [62] and hyperviscosities [185, 264]. Based on that, three-dimensional BF stability maps are obtained and gathered in Figure 4.16, where the x -, y -, z -coordinate axes correspond to $\zeta_{q,\mu}$, ζ_e , $\zeta_{\varepsilon,\Pi}$, respectively.

The BF computations compiled in Figure 4.16 are carried out for $Re = 1600$, and comprise several values for Ma and N to obtain a scan over acoustic scaling (AS) as well as diffusive scaling (DS). The general numerical and flow parameters are given in Table 4.8. Note that column-wise reading of Table 4.8 and Figure 4.16 corresponds to refining the grid according to AS, whereas $(\tau_P, \Delta x, \Delta t)$ -triples read along diagonal (Ma, N) -pairs obey DS, respectively. The variety of numerical effects visualized in Figure 4.16, can be summarized along the parameter changes through Table 4.8 as follows.

1. AS ($Ma = \text{const}$, $N \rightarrow \infty$): The visible volume of the BF stability map increases on average (except for $Ma = 0.4$) and is moved collectively to the origin (i.e. the SRT BGK configuration). Whereas the top regions (toward $\zeta = (10, 10, 10)^T$) are roughly similar in shape, distinct features of each map are located around the origin of the parameter space. The error minimum shifts to the SRT BGK configuration. The translation toward the origin is observed for all tested Ma .
2. $Ma \rightarrow 0$, $N = \text{const}$: For individual resolutions, the visible volume of the BF stability map increases on average, where its form is contracted toward the origin in the $\zeta_{\varepsilon,\Pi}$ -direction and elongated in the $\zeta_{q,\mu}$ -direction. Although a variation in the clustering of the error minimal cubes is observable for $N = 32$ (Figures 4.16a, 4.16d, 4.16g, 4.16j), for $N > 32$ the minimum location is less scattered on average.
3. DS ($Ma \sim 1/N \rightarrow 0$): As a composition of the two previous parameter scalings, the DS features error minima near SRT BGK collision as well as Ma -dependent shrinkage of the BF stability region in the $\zeta_{\varepsilon,\Pi}$ -coordinate and an overall movement to the origin. For large N , the error minimum is located on average at minimal distance to the SRT BGK parameters with diminishing correlation to the change in Ma . In contrast to that, small N lead to larger Ma -correlated clustering of the error minimum.

In general, Figure 4.16 provides evidence that the error minimum is highly correlated to the minimum distance from the SRT BGK point. For low resolutions, this correlation weakens and can be outsourced to move within the stability region while upholding minimal error magnitudes. With the increase of resolution, the clustering of the error minimal cubes around the SRT BGK location decreases and indicates an increase of correlation strength. Interestingly, for $N \geq 64$ a second region with decreased error magnitudes appears (see Figures 4.16b, 4.16c, 4.16e, 4.16f, 4.16h,

4.16i, 4.16l). Since this region is adjacent to error maxima, we assume numerical artifacts as a reason. Alternatively, according to the above reasoning, decreased numerical dissipation might be another possible cause. Nevertheless, throughout all tested parameter configurations, the error minima are located within the nearest distance region to the SRT BGK configuration. Taking all observations into account, we conclude that the least numerical dissipation is injected when choosing stable relaxation frequencies as near to SRT BGK parameters as possible, in DS as well as AS. For very coarse resolutions, the possibilities of stabilizing the method with numerical dissipation while keeping the error constant are increased. In contrast to that, for increasing resolutions, the error minimization will inevitably lead to the SRT BGK origin where also the numerical dissipation is minimized via reduction of hyperviscosities.

Considering solely the shape of the BF stability regions, a shift as well as a change of the overall box size is observed when comparing Ma -sequences for individual N . The range of BF stable values for $\zeta_{q,\mu}$ increases with $Ma \rightarrow 0$, whereas the possible choices of $\zeta_{\varepsilon,\Pi}$ decrease. Further, the stability range for ζ_e seems to be marginally affected by the change in Ma for small N , where the Ma -influence increases with decreasing N . In summary, for a DS approach – first and second diagonal, i.e.: Figures 4.16a, 4.16e, 4.16i, and Figures 4.16d, 4.16h, 4.16l, respectively – the BF stability map contracts in $\zeta_{\varepsilon,\Pi}$ -direction and shifts toward the SRT BGK point with increasing N [63].

However, even with the inclusion of artificial viscosity scaling into the parametrization of kinetic relaxation frequencies, the BF stability map still shifts in position dependent on N . Especially when using coarse resolutions, the distance to the SRT BGK configuration becomes crucial. This indicates that the ghost Reynolds numbers for controlling the hyperviscosities can be amended by resolution dependent relaxation functions to automatically stay in the stability region in a three-dimensional turbulence simulation.

4.3.3.3 Empirical multiple relaxation function collision

Based on the data obtained with the BF and VN computations and visualized in Figures 4.12, 4.15, 4.16, we construct two MRF collision schemes. For the first scheme, the third order relaxation frequencies s_μ and s_q are dynamically defined via extrapolating the values \hat{s}_μ and \hat{s}_q from [52] (which were optimized by the k -1% dispersion-error rule) over a range of $Ma \in [0.3, 0)$. The extrapolation is based on the dependency on Ma observed above and uses the origin as a fourth point. The resulting functions

$$\hat{s}_\mu^{\text{pf3}}(Ma) = \frac{200}{3}Ma^3 - 45Ma^2 + \frac{71}{6}Ma, \quad (4.39)$$

$$\hat{s}_q^{\text{pf3}}(Ma) = 35Ma^3 - \frac{53}{2}Ma^2 + \frac{17}{2}Ma \quad (4.40)$$

are plotted in the parameter space $\mathfrak{M} \times \mathfrak{S}$ in Figure 4.17a. The such obtained MRF collision scheme is further tested and used as background stabilization for the TLES simulations in Section 4.4. It is to be noted that this variant still contains constant relaxation frequencies, which are affecting stability up to negligible orders only. Consistency however has to be ensured via additional means of creating a reduction point toward SRT BGK collision.

The second MRF scheme is based on the minimal error configurations within the computed BF stability sets shown in Figure 4.16. This version is fully consistent toward SRT BGK collision and thus toward the TEQ. Polynomial fits through the error minima from the BF stability sets over the second, third and fourth order relaxation are visualized in Figure 4.17b. The mean exponents $\bar{\zeta}$ are obtained from averaging over the minimal error exponents along the diffusive scaling paths in the computed parameter grid (see Table 4.8). Due to the intended hybridization to an SRT BGK scheme which is found to be stable from $N = 128$ onwards for $Re = 1600$, null points in $\bar{\zeta}$ are added at $N = 256, 512, 1024$ in the polynomial fit. The resulting relaxation function exponents are

$$\bar{\zeta}_{q,\mu}^{\text{pf3}}(N) = -2.50 \times 10^{-8}N^3 + 4.33 \times 10^{-5}N^2 - 2.07 \times 10^{-2}N + 2.65, \quad (4.41)$$

$$\bar{\zeta}_e^{\text{pf3}}(N) = -7.11 \times 10^{-8}N^3 + 1.21 \times 10^{-4}N^2 - 5.65 \times 10^{-2}N + 6.85, \quad (4.42)$$

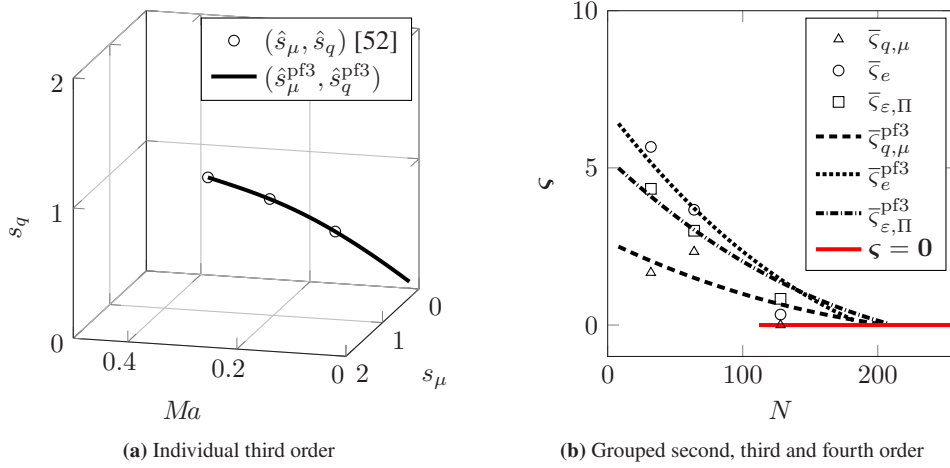


Figure 4.17: (a) Third order polynomial fit (\cdot^{pf3}) through relaxation frequency prefactors \hat{s}_q and \hat{s}_μ dependent on the Mach number. (b) Third order polynomial fit (\cdot^{pf3}) through Ma -averaged $\text{err}_{L^2}(\epsilon)$ -minimal ζ -configurations $\bar{\zeta}$ in diffusive scaling.

$$\bar{\zeta}_{\epsilon, \Pi}^{\text{pf3}}(N) = -4.91 \times 10^{-8} N^3 + 8.52 \times 10^{-5} N^2 - 4.09 \times 10^{-2} N + 5.31. \quad (4.43)$$

To render the empirically derived MRF definitions grid-independent for a given bulk flow with a predefined Reynolds number, the lowest stable resolution should be determined and used as the reduction point to the SRT BGK mode. Assuming that the stability sets computed above are transferable to wave space, a similar argument as for VN stability can be used to draw an analogy between increasing the Reynolds number at fixed resolution and vice versa. The effect on the computed relaxation functions is to be determined in future studies.

Table 4.9: Dissipation rate error minima ϵ_{\min} and corresponding orderwise relaxation pairs $\zeta = (\zeta_{q, \mu}, \zeta_\epsilon, \zeta_{\epsilon, \Pi})^T$ for MRT LBM simulations of the TGV flow at $Re = 1600$.

$Ma \backslash N$	32		64		128	
	ζ^T	$\text{err}_{L^2}(\epsilon)$	ζ^T	$\text{err}_{L^2}(\epsilon)$	ζ^T	$\text{err}_{L^2}(\epsilon)$
0.4	(1, 7, 4)	8.04×10^{-2}	(0, 4, 3)	6.64×10^{-2}	(0, 2, 0)	2.96×10^{-2}
0.2	(3, 3, 5)	8.38×10^{-2}	(1, 4, 3)	5.03×10^{-2}	(0, 0, 1)	2.54×10^{-2}
0.1	(0, 7, 4)	8.16×10^{-2}	(6, 3, 3)	4.84×10^{-2}	(0, 0, 1)	2.51×10^{-2}
0.05	(3, 7, 4)	8.18×10^{-2}	(0, 4, 3)	4.62×10^{-2}	(0, 0, 1)	2.52×10^{-2}

Concerning accuracy, the error map with $\text{err}_{L^2}(\epsilon)$ with respect to the reference DNS results [40] of the parameter grid (Table 4.8) is shown in Figure 4.18. The corresponding values are given in Table 4.9. As directly observable, the EOC is around one. Notably, the MRF scheme as defined above is neither intended to improve the convergence order nor to even show such a behavior for coarse grids. Instead, the aim is to ensure the underresolved stability of the scheme and to reduce the error of the dissipation rate to a minimum at the same time. Hence, for low resolutions the error is smaller than for using constant relaxation frequencies, which in turn reduces the second order EOC visibly to first order (see e.g. Figure 4.18). Due to the hybridization, this construction is expected to increase the EOC to second order automatically as soon as the SRT BGK mode region is reached for high enough N compared to the lowest stable configuration with respect to the Kolmogorov scale. Additionally, a clean estimation of the convergence order cannot be expected due to the difference in the methodology and way of computation with respect to the reference DNS (see [114] for a detailed discussion). In summary, the most prolific advantage of the proposed MRF collision is the increased accuracy in addition to its stability for coarse grids. Compared to previous observations made with for example, constant relaxation MRT LBMs, two-relaxation-time LBMs, regularized LBMs, entropic equilibria or with

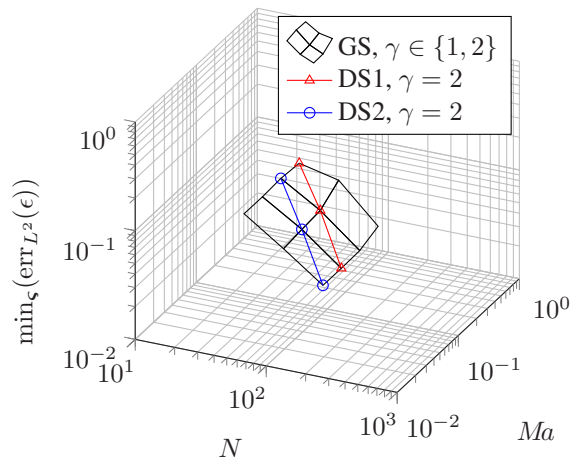


Figure 4.18: Orthogonal moment MRT LBM (see Table 3.4) error landscape of $\text{err}_{L^2}(\epsilon)$ -minimal relaxation frequency configurations ς listed in Table 4.9 and denoted with black cubes in Figure 4.16. Diffusive scaling (DS) and generic scaling (GS) determines the scaling function $\sigma = h^\gamma$ via $\gamma = 2$ for DS and $\gamma \in \{1, 2\}$ for GS, respectively, where DS1 starts at $(N = 32, Ma = 0.4)$ and DS2 starts at $(N = 32, Ma = 0.2)$.

SRT BGK collision [114], in the stable region before the reduction point, the accuracy measured in $\text{err}_{L^2}(\epsilon)$ increased by an average factor of $\mathcal{O}(10)$ for the resolutions $N = 64, 128$ (cf. [114, Table 6.3 and 6.4]). It is thus found to be crucial to tune the kinetic relaxation times of MRT LBMs before its usage with constant values. Once tuned, the stability and accuracy increase comes at the price of virtually no computational overhead apart from the additional moment–population mapping for the collision phase. Whereas the here presented methodology of *a priori* VN stability is found suitable for linear stability in the bulk flow domain, it is currently not covering wall-bounded flows, where the boundary conditions determine the convergence of the solver. The second methodology of *a posteriori* BF stability is by construction (under the premise of the availability of modern HPC resources and efficient parallel software) applicable to any test configuration, for example also canonical wall-bounded turbulence. The notion of BF stability is planned to be used for the prediction of nonlinear stability of LBMs for simulating complex flows as well as for the approximation of other mathematical models based on coupled PDEs.

4.3.4 Spectral effects of controlled relaxation

Besides the definition of relaxation functions with respect to nondimensional parameters (see Section 3.2.7.1 and Section 4.3.3.3), a space-time dependency can be imposed to enforce stability. The present section studies the effect of an entropy controlled relaxation of higher order moments on the turbulence quantities of the TGV flow summarized above (see Section 4.3.2). The KBC-N1 collision scheme [36] (Algorithm 1) is used with a $D3Q19$ velocity stencil (Definition 3.2.3) and natural moments (Table 3.2). Besides validating the implementation of Algorithm 1 in OpenLB [162], the present results contribute to (CTN3) and (CTN4) in terms of the explicit computational analysis of spectral properties of the space-time dependent relaxation. For this purpose, we recompute and extend the preliminary study in [163] and carefully analyze the produced results. Hence, for the first time, numerical effects of the entropy maximization through controlled higher order moment relaxation frequencies are analyzed in wave space via Fourier-transforming not only the flow quantities but also the entropy controller. Below, we compute a total of 27 simulation runs and post-process each flow field via computing the kinetic energy, the enstrophy, the total dissipation rate and maximum vorticity. Additionally, the entropy controller activation throughout the space-time domain is measured in terms of mean and variance. At last, the energy and control spectra at a sequence of discrete time steps of the KBC-N1 scheme are contrasted to energy spectra of the SRT BGK scheme to isolate the nonlinear stabilization mechanisms.

4.3.4.1 Discretization parameters and reference solutions

The parameter spaces used in the following computations are summarized in Table 4.10. To cover acoustic (AS) and diffusive scaling (DS) for three Reynolds numbers $Re = 1600, 3000, 6000$, the tested Mach numbers $Ma = 0.2, 0.1, 0.05$ are paired with all resolutions $N = 32, 64, 128$. The tested resolutions resemble an underresolved setting with a grid Reynolds number $Re_{\Delta} = Re/N = \mathcal{O}(100)$ on purpose which typically leads to divergence of the SRT BGK scheme in the standard formulation.

Table 4.10: Parameter grid for the numerical experiments with KBC-N1 on $D3Q19$ with natural moments (Table 3.2), entropy controlled relaxation (3.201) and truncated equilibrium (3.98).

N	Δt	Ma	τ		
			$Re = 1600$	$Re = 3000$	$Re = 6000$
32	2.34×10^{-2}	0.2	0.501068	0.500570	0.500285
	1.17×10^{-2}	0.1	0.500534	0.500285	0.500142
	5.85×10^{-3}	0.05	0.500267	0.500142	0.500071
64	1.15×10^{-2}	0.2	0.502171	0.501158	0.500579
	5.75×10^{-3}	0.1	0.501085	0.500579	0.500289
	2.87×10^{-4}	0.05	0.500543	0.500289	0.500146
128	5.71×10^{-3}	0.2	0.504376	0.502334	0.501167
	2.85×10^{-3}	0.1	0.502188	0.501167	0.500582
	1.42×10^{-4}	0.05	0.501094	0.500583	0.500292

The LBM results are assessed in terms of an error computation with respect to a psDNS reference solution⁴. The error computation below is done for $Re = 1600$ only. For $Re = 3000$, the DNS data from [233] computed with the SEM (Nek5000) is used for qualitative comparison.

4.3.4.2 Integral turbulence quantities

Simulations of the TGV flow are computed with the KBC-N1 LBM for the parameter grid in Table 4.10. The obtained flow fields approximate weak solutions to (2.12). To assess the quality of approximation, each flow field is post-processed via computing the kinetic energy (4.20), the enstrophy (4.21), the total dissipation rate (4.22) and the maximum vorticity (4.25). Concerning the latter for the TGV flow at high Reynolds numbers, Thantapanally *et al.* [247] have observed that the maximum vorticity shows a single separated peak at $t \approx 6.5$ after an initial virtually inviscid phase. This isolated peak region (IPR) is followed by a series of sub-peaks with similar magnitude. For Reynolds numbers smaller than $Re = 5000$, the IPR is shifted forward in time. For example at $Re = 800$ the separated peak is observed at $t \approx 7$. Hence, the computed vorticity is expected to recover an isolated peak in the IPR ranging in [6, 7]. For $Re = 1600$, the psDNS reference [61] provides kinetic energy, enstrophy and total dissipation rate results for comparison.

Figures 4.19, 4.20, 4.21 visualize the integral turbulence quantities computed for $Re = 1600, 3000, 6000$, respectively, with the Mach numbers and resolutions summarized in Table 4.10. The only stable SRT BGK results are obtained with the configurations $N = 128$ with $Ma = 0.2, 0.1, 0.05$ for $Re = 1600$. A higher Reynolds number or lower resolution

⁴ The presently used grid-converged reference solution (see for example [61, 253]) has been produced with a dealiased psDNS on 512^3 spatial grid points with a three-step Runge-Kutta scheme for time integration at $\Delta t = 1.0 \times 10^{-3}$. The data can be downloaded at http://www.as.dlr.de/hio CFD/spectral1_Re1600_512.gdiag. For simplicity, we will refer to [61] for this reference solution below.

led to divergence of the SRT BGK scheme used for the TGV flow. In contrast to that, all computations with KBC-N1 are stable and convergent.

The present results suggest that the reasonable stability bound $Re_{\Delta x} = \mathcal{O}(10)$ of the SRT BGK LBM for approximating the incompressible NSE (2.12) [164] is removed or at least drastically increased by the entropy controlled relaxation of kinetic moments. This observation has been predicted by Lyapunov stability for a suitable equilibrium formulation. The novelty in the present results is the numerically indicated validity for the computationally more efficient configuration with a second order truncated Maxwellian and $D3Q19$. As $Re_{\Delta x}$ increases further, accuracy is however still not preserved. For very coarse resolutions ($N = 32$), the kinetic energy is overpredicted (see Figures 4.19a, 4.19b, 4.19c, 4.20a, 4.20b, 4.20c, 4.21a, 4.21b, 4.21c), which shifts the total dissipation rate forward in time (see Figures 4.19g, 4.19h, 4.19i, 4.20g, 4.20h, 4.20i, 4.21g, 4.21h, 4.21i). It is remarkable however, that the shapes and magnitudes of both curves are well recovered. This is not the case for the enstrophy and the maximum vorticity, which are heavily reduced, see Figures 4.19d, 4.19e, 4.19f, 4.20d, 4.20e, 4.20f, 4.21d, 4.21e, 4.21f and Figures 4.19j, 4.19k, 4.19l, 4.20j, 4.20k, 4.20l, 4.21j, 4.21k, 4.21l, respectively. In addition, for decreasing the Mach number at fixed resolution, the reduction of enstrophy and vorticity increases (see Figures 4.19d, 4.19e, 4.19f, 4.20d, 4.20e, 4.20f, 4.21d, 4.21e, 4.21f and Figures 4.19j, 4.19k, 4.19l, 4.20j, 4.20k, 4.20l, 4.21j, 4.21k, 4.21l). The enstrophy reduction has also been reported by Geier *et al.* [97, Figures 2 and 3] for the K15 regularized cumulant LBM with unit relaxation times. In the above studies for the BF and VN stability, a Mach decrease under constant resolution even led to instabilities (Section 4.3.3.1). Remarkably, the error minimized MRF scheme does not show this effect and instead decreases the error with Mach decrease (see Section 4.3.3.2 and Figure 4.18). Another noticeable feature of the results for $N = 32$ are strong oscillations of the total dissipation rate in the initial time steps $t < 5$ (see Figures 4.19g, 4.19h, 4.19i, 4.20g, 4.20h, 4.20i, 4.21g, 4.21h, 4.21i). The oscillations vanish for larger resolutions, which has been just recently observed also by [187]. Here, the effects are present for both SRT BGK and KBC-N1 collision. Notably, the derivative of the kinetic energy is approximated with second order central differences, where the oscillations are independent on the edge stencil. The root of these numerical artifacts is investigated currently, and meanwhile attributable to the initialization procedure (3.303).

All of the observed effects vanish with increasing resolutions according to DS and the numerical KBC-N1 solution visibly approximates the DNS reference. Particularly the IPR of the maximum vorticity is rendered increasingly pronounced already at $N = 64, 128$. In summary, all tested integral turbulence quantities are approximated very well measured against the very coarse resolutions. In regard to the limit consistent approximation, the reduction of the entropy controller in the relaxation limit as well as the EOC of the total dissipation rate are further discussed below.

4.3.4.3 Entropy controller statistics

The relaxation function defined by the entropy controller (3.201) is measured in each time step of the simulation in terms of a statistical distance from the SRT BGK value $\gamma^* = 2$. To this end, we compute the mean controller via averaging over all nodes in space

$$\overline{\gamma^*}(t) = \frac{1}{|\Omega_{\Delta x}|} \sum_{\mathbf{x} \in \Omega_{\Delta x}} \gamma^*(\mathbf{x}, t). \quad (4.44)$$

The spatial average $\overline{\gamma^*}$ is then further processed to compute the root-mean-square error in the form of the variance

$$\llbracket \gamma^* \rrbracket(t) = \frac{1}{|\Omega_{\Delta x}|} \sum_{\mathbf{x} \in \Omega_{\Delta x}} [\overline{\gamma^*}(t) - \gamma^*(\mathbf{x}, t)]^2. \quad (4.45)$$

The mean and the variance of γ^* computed in all simulations with the parameters summarized in Table 4.10 are plotted in Figure 4.22. The asymptotic decrease of $|2 - \overline{\gamma^*}|$ for increasing N is clearly visible for all Reynolds numbers (cf. Figures 4.22a, 4.22b, 4.22c, Figures 4.22d, 4.22e, 4.22f, and Figures 4.22g, 4.22h, 4.22i, respectively). In addition, the variance $\llbracket \gamma^* \rrbracket$ decreases with increasing resolution. Notably, the configuration where the SRT BGK relaxation is

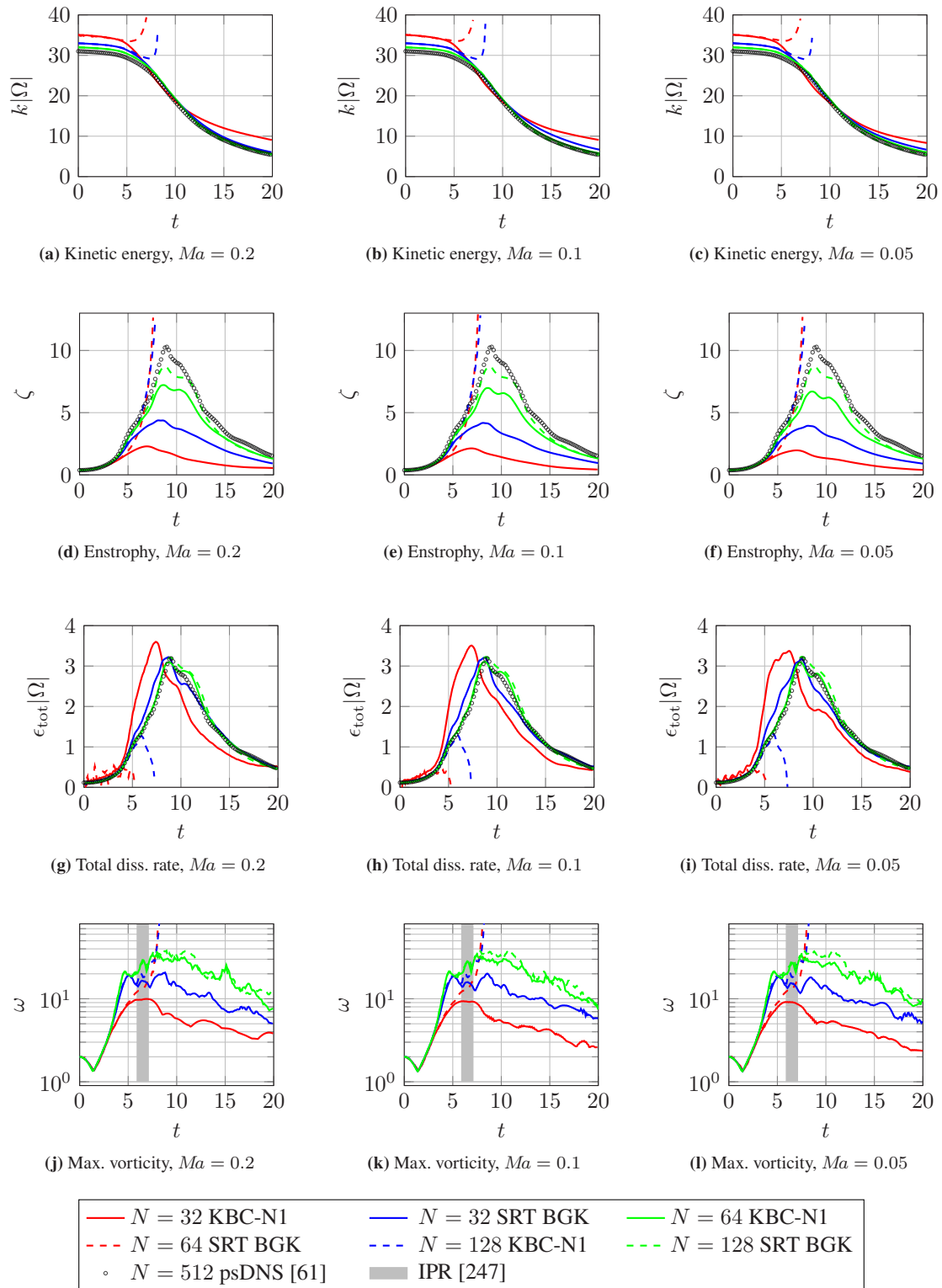


Figure 4.19: Integral turbulence quantities of KBC-N1 and SRT BGK collision for $Re = 1600$ at several resolutions $N = 32, 128, 256$ and Mach numbers $Ma = 0.2, 0.1, 0.05$.

stable ($N = 128$) still shows $\overline{\gamma^*} \neq 2$. However, for increasing Re at fixed N and Ma an increase in $|2 - \overline{\gamma^*}|$ is visible, where the effect is more pronounced for large N . Similarly to the correlation of Re and $|2 - \overline{\gamma^*}|$, the latter decreases with decreasing Ma . In summary, the stabilization via γ^* according to (3.201) is more active for large Re and large

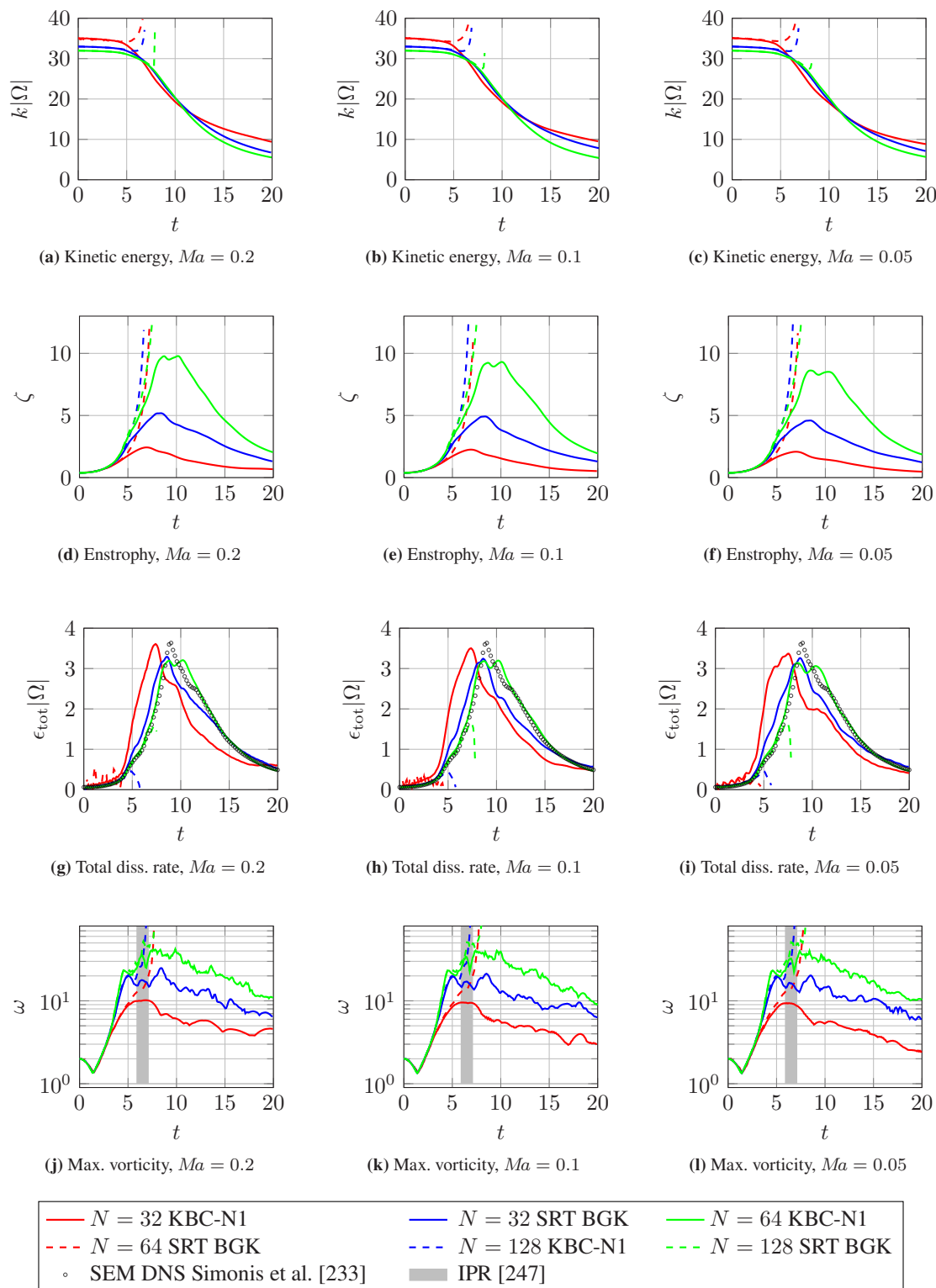


Figure 4.20: Integral turbulence quantities of KBC-N1 and SRT BGK collision for $Re = 3000$ at several resolutions $N = 32, 128, 256$ and Mach numbers $Ma = 0.2, 0.1, 0.05$.

Ma and vanishes in the smallness limit of both. The point in time, where the entropy controller is most active in terms of the steepness of $|2 - \bar{\gamma}^*|$ is visibly matching with the divergence point of the SRT BGK collision (see for example Figure 4.21a) on the one hand, and with the first peak region of the maximum vorticity (see for example Figure 4.21j)

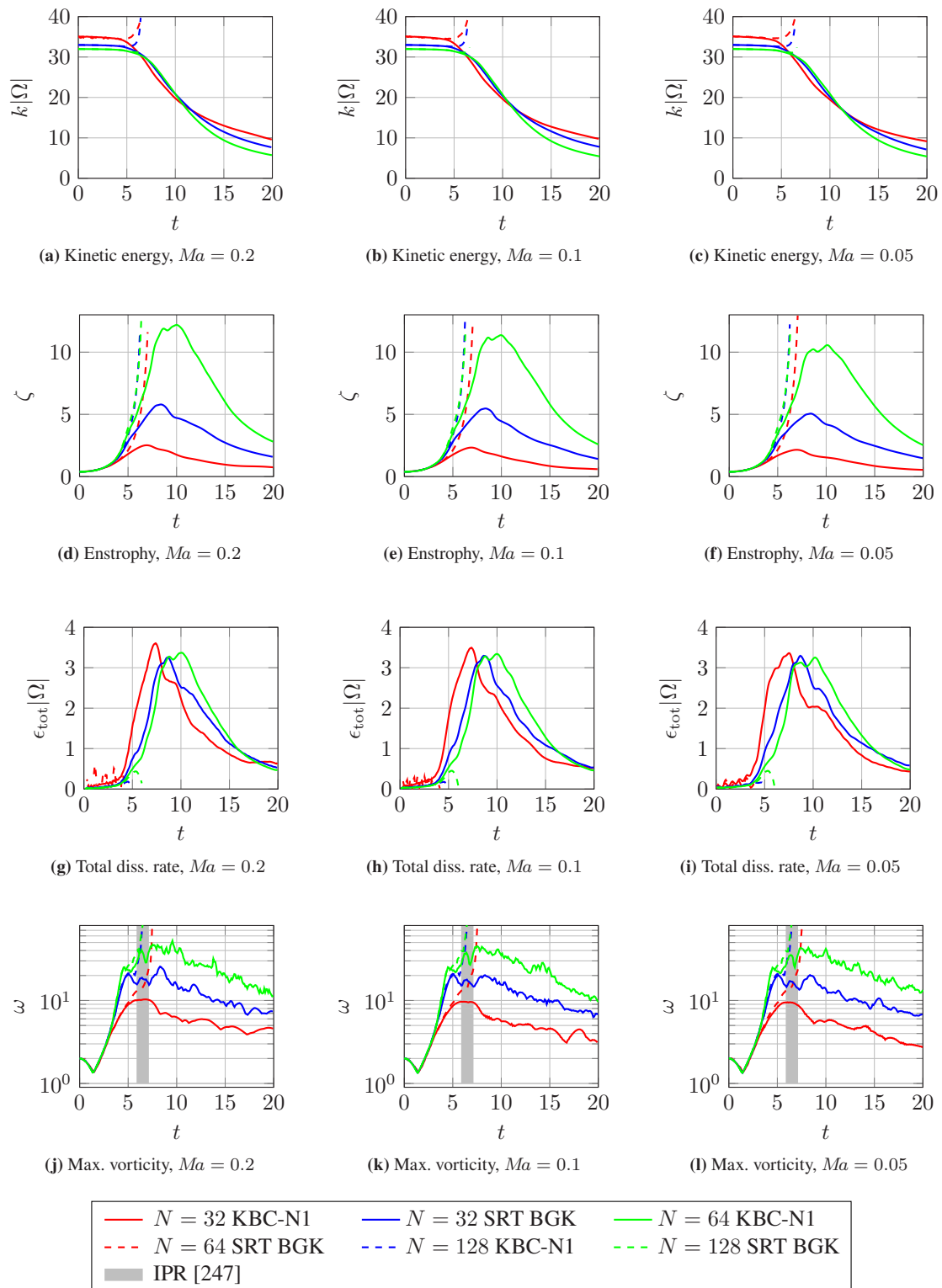


Figure 4.21: Integral turbulence quantities of KBC-N1 and SRT BGK collision for $Re = 6000$ at several resolutions $N = 32, 128, 256$ and Mach numbers $Ma = 0.2, 0.1, 0.05$.

on the other. The connection of $\bar{\gamma}^*$ to the latter seems even more natural when comparing the shape of the slopes. The entropy controller seems to track the vorticity and in case of low resolutions compensate its effect within the flow

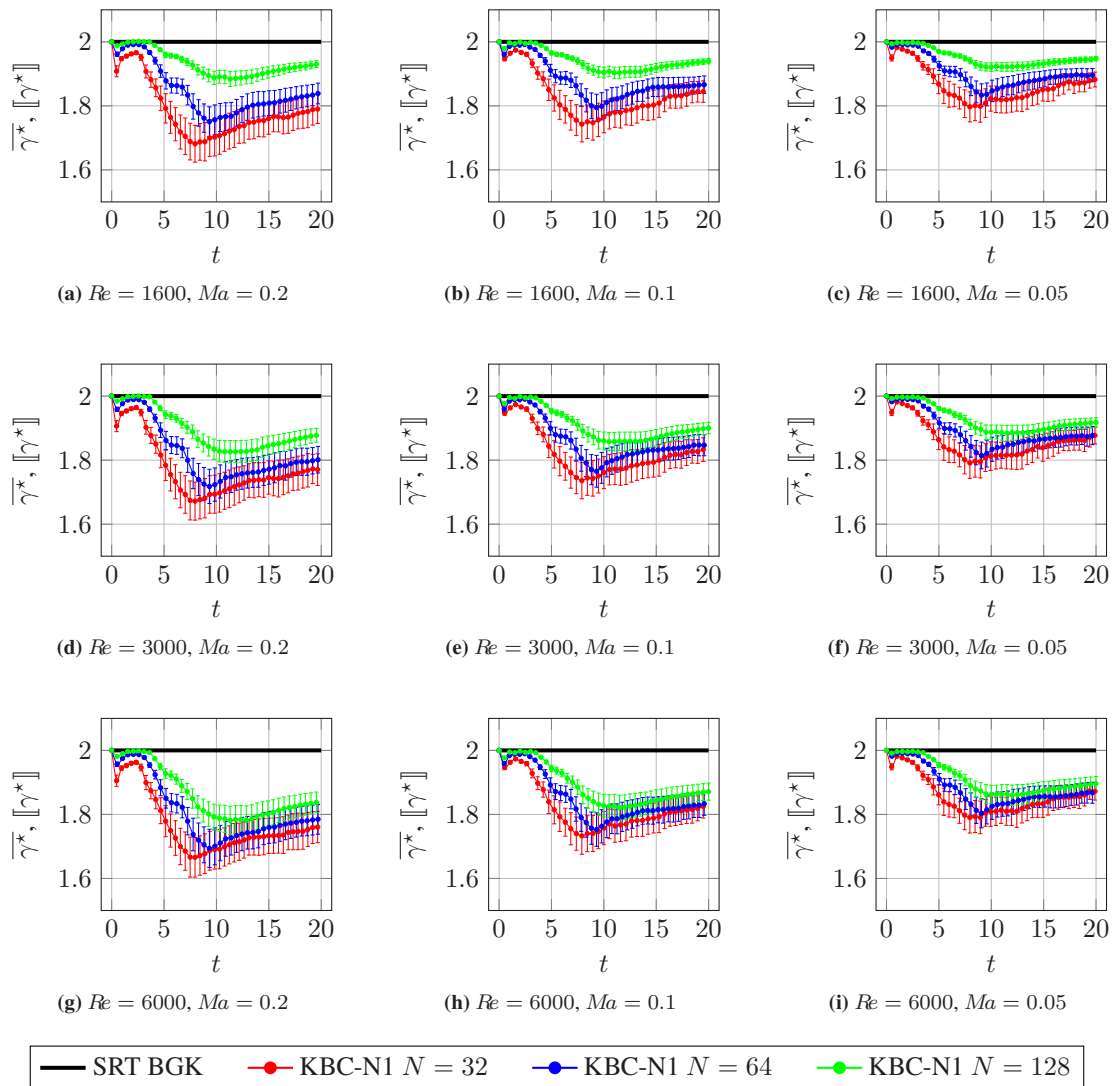


Figure 4.22: Spatial mean (4.44) and standard deviation (4.45) of KBC-N1 entropy controller γ^* (3.201) for TGV flow simulations at several Reynolds number $Re = 1600, 3000, 6000$ and Mach numbers $Ma = 0.2, 0.1, 0.05$.

field, similarly to a turbulence model. In addition, an exemplary EOC computation of the entropy controller statistics at $t \approx 5.1$ in DS yields

$$|2 - \overline{\gamma^*}(t)| = \mathcal{O}(N^{1.34}), \quad (4.46)$$

$$|\llbracket \gamma^* \rrbracket(t)| = \mathcal{O}(N^{1.61}), \quad (4.47)$$

which suggests convergence with order larger than one of the KBC-N1 relaxation understood as an MRF model toward the SRT BGK configuration. The crucial difference to classical explicit turbulence models with a grid coupled filter width is with respect to the order of viscosity. The relaxation functions only affect kinetic moments uncoupled from the viscosity. Since the latter in turn appear as higher order gradients in the closed form equation for the conserved moments, the KBC-N1 scheme is rather interpretable as a consistent, space-time adaptive hyperviscosity model.

4.3.4.4 Computational spectral analysis

Due to the apparent energy cascade along the vortical scales in DHIT for large Re , the above observed similarity between the entropy controller mean value and the maximum vorticity motivates the novel Definition 4.3.1 of the control spectrum (4.30) and its computational analysis. For the latter, all time dependent flow fields obtained with the computational parameter grid (Table 4.10) are Fourier transformed. The control spectrum $C(\kappa, t)$ is computed over the discrete wavenumber range at several points in time, which results in an array of three-dimensional data sets also for the energy spectra $E(\kappa, t)$ of the KBC-N1 solution and the SRT BGK solution. For DS, this data is visualized as waterfall plots in the Figures 4.23, 4.24, 4.25 for $Re = 1600, 3000, 6000$, respectively.

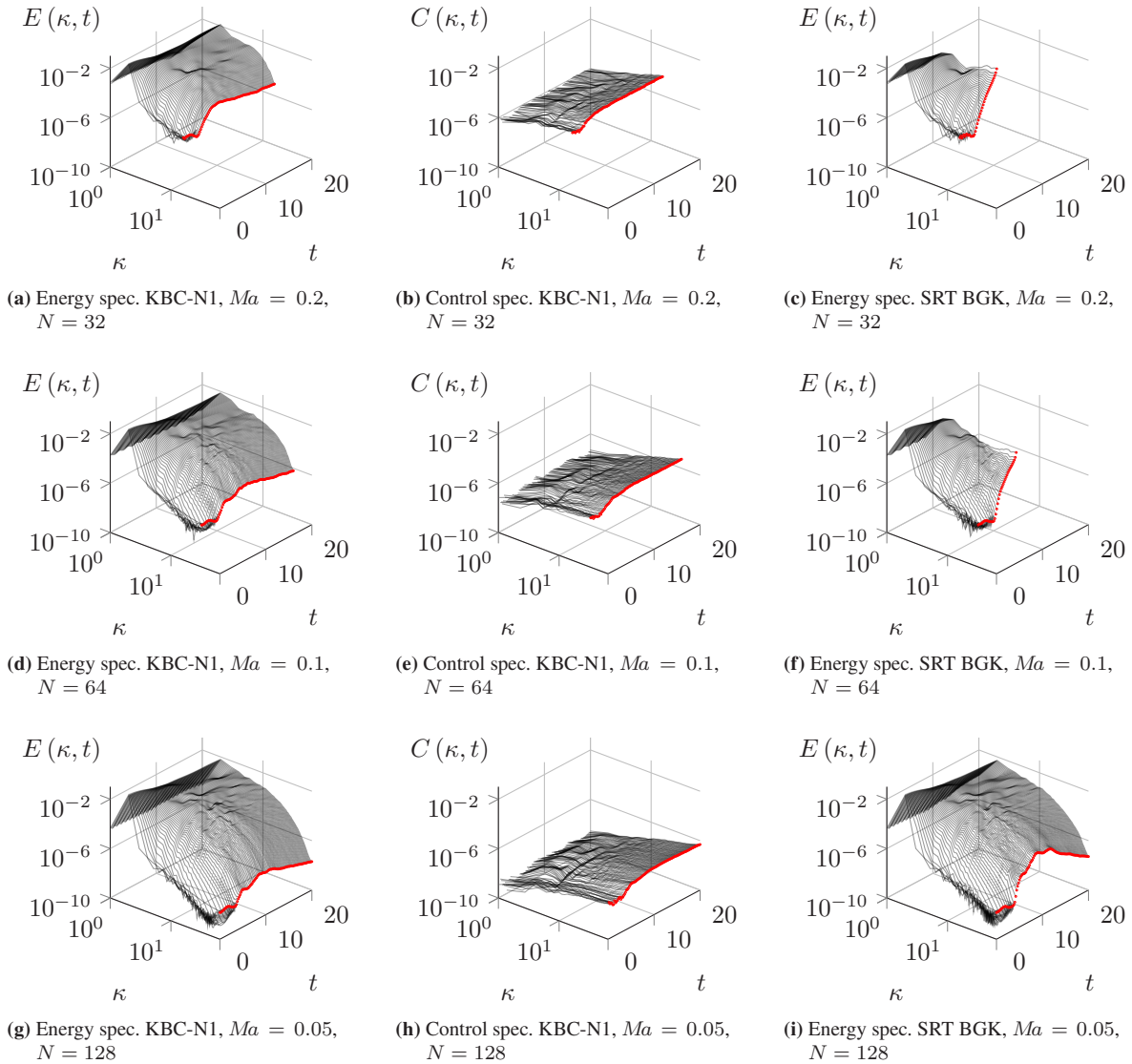


Figure 4.23: Energy spectra (4.26) and control spectra (4.30) for KBC-N1 scheme (left and middle column) as well as energy spectra (4.26) for SRT BGK collision (right column) of the TGv flow simulations at $Re = 1600$ in DS (top to bottom) for $(Ma, N) \in \{(0.2, 32), (0.1, 64), (0.05, 128)\}$. The red circles denote the values of the spectra at the respective cutoff wavenumber $\kappa_c = N/2$.

The activity of the entropy controller on particular wave lengths as well as its effect on the energy spectrum are observed for all tested Reynolds numbers and discretization parameters along DS. For small κ and initial times, $C(\kappa, t)$ is minimal on average. With increasing wavenumbers, the control spectrum increases as well, which approves the

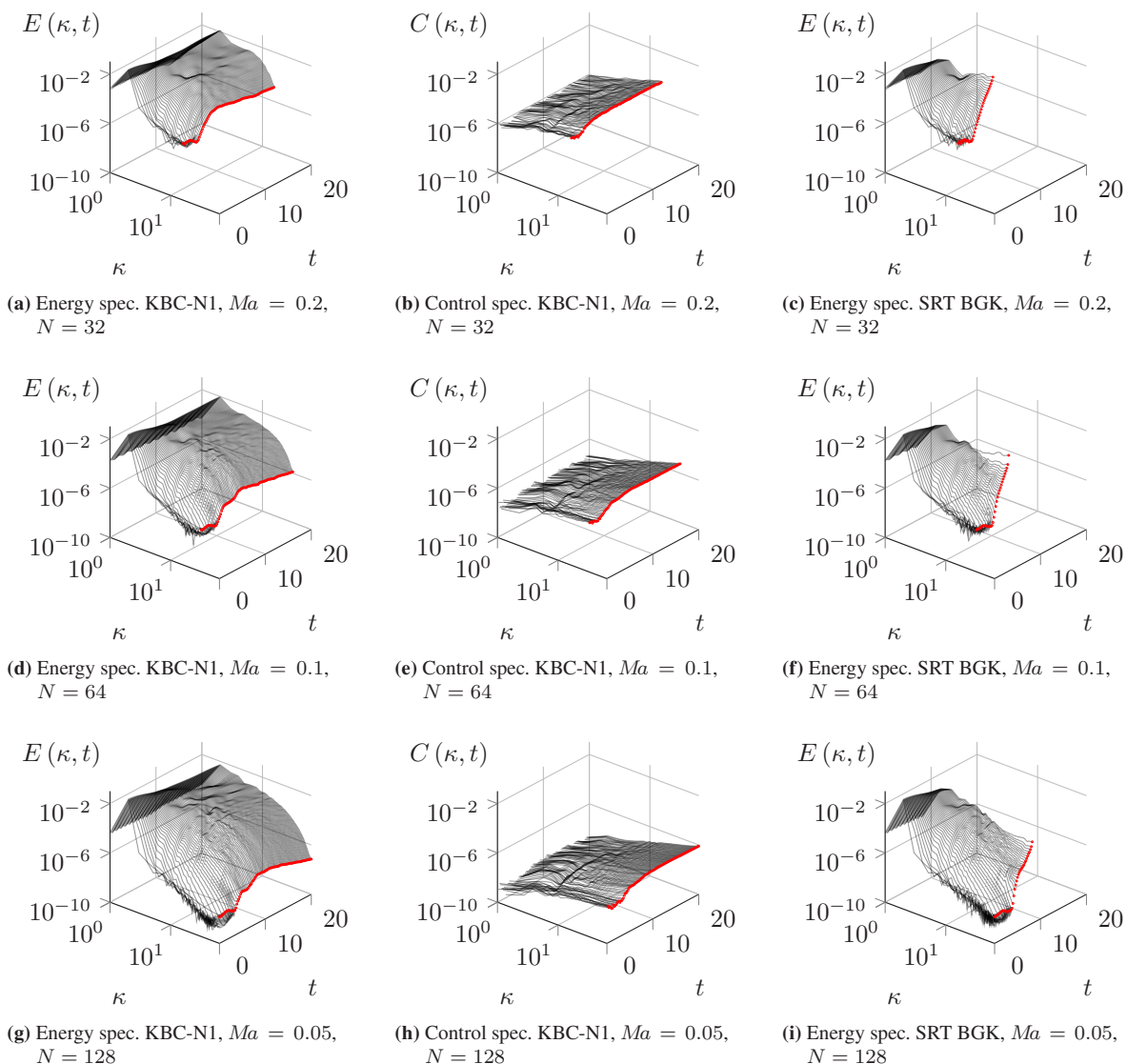


Figure 4.24: Energy spectra (4.26) and control spectra (4.30) for the KBC-N1 scheme (left and middle column) as well as energy spectra (4.26) for SRT BGK collision (right column) of the TGV flow simulations at $Re = 3000$ in DS (top to bottom) for $(Ma, N) \in \{(0.2, 32), (0.1, 64), (0.05, 128)\}$. The red circles denote the values of the spectra at the respective cutoff wavenumber $\kappa_c = N/2$.

above observed correlation of the entropy controller γ^* and the maximum vorticity ω . Similarly to the power law $E(\kappa, \cdot) = \mathcal{O}(\kappa^{-5/3})$ predicted by Kolmogorov [155, 156], the relaxation spectrum $C(\kappa, \cdot)$ reaches an asymptotic shape toward the end of the simulated time horizon. The shape of course differs from the one of the energy spectra and scales inversely. For the most resolved configuration ($Re = 1600$, $N = 128$), where the SRT BGK relaxation is stable (Figures 4.23i), the control spectrum landscape in κ and t is mostly flattened (see Figures 4.23g, 4.23h). In addition, the wave-time averaged magnitude of the control spectra decreases heavily with increasing the resolution. Notably, the correlation between the maximum vorticity and the entropy controller mean over time reappears for the largest wavenumbers in each grid configuration (the visible edge of the waterfall marked in red). At the cutoff wavenumber κ_c , the slope of the energy spectrum $E(\kappa_c, t)$ over time has substantial similarity to the maximum vorticity curve in Figures 4.19, 4.20, 4.21. Likewise, the control spectrum $C(\kappa_c, t)$ tracks the initial vorticity minimum and upholds an asymptotically constant level as soon as the IPR is reached. The above observed reduction to SRT BGK collision in the sense of an MRF scheme is thus also observed for Fourier transformed quantities. Further, the influence of

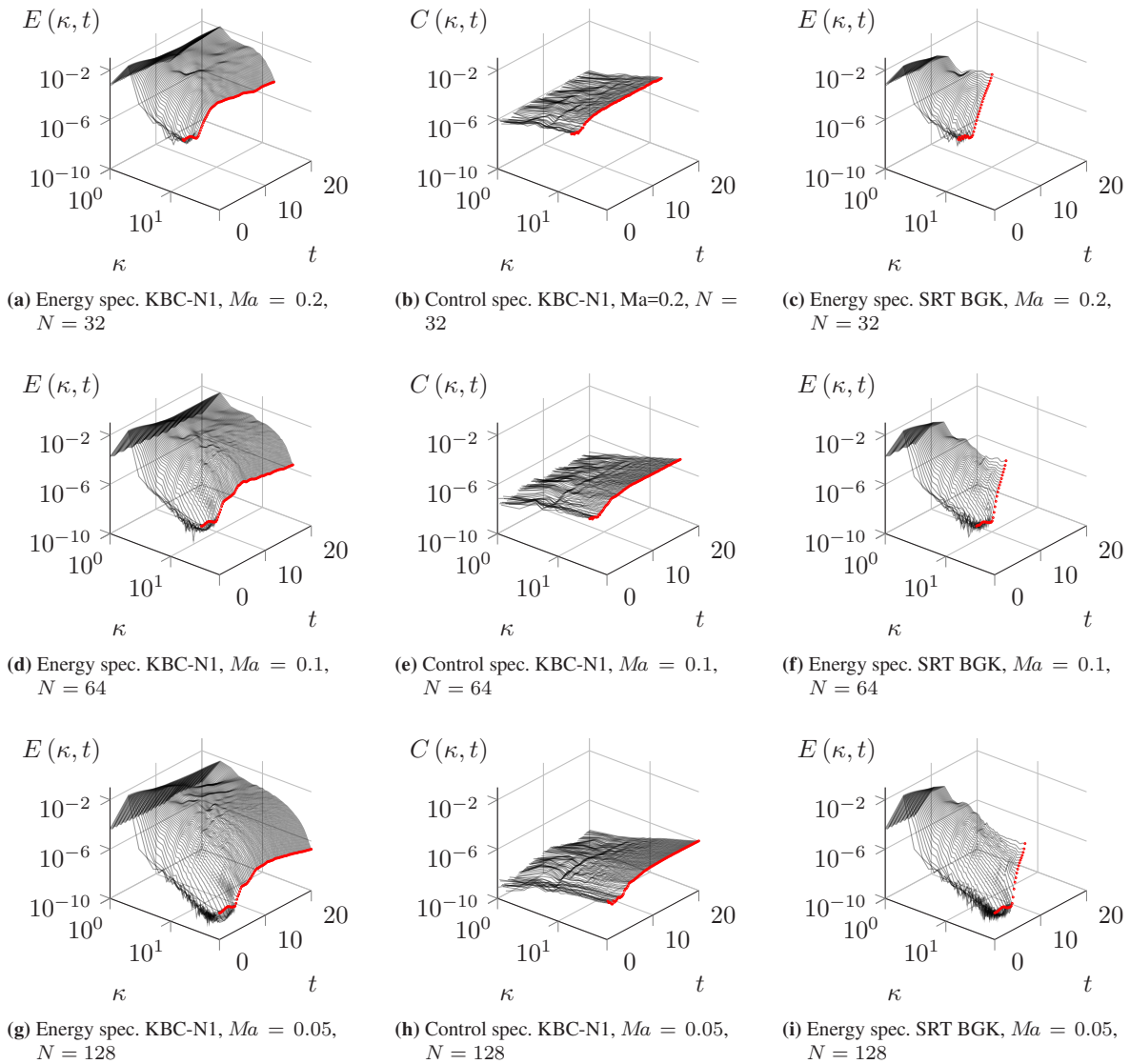


Figure 4.25: Energy spectra (4.26) and control spectra (4.30) for KBC-N1 scheme (left and middle column) as well as energy spectra (4.26) for SRT BGK collision (right column) of the TGV flow simulations at $Re = 6000$ in DS (top to bottom) for $(Ma, N) \in \{(0.2, 32), (0.1, 64), (0.05, 128)\}$. The red circles denote the values of the spectra at the respective cutoff wavenumber $\kappa_c = N/2$.

the entropy controlled stabilization is found to be connected to the underresolved vorticity via being maximal at large wavenumbers near the cutoff.

For the purpose of cross-comparing the energy spectra produced by the SRT BGK and the KBC-N1 relaxation, Figure 4.26 shows waterfall sections at the latest stable time steps of the SRT BGK simulations before divergence occurs. Only DS parameter configurations are shown for each Reynolds number. The reduction of the magnitude of the control spectrum is clearly visible (row-wise, left to right). For highly resolved settings, the control spectrum is thus expected to be constantly zero in machine precision as already indicated by the convergence of $|2 - \bar{\gamma}^*| \searrow 0$. Additionally, a common intersection point of the control spectrum and the energy spectrum of the KBC-N1 scheme at the respective cutoff wavenumber for almost all shown parameters is observed. The only exception for this observation is the configuration where the SRT BGK collision is stable (Figure 4.26c) and the intersection point is shifted to smaller $\kappa < \kappa_c$. For this less underresolved setting the production of smoothed energy and control spectra for both collision schemes is also noticeable. In conclusion, the asymptotic power-law form of all three spectra is well pronounced and

suggests that the control spectrum approximates $C(\kappa, \cdot) = \mathcal{O}(\kappa^{5/3})$ for a further refinement of the space-time mesh and an inverse increase of the Reynolds number at the same time.

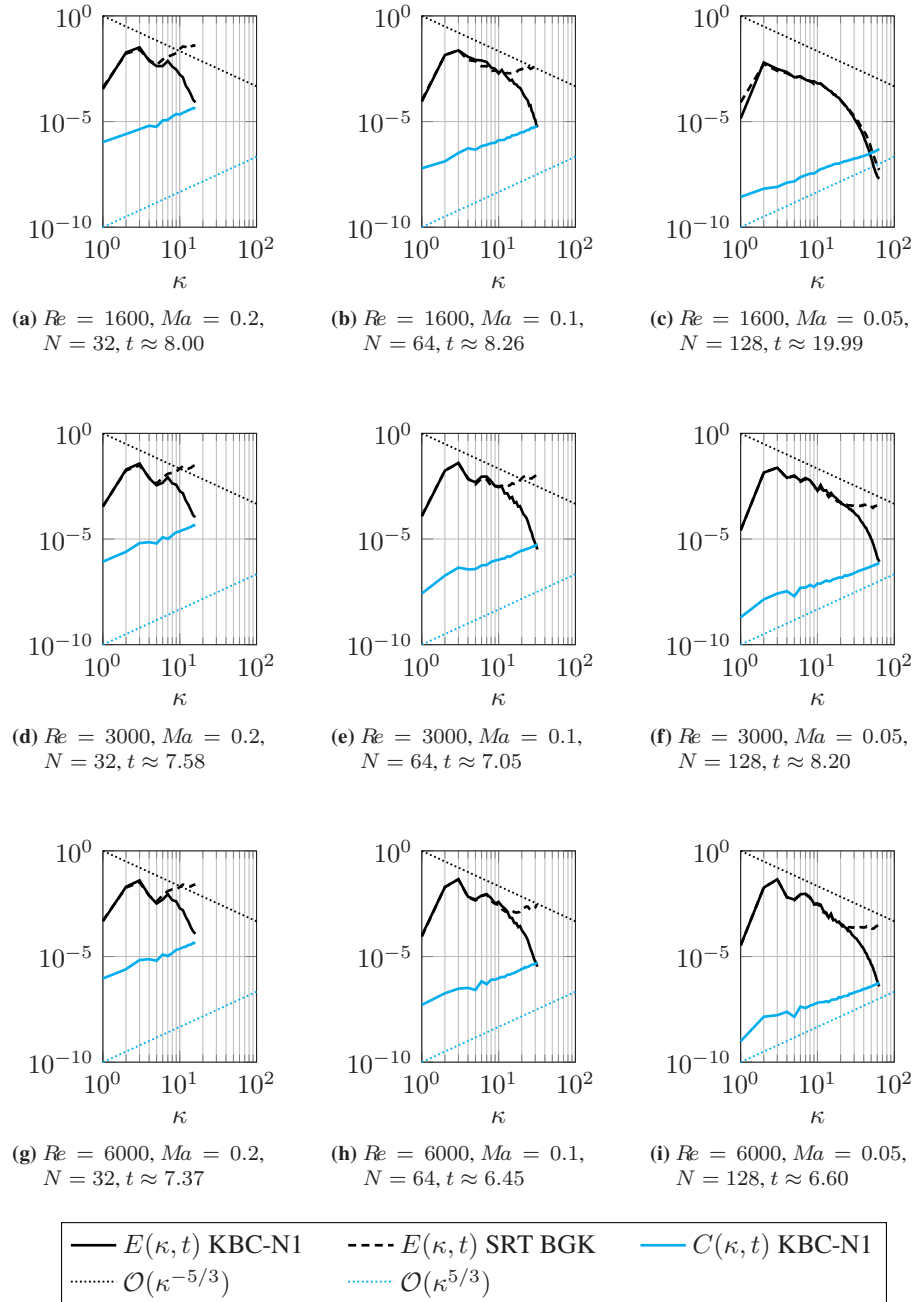


Figure 4.26: Computed energy spectra $E(\kappa, t)$ and control spectra $E(\kappa, t)$ of KBC-N1 and energy spectra $E(\kappa, t)$ of SRT BGK plotted at the last stable SRT BGK time step, respectively for several $Re = 1600, 3000, 6000$ (top to bottom) in DS $(Ma, N) \in \{(0.2, 32), (0.1, 64), (0.05, 128)\}$ (left to right).

4.3.4.5 Experimental order of convergence

The convergence of the KBC-N1 LBM is experimentally studied via computing the time dependent relative error

$$\text{err}(\epsilon_{\text{tot}}(t)) = \frac{|\epsilon_{\text{tot}}(t) - \epsilon_{\text{tot}}^*(t)|}{|\epsilon_{\text{tot}}^*(t)|} \quad (4.48)$$

and the temporal L^2 -error $\text{err}_{L^2}(\epsilon_{\text{tot}})$ (4.33) with respect to the psDNS solution [61]. Figure 4.27 visualizes the strong

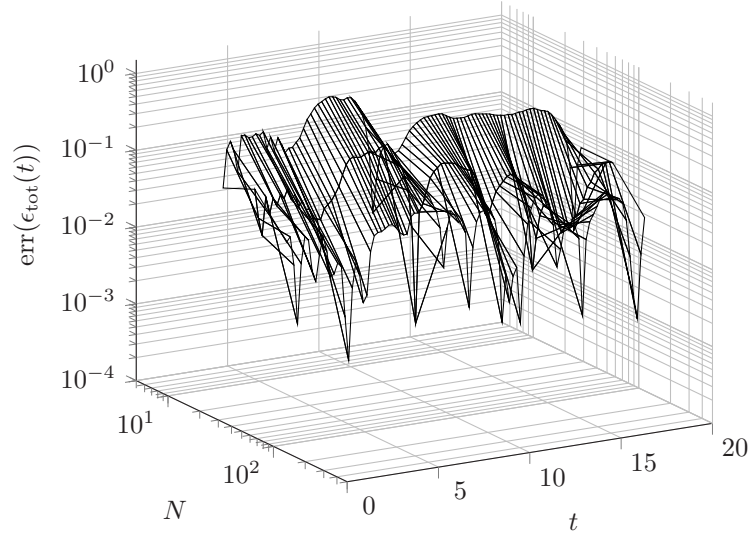


Figure 4.27: Time dependent error of total dissipation rate $\text{err}(\epsilon_{\text{tot}})$ of the KBC-N1 scheme with respect to the psDNS reference [61]. Discretization parameters are chosen from Table 4.10 in DS, hence $(Ma, N) \in \{(0.2, 32), (0.1, 64), (0.05, 128)\}$. Only a subsequence of time steps $t \in [0.1, 19.7]$ is shown with a step size of $\Delta t = 0.2$.

temporal dependence of the error values for discretization parameters in DS. Figure 4.28 plots the section lines of for several resolutions in one plane. The error behavior is visibly more structured in before and in the IPR ($t \in (0, 7)$). The peak region of the total dissipation rate ($t \approx 9$) induces a very pronounced disturbance of the error landscape. A second increased error region in this sense is located from $t \approx 14$ onwards. These observations indicate that a time averaged error of an integral quantity might not be representative for the error behavior in subintervals in the time domain. The effect of the temporal variation in the error magnitude on the EOC is visible in Figure 4.29. The time dependent EOC oscillates between superquadratic and even divergence in the region around the peak of the total dissipation rate. Still, on average the EOC ranges between one and two. Table 4.11 gives sample data for the local in time EOC and the EOC computed with the L^2 -error.

The present observation of local in time second order spatial accuracy of the KBC-N1 LBM toward the incompressible NSE solution approximated with a psDNS matches the results from Bösch *et al.* [36]. In the latter, a local consistency error to high resolution SRT BGK results has been computed and found to be of second order for initial time steps

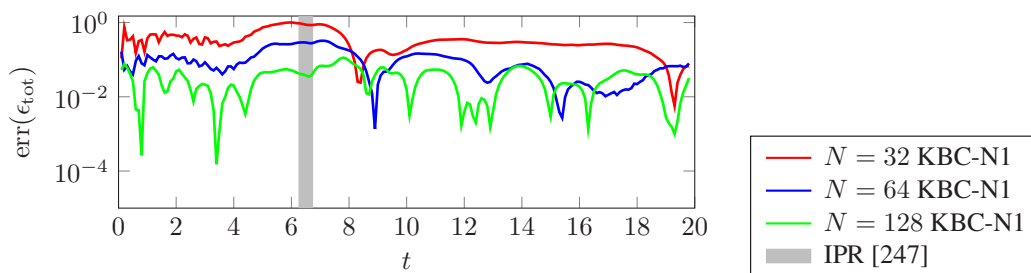


Figure 4.28: Time dependent error of total dissipation rate $\text{err}(\epsilon_{\text{tot}}(t))$ of the KBC-N1 scheme with respect to the 'psDNS reference [61].

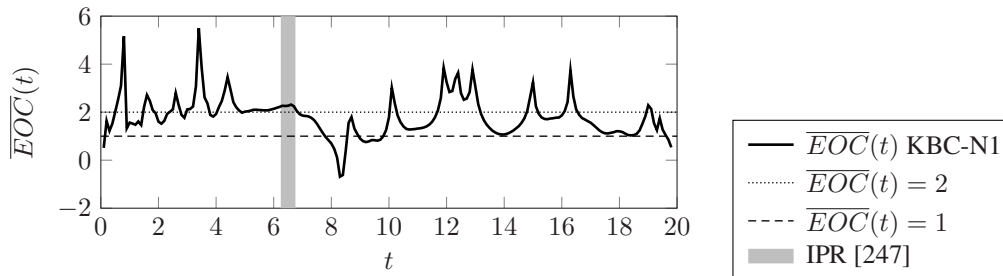


Figure 4.29: Time dependent EOC of total dissipation rate $\text{err}(\epsilon_{\text{tot}})$ of KBC-N1 with respect to psDNS reference [61].

Table 4.11: Sample error data of the KBC-N1 scheme with respect to the psDNS reference [61] with computed EOC values locally $\overline{EOC}(t)$ (for dedicated points in time $t_1 = 1, t_2 = 6, t_3 = 11, t_4 = 16$) and on average \overline{EOC} for $t \in [0.1, 19.8]$.

(N, Ma)	$\text{err}(\epsilon_{\text{tot}}(t))$				$\text{err}_{L^2}(\epsilon_{\text{tot}})$
	$t = t_1$	$t = t_2$	$t = t_3$	$t = t_4$	$t \in [0.1, 19.8]$
(32, 0.2)	3.75×10^{-1}	1.00×10^0	3.35×10^{-1}	2.46×10^{-1}	3.97×10^{-1}
(64, 0.1)	1.33×10^{-1}	2.63×10^{-1}	1.39×10^{-1}	2.53×10^{-2}	1.41×10^{-1}
(128, 0.05)	4.30×10^{-2}	5.18×10^{-2}	5.40×10^{-2}	1.86×10^{-2}	4.95×10^{-2}
$\overline{EOC}(t)$	1.56	2.13	1.31	1.86	—
\overline{EOC}	—	—	—	—	1.50

$t < 1$. In contrast to that, the present work shows a local and an averaged accuracy error toward the actually targeted PDE (2.12). It thus becomes clear from the present results, that averaging the error over time results in an order reduction by approximately 0.5. The variation of magnitude in the peak region of the computed total dissipation rate is exemplarily responsible for the error reduction. We attribute this time delay in the approximation of the time dependent total dissipation rate to the consistency reduction of the SRT BGK collision to first order in time in DS. Nonetheless, based on the numerically observed consistency of order two in [36], and the here measured local and averaged accuracy, it can be concluded that the space-time dependent relaxation functions for the kinetic moments increase the stability drastically and do not overly affect the EOC.

4.3.5 Computation of statistical solutions

Computing statistical solutions to the incompressible NSE (2.12) and the incompressible EE ($\nu \searrow 0$) with numerical simulations poses an extreme challenge due to the tremendous number of floating point operations required and the thus drastically increased energy-to-solution. Applying SLMC methods to evolve a sufficiently large number of random samples of \mathbf{u}_0 in time with a deterministic solver brings forth a quickly increasing amount of computations. Several approaches have been made to meet this challenge. Combined with multi level Monte Carlo (MLMC) methods, a finite difference discretization of the vorticity form of the incompressible NSE for $d = 2$ with periodic boundaries has been proposed in [176]. In [18], statistical solutions of the incompressible NSE for $d = 2$ with boundaries are computed with SLMC and an $H(\text{div})$ -based finite element method. Statistical solutions to the incompressible EE for $d = 2$ with periodic boundaries have been approximated successfully in [173] via combining MC with a deterministic spectral hyperviscosity method. The implementation of these methods for periodic incompressible flows has been extended to $d = 3$ within the framework azeban⁵ [220]. Besides, statistical solutions of two-dimensional compressible NSE have been approximated with hp -MLMC and discontinuous Galerkin methods [24]. Further, in [25] methods of uncertainty quantification (UQ) for approximating the three-dimensional compressible NSE have been implemented

⁵ Tobias Rohner, azeban: a spectral viscosity method, <https://github.com/TobiasRohner/azaban> (Accessed April 2023)

for the execution on HPC machines. For the computation of three-dimensional statistical solutions to the compressible EE, a combination of the FVM with SLMC, MLMC and quasi-randomized Monte Carlo (QMC) methods [183] is published in the open-source numerical framework Alsvinn [182]. To the knowledge of the author, LBM has not been used before to compute statistical solutions of incompressible NSE in three dimensions.

Although in general, combinations of LBM with both, intrusive and nonintrusive methods, have rarely been studied in the past, the few obtained results are throughout promising. For example, an LBM is proposed in [276] to approximate Galerkin projected stochastic convection–diffusion equations. The scheme offers rigorous weighted L^2 -stability and applicability to stochastic problems with complex boundaries. In [274] a probabilistic collocation method has been combined with LBM to efficiently obtain statistical properties for fluid flows through porous media. A reduction of the computational effort by $\geq \mathcal{O}(100)$ compared to SLMC LBM is reported for 2D flow simulations. Further, in [251] newly developed sparse quadrature and cubature rules are used in stochastic collocation methods combined with LBM for 2D cavity flows. Compared to SLMC, the reduced parameter grids show spectral convergence, achieving comparable performance to Smolyak sparse grid procedures.

Above, primary numerical evidence is given that the entropic estimate of the KBC collision successfully detects and counteracts high wavenumber spectral energy overloads and thus nonlinearly stabilizes the LBM. Additionally, the data-based convergence of integral turbulence quantities is approved up to second order when successively increasing resolutions in diffusive scaling. These advantages over the standard SRT BGK collision combined with the near-to-perfect parallelizability of LBM [166], render the KBC-N1 scheme a promising approach for computing statistical solutions explicitly for $d = 3$.

Hence, in the present work, the KBC-N1 LBM is used for the first time in an SLMC method to approximate statistical solutions to the three-dimensional incompressible EE. The latter is achieved via computing a sequence of sample solutions to the incompressible NSE (2.12) for increasing but fixed values of viscosity $\nu > 0$. The approximate sample solutions to (2.12) are obtained via statistically perturbing periodic TGV flow initial conditions and evolving them in time via the KBC-N1 LBM. If a power law in the energy spectrum is observed, we deduce that a weak solution is found for a deterministic sample initial condition. Conclusively, if the power law is also observed for an array of $M = N$ samples, this hypothetically implies that the second order structure functions of the statistical solution obey a scaling hypothesis as well. Thus, according to [85], we should approximate a strong (hence unique) statistical solution to the three-dimensional EE if $Re \rightarrow \infty$. Recalling Definition 2.2.1 which states that a periodic statistical solution to (2.12) (Foiş and Prodi [86, 87]) for fixed $\nu > 0$ is a family of probability measures $\mu^\nu = (\mu_t^\nu)_{0 \leq t \leq T}$ on $L^2_{\text{div}}(\Omega; U)$ with initial data

$$\mu_0^\nu \sim \mathcal{P}(L^2_{\text{div}}(\Omega; U)). \quad (4.49)$$

This initial distribution can be used with the solution operator S_t to compute the push-forward measure $S_t \mu_0^\nu$. In the present work, the probability measure μ^ν is approximated with M samples $\mathbf{u}^{(m)}$, where $m = 1, 2, \dots, M$, of mesh resolution N for $t \in I$ via

$$\mu_t^\nu \approx \mu_t^{N,M} := \frac{1}{M} \sum_{m=1}^M \delta_{\mathbf{u}^{(m)}(t)}, \quad (4.50)$$

where $\mathbf{u}^{(m)}$ is obtained from evolving independent and identically distributed (IID) initial data $\mathbf{u}_0^{(m)}$ of (2.12) in time with LBM, and $\delta_{\mathbf{u}^{(m)}(t)}$ is the Dirac measure (unit mass) at $\mathbf{u}^{(m)}(t)$.

The novel SLMC LBM prototype is implemented in OpenLB as arranged in Figure 3.9. Even though SLMC methods are computationally most expensive for UQ, it has been suggested [183] that for the particular purpose of computing statistical solutions of fluid flows governed by the NSE or the EE, whether compressible or incompressible, improvements such as QMC, or MLMC are not superior in terms of the ratio of convergence speed and computational effort. It is thus natural to use highly scalable methods akin to LBMs as the black box in a nonintrusive framework. Below,

a numerical experiment setup contained in the azeban repository⁶ [220] is computed with an LBM for the first time. The results serve as proof of concept that the KBC-N1 LBM is a suitable option for this purpose.

The TGV flow initial condition $\mathbf{u}_0 \in \mathbb{R}^d$ (4.18) is perturbed with $8d$ IID random variables

$$X_{\alpha,i,j,k} \in \mathcal{U}_{[-w,w]} \quad (4.51)$$

to obtain a randomized TGV (RTGV) initial velocity field

$$\mathbf{u}_0 = \mathbf{u}_0 + \mathbf{s} \in \mathbb{R}^d, \quad (4.52)$$

where the α th perturbation in $\mathbf{s} = (\mathbf{s}_\alpha)_{1 \leq \alpha \leq d}$ is

$$\mathbf{s}_\alpha = \frac{1}{8} \sum_{(i,j,k) \in \{0,1\}^3} X_{\alpha,i,j,k} \mathbf{a}_i(2x) \mathbf{a}_j(2y) \mathbf{a}_k(2z), \quad (4.53)$$

with

$$\mathbf{a}_i(x) = \begin{cases} \sin(x), & \text{if } i = 0, \\ \cos(x), & \text{if } i = 1. \end{cases} \quad (4.54)$$

The computational domain is still $\Omega = [0, 2\pi]^d$ and the support parameter of the uniform distribution is set to $w = 0.025$. Given this uncertainty in the initial data, we draw M samples

$$\left\{ \mathbf{u}_0^{(m)} \mid m = 1, 2, \dots, M \right\} \sim \mu_0^\nu \quad (4.55)$$

and Leray project each onto its solenoidal part $P_{\text{div}} \mathbf{u}_0^{(m)}$ via the projection operator

$$P_{\text{div}}: \begin{cases} L^2(\Omega; U) \rightarrow L^2_{\text{div}}(\Omega; U), \\ \mathbf{u} \mapsto P_{\text{div}} \mathbf{u} = \nabla_{\mathbf{x}} \times \boldsymbol{\psi}, \end{cases} \quad (4.56)$$

where the splitting

$$\mathbf{u} = \nabla_{\mathbf{x}} \phi + \nabla_{\mathbf{x}} \times \boldsymbol{\psi} \quad (4.57)$$

contains $\boldsymbol{\psi} \in H(\text{curl}, \Omega)$ and $\phi \in H^1(\Omega)$. Using the Fourier transform $\hat{\mathbf{u}}$ of \mathbf{u} , we replace the classical Poisson solver with an algebraic modification

$$P_{\text{div}} \hat{\mathbf{u}} = \left(\mathbf{1} - \frac{\mathbf{k} \otimes \mathbf{k}}{|\mathbf{k}|^2} \right) \cdot \hat{\mathbf{u}} \quad (4.58)$$

in wave space $\mathbf{k} \in \mathcal{K}$ and Fourier invert the result. All initial samples are thus Fourier transformed, Leray projected, Fourier inverted, consistently initialized and evolved in time with the deterministic KBC-N1 LBM until $t = T$ to obtain

$$\left\{ \mathbf{u}^{(m)}(t) \mid m = 1, 2, \dots, M \right\} \sim \mu_t^{N,M}. \quad (4.59)$$

Figure 4.30 highlights the random perturbation in the Q -criterion [131] of a single sample RTGV flow field, where

$$Q = \frac{1}{2} \left(\|\mathbf{D}\|_2^2 + \|\mathbf{N}\|_2^2 \right) \quad (4.60)$$

⁶ <https://github.com/TobiasRohner/azeban>

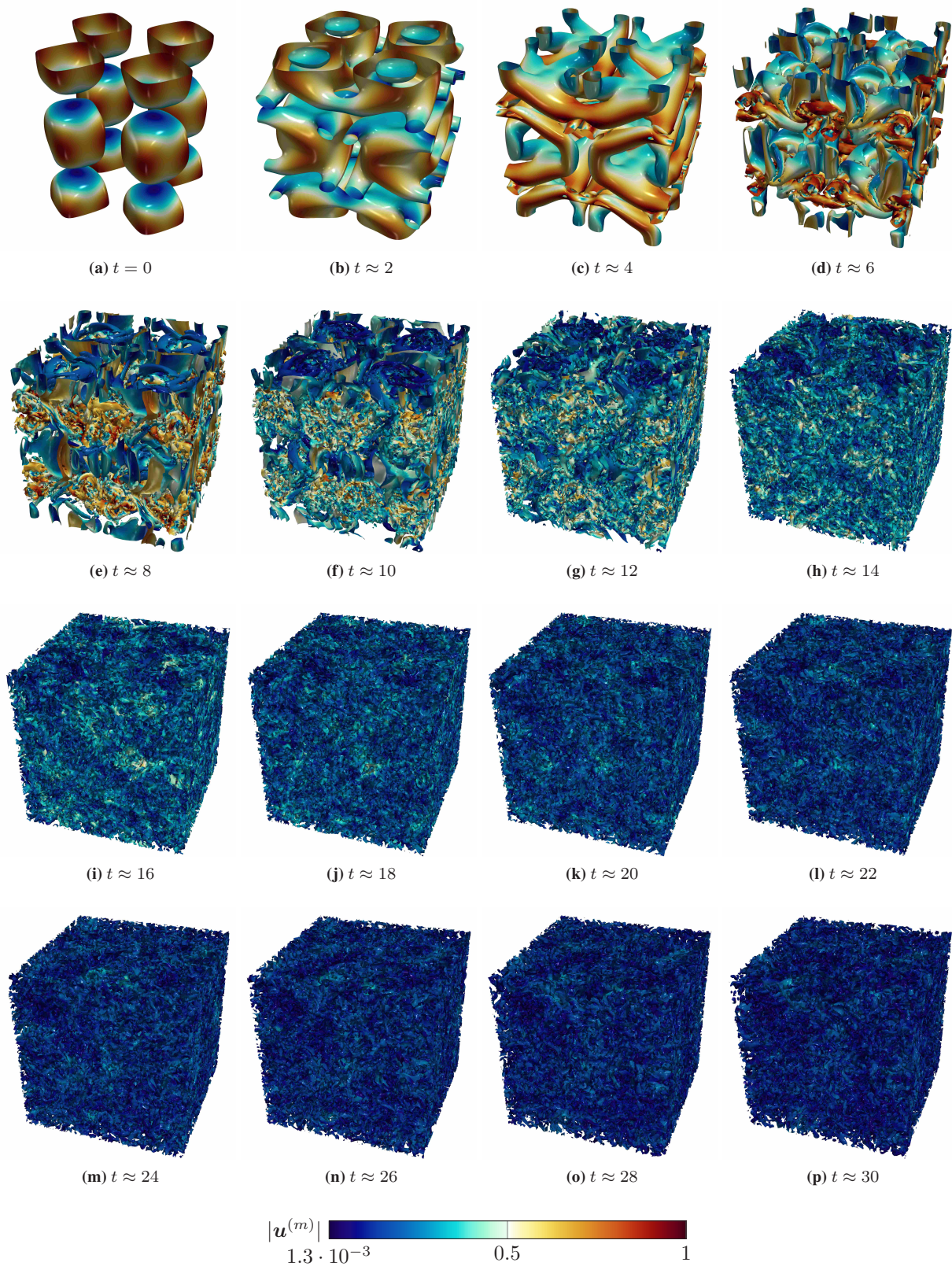


Figure 4.30: Time evolution of Q -criterion ($Q = 0.1$) colored by $|\mathbf{u}^{(m)}|$ of one RTGV flow sample computed with the KBC-N1 LBM for $Re = 10240$, resolution $N = 256$, and $Ma = 0.0125$.

is computed with the spectral norm $\|\cdot\|_2$ of the rate of strain (2.52) and its antisymmetric counterpart

$$\mathbf{N} = \frac{1}{2} \left[\nabla_{\mathbf{x}} \mathbf{u}^{(m)} - \left(\nabla_{\mathbf{x}} \mathbf{u}^{(m)} \right)^T \right]. \quad (4.61)$$

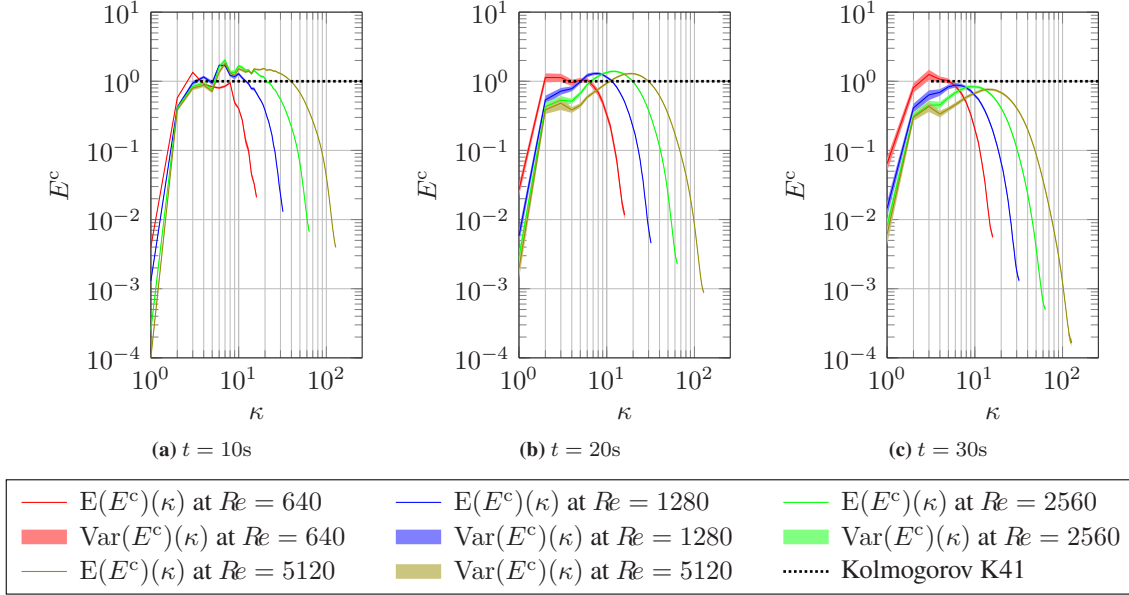


Figure 4.31: Mean (solid lines) and standard deviation (shaded areas) of compensated energy spectra of the RTGV flow field at several Reynolds numbers and time steps, computed with the novel SLMC LBM.

Figure 4.31 shows mean $E(\cdot)$ and variance $\text{Var}(\cdot)$ of the compensated energy spectra

$$E^c = C_{\text{Kol}}^{-1} \epsilon^{-2/3}(t) \kappa^{5/3} E(\kappa) \quad (4.62)$$

for four consecutive Reynolds numbers $Re = 20N$ in DS, where $N = 32, 64, 128, 256$. The K41 constant [155, 156] is $C_{\text{Kol}} = 1.5$, and the dissipation rate is taken from the deterministic inviscid high-resolution simulations by Fehn *et al.* [81]. Via connecting the Reynolds number and the grid resolution per spatial dimension, an inviscid limit is superimposed for $N \rightarrow \infty$. The amount of samples is chosen as $M = N$. An extended terminal time $T > 30$, which is larger than the commonly used values for benchmarking, results in fully developed small scales and a smooth energy cascade (see cyan squares in Figure 4.32).

Moreover, from Figure 4.31, it becomes evident that a sufficiently long simulation time horizon is necessary ($T \geq 30$) to propagate the initial perturbation \mathfrak{s} through the spectrum. The latter in turn shows an asymptotic trend toward the K41-predicted inertial subrange. Due to [173, Theorem 4.4, Remark 4.4, Remark 4.5] with $\beta = 5/6$ in the respective notation, we have that

$$E_T(\mu_t^\nu, \kappa) = \int_0^T \int_{L_{\text{div}}^2} E(\kappa) d\mu_t^\nu(\mathbf{u}) dt \lesssim \kappa^{-2\beta} \Rightarrow S^2(T, r) \lesssim r^{\beta-1/2}, \quad \text{if } 1 < 2\beta < 3, \quad (4.63)$$

where $S^2(T, r)$ is a global structure function of order two (see for example [173] and references therein). Hence, in case of approximating the local structure functions of second order with $S_{r,t}^2(\mu_t^{N,M})$, it is conjectured that a similar scaling will appear. In turn, a statistical solution of the incompressible Euler equation is approximated as $\nu \searrow 0$. In conclusion of the present energy spectrum decay for randomized initial data, the above results suggest that the SLMC

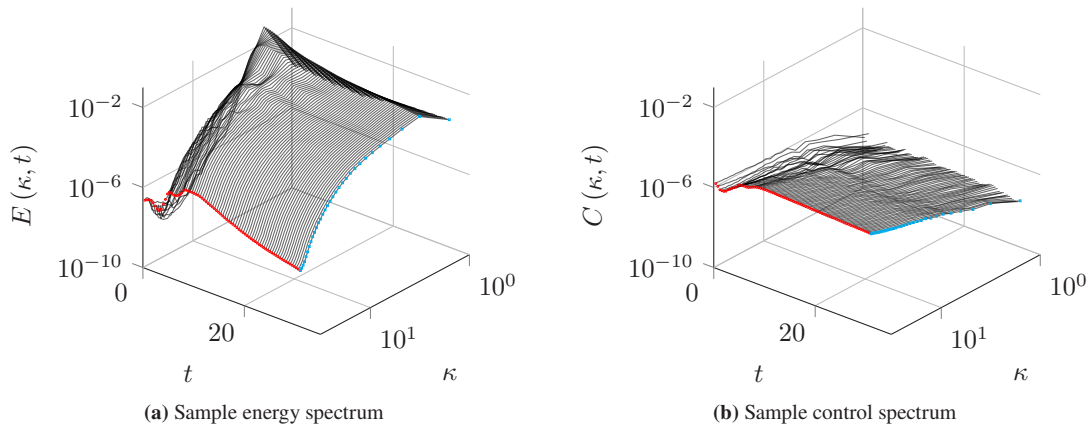


Figure 4.32: Sample spectra of (a) energy (4.26) and (b) control spectra (4.30) of the RTGV flow at $Re = 1280$ computed with the KBC-N1 LBM for $(Ma, N) = (0.1, 64)$. The red circles denote the values of the spectra at the respective cutoff wavenumber $\kappa_c = 1/N$. The cyan squares denote the spectra at $t = T \approx 31$.

LBM is well-suited for computing statistical solutions to three-dimensional incompressible fluid flows. Forthcoming research will put in evidence the structure function decay and provide runtime comparisons to conventional solvers.

4.4 Time-filtered Navier–Stokes equations

This section summarizes the results from Simonis *et al.* [233] that are obtained from conducting benchmark tests for artificial DHIT to evaluate the quality of the proposed TLES LBM (see Section 3.3.1.5) with respect to DNS results with SEM⁷. The numerical experiments are based on approximating the incompressible NSE (2.12) with deterministic TGV flow initial data (4.18).

4.4.1 Reference data

In the following, a high resolution DNS with the SEM, resolving the appearing scales, serves as a reference. The simulations denoted with SEM were performed using the spectral element code Nek5000. The solver employs third order backward differentiation formulas in time and a spatial discretization which depends on the chosen polynomial order [65]. Two Reynolds numbers are tested, $Re = 800$ and $Re = 3000$, respectively. The discretization for the former is based on 18 spectral elements in each coordinate direction with a polynomial order of seven, which equals a number of $N = 127$ grid points. For the second tested Reynolds number $Re = 3000$, the resolution of the reference SEM DNS is $N = 351$ in each coordinate direction, consisting of 50 elements and a polynomial order of seven. Both reference simulations use a time step size of $\Delta t = 0.001$. Figure 4.11 exemplarily visualizes the time-dependent spectra of energy and dissipation for $Re = 800$ computed with SEM DNS. The sampling rate of the kinetic energy is 0.05. The time dependence of the TGV flow in terms of spectral properties is clearly evident. It is also notable that, due to the low Reynolds number, the majority of dissipation takes place within the low to intermediate wavenumber region (see Figure 4.11b).

⁷ Large parts of the text, figures and tables in this Section are reproduced from [233], Copyright (2022), with permission from the authors and Elsevier Inc.

4.4.2 Model calibration

To scrutinize the numerical behavior of the TLES LBM proposed in Section 3.3.1.5, a parameter study is conducted. The observed effects of the temporal filter for varying lattice Mach number and filter width are categorized below. Therefore, ϵ_{tot} , ϵ_{res} , ϵ_{mod} , E , and D are evaluated for a Reynolds number of $Re = 800$. If not stated otherwise, all quantities are deconvolved according to (3.291). For clarity, Table 4.12 summarizes a selection of conversion factors for the TLES LBM used in the present work. All LBM computations are carried out with OpenLB [161, 162] on at most 75 nodes with two Intel Xeon E5-2660 v3 each.

Table 4.12: Summary of TLES LBM discretization parameters. This table is reproduced from [233], Copyright (2022), with permission from the authors and Elsevier Inc.

N	u^L	Ma	Δx	Δt	τ	
					$Re = 800$	$Re = 3000$
64	0.11547	0.2	0.09973	0.01154	0.50434	0.50116
	0.08660	0.15	0.09973	0.00864	0.50326	0.50087
	0.05776	0.1	0.09973	0.00576	0.50217	0.50058
	0.04330	0.075	0.09973	0.00432	0.50163	0.50043
	0.02887	0.05	0.09973	0.00288	0.50109	0.50029
128	0.11547	0.2	0.04947	0.00571	0.50875	0.50233
	0.08660	0.15	0.04947	0.00428	0.50656	0.50175
	0.05776	0.1	0.04947	0.00288	0.50438	0.50117
	0.04330	0.075	0.04947	0.00214	0.50328	0.50088
	0.02887	0.05	0.04947	0.00144	0.50219	0.50058

4.4.2.1 Filter width

Let

$$\Theta = \tilde{\Theta} \Delta t, \quad (4.64)$$

where $\tilde{\Theta} > 0$ denotes the dimensionless filter width. To calibrate the model, we test a sequence of $\tilde{\Theta} = 5, 10, 20, 40$ in the MRT LBM TLES with a fixed Mach number of $Ma = 0.1$ and a resolution of $N = 64$ for the TGV flow with $Re = 800$.

The resulting effects on dissipative properties and spectral energy recovery are plotted in Figures 4.34 and 4.33, respectively. For $\tilde{\Theta} = 5$ the impact of the TLES on the dissipation rate is marginally visible when comparing Figures 4.34a and 4.34b. Also the spectral properties of underresolved DNS (UDNS) and TLES are similar for the smallest investigated filter width. Nevertheless, a slight increase of ϵ_{mod} shortly after the initialization is evident. In case of $\tilde{\Theta} = 10, 20$, the peak of ϵ_{tot} approaches the reference DNS solution, see Figures 4.34c and 4.34d. At the same time, the model dissipation rate oscillations in the initial time zone accumulate until a complete overdrive, which proceeds with time, is visible for $\tilde{\Theta} = 40$ (Figure 4.34e). Conclusively it can be stated that for $\tilde{\Theta} > 10$ the dissipation rate oscillations are clearly unphysical. The effects also project to wavespace, where a respective increase within the energy (Figure 4.33a) as well as the dissipation spectrum (Figure 4.33b) appears at high wavenumbers $\kappa \gtrsim 30$. Further, Figure 4.33 suggests that for $\tilde{\Theta} \rightarrow 40$ the model draws energy from the inertial range and transports it to small scales. Hence, increasing the filter width leads to a larger amount of energy injection into the dissipation range.

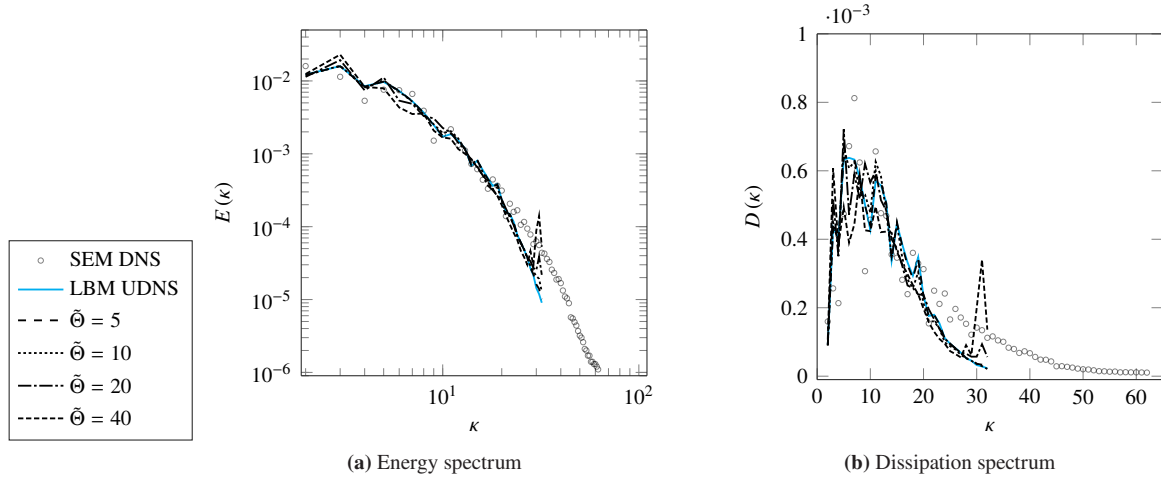


Figure 4.33: Energy spectrum $E(\kappa)$ (a) and dissipation spectrum $D(\kappa)$ (b) at $t = 9$ for the TGV flow with $Re = 800$. Computations for $Ma = 0.1$ and $N = 64$ with the LBM as UDNS and TLES with $\tilde{\Theta} = 5, 10, 20, 40$ in comparison to the SEM DNS with a corresponding resolution of $N = 127$. This figure is reproduced from [233], Copyright (2022), with permission from the authors and Elsevier Inc.

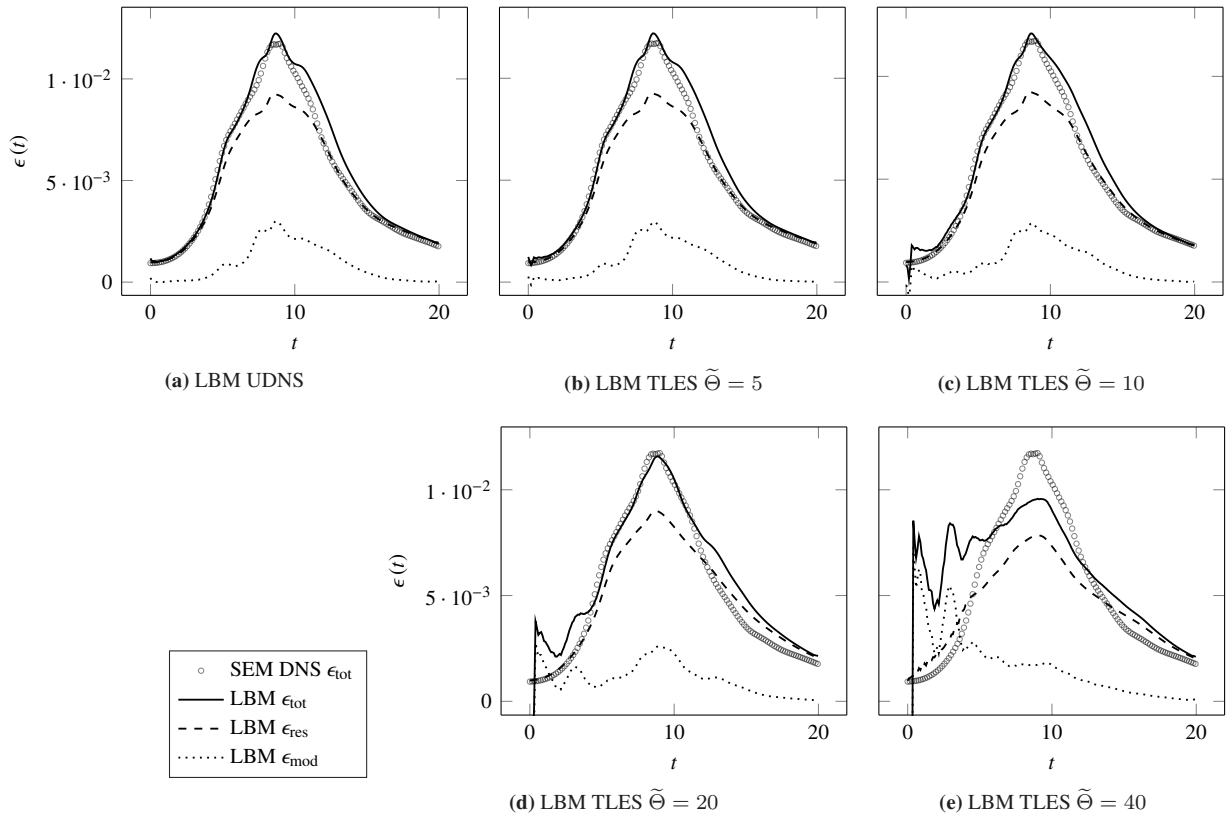


Figure 4.34: Total, resolved and model dissipation rate for the TGV flow with $Re = 800$. Computations for $Ma = 0.1$ and $N = 64$ with the LBM as UDNS (a) and TLES with $\tilde{\Theta} = 5, 10, 20, 40$ (b-e, respectively) in comparison to the SEM DNS with a corresponding resolution of $N = 127$. This figure is reproduced from [233], Copyright (2022), with permission from the authors and Elsevier Inc.

Conclusively, since the spectra remain close to the UDNS, initial oscillations are kept in a reasonable intensity and the dissipation rate peak is a closer match than without the model, the filter width is set to $\tilde{\Theta} = 10$ for all following LBM TLES runs.

4.4.2.2 Lattice Mach number dependency

We test the method for a range of $Ma = 0.05, 0.075, 0.1, 0.15, 0.2$ to investigate the dependency on the timestep size which changes along the Mach number variation. Due to the fact that orthogonal moment MRT LBMs exhibit lattice Mach number instabilities [63, 114], the free parameters of the MRT scheme are modified toward the MRF collision as proposed in Section 3.2.7.1 to obtain stable results. The optimized third order relaxation frequencies proposed by Chávez-Modena *et al.* [52] are Ma -dependent [232]. To respect this dependency, a polynomial fit is used as described in Section 4.3.3.3, assigning the corresponding value for each of the tested Ma to the third order relaxation frequencies. Overall, the here used relaxation frequencies are at second order $s_e = 1.19$ (static) and $s_P = 2c_s^2/(2\nu + c_s^2)$ (shear viscosity conforming to (3.289)), third order $s_q(Ma) = \hat{s}_q^{\text{pf3}}(Ma)$ and $s_\mu(Ma) = \hat{s}_\mu^{\text{pf3}}(Ma)$ (dynamic relaxation functions (4.40) and (4.39), respectively), and fourth order $s_\varepsilon = s_\Pi = 1.4$ (static). A detailed analysis of the such obtained model is given above (Section 4.3.3 and Section 4.3.3.3) and in [232].

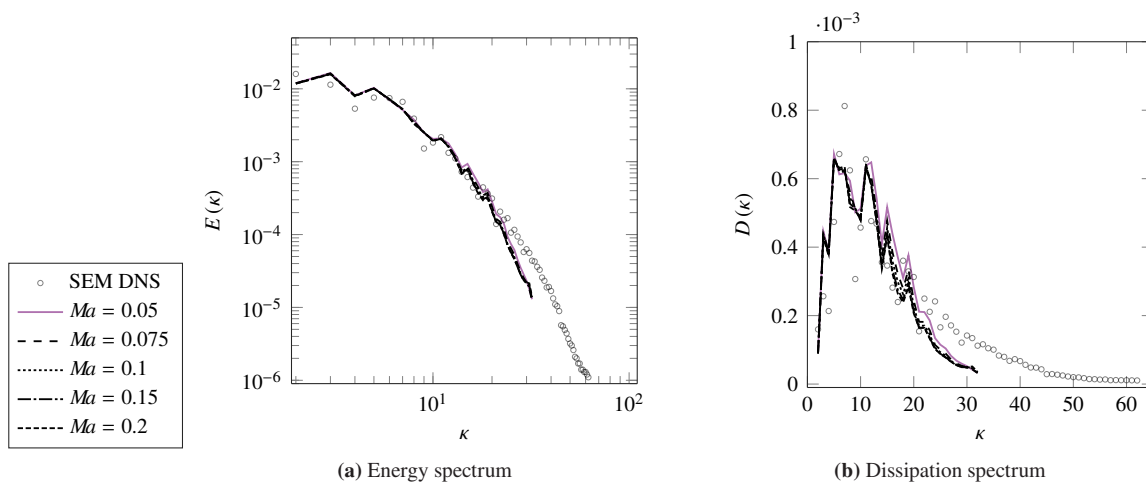


Figure 4.35: Energy spectrum $E(\kappa)$ (a) and dissipation spectrum $D(\kappa)$ (b) at $t = 9$ for the TGV flow with $Re = 800$. Computations for $N = 64$ with the LBM TLES ($\tilde{\Theta} = 10$) for $Ma = 0.05, 0.075, 0.1, 0.15, 0.2$ in comparison to the SEM DNS with a corresponding resolution of $N = 127$. This figure is reproduced from [233], Copyright (2022), with permission from the authors and Elsevier Inc.

Figure 4.36 summarizes the dissipation rate changes along the variation of Ma . Spectral energy and dissipation are visualized in Figure 4.35. Tracking the previous observations for the filter width variation, we detect an amplification of the dissipation rate oscillations at $t \rightarrow 0$ with increasing Ma (see e.g. Figure 4.36d). Though a similar effect of analogously increasing energy and dissipation in high wavenumbers is shown in Figure 4.35, the spectral quantities are less affected by varying Ma .

In contrast to the unphysical oscillations for increasing Ma , the lowest evaluated Mach number causes clearly negative model dissipation. This behavior roots in the model's compensation of an unphysically increased resolved dissipation rate for $t > 10$ (see Figure 4.36a). The fact that the model is applied to the TGV flow, where the effective Mach number decreases with time underlines the statement. The lowest tested Mach number which does not exhibit an overly increased dissipation rate tail is $Ma = 0.1$. Another argument for choosing Ma rather smaller than the usually incompressible enough value of 0.3 is constituted by the fact that we obtained an expression for the residual stress \mathbf{T} from the filtered incompressible NSE in the first place. Contrary to this, for fixed discretization, the LBM forms a moment hierarchy which approximates the weakly compressible NSE [184], solely reaching the incompressible limit under DS [172], i.e. diminishing the Mach number via $\Delta t = \mathcal{O}(\Delta x^2)$ along $\Delta x \rightarrow 0$ (see Section 3).

As a compromise between the computational effort, which increases with decreasing Mach number, and the circumstances addressed above, we fix $Ma = 0.1$ for the following simulations.

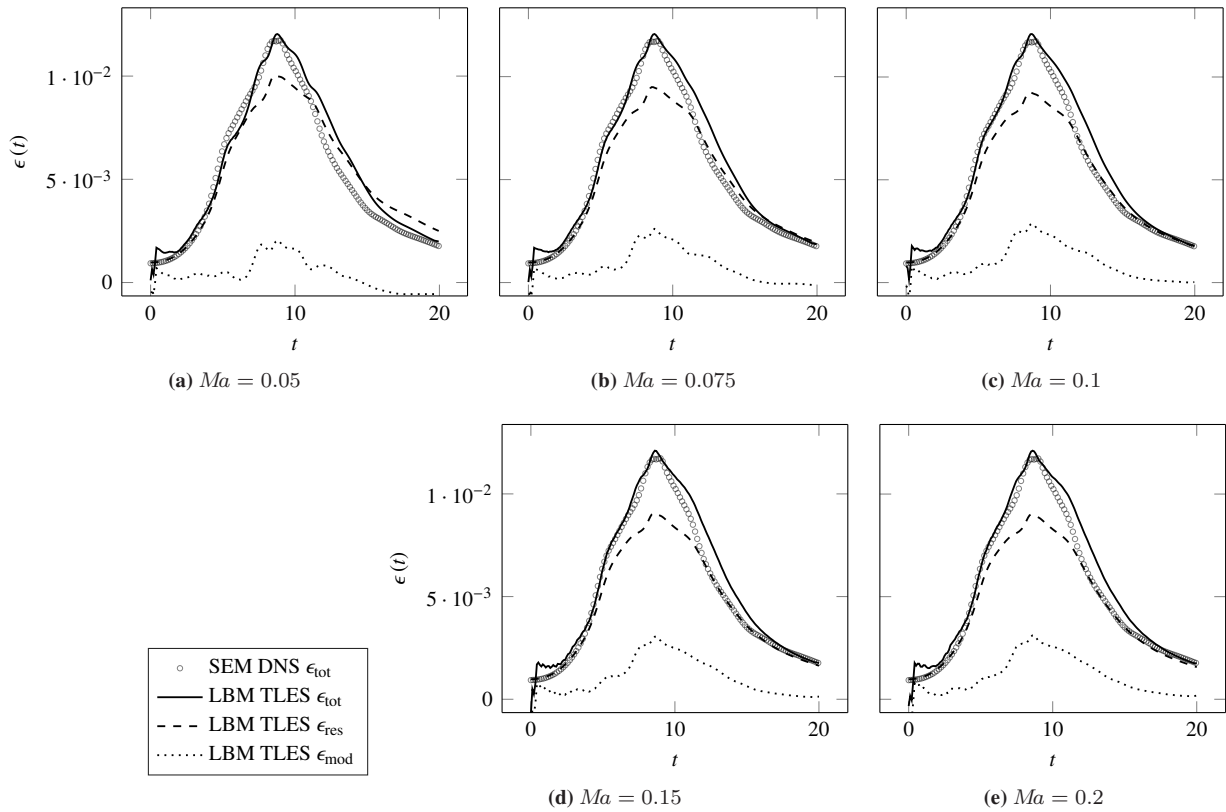


Figure 4.36: Total, resolved and model dissipation rate for the TGv flow with $Re = 800$. Computations for $N = 64$ with LBM TLES ($\tilde{\Theta} = 10$) for $Ma = 0.05, 0.075, 0.1, 0.15, 0.2$ (a-e, respectively) in comparison to the SEM DNS with a corresponding resolution of $N = 127$. This figure is reproduced from [233], Copyright (2022), with permission from the authors and Elsevier Inc.

4.4.2.3 Deconvolution of filtered quantities

Figure 4.37 gives an overview of all computed quantities in filtered and deconvolved form. With respect to the observations above (already in Section 4.3.4.2), it becomes clear that the initial dissipation rate deviation in Figure 4.37a roots in the LBM itself and is amplified by the turbulence model. In particular, despite initializing the velocity field, pressure and strain rate with respective populations, the intrinsic feature of LBMs applied to a nonstationary TEQ – transporting initialization errors with time throughout the whole simulation – remains present. Consequently, the first order finite differences in the evolution equation for \mathbf{T} (3.290) as well as in the discrete deconvolution (3.291) act as amplifiers for initialization errors of LBMs. The intensifying initial time oscillations with increased Mach numbers are also in line with this argument. A larger Ma increases Δt as well as the compressibility error, and consequently the initialization error [186]. In turn, larger filter widths amplify that error and lead to higher deviation at early timesteps.

Except for the initial dissipation rate oscillations and the corresponding spectra deviations at the highest wavenumbers $\kappa \approx 30$, only marginal differences are observable in Figure 4.37. Within the remaining region of resolved wavenumbers, the deconvolved and filtered spectra of energy (Figure 4.37b) and dissipation (Figure 4.37c), respectively, are overall in close agreement.

4.4.3 Comparison to the spectral element method

The Reynolds number is increased to $Re = 3000$ to reach the turbulent regime and shift the dissipation to higher wavenumbers. The optimal parameters for the LBM TLES with respect to above investigations where set to $\Theta = 10$ and $Ma = 0.1$.

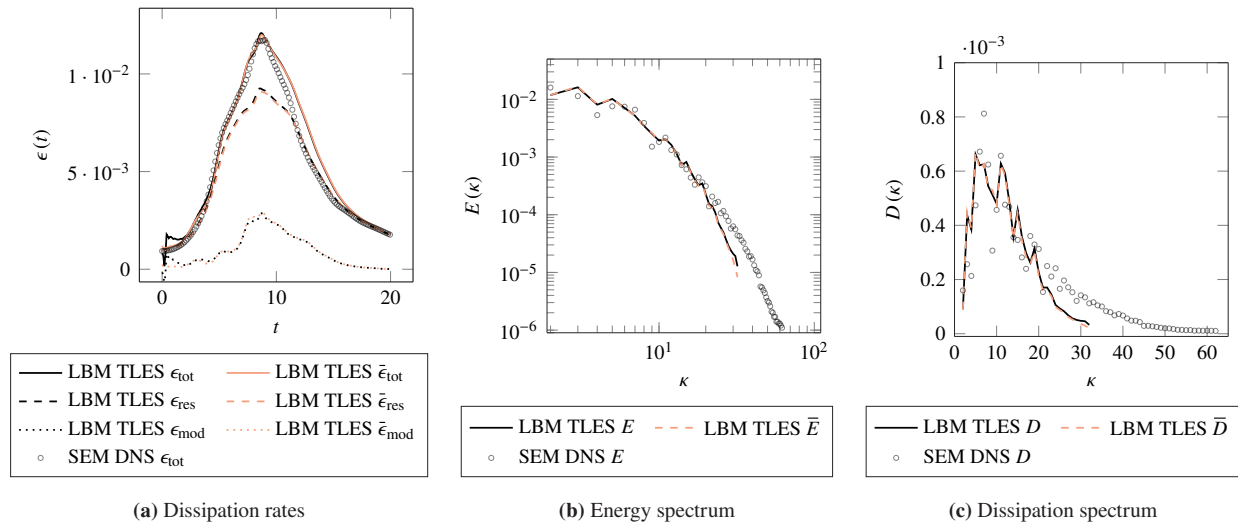


Figure 4.37: Dissipation rates $\epsilon_{\text{tot}}(t)$, $\epsilon_{\text{res}}(t)$, $\epsilon_{\text{mod}}(t)$ (a), energy spectrum $E(\kappa)$ (b) and dissipation spectrum $D(\kappa)$ (c) (at $t = 9$) for the TGv flow with $Re = 800$. Computations for $N = 64$ with the LBM TLES ($\Theta = 10$) for $Ma = 0.1$. Deconvolved and filtered quantities in comparison to the SEM DNS with a corresponding resolution of $N = 127$. This figure is reproduced from [233], Copyright (2022), with permission from the authors and Elsevier Inc.

A comparison to the recently proposed SEM TLES [200] is conducted. The only modification compared to the implementation in [200] is the regularization term. As expected, relaxing the unfiltered velocity fields to the filtered ones within the regularization, introduces a phase lag. Although its effect is negligible in statistically stationary test cases, it proved to be severe for the results of the TGv flow due to its transient nature. This effect can be prevented by using the regularization term from the temporal approximate deconvolution method [211]. In this term, the filtered fields are relaxed to their filtered approximate deconvolution.

To find common ground for both methods, the respective number of elements was chosen such that the overall resolution of the SEM closely matches the number of Cartesian gridpoints of the LBM. The resolution $N = 64$ of the UDNS and the TLES with the SEM consists of nine spectral elements in each coordinate direction and a polynomial order of seven. The parameters used for the SEM TLES comprise the filter width $\Theta = 10\Delta t$ and the regularization parameter $\chi = 4.0$, with a time step size of $\Delta t = 0.005$. In contrast to that, the resolution $N = 127$ of the UDNS and the TLES combined with the SEM consists of 18 spectral elements in each coordinate direction and a polynomial order of seven. The parameter choices for the SEM TLES in this case are $\Theta = 10\Delta t$, $\chi = 2.0$, and $\Delta t = 0.005$. Below, both, the underresolved DNS (denoted as UDNS) results and the TLES computations, for the SEM as well as the LBM, are cross-compared with respect to the reference high resolution SEM DNS.

4.4.3.1 Underresolved direct numerical simulation

Figure 4.38 summarizes dissipation rates, energy spectrum and dissipation spectrum for the TGv flow computed without turbulence model with the LBM and the SEM as UDNS for resolutions of $N = 64$ and $N \approx 128$, respectively.

Figure 4.38a gathers the dissipation rates ϵ_{tot} , ϵ_{mod} and ϵ_{res} computed with the LBM and ϵ_{tot} computed with the SEM, respectively. The total dissipation rates in the initial region of both methods are similar for each resolution. However, the peak region is underpredicted by the LBM in contrast to the SEM results. This effect is less pronounced for $N \approx 128$. For $N = 64$ the SEM seems to detect the dissipation rate peak better in terms of magnitude and narrowness around $t = 9$. Within the remaining time interval both methods show a certain variance from the DNS reference, where the LBM overpredicts and the SEM underpredicts the dissipation rate. For $N = 128$, the LBM approaches the peak magnitude of the dissipation rate and closely matches the slope in the time interval subsequent to the overpredicted plateau at $t \approx 13$. Similarly, the SEM closely follows the DNS roughly up to $t \approx 10$, and deviates from the reference

dissipation rate in the plateau region. However, the SEM also varies from the reference DNS in the final time interval by first underpredicting and then overpredicting the slope.

The qualities of each methods for the recovery of the energy spectrum can be observed in Figure 4.38b. Within the low wavenumber region, the SEM produces more accurate results than the LBM. This difference vanishes when increasing the resolution. In the high wavenumber region for $N = 64$, the SEM produces an energy pile-up, whereas the LBM predicts an early onset of the dissipation range with low energy levels. Increasing the resolution to $N \approx 128$ the SEM bends the pile-up toward the DNS which substantially increases the approximation quality. The energy spectrum recovered by the LBM still exhibits an early decay though its onset is shifted from $\kappa \approx 20$ (for $N = 64$) to $\kappa \approx 50$ (for $N = 128$).

For the dissipation spectra plotted in Figure 4.38c similar effects are visible. The characteristic differences between the methods in terms of a pile-up with the SEM versus an early energy dissipation with the LBM are clearly apparent for $N = 64$. The increased resolution $N \approx 128$ still exhibits a separation of curves at higher wavenumbers. Up to $\kappa \approx 40$ both methods closely follow the DNS reference, where the LBM slightly overpredicts the DNS dissipation spectrum for $\kappa \gtrsim 25$. Afterwards, the SEM dissipation spectrum still roughly matches the reference slope with a diminished pile-up at the highest captured wavenumbers, whereas the LBM triggers an early onset of flattening.

Overall, both, the LBM and the SEM, recover the tested quantities remarkably well in comparison to results computed with other methods but similar resolutions found in the literature [79, 90]. Distinct attributes can be observed which root in the derivation of each method and leave scope for specific improvements or additional features.

4.4.3.2 Temporal large eddy simulation

Figure 4.39 summarizes the dissipation rates, as well as the energy spectra and the dissipation spectra for the TGV flow computed with TLES based on the LBM and the SEM for resolutions of $N = 64$ and $N \approx 128$, respectively. With respect to the dissipation rates plotted in Figure 4.39a, the LBM TLES recovers the formation of a distinct peak around $t \approx 9$ already at a resolution of $N = 64$, although with slightly differing magnitude. In contrast to that, the SEM exhibits a distorted crown within the peak region. As expected, initial time oscillations are clearly visible for the LBM. The SEM shows similar but far less pronounced issues. The dissipation rate tail is overpredicted by the LBM and slightly underpredicted by the SEM. Increasing the resolution to $N \approx 128$, both methods closely follow the DNS reference up to $t \approx 9$. Afterwards, the LBM fails in capturing the plateau subsequent to the peak region, but aligns again with the reference slope for $t \gtrsim 13$. The SEM overpredicts and then underpredicts the DNS reference within this region.

Comparing the energy spectra in Figure 4.39b for $N = 64$, the distinct features of each method reappear, i.e. the SEM forms an energy pile-up at high wave-numbers, whereas the LBM induces an early energy dissipation in that region. Again, these effects shift and decrease with an increased resolution of $N \approx 128$. The dissipation spectra produced with the TLES (see Figure 4.39c) also exhibit similar properties as for UDNS. Nevertheless, a trend toward a closer match of the DNS reference is visible. The dissipation pile-up of the SEM TLES is less distinctive compared to the SEM UDNS. Analogously, the LBM TLES flattening is slightly shifted upwards compared to the LBM UDNS.

Overall, the most prominent differences between the LBM TLES and the LBM UDNS can be observed in the dissipation rates. Comparing UDNS and TLES results with the LBM for $N = 64$ (Figure 4.38a vs Figure 4.39a, left respectively), we notice a sharpening effect of ϵ_{tot} in the peak region toward the DNS reference. This observation can be linked to ϵ_{mod} , which forms a peak closer to the reference peak at $t \approx 9$ with the TLES than with the UDNS. At the same time, the resolved dissipation rate ϵ_{res} appears to be smoother for the TLES LBM than for the UDNS LBM. Similarly, the SEM TLES results show better agreement with the DNS values for ϵ_{tot} than the SEM UDNS data.

Hence, for both methods, the TLES evidently improves the dissipation rate recovery, while upholding or slightly enhancing the good approximation of DNS reference energy and dissipation spectra. This improvement can be traced

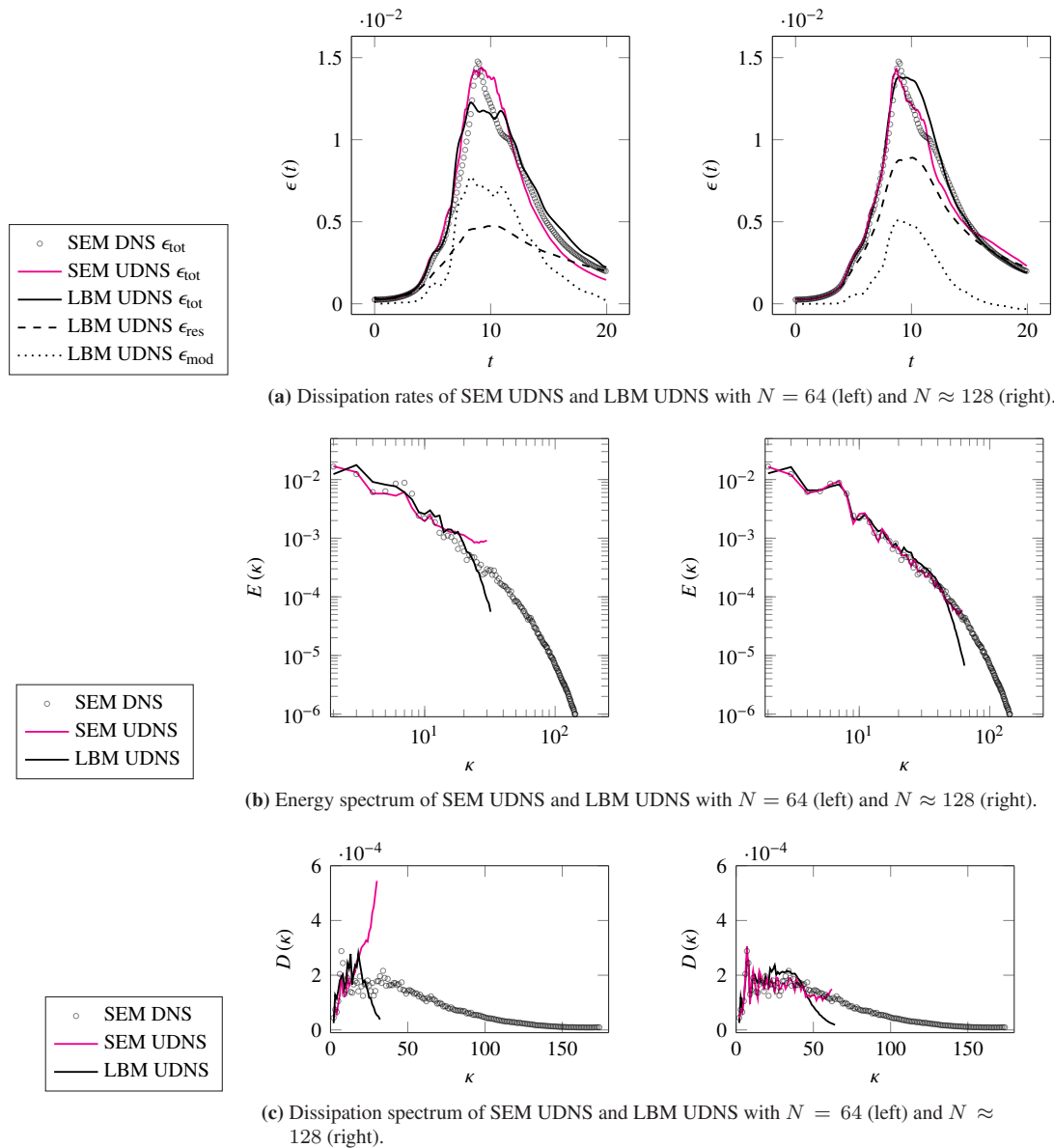


Figure 4.38: Dissipation rates $\epsilon_{\text{tot}}(t)$, $\epsilon_{\text{res}}(t)$, $\epsilon_{\text{mod}}(t)$, energy spectrum $E(\kappa)$ and dissipation spectrum $D(\kappa)$ (at $t = 9$) for the TGv flow with $Re = 3000$. Computations for $N = 64$ (left column) and $N = 128$ (right column) with the LBM UDNS for $Ma = 0.1$ compared to the SEM UDNS with the number of spectral elements corresponding to a resolution of $N = 64$ and $N = 127$, respectively. The resolution of the reference SEM DNS corresponds to $N = 351$. This figure is reproduced from [233], Copyright (2022), with permission from the authors and Elsevier Inc.

back to the injection of model dissipation rate. After comparing the MRT LBM results of the UDNS and the TLES, we can numerically approve that the employed MRT LBM UDNS, already acts as an implicit LES *on its own* via introducing hyperviscous terms. The model dissipation rate for $N = 64$ in Figure 4.38a which makes approximately half of ϵ_{tot} underpins this observation.

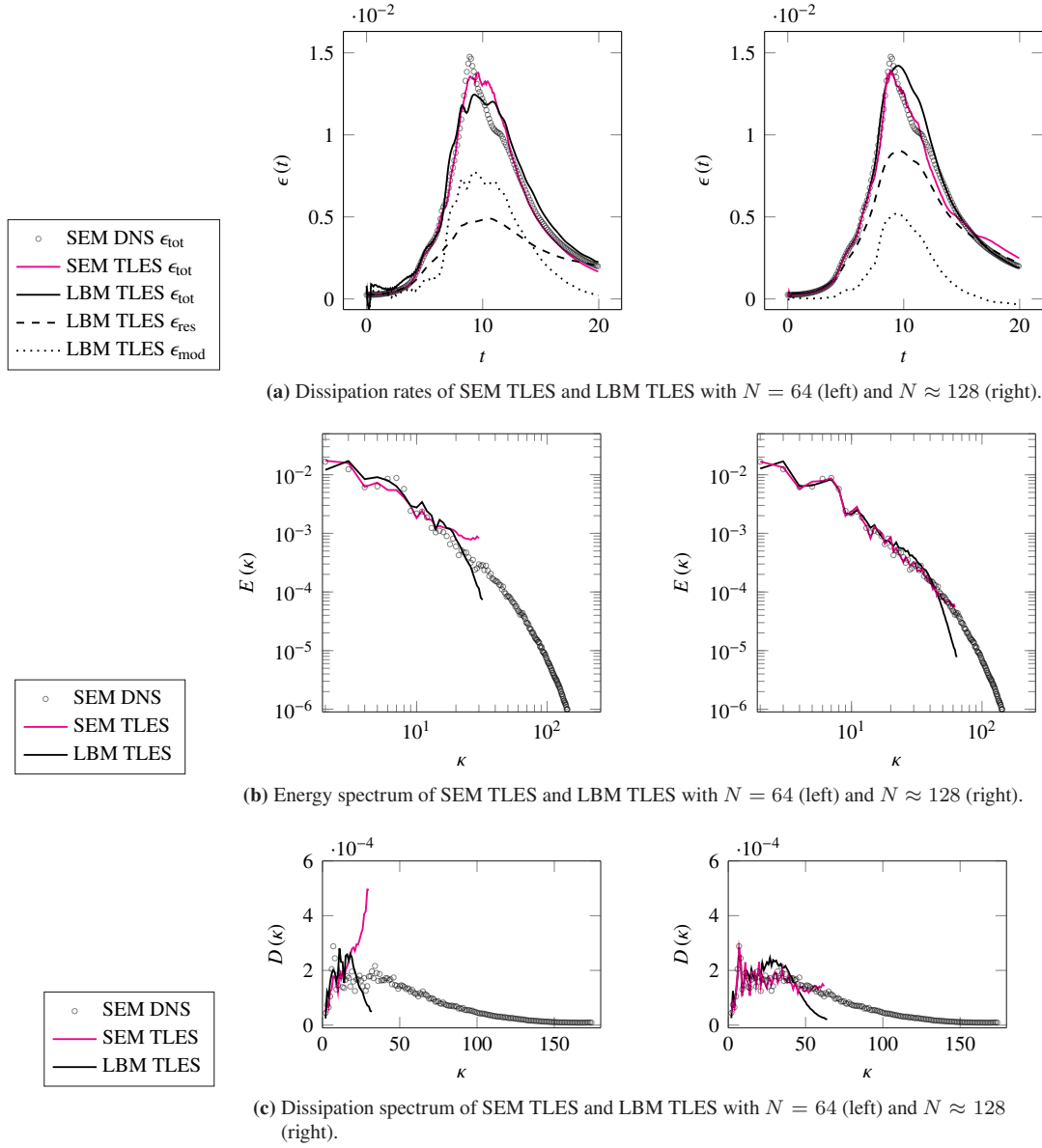
(a) Dissipation rates of SEM TLES and LBM TLES with $N = 64$ (left) and $N \approx 128$ (right).(b) Energy spectrum of SEM TLES and LBM TLES with $N = 64$ (left) and $N \approx 128$ (right).(c) Dissipation spectrum of SEM TLES and LBM TLES with $N = 64$ (left) and $N \approx 128$ (right).

Figure 4.39: Dissipation rates $\epsilon_{\text{tot}}(t)$, $\epsilon_{\text{res}}(t)$, $\epsilon_{\text{mod}}(t)$, energy spectrum $E(\kappa)$ (at $t = 9$) and dissipation spectrum $D(\kappa)$ for the TGV flow with $Re = 3000$. Computations for $N = 64$ (left column) and $N = 128$ (right column) with the LBM TLES ($\tilde{\Theta} = 10$) for $Ma = 0.1$ compared to the SEM TLES with the number of spectral elements corresponding to a resolution of $N = 64$ and $N = 127$, respectively. The resolution of the reference SEM DNS corresponds to $N = 351$. This figure is reproduced from [233], Copyright (2022), with permission from the authors and Elsevier Inc.

4.4.4 Numerical error quantification

The mesh convergence of UDNSs with the MRT LBM for the TGV flow under acoustic scaling (AS) up to a measurable compressibility error has been investigated by Haussmann *et al.* [114]. Following up the work, the present investigations predict the accuracy of the MRT LBM with the proposed TLES and link the activity of the model to an error extracted from the energy spectrum. The results of the experimental numerical analysis are gathered in Figure 4.40.

Besides the classical evaluation of a turbulence model based on nonanalytic graphical observations, a possible tool for measuring its accuracy is suggested by Geurts *et al.* [99]. The accuracy prediction is based on the subgrid activity

$$s(N, t) = \frac{|\epsilon_{\text{mod}}^{(N)}(t)|}{|\epsilon_{\text{tot}}^{(N)}(t)|}, \quad (4.65)$$

where $\epsilon^{(N)}(t)$ denotes the respective dissipation rate portions for a resolution N at time t . Note that we reframe the notions introduced in [99] specifically for the classical Smagorinsky model according to the observations for the present TDDM. Subsequently, the accuracy of a run with resolution N is compiled into a time dependent L^2 -error over the resolved wavenumbers κ with respect to the energy spectrum $E^{(N)}(\kappa, t)$, i.e.

$$\text{err}_{L^2}(N, t) = \sqrt{\frac{\sum_{i=2}^c |E^{(N)}(\kappa_i, t) - E^{\text{DNS}}(\kappa_i, t)|^2}{\sum_{i=2}^c |E^{\text{DNS}}(\kappa_i, t)|^2}}, \quad (4.66)$$

where $\kappa_c = \kappa_c(N)$ denotes the cutoff wavenumber for the respective resolution.

The subgrid activity $s(N, t)$ of the MRT LBM TLES and the MRT LBM UDNS are plotted over time t for a resolution sequence of $N = 24, 48, 64, 96, 128, 192$ in Figure 4.40a and Figure 4.40b, respectively. The specific data at time $t = 9$ is compiled in Figure 4.40c. The parameters for the spatial refinement obey AS with a constant Mach number $Ma = 0.1$ and the filter width is chosen as $\tilde{\Theta} = 10$. Exemplary parameter settings for $N = 64$ and $N = 128$ are listed in Table 4.12. Apart from the artifacts discussed in Section 4.4.2.2 which are clearly visible in Figures 4.40a, 4.40b – namely the initialization errors at the beginning of the simulated time interval and the negative model dissipation rate values at its end – the subgrid activity is monotonically decreasing on average when the resolution is increased. This suggests a consistently vanishing subgrid contribution toward DNS level resolutions for the present TLES. Due to its time discretization dependence, the temporal filter width Θ is affected by increasing the temporal resolution along the spatial one during AS. The effect of this coupling is clearly visible in Figure 4.40c.

It is notable that, when refining the grid via AS, the subgrid activity of both simulation techniques with the MRT LBM is diminished with increasing (up to presumably second) order. Further, comparing Figure 4.40a and Figure 4.40b we observe solely shape differences within the artifact-free region $t \in (5, 15)$, whereas the general magnitude of the subgrid activity with and without explicit turbulence model remains approximately equal. Again, the above mentioned interpretation of MRT LBMs as a stand-alone implicit turbulence models seems natural and is strongly supported by the data compiled in Figure 4.40c.

To isolate the previously observed dissipation injection at the peak region of $\epsilon_{\text{tot}}(t)$, the energy spectra produced by the MRT LBM with and without TLES are evaluated at $t = 9$, see Figure 4.40d and Figure 4.40e, respectively. Within the dissipation regime for the highest wavenumbers, a slight increase of the slope produced by the TLES compared to the UDNS result can be observed for all resolutions. The corresponding errors are computed according to (4.66) and are gathered in Figure 4.40f by plotting $\text{err}_{L^2}(N, t = 9)$ over the subgrid activity $s(N, t = 9)$. For lower resolutions $N \leq 64$ an accuracy order of two is evident. Increasing the resolution, the second order accuracy in terms of $\text{err}_{L^2}(N)$ is diminished until an error plateau is reached.

Since the error plateau appears for both, the UDNS and the TLES, a further characterization is required. As a first investigation of isolating the impact of the TLES on LBMs, Figure 4.40i visualizes the relative deviation of the MRT LBM TLES from its UDNS counterpart in terms of subgrid activity and energy spectrum error. For both quantities, a clear diminishing trend is observable. Whereas the subgrid activity deviation shows a linear regression slope of approximately $\mathcal{O}(N^{-0.47})$, the regression slope of the energy spectrum error deviation exhibits a much clearer order $\mathcal{O}(N^{-0.83})$.

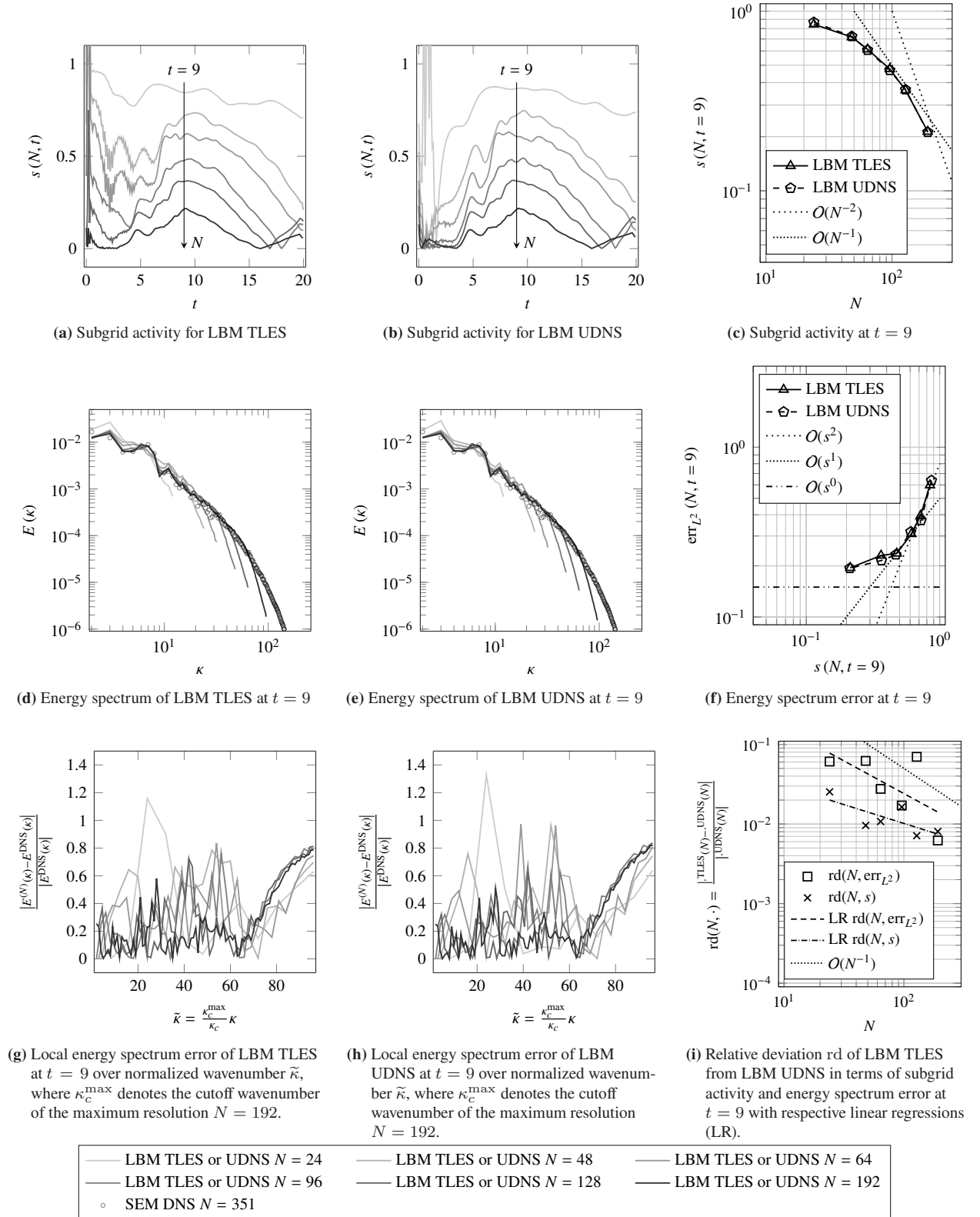


Figure 4.40: Subgrid activity and energy spectrum error measurements for a sequence of resolutions $N = 24, 48, 64, 96, 128, 192$. The LBM TLES runs with $\tilde{\Theta} = 10$ and the LBM UDNS computations are carried out with $Ma = 0.1$ for the TGv flow at $Re = 3000$. This figure is reproduced from [233], Copyright (2022), with permission from the authors and Elsevier Inc.

Further, the overall magnitude of the energy spectrum error plateau is almost doubled compared to the dissipation rate error values obtained in [114]. Figures 4.40g, 4.40h gather additional information on the energy spectrum error composition in terms of normalized wavenumbers $\tilde{\kappa}$. Within the regime up to approximately 75% of the resolved wavenumbers, the error is on average consistently diminished with an increasing resolution. Opposed to that, the remaining 25% up to the cutoff wavenumber form an asymptotically constant error contribution and perturb the error measurement due to the dissipation rate tail. Hence, we expect that advanced analysis techniques (e.g. [98]) could be employed to focus on certain wavenumber ranges.

In summary, the information compressed in Figures 4.40g, 4.40h, 4.40i suggests that the presence of numerical dissipation within the underlying method renders the experimental error analysis of the compound methodology, including the TLES, rather difficult. Nevertheless, we can state that, along the limit toward the error bound of the MRT LBM with AS [114], the TLES consistently loses its model effectiveness represented by the subgrid activity. In terms of a *temporal subgrid resolution* defined as $\tilde{h} = \Delta t / \Theta$, the present work proves that with $\tilde{h} = 0.1$ being fixed as a constant, the solution to the incompressible NSE is approached by the proposed MRT LBM TLES up to a known combination of errors. Since the error plateau similarly appears for the MRT LBM UDNS we conclude that, besides the dissipative nature of LBMs, the compressibility defect [114] represents the main contribution of the energy spectrum error. A consistency error investigation with respect to the total dissipation rate is provided in 4.4.5. However, the complete interaction of all possible roots of errors near the DNS level remains to be clarified in future studies.

4.4.5 Scaling, consistency and experimental order of convergence

Since we aim at approximating the incompressible NSE, DS is mathematically consistent in the relaxation limit and reduces the accuracy in time to first order ($\Delta t \sim \Delta x^2$) with respect to the TEQ (see [120, 143, 250]). In contrast to that, AS suggests spatio-temporal accuracy orders of two (since $\Delta t \sim \Delta x$), but prevents convergence as soon as the constant compressibility error plateau is reached (see theoretically [120] and numerically [114]). According to this fact, a second order TDDM discretization should be more consistent in underresolved configurations and AS. Whereas a first investigation of this conjecture is provided below, the detailed analysis is deferred to future studies. Moreover, despite AS being nonconvergent, it is employed in the present study due to its common usage in underresolved applications with limited parameter spaces. Thus, the above investigations include numerical tests for the AS-typical error behavior which was previously documented in [114].

Nevertheless, from a mathematically rigorous point of view, the LBM as a numerical method to approximate the incompressible NSE is restricted to DS, which hence implies accuracy of second order in space and first order in time, and henceforth in this case renders the first order discretization of the TDDM (deconvolution and residual stress calculation) reasonable.

To investigate and verify these statements, the modular LBM combinations of SRT and MRT collision as UDNS and with the TDDM finite difference discretization of first (TLESo1) and second order (TLESo2), respectively, are compared in terms of error measurements along AS and DS with respect to a Kolmogorov scale resolving high resolution simulation (SRT LBM with $N = 512$ and parameters according to Table 4.13). The validity of the highly resolved SRT LBM as DNS was numerically proven in [114] with respect to reference results obtained with pseudo-spectral methods. Note that, due to the observations made in [97], within the present work spatial velocity gradients are computed with eighth order central differences (3.313). Furthermore, (4.22) is approximated with second order central differences. The simulations are carried out on a maximum of 264 nodes with two Intel Xeon Platinum 8368 processors each.

Figure 4.41 gathers the results of resolution dependent computations of the total dissipation rate error

$$\text{err}_{\epsilon_{\text{tot}}}(N) = \sqrt{\frac{\sum_{i=1}^m |\epsilon_{\text{tot}}^{(N)}(t_i) - \epsilon_{\text{tot}}^{\text{DNS}}(t_i)|^2}{\sum_{i=1}^m |\epsilon_{\text{tot}}^{\text{DNS}}(t_i)|^2}} \quad (4.67)$$

for each tested modification, where $[t_1, t_m] = [0.1, 20]$ is discretized to equidistant time intervals of size 0.1, and $\epsilon_{\text{tot}}^{\text{DNS}}$ refers to the total dissipation rate computed with the high resolution SRT LBM. The corresponding discretization parameters are summarized in Table 4.12. Via linear regression, approximate EOC slopes are obtained from $\text{err}_{\epsilon_{\text{tot}}}(N)$ for the overall stable subsequence $N = 64, 128, 256$ (see Table 4.14).

Table 4.13: LBM discretization parameters used in Figure 4.41. This table is reproduced from [233], Copyright (2022), with permission from the authors and Elsevier Inc.

N	scaling	Ma	τ	Δx	Δt
32	DS/AS	0.1	0.50106	0.20268	0.01170
64	AS	0.1	0.50217	0.09973	0.00575
	DS	0.05	0.50108	0.09973	0.00287
128	AS	0.1	0.50437	0.04947	0.00285
	DS	0.025	0.50109	0.04947	0.00071
256	AS	0.1	0.50878	0.02463	0.00142
	DS	0.0125	0.50109	0.02463	0.00017
512	DS	0.00625	0.50110	0.01229	0.00004

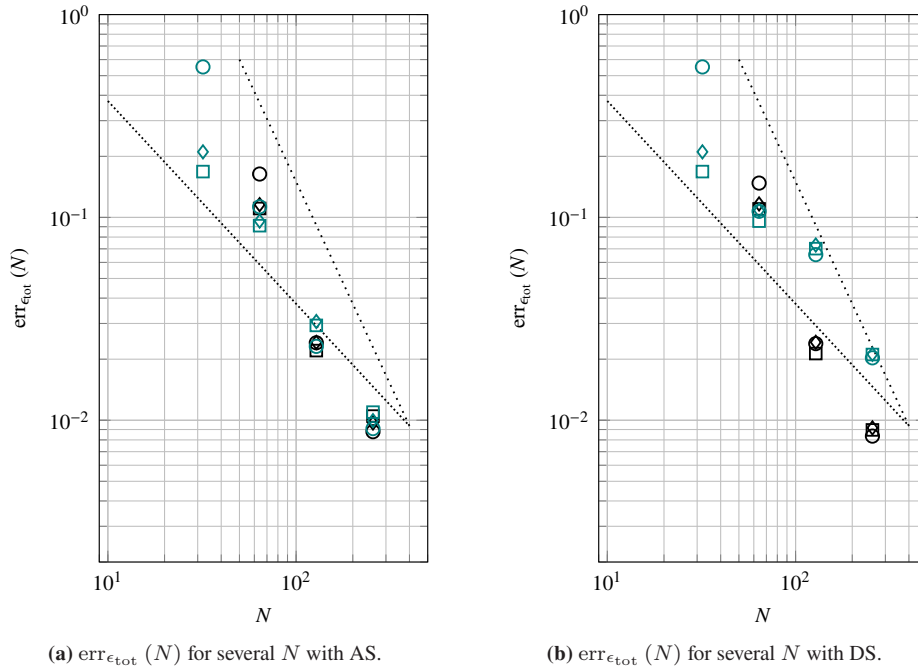


Figure 4.41: EOC comparison for TGV flow computations at $Re = 800$ with modular LBM combinations of SRT or MRT collision without (UDNS) and with TLES with TDDM finite difference discretization of first (TLESo1) and second order (TLESo2), respectively. Only stable configurations are included. Total dissipation rate errors are calculated according to (4.67) with respect to high resolution reference data from the SRT LBM run at $N = 512$ and $Ma = 0.00625$. AS (left) and DS (right) are based on a respective sequence of resolutions $N = 32, 64, 128, 256$ starting at $Ma = 0.1$ and conforming to Table 4.13. This figure is reproduced from [233], Copyright (2022), with permission from the authors and Elsevier Inc.

Table 4.14: Regression slopes $\mathcal{O}(N^{-\gamma})$ of EOC comparison (cf. Figure 4.41) computed with $\text{err}_{\epsilon_{\text{tot}}}(N)$ for $N = 64, 128, 256$. This table is reproduced from [233], Copyright (2022), with permission from the authors and Elsevier Inc.

method	AS	DS
SRT UDNS	1.70	1.80
SRT TLESo1	1.78	1.83
SRT TLESo2	2.11	2.07
MRT UDNS	1.52	1.09
MRT TLESo1	1.63	1.17
MRT TLESo2	1.81	1.20

In advance of discussing Figure 4.41 and Table 4.14, the statistical nature of EOC results for turbulent flow test cases without (known) analytical solution for all times has to be recalled. The rationale of this statement is based on several aspects, for example that the EOC computation via regression slopes is prone to interference by statistical outliers. Hence, in order to uphold a mathematical viewpoint, the perception of data obtained from such numerically experimental validations should remain rather fuzzy than accurate up to specific decimal places.

Nevertheless, considering the results compiled in Figure 4.41, the following observations can be made. Firstly, comparing the SRT error results of the largest tested resolution $N = 256$ for AS and DS, we deduce that the compressibility error plateau is only marginally pronounced, which matches the observations in [114] where the DNS level for the present setting has been approximated to $N \approx 313$. This feature of the results proves the choice of an incompressible turbulence model for a weakly compressible method reasonable when using $Ma \leq 0.1$. Secondly, despite using MRT collision reduces the EOC (see Table 4.14), it yields a stability gain for highly underresolved settings (here $N = 32$) in comparison to the SRT BGK scheme. Additionally, with the help of dynamic relaxation frequencies, the present MRT formulation is stable for all tested Mach numbers. Still, unexpectedly, the usage of MRT collision lowers the EOC in DS compared to AS by about 0.5 (see Table 4.14). This is not the case for the SRT LBM. We interpret the effect as a consequence of choosing specific sets of relaxation frequencies which modify numerical dissipation, reduce the error for a fixed resolution, and thus yield crooked error curves. Moreover, the reduced EOC indicates that the present kinetic relaxation frequencies might be suboptimal with respect to a filtered TEQ. Thirdly, it has to be stressed that the TLES consistently improves the EOC in contrast to the UDNS for all tested methods and scalings. The positive impact of the model is larger for AS than for DS, which is likely due to the Ma reduction during DS. Further, the model effectiveness increases with the discretization order.

In summary it can be stated that, when using the MRT scheme with AS to ensure stability throughout a broad sequence of resolutions, the proposed concept of TLES for LBMs significantly and consistently increases the EOC.

4.5 Homogenized Navier–Stokes equations

The HLBM derived in Section 3.3.1.4 by limit consistent discretization is numerically tested for several specific configurations. To study the limit composition of homogenization, relaxation, and discretization, the results of the present HLBM for porous media are compared to fully resolved simulations with the HLBM for particulate flows proposed by Krause *et al.* [159] and revisited by Trunk *et al.* [249]. An example visualization of the solid matrix arrangements in the conducted tests is provided in Figure 4.42 (see Figure 4.42a, 4.42b).

4.5.1 Porous Poiseuille flow

The geometric arrangement of the porous matrix consists of an array of equally sized spheres. Complemented with the solid matrix, the fluid void fills the cuboidal domain $\Omega = [0, 2.5] \times [0, 1] \times [0, 1]$. The numerical setup in the inner domain conforms to the mathematical model for homogenization from Section 2.5. Additionally, for all simulations, a quadratic duct flow profile [259] in the yz -plane

$$u_x(y, z) = \frac{16a^2}{\nu\pi^3} (-\partial_x p) \sum_{\substack{i=1 \\ i \bmod 2=1}}^{\infty} (-1)^{\frac{i-1}{2}} \left[1 - \frac{\cosh\left(\frac{i\pi z}{2a}\right)}{\cosh\left(\frac{i\pi b}{2a}\right)} \right] \frac{\cos\left(\frac{i\pi y}{2a}\right)}{i^3} \quad (4.68)$$

is approximated and used as an inlet velocity at $x = 0$, where $a = b = 0.5$. The outflow at $x = 2.5$ comprises a pressure boundary only and at the side walls no slip conditions are set for the velocity field. Based on firstly, the regular sphere packing for $a_\epsilon = \epsilon$ which allows to study the model problem without loss of generality (see Section 2.5) and secondly, the x -directional inflow in the resolved simulations, the following statements can be made [198]. Within the model problem, for a given porosity, (2.136) simplifies to an expression for the sphere radius

$$a_\epsilon = \left[\frac{3}{4\pi} (1 - \phi) |Y_i^\epsilon| \right]^{\frac{1}{3}}. \quad (4.69)$$

We recall Ergun's [77] equation

$$-\partial_x p = \frac{\beta\nu\rho(1-\phi)^2}{a_\epsilon^2\phi^3} \bar{u}_x + \frac{\alpha\rho(1-\phi)}{a_\epsilon\phi^3} u_x |\bar{u}_x|, \quad (4.70)$$

with $\alpha = 1.75$ and $\beta = 150$, where the superficial velocity u_s describes the average flow speed through the empty void in x -direction. Via (4.70), the pressure drop $\Delta p \approx L\partial_x p$ over the domain in x -length L (including the resolved matrix) is connected to the porosity. Similarly, we can deduce a suitable permeability for the lattice porosity (3.211) via the Carman–Kozeny relation

$$K = \frac{a_\epsilon^2\phi^3}{\tilde{\beta}(1-\phi)^2}, \quad (4.71)$$

where $\tilde{\beta} = 180$ is obtained from a fit to experimental results [198]. Forchheimer's prediction for taking a quadratic drag into account reads

$$\nabla_x p = -\nu\rho K^{-1} \mathbf{u} - c_F K^{-\frac{1}{2}} \rho |\mathbf{u}| \mathbf{u}. \quad (4.72)$$

Combining (4.70), (4.71), and (4.72), suggests $\beta \approx \tilde{\beta}$. The dimensionless form-drag constant hence obeys the expression

$$c_F = \alpha \tilde{\beta}^{-\frac{1}{2}} \phi^{-\frac{3}{2}}. \quad (4.73)$$

4.5.2 Consistency of the pressure difference

The following computations with the present HLBM for fluid flow through porous media are contrasted to the reference values from the resolved simulations via (4.70) and (4.71). A parameter grid comprised by the values $(K, N) \in \mathfrak{K} \times \mathfrak{N} = (2.7 \times 10^{-4}, 4.0 \times 10^{-2}) \times (21, 105)$ is used with a Reynolds number of $Re = 1$ with respect to the duct height. The Mach number is reduced along DS which leads to a minimum of $Ma = 1.6 \times 10^{-3}$ for $N = 105$.

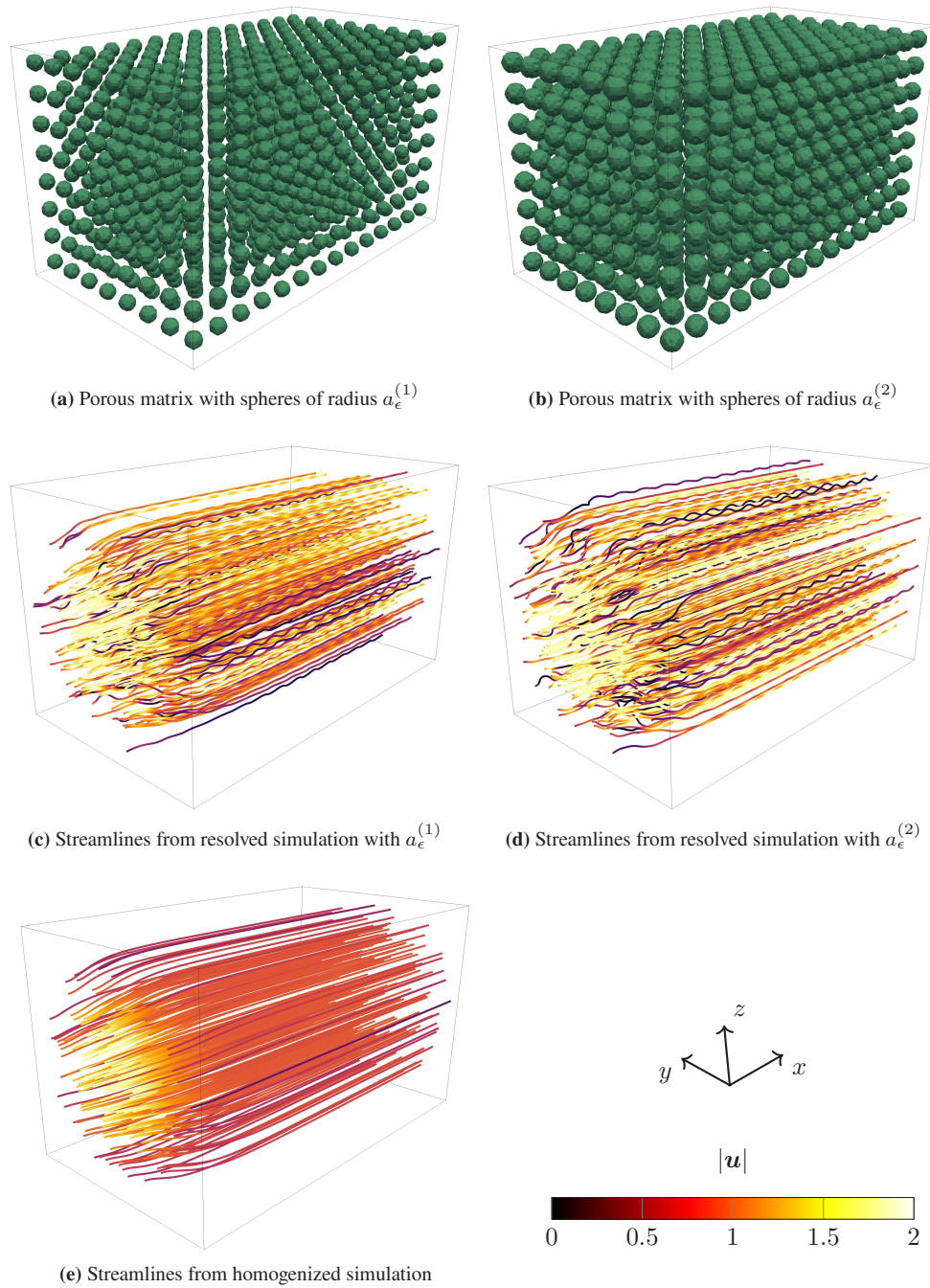


Figure 4.42: Exemplary streamlines of \mathbf{u} computed with HLB simulations through homogenized (e) and resolved (c,d) regular arrangements of spheres (a,b), respectively.

The quantitative assessment of the simulation is given in Figure 4.43 and Table 4.15. A relative consistency error of the computed pressure drop

$$\text{err}_{\Delta p}(N) = \frac{|\Delta p^{(N)} - \Delta p^*|}{|\Delta p^*|} \quad (4.74)$$

is extracted, where p^* is the result with the highest resolution. Based on that, the pressure drop prediction for respective permeabilities is studied for consistency. Figure 4.43a visualizes the computed pressure differences with respect to the permeability computed from (4.71). Compared to the resolved simulation for $N = 105$, the HLB results show

the expected smoothed curve due to the geometric homogenization of the porous matrix. The consistency error of the

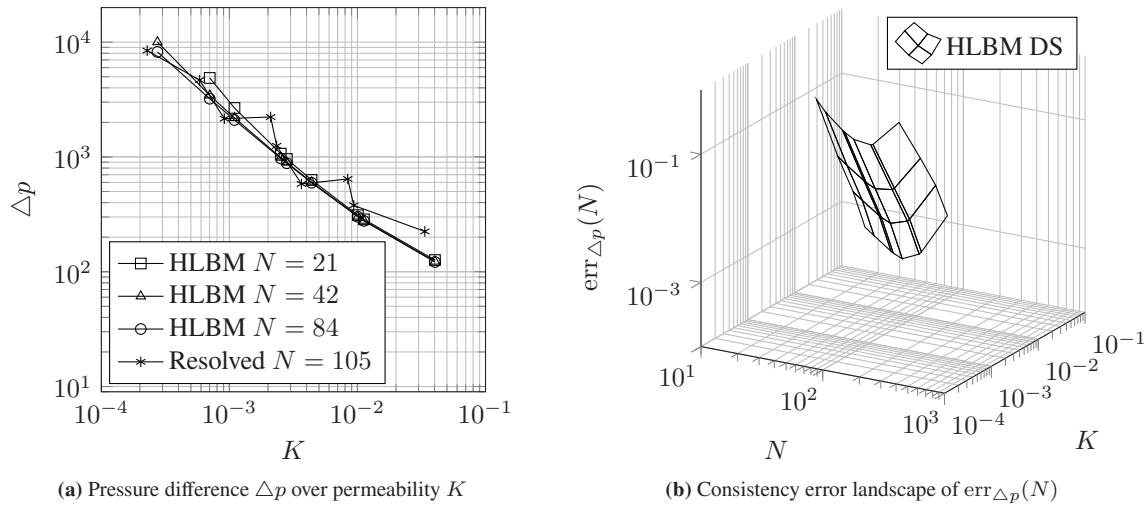


Figure 4.43: (a) Pressure difference for Poiseuille flow through rectangular duct with a regular sphere matrix simulated with present HLBM for several resolutions and permeabilities and particle-resolved HLBM [159, 249]. (b) Consistency error $\text{err}_{\Delta p}(N)$ landscape of the pressure drop Δp computed with HLBM for several permeabilities K and resolutions N .

HLBM approximation toward the highest resolution is plotted in Figure 4.43b. The dependency on the permeability eigenvalue K is clearly visible. Whereas for large K , the error decreases on average, smaller permeabilities result in an increased $EOC(K)$. The latter is summarized in Table 4.15. We observe the expected EOC of order two on average,

Table 4.15: Consistency error of the pressure drop Δp computed with HLBM for several permeabilities K , and resulting EOC values.

K	$\text{err}_{\Delta p}(N)$				$EOC(K)$
	$N = 21$	$N = 42$	$N = 63$	$N = 84$	
7.02×10^{-4}	5.28×10^{-1}	7.86×10^{-2}	2.47×10^{-2}	7.55×10^{-3}	2.43
1.09×10^{-3}	2.78×10^{-1}	4.76×10^{-2}	1.51×10^{-2}	4.61×10^{-3}	2.37
2.51×10^{-3}	1.02×10^{-1}	1.93×10^{-2}	6.14×10^{-3}	1.85×10^{-3}	2.34
2.80×10^{-3}	9.10×10^{-2}	1.73×10^{-2}	5.50×10^{-3}	1.66×10^{-3}	2.34
4.38×10^{-3}	5.84×10^{-2}	1.15×10^{-2}	3.69×10^{-3}	1.12×10^{-3}	2.32
1.00×10^{-2}	3.38×10^{-2}	7.87×10^{-3}	2.82×10^{-3}	9.33×10^{-4}	2.11
1.12×10^{-2}	3.27×10^{-2}	7.88×10^{-3}	2.88×10^{-3}	9.64×10^{-4}	2.08
4.02×10^{-2}	4.21×10^{-2}	1.35×10^{-2}	5.68×10^{-3}	2.06×10^{-3}	1.82

which matches the limit consistency predictions from Section 3.3.1.4. Notably, each simulation is ran until stationary convergence is observed and the flow conditions are in the Stokes regime. Simulations with increased Reynolds numbers to computationally recover all terms in the approximated HNSE (2.138) are planned in future research.

4.6 Navier–Stokes–Cahn–Hilliard equations

In Section 4.6, the HSFRM is derived as a higher order extension of the SFRM and formally linked to the binary KFRM in the incompressible limit. The LBE, discretizing the (H)SFRM for approximating solutions to (2.178) is given in Section 3.3.1.6. Below, numerical experiments with the thus obtained (H)SFRM LBM are conducted⁸.

The dynamic effects on an immiscible mixture of two components can be abstracted into shear- and extension-dominated flows. For these two types of dynamic mixture flows, the (H)SFRM LBM is implemented and tested with a simplified binary fluid composition (equal density and viscosity). To this end, two classical configurations are digitally twinned: a parallel-band device for binary shear flow and a four-roller apparatus for binary extensional flow. The free energy LBM and the test cases are implemented in the open-source parallel C++ framework OpenLB (see Algorithm 2 for the collision kernel) and evaluated for several nondimensional numbers. In particular, deformation as well as breakup phenomena are distinctively assessed to determine the models applicability for more complex applications.

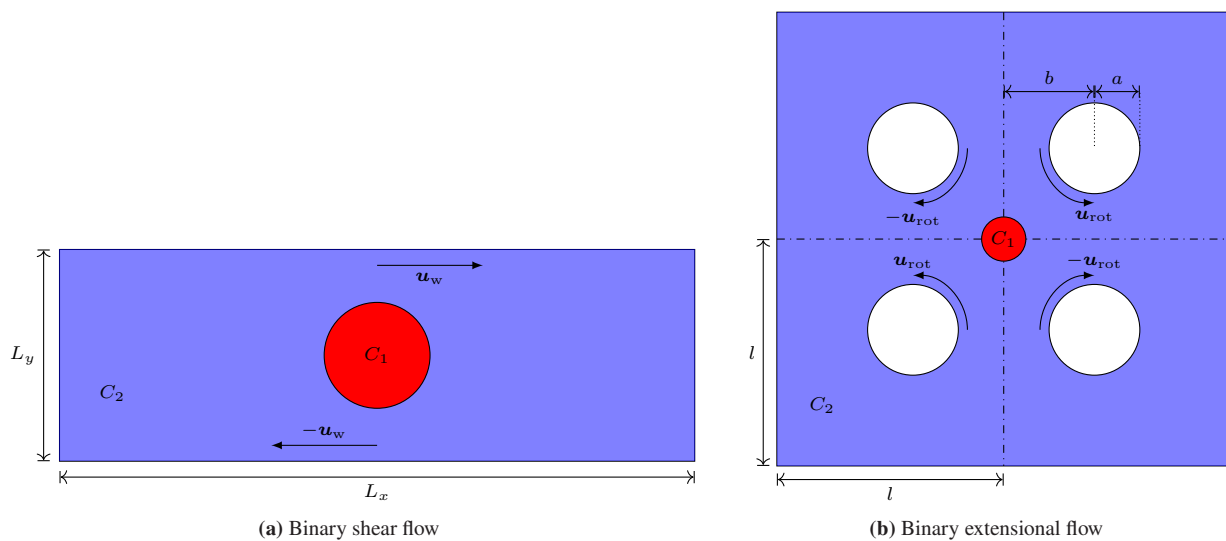


Figure 4.44: Geometric setup of numerical test cases for binary flow in two dimensions. Scales differ for the purpose of representation. This figure is reproduced from [235], Copyright (2023), with permission from the authors and the American Institute of Mathematical Sciences.

To assess the capability of the FRM LBM for recovering shear and extensional binary flows, we emulate Taylor’s parallel-band and four-roller devices [245] by means of numerical simulations in two dimensions (2D). The former is also tested for three dimensions (3D). The geometric setup of the 2D simulations is sketched in Figure 4.44. All computations are done with OpenLB release 1.4 [161] on several HPC machines, using for example up to 16 nodes with five quad-core Intel Xeon E5-2609v2 cores each, or a maximum of 75 nodes with respectively two deca-core Intel Xeon E5-2660v3.

The deformation of the C_1 droplet

$$D = \frac{L - B}{L + B}, \quad (4.75)$$

where L is the longer axis halved and B the shorter one, is measured via intrinsic functors of OpenLB [162]. In case of a horizontally measured inclination angle $\theta = 0^\circ$, an interpolation along the space directions recovers the location of

⁸ Parts of this section are reproduced from [235], Copyright (2023), with permission from the authors and the American Institute of Mathematical Sciences.

the interface. If a simultaneous deformation and inclination of the droplet occurs, L and B are approximated through concentric circles and θ can be computed at the respective intersection points with the interface.

Though essential differences between 2D and 3D deformations are known [237], certain nondimensional regimes still allow a side-by-side comparison. Based on that we compare the FRM LBM solutions to 3D reference computations [157, 179] and analytical predictions [226, 245].

4.6.1 Volume loss of small droplets

The extensions of both, the SFRM and the KFRM with the higher order free energy functional approach by Shin *et al.* [227] is proposed in Section 2.6.2. Via using higher orders in leading powers of the order parameter in the free energy functional, we obtain the HSFRM and the HKFRM (see Definition 2.6.9 and Definition 2.6.8, respectively), where the connection of both in the formal incompressible limit is upheld also for higher orders. In [227], a higher-order free energy polynomial setting $m > 2$ counteracts the vanishing sub-critical sized droplets via penalizing the steepness near the minima of the double-well potential. Conclusively, a positive recommendation is given toward $m = 6$, while $m \gg 6$ results in nonphysical effects on the interface shape. Based on (2.173), let

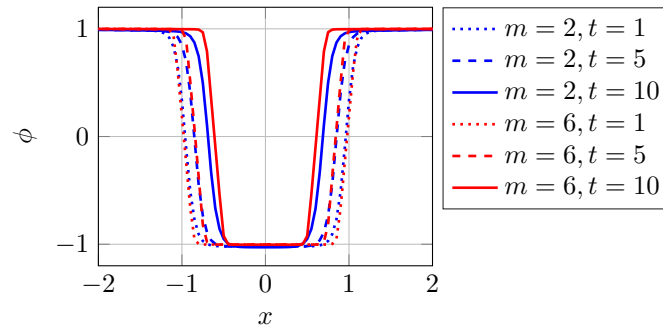


Figure 4.45: Static droplet test case in 2D computed with the SFRM LBM. The order parameter ϕ is plotted over the cross section $y = 0$ for the free energy functional $\Psi^{(m)}$ with $m = 2$ and $m = 6$ at several time steps. This figure is reproduced from [235]. Copyright (2023), with permission from the authors and the American Institute of Mathematical Sciences.

$$\Psi^{(m)} = \int_{\Omega} (f_{B,m}^{\text{HS}} + f_{\text{I}}^{\text{S}}) \, d\mathbf{x} \quad (4.76)$$

denote the free energy functional for the HSFRM. To investigate the effects of the higher order polynomial in $f_{B,m}^{\text{HS}}$ for the present HSFRM LBM, the modified $\Psi^{(6)}$ is evaluated against the standard SFRM LBM $\Psi = \Psi^{(2)}$ in a static 2D test case where a circular droplet ($\phi = 1$) is immersed in a quadratic domain filled with the other component ($\phi = -1$). The velocity field and the external forces are nulled out. The droplet has a radius of $a = 20$ with an interface thickness $\xi = 2.27$ which results in $Ch = 0.1135$ and thus is prone to strong shrinkage. Figure 4.45 visualizes the cross section of ϕ at different time steps. In the case of $m = 2$, we observe that the order parameter reaches a shifted value of $\phi \approx -1.027$ at the center of the droplet, as well as a decreased value in the surrounding fluid region. This observation agrees well with results from Komrakova *et al.* [157] who identified the so-called contamination to be caused by residual diffusion of the interface. It is to be stressed that, though the higher order polynomial with $m = 6$ corrects the unwanted shift from the local minima and prevents the contamination, the shrinkage of the droplet is still present and seems to even be increased for larger times. Thus, a recommendation for using the proposed HSFRM can only be made for simulations where the size of the droplets also after a possible breakup remains above the threshold of the critical radius. Presently, to capture breakup also at coarse resolutions under the trade-off against more diffuse interfaces we use $m = 2$ unless stated otherwise. For this configuration, the approximation of a sharp interface solution

is numerically approved in Section 4.2 above. Further development and a detailed numerical analysis of the higher order FRM for dynamic multicomponent fluid flow is planned for future research.

4.6.2 Binary shear flow

We define the nondimensional Reynolds number, capillary number, Péclet number, and Cahn number, respectively as

$$Re = \frac{\gamma a^2 \rho}{\eta}, \quad (4.77)$$

$$Ca = \frac{a\gamma\eta}{\sigma}, \quad (4.78)$$

$$Pe = \frac{\gamma a \xi}{M_\phi A}, \quad (4.79)$$

$$Ch = \frac{\xi}{a}, \quad (4.80)$$

where γ , a , η , σ , ξ are shear rate, droplet radius, dynamic viscosity, surface tension, interface thickness, respectively, and $A = 3\sigma/(2\xi)$ is a mobility parameter. The ratios of viscosity and density of the components are unity and time is understood as normalized via $\bar{t} = \gamma t$.

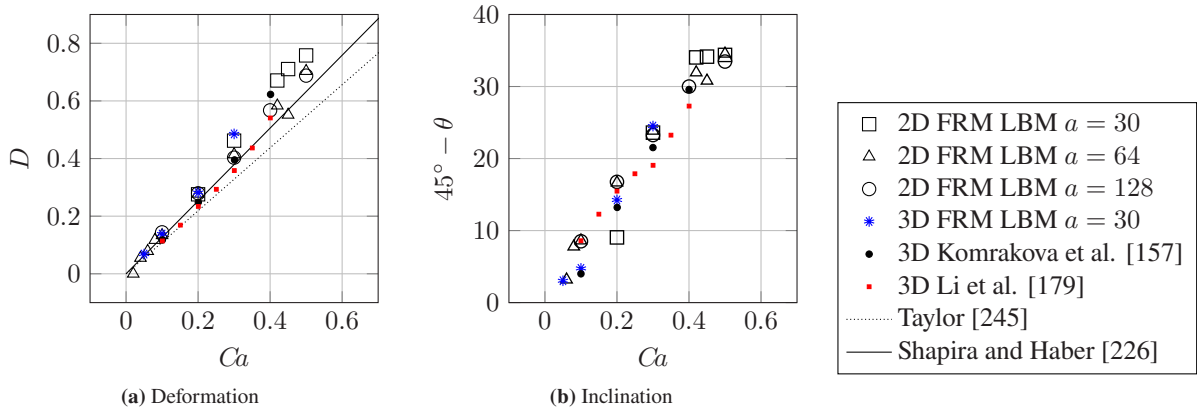


Figure 4.46: Deformation and inclination of a droplet in 2D and 3D binary shear flow simulated with the SFRM LBM and compared to reference results for varying capillary numbers. This figure is reproduced from [235], Copyright (2023), with permission from the authors and the American Institute of Mathematical Sciences.

Steady state validation In the case of $Ca < Ca_c$, the droplet deforms until it reaches a steady state. For $Re = 0.1$, $Pe = 0.43$, and $Ch = 0.0379$, Ca is varied over the interval $(0.02, 0.6)$. The results are plotted in Figure 4.46b and agree well with the literature for small Ca . Refining the mesh over several droplet radii in lattice units $a = 30, 64, 128$, indicates convergence to the reference results and allows to simulate validly for higher Ca . Notably, in the transition regime toward Ca_c , the droplet tilts and deforms toward an elongated thread and falls back into the stationary shape. This physical effect leads to an increased difference in results for lower grid resolutions.

Breakup The breakup occurs for $a = 30$ approximately at $Ca_c \sim 0.7$ (2D) and $Ca_c \sim 0.42$ (3D). Three different categories are commonly observed [32, 277], namely

- (i) pseudo steady-state $Ca \sim Ca_c$,
- (ii) end-pinching $Ca_c < Ca < 2Ca_c$, and

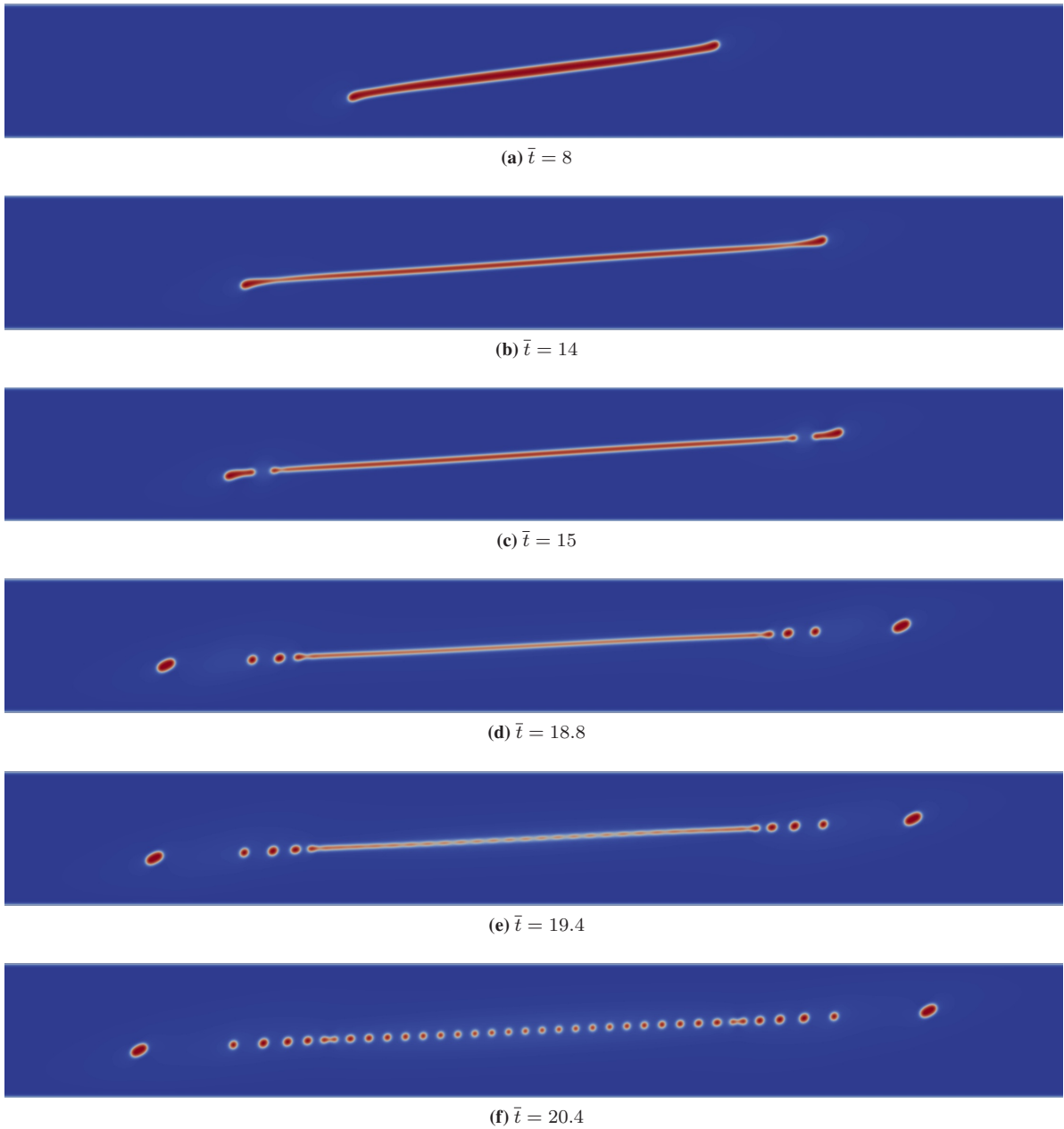


Figure 4.47: Droplet breakup in 2D binary shear flow at $Ca = 3.5$ computed with the SFRM LBM. Components C_1 (red) and C_2 (blue) are plotted at normalized time steps.

(iii) capillary wave breakup $Ca > 2Ca_c$.

However, the bounds between these regimes are not sharp, such that the droplet may pass through multiple types during the breakup process. Due to differences between 2D and 3D droplet deformations, Ca_c in 2D is significantly larger than in 3D. The latter agrees well with the literature [157], and so does the breakup scenario (see Figure 4.48). In 2D for $Ca = 5Ca_c$ at $Re = 1$, $Pe = 0.2$ and $a = 40$ we observe end-pinching as well as a capillary wave breakup (see Figure 4.47).

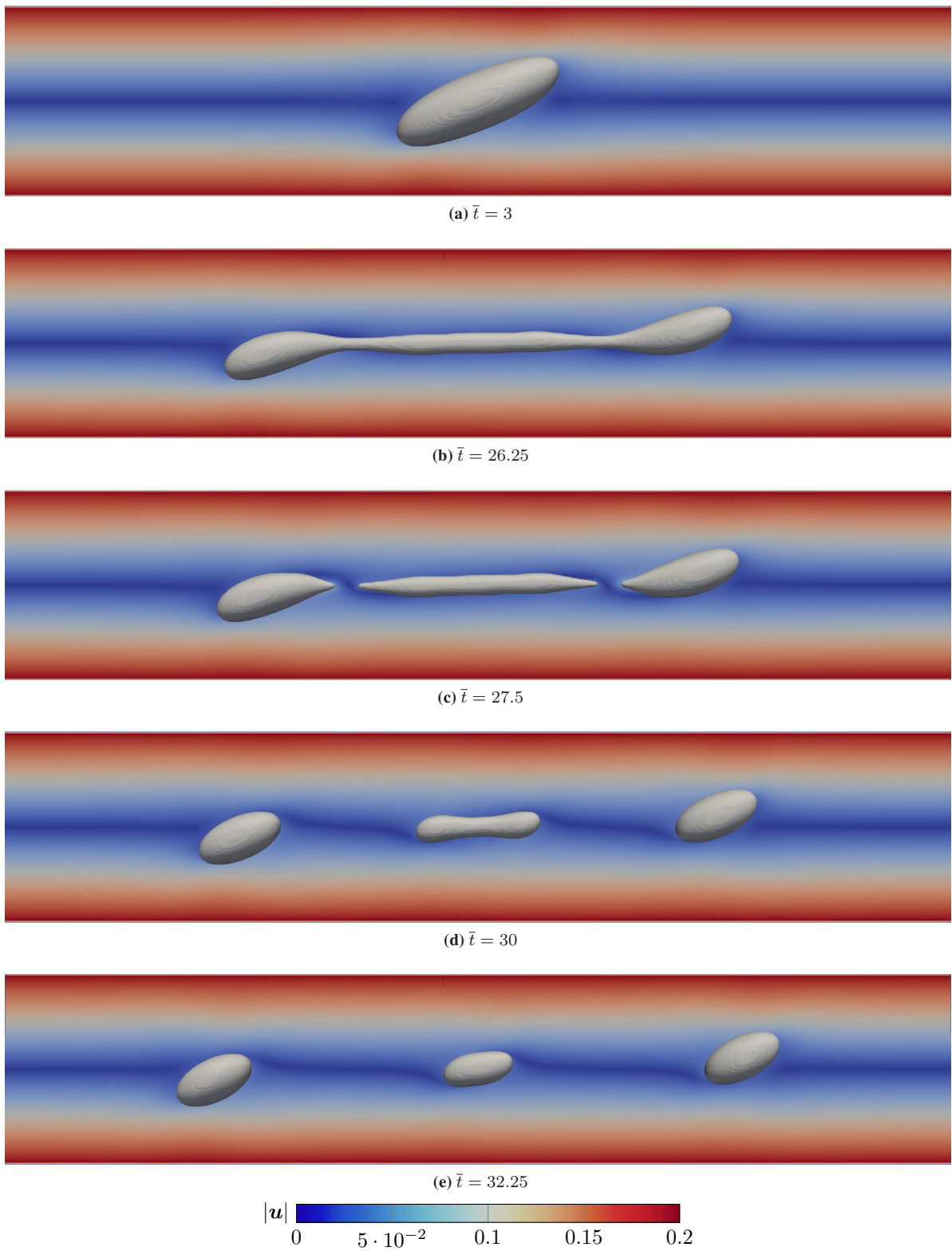


Figure 4.48: Droplet breakup in 3D binary shear flow computed with the SFRM LBM at normalized time steps for $Re = 0.0625$, $Ca = 0.42$, $Ch = 0.0379$, $Pe = 0.43$. This figure is reproduced from [235], Copyright (2023), with permission from the authors and the American Institute of Mathematical Sciences.

4.6.3 Binary extensional flow

The sizing of the four-roller device ensures a uniform extension rate ϵ [118] which now replaces γ [29, 119, 248] in the π -group. For fixed $Re = 0.0625$, $Ch = 0.57$, $Pe = 0.1$ and $Ca \in [0.01, 0.3]$ the droplet is observed to break for $Ca > 0.25$.

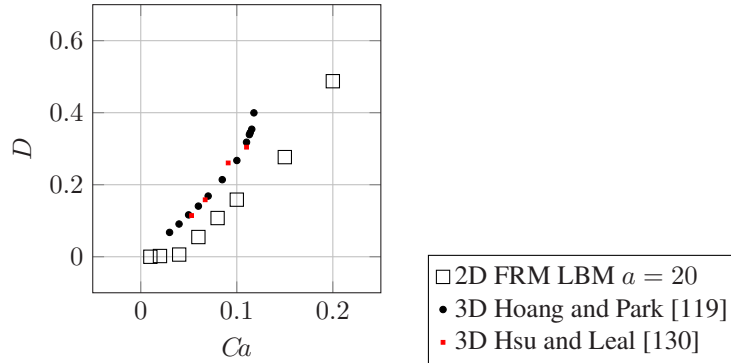


Figure 4.49: Deformation of a droplet in 2D binary extensional flow simulated with the SFRM LBM and comparison to 3D reference results for varying capillary numbers. This figure is reproduced from [235], Copyright (2023), with permission from the authors and the American Institute of Mathematical Sciences.

Steady state validation The droplet radius is set to $a = 20$, which corresponds to a ratio of 40 between domain length and radius. Figure 4.49 summarizes the deformation in the subcritical capillary regime. For $Ca = 0.01, 0.02, 0.04$ the droplet shows little to no deformation. Beginning at $Ca = 0.05$ the deformation becomes significant and increases rapidly with increasing Ca and with a considerably faster rate than in the shear flow. Our simulation results and the reference data from [119, 130] agree from the perspective of an overall trend but differ at individual values. Based on the same reasoning as above, we conclude that a 3D extensional flow produces a higher deformation at lower Ca than in 2D.

Breakup Figure 4.50 visualizes a breakup for $Ca = 0.42$. At first, the droplet stretches into a long thread of equal width with rounded ends. Instead of end-pinching, the droplet breaks by overstretching, forming several sub-satellite droplets. After the droplets exceed the rollers' gap, their velocity declines and the tails retract quickly. Despite the successful reproduction of these phenomena, the results show heavy satellite shrinkage due to the high domain-droplet ratio. The apparent shrinkage of sub-critical droplets is further discussed in Appendix 4.6.1.

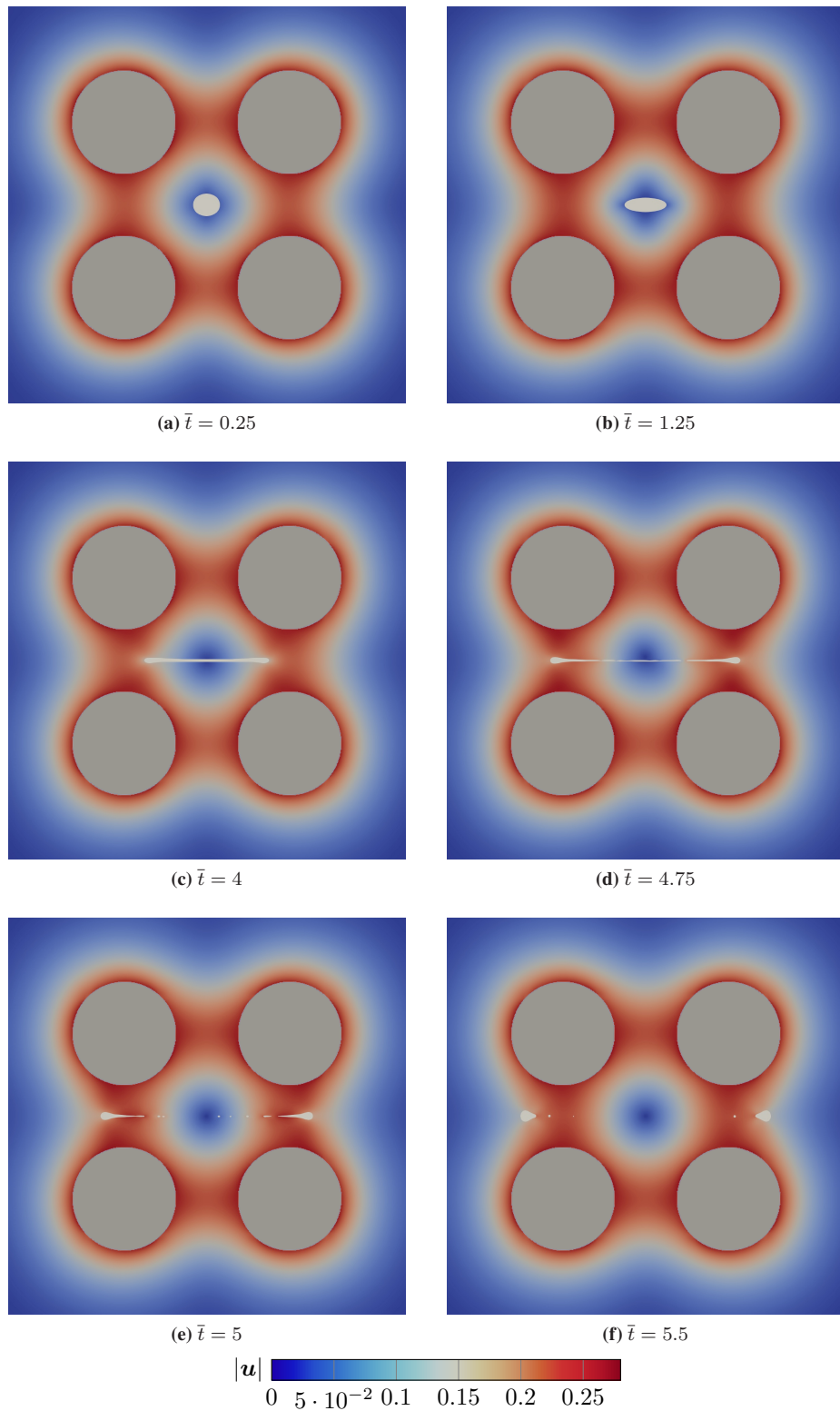


Figure 4.50: Droplet breakup in 2D binary extensional flow simulated with the SFRM LBM at normalized time steps for $Re = 0.0625$, $Ca = 0.42$, $Ch = 0.057$, $Pe = 0.43$. This figure is reproduced from [235], Copyright (2023), with permission from the authors and the American Institute of Mathematical Sciences.

5 Conclusions

The main result of the present work is the introduction of a novel coherent mathematical framework to analyze the constructability, stability and limit consistency of LBMs (see Chapter 3, specifically Sections 3.1 and 3.2). The relaxation principles of the LBM render the method a bottom-up approach. To advance the LBM into a generic methodology for approximating broad classes of PDEs, this relaxation limit must be retained at all steps in its construction. For the example of an advection–diffusion equation in d dimensions, the novel constructive ansatz offers a completely top-down mathematical path from the PDE toward the final LBE, which forms the centerpiece of the LBM. Modular convergence arguments are used at each step to further analyze the key ingredients of relaxation frequencies, equilibria, and moment bases in the ansatz. Hence, complementary to the rigorous procedure for the simple ADE, necessary LBM ingredients to approximate other PDEs are analyzed by means of possibly nonrigorous but pragmatic and expedient methodology. Specific results either being a consequence of the novel framework, or complementing it, are summarized below. Additionally, the contributions are assessed with respect to the initially formulated objectives, and future research directions are given.

5.1 Summary

In Section 3.1, the contraction limit of the relaxation terms added in the constructive ansatz is analyzed in detail. For uniform relaxation, existing rigorous results can be used to prove the convergence of the constructed RS to the entropy solution of the nonlinear advection–diffusion equation in d dimensions (Proposition 3.1.3). Nonuniform relaxation with MRT collision is analyzed in terms of linear von Neumann stability, which forms the basis for the definition of stability sets used for example, in Corollary 3.1.2. In Section 3.2, the presently used discrete velocity models and moment spaces are summarized. As a main contribution, the second order limit consistent discretization of the constructed and spectrally decomposed RS is proposed. The procedure is based on chaining finite difference operators and Taylor expansions on three neighboring time steps to consistently derive an LBE with MRT collision and generic scaling. At each level of discretization, the error contribution on top of the relaxation limit is isolated. The method is contrasted with other approaches such as asymptotic preserving notions. Stability and convergence is proven linearly, as commonly done for finite difference discretizations. Based on the composition of limits, the notion of limit consistency is introduced to track both, the respective and joint order of approximation. Extensions for nonlinearly stabilized collisions in terms of entropy controlled relaxation are discussed and combined with a computationally efficient velocity stencil and equilibrium. Additionally, the MRF collision is proposed as a complete abstraction of the relaxation times to space-time dependent functions. In Section 3.3, existing LBEs for the here approximated PDEs are summarized and novel LBEs are proposed, for example, to approximate the temporally filtered NSE. Additionally, in Section 3.3.4, algorithmic concepts for LBM-based extensive computations to numerically observe analytically unseen stability and for computing statistical solutions of the NSE and the EE with LBMs are devised.

Preceding to the numerical analysis, in Chapter 2, mathematical models are derived in the form of PDEs. The focus is placed on PDEs with convection and advection terms in the broadest sense, where existing models are revisited and in parts newly derived. Exemplary for the latter, higher order free energy functionals are used for binary fluid flow models in Section 2.6.1, and the homogenization of the nonstationary incompressible NSE in various regimes is assessed from the viewpoint of applicability in Section 2.5.

Complementary to deriving the mathematical models, constructing the LBM and the numerical analysis thereof, Chapter 4 documents an array of numerical experiments. The combination of the intrinsic parallelizability of LBMs with the platform-agnostic and scalable open source framework OpenLB enables in-depth computational tests. The approximation of various PDEs with LBMs is computationally analyzed in terms of stability, consistency, and accuracy. The top-down constructed LBM for advection, pure diffusion, or with both features in the targeted PDE is numerically tested in Section 4.1. The theoretical stability bounds are approved for smooth and nonsmooth initial data in up to three dimensions and in several ranges of grid normalized nondimensional numbers. The additional limit toward a sharp interface solution of the CHE is computationally analyzed and observed for a periodic droplet movement in two dimensions in Section 4.2. The overall second order convergence in space is indicated. In Section 4.3, deterministic and statistical TGV solutions of the incompressible NSE are approximated with various LBMs. Existing and novel schemes are extensively tested in terms of stability and convergence over large range of parameter configurations. In particular, advanced relaxation with the KBC collision is spectrally analyzed on the basis of Fourier transforming both, the hydrodynamic target quantities and the kinetic relaxation frequencies. Primary numerical evidence is given that the entropy controller detects and counteracts spectral energy overloads at high wavenumbers where an inverse K41 power law is observed in the relaxation spectrum. The time dependent EOC toward a pseudo-spectral resolved reference solution is found to be unaffectedly of second order in the maximum vorticity peak region, even for the presently used truncated polynomial equilibrium. Moreover, from the numerically observed stability on a broad range of parameter scans, empirical relaxation functions are proposed for MRF collision, which retains an error minimum in terms of the total dissipation rate computed in artificial three-dimensional turbulence. Finally, statistical solutions to the incompressible EE are approximated along the low viscosity limit. A randomized TGV initialization is used to impose uncertainty into the flow field. For the computed range of configurations, the convergence of the mean and variance of compensated energy spectra is indicated. In addition to the computational analysis of several LBM collision schemes, theoretical insights are computationally explored. This work provides an investigation of the capabilities of classical von Neumann techniques for the stability analysis of MRT LBMs based on orthogonal moments. A comparison of theoretically derived linear stability to numerically observed computations through several parameter spaces reveals the spectral sampling of grid effects in the former. The latter in turn indicates that the dissipation error is minimal within regions of nonlinear stability sets for hyperviscous configurations that are near the SRT BGK configuration.

The numerical experiments include a pilot study on the first LBM TLES with SRT and MRF collision in Section 4.4. The proposed LBM TLES is based on the closure of the FDVBE with the TDDM and found suitable for increasing the EOC in terms of accuracy to SEM DNS reference solutions of artificial DHIT. A numerical calibration is carried out by investigating the interplay of the lattice Mach number affecting the MRT LBM and the filter width, which characterizes the TLES. Capabilities of the novel methods with respect to turbulence quantity recovery are assessed and a good agreement to the DNS reference data is found. An error measurement with respect to the energy spectrum is conducted and linked to the subgrid activity. Additionally, the consistency of the LBM paired with first and second order multistep finite difference discretizations of the TDDM toward the DNS regime is numerically confirmed.

In Section 2.5, the characteristic regimes of the homogenization of the nonstationary NSE with specific porosities are merged into one homogenized NSE, which is approximated by the HLBM for fluid flow through porous media. Based on an application-oriented rationale, the porosity range recoverable by the mathematical model is dictated by the maximal sphere packing for the nonvanishing obstacle case. The here proposed HLBM is derived with limit consistent discretization from approximating the homogenized nonstationary NSE in Section 3.3.1.4. The present scheme is found to reduce to an existing one for simplified flow configurations. The numerical tests in Section 4.5 approve the approximation of the pressure difference with second order consistency in a porous Poiseuille flow through a square duct.

The implementation of classical experimental setups for binary extensional and shear flows with the SFRM LBM in OpenLB allows for the computational modeling of stationary states and breakup mechanisms of droplets and bubbles in two and three dimensions. In Section 4.6, Taylor's parallel-band and four-roller devices are digitally twinned and used for the validation of the numerical scheme when approximating an NSCHE system that models a binary mixture

flow. To the author's knowledge, this work is the first application of LBMs for simulating a four-roller apparatus. Characteristic deformations for steady states and breakup scenarios in critical capillary regimes are captured, and the known volume loss of small droplet-domain ratios is observed and circumvented with suitably fine meshes. The known differences between two and three-dimensional droplet deformations and good agreement to reference results are observed.

Conclusively, the modifications of scaling and relaxation parameters as well as specific moments and equilibria to cause the limit of the LBM to distinct TEQs are theoretically analyzed and excessively tested in this work. Options that finally yield control over the relaxation terms appearing in the PDE, which is to be approximated are proposed (relaxation functions) and discussed (entropy control) together with numerical procedures for the indication and analysis of such. In summary, a novel coherent framework is built from a combination of a constructive ansatz (CTN1), modular convergence proofs (CTN2), and the enablement of extensive numerical tests (CTN3). This framework allows for the analysis and construction of new schemes (CTN4) and contributes to unfolding and analyzing the specific enforcing of numerical features for example numerical dissipation under the preservation of limit consistency of LBMs already at the level of construction for a vast range of applications.

5.2 Limitations and outlook

The progress gained from trailblazing the combination of top-down construction and relaxation limit consistent and stable discretizations in a coherent methodology, motivated this research in the first place. Thus, it contributes toward the transformation of the LBM to a generically applicable solver for various classes of PDEs. Looking back, the objectives stated in Chapter 1 have been reached, namely: (OBJ1) Top-down construction for LBMs from a targeted PDE, (OBJ2) Convergence analysis of the combined limits in LBMs, (OBJ3) Description of the kinetic information in LBMs, (OBJ4) Establishment of novel LBMs for newly targeted PDEs. Nevertheless, the conducted research also brings forth the limitations of the proposed methodology. Below, these limitations are summarized and serve as a basis for suggesting further research directions.

- The present work focuses on approximating PDEs, which are already in – or have been transformed to – transport form consisting of $(\partial_t + \nabla_{\mathbf{x}} \cdot)$ with optional diffusion or higher order derivatives in space. Several studies (for example [49]) have shown that adapting the equilibrium function is beneficial for approximating nontransport PDEs (without ∂_t) where otherwise, the time derivative must be numerically suppressed. As the change in equilibrium is merely a change in the added perturbation terms in the proposed ansatz (see Section 3.1), categorizing the appearance of these terms would enable a unified construction for PDEs of second order at least.
- As a matter of fact, the equilibria used for example, in approximations for the CHE or for nontransport PDEs typically require a null velocity where the equilibrium function is specialized and differs from the remaining velocity space. Since by construction, the relaxation system introduces an optional rest velocity, the present methodology serves as a first step in this direction.
- Including arbitrary equilibrium formulations besides the generalized Maxwellian form, would in turn allow for formulating new collision schemes, which are optimal in terms of stability and consistency for approximating nontransport PDEs. To the knowledge of the author, apart from classical MRT schemes, advanced collision has rarely been studied for approximating PDEs of nontransport type with LBMs.
- This work contains stability analyses of uniform and nonuniform relaxation, in terms of both, linear theoretical and nonlinear numerical techniques (see Chapter 3). Whereas linear theoretical analysis is useful for simplified problems and proving the stability of the scheme for classical convergence results, nonlinear numerical observations are found to be crucial for applicative insights on the scheme taking into account all sources of errors. Needless to say, nonlinear Lyapunov stability yields a third notion for analyzing nonuniform relaxation and

enables to adaptively stabilize underresolved flow simulations with hyperviscosity. However, to handle boundary induced instability in approximating IBVPs involving complex PDEs, the method of numerically observing stability is unrestrictedly applicable. Forthcoming research should combine the techniques to analyze and propose solutions to numerical instabilities at the domain boundary when approximating IBVPs with LBMs.

- For targeted PDEs akin to the NSE, the thermodynamic information is helpful to consistently couple additional multiphysics to the relaxation limit. Thus, removing the thermodynamic parts of the LBM completely to enable better analyzability will introduce new challenges in modeling for additional terms or couplings. Further, the methods for including boundary conditions into LBMs benefit from the coarse-grained information from mesoscopic or even microscopic levels of modeling. These challenges could for example be approached by extending established theory from kinetic equations toward mathematically generic relaxation specifically in the context of LBMs.
- Presently, the limit consistent discretization is carried out with second order accuracy. In principle, whereas a higher order discretization is reachable, the limit consistency with respect to relaxation still must be ensured. Higher order discretizations have been proposed (see for example [70]) and should be included in the constructive ansatz.
- Although not combined yet, the proposed methodology of time filtering for LBMs is naturally compatible with computing statistical solutions, which are a result of random spatial perturbations in the initial data. It is conjecturable that the benefits from direct deconvolution of the temporally filtered variables will allow for filtering statistical turbulence quantities in a controllable and consistent way, similar to the deterministic case. Based on that, an improvement in coarse grid computations with a stabilized TLES LBM would reduce the time-to-statistical-solution. Additionally, with respect to limit consistent discretization in the scaling coupled space-time domain, the construction of an LES in space and time might reveal improved consistency toward the TEQ.
- Since the computation of statistical solutions to the NSE and EE in three dimensions is presently performed with SLMC LBMs only, the question for advanced UQ methodology to be paired with the LBM is immediately raised. MLMC or QMC, or at best both [169], should be used along with LBMs to allow for high resolution simulations of statistical solutions involving more complex initial distributions and boundaries. Additionally, intrusive approaches should yield advantages when used with LBMs compared to discretizing the modified target PDEs containing nonlinear gradient terms in the transport part (which is not the case for LBMs).
- Here, the HLBM for fluid flow in porous media is numerically tested for stationary flows only. Since the limit toward the nonstationary HNSE is uncovered in Section 3.3, numerical tests for turbulent flows in mathematical porous media models are planned. Future studies should additionally involve model extensions in terms of taking porosity gradients [58] or anisotropic permeability tensors [17] into account.
- Albeit sharpening the diffuse interface considerably, the proposed HSFRM LBM with higher order free energy functionals (see e.g. Section 2.6.1) still does not completely solve the model-intrinsic problem of the CHE in terms of volume loss. Remedies to this observation have been proposed for direct NSCHE discretization with finite differences [180] and are transferable to LBMs. Along with the higher order free energy functionals, correction terms should be included to turn the FRM LBM into an approximation for the conservative CHE. Moreover, model extensions to nonuniform viscosity and density ratios as well adaptive discretizations are necessary to reach the complexity of industrial applications.

In summary, the here established explicit combination of mathematical modeling, numerical analysis and computational experiments (see Figure 1.2) is found to be essential for the proposal and investigation of novel LBMs for PDEs. Considering the mathematical modeling, an advanced conceptualization of models is required, which are firstly, mapping accurately from the problem at hand, and secondly come with suitable structures and well-behaved properties to be optimally approximated with LBMs. Although the numerical analysis of the LBM has brought up several

rigorous contributions already, a unifying coherent path for pragmatic usage on any given PDE problem, including boundary conditions, is still to be established. Albeit the intrinsic structure of LBMs enables remarkable scalability of simulations on contemporary HPC machines, this feature is not outsourced yet. To this end, the most prolific advantage of the LBM – its parallelizability – must be applied not only to approximate the PDE at hand but also to analyze the method itself with the help of sustainably developed and optimized software. Furthermore, such obtained robust and computationally efficient collision kernels are valuable modular pieces to be embedded into and thus accelerate larger computational data structures. This work is a first step into all three of the above directions, and is hoped to serve as a starting point for future research on transforming the LBM into a modern, efficient and robust solver for large classes of PDEs.

Bibliography

- [1] A. Abdelsamie, G. Lartigue, C. E. Frouzakis, and D. Thévenin. The Taylor–Green vortex as a benchmark for high-fidelity combustion simulations using low-Mach solvers. *Computers & Fluids*, 223:104935, 2021. doi: 10.1016/j.compfluid.2021.104935.
- [2] J. Ahrens, B. Geveci, and C. Law. ParaView: An End-User Tool for Large Data Visualization. In C. D. Hansen and C. R. Johnson, editors, *Visualization Handbook*, pages 717–731. Elsevier Inc., Burlington, MA, USA, 2005. URL <https://www.sciencedirect.com/book/9780123875822/visualization-handbook>.
- [3] C. K. Aidun and J. R. Clausen. Lattice-Boltzmann Method for Complex Flows. *Annual Review of Fluid Mechanics*, 42(1):439–472, 2010. doi: 10.1146/annurev-fluid-121108-145519.
- [4] G. Allaire. *Homogénéisation des équations de Stokes et de Navier-Stokes*. PhD thesis, Centre d’Etudes Nucléaires de Saclay, 1990. URL http://inis.iaea.org/search/search.aspx?orig_q=RN:22020229. CEA-N–2638.
- [5] G. Allaire. Continuity of the Darcy’s law in the low-volume fraction limit. *Annali della Scuola Normale Superiore di Pisa - Classe di Scienze*, Ser. 4, 18(4):475–499, 1991. URL http://www.numdam.org/item/ASNSP_1991_4_18_4_475_0.
- [6] G. Allaire. Homogenization of the Navier-Stokes Equations in Open Sets Perforated with Tiny Holes I: Abstract Framework, a Volume Distribution of Holes. *Archive for Rational Mechanics and Analysis*, 113(3):209–259, 1991. doi: 10.1007/BF00375065.
- [7] G. Allaire. Homogenization of the Navier-Stokes Equations in Open Sets Perforated with Tiny Holes II: Non-Critical Sizes of the Holes for a Volume Distribution and a Surface Distribution of Holes. *Archive for Rational Mechanics and Analysis*, 113(3):261–298, 1991. doi: 10.1007/BF00375066.
- [8] G. Allaire. Homogenization of the Navier–Stokes equations and derivation of Brinkman’s law. In C. Carasso, C. Conca, J.-P. Puel, and R. Correa, editors, *Mathématiques appliquées aux sciences de l’ingénieur: 2e colloque franco-chilien de mathématiques appliquées (Santiago, 1989)*, pages 7–20. Cépaduès, 1991.
- [9] G. Allaire. Homogenization of the unsteady Stokes equations in porous media. In C. Bandle, J. Bemelmans, M. Chipot, M. Grüter, and J. Saint Jean Paulin, editors, *Progress in partial differential equations: calculus of variations, applications*, Pitman Research Notes in Mathematics Series 267, pages 109–109. Longman Scientific & Technical, 1992.
- [10] G. Allaire. Homogenization and Two-Scale Convergence. *SIAM Journal on Mathematical Analysis*, 23(6): 1482–1518, 1992. doi: 10.1137/0523084.
- [11] G. Allaire. Lecture 2. *CEA-EDF-INRIA School on Homogenization, December 13–16, 2010*. URL <http://www.cmap.polytechnique.fr/~allaire/homog/>.
- [12] A. R. Appadu, J. K. Djoko, H. Gidey, and J. M.-S. Lubuma. Analysis of multilevel finite volume approximation of 2D convective Cahn–Hilliard equation. *Japan Journal of Industrial and Applied Mathematics*, 34:253–304, 2017. doi: 10.1007/s13160-017-0239-y.

- [13] M. K. Arthur. Point Picking and Distributing on the Disc and Sphere. Technical report, Army Research Lab Aberdeen Proving Ground MD Weapons and Materials Research, 2015. URL <https://apps.dtic.mil/sti/citations/ADA626479>.
- [14] H. Babovsky. *Die Boltzmann-Gleichung: Modellbildung-Numerik-Anwendungen*. Springer/Vieweg+Teubner, 1998. doi: 10.1007/978-3-663-12034-6.
- [15] M. K. Banda, W.-A. Yong, and A. Klar. A stability notion for lattice Boltzmann equations. *SIAM Journal on Scientific Computing*, 27(6):2098–2111, 2006. doi: 10.1137/040606211.
- [16] M. K. Banda, A. Klar, L. Pareschi, and M. Seaïd. Lattice-Boltzmann type relaxation systems and high order relaxation schemes for the incompressible Navier–Stokes equations. *Mathematics of Computation*, 77(262):943–965, 2008. doi: 10.1090/S0025-5718-07-02034-0.
- [17] B. Bang and D. Lukkassen. Application of homogenization theory related to Stokes flow in porous media. *Applications of Mathematics*, 44(4):309–319, 1999. doi: 10.1023/A:1023084614058.
- [18] P. Bansal. Numerical approximation of statistical solutions of the incompressible Navier-Stokes Equations. *arXiv*, preprint, 2021. doi: 10.48550/arXiv.2107.06073. URL <https://arxiv.org/abs/2107.06073>.
- [19] M. F. Barad, J. G. Kocheemoolayil, and C. C. Kiris. Lattice Boltzmann and Navier–Stokes Cartesian CFD approaches for airframe noise predictions. *23rd AIAA Computational Fluid Dynamics Conference, 2017*, June 2017:1–16, 2017. doi: 10.2514/6.2017-4404.
- [20] C. Bardos, F. Golse, and C. D. Levermore. Fluid dynamic limits of kinetic equations II: Convergence proofs for the Boltzmann equation. *Communications on Pure and Applied Mathematics*, 46(5):667–753, 1993. doi: 10.1002/cpa.3160460503.
- [21] S. Bartels. *Numerical methods for nonlinear partial differential equations*, volume 47. Springer Cham, 2015. doi: 10.1007/978-3-319-13797-1.
- [22] R. Bauer. Distribution of Points on a Sphere with Application to Star Catalogs. *Journal of Guidance, Control, and Dynamics*, 23(1):130–137, 2000. doi: 10.2514/2.4497.
- [23] J. Bear. *Dynamics of fluids in porous media*. American Elsevier Publishing Co, 1972.
- [24] A. Beck, J. Dürrwächter, T. Kuhn, F. Meyer, C.-D. Munz, and C. Rohde. *hp*-Multilevel Monte Carlo Methods for Uncertainty Quantification of Compressible Navier–Stokes Equations. *SIAM Journal on Scientific Computing*, 42(4):B1067–B1091, 2020. doi: 10.1137/18M1210575.
- [25] A. Beck, J. Dürrwächter, T. Kuhn, F. Meyer, C.-D. Munz, and C. Rohde. Uncertainty Quantification in High Performance Computational Fluid Dynamics. In W. E. Nagel, D. H. Kröner, and M. M. Resch, editors, *High Performance Computing in Science and Engineering '19*, pages 355–371, Cham, 2021. Springer International Publishing. doi: 10.1007/978-3-030-66792-4_24.
- [26] T. Bellotti. Truncation errors and modified equations for the lattice Boltzmann method via the corresponding Finite Difference schemes. *ESAIM: Mathematical Modelling and Numerical Analysis (M2AN)*, 57(3):1225–1255, 2023. doi: 10.1051/m2an/2023008.
- [27] T. Bellotti. Initialisation from lattice Boltzmann to multi-step Finite Difference methods: modified equations and discrete observability. *arXiv*, preprint, 2023. doi: 10.48550/arXiv.2302.07558. URL <https://arxiv.org/abs/2302.07558>.
- [28] T. Bellotti, B. Graille, and M. Massot. Finite Difference formulation of any lattice Boltzmann scheme. *Numerische Mathematik*, 152:1–40, 2022. doi: 10.1007/s00211-022-01302-2.

- [29] B. J. Bentley and L. G. Leal. An experimental investigation of drop deformation and breakup in steady, two-dimensional linear flows. *Journal of Fluid Mechanics*, 167:241–283, 1986. doi: 10.1017/S0022112086002811.
- [30] L. C. Berselli and S. Spirito. On the convergence of a fully discrete scheme of LES type to physically relevant solutions of the incompressible Navier–Stokes. *Zeitschrift für angewandte Mathematik und Physik*, 69:1–15, 2018. doi: 10.1007/s00033-018-0955-4.
- [31] P. L. Bhatnagar, E. P. Gross, and M. Krook. A Model for Collision Processes in Gases. I. Small Amplitude Processes in Charged and Neutral One-Component Systems. *Physical Review*, 94:511–525, 1954. doi: 10.1103/PhysRev.94.511.
- [32] D. I. Bigio, C. R. Marks, and R. V. Calabrese. Predicting drop breakup in complex flows from model flow experiments. *International Polymer Processing*, 13(2):192–198, 1998. doi: 10.3139/217.980192.
- [33] J. F. Blowey and C. M. Elliott. The Cahn–Hilliard gradient theory for phase separation with non-smooth free energy Part I: Mathematical analysis. *European Journal of Applied Mathematics*, 2(3):233–280, 1991. doi: 10.1017/S095679250000053X.
- [34] B. M. Boghosian, J. Yezep, P. V. Coveney, and A. Wagner. Entropic lattice Boltzmann methods. *Proceedings of the Royal Society A*, 457(2007):717–766, 2001. doi: 10.1098/rspa.2000.0689.
- [35] F. Bösch, S. S. Chikatamarla, and I. Karlin. Entropic multi-relaxation models for simulation of fluid turbulence. *ESAIM: Proceedings and Surveys*, 52:1–24, 2015. doi: 10.1051/proc/201552001.
- [36] F. Bösch, S. S. Chikatamarla, and I. V. Karlin. Entropic multirelaxation lattice Boltzmann models for turbulent flows. *Physical Review E*, 92:043309, 2015. doi: 10.1103/PhysRevE.92.043309.
- [37] F. Bouchut, F. R. Guarguaglini, and R. Natalini. Diffusive BGK approximations for nonlinear multidimensional parabolic equations. *Indiana University Mathematics Journal*, 49(2):723–749, 2000. doi: 10.1512/iumj.2000.49.1811.
- [38] M. Bouzidi, M. Firdaouss, and P. Lallemand. Momentum transfer of a Boltzmann-lattice fluid with boundaries. *Physics of Fluids*, 13(11):3452–3459, 2001. doi: 10.1063/1.1399290.
- [39] M. E. Brachet. Direct simulation of three-dimensional turbulence in the Taylor–Green vortex. *Fluid Dynamics Research*, 8(1–4):1–8, 1991. doi: 10.1016/0169-5983(91)90026-F.
- [40] M. E. Brachet, D. I. Meiron, S. A. Orszag, B. Nickel, R. H. Morf, and U. Frisch. Small-scale structure of the Taylor–Green vortex. *Journal of Fluid Mechanics*, 130:411–452, 1983. doi: 10.1017/S0022112083001159.
- [41] H. Brinkman. On the permeability of media consisting of closely packed porous particles. *Flow, Turbulence and Combustion*, 1(1):81, 1949. doi: 10.1007/BF02120318.
- [42] F. Bukreev, S. Simonis, A. Kummerländer, J. Jeßberger, and M. J. Krause. Consistent lattice Boltzmann methods for the volume averaged Navier–Stokes equations. *Journal of Computational Physics*, 490:112301, 2023. doi: 10.1016/j.jcp.2023.112301.
- [43] F. Caetano, F. Dubois, and B. Graille. A result of convergence for a mono-dimensional two-velocities lattice Boltzmann scheme. *Discrete and Continuous Dynamical Systems - S*, 2023. doi: 10.3934/dcdss.2023072.
- [44] A. Caiazzo. Analysis of lattice Boltzmann initialization routines. *Journal of Statistical Physics*, 121(1-2):37–48, 2005. doi: 10.1007/s10955-005-7010-5.
- [45] A. Caiazzo, M. Junk, and M. Rheinländer. Comparison of analysis techniques for the lattice Boltzmann method. *Computers & Mathematics with Applications*, 58(5):883–897, 2009. doi: 10.1016/j.camwa.2009.02.011.

- [46] S. G. K. Calhoun, K. K. Brower, V. C. Suja, G. Kim, N. Wang, A. L. McCully, H. Kusumaatmaja, G. G. Fuller, and P. M. Fordyce. Systematic characterization of effect of flow rates and buffer compositions on double emulsion droplet volumes and stability. *Lab on a Chip*, 22:2315–2330, 2022. doi: 10.1039/D2LC00229A.
- [47] M. E. Cates and E. Tjhung. Theories of binary fluid mixtures: from phase-separation kinetics to active emulsions. *Journal of Fluid Mechanics*, 836:P1, 2018. doi: 10.1017/jfm.2017.832.
- [48] D. Chae. The vanishing viscosity limit of statistical solutions of the Navier-Stokes equations. I. 2-D periodic case. *Journal of Mathematical Analysis and Applications*, 155(2):437–459, 1991. doi: 10.1016/0022-247X(91)90012-O.
- [49] Z. Chai and B. Shi. A novel lattice Boltzmann model for the Poisson equation. *Applied Mathematical Modelling*, 32(10):2050–2058, 2008. doi: 10.1016/j.apm.2007.06.033.
- [50] Z. Chai, N. He, Z. Guo, and B. Shi. Lattice Boltzmann model for high-order nonlinear partial differential equations. *Physical Review E*, 97(1):013304, 2018. doi: 10.1103/PhysRevE.97.013304.
- [51] M. Chávez-Modena, E. Ferrer, and G. Rubio. Improving the stability of multiple-relaxation lattice Boltzmann methods with central moments. *Computers & Fluids*, 172:397–409, 2018. doi: 10.1016/j.compfluid.2018.03.084.
- [52] M. Chávez-Modena, A. Martínez-Cava, G. Rubio, and E. Ferrer. Optimizing free parameters in the D3Q19 Multiple-Relaxation lattice Boltzmann methods to simulate under-resolved turbulent flows. *Journal of Computational Science*, 45:101170, 2020. doi: 10.1016/j.jocs.2020.101170.
- [53] B. Chopard, J.-L. Falcone, and J. Latt. The lattice Boltzmann advection-diffusion model revisited. *The European Physical Journal Special Topics*, 171(1):245–249, 2009. doi: 10.1140/epjst/e2009-01035-5.
- [54] C. Coreixas and J. Latt. Compressible lattice Boltzmann methods with adaptive velocity stencils: An interpolation-free formulation. *Physics of Fluids*, 32(11):116102, 2020. doi: 10.1063/5.0027986.
- [55] C. Coreixas, B. Chopard, and J. Latt. Comprehensive comparison of collision models in the lattice Boltzmann framework: Theoretical investigations. *Physical Review E*, 100:033305, 2019. doi: 10.1103/PhysRevE.100.033305.
- [56] C. Coreixas, G. Wissocq, B. Chopard, and J. Latt. Impact of collision models on the physical properties and the stability of lattice Boltzmann methods. *Philosophical Transactions of the Royal Society A*, 378(2175):20190397, 2020. doi: 10.1098/rsta.2019.0397.
- [57] T. H. Cormen, C. E. Leiserson, R. L. Rivest, and C. Stein. *Introduction to algorithms*. The MIT Press, 2022.
- [58] M. P. Dalwadi, I. M. Griffiths, and M. Bruna. Understanding how porosity gradients can make a better filter using homogenization theory. *Proceedings of the Royal Society A*, 471(2182):20150464, 2015. doi: 10.1098/rspa.2015.0464.
- [59] D. Dapelo, S. Simonis, M. J. Krause, and J. Bridgeman. Lattice-Boltzmann coupled models for advection–diffusion flow on a wide range of Péclet numbers. *Journal of Computational Science*, 51:101363, 2021. doi: 10.1016/j.jocs.2021.101363.
- [60] H. P. G. Darcy. *Les Fontaines publiques de la ville de Dijon. Exposition et application des principes à suivre et des formules à employer dans les questions de distribution d’eau, etc.* V. Dalmont, 1856.
- [61] J. DeBonis. Solutions of the Taylor–Green vortex problem using high-resolution explicit finite difference methods. In *51st AIAA Aerospace Sciences Meeting including the New Horizons Forum and Aerospace Exposition*, 2013. doi: 10.2514/6.2013-382.

- [62] P. J. Dellar. Bulk and shear viscosities in lattice Boltzmann equations. *Physical Review E*, 64:031203, 2001. doi: 10.1103/PhysRevE.64.031203.
- [63] P. J. Dellar. Incompressible limits of lattice Boltzmann equations using multiple relaxation times. *Journal of Computational Physics*, 190:351–370, 2003. doi: 10.1016/S0021-9991(03)00279-1.
- [64] P. J. Dellar. An interpretation and derivation of the lattice Boltzmann method using Strang splitting. *Computers & Mathematics with Applications*, 65(2):129–141, 2013.
- [65] M. O. Deville, P. F. Fischer, and E. H. Mund. *High-order methods for incompressible fluid flow*, volume 9. Cambridge University Press, 2002.
- [66] D. d’Humières. Multiple-relaxation-time lattice Boltzmann models in three dimensions. *Philosophical Transactions of the Royal Society A*, 360(1792):437–451, 2002. doi: 10.1098/rsta.2001.0955.
- [67] Y.-H. Dong, P. Sagaut, and S. Marie. Inertial consistent subgrid model for large-eddy simulation based on the lattice Boltzmann method. *Physics of Fluids*, 20(3):35104, 2008. doi: 10.1063/1.2842379.
- [68] B. Dorschner, F. Bösch, and I. V. Karlin. Particles on Demand for Kinetic Theory. *Physical Review Letters*, 121:130602, 2018. doi: 10.1103/PhysRevLett.121.130602.
- [69] F. Dubois. Equivalent partial differential equations of a lattice Boltzmann scheme. *Computers & Mathematics with Applications*, 55(7):1441–1449, 2008. doi: 10.1016/j.camwa.2007.08.003.
- [70] F. Dubois and P. Lallemand. Towards higher order lattice Boltzmann schemes. *Journal of Statistical Mechanics: Theory and Experiment*, 2009(06):P06006, 2009. doi: 10.1088/1742-5468/2009/06/P06006.
- [71] A. Eden and V. Kalantarov. The convective Cahn–Hilliard equation. *Applied Mathematics Letters*, 20(4):455–461, 2007. doi: 10.1016/j.aml.2006.05.014.
- [72] A. Eden and V. K. Kalantarov. 3D convective Cahn–Hilliard equation. *Communications on Pure and Applied Analysis*, 6(4):1075–1086, 2007. doi: 10.3934/cpaa.2007.6.1075.
- [73] A. Eden, C. Foias, B. Nicolaenko, and Z. She. Exponential attractors and their relevance to fluid dynamics systems. *Physica D: Nonlinear Phenomena*, 63:350–360, 1993. doi: 10.1016/0167-2789(93)90116-I.
- [74] A. Eden, C. Foias, and B. Nicolaenko. Exponential attractors of optimal Lyapunov dimension for Navier-Stokes equations. *Journal of Dynamics and Differential Equations*, 6:301–323, 1994. doi: 10.1007/BF02218532.
- [75] A. Eden, C. Foias, B. Nicolaenko, and R. Temam. *Exponential Attractors for Dissipative Evolution Equations*. Research in Applied Mathematics. John Wiley & Sons, 1994. URL <https://cir.nii.ac.jp/crid/1570291224960836224>.
- [76] B. H. Elton, C. D. Levermore, and G. H. Rodrigue. Convergence of Convective–Diffusive Lattice Boltzmann Methods. *SIAM Journal on Numerical Analysis*, 32(5):1327–1354, 1995. doi: 10.1137/0732062.
- [77] S. Ergun. Fluid flow through packed columns. *Chemical Engineering Progress*, 48(2):89–94, 1952.
- [78] L. C. Evans. *Partial Differential Equations*, volume 19 of *Graduate Studies in Mathematics*. American Mathematical Society, Providence, Rhode Island, USA, second edition, 2010.
- [79] D. Fauconnier, C. Bogey, and E. Dick. On the performance of relaxation filtering for large-eddy simulation. *Journal of Turbulence*, 14(1):22–49, 2013. doi: 10.1080/14685248.2012.740567.
- [80] C. L. Fefferman. Existence and smoothness of the Navier–Stokes equation. *The millennium prize problems*, 57:67, 2000. URL <https://www.claymath.org/wp-content/uploads/2022/06/navierstokes.pdf>.

- [81] N. Fehn, M. Kronbichler, P. Munch, and W. A. Wall. Numerical evidence of anomalous energy dissipation in incompressible Euler flows: towards grid-converged results for the inviscid Taylor–Green problem. *Journal of Fluid Mechanics*, 932:A40, 2022. doi: 10.1017/jfm.2021.1003.
- [82] E. Feireisl, Y. Namlyeyeva, and Š. Nečasová. Homogenization of the evolutionary Navier–Stokes system. *Manuscripta Mathematica*, 149(1–2):251–274, 2016. doi: 10.1007/s00229-015-0778-y.
- [83] F. Feppon. High Order Homogenization of the Stokes System in a Periodic Porous Medium. *SIAM Journal on Mathematical Analysis*, 53(3):2890–2924, 2021. doi: 10.1137/20M1348078.
- [84] F. Feppon and W. Jing. High Order Homogenized Stokes Models Capture all Three Regimes. *SIAM Journal on Mathematical Analysis*, 54(4):5013–5040, 2022. doi: 10.1137/21M1390232.
- [85] U. S. Fjordholm, S. Mishra, and F. Weber. On the vanishing viscosity limit of statistical solutions of the incompressible Navier-Stokes equations. *arXiv*, preprint, 2021. doi: 10.48550/arXiv.2110.04674. URL <https://arxiv.org/abs/2110.04674>.
- [86] C. Foias and G. Prodi. Sur les solutions statistiques des équations de Navier-Stokes. *Annali di Matematica Pura ed Applicata*, 111(1):307–330, 1976. doi: 10.1007/BF02411822.
- [87] C. Foias, O. Manley, R. Rosa, and R. Temam. *Navier-Stokes equations and turbulence*, volume 83. Cambridge University Press, 2001.
- [88] G. B. Folland. *Advanced Calculus*. Pearson Education (US), 2001.
- [89] P. Forchheimer. Wasserbewegung durch Boden. *Zeitschrift des Vereins deutscher Ingenieure*, 45:1782–1788, 1901.
- [90] L. Fu, X. Y. Hu, and N. A. Adams. A new class of adaptive high-order targeted ENO schemes for hyperbolic conservation laws. *Journal of Computational Physics*, 374:724–751, 2018. doi: 10.1016/j.jcp.2018.07.043.
- [91] R. Fučík and R. Straka. Equivalent finite difference and partial differential equations for the lattice Boltzmann method. *Computers & Mathematics with Applications*, 90:96–103, 2021. doi: 10.1016/j.camwa.2021.03.014.
- [92] R. Fučík, P. Eichler, J. Klinkovský, R. Straka, and T. Oberhuber. Lattice Boltzmann Method Analysis Tool (LBMAT). *Numerical Algorithms*, pages 1–17, 2022. doi: 10.1007/s11075-022-01476-8.
- [93] M. Gaedtke, S. Wachter, M. Rädle, H. Nirschl, and M. J. Krause. Application of a lattice Boltzmann method combined with a Smagorinsky turbulence model to spatially resolved heat flux inside a refrigerated vehicle. *Computers & Mathematics with Applications*, 76(10):2315–2329, 2018. doi: 10.1016/j.camwa.2018.08.018.
- [94] M. Gaedtke, S. Abishek, R. Mead-Hunter, A. J. C. King, B. J. Mullins, H. Nirschl, and M. J. Krause. Total enthalpy-based lattice Boltzmann simulations of melting in paraffin/metal foam composite phase change materials. *International Journal of Heat and Mass Transfer*, 155:119870, 2020. doi: 10.1016/j.ijheatmasstransfer.2020.119870.
- [95] M. Geier and A. Pasquali. Fourth order Galilean invariance for the lattice Boltzmann method. *Computers & Fluids*, 166:139–151, 2018. doi: 10.1016/j.compfluid.2018.01.015.
- [96] M. Geier, A. Pasquali, and M. Schönherr. Parametrization of the cumulant lattice Boltzmann method for fourth order accurate diffusion part I: Derivation and validation. *Journal of Computational Physics*, 348:862–888, 2017. doi: 10.1016/j.jcp.2017.05.040.
- [97] M. Geier, S. Lenz, M. Schönherr, and M. Krafczyk. Under-resolved and large eddy simulations of a decaying Taylor–Green vortex with the cumulant lattice Boltzmann method. *Theoretical and Computational Fluid Dynamics*, 35:169–208, 2021. doi: 10.1007/s00162-020-00555-7.

- [98] B. J. Geurts. Analysis of errors occurring in large eddy simulation. *Philosophical Transactions of the Royal Society A*, 367(1899):2873–2883, 2009. doi: 10.1098/rsta.2009.0001.
- [99] B. J. Geurts and J. Fröhlich. A framework for predicting accuracy limitations in large-eddy simulation. *Physics of Fluids*, 14(6):L41–L44, 2002. doi: doi.org/10.1063/1.1480830.
- [100] T. A. Ghezzehei and D. Or. Pore-Space Dynamics in a Soil Aggregate Bed under a Static External Load. *Soil Science Society of America Journal*, 67(1):12–19, 2003. doi: 10.2136/sssaj2003.1200.
- [101] H. H. Gidey. *Numerical solution of advection-diffusion and convective Cahn-Hilliard equations*. PhD thesis, University of Pretoria, 2016. URL <http://hdl.handle.net/2263/60805>.
- [102] H. H. Gidey and B. D. Reddy. Operator-splitting methods for the 2D convective Cahn–Hilliard equation. *Computers & Mathematics with Applications*, 77(12):3128–3153, 2019. doi: 10.1016/j.camwa.2019.01.023.
- [103] I. Ginzburg. Truncation Errors, Exact And Heuristic Stability Analysis Of Two-Relaxation-Times Lattice Boltzmann Schemes For Anisotropic Advection-Diffusion Equation. *Communications in Computational Physics*, 11(5):1439–1502, 2012. doi: 10.4208/cicp.211210.280611a.
- [104] I. Ginzburg, D. d’Humières, and A. Kuzmin. Optimal Stability of Advection-Diffusion Lattice Boltzmann Models with Two Relaxation Times for Positive/Negative Equilibrium. *Journal of Statistical Physics*, 139(6): 1090–1143, 2010. doi: 10.1007/s10955-010-9969-9.
- [105] J. Glimm, J. Petrillo, and M. C. Lee. Smooth vs. Physical Solutions of the Navier-Stokes Equation. *arXiv*, preprint, 2023. doi: 10.48550/arXiv.2212.14734. URL <https://arxiv.org/abs/2212.14734v3>.
- [106] F. W. Glines, P. Grete, and B. W. O’Shea. Magnetized decaying turbulence in the weakly compressible Taylor-Green vortex. *Physical Review E*, 103:043203, 2021. doi: 10.1103/PhysRevE.103.043203.
- [107] A. N. Gorban. Hilbert’s sixth problem: the endless road to rigour. *Philosophical Transactions of the Royal Society A*, 376(2118):20170238, 2018. doi: 10.1098/rsta.2017.0238.
- [108] M. Griebel and M. Klitz. Homogenisation and numerical simulation of flow in geometries with textile microstructures. *SIAM Multiscale Modeling & Simulation*, 8(4), 2010. doi: 10.1137/09077059X.
- [109] Y. Guangwu. A lattice Boltzmann equation for waves. *Journal of Computational Physics*, 161(1):61–69, 2000. doi: 10.1006/jcph.2000.6486.
- [110] G. Guennebaud, B. Jacob, et al. Eigen v3. <http://eigen.tuxfamily.org>, 2010.
- [111] Z. Guo and T. Zhao. Lattice Boltzmann model for incompressible flows through porous media. *Physical Review E*, 66(3):036304, 2002.
- [112] Z. Guo, C. Zheng, and B. Shi. Discrete lattice effects on the forcing term in the lattice Boltzmann method. *Physical Review E*, 65(4):046308, 2002. doi: 10.1103/PhysRevE.65.046308.
- [113] Z. Guo, J. Li, and K. Xu. Unified preserving properties of kinetic schemes. *Physical Review E*, 107:025301, 2023. doi: 10.1103/PhysRevE.107.025301.
- [114] M. Haussmann, S. Simonis, H. Nirschl, and M. J. Krause. Direct numerical simulation of decaying homogeneous isotropic turbulence – numerical experiments on stability, consistency and accuracy of distinct lattice Boltzmann methods. *International Journal of Modern Physics C*, 30(09):1–29, 2019. doi: 10.1142/S0129183119500748.
- [115] M. Haussmann, F. Ries, J. B. Jeppener-Haltenhoff, Y. Li, M. Schmidt, C. Welch, L. Illmann, B. Böhm, H. Nirschl, M. J. Krause, and A. Sadiki. Evaluation of a Near-Wall-Modeled Large Eddy Lattice Boltzmann Method for the Analysis of Complex Flows Relevant to IC Engines. *Computation*, 8(2), 2020. doi: 10.3390/computatio n8020043.

- [116] M. Haussmann, P. Reinshaus, S. Simonis, H. Nirschl, and M. J. Krause. Fluid–Structure Interaction Simulation of a Coriolis Mass Flowmeter Using a Lattice Boltzmann Method. *Fluids*, 6(4):167, 2021. doi: 10.3390/fluid6040167.
- [117] X. He and L.-S. Luo. Theory of the lattice Boltzmann method: From the Boltzmann equation to the lattice Boltzmann equation. *Physical Review E*, 56:6811–6817, 1997. doi: 10.1103/PhysRevE.56.6811.
- [118] J. J. L. Higdon. The kinematics of the four-roll mill. *Physics of Fluids A*, 5(1):274–276, 1993. doi: 10.1063/1.858782.
- [119] V. T. Hoang and J. M. Park. A Taylor analogy model for droplet dynamics in planar extensional flow. *Chemical Engineering Science*, 204:27–34, 2019. doi: 10.1016/j.ces.2019.04.015.
- [120] D. J. Holdych, D. R. Noble, J. G. Georgiadis, and R. O. Buckius. Truncation error analysis of lattice Boltzmann methods. *Journal of Computational Physics*, 193(2):595–619, 2004. doi: 10.1016/j.jcp.2003.08.012.
- [121] E. Hopf. Über die Anfangswertaufgabe für die hydrodynamischen Grundgleichungen. *Mathematische Nachrichten*, 4(1-6):213–231, 1950. doi: 10.1002/mana.3210040121.
- [122] U. Hornung. *Homogenization and porous media*, volume 6. Springer, New York, 1997. doi: 10.1007/978-1-4612-1920-0.
- [123] S. A. Hosseini and I. V. Karlin. Entropic equilibrium for the lattice Boltzmann method: Hydrodynamics and numerical properties. *arXiv*, preprint, 2023. doi: 10.48550/arXiv.2303.08163. URL <https://arxiv.org/abs/2303.08163>.
- [124] S. A. Hosseini, N. Darabiha, D. Thévenin, and A. Eshghinejadfard. Stability limits of the single relaxation-time advection–diffusion lattice Boltzmann scheme. *International Journal of Modern Physics C*, 28(12):1750141, 2017. doi: 10.1142/S0129183117501418.
- [125] S. A. Hosseini, C. Coreixas, N. Darabiha, and D. Thévenin. Extensive analysis of the lattice Boltzmann method on shifted stencils. *Physical Review E*, 100:063301, 2019. doi: 10.1103/PhysRevE.100.063301.
- [126] S. A. Hosseini, C. Coreixas, N. Darabiha, and D. Thévenin. Stability of the lattice kinetic scheme and choice of the free relaxation parameter. *Physical Review E*, 99:063305, 2019. doi: 10.1103/PhysRevE.99.063305.
- [127] S. A. Hosseini, N. Darabiha, and D. Thévenin. Compressibility in lattice Boltzmann on standard stencils: effects of deviation from reference temperature. *Philosophical Transactions of the Royal Society A*, 378(2175):20190399, 2020. doi: 10.1098/rsta.2019.0399.
- [128] S. A. Hosseini, M. Atif, S. Ansumali, and I. V. Karlin. Entropic lattice Boltzmann methods: A review. *Computers & Fluids*, page 105884, 2023. doi: 10.1016/j.compfluid.2023.105884.
- [129] S. Hou, J. Sterling, S. Chen, and G. D. Doolen. A lattice Boltzmann subgrid model for high Reynolds number flows. *arXiv*, preprint, 1994. doi: 10.48550/arXiv.comp-gas/9401004. URL <https://arxiv.org/abs/comp-gas/9401004>.
- [130] A. S. Hsu and L. G. Leal. Deformation of a viscoelastic drop in planar extensional flows of a Newtonian fluid. *Journal of Non-Newtonian Fluid Mechanics*, 160(2-3):176–180, 2009. doi: 10.1016/j.jnnfm.2009.03.004.
- [131] J. C. Hunt, A. A. Wray, and P. Moin. Eddies, streams, and convergence zones in turbulent flows. *Studying Turbulence Using Numerical Simulation Databases, 2. Proceedings of the 1988 Summer Program*, N89(24555):193–208, 1988. URL <https://ntrs.nasa.gov/citations/19890015184>.
- [132] T. M. Inc. Matlab version: 9.9.0 (r2020b), 2020. URL <https://www.mathworks.com>.

- [133] L. Jahanshaloo, E. Pouryazdanpanah, and N. A. Che Sidik. A review on the application of the lattice Boltzmann method for turbulent flow simulation. *Numerical Heat Transfer; Part A: Applications*, 64(11):938–953, 2013. doi: 10.1080/10407782.2013.807690.
- [134] S. Jin. Asymptotic preserving (AP) schemes for multiscale kinetic and hyperbolic equations: a review. *Rivista di Matematica della Universita di Parma*, 3:177–216, 2012. URL <https://ins.sjtu.edu.cn/people/shijin/PS/AP.pdf>.
- [135] A. Jonnalagadda, A. Sharma, and A. Agrawal. Single relaxation time entropic lattice Boltzmann methods: A developer’s perspective for stable and accurate simulations. *Computers & Fluids*, 215:104792, 2021. doi: 10.1016/j.compfluid.2020.104792.
- [136] M. Junk. On the construction of discrete equilibrium distributions for kinetic schemes. *Institut für Techno- und Wirtschaftsmathematik Kaiserslautern, ITWM Report*, 14, 1999. URL <http://nbn-resolving.de/urn:nbn:de:bsz:352-254804>.
- [137] M. Junk. A finite difference interpretation of the lattice Boltzmann method. *Numerical Methods for Partial Differential Equations*, 17(4):383–402, 2001. doi: 10.1002/num.1018.
- [138] M. Junk and A. Klar. Discretizations for the Incompressible Navier-Stokes Equations Based on the Lattice Boltzmann Method. *SIAM Journal on Scientific Computing*, 22(1):1–19, 2000. doi: 10.1137/S1064827599357188.
- [139] M. Junk and M. K. Rheinlander. Regular and multiscale expansions of a lattice Boltzmann method. *Progress in Computational Fluid Dynamics, an International Journal*, 8(1-4):25–37, 2008. doi: 10.1504/PCFD.2008.018076.
- [140] M. Junk and Z. Yang. Convergence of lattice Boltzmann methods for Stokes flows in periodic and bounded domains. *Computers & Mathematics with Applications*, 55(7):1481–1491, 2008. doi: 10.1016/j.camwa.2007.08.002.
- [141] M. Junk and W.-A. Yong. Rigorous Navier–Stokes limit of the lattice Boltzmann equation. *Asymptotic Analysis*, 35(2):165–185, 2003.
- [142] M. Junk and W.-A. Yong. Weighted L^2 -stability of the lattice Boltzmann method. *SIAM Journal on Numerical Analysis*, 47(3):1651–1665, 2009. doi: 10.1137/060675216.
- [143] M. Junk, A. Klar, and L.-S. Luo. Asymptotic analysis of the lattice Boltzmann equation. *Journal of Computational Physics*, 210(2):676–704, 2005. doi: 10.1016/j.jcp.2005.05.003.
- [144] A. Kajzer, J. Pozorski, and K. Szewc. Large-eddy simulations of 3D Taylor-Green vortex: Comparison of smoothed particle hydrodynamics, lattice Boltzmann and finite volume methods. In *Journal of Physics: Conference Series*, volume 530, page 012019, 2014. doi: 10.1088/1742-6596/530/1/012019.
- [145] N. G. Kallikounis, B. Dorschner, and I. V. Karlin. Particles on demand for flows with strong discontinuities. *Physical Review E*, 106:015301, 2022. doi: 10.1103/PhysRevE.106.015301.
- [146] I. V. Karlin, S. Ansumali, C. E. Frouzakis, and S. S. Chikatamarla. Elements of the Lattice Boltzmann Method I: Linear Advection Equation. *Communications in Computational Physics*, 1(4):616–655, 2006. URL http://global-sci.org/intro/article_detail/cicp/7972.html.
- [147] I. V. Karlin, S. S. Chikatamarla, and S. Ansumali. Elements of the Lattice Boltzmann Method II: Kinetics and Hydrodynamics in One Dimension. *Communications in Computational Physics*, 2(2):196–238, 2007. URL http://global-sci.org/intro/article_detail/cicp/7903.html.
- [148] I. V. Karlin, F. Bösch, and S. S. Chikatamarla. Gibbs’ principle for the lattice-kinetic theory of fluid dynamics. *Physical Review E*, 90:031302, 2014. doi: 10.1103/PhysRevE.90.031302.

- [149] I. V. Karlin, F. Bösch, S. S. Chikatamarla, and S. Succi. Entropy-Assisted Computing of Low-Dissipative Systems. *Entropy*, 17(12):8099–8110, 2015. doi: 10.3390/e17127867.
- [150] V. M. Kendon, M. E. Cates, I. Pagonabarraga, J.-C. Desplat, and P. Bladon. Inertial effects in three-dimensional spinodal decomposition of a symmetric binary fluid mixture: a lattice Boltzmann study. *Journal of Fluid Mechanics*, 440:147–203, 2001. doi: 10.1017/S0022112001004682.
- [151] H. K. Khalil. *Nonlinear systems*. Prentice-Hall, Upper Saddle River, New Jersey, third edition, 2002.
- [152] A. Klar. Relaxation Scheme for a Lattice–Boltzmann-type Discrete Velocity Model and Numerical Navier–Stokes Limit. *Journal of Computational Physics*, 148(2):416–432, 1999. doi: 10.1006/jcph.1998.6123.
- [153] F. Klemens. *Combining computational fluid dynamics and magnetic resonance imaging data using lattice Boltzmann based topology optimisation*. Doctoral thesis, Karlsruhe Institute of Technology (KIT), 2020. URL <https://publikationen.bibliothek.kit.edu/1000125499>.
- [154] M. Klitz. Homogenised Fluid Flow Equations in Porous Media with Application to Permeability Computations in Textiles. Diplomarbeit, Institut für Numerische Simulation, Universität Bonn, 2006. URL http://wissrech.ins.uni-bonn.de/teaching/diplom/diplom_klitz.pdf.
- [155] A. N. Kolmogorov. The Local Structure of Turbulence in Incompressible Viscous Fluid for Very Large Reynolds Numbers. *Proceedings of the USSR Academy of Sciences*, 30:301–305, 1941.
- [156] A. N. Kolmogorov, V. Levin, J. C. R. Hunt, O. M. Phillips, and D. Williams. The local structure of turbulence in incompressible viscous fluid for very large Reynolds numbers. *Proceedings of the Royal Society A*, 434(1890): 9–13, 1991. doi: 10.1098/rspa.1991.0075.
- [157] A. E. Komrakova, O. Shardt, D. Eskin, and J. J. Derksen. Lattice Boltzmann simulations of drop deformation and breakup in shear flow. *International Journal of Multiphase Flow*, 59:24–43, 2014. doi: 10.1016/j.ijmultiphaseflow.2013.10.009.
- [158] M. J. Krause. *Fluid flow simulation and optimisation with lattice Boltzmann methods on high performance computers: application to the human respiratory system*. Doctoral thesis, Karlsruhe Institute of Technology (KIT), 2010. URL <https://publikationen.bibliothek.kit.edu/1000019768>.
- [159] M. J. Krause, F. Klemens, T. Henn, R. Trunk, and H. Nirschl. Particle flow simulations with homogenised lattice Boltzmann methods. *Particuology*, 34:1–13, 2017. doi: 10.1016/j.partic.2016.11.001.
- [160] M. J. Krause, S. Avis, D. Dapalo, N. Hafen, M. Haußmann, M. Gaedtke, F. Klemens, A. Kummerländer, M.-L. Maier, A. Mink, J. Ross-Jones, S. Simonis, and R. Trunk. OpenLB Release 1.3: Open Source Lattice Boltzmann Code, May 2019. URL <https://doi.org/10.5281/zenodo.3625967>.
- [161] M. J. Krause, S. Avis, H. Kusumaatmaja, D. Dapalo, M. Gaedtke, N. Hafen, M. Haußmann, J. Jeppener-Haltenhoff, L. Kronberg, A. Kummerländer, J. Marquardt, T. Pertz, S. Simonis, R. Trunk, M. Wu, and A. Zarth. OpenLB Release 1.4: Open Source Lattice Boltzmann Code, Nov. 2020. URL <https://doi.org/10.5281/zenodo.4279263>.
- [162] M. J. Krause, A. Kummerländer, S. J. Avis, H. Kusumaatmaja, D. Dapalo, F. Klemens, M. Gaedtke, N. Hafen, A. Mink, R. Trunk, J. E. Marquardt, M.-L. Maier, M. Haussmann, and S. Simonis. OpenLB—Open source lattice Boltzmann code. *Computers & Mathematics with Applications*, 81:258–288, 2021. doi: 10.1016/j.camwa.2020.04.033.
- [163] L. Kronberg. *Entropic Stabilizers for Lattice Boltzmann Methods*. B.Sc. thesis (unpublished), Karlsruhe Institute of Technology (KIT), 2022.

- [164] T. Krüger, H. Kusumaatmaja, A. Kuzmin, O. Shardt, G. Silva, and E. M. Viggen. *The Lattice Boltzmann Method: Principles and Practice*. Springer International Publishing, 2017.
- [165] A. Kummerländer, S. Avis, H. Kusumaatmaja, F. Bukreev, D. Dapelo, S. Großmann, N. Hafen, C. Holeksa, A. Husfeldt, J. Jeßberger, L. Kronberg, J. Marquardt, J. Mödl, J. Nguyen, T. Pertzel, S. Simonis, L. Springmann, N. Suntoyo, D. Teutscher, M. Zhong, and M. J. Krause. OpenLB Release 1.5: Open Source Lattice Boltzmann Code, Nov. 2022. URL <https://doi.org/10.5281/zenodo.6469606>.
- [166] A. Kummerländer, M. Dorn, M. Frank, and M. J. Krause. Implicit propagation of directly addressed grids in lattice Boltzmann methods. *Concurrency and Computation: Practice and Experience*, page e7509, 2022. doi: 10.1002/cpe.7509.
- [167] A. Kummerländer, F. Bukreev, S. Berg, M. Dorn, and M. J. Krause. Advances in Computational Process Engineering using Lattice Boltzmann Methods on High Performance Computers for Solving Fluid Flow Problems. In *High Performance Computing in Science and Engineering '22 (accepted)*. Springer, 2023.
- [168] A. Kummerländer, S. Avis, H. Kusumaatmaja, F. Bukreev, M. Crocoll, D. Dapelo, N. Hafen, S. Ito, J. Jeßberger, J. E. Marquardt, J. Mödl, T. Pertzel, F. Prinz, F. Raichle, M. Schecher, S. Simonis, D. Teutscher, and M. J. Krause. OpenLB Release 1.6: Open Source Lattice Boltzmann Code, Apr. 2023. URL <https://doi.org/10.5281/zenodo.7773497>.
- [169] F. Kuo, R. Scheichl, C. Schwab, I. Sloan, and E. Ullmann. Multilevel quasi-Monte Carlo methods for lognormal diffusion problems. *Mathematics of Computation*, 86(308):2827–2860, 2017. doi: 10.1090/mcom/3207.
- [170] H. Lai and C. Ma. Lattice Boltzmann model for generalized nonlinear wave equations. *Physical Review E*, 84: 046708, 2011. doi: 10.1103/PhysRevE.84.046708.
- [171] P. Lallemand and L.-S. Luo. Theory of the lattice Boltzmann method: Dispersion, dissipation, isotropy, Galilean invariance, and stability. *Physical Review E*, 61(6):6546, 2000. doi: 10.1103/PhysRevE.61.6546.
- [172] P. Lallemand, L.-S. Luo, M. Krafczyk, and W.-A. Yong. The Lattice Boltzmann Method for Nearly Incompressible Flows. *Journal of Computational Physics*, (In press):109713, 2020. doi: 10.1016/j.jcp.2020.109713.
- [173] S. Lanthaler, S. Mishra, and C. Parés-Pulido. Statistical solutions of the incompressible Euler equations. *Mathematical Models and Methods in Applied Sciences*, 31(02):223–292, 2021. doi: 10.1142/S0218202521500068.
- [174] V. Laptev. *Numerical solution of coupled flow in plain and porous media*. Doctoral thesis, Technische Universität Kaiserslautern, 2003. URL <http://nbn-resolving.de/urn:nbn:de:hbz:386-kluedo-17312>.
- [175] P. D. Lax and R. D. Richtmyer. Survey of the stability of linear finite difference equations. *Communications on Pure and Applied Mathematics*, 9(2):267–293, 1956. doi: 10.1002/cpa.3160090206.
- [176] F. Leonardi, S. Mishra, and C. Schwab. Numerical approximation of statistical solutions of planar, incompressible flows. *Mathematical Models and Methods in Applied Sciences*, 26(13):2471–2523, 2016. doi: 10.1142/S0218202516500597.
- [177] J. Leray. Sur le mouvement d’un liquide visqueux emplissant l’espace. *Acta Mathematica*, 63(1):193–248, 1934. doi: 10.1007/BF02547354.
- [178] R. J. LeVeque. *Finite difference methods for ordinary and partial differential equations: steady-state and time-dependent problems*, volume 98. SIAM, 2007.
- [179] J. Li, Y. Y. Renardy, and M. Renardy. Numerical simulation of breakup of a viscous drop in simple shear flow through a volume-of-fluid method. *Physics of Fluids*, 12(2):269–282, 2000. doi: 10.1063/1.870305.

- [180] Y. Li, J.-I. Choi, and J. Kim. A phase-field fluid modeling and computation with interfacial profile correction term. *Communications in Nonlinear Science and Numerical Simulation*, 30(1):84–100, 2016. doi: 10.1016/j.cnsns.2015.06.012.
- [181] R. Löhner. Towards overcoming the LES crisis. *International Journal of Computational Fluid Dynamics*, 33(3):87–97, 2019. doi: 10.1080/10618562.2019.1612052.
- [182] K. O. Lye. Alsvinn: A Fast multi-GPGPU finite volume solver with a strong emphasis on reproducibility. *arXiv*, preprint, 2019. doi: 10.48550/arXiv.1912.07645. URL <https://arxiv.org/abs/1912.07645>.
- [183] K. O. Lye. *Computation of statistical solutions of hyperbolic systems of conservation laws*. Doctoral thesis, ETH Zurich, 2020. URL <https://www.research-collection.ethz.ch/handle/20.500.11850/432014>.
- [184] O. Malaspinas and P. Sagaut. Consistent subgrid scale modelling for lattice Boltzmann methods. *Journal of Fluid Mechanics*, 700:514–542, 2012. doi: 10.1017/jfm.2012.155.
- [185] P.-A. Masset and G. Wissocq. Linear hydrodynamics and stability of the discrete velocity Boltzmann equations. *Journal of Fluid Mechanics*, 897:A29, 2020. doi: 10.1017/jfm.2020.374.
- [186] R. Mei, L.-S. Luo, P. Lallemand, and D. d’Humières. Consistent initial conditions for lattice Boltzmann simulations. *Computers & Fluids*, 35:855–862, 2006. doi: 10.1016/j.compfluid.2005.08.008.
- [187] J. Meng, X.-J. Gu, and D. R. Emerson. Impact of reconstruction schemes on interpreting lattice Boltzmann results – A study using the Taylor-Green vortex problem. *arXiv*, preprint, 2023. doi: 10.48550/arXiv.2302.13910. URL <https://arxiv.org/abs/2302.13910>.
- [188] A. Mikelić. Homogenization of nonstationary Navier-Stokes equations in a domain with a grained boundary. *Annali di Matematica Pura ed Applicata*, 158(1):167–179, 1991. doi: 10.1007/BF01759303.
- [189] A. Mikelić. Mathematical derivation of the Darcy-type law with memory effects, governing transient flow through porous medium. *Glasnik Matematički*, 29(49):57–77, 1994.
- [190] A. Mink, K. Schediwy, C. Posten, H. Nirschl, S. Simonis, and M. J. Krause. Comprehensive Computational Model for Coupled Fluid Flow, Mass Transfer, and Light Supply in Tubular Photobioreactors Equipped with Glass Sponges. *Energies*, 15(20):7671, 2022. doi: 10.3390/en15207671.
- [191] A. Miranville. The Cahn–Hilliard equation and some of its variants. *AIMS Mathematics*, 2(3):479–544, 2017. doi: 10.3934/Math.2017.2.479.
- [192] A. Miranville. *The Cahn–Hilliard Equation: Recent Advances and Applications*. Society for Industrial and Applied Mathematics, Philadelphia, 2019. doi: 10.1137/1.9781611975925.
- [193] S. Mischler. Uniqueness for the BGK-equation in \mathbb{R}^N and rate of convergence for a semi-discrete scheme. *Differential and Integral Equations*, 9(5):1119–1138, 1996. doi: 10.57262/die/1367871533.
- [194] M. Mohrhard, G. Thäter, J. Bludau, B. Horvat, and M. J. Krause. Auto-vectorization friendly parallel lattice Boltzmann streaming scheme for direct addressing. *Computers & Fluids*, 181:1–7, 2019. doi: 10.1016/j.compfluid.2019.01.001.
- [195] A. Mojtabi and M. O. Deville. One-dimensional linear advection–diffusion equation: Analytical and finite element solutions. *Computers & Fluids*, 107:189–195, 2015. doi: 10.1016/j.compfluid.2014.11.006.
- [196] K. W. Morton. *Numerical Solution of Convection-Diffusion Problems*. Chapman & Hall, 1996.
- [197] H. Müller, A. Touil, A. Schlüter, and R. Müller. Dynamic propagation of mode III cracks in a Lattice Boltzmann method for solids. *Archive of Applied Mechanics*, pages 1–14, 2022. doi: 10.1007/s00419-022-02306-y.

- [198] D. Nield. *Convection in Porous Media, Fifth Edition*. Springer, New York, 2017. doi: 10.1007/978-3-319-49562-0.
- [199] P. Nithiarasu, K. Seetharamu, and T. Sundararajan. Natural convective heat transfer in a fluid saturated variable porosity medium. *International Journal of Heat and Mass Transfer*, 40(16):3955–3967, 1997. doi: 10.1016/S0017-9310(97)00008-2.
- [200] D. Oberle, C. D. Pruett, and P. Jenny. Temporal large-eddy simulation based on direct deconvolution. *Physics of Fluids*, 32(6):065112, 2020. doi: 10.1063/5.0006637.
- [201] H. Otomo, B. M. Boghosian, and F. Dubois. Two complementary lattice-Boltzmann-based analyses for nonlinear systems. *Physica A: Statistical Mechanics and its Applications*, 486:1000–1011, 2017. doi: 10.1016/j.physa.2017.06.010.
- [202] H. Otomo, B. M. Boghosian, and S. Succi. A kinetic generator for classical field theories with conservation laws. *Europhysics Letters*, 132(6):60002, 2021. doi: 10.1209/0295-5075/132/60002.
- [203] P. Otte and M. Frank. Derivation and analysis of Lattice Boltzmann schemes for the linearized Euler equations. *Computers & Mathematics with Applications*, 72(2):311–327, 2016. doi: 10.1016/j.camwa.2015.12.004.
- [204] P. Otte and M. Frank. A structured approach to the construction of stable linear Lattice Boltzmann collision operator. *Computers & Mathematics with Applications*, 79(5):1447–1460, 2020. doi: 10.1016/j.camwa.2019.09.009.
- [205] D. V. Patil, K. N. Premnath, and S. Banerjee. Multigrid lattice Boltzmann method for accelerated solution of elliptic equations. *Journal of Computational Physics*, 265:172–194, 2014. doi: 10.1016/j.jcp.2014.01.049.
- [206] F. S. Pereira, F. F. Grinstein, D. M. Israel, R. Rauen Zahn, and S. S. Girimaji. Modeling and simulation of transitional Taylor-Green vortex flow with partially averaged Navier-Stokes equations. *Physical Review Fluids*, 6:054611, 2021. doi: 10.1103/PhysRevFluids.6.054611.
- [207] B. Perthame. Global existence to the BGK model of Boltzmann equation. *Journal of Differential Equations*, 82(1):191–205, 1989. doi: 10.1016/0022-0396(89)90173-3.
- [208] B. Perthame and M. Pulvirenti. Weighted L^∞ bounds and uniqueness for the Boltzmann BGK model. *Archive for Rational Mechanics and Analysis*, 125:289–295, 1993. doi: 10.1007/BF00383223.
- [209] S. B. Pope. *Turbulent Flows*. Cambridge University Press, 2000. doi: 10.1017/CBO9780511840531.
- [210] N. Provatas and K. Elder. *Phase-Field Methods in Materials Science and Engineering*. John Wiley & Sons, Ltd, 2010. doi: 10.1002/9783527631520.
- [211] C. Pruett. Temporal large-eddy simulation: theory and implementation. *Theoretical and Computational Fluid Dynamics*, 22(3-4):275–304, 2008. doi: 10.1007/s00162-007-0063-0.
- [212] F. Rao and Y. Jin. Possibility for survival of macroscopic turbulence in porous media with high porosity. *Journal of Fluid Mechanics*, 937:A17, 2022. doi: 10.1017/jfm.2022.87.
- [213] R. Reams. Hadamard inverses, square roots and products of almost semidefinite matrices. *Linear Algebra and Its Applications*, 288:35–43, 1999. doi: 10.1016/S0024-3795(98)10162-3.
- [214] T. Reis. A Conservative Interface Sharpening Lattice Boltzmann Model. *SIAM Journal on Scientific Computing*, 40(6):B1495–B1516, 2018. doi: 10.1137/18M1184928.
- [215] T. Reis. On the Lattice Boltzmann Deviatoric Stress: Analysis, Boundary Conditions, and Optimal Relaxation Times. *SIAM Journal on Scientific Computing*, 42(2):B397–B424, 2020. doi: 10.1137/19M1244846.

- [216] T. Reis. A lattice Boltzmann formulation of the one-fluid model for multiphase flow. *Journal of Computational Physics*, 453:110962, 2022. doi: 10.1016/j.jcp.2022.110962.
- [217] T. Reis and P. J. Dellar. A volume-preserving sharpening approach for the propagation of sharp phase boundaries in multiphase lattice Boltzmann simulations. *Computers & Fluids*, 46(1):417–421, 2011. doi: 10.1016/j.compfluid.2010.12.005.
- [218] M. K. Rheinländer. *Analysis of Lattice-Boltzmann Methods: Asymptotic and Numeric Investigation of a Singularly Perturbed System*. Doctoral thesis, Universität Konstanz, 2007. URL <http://nbn-resolving.de/urn:nbn:de:bsz:352-opus-36351>.
- [219] M. K. Rheinländer. On the stability structure for lattice Boltzmann schemes. *Computers & Mathematics with Applications*, 59(7):2150–2167, 2010. doi: 10.1016/j.camwa.2009.08.040.
- [220] T. Rohner. *Efficient Computation of Statistical Solutions of Incompressible Fluids*. M.Sc. thesis (unpublished), ETH Zurich, 2021.
- [221] A. Ruhi, S. Raghurama Rao, and S. Muddu. A lattice Boltzmann relaxation scheme for incompressible fluid flows. *International Journal of Advances in Engineering Sciences and Applied Mathematics*, 14(1):34–47, 2022. doi: 10.1007/s12572-022-00320-5.
- [222] L. Saint-Raymond. Discrete time Navier–Stokes limit for the BGK Boltzmann equation. *Communications in Partial Differential Equations*, 27(1-2):149–184, 2002. doi: 10.1081/PDE-120002785.
- [223] L. Saint-Raymond. From the BGK model to the Navier-Stokes equations. *Annales Scientifiques de l’École Normale Supérieure*, Ser. 4, 36(2):271–317, 2003. doi: 10.1016/S0012-9593(03)00010-7.
- [224] C. Semperebon, T. Krüger, and H. Kusumaatmaja. Ternary free-energy lattice Boltzmann model with tunable surface tensions and contact angles. *Physical Review E*, 93(3):033305, 2016. doi: 10.1103/PhysRevE.93.033305.
- [225] C. E. Shannon. Communication in the Presence of Noise. *Proceedings of the IRE*, 37(1):10–21, 1949. doi: 10.1109/JRPROC.1949.232969.
- [226] M. Shapira and S. Haber. Low Reynolds number motion of a droplet in shear flow including wall effects. *International Journal of Multiphase Flow*, 16(2):305–321, 1990. doi: 10.1016/0301-9322(90)90061-M.
- [227] J. Shin, J. Yang, C. Lee, and J. Kim. The Navier–Stokes–Cahn–Hilliard model with a high-order polynomial free energy. *Acta Mechanica*, 231:2425–2437, 2020. doi: 10.1007/s00707-020-02666-y.
- [228] D. N. Siebert, L. A. Hegele, and P. C. Philippi. Lattice Boltzmann equation linear stability analysis: Thermal and athermal models. *Physical Review E*, 77:026707, 2008. doi: 10.1103/PhysRevE.77.026707.
- [229] S. Simonis and M. J. Krause. Forschungsnahe Lehre unter Pandemiebedingungen. *Mitteilungen der Deutschen Mathematiker-Vereinigung*, 30(1):43–45, 2022. doi: 10.1515/dmvm-2022-0015.
- [230] S. Simonis and M. J. Krause. Limit Consistency of Lattice Boltzmann Equations. *arXiv*, preprint, 2022. doi: 10.48550/arXiv.2208.06867. URL <https://arxiv.org/abs/2208.06867>.
- [231] S. Simonis, M. Frank, and M. J. Krause. On relaxation systems and their relation to discrete velocity Boltzmann models for scalar advection–diffusion equations. *Philosophical Transactions of the Royal Society A*, 378: 20190400, 2020. doi: 10.1098/rsta.2019.0400.
- [232] S. Simonis, M. Haussmann, L. Kronberg, W. Dörfler, and M. J. Krause. Linear and brute force stability of orthogonal moment multiple-relaxation-time lattice Boltzmann methods applied to homogeneous isotropic turbulence. *Philosophical Transactions of the Royal Society A*, 379:20200405, 2021. doi: 10.1098/rsta.2020.0405.

- [233] S. Simonis, D. Oberle, M. Gaedtke, P. Jenny, and M. J. Krause. Temporal large eddy simulation with lattice Boltzmann methods. *Journal of Computational Physics*, 454:110991, 2022. doi: 10.1016/j.jcp.2022.110991.
- [234] S. Simonis, M. Frank, and M. J. Krause. Constructing relaxation systems for lattice Boltzmann methods. *Applied Mathematics Letters*, 137:108484, 2023. doi: 10.1016/j.aml.2022.108484.
- [235] S. Simonis, J. Nguyen, S. J. Avis, W. Dörfler, and M. J. Krause. Binary fluid flow simulations with free energy lattice Boltzmann methods. *Discrete Contin. Dyn. Syst. - S*, 2023. doi: 10.3934/dcdss.2023069.
- [236] M. Siodlaczek, M. Gaedtke, S. Simonis, M. Schweiker, N. Homma, and M. J. Krause. Numerical evaluation of thermal comfort using a large eddy lattice Boltzmann method. *Building and Environment*, 192:107618, 2021. doi: 10.1016/j.buildenv.2021.107618.
- [237] G. Soligo, A. Roccon, and A. Soldati. Deformation of clean and surfactant-laden droplets in shear flow. *Meccanica*, 55(2):371–386, 2020. doi: 10.1007/s11012-019-00990-9.
- [238] M. A. Spaid and F. R. Phelan Jr. Lattice Boltzmann methods for modeling microscale flow in fibrous porous media. *Physics of Fluids*, 9(9):2468–2474, 1997. doi: 10.1063/1.869392.
- [239] Steinbuch Centre for Computing (SCC), 2023. URL <https://www.scc.kit.edu/>.
- [240] J. D. Sterling and S. Chen. Stability analysis of lattice Boltzmann methods. *Journal of Computational Physics*, 123(1):196–206, 1996. doi: 10.1006/jcph.1996.0016.
- [241] S. Suga. Numerical schemes obtained from lattice Boltzmann equations for advection diffusion equations. *International Journal of Modern Physics C*, 17(11):1563–1577, 2006. doi: 10.1142/S0129183106010030.
- [242] M. R. Swift, E. Orlandini, W. R. Osborn, and J. M. Yeomans. Lattice Boltzmann simulations of liquid-gas and binary fluid systems. *Physical Review E*, 54(5):5041, 1996. doi: 10.1103/PhysRevE.54.5041.
- [243] E. Tadmor. A review of numerical methods for nonlinear partial differential equations. *Bulletin of the American Mathematical Society*, 49(4):507–554, 2012. doi: 10.1090/S0273-0979-2012-01379-4.
- [244] X. Tang, Y. Yu, and A. Oztekin. Asymptotic method for entropic multiple relaxation time model in lattice Boltzmann method. *Physical Review E*, 106:015303, 2022. doi: 10.1103/PhysRevE.106.015303.
- [245] G. I. Taylor. The formation of emulsions in definable fields of flow. *Proceedings of the Royal Society A*, 146(858):501–523, 1934. doi: 10.1098/rspa.1934.0169.
- [246] G. I. Taylor and A. E. Green. Mechanism of the production of small eddies from large ones. *Proceedings of the Royal Society A*, 158(895):499–521, 1937. doi: 10.1098/rspa.1937.0036.
- [247] C. Thantapanally, D. V. Patil, S. Succi, and S. Ansumali. Universal mechanism for saturation of vorticity growth in fully developed fluid turbulence. *Journal of Fluid Mechanics*, 728, 2013. doi: 10.1017/jfm.2013.321.
- [248] D. C. Trethewey and L. G. Leal. Deformation and relaxation of Newtonian drops in planar extensional flows of a Boger fluid. *Journal of Non-Newtonian Fluid Mechanics*, 99(2-3):81–108, 2001. doi: 10.1016/S0377-0257(01)00123-9.
- [249] R. Trunk, T. Weckerle, N. Hafen, G. Thäter, H. Nirschl, and M. J. Krause. Revisiting the Homogenized Lattice Boltzmann Method with Applications on Particulate Flows. *Computation*, 9(2), 2021. doi: 10.3390/computat.ion9020011.
- [250] S. Ubertini, P. Asinari, and S. Succi. Three ways to lattice Boltzmann: A unified time-marching picture. *Physical Review E*, 81:016311, 2010. doi: 10.1103/PhysRevE.81.016311.

- [251] L. van den Bos, B. Koren, and R. Dwight. Non-intrusive uncertainty quantification using reduced cubature rules. *Journal of Computational Physics*, 332:418–445, 2017. doi: 10.1016/j.jcp.2016.12.011.
- [252] P. Van Leemput, M. Rheinländer, and M. Junk. Smooth initialization of lattice Boltzmann schemes. *Computers & Mathematics with Applications*, 58(5):867–882, 2009. doi: 10.1016/j.camwa.2009.02.022.
- [253] W. M. van Rees, A. Leonard, D. Pullin, and P. Koumoutsakos. A comparison of vortex and pseudo-spectral methods for the simulation of periodic vortical flows at high reynolds numbers. *Journal of Computational Physics*, 230(8):2794–2805, 2011. doi: 10.1016/j.jcp.2010.11.031.
- [254] Y. Vanderhoydonc and W. Vanroose. Initialization of Lattice Boltzmann Models with the Help of the Numerical Chapman–Enskog Expansion. *Procedia Computer Science*, 18:1036–1045, 2013. doi: 10.1016/j.procs.2013.05.269.
- [255] A. J. Wagner. An H-theorem for the lattice Boltzmann approach to hydrodynamics. *Europhysics Letters*, 44(2): 144–149, 1998. doi: 10.1209/epl/i1998-00448-8.
- [256] L. Wang. Enhanced multi-relaxation-time lattice Boltzmann model by entropic stabilizers. *Physical Review E*, 102:023307, 2020. doi: 10.1103/PhysRevE.102.023307.
- [257] N. Wang, C. Semperebon, H. Liu, C. Zhang, and H. Kusumaatmaja. Modelling double emulsion formation in planar flow-focusing microchannels. *Journal of Fluid Mechanics*, 895:A22, 2020. doi: 10.1017/jfm.2020.299.
- [258] J.-P. Weiß. *Numerical Analysis of Lattice Boltzmann Methods for the Heat Equation on a Bounded Interval*. KIT Scientific Publishing, Karlsruhe, 2006. doi: 10.5445/KSP/1000005304.
- [259] F. M. White. *Viscous Fluid Flow*, volume 3. McGraw-Hill New York, 2006.
- [260] D. Wilde, A. Krämer, D. Reith, and H. Foyssi. High-order semi-Lagrangian kinetic scheme for compressible turbulence. *Physical Review E*, 104:025301, 2021. doi: 10.1103/PhysRevE.104.025301.
- [261] D. Wilde, S. Nidhan, H. T. Pham, H. Foyssi, D. Reith, and S. Sarkar. Stratified Taylor–Green vortex by lattice Boltzmann methods: Influence of stencils, forcing schemes, and collision models. *Computers & Fluids*, 256: 105838, 2023. doi: 10.1016/j.compfluid.2023.105838.
- [262] G. Wissocq and P. Sagaut. Hydrodynamic limits and numerical errors of isothermal lattice Boltzmann schemes. *Journal of Computational Physics*, 450:110858, 2022. doi: 10.1016/j.jcp.2021.110858.
- [263] G. Wissocq, P. Sagaut, and J.-F. Boussuge. An extended spectral analysis of the lattice Boltzmann method: modal interactions and stability issues. *Journal of Computational Physics*, 380:311–333, 2019. doi: 10.1016/j.jcp.2018.12.015.
- [264] G. Wissocq, C. Coreixas, and J.-F. Boussuge. Linear stability and isotropy properties of athermal regularized lattice Boltzmann methods. *Physical Review E*, 102(5):053305, 2020. doi: 10.1103/PhysRevE.102.053305.
- [265] D. A. Wolf-Gladrow. *Lattice-Gas Cellular Automata and Lattice Boltzmann Models: An Introduction*. Lecture Notes in Mathematics. Springer Berlin, Heidelberg, 2000. doi: 10.1007/b72010.
- [266] M. A. Woodbury. *Inverting Modified Matrices*. Princeton University: Department of Statistics, Princeton, 1950.
- [267] R. A. Worthing, J. Mozer, and G. Seeley. Stability of lattice Boltzmann methods in hydrodynamic regimes. *Physical Review E*, 56(2):2243, 1997. doi: 10.1103/PhysRevE.56.2243.
- [268] H. Xu and P. Sagaut. Optimal low-dispersion low-dissipation LBM schemes for computational aeroacoustics. *Journal of Computational Physics*, 230(13):5353–5382, 2011. doi: 10.1016/j.jcp.2011.03.040.

-
- [269] H. Xu, O. Malaspinas, and P. Sagaut. Sensitivity analysis and determination of free relaxation parameters for the weakly-compressible MRT–LBM schemes. *Journal of Computational Physics*, 231(21):7335–7367, 2012. doi: 10.1016/j.jcp.2012.07.005.
- [270] W. Yang and C. Li. A Unified Lattice Boltzmann Model for Fourth Order Partial Differential Equations with Variable Coefficients. *Entropy*, 24(9), 2022. doi: 10.3390/e24091176.
- [271] P. Yue, C. Zhou, and J. J. Feng. Spontaneous shrinkage of drops and mass conservation in phase-field simulations. *Journal of Computational Physics*, 223(1):1–9, 2007. doi: 10.1016/j.jcp.2006.11.020.
- [272] P. Yue, C. Zhou, and J. J. Feng. Sharp-interface limit of the Cahn–Hilliard model for moving contact lines. *Journal of Fluid Mechanics*, 645:279–294, 2010. doi: 10.1017/S0022112009992679.
- [273] C. Zhang, Z. Guo, and H. Liang. High-order lattice-Boltzmann model for the Cahn-Hilliard equation. *Physical Review E*, 99:043310, 2019. doi: 10.1103/PhysRevE.99.043310.
- [274] L. Zhao and H. Li. Stochastic modeling of the permeability of randomly generated porous media via the lattice Boltzmann method and probabilistic collocation method. *Transport in Porous Media*, 128(2):613–631, 2019. doi: 10.1007/s11242-019-01261-7.
- [275] W. Zhao and W.-A. Yong. Maxwell iteration for the lattice Boltzmann method with diffusive scaling. *Physical Review E*, 95:033311, 2017. doi: 10.1103/PhysRevE.95.033311.
- [276] W. Zhao, J. Huang, and W.-A. Yong. Lattice Boltzmann Method for Stochastic Convection-Diffusion Equations. *SIAM/ASA Journal on Uncertainty Quantification*, 9(2):536–563, 2021. doi: 10.1137/19M1270665.
- [277] X. Zhao. Drop breakup in dilute Newtonian emulsions in simple shear flow: New drop breakup mechanisms. *Journal of Rheology*, 51(3):367–392, 2007. doi: 10.1122/1.2714641.
- [278] X. Zhao. Global well-posedness and decay of solutions to the Cauchy problem of convective Cahn-Hilliard equation. *arXiv*, preprint, 2019. doi: 10.48550/arXiv.1910.09409. URL <https://arxiv.org/abs/1910.09409>.
- [279] L. Zheng, T. Lee, Z. Guo, and D. Rumschitzki. Shrinkage of bubbles and drops in the lattice Boltzmann equation method for nonideal gases. *Physical Review E*, 89:033302, 2014. doi: 10.1103/PhysRevE.89.033302.

A Acronyms and Symbols

Some of the frequently used acronyms and symbols are summarized below. The list raises no claim to completeness. For the purpose of readability, symbols are renamed occasionally. In this case, the definition or notation is explicitly stated within the respective section and is mostly used therein.

Frequently used acronyms

Acronym	Definition	Page
LBM	lattice Boltzmann method	p. 1
CFD	computational fluid dynamics	p. 1
HPC	high performance computing	p. 1
LES	large eddy simulation	p.1
FVM	finite volume method	p. 1
PDE	partial differential equation	p. 1
IBVP	initial boundary value problem	p. 1
FDM	finite difference method	p. 1
HPC	high performance computing	p. 1
OBJ	objective	p. 2
CTN	contribution	p. 2
TEQ	target equation	p. 2
IVP	initial value problem	p. 2
PDO	partial differential operator	p. 5
RS	relaxation system	p. 5
ADE	advection–diffusion equation	p. 7
CHE	Cahn–Hilliard equation	p. 7
NSE	Navier–Stokes equations	p. 8
EE	Euler equations	p. 8
K41	Kolmogorov’s theory in [155, 156]	p. 9
BE	Boltzmann equation (BE)	p. 9
BGK	Bhatnagar–Gross–Krook [31]	p. 11
BGKBE	Bhatnagar–Gross–Krook–Boltzmann equation	p. 11
TLES	temporal large eddy simulation	p. 17
TDDM	temporal direct deconvolution model [200]	p. 17
BL	Brinkman law	p. 20
DL	Darcy’s law	p. 20

HNSE	homogenized Navier–Stokes equations	p. 29
NSCHE	Navier–Stokes–Cahn–Hilliard equations	p. 29
FRM	free energy model	p. 29
KFRM	free energy model of Kendon <i>et al.</i> [150]	p. 30
SFRM	free energy model of Semprebon <i>et al.</i> [224]	p. 31
HKFRM	higher order KFRM	p. 34
HSFRM	higher order SFRM	p. 34
LBE	lattice Boltzmann equation	p. 38
AV	introduction of artificial variables	p. 39
AP	addition of perturbation terms	p. 39
TRS	transformed relaxation system	p. 46
MRT	multi-relaxation-time	p. 47
SRT	single-relaxation-time	p. 47
VN	von Neumann	p. 49
KBC	Karlin–Bösch–Chikatamarla [148]	p. 52
DVBE	discrete velocity BGK-Boltzmann equation	p. 52
MRF	multi-relaxation-function	p. 71
HLBM	homogenized LBM	p. 76
HBGKBE	homogenized BGKBE	p. 78
FDVBE	filtered DVBE	p. 87
FLBE	filtered LBE	p. 87
SLMC	single level Monte Carlo	p. 94
GPU	graphical processing unit	p. 95
CPU	central processing unit	p. 98
EOC	experimental order of convergence	p. 99
DNS	direct numerical simulation	p. 110
SEM	spectral element method	p. 110
BF	brute force	p. 114
AS	acoustic scaling	p. 121
DS	diffusive scaling	p. 121
IPR	initial peak region [247]	p. 125
MLMC	multi level Monte Carlo	p. 136
UQ	uncertainty quantification	p. 136
QMC	quasi-randomized Monte Carlo	p. 137
UDNS	underresolved DNS	p. 142

Frequently used symbols

Symbol	Definition	Page
$x \in \Omega$	spatial coordinate, where $\Omega \subseteq \mathbb{R}^d$ denotes an Euclidean space domain	p. 5

$d \in \mathbb{N}$	spatial dimension	p. 5
$t \in I$	temporal coordinate, where $I \subseteq \mathbb{R}_{\geq 0}$ denotes a time horizon	p. 5
$\Omega_T = \Omega \times I$	space-time cylinder	p. 5
$\rho(\mathbf{x}, t)$	conserved variable, zeroth order moment (e.g. density)	p. 5
C^m	class of m times differentiable functions	p. 5
F_{\sharp}	partial differential operator	p. 5
F_{\sharp}^{ϵ}	relaxation operator depending on scaling parameter $\epsilon > 0$	p. 5
$\epsilon > 0$	smallness parameter tending to zero	p. 5
$\partial_{\cdot} = \frac{\partial}{\partial \cdot}$	partial derivative with respect to \cdot	p. 5
\cdot^{ar}	remainder terms in the relaxation limit $\epsilon \searrow 0$	p. 6
$L(\rho)$	linear second order partial differential operator	p. 6
$\sharp \in \{\text{ell, par, hyp}\}$	type of partial differential operator	p. 6
$\mathcal{O}(\cdot)$	set of functions with order of magnitude in terms of \cdot	p. 6
\cdot_0	e.g. initial value at ($t = 0$) of a function \cdot of t	p. 7
$\mathbf{F}(\rho)$	flux function	p. 7
$\mu, M_{\phi} > 0$	diffusivity	p. 7
$\phi(\mathbf{x}, t)$	order parameter	p. 7
$\mu_{\phi}(\mathbf{x}, t)$	chemical potential	p. 7
\mathbf{u}	flow velocity	p. 8
$\text{div}_{\mathbf{x}} = \nabla_{\mathbf{x}} \cdot$	divergence operator	p. 8
p	pressure (rescaled with density, i.e. times $\frac{1}{\rho}$)	p. 8
$\nu > 0$	kinematic viscosity	p. 8
Re	Reynolds number	p. 8
$L_{\text{div}}^2(\Omega, U)$	divergence-free functions in $L^2(\Omega; U)$	p. 8
μ^{ν}	statistical solution to the Navier–Stokes equations	p. 8
$f(\mathbf{x}, \mathbf{v}, t)$	probability density function	p. 9
$\mathfrak{R} = \Omega \times \Xi \times I$	phase-time space	p. 9
\cdot_f	moments (integration over Ξ) of f	p. 9
\mathbf{v}	particle velocity in $\Xi \subseteq \mathbb{R}^d$	p. 9
$\mathbf{F}(\mathbf{x}, t)$	external force field	p. 9
$Q(f)$	Bhatnagar–Gross–Krook collision operator	p. 11
$\frac{D}{Dt}$	material derivative	p. 11
\cdot^*	denotes a solution to e.g. a partial differential equation	p. 11
\cdot^{eq}	(Maxwellian) equilibrium of \cdot	p. 10
Kn	Knudsen number	p. 12
Ma	Mach number	p. 12
\mathbf{P}	pressure tensor	p. 14
$L_{\text{loc}}^1(X)$	locally integrable functions on X	p. 15
$\Theta > 0$	temporal filter width	p. 17
\mathbf{T}	temporal residual stress tensor	p. 18

σ_ϵ	homogenization ratio	p. 21
φ	porosity of solid matrix in fluid void	p. 28
$\Psi(\phi)$	free energy functional	p. 29
$\cdot^\epsilon, \cdot_\epsilon$	perturbed variable	p. 38
α	stability parameters in the constructive approach for relaxation systems	p. 39
$\gamma > 0$	scaling parameter	p. 39
$\delta = 2(\gamma - 1)$	scaling parameter	p. 39
\mathbf{A}_α	transport matrix in the relaxation system	p. 40
\mathbf{S}	relaxation matrix	p. 40
τ	relaxation time contained in \mathbf{S}	p. 40
$\mathcal{R}^{\epsilon\epsilon}$	remainder terms of the relaxation within the closed form of an RS	p. 41
\diamond	Hadamard operations on and between tensors	p. 45
diag	diagonal matrix and diagonal of a matrix	p. 45
\mathbf{D}	unified diagonalizer for several matrices	p. 46
\cdot^d	diagonalized version of matrix \cdot	p. 46
$\mathbf{g} = \mathbf{D}^1 \rho^{\epsilon\epsilon}$	transformed variable of the TRS	p. 46
\mathcal{G}	generalized Maxwellian	p. 47
$\mathbf{K} = \mathbf{D}^{-1} \mathbf{S} \mathbf{D}$	collision matrix in the TRS	p. 47
$\cdot^{\text{neq}} = \cdot - \cdot^{\text{eq}}$	nonequilibrium contribution of a variable \cdot	p. 47
\mathbf{J}	Jacobian matrix of a vector-valued function \cdot	p. 47
\mathbf{V}	amplification matrix for the TRS	p. 50
\mathcal{S}	stability set containing stable configurations of \mathbf{S}	p. 50
$s = \frac{1}{\tau}$	relaxation frequency contained in \mathbf{S}	p. 52
$DdQq$	discrete velocity set of dimension d and size q	p. 53
\mathbf{c}_i	discrete velocity contained in $DdQq$	p. 53
q	number of discrete velocities contained in $DdQq$	p. 53
w_i	weight for the i th velocity in $DdQq$	p. 53
$\mathbf{f} = (f_i)_{1 \leq i \leq q}^T$	discrete velocity distribution function vector, population vector	p. 54
\mathbf{M}	moment matrix	p. 54
\mathbf{V}_α	discrete velocity matrix in α th direction	p. 54
\mathbf{f}^{eq}	truncated Maxwellian equilibrium	p. 54
\mathbf{W}_j	j th column of \mathbf{M}^{-1}	p. 55
γ^*	entropy controller for kinetic moment relaxation	p. 56
\mathcal{C}	abstract TEQ (to be approximated)	p. 60
\mathcal{A}^ϵ	abstract TRS (to be discretized)	p. 60
\mathcal{D}_h	abstract discrete scheme for TEQ (to be extended)	p. 60
\mathcal{B}_h^ϵ	abstract relaxation scheme (discrete and extended)	p. 60
E_h^ϵ	global error of \mathcal{B}_h^ϵ with respect to \mathcal{C}	p. 62
h	artificial discretization parameter	p. 64
$\epsilon \leftarrow h$	assignment operator mapping h to ϵ	p. 64

$\sigma(\epsilon), \hat{\sigma}(\epsilon)$	scaling monomials in ϵ	p. 64
$\Delta x, \Delta t$	discretization intervals in space and time	p. 65
N	number of discretization points or intervals per coordinate direction	p. 65
Z_h	discrete space-time cylinder	p. 65
$\mathbf{K}^s = \mathbf{M}^{-1}\mathbf{S}^s\mathbf{M}$	shifted collision matrix with shifted relaxation matrix \mathbf{S}^s	p. 67
$R^{(n)}$	n th remainder term with respect to discretization in \cdot , where $n \in \mathbb{N}_{\geq 0}$	p. 67
$\frac{\mathcal{D}}{\mathcal{D}t}$	vector material derivative	p. 68
\mathbf{H}	discrete amplification matrix	p. 70
$\mathbf{k} \in \mathcal{K}$	wavevector in wave space	p. 70
\cdot^{poc}	post-collision value of \cdot	p. 74
d_h	lattice porosity in HLBM	p. 77
ϖ	porosity control	p. 77
\mathcal{F}	family/sequence of HBGKBEs	p. 81
\mathcal{FG}	family/sequence of discrete velocity HBGKBEs	p. 83
\mathcal{G}	family/sequence of HLBEs	p. 85
Pe	Péclet number	p. 99
$\text{err}_{L^p}(t_i)$	local in time, spatial L^p error	p. 101
$\overline{\text{err}}$	global error (averaged)	p. 102
Ch	Cahn number	p. 106
$k, \zeta, \mathbf{r}, \epsilon, w$	kinetic energy, enstrophy, vorticity, dissipation rate, maximum vorticity	p. 111
E, D, C	energy spectrum, dissipation spectrum, control spectrum	p. 112
$\overline{EOC}(t)$	time dependent experimental order of convergence	p. 136
Ca	capillary number	p. 160

B Publications

Parts of this work have already been published in journals and software releases. The references are given in the main body where applicable. For the sake of completeness, own publications are also summarized below. First authorship indicates at least major contribution and else positions denote up to major contributions.

Peer-reviewed publications

- (i) **S. Simonis**, J. Nguyen, S. J. Avis, W. Dörfler, M. J. Krause. Binary fluid flow simulations with free energy lattice Boltzmann methods. *Discrete and Continuous Dynamical Systems - Series S* (2023). doi: 10.3934/dcdss.2023069. [235]
- (ii) F. Bukreev, **S. Simonis**, J. Jeßberger, A. Kummerländer, M. J. Krause. Consistent lattice Boltzmann method for the volume averaged Navier–Stokes equations. *Journal of Computational Physics* 490 (2023) 112301. doi: 10.1016/j.jcp.2023.112301. [42]
- (iii) **S. Simonis**, M. Frank, M. J. Krause. Constructing relaxation systems for lattice Boltzmann methods. *Applied Mathematics Letters* 137 (2023) 108484. doi: 10.1016/j.aml.2022.108484. [234]
- (iv) A. Mink, K. Schediwy, C. Posten, H. Nirschl, **S. Simonis**, M. J. Krause. Comprehensive Computational Model for Coupled Fluid Flow, Mass Transfer, and Light Supply in Tubular Photobioreactors Equipped with Glass Sponges. *Energies* 15(20) (2022) 7671. doi: 10.3390/en15207671. [190]
- (v) **S. Simonis**, D. Oberle, M. Gaedtke, P. Jenny, M. J. Krause. Temporal large eddy simulation with lattice Boltzmann methods. *Journal of Computational Physics* 454 (2022) 110991. doi: 10.1016/j.jcp.2022.110991. [233]
- (vi) **S. Simonis**, M. Haussmann, L. Kronberg, W. Dörfler, M. J. Krause. Linear and brute force stability of orthogonal moment multiple-relaxation-time lattice Boltzmann methods applied to homogeneous isotropic turbulence. *Philosophical Transactions of the Royal Society A* 379 (2021) 20200405. doi: 10.1098/rsta.2020.0405. [232]
- (vii) M. Haussmann, P. Reinshaus, **S. Simonis**, H. Nirschl, M. J. Krause. Fluid–Structure Interaction Simulation of a Coriolis Mass Flowmeter Using a Lattice Boltzmann Method. *Fluids* 6(4) (2021) 167. doi: 10.3390/fluids6040167. [116]
- (viii) D. Dapelo, **S. Simonis**, M. J. Krause, J. Bridgeman. Lattice-Boltzmann coupled models for advection–diffusion flow on a wide range of Péclet numbers. *Journal of Computational Science* 51 (2021) 101363. doi: 10.1016/j.jocs.2021.101363. [59]
- (ix) M. Siodlaczek, M. Gaedtke, **S. Simonis**, M. Schweiker, N. Homma, M. J. Krause. Numerical evaluation of thermal comfort using a large eddy lattice Boltzmann method. *Building and Environment* 192 (2021) 107618. doi: 10.1016/j.buildenv.2021.107618. [236]
- (x) M. J. Krause, A. Kummerländer, S. J. Avis, H. Kusumaatmaja, D. Dapelo, F. Klemens, M. Gaedtke, N. Hafen, A. Mink, R. Trunk, J. E. Marquardt, M.-L. Maier, M. Haussmann, **S. Simonis**. OpenLB—Open source lattice Boltzmann code. *Computers and Mathematics with Applications* 81 (2021) 258–288. doi: 10.1016/j.camwa.2020.04.033. [162]

- (xi) **S. Simonis**, M. Frank, M. J. Krause. On relaxation systems and their relation to discrete velocity Boltzmann models for scalar advection–diffusion equations. *Philosophical Transactions of the Royal Society A* 378 (2020) 20190400. doi: 10.1098/rsta.2019.0400. [231]
- (xii) M. Haussmann, **S. Simonis**, H. Nirschl, M. J. Krause. Direct numerical simulation of decaying homogeneous isotropic turbulence – numerical experiments on stability, consistency and accuracy of distinct lattice Boltzmann methods. *International Journal of Modern Physics C* 30(09) (2019) 1–29. doi: 10.1098/rsta.2019.0400. [114]

Proceedings, preprints and others

- (xiii) **S. Simonis**, M. J. Krause. Forschungsnahe Lehre unter Pandemiebedingungen. *Mitteilungen der Deutschen Mathematiker-Vereinigung* 30(1) (2022) 43–45. doi: 10.1515/dmvm-2022-0015. [229]
- (xiv) **S. Simonis**, M. J. Krause. Limit consistency of lattice Boltzmann equations. *arXiv preprint* (2022). doi: 10.48550/arXiv.2208.06867. [230]

Software

Table B.1: Selected parts of the author’s contribution to OpenLB.

Keyword	Commit hash
ade1d	a7306c54db19b840125ccab177ffded176bcdfc3
ade2d	28c72adb44879c26796bc59b5afd046128018d48
ade3d	9e6e0f5e766d505ba48ddaca8884f488ad8df0d8
kpv3d	b971b7f9b03b76122032b8922edf0e526bd3d5a8
rtgv3d	a2c3c31732a68d6d787c64ea40539254f0c6b076
binaryShear2d	2593b4c25d33549271885f93f0356ec33719d3e7
binaryShear3d	a6b687b81f1907d1960a54bb2bba9dcdd33ef58a
fourRollMill2d	1ada160561cebcefb471653766d7df58ba9c01b4
highPressure2d	fd490e46e8e698329253032a03a86914f5c339c
highPressure3d	e9bb973ab7441d5f8b6437245bdec2d3029f32e9
advectionDiffusionConverter	c510a87b3ac2d4d4610a604b967b608b20b0f7b8
temporalDirectDeconvolutionBGKdynamics	6bb2cb1f580c0f9891b40d82ae227b09dab6e790
temporalDirectDeconvolutionMRTdynamics	6bb2cb1f580c0f9891b40d82ae227b09dab6e790
kineticLES	ece6445a4fd10c8af9a96f4456bc09a07a83bcae
entropicBoostDynamics	8fd68da7f279af51711df5dd32e2c82ea1745c8b
KBCdynamics	b09a3bbd95527eff9bd71f103fa21ea798bc2598
vnaFunctor	a37715d9255856375b094b49f06aad13523b084e
cumulantDynamics	0ddb1620d1ef26ac36f0592879212ac6eabe3ccc

If not stated otherwise, the computer simulations used for the present results all are based upon, embedded in, or coupled to the open-source C++ library OpenLB [162]. The author contributed to the releases 1.3 [160], 1.4 [161], 1.5 [165] and 1.6 [168] of said library. Some specific commit hashes for parts of the code (also unreleased) are listed in Table B.1 together with keywords.

List of Figures

1.1	From application to numerical algorithm.	1
1.2	Present contributions toward a coherent mathematical framework for LBMs.	3
2.1	Illustrations of the geometric model of a porous structure in $d = 3$ dimensions. The i th void cell is denoted with Y_i^ϵ containing a spherical matrix obstacle $Y_{S,i}^\epsilon$ with radius a_ϵ . Each cell is cubic with side length ϵ	21
2.2	Graph of ratio $\sigma_\epsilon(\epsilon)$ (2.135) for $d = 3$ and $C = 1$	27
2.3	Double-well bulk free energy potentials of (a) the KFRM and (b) the SFRM. For the purpose of illustration, the values are scaled around null ($\tilde{f}_B^K = f_B^K - ((1 - 10^{-3})/3)\rho \ln(\rho)$ and $\tilde{f}_B^S = f_B^S - (\kappa_1 + \kappa_2)/32$) and cut off. The exemplary parameters $A = 0.002$, $B = -A$, $\kappa_1 = 0.008 = \kappa_2$ are chosen.	33
2.4	Double-well bulk free energy potentials of (a) the HKFRM and (b) the HSFRM, both for $m = 6$. For the purpose of illustration, the values are scaled around null ($\tilde{f}_B^{HK} = f_B^{HK} - ((1 - 10^{-3})/3)\rho \ln(\rho)$ and $\tilde{f}_B^{HS} = f_B^{HS} - (\kappa_1 + \kappa_2)/32$) and cut off. The exemplary parameters $A = 0.002$, $B = -A$, $\kappa_1 = 0.008 = \kappa_2$ are chosen.	34
3.1	Schematic overview of the constructive approach (from left to right) proposed in [231]. Parts of this figure are reproduced from [231], Copyright (2020), with permission from the authors and the Royal Society.	38
3.2	Discrete velocity sets $DdQ(2d + 1)$ for $d = 1, 2, 3$, respectively (a–c), $D2Q9$ (d) and $D3Q19$ (e). Coloring refers to the corresponding energy shell, where orange, cyan and green denote zeroth, first and second order nodes, respectively.	53
3.3	Schematic concept of kinetic and relaxation limits. The limit PDE of the relaxation operator is denoted with \mathcal{C} , the kinetic equation or RS is denoted with \mathcal{A}^ϵ , the kinetic scheme or relaxation scheme is denoted with \mathcal{B}_h^ϵ and the corresponding macroscopic scheme or relaxed scheme is \mathcal{D}_h . Here, h defines a space-time discretization. The diagonal limit $\mathcal{B}_h^\epsilon \rightarrow \mathcal{C}$ for $\epsilon = h \searrow 0$ is the present focus.	60
3.4	Schematic concept of limit consistency. Notation is similar to Figure 3.3. This figure is reproduced from [230].	61
3.5	Time steps used for the discretization. The final LBE operates on the green squares only. Red points are canceled in the derivation.	66
3.6	Schematic view of diffusive scaling limits ($Ma \sim h \searrow 0$) of LBM schemes (SRT BGK LBE and exemplary instances of $n \in \mathbb{N}$ parametrized MRT_{ζ^n} LBE) toward the NSE, respectively. Dashed lines denote instability regions along the limit. The points B and M_{ζ^n} mark the (coarse resolution dependent [114, 267]) instability onset of the SRT BGK scheme and the (Mach induced [62, 114]) instability onsets of fixed MRT_{ζ^n} schemes, respectively. Solid lines specify stable configurations.	72
3.7	Schematic concept for merging relaxation, discretization and filtering of PDE. The abbreviations denote: filtered NSE (FNSE) {(2.90), (2.91), (2.94)}; filtered DVBE (FDVBE) {(3.286), (2.94)}; filtered LBE (FLBE) {(3.288), (3.293)}; NSE (2.12); DVBE (3.92); LBE (3.160). The parameters are defined as ϵ for the relaxation scaling, h for the space-time discretization and Θ for the filter width. The nature of arrows is hidden for the purpose of representation. The overall limit of the FLBE to the NSE is denoted as dashed line.	89
3.8	Illustration of a curved boundary layout [116].	93
3.9	Schematic overview of SLMC LBM. The m th initial data sample is denoted with $f_0^{(m)}$	97
4.1	Relaxation stability maps for LBM (see Theorem 3.2.1) approximating the d -dimensional ADE (2.10). The volume of the stability octahedron (c) in \mathbf{u} -coordinates grows inversely proportional to Δx . Plot (a) is redrawn from [231], Copyright (2020), with permission from the authors and the Royal Society.	101

4.2	Exemplary computations with SRT BGK collision (images are downsampled for visualization) approximating (a) a diffusion equation ($\mathbf{F} = \mathbf{0}$, $\tau > 0.5$, $\gamma = 2$), (b) a hyperbolic balance law ($\mathbf{F} \neq \mathbf{0}$, $\tau = 0.5$, $\gamma = 1$) or (c) the full ADE (2.10) ($\mathbf{F} \neq \mathbf{0}$, $\tau > 0.5$, $\gamma = 2$). This figure is redrawn from [231], Copyright (2020), with permission from the authors and the Royal Society.	101
4.3	Local in time error $\text{err}_{L^2}(\hat{t})$ plots at $\hat{t} = 0.3$ for several Péclet numbers or corresponding characteristic scales (\cdot_L denotes nondimensional lattice units). Computations with SRT BGK collision approximating (a) a diffusion equation ($\mathbf{F} = \mathbf{0}$, $\tau > 0.5$, $\gamma = 2$), (b) a hyperbolic balance law ($\mathbf{F} \neq \mathbf{0}$, $\tau \searrow 0.5$, $\gamma = 1$) or (c) the full ADE (2.10) ($\mathbf{F} \neq \mathbf{0}$, $\tau > 0.5$, $\gamma = 2$). This figure is reproduced from [231], Copyright (2020), with permission from the authors and the Royal Society.	102
4.4	Approximated solution to Example 4.1.1 with resolution $N = 200$ for $Pe = 100$. Parts of this figure are reproduced from [59], Copyright (2021), with permission from the authors and Elsevier Ltd.	105
4.5	Approximated solution to Example 4.1.2 with resolution $N = 200$ for $Pe = 1000$	105
4.6	Errors of $D3Q7$ SRT LBM approximating (2.10) with smooth (sm) and nonsmooth (ns) initial data. This figure is reproduced from [234], Copyright (2022), with permission from the authors and Elsevier Ltd.	106
4.7	(a): Static ($\mathbf{u} = \mathbf{0}$) and moving interface ($\mathbf{u} = \mathbf{u}_0$) simulation setup, where the white circle denotes $\phi = 0$. The velocity \mathbf{u}_0 is constant and boundaries are periodic. (b): Cross section of the interface at $y = 0$ with profile of initial order parameter $\phi = \phi_0$ (dashed line). Scales differ for the purpose of representation.	107
4.8	(a): Order parameter approximated with the SFRM LBM after 40 normalized timesteps for subsequent resolutions N . (b): Relative approximation error err_{L^2} with respect to tanh-profile within normalized time interval $t \in [1, 50]$	107
4.9	Normalized time of error measurements is $\hat{t} = 40$. (a): Time local error $\text{err}_L^p(\hat{t})$ of ϕ with respect to the initial analytical tanh-profile for circular interface for accuracy prediction toward sharp interface. (b): Time local error $\text{err}_L^p(\hat{t})$ of ϕ with respect to highest tested resolution $N = 400$ for consistency prediction of discretization.	108
4.10	Warped order parameter ϕ from SFRM LBM simulations of moving circular interfaces ($\mathbf{u} = \mathbf{u}_0$) at fixed normalized timesteps $\hat{t} = 0, 12, 36$ (column-wise) which comprise several cycles of reaching the initial interface location for several resolutions $N = 50, 100, 200, 400$ (row-wise). The colorbar is cut off for the purpose of representation.	109
4.11	DNS results of the TGV flow computed with SEM ($N = 127$, $Re = 800$). Energy spectrum $E(\kappa, t)$ and dissipation spectrum $D(\kappa, t)$ plotted over time t and wavenumber κ . This figure is reproduced from [233], Copyright (2022), with permission from the authors and Elsevier Inc.	111
4.12	Top row (a–d): BF stability maps (Algorithm 4) for $Re = 1600$ and $N = 64$, where the pixel resolution of each map is 41×41 , one pixel equals one TGV computation with the MRT LBM (Table 3.4), and coloring refers to maximal stable computation time t_{end} . Bottom row (e–h): Corresponding BF error maps, with the same map resolution as above (only BF stable configurations shown). Coloring refers to the logarithm of $\text{err}_{L^2}(\epsilon)$ over the interval $t \in [0, 10]$. For all subfigures $Ma = 0.3, 0.2, 0.1, 0.05$, respectively, from left to right. White squares denote $\tilde{\mathbf{s}}$ used in the classical MRT formulation [66]. The optimized MRT LBM [52] comprising $\hat{\mathbf{s}}$ is plotted as white circles. The optimized value for $Ma = 0.05$ is obtained by a polynomial fit through $\hat{\mathbf{s}}_q$ and $\hat{\mathbf{s}}_\mu$ for larger Ma , respectively. This figure is reproduced from [232], Copyright (2021), with permission from the authors and the Royal Society.	115
4.13	(a) Schematic visualization of $\mathcal{B}_{\Delta\chi, \Delta\theta}$ (elements are denoted with black dots). The discretization steps are $\Delta\chi = 0.1$ and $\Delta\theta = \pi/20$. The set comprises normalized vectors $\mathbf{b} = (b_x, b_y, b_z)^T$ for the mean flow variation used in the (scaled) octant specifier according to Table 4.6. (b) Schematic visualization of $\mathcal{V}_{\Delta p}$ (elements are denoted with black dots). The number of points on the whole sphere is $p = 8.88 \times 10^2$. The set comprises normalized vectors $\mathbf{v} = (v_x, v_y, v_z)^T$. Figure (a) is reproduced from [232], Copyright (2021), with permission from the authors and the Royal Society.	116

4.14	From top to bottom, row-wise: VN stability maps (Algorithm 3) for $Re = 1600$ and $N_{\mathcal{K}} = 257$ with scan regions according to Table 4.6: <i>x-directional</i> (a–d), <i>orthogonal</i> (e–h), <i>parallel</i> (i–l), κ - <i>partial</i> (m–p), <i>full</i> (q–t). From left to right, column-wise: $Ma = 0.3, 0.2, 0.1, 0.05$, respectively. Coloring refers to respectively normalized spectral radius approximation $\tilde{r}_{\text{spec}}^*(\mathbf{H})$ (4.38). White squares denote \tilde{s} used in the classical MRT formulation [66]. The optimized MRT LBM [52] comprising \hat{s} is plotted as white circles. Note that the optimized value for $Ma = 0.05$ is obtained by a polynomial fit through \hat{s}_q and \hat{s}_μ for larger Ma , respectively. This figure is reproduced from [232], Copyright (2021), with permission from the authors and the Royal Society.	117
4.15	From top to bottom, row-wise: VN stability maps (Algorithm 3) for $Re = 1600$ and $N_{\mathcal{K}} = 257$ with scan region <i>octant</i> (a–d) and <i>scaled octant</i> (e–h) according to Table 4.6. From left to right, column-wise: $Ma = 0.3, 0.2, 0.1, 0.05$, respectively. Coloring refers to respectively normalized spectral radius approximation $\tilde{r}_{\text{spec}}^{**}(\mathbf{H})$. White squares denote \tilde{s} used in the classical MRT formulation [66]. The optimized MRT LBM [52] comprising \hat{s} is plotted as white circles. Note that the optimized value for $Ma = 0.05$ is obtained by a polynomial fit through \hat{s}_q and \hat{s}_μ for larger Ma , respectively. This figure is reproduced from [232], Copyright (2021), with permission from the authors and the Royal Society.	118
4.16	BF stability maps (Algorithm 4), only stable configurations shown) of ς -parametrized MRT LBM computations for TGV flow simulations with $Re = 1600$, $Ma = 0.4, 0.2, 0.1, 0.05$ (from top to bottom), and $N = 32, 64, 128$ (from left to right). The Cartesian x -, y -, and z -coordinate axes correspond to $\varsigma_{q,\mu}$, ς_e , and $\varsigma_{\Pi,e}$, respectively, and are shown for the interval $[0, 10]^3$. One map contains 11^3 TGV computations visualized as voxels. Coloring refers to $\text{err}_{L^2}(\epsilon)$ over the interval $t \in [0, 10]$. Black cubes denote stable ς configurations such that $\text{err}_{L^2}(\epsilon)$ is minimal. Black spheres indicate the corresponding origins $\varsigma = \mathbf{0}$, i.e. SRT BGK configurations. This figure is reproduced from [232], Copyright (2021), with permission from the authors and the Royal Society.	120
4.17	(a) Third order polynomial fit ($\cdot^{\text{P}f3}$) through relaxation frequency prefactors \hat{s}_q and \hat{s}_μ dependent on the Mach number. (b) Third order polynomial fit ($\cdot^{\text{P}f3}$) through Ma -averaged $\text{err}_{L^2}(\epsilon)$ -minimal ς -configurations $\bar{\varsigma}$ in diffusive scaling.	123
4.18	Orthogonal moment MRT LBM (see Table 3.4) error landscape of $\text{err}_{L^2}(\epsilon)$ -minimal relaxation frequency configurations ς listed in Table 4.9 and denoted with black cubes in Figure 4.16. Diffusive scaling (DS) and generic scaling (GS) determines the scaling function $\sigma = h^\gamma$ via $\gamma = 2$ for DS and $\gamma \in \{1, 2\}$ for GS, respectively, where DS1 starts at $(N = 32, Ma = 0.4)$ and DS2 starts at $(N = 32, Ma = 0.2)$	124
4.19	Integral turbulence quantities of KBC-N1 and SRT BGK collision for $Re = 1600$ at several resolutions $N = 32, 128, 256$ and Mach numbers $Ma = 0.2, 0.1, 0.05$	127
4.20	Integral turbulence quantities of KBC-N1 and SRT BGK collision for $Re = 3000$ at several resolutions $N = 32, 128, 256$ and Mach numbers $Ma = 0.2, 0.1, 0.05$	128
4.21	Integral turbulence quantities of KBC-N1 and SRT BGK collision for $Re = 6000$ at several resolutions $N = 32, 128, 256$ and Mach numbers $Ma = 0.2, 0.1, 0.05$	129
4.22	Spatial mean (4.44) and standard deviation (4.45) of KBC-N1 entropy controller γ^* (3.201) for TGV flow simulations at several Reynolds number $Re = 1600, 3000, 6000$ and Mach numbers $Ma = 0.2, 0.1, 0.05$	130
4.23	Energy spectra (4.26) and control spectra (4.30) for KBC-N1 scheme (left and middle column) as well as energy spectra (4.26) for SRT BGK collision (right column) of the TGV flow simulations at $Re = 1600$ in DS (top to bottom) for $(Ma, N) \in \{(0.2, 32), (0.1, 64), (0.05, 128)\}$. The red circles denote the values of the spectra at the respective cutoff wavenumber $\kappa_c = N/2$	131
4.24	Energy spectra (4.26) and control spectra (4.30) for the KBC-N1 scheme (left and middle column) as well as energy spectra (4.26) for SRT BGK collision (right column) of the TGV flow simulations at $Re = 3000$ in DS (top to bottom) for $(Ma, N) \in \{(0.2, 32), (0.1, 64), (0.05, 128)\}$. The red circles denote the values of the spectra at the respective cutoff wavenumber $\kappa_c = N/2$	132
4.25	Energy spectra (4.26) and control spectra (4.30) for KBC-N1 scheme (left and middle column) as well as energy spectra (4.26) for SRT BGK collision (right column) of the TGV flow simulations at $Re = 6000$ in DS (top to bottom) for $(Ma, N) \in \{(0.2, 32), (0.1, 64), (0.05, 128)\}$. The red circles denote the values of the spectra at the respective cutoff wavenumber $\kappa_c = N/2$	133

4.26	Computed energy spectra $E(\kappa, t)$ and control spectra $E(\kappa, t)$ of KBC-N1 and energy spectra $E(\kappa, t)$ of SRT BGK plotted at the last stable SRT BGK time step, respectively for several $Re = 1600, 3000, 6000$ (top to bottom) in DS $(Ma, N) \in \{(0.2, 32), (0.1, 64), (0.05, 128)\}$ (left to right).	134
4.27	Time dependent error of total dissipation rate $\text{err}(\epsilon_{\text{tot}})$ of the KBC-N1 scheme with respect to the psDNS reference [61]. Discretization parameters are chosen from Table 4.10 in DS, hence $(Ma, N) \in \{(0.2, 32), (0.1, 64), (0.05, 128)\}$. Only a subsequence of time steps $t \in [0.1, 19.7]$ is shown with a step size of $\Delta t = 0.2$	135
4.28	Time dependent error of total dissipation rate $\text{err}(\epsilon_{\text{tot}}(t))$ of the KBC-N1 scheme with respect to the psDNS reference [61].	135
4.29	Time dependent EOC of total dissipation rate $\text{err}(\epsilon_{\text{tot}})$ of KBC-N1 with respect to psDNS reference [61].	136
4.30	Time evolution of Q -criterion ($Q = 0.1$) colored by $ \mathbf{u}^{(m)} $ of one RTGV flow sample computed with the KBC-N1 LBM for $Re = 10240$, resolution $N = 256$, and $Ma = 0.0125$	139
4.31	Mean (solid lines) and standard deviation (shaded areas) of compensated energy spectra of the RTGV flow field at several Reynolds numbers and time steps, computed with the novel SLMC LBM.	140
4.32	Sample spectra of (a) energy (4.26) and (b) control spectra (4.30) of the RTGV flow at $Re = 1280$ computed with the KBC-N1 LBM for $(Ma, N) = (0.1, 64)$. The red circles denote the values of the spectra at the respective cutoff wavenumber $\kappa_c = 1/N$. The cyan squares denote the spectra at $t = T \approx 31$	141
4.33	Energy spectrum $E(\kappa)$ (a) and dissipation spectrum $D(\kappa)$ (b) at $t = 9$ for the TGV flow with $Re = 800$. Computations for $Ma = 0.1$ and $N = 64$ with the LBM as UDNS and TLES with $\tilde{\Theta} = 5, 10, 20, 40$ in comparison to the SEM DNS with a corresponding resolution of $N = 127$. This figure is reproduced from [233], Copyright (2022), with permission from the authors and Elsevier Inc.	143
4.34	Total, resolved and model dissipation rate for the TGV flow with $Re = 800$. Computations for $Ma = 0.1$ and $N = 64$ with the LBM as UDNS (a) and TLES with $\tilde{\Theta} = 5, 10, 20, 40$ (b-e, respectively) in comparison to the SEM DNS with a corresponding resolution of $N = 127$. This figure is reproduced from [233], Copyright (2022), with permission from the authors and Elsevier Inc.	143
4.35	Energy spectrum $E(\kappa)$ (a) and dissipation spectrum $D(\kappa)$ (b) at $t = 9$ for the TGV flow with $Re = 800$. Computations for $N = 64$ with the LBM TLES ($\tilde{\Theta} = 10$) for $Ma = 0.05, 0.075, 0.1, 0.15, 0.2$ in comparison to the SEM DNS with a corresponding resolution of $N = 127$. This figure is reproduced from [233], Copyright (2022), with permission from the authors and Elsevier Inc.	144
4.36	Total, resolved and model dissipation rate for the TGV flow with $Re = 800$. Computations for $N = 64$ with LBM TLES ($\tilde{\Theta} = 10$) for $Ma = 0.05, 0.075, 0.1, 0.15, 0.2$ (a-e, respectively) in comparison to the SEM DNS with a corresponding resolution of $N = 127$. This figure is reproduced from [233], Copyright (2022), with permission from the authors and Elsevier Inc.	145
4.37	Dissipation rates $\epsilon_{\text{tot}}(t)$, $\epsilon_{\text{res}}(t)$, $\epsilon_{\text{mod}}(t)$ (a), energy spectrum $E(\kappa)$ (b) and dissipation spectrum $D(\kappa)$ (c) (at $t = 9$) for the TGV flow with $Re = 800$. Computations for $N = 64$ with the LBM TLES ($\tilde{\Theta} = 10$) for $Ma = 0.1$. Deconvolved and filtered quantities in comparison to the SEM DNS with a corresponding resolution of $N = 127$. This figure is reproduced from [233], Copyright (2022), with permission from the authors and Elsevier Inc.	146
4.38	Dissipation rates $\epsilon_{\text{tot}}(t)$, $\epsilon_{\text{res}}(t)$, $\epsilon_{\text{mod}}(t)$, energy spectrum $E(\kappa)$ and dissipation spectrum $D(\kappa)$ (at $t = 9$) for the TGV flow with $Re = 3000$. Computations for $N = 64$ (left column) and $N = 128$ (right column) with the LBM UDNS for $Ma = 0.1$ compared to the SEM UDNS with the number of spectral elements corresponding to a resolution of $N = 64$ and $N = 127$, respectively. The resolution of the reference SEM DNS corresponds to $N = 351$. This figure is reproduced from [233], Copyright (2022), with permission from the authors and Elsevier Inc.	148
4.39	Dissipation rates $\epsilon_{\text{tot}}(t)$, $\epsilon_{\text{res}}(t)$, $\epsilon_{\text{mod}}(t)$, energy spectrum $E(\kappa)$ (at $t = 9$) and dissipation spectrum $D(\kappa)$ for the TGV flow with $Re = 3000$. Computations for $N = 64$ (left column) and $N = 128$ (right column) with the LBM TLES ($\tilde{\Theta} = 10$) for $Ma = 0.1$ compared to the SEM TLES with the number of spectral elements corresponding to a resolution of $N = 64$ and $N = 127$, respectively. The resolution of the reference SEM DNS corresponds to $N = 351$. This figure is reproduced from [233], Copyright (2022), with permission from the authors and Elsevier Inc.	149

4.40	Subgrid activity and energy spectrum error measurements for a sequence of resolutions $N = 24, 48, 64, 96, 128, 192$. The LBM TLES runs with $\Theta = 10$ and the LBM UDNS computations are carried out with $Ma = 0.1$ for the TGV flow at $Re = 3000$. This figure is reproduced from [233], Copyright (2022), with permission from the authors and Elsevier Inc.	151
4.41	EOC comparison for TGV flow computations at $Re = 800$ with modular LBM combinations of SRT or MRT collision without (UDNS) and with TLES with TDDM finite difference discretization of first (TLESo1) and second order (TLESo2), respectively. Only stable configurations are included. Total dissipation rate errors are calculated according to (4.67) with respect to high resolution reference data from the SRT LBM run at $N = 512$ and $Ma = 0.00625$. AS (left) and DS (right) are based on a respective sequence of resolutions $N = 32, 64, 128, 256$ starting at $Ma = 0.1$ and conforming to Table 4.13. This figure is reproduced from [233], Copyright (2022), with permission from the authors and Elsevier Inc.	153
4.42	Exemplary streamlines of \mathbf{u} computed with HLBM simulations through homogenized (e) and resolved (c,d) regular arrangements of spheres (a,b), respectively.	156
4.43	(a) Pressure difference for Poiseuille flow through rectangular duct with a regular sphere matrix simulated with present HLBM for several resolutions and permeabilities and particle-resolved HLBM [159, 249]. (b) Consistency error $\text{err}_{\Delta p}(N)$ landscape of the pressure drop Δp computed with HLBM for several permeabilities K and resolutions N	157
4.44	Geometric setup of numerical test cases for binary flow in two dimensions. Scales differ for the purpose of representation. This figure is reproduced from [235], Copyright (2023), with permission from the authors and the American Institute of Mathematical Sciences.	158
4.45	Static droplet test case in 2D computed with the SFRM LBM. The order parameter ϕ is plotted over the cross section $y = 0$ for the free energy functional $\Psi^{(m)}$ with $m = 2$ and $m = 6$ at several time steps. This figure is reproduced from [235], Copyright (2023), with permission from the authors and the American Institute of Mathematical Sciences.	159
4.46	Deformation and inclination of a droplet in 2D and 3D binary shear flow simulated with the SFRM LBM and compared to reference results for varying capillary numbers. This figure is reproduced from [235], Copyright (2023), with permission from the authors and the American Institute of Mathematical Sciences.	160
4.47	Droplet breakup in 2D binary shear flow at $Ca = 3.5$ computed with the SFRM LBM. Components C_1 (red) and C_2 (blue) are plotted at normalized time steps.	161
4.48	Droplet breakup in 3D binary shear flow computed with the SFRM LBM at normalized time steps for $Re = 0.0625$, $Ca = 0.42$, $Ch = 0.0379$, $Pe = 0.43$. This figure is reproduced from [235], Copyright (2023), with permission from the authors and the American Institute of Mathematical Sciences.	162
4.49	Deformation of a droplet in 2D binary extensional flow simulated with the SFRM LBM and comparison to 3D reference results for varying capillary numbers. This figure is reproduced from [235], Copyright (2023), with permission from the authors and the American Institute of Mathematical Sciences.	163
4.50	Droplet breakup in 2D binary extensional flow simulated with the SFRM LBM at normalized time steps for $Re = 0.0625$, $Ca = 0.42$, $Ch = 0.057$, $Pe = 0.43$. This figure is reproduced from [235], Copyright (2023), with permission from the authors and the American Institute of Mathematical Sciences.	164

List of Tables

3.1	Computation of closed equation in $\rho^{\epsilon\epsilon}$ for Theorem 3.1.2. The n th row of (3.10) is denoted with R_n for $n \in \mathbb{N}$. Equations for $\phi^{\epsilon\epsilon}$ and $\psi^{\epsilon\epsilon}$ are not shown in the last two steps.	43
3.2	Summary of natural moments and physical tensor notation used in the $D3Q19$ MRT collision.	56
3.3	Summary of relaxation frequencies and orders of physical tensors resembling natural moments in the $D3Q19$ MRT collision. Note that moments of kinematic and shear type are considered to be hydrodynamic.	56
3.4	Summary of moments and corresponding relaxation frequencies used in $D3Q19$ MRT formulations in [66], [52], and the present work, respectively. The frequencies are in discrete form, where the lattice sound speed is denoted by c_s and physical interpretations for the tensors ρ , $\rho\mathbf{u}$, e , P , \mathbf{q} , μ , ε , and Π are given in [66]. This table is reproduced from [232], Copyright (2021), with permission from the authors and the Royal Society.	56
4.1	Summary of LBM discretization parameters for diffusive scaling (\cdot_L denotes lattice units). Note that $\mu = \mu_L$ and $\omega_{\Delta x} = 1/\tau_{\Delta x}$. This table is reproduced from [231], Copyright (2020), with permission from the authors and the Royal Society.	103
4.2	Summary of LBM discretization parameters in acoustic scaling (\cdot_L denotes lattice units). Note that $u = u_L$. This table is reproduced from [231], Copyright (2020), with permission from the authors and the Royal Society.	103
4.3	Numerical errors of LBM computations in diffusive scaling to approximate the advection–diffusion equation (2.10) ($\mathbf{F} \neq \mathbf{0}$ linear, $\tau > 0.5$) measured in terms of global error $\overline{\text{err}}$ until terminal time t_M , local error $\text{err}_{L_2}(\hat{t})$ at $\hat{t} = 0.3$, and experimental order of convergence \overline{EOC} . This table is reproduced from [231], Copyright (2020), with permission from the authors and the Royal Society.	104
4.4	Numerical errors of LBM computations in diffusive scaling to approximate the diffusion equation (2.10) ($\mathbf{F} = \mathbf{0}$, $\tau > 0.5$, $\gamma = 2$), measured in terms of global error $\overline{\text{err}}$ until terminal time t_M , local error $\text{err}_{L_2}(\hat{t})$ at $\hat{t} = 0.3$, and experimental order of convergence \overline{EOC} . This table is reproduced from [231], Copyright (2020), with permission from the authors and the Royal Society.	104
4.5	Numerical errors of LBM computations in acoustic scaling to approximate the hyperbolic conservation law (2.10) ($\mathbf{F} \neq \mathbf{0}$, $\mu = 0$, $\gamma = 1$) or the full ADE (2.10) ($\mathbf{F} \neq \mathbf{0}$, $\mu > 0$, $\gamma = 1$), measured in terms of global error $\overline{\text{err}}$ until terminal time $\hat{t}_M = 8.12$, local error $\text{err}_{L_2}(\hat{t})$ at $\hat{t} = 0.3$, and experimental order of convergence \overline{EOC} . This table is reproduced from [231], Copyright (2020), with permission from the authors and the Royal Society.	104
4.6	List of specifiers for scan regions of the VN stability maps plotted in Figure 4.14. Note that $\mathbf{b} \in \mathcal{B}$ denotes the mean flow variation in the first octant (4.35) and $\text{ave}(\mathbf{u}_0)$ accounts for scaling via the averaged TGV initial flow field magnitude (4.36). This table is reproduced from [232], Copyright (2021), with permission from the authors and the Royal Society.	115
4.7	Exemplary relaxation parameters calculated with (3.192) for $Re = 1600$, $Ma = 0.05$, $N = 128$, where $s_P = 1/\tau_P$ with $\tau_P = 0.50109$ according to Table 4.8. This table is reproduced from [232], Copyright (2021), with permission from the authors and the Royal Society.	119
4.8	LBM discretization parameters for TGV flow simulations at $Re = 1600$, where $\tau_P = 1/s_P$. This table is reproduced from [232], Copyright (2021), with permission from the authors and the Royal Society.	121
4.9	Dissipation rate error minima ϵ_{\min} and corresponding orderwise relaxation pairs $\boldsymbol{\varsigma} = (\varsigma_{q,\mu}, \varsigma_e, \varsigma_{\varepsilon,\Pi})^T$ for MRT LBM simulations of the TGV flow at $Re = 1600$	123
4.10	Parameter grid for the numerical experiments with KBC-N1 on $D3Q19$ with natural moments (Table 3.2), entropy controlled relaxation (3.201) and truncated equilibrium (3.98).	125

4.11	Sample error data of the KBC-N1 scheme with respect to the psDNS reference [61] with computed EOC values locally $\overline{EOC}(t)$ (for dedicated points in time $t_1 = 1, t_2 = 6, t_3 = 11, t_4 = 16$) and on average \overline{EOC} for $t \in [0.1, 19.8]$	136
4.12	Summary of TLES LBM discretization parameters. This table is reproduced from [233], Copyright (2022), with permission from the authors and Elsevier Inc.	142
4.13	LBM discretization parameters used in Figure 4.41. This table is reproduced from [233], Copyright (2022), with permission from the authors and Elsevier Inc.	153
4.14	Regression slopes $\mathcal{O}(N^{-\cdot})$ of EOC comparison (cf. Figure 4.41) computed with $\text{err}_{\epsilon_{\text{tot}}}(N)$ for $N = 64, 128, 256$. This table is reproduced from [233], Copyright (2022), with permission from the authors and Elsevier Inc.	154
4.15	Consistency error of the pressure drop Δp computed with HLBM for several permeabilities K , and resulting EOC values.	157
B.1	Selected parts of the author's contribution to OpenLB.	196